THE PHYSICAL REVIEW

VOLUME 91 Second Series NUMBER 3

AUGUST 1, 1953

Published for the

AMERICAN PHYSICAL SOCIETY

by the

AMERICAN INSTITUTE OF PHYSICS

LANCASTER, PA., AND NEW YORK, N. Y.

A journal of c

for the

AMERICAN PHYSICAL SO

Officers

President

Enrico Fermi
Institute for Nuclear Studies
University of Chicago
Chicago 37, Illinois

Vice-President

H. A. Bethe
Cornell University
Ithaca, New York

Secretary

K. K. Darrow
Bell Telephone Laboratories
Office:
Columbia University
New York 27, New York

Treasurer

G. B. Pegram
Columbia University
New York 27, New York

Local Secretary
for the Pacific Coast

S. Kaplan
University of California at
Angeles
Los Angeles, California

Managing Editor

S. A. Goudsmit
Brookhaven National Labora
Upton, Long Island
New York

THE
PHYSICAL REVIEW

A journal of experimental and theoretical physics established by E. L. Nichols in 1893

SECOND SERIES, VOL. 91, NO. 3 AUGUST 1, 1953

Straggling Distributions for Electrons in Passing through Thin Foils

F. KALIL,*
Physics Department, Vanderbilt University, Nashville, Tennessee

AND

R. D. BIRKHOFF,
Oak Ridge National Laboratory, Oak Ridge, Tennessee and Physics Department, University of Tennessee, Knoxville, Tennessee

(Received March 18, 1953)

Straggling distributions for the 624-kev conversion electrons from Cs^{137} are examined with a high-resolution beta spectrometer for foils of Be, Al, Cu, Sn, Ta, and Pb. Agreement is found with the Blunck-Leisegang theory for the heavy elements, but the energy loss distributions for light elements are found to be about 1.8 times as wide as expected.

INTRODUCTION

THE fluctuation in energy loss which occurs for electrons passing through absorbers thin compared to the range of the electrons has been the subject of several recent experimental investigations. Paul and Reich[1] measured the straggling of electrons at 2.8 and 4.7 Mev in foils of Be, C, Fe, and Pb. Their data were subsequently interpreted by Blunck and Leisegang,[2] who showed that the broadening of the energy loss distributions was in agreement with an extension of the Landau[3] theory, which takes into account the resonance transfer of energy during distant collisions. Chen and Warshaw,[4] using conversion electrons of 624 kev, demonstrated the validity of the Landau formula regarding the prediction of the most probable energy loss but were unable to decide between the distributions obtained by Landau and Blunck-Leisegang with reference to the widths of the experimental curves. Kageyama and Nishimura,[5] using conversion electrons of energies 606, 1414, and 1761 kev, obtained straggling curves whose widths were appreciably greater than those calculated from the Landau theory, but no comparison was made with the Blunck-Leisegang theory. The most recent work, carried out with 9.6- and 15.7-Mev electrons by Goldwasser, Mills, and Hansen,[6] showed good agreement with the Landau theory, provided corrections were made for the polarization effect, increase in path length in the absorber as a result of scattering, and bremsstrahlung.

In the present work foils of Be, Al, Cu, Sn, Ta, and Pb of various thicknesses have been placed in a beam of 624-kev conversion electrons from Cs^{137} and the resulting energy loss distributions examined with a high-resolution beta spectrometer. Comparison is made of the straggling distributions obtained in this experiment and those of Kageyama and Nishimura with the Blunck-Leisegang theory.

THEORY

The problem of the energy loss of electrons as a result of ionization and excitation in passing through thin absorbers has been treated by Landau, who defined $W(R,Q)dQ$ as the probability that an electron in penetrating a thickness R will lose an amount of energy between Q and $Q+dQ$. The change in this probability in the distance dR after the electron has moved a distance R then may be written

$$\frac{\partial W}{\partial R}=\int_0^\infty \Phi(K)[W(Q-K)-W(Q)]dK,$$

* U. S. Atomic Energy Commission Fellow in Radiological Physics.

[1] W. Paul and H. Reich, Z. Physik **127**, 429 (1950).

[2] O. Blunck and S. Leisegang, Z. Physik **128**, 500 (1950).

[3] L. Landau, J. Physics (U.S.S.R.) **8**, 201 (1944).

[4] J. J. S. Chen and S. D. Warshaw, Phys. Rev. **84**, 355 (1951).

[5] S. Kageyama and K. Nishimura, J. Phys. Soc. Japan **7**, 292 (1952).

[6] Goldwasser, Mills, and Hansen, Phys. Rev. **88**, 1137 (1952).

TABLE I. Constants appearing in representation of Landau's distribution.

ν	1	2	3	4
C_ν	0.174	0.058	0.019	0.007
λ_ν	0.0	3.0	6.5	11.0
γ_ν	1.8	2.0	3.0	5.0

where $\Phi(K)$ is the cross section per unit length of path for a loss K. In this treatment, in order that Φ may be assumed independent of the change in the energy of the particle as it passes through the absorber, this change must be small compared with the incident energy. By taking the Fourier transform of the function W with respect to the variable Q, an expression equivalent to the one found by Landau may be obtained:

$$W(Q)=\frac{1}{2\pi}\int_{-\infty}^{\infty}\exp(isQ-Rf(s))ds,$$

with

$$f(s)=\int_{-\infty}^{\infty}[1-\exp(-isK)]\Phi(K)dK.$$

According to Bohr,[7] the cross section $\Phi(K)$ may be separated into a part which is due to the resonance interactions Φ_r, where the amount of energy transferred is of the order of the binding energies of the various atomic shells, and a part which due to the large energy exchanges with essentially free electrons Φ_f. By expanding the exponential in the latter integral, the part of the function $f(s)$ which is due to the resonance transfer is expressible in terms of the various moments of the $\Phi_r(K)$ distribution:

$$f_r(s)=\sum_{n=1}^{\infty}\langle K_r{}^n\rangle_{Av}\frac{(-is)^n}{n!},\quad\text{with}\quad\langle K_r{}^n\rangle_{Av}=\int K_r{}^n\Phi_r(K)dK.$$

For determining $f_f(s)$, Landau[3] uses an expression calculated by Thomson and discussed by Bohr:[7]

$$\Phi_f(K)=\frac{2\pi Ne^4\rho}{mv^2}\frac{Z}{A}\frac{1}{K^2}\equiv\frac{a}{K^2},$$

where N = Avogadro's number, e, m, v = charge, mass, and velocity of the incident electron, ρ = density of the material, and Z, A = atomic number and weight of the material.

For the resonance transfers Landau takes into account only the first moment $\langle K_r{}^1\rangle_{Av}$ by the use of the Bethe-Bloch[8] formula for the average energy loss per unit path on the interval $0\leq K\leq K_1$, with K_1 an energy large compared with the binding energies of the atomic electrons but small compared to the incident energy:

$$\langle K_r{}^1\rangle_{Av}=\frac{2\pi Ne^4\rho}{mv^2}\frac{Z}{A}\left[\ln\frac{K_1 2mv^2}{(1-\beta^2)I^2Z^2}-\beta^2\right]$$

$$=a\left[\ln\frac{K_1 2mc^2\beta^2}{(1-\beta^2)I^2Z^2}-\beta^2\right],$$

with IZ = the average ionization energy of the atom ($I\simeq 13.5$ ev).

After a numerical integration, Landau obtains a single universal straggling curve whose dependence on atomic number, incident energy, and foil thickness is contained in a dimensionless parameter λ related to the energy loss, given by

$$\lambda=\left\{Q-aR\left[\ln\frac{aR2mc^2\beta^2}{(1-\beta^2)I^2Z^2}+1-\beta^2-C\right]\right\}\Big/aR$$

$$=\frac{Q-R\bar{Q}}{aR}+\ln\frac{U}{aR}-1.116,$$

where C is Euler's constant, and U is the incident energy; $\bar{Q}$ is the average energy loss per cm.

Blunck and Leisegang,[2] whose notation is used throughout the above discussions, include the second moment of the resonance cross section, and by representing Landau's curve as a sum of Gaussian functions, obtain a family of straggling curves whose width depends upon a parameter b^2.

$$b^2=2\langle K_r{}^2\rangle_{Av}/a^2R,$$

$$W(Q)dQ=\sum_{\nu=1}^{4}\frac{C_\nu\gamma_\nu}{(\gamma_\nu{}^2+b^2)^{\frac{1}{2}}}\exp\left[-\frac{(\lambda-\lambda_\nu)^2}{\gamma_\nu{}^2+b^2}\right]d\lambda.$$

The constants C_ν, γ_ν, and λ_ν are given in Table I. It should be noted that, for $b^2\ll 3$, the Blunck-Leisegang distribution becomes identical with that of Landau.

The second moment $\langle K_r{}^2\rangle_{Av}$ may be obtained by representing the cross section,

$$\Phi_r(K)=\sum_s\langle K_{rs}\rangle_{Av}\frac{\delta(K-1.5I_s)}{1.5I_s},$$

with

$$\langle K_{rs}\rangle_{Av}=a\frac{n_s}{Z}\ln\left[\frac{2U}{I_s(1-\beta^2)}\right],$$

where n_s is the number of electrons in shell s having ionization energy I_s. After integration, $\langle K_r{}^2\rangle_{Av}$ is found to be

$$\langle K_r{}^2\rangle_{Av}=1.5\sum_s I_s\langle K_{rs}\rangle_{Av}.$$

The evaluation of this quantity is relatively tedious for heavy atoms. Hence, Blunck and Westphal[9] give, without proof, in a later paper an alternative repre-

[7] N. Bohr, Kgl. Danske Videnskab. Selskab, Mat.-fys. Medd. **18**, No. 8 (1948).
[8] W. Heitler, *The Quantum Theory of Radiation* (Oxford University Press, London, 1944).
[9] O. Blunck and K. Westphal, Z. Physik **130**, 641 (1951).

sentation for b^2 based on a Fermi-Thomas model of the atom.

$$b^2 = q\bar{Q}Z^{4/3}/(aR)^2 \quad \text{with} \quad q \simeq 20 \text{ ev}.$$

For the foils used, the b^2 was calculated from both expressions, the differences in values for a given foil causing a change in the width of the theoretical curve of less than 0.1 λ unit. A graph of straggling curve width at half-height *versus* b^2 is given in Fig. 1 as calculated from the Blunck-Leisegang formula.

APPARATUS

The beta spectrometer used in this investigation was of the solenoidal type described by DuMond,[10,11] with a helical diameter R of 20 cm and trajectory angle with the magnetic field of 45°. Values of energy resolution and transmission were calculated to be 0.1 percent and 1 percent of the total solid angle, respectively, although, in practice, these parameters were found to be 0.6 percent and 0.2 percent due in part to the difficulties encountered in making a strongly radioactive source disk which would conform to the calculated requirements. Ideally, the source material would be deposited on a thin electrically grounded backing, with neither source nor backing thickness exceeding about 1 mg/cm² and with a source diameter of 0.4 mm. The source backing, consisting of about 0.5-mg/cm² rubber hydrochloride with a 100-μg/cm² conducting gold film, satisfied the above considerations, but intensity requirements necessitated the deposition of several drops of $CsCl_2$ solution onto the backing, thus building up an absorbing thickness estimated to be almost 5 mg/cm² and having a diameter of about 1 mm. Generator ripple

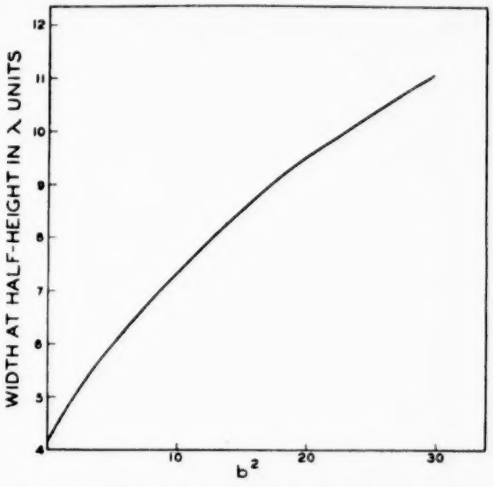

FIG. 1. Width at half-height as a function of parameter b^2 as calculated from the Blunck-Leisegang theory.

[10] J. W. M. DuMond, Rev. Sci. Instr. **20**, 160 (1949).
[11] J. W. M. DuMond, Rev. Sci. Instr. **20**, 616 (1949).

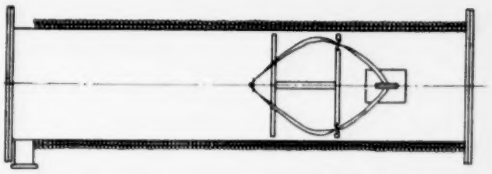

FIG. 2. Cross section of magnet and slit system (not to scale).

current and a 0.25 percent inhomogeneity in the magnetic field contributed additional width to the K conversion line.

A Tracerlab TGC-6 G-M tube having a wall thickness of 30 mg/cm² was used as detector. A Fermi plot of Cs^{134} showed a departure from linearity at 450 kev,[12] but inasmuch as no data was obtained at energies this low throughout the experiment, the tube was assumed to have a constant efficiency. A conical aperture was cut in a lead cylinder 6 inches in diameter and 7½ inches long, and a ¾-inch hole was drilled along the axis to accommodate the G-M tube. Background count with this arrangement ran about 70 counts per minute, half of this being attributable to cosmic rays and the remainder to the 0.66-Mev gamma-rays from the Cs^{137} source.

The circular slits were milled from 24ST aluminum ⅜ in. thick to the dimensions specified by DuMond. The energy selecting slit was cut by milling a ¼-in. wide slot halfway through the sheet, placing supporting bars across the slot, thus joining the circular center portion to the ring-shaped outer section when they were separated by a subsequent slot milled on the opposite side on a ¼-in. larger radius deep enough to meet the first cut. This procedure left a slit with a radial width of 0.004 inch and axial width of 0.009 inch. Slit and counter arrangement is shown in Fig. 2.

Alignment of the slit axis with the magnetic field was accomplished by supporting the source end of the assembly in a universal joint and bringing out an axial rod attached to the detector end through a sylphon seal to horizontal and vertical positioning screws. The latter were varied until the Cs^{137} conversion lines showed a maximum number of counts, this slit position also providing the best resolution.

A cylindrical vacuum chamber two meters long and 0.5 meter in diameter was rolled from ½-in. aluminum sheet and welded down the seam. The vacuum was maintained at 0.1 micron by an oil diffusion pump and forepump. The chamber was covered with an electrically insulating asbestos sheet and the latter wrapped with two layers of ⅜-in. copper tubing which was water cooled. A 125-volt 160-ampere dc generator supplied magnet current which was kept constant to 0.1 percent.

[12] The authors wish to express their gratitude to R. E. Maerker of the Physics Department, University of Tennessee for making this check.

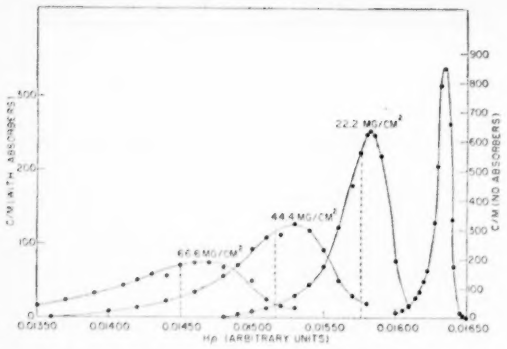

FIG. 3. Typical uncorrected spectrometer data for Be. Line at right is incident distribution. Foil thicknesses are actual thicknesses times $\sqrt{2}$ to correct for non-normal incident and exit angles.

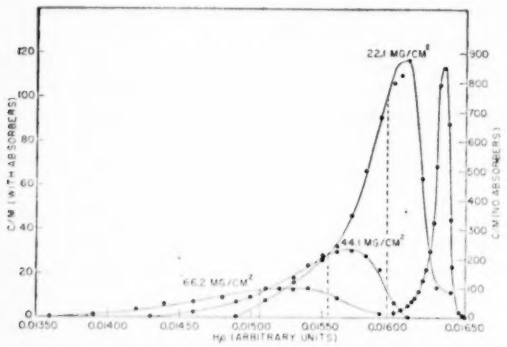

FIG. 4. Typical uncorrected spectrometer data for Pb. Line at right is incident distribution. Foil thicknesses are actual thicknesses times $\sqrt{2}$ to correct for non-normal incident and exit angles.

RESULTS

Figures 3 and 4 show typical straggling curves without corrections as obtained from the spectrometer. The foil thicknesses given are the actual thicknesses multiplied by $\sqrt{2}$ to take into account the 45° incidence and exit angle from the foil. Thicknesses lay between 20 and 66 mg/cm² after making this correction. All ordinates are divided by the potentiometer reading (proportional to the momentum) before making a momentum plot, in order to correct for the change with energy of the momentum increment accepted by the spectrometer. In calculating the aR values for the various foils, an additional thickness is added to the thickness specified above to correct for the finite width of the incident distribution, a practice which has been discussed recently.[13] This additional foil thickness is determined experimentally by extrapolating the graph of observed curve widths *versus* thickness to zero width. These thicknesses were calculated to be about 7.7 ± 0.3 mg/cm², without any consistent variation with Z being noted. On the basis of stopping power considerations alone, one would expect the constant width of the incident distribution to correspond to a "virtual" foil thickness of Be smaller than that of Pb. However, the larger straggling widths of the observed distributions for the light elements compensated for this expected effect, thus making the correction in mg/cm² about constant for all elements. The value of the incident energy used in the calculations was increased by using the above "virtual" thicknesses and the most probable stopping power.

Straggling distributions are compared with the Blunck-Leisegang theory in Figs. 5 and 6. All distributions had maximum ordinates between $\lambda=0$ and $\lambda=1$ as predicted from the theory, although the width of the distribution for Be is seen to be considerably larger than expected. All curves are drawn to a maximum ordinate of 0.18.

A graph of the ratio of experimental width at half-height to width calculated from the Blunck-Leisegang theory is given as a function of atomic number in Fig. 7. Included also are some values obtained by Kageyama and Nishimura at 1414 kev. It can be seen that straggling curves for the light elements are about 1.8 times as wide as anticipated, the ratio decreasing to unity for the heavy elements.

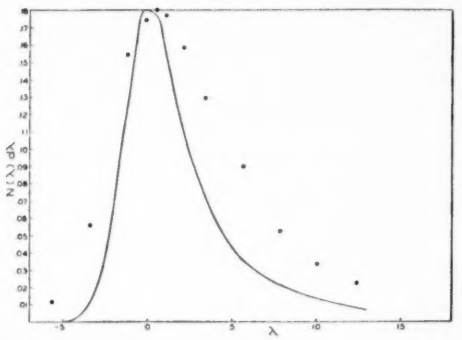

FIG. 5. Corrected data plotted against the Blunck-Leisegang distribution for Be ($b^2=0.84$). Curve normalized to maximum ordinate of 0.18.

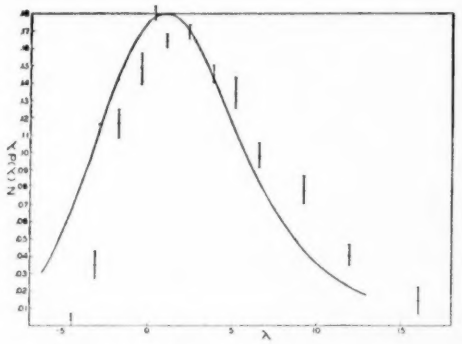

FIG. 6. Corrected data plotted against the Blunck-Leisegang distribution for Pb ($b^2=22$). Curve normalized to maximum ordinate of 0.18.

[13] W. Schultz, Z. Physik **129**, 530 (1951).

Recent calculations by Yang[14] of the effect of multiple scattering on the length of path in the absorber raise considerable doubt concerning the applicability to medium and high atomic numbers of the Landau and Blunck-Leisegang distributions taken by themselves for low-energy electrons. Yang obtains distributions in path length for electrons which have entered the foil normally, and either are detected irrespective of angle of emergence (Case I) or are detected only when leaving normally (Case II). Although our experimental arrangement does not enable us to use Yang's distributions exactly, we can use the average path increase he obtains as an order of magnitude estimate of the importance of this effect. Considering that our geometry more closely approximates his Case I, we find that we should expect theoretically an increase of about 5 percent in path length in the thinnest Be absorber, about 12 percent in the thinnest Al absorber, and up to 100 percent in Pb. Clearly, one should expect a corresponding broadening of the experimental straggling distribution and a shift toward lower energy. No displacement of the experimental energy loss curve was noted, in agreement with Chen and Warshaw and Kageyama and Nishimura, although the anomalous width of the curves may possibly be attributable to this effect. An experiment in which the angles of incidence and exit are sharply defined is needed to determine the validity of this correction. The Blunck-Leisegang distribution can then be integrated over the Yang distribution for the conditions of the experiment and the data then compared with this new straggling curve.

CONCLUSIONS

Straggling curves for 624-kev electrons have been measured for several foils of each of Be, Al, Cu, Sn, Ta, and Pb. The peaks of the observed distributions are found to be displaced as predicted by the Landau theory, although the observed distributions had widths at half-height between 8 and 11 λ-units as compared with the 4.1 λ-unit width obtained by Landau. A correction to the simple theory by Blunck and Leisegang brings agreement with the data for the heavy elements but fails to account for the excessive width of straggling distributions for light elements, the latter still being about 1.8 times as wide as the Blunck-Leisegang theory.

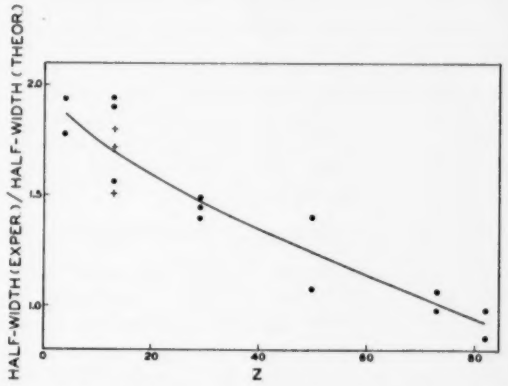

FIG. 7. Ratio of experimental to theoretical widths at half-height as a function of atomic number. Crosses are values of Kageyama and Nishimura for 1414-kev electrons.

The authors wish to express their thanks to R. H. Ritchie and P. N. Hensley of the Oak Ridge National Laboratory staff, the former for his many interesting discussions regarding the theory of electron energy loss, and the latter for his help in the design and construction of the spectrometer.

[14] C. N. Yang, Phys. Rev. **84**, 599 (1951).

Current Density Tables for Field Emission Theory*

W. W. DOLAN
Physics Department, Linfield College, McMinnville, Oregon
(Received December 1, 1952; revised manuscript received April 24, 1953)

The Fowler-Nordheim field emission equation permits calculation of current density J as a function of surface electric field F and work function ϕ. Computed values of J for $1.00\times10^7<F<1.00\times10^8$ v/cm and for $2.00<\phi<6.30$ ev are tabulated; the table is of use in connection with several theoretical and experimental aspects of field emission.

INVESTIGATION of field emission phenomena requires frequent reference to the fundamental Fowler-Nordheim theory[1,2] in which the emission current density J in amperes/cm^2 is given as a function of the surface electric field F in v/cm and the work function ϕ in ev by the equation:[3]

$$J=(1.54\times10^{-6}F^2/\phi)\exp[-6.83\times10^7\phi^{\frac{1}{2}}f(y)/F], \quad (1)$$

where $f(y)$ is the Nordheim elliptic function[2,4] of the variable $y=3.79\times10^{-4}F^{\frac{1}{2}}/\phi$. In these expressions, the numerical coefficients have been altered to conform with recent values of the physical constants. The comparison of experiment with theory necessitates repeated calculations of current densities from Eq. (1), or its logarithmic equivalent, for a wide range of F and for values of ϕ which depend upon the nature of the emitting surface.

Experimental results in these laboratories[5] have stimulated renewed interest in field emission theory for several reasons. First, pulse techniques have produced stable field current densities of the order of 10^8 amperes/cm^2 at fields of 8×10^7 v/cm for which the approximations involved in the derivation of Eq. (1) become questionable. Second, space charge effects[5] cause marked deviations from the current-voltage relationship expected in view of Eq. (1). Third, previous results here indicate that the transition from normal field emission to the vacuum arc occurs when the emitter is resistively heated, the problem thus involving electron emission in the presence of simultaneous high fields and high temperatures. This problem has had only partial theoretical treatment.[6-8]

In each of these studies, Eq. (1) is the basic reference for cold cathode emission in the absence of space charge. Table I has therefore been prepared, comprising

TABLE I. Common logarithms of field current density J in amperes/cm^2, from Eq. (1), for various values of electric field F in v/cm and work function ϕ in ev.

$F\times10^{-7}$ (v/cm)	ϕ(ev) 2.00	2.50	3.00	3.50	4.00
1.0	3.04	−0.54	−4.45	−8.64	
1.2	4.51	+1.48	−1.80	−5.32	
1.4	5.56	2.94	+0.10	−2.94	
1.6	6.36	4.04	1.53	−1.14	
1.8	6.98	4.90	2.66	+0.26	
2.0	7.48	5.59	3.56	1.39	−0.90
2.2	7.90	6.16	4.30	2.32	+0.22
2.4	8.25	6.64	4.92	3.09	1.16
2.6	8.54	7.05	5.45	3.75	1.96
2.8		7.40	5.91	4.32	2.65
3.0		7.71	6.30	4.82	3.25
3.2		7.98	6.65	5.25	3.78
3.4		8.22	6.96	5.64	4.24
3.6		8.43	7.24	5.98	4.66
3.8		8.63	7.49	6.29	5.03
4.0		8.80	7.71	6.57	5.37
4.2		8.96	7.92	6.82	5.67
4.4			8.11	7.06	5.96
4.6			8.28	7.27	6.21
4.8			8.44	7.46	6.44
5.0			8.59	7.65	6.66
5.2			8.72	7.82	6.87
5.4			8.85	7.97	7.05
5.6			8.97	8.12	7.23
5.8			9.08	8.25	7.39
6.0			9.18	8.38	7.55
6.2			9.28	8.50	7.69
6.4				8.61	7.83
6.6				8.72	7.95
6.8				8.82	8.07
7.0				8.92	8.19
7.2				9.01	8.30
7.4				9.09	8.40
7.6				9.18	8.50
7.8				9.25	8.59
8.0				9.33	8.68
8.2				9.40	8.76
8.4				9.47	8.84
8.6					8.92
8.8					9.00
9.0					9.07
9.2					9.14
9.4					9.20
9.6					9.27
9.8					9.33
10.0					9.39

* This work was supported by the U. S. Air Force, in part through the Microwave Laboratory, University of California.
[1] R. H. Fowler and L. W. Nordheim, Proc. Roy. Soc. (London) **A119**, 173 (1928).
[2] L. W. Nordheim, Proc. Roy. Soc. (London) **A121**, 626 (1928).
[3] A. Sommerfeld and H. Bethe, *Handbuch der Physik* (Verlag. Julius Springer, Berlin, 1933), Vol. 24, No. 2, p. 441.
[4] J. M. Houston, Phys. Rev. **88**, 349 (1952); Burgess, Kroemer, and Houston, Phys. Rev. **90**, 515 (1953); also private communication from J. M. Houston.
[5] W. P. Dyke and J. K. Trolan, Phys. Rev. **89**, 799 (1953).
[6] E. Guth and C. J. Mullin, Phys. Rev. **61**, 339 (1942).
[7] A. E. Glaubermann and I. I. Talynasky, Doklady Acad. Nauk. S.S.S.R. **78**, 661 (1951).
[8] J. Nakai, Technol. Repts. Osaka Univ. **1**, 213 (1951).

TABLE I.—*Continued.*

$F\times10^{-7}$ (v/cm)	ϕ(ev) 4.35	4.50	4.65	5.00	5.50	6.30
2.0	−2.58	−3.32	−4.06	−5.85	−8.50	−12.97
2.2	−1.31	−1.99	−2.66	−4.30	−6.71	−10.78
2.4	−0.25	−0.87	−1.50	−2.99	−5.22	−8.96
2.6	+0.65	+0.08	−0.50	−1.89	−3.95	−7.41
2.8	1.43	0.90	+0.36	−0.94	−2.86	−6.08
3.0	2.11	1.61	1.10	−0.11	−1.91	−4.92
3.2	2.70	2.23	1.75	+0.61	−1.08	−3.91
3.4	3.22	2.78	2.33	1.25	−0.34	−3.02
3.6	3.69	3.27	2.84	1.82	+0.32	−2.22
3.8	4.11	3.71	3.30	2.34	0.90	−1.50
4.0	4.49	4.11	3.72	2.80	1.44	−0.85
4.2	4.84	4.47	4.10	3.22	1.92	−0.27
4.4	5.15	4.80	4.45	3.60	2.35	+0.26
4.6	5.44	5.11	4.76	3.95	2.76	0.75
4.8	5.71	5.38	5.06	4.28	3.13	1.20
5.0	5.95	5.64	5.33	4.58	3.47	1.62
5.2	6.18	5.88	5.58	4.85	3.78	2.00
5.4	6.39	6.10	5.80	5.11	4.08	2.35
5.6	6.59	6.31	6.02	5.35	4.35	2.68
5.8	6.77	6.50	6.22	5.57	4.60	2.99
6.0	6.94	6.68	6.41	5.78	4.83	3.28
6.2	7.10	6.85	6.59	5.97	5.06	3.55
6.4	7.26	7.01	6.76	6.16	5.28	3.81
6.6	7.40	7.16	6.91	6.33	5.48	4.04
6.8	7.53	7.30	7.06	6.50	5.66	4.27

$F\times10^{-7}$ (v/cm)	ϕ(ev) 4.35	4.50	4.65	5.00	5.50	6.30
7.0	7.66	7.43	7.20	6.65	5.84	4.48
7.2	7.78	7.56	7.33	6.80	6.00	4.68
7.4	7.90	7.68	7.46	6.93	6.16	4.88
7.6	8.01	7.80	7.58	7.07	6.31	5.06
7.8	8.11	7.90	7.69	7.19	6.46	5.23
8.0	8.21	8.01	7.80	7.31	6.60	5.40
8.2	8.31	8.11	7.91	7.43	6.72	5.55
8.4	8.40	8.20	8.00	7.54	6.85	5.70
8.6	8.48	8.29	8.10	7.64	6.97	5.85
8.8	8.57	8.38	8.19	7.74	7.08	5.98
9.0	8.65	8.46	8.28	7.84	7.19	6.12
9.2	8.72	8.54	8.36	7.93	7.30	6.24
9.4	8.80	8.62	8.44	8.02	7.40	6.36
9.6	8.67	8.69	8.52	8.10	7.49	6.48
9.8	8.94	8.76	8.59	8.18	7.58	6.59
10.0	9.00	8.83	8.66	8.26	7.67	6.69
12.0	9.54	9.40	9.25	8.91	8.41	7.58
14.0		9.83	9.69	9.39	8.95	8.23
16.0				9.76	9.37	8.72
18.0					9.70	9.12
20.0					9.97	9.44

common logarithms of J predicted by Eq. (1) for a range of fields and work functions found useful in the present series of investigations here. Recent corrections by Houston[4] of Nordheim's elliptic function have been employed. The values of ϕ included in the table were chosen for various experimental reasons. $\phi=4.5$ ev is the accepted average value for tungsten, the cathode material most commonly used here. The values 4.35 and 4.65 ev are those found by Nichols[9] for tungsten crystal faces (116) and (110), respectively, which become individually significant for single crystal cathodes. $\phi=5.0$ ev is an estimate[10,11] of a possible corrected value for the (110) face. $\phi=6.3$ ev is a published[12] average value for platinum, one of the materials of higher work function. The values below 4.5 ev are useful in the interpretation of experiments with the barium-coated tungsten cathode. In the latter cases, the table is terminated at values of F such that $f(y)=0$, a limit imposed on Eq. (1) by the lowering of the surface potential barrier to the top Fermi level. For higher work functions, this limit falls outside the range of the table.

Acknowledgment for much of the tedious numerical work is due the author's assistants, Lorraine McPhee and Jack Brandt. The cooperation of W. P. Dyke and other staff members of this laboratory is appreciated.

[9] M. H. Nichols, Phys. Rev. **57**, 297 (1940).
[10] E. W. Mueller, Z. Physik **120**, 270 (1943).
[11] G. F. Smith, Abstracts of Field Emission Seminar, Linfield College, 1952 (unpublished).
[12] L. A. DuBridge, Phys. Rev. **31**, 236 (1928).

The Surface Tension of Liquid Silicon and Germanium*

PAUL H. KECK AND WENDELL VAN HORN
Signal Corps Engineering Laboratories, Fort Monmouth, New Jersey
(Received April 27, 1953)

The surface tensions of liquid silicon and germanium were determined using the drop weight method. 600 dynes/cm was found for germanium and 720 dynes/cm for silicon at their freezing points and argon atmosphere. The parachors of the group IVb elements as derived from surface tension measurements of the molten elements are compared with the atomic parachors calculated from compounds. The differences are interpreted as structural parachors which indicate that the bonding between neighboring atoms in the liquid state increases in nearly uniform steps from lead to tin and to germanium. No further increase of the structural parachor takes place in silicon which is consistent with the fact that only four electrons per atom are available for bonding.

IN connection with the problem of producing single crystals of germanium and silicon from the melt, the values of the surface tensions of these elements in the liquid state at their freezing points are of interest. Since no data could be found in the literature the surface tensions were measured via the well-known drop weight method.

A short tantalum cylinder of approximately 25 mm diameter was suspended in a quartz glass flask, and a concentric induction coil on the outside served to heat the cylinder to incandescence in argon as an inert atmosphere. Rods of high-purity polycrystalline germanium and of silicon, up to about 5 mm diameter, were slowly lowered into the incandescent cylinder whereby the tip melted and a drop of gradually increasing size was formed. The process was slowly continued until the drop fell off. Proper melting was obtained with the temperature of the tantalum cylinder adjusted to approximately 1400°C for germanium and 2000°C for silicon.

The surface tension γ was calculated from the radius r of the rod and the weight W in grams ($=gW$ in dynes) of a drop according to the equation,

$$\gamma=\phi gW/2\pi r[\text{dynes/cm}], \tag{1}$$

where ϕ is a correction factor which is dependent upon the cross section of the rod and upon the volume of the drop. Values of ϕ were calculated and measured for various substances by Lohnstein and Harkins and co-workers.[1]

The results of our measurements of the surface tensions are

$$\gamma=600 \text{ dynes/cm for germanium,}$$
$$\gamma=720 \text{ dynes/cm for silicon.}$$

These values refer to the liquids at the freezing point in argon of atmospheric pressure and are believed to be accurate at least within ±5 percent.†

Since various relations are known between the surface tension and other physical and chemical quantities, a number of conclusions can be deduced from the knowledge of the surface tension. Macleod found that the fourth root of the surface tension divided by the density is independent of temperature,

$$\gamma^{\frac{1}{4}}/(\rho_L-\rho_G)=\text{constant}, \tag{2}$$

where ρ_L and ρ_G refer to the densities of the liquid and the gas phase. ρ_G can ordinarily be neglected.

Sugden[2] introduced the parachor P which is the expression in (2) multiplied by the molecular weight M and showed that P can provide some insight into the bonding between the atoms,

$$P=\gamma^{\frac{1}{4}}M/(\rho_L-\rho_G)$$

or

$$P=\gamma^{\frac{1}{4}}V, \tag{3}$$

where V is the molar volume of the compound or the atomic volume in the case of an element. The parachor of a compound is an additive property, being the sum of the atomic parachors with some additional terms which account for binding forces between the atoms.

Table I summarizes the values for the elements of group IVb of the periodic table. The second column contains the surface tension as measured in the liquid state near the freezing point. The values of the fourth column are the parachors as derived from columns two and three. If we subtract from these values the atomic parachors deduced by Sugden[2] from the surface tension of covalent compounds and listed in column five, we obtain the data of the sixth column. These values can be interpreted as structural parachors and are indicative of the nature of bonding between the atoms of the elements in the liquid state. The increase of the structural parachor from lead to germanium in nearly equal steps is striking. Sugden assumed a structural parachor of zero for the sharing of one electron pair and derived structural parachors of 11.6 and 23.3 for the sharing of

* Presented at the American Physical Society meeting at Durham, North Carolina, March 26–28 (1953).

[1] See A. Weissberger, *Physical Methods of Organic Chemistry. I* (Interscience Publishers, New York, 1945).

† After completion of this paper we learned that W. D. Kingery and M. Humenik, J. Phys. Chem. **57**, 359 (1953), found 730±10 dynes/cm for the surface tension of silicon in helium, using the sessile drop method. This is in very good agreement with our results.

[2] S. Sugden, *The Parachor and Valency* (G. Routhledge and Sons, London, 1930).

two and three electron pairs, respectively. He therefore concluded that in liquid lead two pairs of electrons are shared between neighboring atoms, while in tin three pairs are shared. The value for liquid germanium then indicates that four electron pairs are being shared between neighbors. Moreover, the fact that the structural parachor of liquid silicon does not exhibit any appreciable additional increase over that of germanium is consistent with the fact that four is the maximum number of available electrons which can be shared. These results are not in disagreement with the metalic conductivity of liquid germanium[3] and the presumably metallic conductivity of liquid silicon, since only a small fraction of free electrons is sufficient to explain the conductivity in the liquid state.

The values in parentheses for carbon must be considered a speculative extrapolation.

The results derived from the parachors do not give any answer as far as the geometrical arrangement of the atoms in the liquid state is concerned. Hendus[4] has shown that in germanium the coordination number changes from four to eight upon melting. The same result should be expected for silicon. No immediate connection between these results and the values of the parachor can be expected.

TABLE I. Surface tension and parachor of the elements of group IVb.

IVb elements	Surface tension in the liquid phase dynes/cm	Atomic volume[a]	Parachor of the elements in the liquid phase	Atomic parachor from compounds[b]	Structural parachor	Sugden's values
C	(2100)	5.41	(36.8)	4.8	(32)	
Si	720	12.0	61	33–35	28–36	
Ge	600	13.5	67	38–36	29–31	
Sn	530	16.2	79–84[b]	58	21–26	23.3
Pb	450	18.3	84–91.4[b]	76.2	8–15	11.6

[a] H. D. Hubbard and W. F. Meggers, *Periodic Chart of the Atoms* (W. W. Welch Scientific Company, Chicago, 1950).
[b] See reference 2.

[3] R. W. Keyes, Phys. Rev. **84**, 367 (1951).

[4] H. Hendus, Z. Naturforsch. **2a**, 505–521 (1947).

PHYSICAL REVIEW VOLUME 91, NUMBER 3 AUGUST 1, 1953

Double Hysteresis Loop of $BaTiO_3$ at the Curie Point

WALTER J. MERZ
Bell Telephone Laboratories, Murray Hill, New Jersey
(Received April 23, 1953)

It is known that the Curie point θ of the ferroelectric $BaTiO_3$ shifts to higher temperatures when a dc bias field is applied. If the crystal shows a sharp transition, we expect by applying an ac field at the Curie temperature that the crystal would become alternately ferroelectric and nonferroelectric in the cycle of the ac field. This can be seen in the shape of the hysteresis loop at temperatures slightly above θ. In the center of the polarization P *versus* field E plot, we observe a linear behavior corresponding to the paraelectric state of $BaTiO_3$ above θ. At both high voltage ends, however, we observe a hysteresis loop corresponding to the ferroelectric state. A change in temperature causes a change in size and shape of the double hysteresis loops, ranging from a line with curves at the ends (higher temperature) to two overlapping loops (lower temperature). The results obtained allow us to calculate the different constants in the free-energy expression of Devonshire and Slater. One of the results shows that the transition is of the first order since the P^4 term turns out to be negative. The properties of the hysteresis loops are discussed, especially the large spontaneous electrical polarization and the low coercive field strength.

I. INTRODUCTION

SEVERAL investigators[1–3] have shown that the Curie point θ of $BaTiO_3$ and some other ferroelectrics[4] is displaced to higher temperatures by application of a biasing field. Having available some unusually good crystals, it has been possible to investigate their behavior at the Curie point more carefully. The crystals used had simple, well-defined domain patterns; i.e., they had only parallel and antiparallel domains.[5] They also showed very sharp transitions and were good insulators even at elevated temperatures.

By working at temperatures a few degrees above the Curie temperature, it has been possible to study the $BaTiO_3$ crystals as they change from nonferroelectric to ferroelectric and back during each cycle of a strong 60 cycle field. At zero or low values of field, the crystal is not ferroelectric, since its temperature is above the normal Curie point. But at the peak values of the field, the Curie temperature is shifted by the field, so that the crystal there is below its Curie point and displays the properties of a ferroelectric.

[1] A. F. Devonshire, Technical Report L/T 185 British Electrical and Allied Industries Research Associates, 1948 (unpublished).
[2] W. Kaenzig and N. Maikoff, Helv. Phys. Acta **24**, 343 (1951).
[3] M. E. Caspari and W. J. Merz, Phys. Rev. **80**, 1082 (1950).
[4] G. Shirane, Phys. Rev. **86**, 219 (1952).

[5] W. J. Merz, Phys. Rev. **88**, 421 (1952).

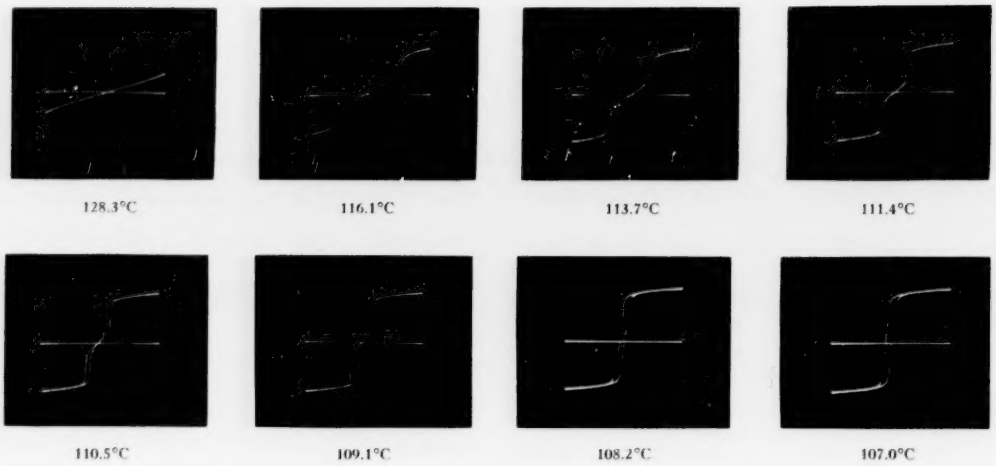

FIG. 1. Double hysteresis loops of $BaTiO_3$.

II. MEASUREMENTS

The experimental data have been obtained from a series of hysteresis loops which are plots of electrical polarization P *versus* applied field E. The loops shown in Fig. 1 at several different temperatures are typical.

At higher temperatures, we observe a straight line: the crystal is paraelectric and at no part of the cycle is the field high enough to shift θ enough to make it ferroelectric. At lower temperatures, we find at the peak values of the field two small hysteresis loops: the crystal becomes ferroelectric when under the influence of a high electrical field. Near the Curie point these two loops overlap. At and below θ, we observe the regular hysteresis loop. If we plot the Curie temperature *versus* electric field at which the crystal becomes ferroelectric, we obtain a linear behavior (Fig. 2).

III. COMPARISON WITH THEORY

For comparison with theory, we express the free energy per cm^3 of $BaTiO_3$ as a function of electrical polarization and stress with the stress equated to zero, as proposed by Devonshire[1,6] and Slater:[7]

$$F=A(T-T_0)P^2-BP^4+CP^6+F_0(T), \qquad (1)$$

where P=electrical polarization; T=temperature; T_0=extrapolated temperature of the $1/\epsilon(T)$ plot; A, B, C=constants. $F_0(T)$=free energy of the unpolarized state.

The derivative of F with respect to P gives, for the electrical field strength E,

$$\partial F/\partial P=E=2A(T-T_0)P-4BP^3+6CP^5. \qquad (2)$$

In order to get dimensionless units, we normalize this equation by multiplying it with a constant K:

$$KE=2AK(T-T_0)P-4BKP^3+6CKP^5. \qquad (3)$$

We then obtain a normalized dimensionless polarization p by setting

$$\begin{aligned} 4BKP^3&=4p^3, \\ 6CKP^5&=2p^5, \end{aligned} \qquad (4)$$

with

$$K=(3C/B^{5/3})^{3/2}\ \text{cm/volt}. \qquad (5)$$

In a similar way, we introduce a normalized dimensionless electrical field e,

$$KE=e, \qquad (6)$$

and a normalized dimensionless temperature t,

$$2AK(T-T_0)P=2pt. \qquad (7)$$

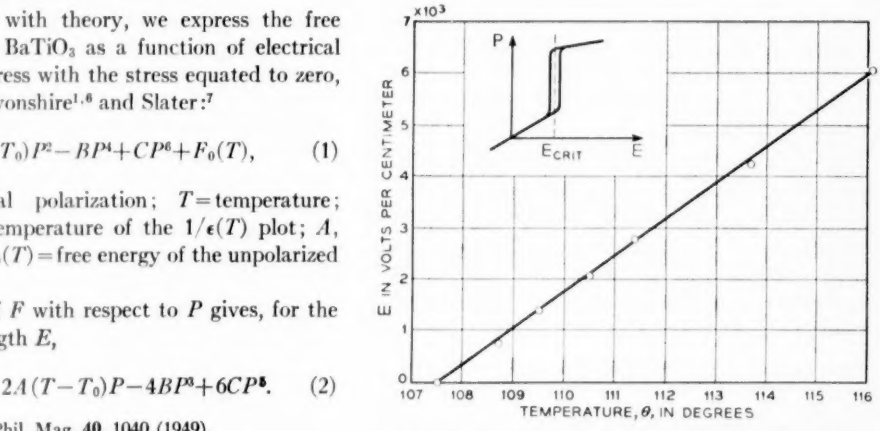

FIG. 2. Shift of Curie temperature θ *versus* applied field E.

[6] A. F. Devonshire, Phil. Mag. **40**, 1040 (1949).
[7] J. C. Slater, Phys. Rev. **78**, 748 (1950).

TABLE I. Values for constants B and C.

Crystal	$(3C/B)^{\frac{1}{2}}$ cm³/coulomb	$(27C^3/B^5)^{\frac{1}{2}}$ cm/volt	B volt cm⁵/coulomb³	C volt cm⁸/coulomb⁵
I	7.8×10^{4}	3.6×10^{-4}	1.3×10^{18}	2.7×10^{27}
II	7.8×10^{4}	3.4×10^{-4}	1.4×10^{18}	2.8×10^{27}

TABLE II. Values for constants A, B, and C.

	A (cgs)	B (cgs)	C (cgs)
Our results	3.7×10^{-6}	1.7×10^{13}	3.8×10^{23}
Devonshire's results	5×10^{-5}	11×10^{13}	61.6×10^{23}
Corrected Devonshire's result	5×10^{-5}	2.7 to 3.1×10^{13}	4.7 to 5.9×10^{23}

With Eq. (5) we get, for Eqs. (4), (6), and (7),

$$p=(3C/B)^{\frac{1}{2}}P, \tag{8a}$$

$$e=(27C^3/B^5)^{\frac{1}{2}}E, \tag{8b}$$

$$t=(3AC/B^2)(T-T_0). \tag{8c}$$

Equation (2) can now be written in the form

$$e=2p^5-4p^3+2pt, \tag{9}$$

and is plotted in Fig. 3 for different values of t. Whenever dp/de becomes negative, which corresponds to an unstable condition, we replace the curve by a vertical line until it crosses the curve at a point where dp/de is positive again. We can now compare this figure with our experimentally obtained curves (Fig. 1).

IV. RESULTS

Experimentally, we can determine the expression $x=2pt-e$ of Eq. (9) from Fig. 1 for different values of

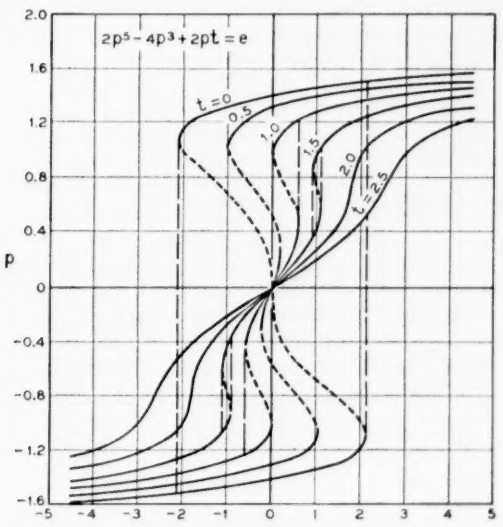

FIG. 3. Plot of function $2p^5-4p^3+2pt=e$.

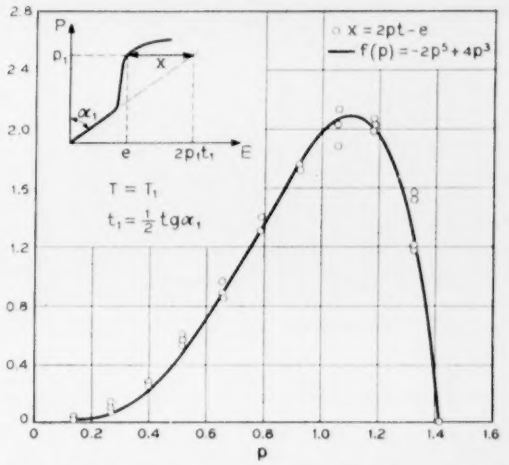

FIG. 4. Plot of values $x=2pt-e$ and function $f(p)=-2p^5+4p^3$.

p and t (related to temperature T) as indicated in Fig. 4, using just the smooth parts of the double loop curves where we have stable conditions. The results obtained are plotted as points in Fig. 4. For comparison, we also plot in Fig. 4 a solid line which represents the theoretical expression $(-2p^5+4p^3)$ as a function of p, which, according to Eq. (9), is equal to $2pt-e$. The agreement is quite good.

In order to fit the experimental points (P,E) to the theoretical curve (p,e), we multiply polarization P and electrical field E of Fig. 1 (x is measured in terms of E) with calibration constants. We then get with Eqs. (8a) and (8b) values for $(3C/B)^{\frac{1}{2}}$ and $(27C^3/B^5)^{\frac{1}{2}}$ from which we can calculate the constants B and C (Table I).

In order to get a value for the constant A, we plot the reciprocal dielectric constant $1/\epsilon_c$, as measured with a bridge, *versus* temperature T (Fig. 5). Since, according to Eq. (2), $1/\chi=2A(T-T_0)$ in first approximation, we

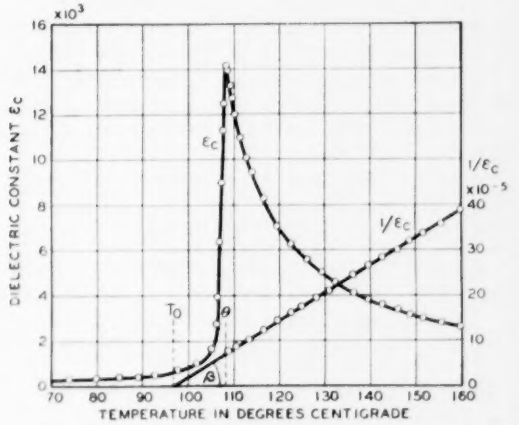

FIG. 5. Dielectric constant ϵ_c and reciprocal dielectric constant $1/\epsilon_c$ *versus* temperature T.

get for A from the slope β of Fig. 5

$$A=2\pi\beta=3.7\times10^{-5}\text{ cgs.} \quad (10)$$

As a check we can compare the temperature T of our curves (Fig. 1) with the t values of the corresponding curves (Fig. 3). Using the corresponding value for T_0 and Eq. (8c), we then get an expression for AC/B^2 which can be compared with the values A, B, and C obtained before. The agreement is good. Table II gives the average values for A, B, and C for the 2 crystals in cgs units with an accuracy of about 5–10 percent. If we compare these values with the values obtained by Devonshire[6] [his Eqs. (7.12), (7.14), (7.16)], where

$$A=\tfrac{1}{2}(\chi'_0/T_1-T_0);\quad B=\xi_{11}'/4;\quad C=\zeta'/6 \quad \text{(Table II)},$$

we find that the values for A agree fairly well. This is to be expected, because A is determined in both cases by measuring the slope of the $1/\epsilon$ *versus* T curve above θ in the nonferroelectric region, where the quality of the crystal is not too important (no domain influence). The difference $\theta-T_0$ is found to be about 11°C, similar to Devonshire's[6] value.

However, our values for B and C differ greatly from Devonshire's results. In order to understand this, we measured the spontaneous electrical polarization. Whereas the dielectric constant as a function of temperature agrees fairly well with old measurements,[8] we find that the value of the spontaneous electrical polarization P_s differs greatly from old measurements.[8,9] We find that the jump of P_s at the Curie point θ is very much steeper because of the fact that the transition is much sharper. The most important difference, however, is that the absolute value of P_s is much bigger, $P_s\sim26\times10^{-6}$ coulomb/cm² at room temperature compared with $P_s\sim15.5\times10^{-6}$ coulomb/cm² before (Fig. 6). Furthermore, the value of P_s after the jump at the Curie point is $P_s\sim18\times10^{-6}$ coulomb/cm² compared with $P_s\sim10\times10^{-6}$ coulomb/cm²; that means that the new P values are 1.7 to 1.8 times bigger than the old ones.

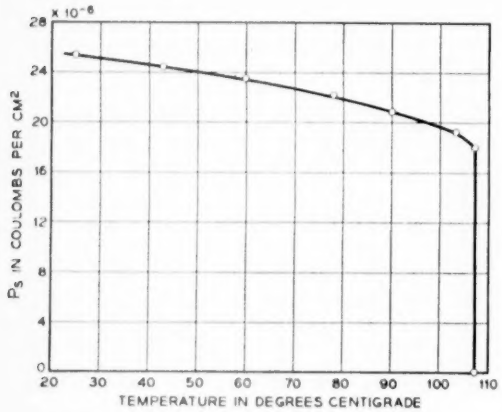

FIG. 6. Spontaneous electrical polarization P_S *versus* temperature T.

Since just the small values for P were available to Devonshire, our constants B and C must be smaller than his. According to Eqs. (6.9) and (6.10) in Devonshire's paper,[6] we have to divide his values B by $[P_s\text{ new}/P_s\text{ old}]^2=(1.7)^2$ to $(1.8)^2$ and C by $[P_s\text{ new}/P_s\text{ old}]^4=(1.7)^4$ to $(1.8)^4$. Furthermore, we change the value χ_0' in Eqs. (6.9) and (6.10) of Devonshire's paper, because our T_1-T_0 value is not 10°C but about 11°C (Fig. 5). Taking our value for $\chi_0'/(T_1-T_0)=2A=0.74\times10^{-4}$ degree^{-1}, we then get for $\chi_0'=8.1\times10^{-4}$ instead of 10×10^{-4}, which means that we also have to multiply B and C with 0.81. The corrected values of Devonshire's constant B and C are listed in Table II and give a fairly good agreement with our values.

Devonshire[1] calculated the shift of the Curie point, when an electric field E is applied, to be

$$\Delta T=(1/A)[2C/B]^{\frac{1}{2}}\times E. \quad (11)$$

Using our values for A, B, and C, we find

$$\Delta T=1.9\times10^{-3}\times E, \quad (12)$$

when E is measured in volts/cm.

The observed temperature shift is, according to Fig. 2,

$$\Delta T=1.43\times10^{-3}\times E. \quad (13)$$

Kaenzig and Maikoff[2] measured $\Delta T=1.2\times10^{-3}\times E$, and, using Devonshire's original values, we get $\Delta T=2.2\times10^{-3}\times E$.

V. ELECTROCALORIC EFFECT

Up to now, we have assumed that the electrocaloric effect near the Curie point can be neglected. It can be calculated in the following way from Eq. (1):

$$S=-(\partial F/\partial T)=-AP^2-(\partial F_0)/(\partial T)_P$$
$$=-AP^2+S_0(T). \quad (14)$$

For adiabatic conditions $S=$ constant. Since all temperature changes will be small, we can write

$$S_0(T)=S_0(T_1)+(c_P\rho/T)\Delta T, \quad (15)$$

where T_1 is the temperature where $P=0$, c_P is the specific heat at constant P, and ρ is density of the crystal.

We then find

$$\Delta T=(AT/c_P\rho)P^2=T-T_1, \quad (16)$$

which is equivalent to the well-known form:[10,11]

$$\Delta T=fP^2/2c_P, \quad (17)$$

[8] W. J. Merz, Phys. Rev. **76**, 1221 (1949).
[9] J. K. Hulm, Nature **160**, 127 (1947).
[10] E. T. Jaynes, *Ferroelectricity* (Princeton University Press, Princeton, 1953).
[11] Blattner, Kaenzig, and Merz, Helv. Phys. Acta **17**, 35 (1949).

where $f=\theta\beta$ is the Lorentz factor and β is the reciprocal Curie constant.

The crystal will take on an average temperature change ΔT somewhere between zero and $(AT/c_P\rho)P_{max}^2$. The correction in temperature resulting the electrocaloric effect will be large just in case of intermediate loops, because at high temperatures (flat line) P_{max} is small and because at low temperature (well-developed loops) P actually never goes through zero and the measured temperature will be the same as the temperature at near the maximum P. The value $(AT/c_P\rho)\times P_{max}^2$ turns out to be about 1.0°, if we use $P_{max}=16\times10^{-6}$ coulomb/cm^2 (P_{max} for intermediate loop), $c_P=0.16$ cal/g degree,[11] and $\rho=6.04$ g/cm^3.

That means that the actual temperature correction in the worst case (intermediate loops) will be of the order of half a degree. From Eq. (16), we get

$$T=T_1+(AT/c_P\rho)P^2, \tag{18}$$

so that Eq. (1) can be written as

$$F=A(T_1-T_0)P^2-(B-A^2T/c_P\rho)P^4+CP^6, \tag{19}$$

which shows that, besides the uncertainty in T_1, the electrocaloric effect gives us a change of B which is never larger than about 10 percent. Since our accuracy is not much better than 10 percent, we neglect these corrections. (See also remarks of Kaenzig and Maikoff.[2])

VI. DISCUSSION

Since the BP^4 term is negative, there seems to be no doubt any more that the transition at the Curie point is of the first order, as discussed by others.[1,2,6,10] The extremely sharp jump of P_S at the Curie point (Fig. 6) substantiates this argument.

However, there is one interesting point of difference. This is the fact that the spontaneous electrical polarization P_S is much larger than previous results indicated. There are two ways to explain this result. Either our new crystals are different crystals, or we are able to switch and align more domains than before. Though the crystals contain a certain amount of impurities to make them nonconductive and bigger, the x-ray pictures show about the same $c/a(\Delta a/a$ or $\Delta c/c)$ ratio as the old crystals. We therefore think that we have probably not changed the crystal appreciably. This is also indicated by the fact that the behavior of the dielectric constant is very similar to the old measurements. It is obvious that the dielectric constant at room temperature is slightly smaller (160), because we have no a domains, whereas before we always had a few.

FIG. 7. Hysteresis loop of $BaTiO_3$ at 60 cps.

Furthermore, the peak value at the Curie temperature is a little higher because the transition is sharp and not smeared out any more. It therefore seems that the high value of P_S has to be explained by the fact that, because of the better quality of the crystal, we can switch all or almost all parallel and antiparallel c domains. Because we have just parallel and antiparallel domains, all the domain movements are much smoother and faster and require smaller field strengths, as can be seen from the hysteresis loop. The coercive force is much smaller than before; we get $E_{coercive}\cong500$ volts/cm, or slightly more at 60 cps. The jump at E_c is very sharp, and the hysteresis loop is extremely steep. (Fig. 7.) This means that all the domains switch at almost the same time. Furthermore, we find an almost perfect saturation. We can increase the field to many times the value of E_c and get very little additional change in P because of domain movements (Fig. 7). However, we still feel that even here we have a few domains which do not change orientation from antiparallel to parallel, especially at higher frequencies.

The flat part of these rectangular loops corresponds to a dielectric constant of about 150–200, whereas the steep part corresponds to a value of the order of a few hundred thousand to almost a million.

Shirane[4] observed similar double hysteresis loops on (Pb-Ba)ZrO_3 ceramics. However, in that case, the ceramics go from an antiferroelectric to a ferroelectric state when an electric field is applied, whereas, in our case, the $BaTiO_3$ crystals go from a paraelectric to a ferroelectric state.

I wish to thank Dr. P. W. Anderson for many helpful discussions and suggestions, Dr. Elizabeth A. Wood for measuring the crystallographical properties of our $BaTiO_3$ crystals, and Mr. J. Remeika for the preparation of the very good single crystals.

n-Type Surface Conductivity on *p*-Type Germanium

W. L. Brown
Bell Telephone Laboratories, Murray Hill, New Jersey
(Received March 17, 1953)

A positive charge on the surface of a *p*-type germanium crystal induces a net negative space charge within the crystal adjacent to the surface. This space charge is composed of ionized acceptor atoms and also of electrons under certain conditions. When electrons occur they provide a layer of *n*-type conductivity immediately under the *p*-type germanium surface. Such a layer has been found on the *p*-type region of some *n*-*p*-*n* transistors. In the *n*-*p*-*n* structure the layer of electrons appears as an extra conducting path—"a channel"—across the *p*-type material between the two *n*-type ends. The conductance of a channel and the capacity between the channel and the *p*-type material have been measured and compared with the theoretical predictions based on a simple model.

1. INTRODUCTION

IN this paper the results of some experimental and theoretical investigations pertaining to surface conductivity will be described. Surface conductivity on germanium has previously been proposed as an explanation for certain aspects of transistor action.[1] These earlier examples now appear to have a different explanation. The phenomena to be discussed in this article, however, appear to be explicable only on the basis of a model in which we suppose that conduction by excess electrons occurs at the surface of a crystal of *p*-type material.

It is proposed that the previous chemical and electrical treatment of a specimen has resulted in a layer of positive charge on the surface of the *p*-type material. The presence of the positive surface charge requires a net deficit of positive charge within the crystal. Part of the deficit is provided by a loss of holes from the valence band near the surface of the crystal. Part of it is also provided by the presence of electrons in the conduction band. It is these electrons which form a layer of *n*-type conductivity at the germanium surface. The situation is represented diagrammatically in Fig. 1(a). If the specimen is in a field free region so that no electric field emerges from the surface, the net charge of the specimen must be zero. Deep in the interior of the crystal the charge density is, of course, zero. Thus, the positive surface charge must be just balanced by a negative space charge composed of negatively charged acceptors and excess electrons in a region adjacent to the surface.

It has been possible to study the layer of *n*-type conductivity shown in Fig. 1(a) by making use of single crystals of germanium having an *n*-*p*-*n* structure. In effect, at the surface of the crystal there is a continuous *n*-type region as a result of the positive surface charge on the *p*-type material. Figure 1(b) shows the potential energy of an electron in this structure. At the surface there is a channel of low potential energy across the *p*-layer. This channel provides a conducting path through which excess electrons may flow from one *n*-region to the other.

The *n*-*p*-*n* structures studied were actually experimental junction transistors. We will have occasion to refer to the two *n*-regions as emitter and collector and to the *p*-region as the base, consistent with transistor terminology.

In a sense the layer of *n*-type conductivity over the *p*-region forms a *p*-*n* junction. Between the excess electrons at the surface and the excess holes in the interior there is a region of substantially zero conductivity where there are neither electrons nor holes. This region acts like a dielectric, and changes in potential between the *n*-type region and the *p*-type region should result in charging currents like those for a condenser. According to the model, there should be a relationship between the conductance of the electrons in the channel and the charge of the condenser. A study of the relationship between conductance and capacity for the experimentally observed channels constitutes one of the strongest pieces of evidence for their existence. In order to explain some of these effects, however, it is necessary to suppose that the charge of the condenser does not reside entirely in mobile electrons but also in the charging and discharging of surface states. This is a familiar phenomenon in connection with the surface of germanium.[2,3]

The details of the calculation of the channel conductance and capacity that are a consequence of the model described above are given in Sec. 4.

2. EXPERIMENTAL EVIDENCE FOR CHANNELS

The presence of channels of *n*-type conductivity across the *p*-type base layers in experimental *n*-*p*-*n* transistors made itself conspicuous in the course of studying current-voltage characteristics of these units. One of the observations was made by leaving the emitter open-circuited while a reverse bias was applied between the base and the collector. This reverse potential tends to extract electrons from the base and

[1] J. Bardeen and W. H. Brattain, Phys. Rev. **75**, 1208 (1949).

[2] W. Shockley and G. L. Pearson, Phys. Rev. **74**, 232 (1948).

[3] J. Bardeen and W. H. Brattain, Bell System Tech. J. **82**, 1 (1953).

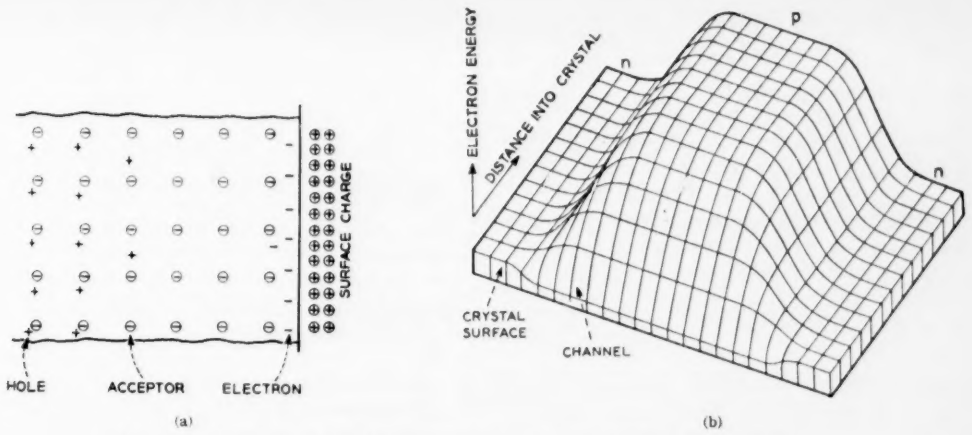

FIG. 1. (a) p-type germanium with a positive surface charge. (b) Potential energy of electrons in an n-p-n with a channel.

in fact to siphon some electrons from the emitter region over the potential maximum in the base layer and into the collector. This loss of electrons serves to charge the emitter positive so that it also assumes a reverse bias. The diffusion theory for p-n junction transistors[4,5] shows that the maximum potential which can be developed by this siphoning action is given by

$$V_f = (kT/q) \ln(1-\alpha),$$

where V_f is the emitter "floating potential," the open circuit potential of the emitter region with respect to the base, and where α is the efficiency of current transmission from emitter to collector through the base. Values of α as high as 0.998 have been observed. Such a value will correspond to a maximum floating potential of about 0.15 volt. It was found in experiments with these transistors that floating potentials as high as several volts could be observed. It was quite impossible to explain them by assuming that the connection between emitter and collector depended upon the diffusion of electrons through the base layer. The extra conducting path that is responsible for these floating potentials and that constitutes a defect in the n-p-n transistor is called a "channel."

In addition to the appearance of anomalously high floating potentials there were other observations which indicated that the connection between emitter and collector was quite different in nature from the predictions of diffusion theory. In particular, there was the phenomenon of aging or "conditioning" the channel: The emitter floating potential would change slowly following a change in the reverse bias of the collector. Furthermore, the emitter floating potential depended upon the bias which had been applied to the emitter immediately before the floating potential measurement was made.

[4] W. Shockley, Bell System Tech. J. **28**, 435 (1949).
[5] Shockley, Sparks, and Teal, Phys. Rev. **83**, 151 (1951).

It is proposed that the conditioning effects described are a result of an increase in the positive charge on the surface of the p-layer when the p-n junctions are biased so as to extract electrons from the base. This can occur in either of two ways. Ions may actually move along the surface of the transistor so as to accumulate over the base layer. Alternatively, the removal of electrons from the base layer will result in a departure from equilibrium at the surface. Electrons emitted by molecules or ions on the surface will tend to drift away and not be replaced. The result will be to produce a positive charge on the surface. It would be possible to investigate the proposal further by shining light on an n-p-n structure while the conditioning voltages were applied, to see whether the presence of electrons produced by the light within the p-layer would prevent the formation of a channel.

As a consequence of their aging effects it is difficult to measure the properties of channels at room temperature. It has been found however that, if a channel is produced at room temperature and the n-p-n structure is then cooled to a temperature considerably below 0°C with the conditioning biases still applied, a much more stable situation is achieved. The low temperature effectively freezes the properties of the channel, and measurements can be made over a period of hours without appreciable drift in the channel characteristics.

If the connection between the emitter and the collector that leads to anomalous floating potentials is an n-type channel across the base, the floating potential of one n-region should exhibit a saturation effect as a function of the bias applied to the other n-region. When a reverse bias is applied between the two n-regions and the base, electrons will be removed from the channel. At a certain critical value of this bias, the pinch-off voltage, the number of electrons in the channel will be reduced substantially to zero. Under these conditions the channel conductance from one n-region to the other

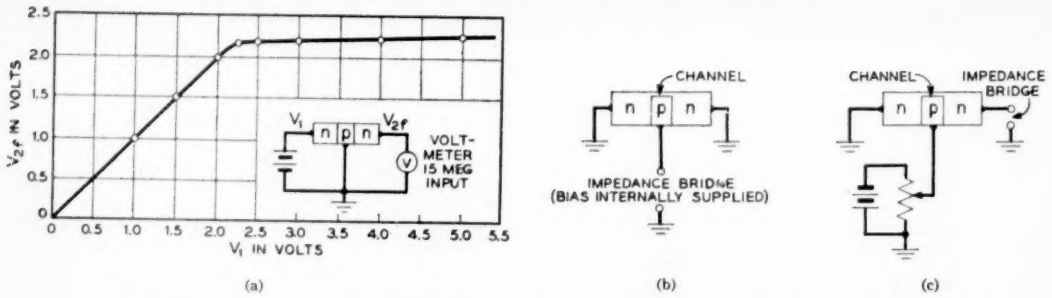

FIG. 2. (a) Experimental floating potential curve. (b) Connections for measurement of channel capacity. (c) Circuit for channel conductance measurement.

should disappear and only the normal conductance by diffusion and conductance due to other leakages should remain.[6] If a potential equal to the pinch-off voltage is applied to the collector and the emitter is allow to float, electrons will flow from the emitter through the channel to the collector. This loss of electrons will make the emitter potential more positive until it approaches the pinch-off voltage. As it approaches this potential very closely, the emitter end of the channel will acquire a progressively lower conductance, and it will be continually more difficult for electrons to escape from the emitter region. If there is a leakage current of any sort between emitter and base, the replacement of electrons through this leakage path will prevent the floating emitter from quite reaching the potential at which electron flow through the channel would be impossible. Consequently, for any value of the collector bias at least as large as the pinch-off voltage, the emitter floating potential will approach the pinch-off voltage but will not quite reach it. For values of collector bias lower than pinch-off, the steady-state floating potential of the emitter must again be such that electrons escaping from the emitter through the channel will just equal the electrons arriving at the emitter from the base along other leakage paths. Since the channel conductance will not approach zero in this case, the emitter must float at a potential approximately equal to the collector potential. This argument has been given considering the emitter as floating, but it will apply equally well with the roles of collector and emitter interchanged.

These considerations account for the shape of the floating potential curves that have been observed. Figure 2(a) is an experimental curve for a channel which has been "frozen" at dry ice temperature to avoid conditioning effects. The potential of the floating *n*-region closely approximates the potential applied to the other *n*-region until a certain critical voltage is reached, after which its potential saturates.

The most important measurements made on channels were measurements at dry ice temperature of the capacity between the channel and the base layer and of the conductance of the channel between the emitter and collector regions. Both capacity and conductance were determined as a function of the reverse bias applied between the *n*-regions and the base. An impedance bridge was used to measure the capacity between the base and the emitter and collector connected together, Fig. 2(b). Since the capacities of the two internal *p-n* junctions are added to the channel capacity in such a measurement, a correction must be made for them. It was accomplished experimentally by letting the unit stand at room temperature without biases applied until the channel had disappeared. Then, cooling the structure to its previous low temperature, a capacity measurement showed the internal junctions alone. The channel capacity is the difference of these two measurements. The conductance of the channel between the *n*-regions was similarly determined with an impedance bridge, Fig. 2(c), as the difference of the conductances with and without a channel.

Figure 3 shows the results of the capacity and conductance measurements as a function of the bias applied between the *n*-regions and the base. These measurements were made on an *n-p-n* unit having a *p*-layer about 1.5 mils thick and 75 mils in circumference. The surface area of the *p*-type material was thus about 7×10^{-4} cm^2. The *p*-type resistivity was approximately 1 ohm cm at room temperature.

The left-hand ordinate of Fig. 3 refers to the experimental channel-to-base capacity and the capacity predicted from the constants of the *p*-layer (see Sec. 4). The experimental points are plotted with bars indicating the estimated limits of uncertainty in the measurements. The experimental curve at low voltages, although it is not well determined because of the uncertainties in the points, does not seem to have quite the theoretical slope. At biases above about 2 volts the theoretical curve should not apply since it is an approximation which neglects pinch-off. The magnitude of the capacity at low voltages agrees with the predictions about as well as the constants of the *p*-layer are known. In computing the theoretical curve the assumption has been made that the channel exists over the entire surface

[6] The channel is similar in its properties to a field-effect transistor. See W. Shockley, Proc. Inst. Radio Engrs. **40**, 1365 (1952).

of the *p*-layer. This of course may not be the case,and assuming a smaller surface area would result in a proportionately smaller predicted channel capacity. The measurements seem to indicate that the whole *p*-layer surface is involved. These capacity measurements are typical of those made on several channels.

The right-hand ordinate of Fig. 3 refers to the measured channel conductance. In the preceding discussion of saturation floating potentials it was noted that the channel conductance was expected to decrease with increasing bias applied between *n*- and *p*-regions and to approach zero as the bias approached the critical pinch-off voltage. In this respect the conductance measurements verify the predictions. The conductance and capacity of Fig. 3 were measured for the same channel shown in Fig. 2(a). It is interesting to note that the saturation floating potential appears to be in good agreement with what one might select as the pinch-off voltage in Fig. 3. The residual conductance at the higher values of bias in Fig. 3 is apparently due to leakage through the coolant surrounding the unit.

We have noted previously that the conductance and the capacity of a channel are expected to be related to one another. In two respects the measurements do not bear out the expectations. In the first place when the channel is pinched off there should be no mobile electrons left to provide the charge on one plate of the germanium condenser. The capacity should thus approach zero as the conductance approaches zero at the pinch-off voltage. In the experimental curve there is no sharp decrease in capacity between 2 and $2\frac{1}{2}$ volts. The capacity which persists to higher voltages may be a result of nonuniformity in the positive surface charge which would tend to make the channel pinch off at the center of the *p*-layer before it would pinch off at the ends. With this type of nonuniformity, the channel conductance from emitter to collector could approach zero as the channel pinched off in the middle, but there would still be electrons near the ends to provide a capacity at higher values of the bias.

In the second place, the magnitude of the conductance is not at all what one would predict from the capacity data below pinch-off. With a change in bias ΔV_a there is a change in the condenser charge $\Delta Q = C\Delta V_a$. Corresponding to a decrease of V_a from $1\frac{1}{2}$ to 1 volts the experimental capacity is 14 $\mu\mu$f so that $\Delta Q = 7\times10^{-12}$ coulomb. On the channel side of the condenser this charge is provided by the addition of electrons to the channel. It should result in an increase in the channel conductance. If this charge is spread uniformly in a layer of length L (the thickness of the *p*-layer) across which there is a potential difference V, the drift velocity of the electrons in the layer will be $v_D = \mu V/L$. On the average each electron will drift through the channel in a time L/v_D, so that the increase in current corresponding to ΔQ is $\Delta I = \Delta Q v_D/L = \Delta Q \mu V/L^2$. This is equivalent to an increase in conductance

$$\Delta g = \mu \Delta Q/L^2.$$

With $L = 1.5$ mils, $\mu = 6700$ cm²/volt sec (electrons at dry ice temperature) and $\Delta Q = 7\times10^{-12}$ coulomb, $\Delta g = 3\times10^{-3}$ mho. The observed increase in channel conductance for a bias change from $1\frac{1}{2}$ to 1 volt is 1×10^{-5} mho or about 300 times smaller.

There are two possible explanations for this discrepancy: (1) the effective mobility of the electrons in the channel may be lower than the mobility in bulk germanium or (2) the change in charge ΔQ may not all be provided by mobile channel electrons. The thickness of the channel within which the electrons must move is the order of a few hundred angstroms, considerably smaller than the mean free path of electrons in bulk germanium at dry ice temperature $l = 3800$A. The electrons will collide many times with the germanium surface for every time they are scattered by lattice vibrations. If the surface collisions are nonspecular, the first possibility indicated above arises. There is a reduction in the effective electron mobility, and hence in the conductance of the channel. The second possibility takes into account the role of surface states for electrons at the surface of the *p*-layer.[7] If

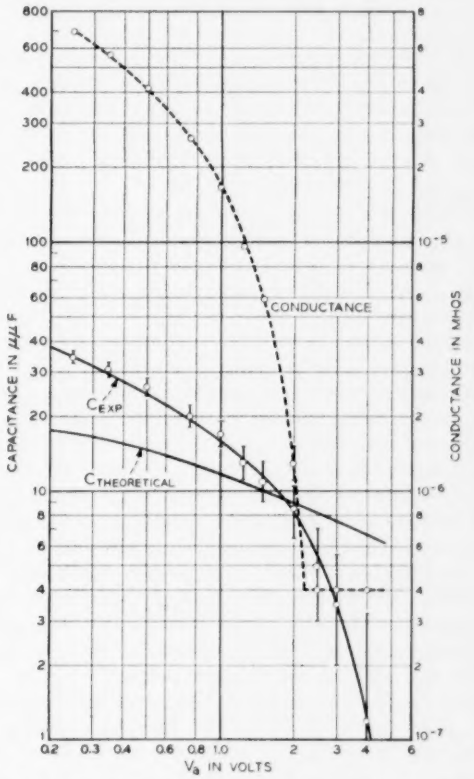

FIG. 3. Experimental channel capacity and conductance.

[7] J. Bardeen, Phys. Rev. **71**, 717 (1947).

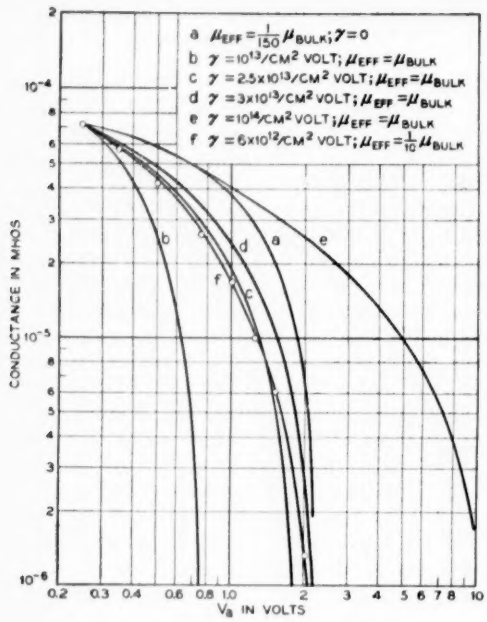

FIG. 4. Theoretical channel conductance.

such states exist, part of the charge associated with a change in bias on the channel will be provided by a change in the charge of the surface states. The corresponding change in conductance will then be smaller than if only mobile electrons had been added to or removed from the channel.

Figure 4 shows the comparison of calculations based on the two possible mechanisms mentioned above with the same experimental conductance points given in Fig. 3. All of the theoretical curves are fitted at the highest conductance point, corresponding to a bias of 0.25 volt. Curve (a) is fitted at this point by assuming the effective electron mobility is lower by a factor of 150 than in bulk germanium at dry ice temperature. It is assumed there are no surface states. There is, however, a second parameter at one's disposal in this calculation. That parameter has been fixed in curve (a) by choosing the pinch-off voltage as 2.2 volts. A factor of 150 reduction in the effective mobility is considerably larger than one would be inclined to select on the basis of the thickness of the channel compared with the normal electron mean free path. A factor an order of magnitude smaller would seem more reasonable. Furthermore, the shape of curve (a) does not agree very well with the experimental points.

Curves (b) through (e) have been computed assuming no reduction in mobility but different surface state densities as indicated. These curves illustrate how rapidly the pinch-off voltage varies with the surface state density. The density 3×10^{13} states/cm² volt gives pinch-off at the desired value of 2.2 volts. This curve (d) more nearly agrees with experimental points than curve (a), but it still is not a particularly good fit.

It is not unreasonable to suppose that both a reduced mobility and surface states play a part in determining the channel conductance. These effects have been introduced simultaneously in computing curve (f). It is fitted at $V_a=0.25$ volt, $V_a=1.0$ volt, and has a pinch-off voltage $V_0=2.2$ volts. The effective mobility for this curve is 10 times smaller than the bulk mobility, and the surface state density is 6×10^{12}/cm² volt. A second channel which has been analyzed in this same way gives an effective mobility about 5 times smaller than the bulk mobility and a surface state density about 2×10^{12}/cm² volt. These surface state densities are an order or magnitude smaller than the densities found by Shockley and Pearson.[2] The differences in the experiments do not make such a factor surprising.

Introducing surface states and a reduced mobility into the model has an insignificant effect on the predicted low voltage channel capacity. Thus by adding these concepts to the original model the relationship between channel capacity and conductance can be made consistent with the data at low voltages. The failure of the capacity to "pinch off" is not resolved by the model and apparently is to be attributed to nonuniformity in the surface charge.

3. ADDITIONAL CHANNEL EXPERIMENTS

The preceding experiments were done with *n-p-n* transistors completely encapsulated in plastic. With the expectation that changing the environment of the germanium surface would produce changes in the properties of the electron channel across the *p*-layer, a few experiments were done with bare *n-p-n* units.

The effect of water vapor on the saturation currents of *n-p-n* transistors was observed by Pietenpol and Ciccolella of the Bell Telephone Laboratories.[8] They found that large increases in current could be produced by increasing the relative humidity. Channels were found to show this same sensitivity to water vapor. An *n-p-n* with a high floating potential at moderate humidity would lose all evidence of a channel when put into a container with a desiccant.

It was also observed that the vapors of nitrobenzene and formamide, organic substances with large dipole moments, gave high floating potentials, but the possibility that water was a contributing factor in these experiments was not entirely eliminated. Benzene, carbon tetrachloride, and toluene, however, produced no channels.

It was found that the encapsulation process used on the *n-p-n* units of the previous experiments did not prevent the penetration of water vapor to the transistors. This strongly suggests that water vapor is responsible for the channels on these units.

[8] W. J. Pietenpol and D. F. Ciccolella (private communication).

In two bare *n-p-n*'s no channels at all were developed by conditioning even in atmospheres of high humidity. These were units having a 25-mil and a 37-mil *p*-layer. This result is consistent with either of the proposed mechanisms by which the surface of the *p*-layer might obtain its positive charge.

In several respects the channels produced by conditioning *n-p-n* units are not altogether satisfactory. In the first place to examine the properties of the channel as a function of the potentials applied to it one must go to low temperatures to achieve stability. Furthermore, the actual surface area of the channel is unknown.

In the hope of producing a channel over which there was a more direct control a number of experiments were done with a drop of the electrolyte glycol borate covering the *p*-layer of a bare *n-p-n*. By means of a gold electrode a potential was applied to the electrolyte with respect to the *p*-type material. When this potential is positive, a layer of positive ions will be formed at the germanium surface, and a channel will be produced if the ions are numerous enough.

The most satisfactory result of these experiments was obtained with an *n-p-n* slab having a 37-mil *p*-layer. The floating potential varied with the potential of the gold electrode in the way expected. With the *p*-layer at ground, grounding the gold electrode or applying a negative voltage to it produced a small floating potential, consistent with the predictions of diffusion theory. Positive voltages on the gold electrode gave floating potentials which increased with increasing applied voltage. The channel conductance and capacity measurements also showed the expected qualitative changes with bias and with the gold electrode potential. However, the channel was not stable enough in time to permit a satisfactory comparison with the detailed calculations made from the model. Furthermore, lowering the temperature did not improve the situation in this case. In fact it eliminated the channel altogether.

Other *n-p-n* units with glycol borate were considerably less satisfactory than this one, a common result being the appearance of an inductance when a capacity was expected. In all cases, including the best one, the currents drawn by the two junctions in reverse increased from 10- to 100-fold when the electrolyte was placed across them.

In addition to these experiments with double function devices, several attempts were made to use an electrolyte in conjunction with a single *p-n* junction. The idea was the following: If a channel could be developed extending out over the material on one side of the junction, hole electron pairs introduced into the channel by light might provide a measurable photo-current with the light farther from the junction than it would if the channel were absent. There was only a slight indication that such an effect occurred.

The use of glycol borate to develop channels was in general unsatisfactory. It did not provide a more direct and stable control over channels (the principal reason it was used). It further complicated the situation by always producing lower reverse junction impedances and often providing inductances when capacities were expected. These effects are not yet understood.

4. THEORETICAL CONSIDERATIONS

In this section the principal features of the *n*-type surface conductivity discussed in the preceding pages will be presented in a more mathematical form. The scheme of representation to be used is indicated in Fig. 5(a). Only the *p*-type base region is shown. The energy of an electron is plotted vertically with E_c the bottom of the conduction band and E_v the top of the valence band. The negatively charged acceptor centers are shown as energy levels in the energy gap just above E_v. The mobile holes are just below E_v in the valence band. The Fermi energy is $-q\varphi$, where φ is the Fermi potential and q the electronic charge. The electrostatic potential ψ in the crystal will be measured so that the energy $-q\psi$ is that appropriate to an electron in the middle of the energy gap.[9] With this definition of ψ,

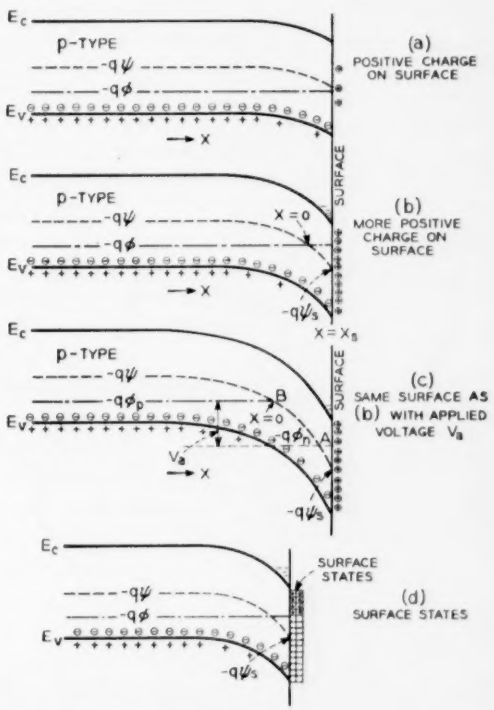

FIG. 5. Effective of positive charge at a *p*-type surface.

[9] This assumes equal effective masses for electrons and holes. If the masses are different, ψ is measured at a level slightly displaced from the center of the forbidden region. Details of this procedure together with a discussion of the quasi-Fermi potentials will be found in W. Shockley, *Electrons and Holes in Semiconductors* (D. van Nostrand Company, Inc., New York, 1950), Chap. 12.

when $\psi=\varphi$ the hole and electron concentrations are equal to the intrinsic concentration n_i. For the equilibrium case:

$$p=n_ie^{q(\varphi-\psi)/kT},\quad n=n_ie^{q(\psi-\varphi)/kT}.$$

In a nonequilibrium case it will be convenient to define two quasi-Fermi potentials φ_n and φ_p such that

$$p=n_ie^{q(\varphi_p-\psi)/kT},\quad n=n_ie^{q(\psi-\varphi_n)/kT}.$$

We will first examine the appearance of a channel from the standpoint of the energy bands in germanium. When positive charge is placed on the surface of p-type germanium it will produce an electric field which distorts the energy bands in the crystal, producing a negative space charge inside the surface to compensate for the positive surface charge. If the surface charge is small, the p-type material will simply have fewer holes near the surface, the space charge being made up entirely of ionized acceptor centers, Fig. 5(a). If the positive surface charge is large enough, the energy bands may be bent to such an extent that the electrostatic potential crosses the Fermi potential, and electrons become more numerous than holes, Fig. 5(b). This situation can apply only very close inside the germanium surface, but it results in a layer of n-type conductivity on the normally p-type material. It will constitute a channel if the p-type material appears as the base in an n-p-n transistor. The details of the space charge region for this case of larger surface charges provide the channel characteristics that have previously been described.

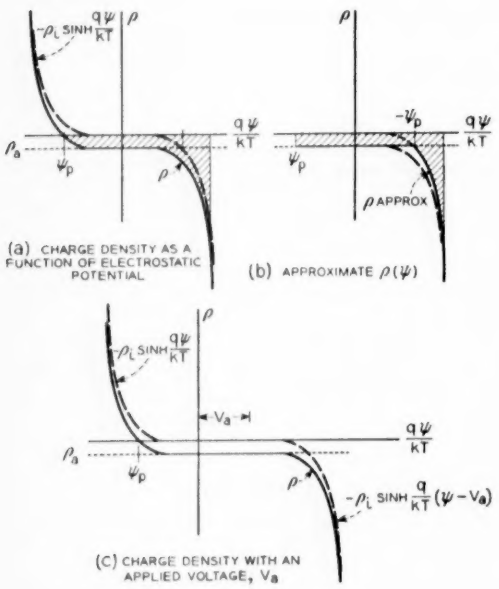

FIG. 6. Theoretical charge densities.

We will assume a one-dimensional problem: p-type germanium with uniform properties extending indefinitely to the left of a plane on which there is a uniform surface charge with a density Q_s. We will also assume that there is no electric field outside of the germanium so that the system as a whole is electrically neutral. We will measure potentials with respect to the Fermi potential in the equilibrium case and will select as origin of the x-coordinate the plane in the p-type material at which $\varphi=\psi$.

Within the semiconductor of dielectric constant κ and having a charge density ρ, Poisson's equation,

$$d^2\psi/dx^2=-4\pi\rho/\kappa, \tag{1}$$

is to be satisfied with the following boundary conditions: (a) $x=-\infty$, $\psi=\psi_p$, $d\psi/dx=0$. Deep in the interior of the p-type material the potential approaches ψ_p, the value which it would have in the absence of a surface charge. The electric field vanishes at this point.

(b) $(d\psi/dx)_{x_s}=4\pi Q_s/\kappa$. Gauss' theorem applied to the charged surface leads to this boundary condition for the electric field in the germanium at $x=x_s$.

Multiplying (1) through by $d\psi/dx$ and integrating,

$$\left(\frac{d\psi}{dx}\right)^2=\frac{-8\pi}{\kappa}\int_{\psi_p}^{\psi}\rho d\psi. \tag{2}$$

In the equilibrium case, $\rho(\psi)$ has the form

$$\rho=\rho_i\sinh(q\psi/kT)+\rho_a \tag{3}$$

where $\rho_i=2qn_i$ and $\rho_a=-qN_a$. N_a is the density of acceptors. Figure 6(a) shows $\rho(\psi)$. The dashed line is the charge density due to mobile carriers, predominately holes for $\psi<0$, predominately electrons for $\psi>0$. The dotted line is the charge density of ionized acceptors. The solid line is the sum of these, the total charge density. Here ψ_p is the value of ψ for which $\rho=0$ since electrical neutrality exists in the undisturbed p-material. The square of the electric field corresponding to some value of ψ is then proportional to the area under the curve and between ψ_p (a negative quantity) and ψ. One such area is shown shaded in Fig. 6(a). It is clear that with known values of Q_s and ρ_a the total electrostatic potential difference between the interior and the surface can be found by simply extending the integral to a value of $\psi=\psi_s$ satisfying the boundary condition (b) above. This is equivalent to saying that in order for the system to be electrically neutral the charge per unit area in the space charge region must be equal and opposite to Q_s.

For values of ψ close to zero the charge density of holes and electrons is small compared with the fixed charge density of acceptors. As ψ approaches $-\psi_p$, n-p increases rapidly and greatly exceeds N_a for values of ψ larger than $-\psi_p$ by a few times kT/q. To simplify the integral (2) we will approximate the actual $\rho(\psi)$ as

given in (3) by: $\rho=\rho_a$ for $|\psi|<\psi_p$, and

$$\rho=-\rho_i\sinh(q\psi/kT)\cong-qn_ie^{q\psi/kT} \quad \text{for} \quad \psi>-\psi_p. \tag{3}$$

This approximates the area shown shaded in Fig. 6(a) by that shaded in Fig. 6(b). For values of $\psi<-\psi_p$, the square of the electric field will be larger in this approximation than it actually is. For $\psi>-\psi_p$, it will be smaller. For the experimental conditions which have been encountered, the field given by this approximation is in error by less than 10 percent for any $\psi>-\psi_p$, and for most values of ψ in this range the error is considerably smaller.

In considering the properties of channels, we will only be concerned with values of Q_s large enough so that electrons will be present at the germanium surface with a density $n>N_a$. This is equivalent to restricting our attention to surface charges so large that boundary condition (b) will require extension of the field integral to values of $\psi>-\psi_p$.

In the nonequilibrium case when a voltage is applied between the p- and n-regions, the carrier densities are to be expressed in terms of the quasi-Fermi potentials φ_n and φ_p. The variations in the quasi-Fermi potentials in the present situation are quite similar to those discussed by Shockley[3] for normal p-n junctions. The applied potential establishes a difference between φ_n in the n-type material and φ_p in the p-type material. Furthermore the quasi-Fermi potentials will have only a small slope in the material for which they specify the density of the majority carrier. In the n-p-n structure with a channel, the high electron density at the surface of the p-region is in effect an n-type layer connected to the normal n-regions at either end. The potential applied between the p-region and the two n-regions connected together thus appears as a difference $V_a=\varphi_n-\varphi_p$ between φ_n which describes the concentration of electrons in the channel and φ_p which describes the hole concentration in the base. The situation is shown in Fig. 5(c). φ_n and φ_p have been drawn horizontal over the range for which they represent the majority carrier. We will not be concerned with the shape of φ_n to the left of A or with the shape of φ_p to the right of B. They will certainly not recross the electrostatic potential line so that between A and B the hole and electron densities will both be less than n_i.

Figure 6(c) indicates the nonequilibrium dependence of ρ on ψ. We now measure potentials with respect to φ_p in the body of the p-material. As in the equilibrium case we get the square of the electric field at any point as the area under ρ between ψ_p and the value of ψ appropriate to the point. Since the surface field is fixed by (b), as V_a is increased the number of electrons in the channel will decrease, a greater fraction of the total space charge that is required by Q_s being provided by acceptor ions. Eventually as V_a is increased to a critical voltage V_0, the surface field will be provided by the acceptor ions alone, no electrons will be required, and the channel will be "pinched off." As in the equilibrium case we will approximate the sum of fixed and mobile charges by the larger of the two.

$$\begin{aligned} &\rho=\rho_a, && \psi_p<\psi<V_a-\psi_p,\\ &\rho=-qn_ie^{q(\psi-V_a)/kT}, && V_a-\psi_p<\psi<\psi_s. \end{aligned} \tag{4}$$

With this approximation the criterion for pinch-off will be that value of $V_a=V_0$ for which $\psi_s=V_0-\psi_p$ or $\psi_s-\varphi_n=-\psi_p$; the difference between the electrostatic potential and the quasi-Fermi level for electrons is just just such as to make $n=N_a$ at the surface.

The actual charge Q_s on the surface has not been measured, but a knowledge of V_0 will suffice since it allows an approximate calculation of the surface field to be made if ρ_a is known. It was indicated in the preceding section that a measurement of the floating potential of one n-region as a function of the bias applied to the other n-region in an n-p-n structure should show a saturation floating potential approximately the pinch-off voltage. If the leakage paths for electrons to the floating n-region have a very low conductance, the saturation floating potential will be a good approximation to V_0. Of course, by measuring the channel conductance directly as a function of bias, V_0 may be determined.

When the channel is pinched off, the charge density making up the whole space charge layer will be approximately ρ_a. The electric field integral (2) is then

$$E_s^2=\left(\frac{d\psi}{dx}\right)_{x_s}^2=\frac{-8\pi}{\kappa}\int_{\psi_p}^{\psi_s=V_0-\psi_p}\rho_a d\psi=\lambda(V_0-2\psi_p), \tag{5}$$

where $\lambda=(8\pi/\kappa)(-\rho_a)$. If the applied voltage is insufficient to pinch off the channel the charge density will be approximately given by (4). The electric field integral gives a value at the surface:

$$E_s^2=\lambda\left\{V_a-2\psi_p+\frac{kT}{q}\left[e^{q[\psi_s-(V_a-\psi_p)]/kT}-1\right]\right\}. \tag{6}$$

Since the surface charge Q_s is assumed to be constant with variations in V_a, the electric field at the surface must be the same for $V_a=V_0$ or for any smaller value: (5) and (6) must be equal. This provides a condition determining ψ_s as a function of V_a;

$$\psi_s=V_a-\psi_p+\frac{kT}{q}\ln\left[\frac{V_0-V_a}{kT/q}+1\right]. \tag{7}$$

This value of the electrostatic potential at the surface, or more directly the difference ψ_s-V_a, gives the electron density at the surface from (4). We could make use of this density to compute the total number of electrons in the channel per unit of surface area, but we will see presently that there is a simplier method of achieving the same result.

We shall have occasion later to use an expression for the electric field at points throughout the space charge region. The field corresponding to any value of ψ is obtained using (2) and (4).

$$E_s^2=\left(\frac{d\psi}{dx}\right)^2=\lambda(\psi-\psi_p) \quad \text{if} \quad \psi_p<\psi<V_a-\psi_p,$$

$$E_s^2=\lambda\left\{V_a-2\psi_p+\frac{kT}{q}\left[e^{q[\psi_s-(V_a-\psi_p)]/kT}-1\right]\right\} \quad \text{if} \quad V_a-\psi_p<\psi<V_0-\psi_p. \tag{8}$$

In Eq. (6) which gives the square of the surface electric field, the first two terms, $\lambda(V_a-2\psi_p)$, represent the contribution that is made by the acceptor ions alone. The difference between the surface field, E_s, and the field produced by the acceptors alone $E_1=[\lambda(V_a-2\psi_p)]^{\frac{1}{2}}$ is proportional to N, the total number of channel electrons per unit of surface area. By Gauss' theorem,

$$4\pi qN/\kappa=E_s-E_1, \tag{9}$$

and using (5):

$$4\pi qN/\kappa=[\lambda(V_0-2\psi_p)]^{\frac{1}{2}}-[\lambda(V_a-2\psi_p)]^{\frac{1}{2}}. \tag{10}$$

The conductance of the channel is directly related to the quantity qN. If Q is the total electron charge in the channel, L is the channel length, and μ the electron mobility, the channel conductance is

$$g=Q\mu/L^2.$$

using the same reasoning applied for a similar case in Sec. 2. However,

$$Q=(qN)wL,$$

where w is the width of the channel, so that

$$g=qN\mu w/L.$$

From (9)

$$g=\mu(w/L)[\kappa(-\rho_a)/2\pi]^{\frac{1}{2}}[(V_0-2\psi_p)^{\frac{1}{2}}-(V_a-2\psi_p)^{\frac{1}{2}}]. \tag{11}$$

This expression indicates a monatonic decrease in conductance as V_a is increased from zero toward V_0. At $V_a=V_0$ the conductance apparently becomes zero. The detailed dependence of g on V_a for very small values of g is not properly represented by (11) because we have neglected electron densities $n<N_a$. The value of the conductance below which this detail becomes important is, however, much smaller than the smallest channel conductance that has been measured.

It was mentioned earlier that the channel electrons were confined to move in a very thin layer adjacent to the germanium surface. We are now in a position to make an approximate evaluation of this thickness. The density of electrons decreases by $1/e$ for a decrease of kT/q in ψ as we go away from the surface. ψ changes by kT/q in a distance which falls within the limits

$$kT/qE_1>\tau>kT/qE_s.$$

The upper limit is the distance over which the potential would change by kT/q is there were only the electric field of the acceptor ions. The lower limit is the distance corresponding to the electric field at the surface. Most of the channel electrons are constrained to move in a layer of thickness τ. E_1 of course increases with V_a, but for material which is 1 ohm cm p-type at room temperature and a floating potential of 2 volts, the upper limit for τ will never exceed a few hundred angstroms. The lower limit for this case will be about 80A.

We have already indicated in Fig. 5(b), (c) that the space charge layer increases in thickness as the applied voltage is increased. As a result, some holes are expelled from the p-material and an equal number of electrons are removed from the channel. This effect is describable as a capacity when V_a has a small ac component. On a unit area basis,

$$C=(-\rho_a)dx/dV_a, \tag{12}$$

since $(-\rho_a)dx$ is just the charge of the holes expelled by an increase dV_a which results in a width increase dx.

We can obtain the width of the space charge layer by a second integration of the field integral (2). If $(d\psi/dx)^2=f(\psi)$, the distance from $x=0$ (the point at which $\psi=0$) to the surface will be

$$x_s=\int_{\psi=0}^{\psi_s}\frac{d\psi}{\sqrt{f(\psi)}}. \tag{13}$$

This is not the total extent of the distortion of the energy band because we have neglected the part corresponding to $\psi<0$. As ψ decreases until it only exceeds ψ_p by the order of kT/q, it subsequently approaches ψ_p exponentially with a characteristic length, the Debye length. Thus the disturbance produced by the surface charge actually extends indefinitely far into the interior of the p-material. However as we change V_a we do not change the electric field for any values of $\psi<0$, so that, whatever the shape of the energy bands to the left of $x=0$, it will remain the same for any V_a and will simply move as a whole with respect to the surface as x_s changes. Thus what we require in (11) is the variation of x_s with V_a.

We can think of x_s as made up of two parts: x_1 the distance to the right of $x=0$ over which the acceptors contribute the predominate charge, and x_2 the width of the channel, i.e., the distance adjacent to the surface over which electrons out-number the acceptors. As V_a increases, x_1 increases and x_2 decreases. Except near pinch-off, x_2 varies much more slowly with V_a than x_1 does. We will make the approximation that dx_s/dV_a

$\sim dx_1/dV_a$. From (8) and (12),

$$x_1=\int_{\psi=0}^{V_a-\psi_p}\frac{d\psi}{\sqrt{f(\psi)}}=\int_0^{V_a-\psi_p}\frac{d\psi}{[\lambda(\psi-\psi_p)]^{\frac{1}{2}}},$$

so that

$$dx_1/dV_a=1/[\lambda(V_a-2\psi_p)]^{\frac{1}{2}},$$

and

$$C=\frac{(-\rho_a\kappa/8\pi)^{\frac{1}{2}}}{(V_a-2\psi_p)^{\frac{1}{2}}}. \tag{14}$$

For 1 ohm-cm p-type material this differential capacity is

$$C=2\times10^{-8}/(V_a-2\psi_p)^{\frac{1}{2}}\quad\text{farad/cm}^2,$$

where the potentials are in volts.

Expression (14) has been plotted in Fig. 3. As a result of neglecting the variation of x_2 with V_a (14) does not include any upper limit for V_a. Such a limit does exist, however, and for $V_a=V_0$ the capacity should be zero. The details of the way in which C approaches zero as V_a approaches V_0 require a more complete treatment than has been given above.

To a rough approximation C varies as $V_a^{-\frac{1}{2}}$ (the dependence to be expected in a p-n junction formed with a sudden change in impurity concentration). However, no values of V_0 have been observed which are large enough to make this approximation valid over any reasonable range of V_a. Simply adding more ions to the surface of the p-region to increase the floating potential by a large amount does not in general produce a simpler situation. In the first place, if V_0 becomes very high, at $V_a=0$ the number of electrons required to satisfy the surface field will be so large that degeneracy will exist, the Fermi level will rise above the bottom of the conduction band, and the simple charge density expression (6) will no longer hold.

In the second place, as the number of ions on the surface increases, the electric field at the surface will also increase and ultimately will exceed the Zener field in germanium. At this point the normal high impedance junction between the channel and the p material will be shunted by the low impedance Zener region, and the simple channel conductance from one n-region to the other will be drastically changed. As V_0 is increased by putting more and more ions on a particular p-layer, at room temperature, the Zener condition will be reached in germanium before degeneracy occurs. In fact, except for values of $N_a>10^{18}/\text{cm}^3$, for a Zener field of 10^5 volt/cm degeneracy will not become the primary consideration until the temperature is lowered below about 80°K.

It is interesting to note how high the electric fields actually are at the surface to give floating potentials of the order measured. From (6)

$$(d\psi/dx)_{x_s}=[8\pi(-\rho_a)/\kappa]^{\frac{1}{2}}(V_0-2\psi_p)^{\frac{1}{2}},$$

which for the same special case we have previously considered ($V_0=2.0v$, 1Ω cm p-type) gives

$$(d\psi/dx)_{x_s}=4\times10^4\quad\text{volt/cm}.$$

This is a field not a great deal smaller than the Zener field.

The effect of introducing surface states into the problem will be considered briefly. We will assume that there are electron surface states distributed uniformly in the energy gap, Fig. 3(d). These states will be assumed neutral when filled with an electron and positively charged when empty. They are characterized by two parameters: γ the density of states per unit area per unit potential, and Q_0 the net charge per unit area in the surface states if they are filled up to the middle of the energy gap. The Fermi potential indicates the actual level of filling, and since ψ by definition lies at the middle of the energy gap, the charge in the surface states in general is

$$Q_0-q\gamma(\psi_s-\varphi_n).$$

This changes the boundary condition (b) to

$$(d\psi/dx)_{x_s}=(4\pi/\kappa)[Q_0-q\gamma(\psi_s-\varphi_n)].$$

Or, measuring potentials with respect to φ_p as we have done before,

$$(d\psi/dx)_{x_s}=(4\pi/\kappa)[Q_0-q\gamma(\psi_s-V_a)]. \tag{b'}$$

If the same approximations are made for $\rho(\psi)$ as were made in the previous case, we again obtain Eqs. (5) and (6) by simply integrating the charge density from deep in the interior of the p-type material to the surface. However, the boundary condition at the surface no longer requires that the surface field be a constant, independent of V_a, because of the presence of the surface states. Expressions (5) and (6) cannot simply be equated. For each V_a, ψ_s must be determined from (6) and (b'). From the value of ψ_s and using (b') and (9) the density of the channel electrons, N, can be found.

In calculating ψ_s the two surface state parameters are at our disposal. As in the previous case Q_0 is directly related to the pinch-off voltage V_0 and may be determined from it. γ can then be chosen so that the channel conductance fits the experimental value at some V_a assuming a value for the electron mobility.

The author is particularly indebted to W. Shockley for his part in this work. His suggestions during its progress and his assistance with the manuscript have contributed materially to the appearance of this paper.

I am also much indebted to M. Sparks and K. D. Smith who provided most of the transistors used in this study.

A Generalized Self-Consistent Field Method*

J. C. SLATER
Massachusetts Institute of Technology, Cambridge, Massachusetts
(Received April 14, 1953)

A self-consistent field method is set up, general enough to be used in case we are treating configuration interaction between any number of states each represented by a single determinantal wave function. Thus it is more general than the Hartree-Fock method, which is limited to a single determinantal wave function. We cannot use a variation method, for if a sufficiently extensive configuration interaction is carried out, an equally good final value of the energy and wave function will be obtained irrespective of the one-electron functions used. Instead, we return to the original postulate of Hartree, that each electron is assumed to move in the averaged charge distribution of all other electrons, and all nuclei. It is shown that when this condition is properly interpreted, it leads to a unique potential for the self-consistent field, all the one-electron orbitals being solutions of the same Schrödinger equation, and hence orthogonal to each other. This field is somewhat different from that of Hartree, who did not literally follow this prescription for finding the potential. For the case where we are using a single determinantal function, the present method reduces to the simplification of the Hartree-Fock method recently proposed by the writer.

THE Hartree-Fock method, and the simplification of it recently suggested by the writer,[1] rest on the assumption that we are dealing with an n electron wave function given by a single determinant, or antisymmetrized product, formed from n one-electron orbital functions of coordinate and spin. Often, however, we wish to deal with a more general case, in which the wave function is approximated by a linear combination of such determinantal wave functions. The process of combining such determinants to get a better approximation than can be secured by one alone is generally called configuration interaction. In this note we shall examine the more general self-consistent field method to be used in such cases of configuration interaction.

If we start with a complete orthogonal set of one-electron spin-orbital functions u_i, then the products $u_j(x_1)u_k(x_2)\cdots u_p(x_n)$, where the indices j, k, $\cdots$, p are to take on all combinations of values, obviously form a complete orthogonal set of n electron functions coordinates and spin, and the antisymmetrized products or determinants $(n!)^{-\frac{1}{2}}\det\{u_j(x_1)u_k(x_2)\cdots u_p(x_n)\}$ form a complete orthogonal set of antisymmetric n electron functions of coordinates and spin. Thus the exact wave function of an n electron problem can be expanded as a linear combination of such determinantal functions, so that a proper treatment of configurational interaction can give an exactly correct solution and can yield a function which takes full account of the correlation between the motion of electrons, though of course it is well known that a single determinantal function by itself does not correctly describe this correlation. The expansion of a given wave function in terms of determinantal wave functions may be slowly convergent; studies of the problem of the ground state of helium by Taylor and Parr,[2] and by Green *et al.*[3] show that in this case the convergence is rather slow. On the other hand, the recent success of Meckler[4] in studying the oxygen molecule suggests that in at least some important cases the method of configuration interaction may converge well enough to be of practical value. It is well known that the Heitler-London and valence-bond methods can be regarded as examples of configuration interaction between a number of different configurations set up in terms of antisymmetrized products of molecular orbitals. Thus any advantages lying in those methods can surely be secured by using configuration interaction, between a relatively limited number of configurations. The case of oxygen studied by Meckler included enough configurations so that his treatment is more general than a valence-bond method, and the same thing is true of various other investigations under way in this laboratory.

Let us then consider the problem of determining the one-electron orbitals u_j by a self-consistent method. It is at once obvious that no variation method, like the Hartree-Fock procedure, can be used in this case, for that depends on choosing those u_i's which allow us to make the best single determinantal function. In the present case, no matter what orbitals we use, provided they form a complete orthogonal set, we can eventually get a precisely correct answer, by carrying the configuration interaction far enough. The only criterion which we can now use to determine the u_i's is that we wish the set in terms of which the process of configuration interaction will give a series which converges most rapidly. This is not a criterion which is readily expressed analytically. Accordingly we turn in quite a different direction for the determination of the u_i's and go back to something much more like Hartree's original intuitive argument for setting up the self-consistent field. We shall demand very simply that the u_i's be solutions of a Schrödinger equation representing the motion of an

* Assisted by the U. S. Office of Naval Research.
[1] J. C. Slater, Phys. Rev. **81**, 385 (1951).
[2] G. R. Taylor and R. C. Parr, Proc. Natl. Acad. Sci. **38**, 154 (1952).
[3] Green, Mulder, Ufford, Slaymaker, Krawitz, and Mertz, Phys. Rev. **85**, 65 (1952).
[4] A. Meckler, Quarterly Progress Reports, Solid-State and Molecular Theory Group, Massachusetts Institute of Technology, July 15, 1952, p. 62; October 15, 1952, p. 19 (unpublished).

electron in the field of all nuclei, and in the field of all other electrons, averaged over the motions of these other electrons.

This very simple requirement leads to a perfectly unique Schrödinger equation. Let the wave function of all n electrons be $U(x_1, \cdots, x_n)$. This is an antisymmetric function, which may well be expressed as a linear combination of determinantal functions of the type we have just been discussing. The quantity $U^*(x_1 \cdots x_n) \times U(x_1 \cdots x_n) dx_1 \cdots dx_n$ measures the probability that simultaneously electron 1 be in dx_1, $\cdots$electron n in dx_n (where we are including the spins with the coordinates). The electrostatic interaction energy between electron 1 and all other electrons is $\sum(j)e^2/r_{1j}$, where j goes from 2 to n, and r_{1j} is the distance from electron 1 to the jth electron. Thus

$$dx_1 \int U^*(x_1 \cdots x_n) \sum(j) e^2/r_{1j} U(x_1 \cdots x_n) dx_2 \cdots dx_n$$

can be considered as the probability that the electron 1 be in dx_1, times the average value of the electrostatic interaction energy as averaged over all positions and spins of the electrons $2 \cdots n$. Since the probability that electron 1 be in dx_1, irrespective of the positions of other electrons, is $dx_1 \int U^*(x_1 \cdots x_n) U(x_1 \cdots x_n) dx_2 \cdots dx_n$, we see that the average potential energy of interaction between electron 1 and all other electrons, when electron 1 has coordinates and spin given by x_1, is

$$V_e(x_1) = \frac{\int U^*(x_1 \cdots x_n) \sum(j) e^2/r_{1j} U(x_1 \cdots x_n) dx_2 \cdots dx_n}{\int U^*(x_1 \cdots x_n) U(x_1 \cdots x_n) dx_2 \cdots dx_n}. \quad (1)$$

If we add this to $V_n(x_1)$, the potential energy of an electron of coordinate and spin x_1 in the field of the nuclei, to get $V(x_1)$, then we see that $V(x_1)$ represents the average potential energy of the electron of coordinates and spin x_1, averaged over the motions and spins of all other electrons. We assume, then, that the correct generalization of the method of the self-consistent field is to set up a one-electron Schrödinger equation moving in this potential $V(x)$.

We have already mentioned (reference 1) the simplification of the Hartree-Fock method, by which a single Schrödinger equation was introduced in place of the Hartree-Fock equations, in the case where the wave function of the many-electron problem could be written as a single determinant. If we replace our function U by a single determinant, then it is easily shown that our Schrödinger equation reduces to that given in Eq. (7) of reference 1, so that the method of reference 1 is a special case of that which is now proposed. We can give the same interpretation to the potential V_e that was done in reference 1. That is, it is the potential energy of interaction of the electron with coordinates and spin x_1, with an electronic distribution of density

$$(n-1) \frac{\int U^*(x_1 \cdots x_n) U(x_1 \cdots x_n) dx_3 \cdots dx_n}{\int U^*(x_1 \cdots x_n) U(x_1 \cdots x_n) dx_2 \cdots dx_n}, \quad (2)$$

with coordinates and spin given by x_2. This electronic distribution consists of a total charge equal to $(n-1)$ electrons, and its density goes to zero when x_2 equals x_1; that is, when electrons 1 and 2 have the same spin and are at the same position of space. That is just as if the electronic distribution consisted of the whole charge of n electrons, diminished by an exchange charge whose properties are like those discussed in reference 1. In other words, the qualitative discussion given in reference 1 is more general than the assumption made there that the wave function could be represented by a single determinant or a single configuration. In particular, the simplification introduced in Sec. 5 of reference 1, replacing the exchange potential by a value calculated from a free-electron gas, is as plausible a simplification in the general case of configuration interaction as it is for the single determinantal function, and is not tied in any way to the Hartree-Fock case.

One way to appreciate the useful features of the expression (1) for the potential V_e is to ask how to calculate the electronic repulsive interaction energy of the whole system. The average values of each term e^2/r_{ij} over the wave function are the same, on account of the antisymmetry of the wave function, and since there are $n(n-1)/2$ pairs, the total interaction energy will be just $n(n-1)/2$ times the integral for one term. Now if we multiply $V_e(x_1)$, as given in Eq. (1), by the denominator $\int U^*(x_1 \cdots x_n) U(x_1 \cdots x_n) dx_2 \cdots dx_n$, and integrate over dx_1, the result will be just the value of $(n-1)$ interaction terms like e^2/r_{ij}. Thus the total interaction energy will be $n/2$ times as great as this. But $n \int U^* U dx_2 \cdots dx_n$ is just the total charge density, in units of the electronic charge. Thus we see that the total electronic interaction energy can be written as

$$\tfrac{1}{2} \int \rho(x_1) V_e(x_1) dx_1, \quad (3)$$

where $\rho(x_1)$ is the electronic charge density at the position and with the spin given by x_1.

The expression (3) is formally just like the interaction energy of a charge distribution with itself in classical electrostatics; only in the classical case, V_e would be related to ρ by Poisson's equation, whereas here it is not. The possibility of writing the electrostatic energy in this form, in the quantum theory, has been discussed by the writer,[5] using arguments closely related to those

[5] J. C. Slater, Revs. Modern Phys. **6**, 209 (1934).

of the present note. The reader should realize clearly that, if the exact wave function of the problem is used in calculating the potential $V_e(x_1)$ of Eq. (1), and in calculating the charge density, then Eq. (3) represents an exact result, including all exchange terms. The total electrostatic energy of the system of course includes in addition to (3) the interactions between electrons and nuclei, which can be computed from the charge density $\rho(x_1)$ alone, and the interactions between pairs of nuclei.

We have now seen that there is a straightforward method in principle for setting up a self-consistent field calculation for any atomic or molecular system. We set up the potential $V_e(x)+V_n(x)$, using Eq. (1) for $V_e(x)$. We solve Schrödinger's equation for the one-electron orbitals in this potential field. By general properties of Schrödinger's equation, these orbitals form a complete orthogonal set. We form from them a complete set of antisymmetrized products of n one-electron functions, and set up and solve the secular problem involved in finding those linear combinations of antisymmetrized products which make the energy of the n electron system stationary. One of the resulting solutions represents the state of the system in which we are particularly interested. We then take the antisymmetric wave function U representing this state, formed as a sum of the antisymmetrized products, and insert it in Eq. (1) to find a new V_e. Our condition of self-consistency implies that this final V_e should be identical with the original value.

The one-electron orbitals which we have obtained in this way are what are usually called molecular orbitals. Most writers, for instance Lennard-Jones[6] and Roothaan,[7] have derived molecular orbitals from the Hartree-Fock method. On account of the involved nature of this method, their discussions are necessarily somewhat complicated. In contrast, the present method, setting up a unique potential and Schrödinger equation of the usual sort, of which the molecular orbitals are eigenfunctions, makes a discussion much simpler. For instance, the potential V_e will usually have the same symmetry as the nuclear system, so that the application of the group theory to the discussion of the symmetry properties of the molecular orbitals follows very straightforwardly. Another advantage of the present method is that it gives us an infinite set of orbitals, in a much more direct way than the Hartree-Fock method, and the configuration interaction gives us (in principle) an infinite number of solutions, representing excited configurations. Since the one-electron orbitals are not chosen to make the problem self-consistent for these excited configurations, the process will presumably not converge as rapidly for these other configurations as for the ground state (if, as usual, it is the ground state which is made self-consistent), but the calculation of these excited configurations is on as firm a theoretical basis as that of the ground state.

The procedure which we have outlined is of course an idealized one which could never be carried through in practice, since we can neither solve the one-electron Schrödinger problem exactly to get the one-electron orbitals, nor carry out exactly the problem of configuration interaction. In an actual case, then, one must compromise, and our general discussion has been more with the aim of suggesting an ideal toward which one may aim in the calculation, than with the hope that it can represent a practicable program. We should ordinarily set up approximate solutions of the self-consistent problem in the form of linear combinations of atomic orbitals. We then note the following situation. If we are using a finite and very limited set of orbitals, and are solving the configuration interaction problem between all configurations which can be set up from these orbitals, as Meckler did in the work referred to, then we can equally well set the problem up in terms of any linear combinations of the orbitals. As Meckler has pointed out, the final result will be independent of what linear combinations we use. In such a case, it is useless extra labor to find those combinations of our orbitals which best represent solutions of the self-consistent field problem. This is the special case, for a limited number of orbitals, of the general statement that if we are completely solving the problem of configuration interaction, it makes no difference what complete orthogonal set of one-electron orbitals we use.

The difficulty with Meckler's procedure, however, is that as the number of electrons and orbitals goes up, the number of interacting configurations increases enormously. In such a case we can obviously handle interaction only between a limited number of configurations, normally those of lowest diagonal energy, and with largest nondiagonal matrix components of energy connecting them with the ground state. We may expect that in such problems, if we are using all configurations arising from N orbitals, then our results will be the more accurate, the more accurately we can write the N lowest molecular orbitals of the self-consistent field problem as linear combinations of these N orbitals. Our aim in setting up linear combinations of atomic orbitals, or other methods of setting up one-electron orbitals, must then be to have a set of unperturbed one-electron functions capable of approximating the lowest N molecular orbitals as accurately as possible.

[6] J. E. Lennard-Jones, Proc. Roy. Soc. (London) **A198**, 1 (1949), and later papers.
[7] C. C. J. Roothaan, Revs. Modern Phys. **23**, 69 (1951).

Band Structures of One-Dimensional Crystals with Square-Well Potentials

G. ALLEN
Lewis Flight Propulsion Laboratory, National Advisory Committee for Aeronautics, Cleveland, Ohio
(Received February 26, 1953)

The energy band structure for a one-dimensional periodic square-well potential is obtained in terms of the well depth for the whole range of possible ratios of well width to hill width. This model bears a closer resemblance to a real crystal since, as potential depth is varied for a fixed ratio of well width to hill width, the curves bounding distinct bands cross while in the case of a delta-function potential no such crossings occur. The location of these crossings is derived. The number of times that a given pair of boundary curves can cross is considered. For the set of boundary curves that belong to a given ratio of well-to-hill widths, this number is unbounded.

I. INTRODUCTION

THE eigenspectrum of the Schrödinger equation for the motion of an electron in a crystal with a periodic potential is continuous except for certain unallowed regions (band structure). Considerable information about many properties of solids (e.g., electrical conductivity and cohesive energy) can be deduced from the structure of the eigenspectrum. In general, approximate methods have to be applied in solving such problems. In order to estimate the validity of a particular method, one can apply it to a one-dimensional model in which the potential is reasonably similar to that assumed for the three-dimensional case. The determination of the band structure in the one-dimensional case may also be useful in providing some insight into the nature of a real crystal.[1]

Mathematically, one has the problem of finding the allowed and unallowed regions of the solution of the equation

$$d^2\psi/dx^2+[E-V(x)]\psi=0, \qquad (1)$$

where E is the total energy and $V(x)$ is a periodic function which in some way possesses properties similar to those of the potential for real crystals. A particularly simple form of $V(x)$ is provided by the function $V_0S(x)$, where V_0 is the depth of the potential well (or height of the potential hill) and $S(x)$ is a periodic function like that shown in Fig. 1 which takes on only the values 0 and 1. In Fig. 1, h is one-half the width of the hill and w is one-half the width of the well.

Equation (1) has been studied in detail for the case where $V(x)$ is sinusoidal, in which case the solutions are Mathieu functions. For $V(x)$ of the form $V_0S(x)$, the allowed and unallowed regions of Eq. (1) have previously been determined for the case[2,3] $h=w$ and for the Kronig-Penney potential.[4,5] For the former case curves of E *vs* V_0 in the interior of a band have also been calculated.[3] We shall here undertake to treat the case of arbitrary w/h,[6] but we shall limit ourselves to curves which bound the zones.

One very important feature of the band structure is the existence of points of contact between different allowed bands (a special type of band crossing). Aside from its general mathematical interest, the question of the distribution of these points of contact deserves attention because of its connection with the problem of surface states, as pointed out by Shockley.[7] The band structures for both the Kronig-Penney and the sinusoidal potential are not qualitatively the same as that of real crystals, since points of contact occur in those of real crystals but not in these models.[5,8] As was shown by Landauer,[9] the band structure in the case of the Kronig-Penney potential is dissimilar to that of real crystals in yet another way. While in the former case, the size of the forbidden regions approaches a constant nonvanishing value as E approaches infinity, in actual crystals if V_0 is kept fixed, the forbidden ranges of E approach zero as E approaches infinity.

The band structure for the case of a finite rectangular well potential, on the other hand, has the proper behavior as E approaches infinity and (as will be shown) has an infinite number of points of contact whenever $h\neq 0$. However, in order to carry out a

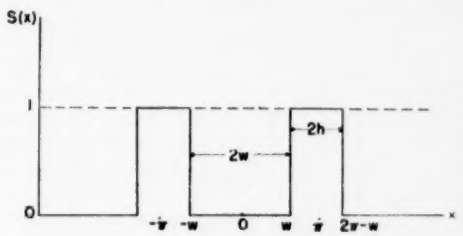

FIG. 1. The function $S(x)$ for a potential function of period 2π.

[1] E. Fues and H. Statz, Z. Naturforsch. **7a**, 2 (1952).
[2] M. T. O. Strutt, *Lamésche-Mathieusche und Verwandte Funktionen* (Verlag. Julius Springer, Berlin, 1932), p. 39. The numbers Strutt uses to label the E axis in his Fig. 4 are too large by a factor of 4.
[3] H. Statz, Z. Naturforsch. **5a**, 534 (1950).
[4] R. Del. Kronig and W. G. Penney, Proc. Roy. Soc. (London) **A130**, 499 (1930).
[5] D. S. Saxon and R. A. Hutner, Philips Research Repts. **4**, 81 (1949).
[6] See also G. Allen and Rolf W. Landauer, Bull. Am. Phys. Soc. **28**, No. 3, 47 (1953).
[7] W. Shockley, Phys. Rev. **56**, 317 (1939).
[8] J. J. Stoker, *Nonlinear Vibrations* (Interscience Publishers, Inc., New York, 1950), Chap. VI.
[9] Rolf W. Landauer, thesis, Harvard University, 1949 (unpublished).

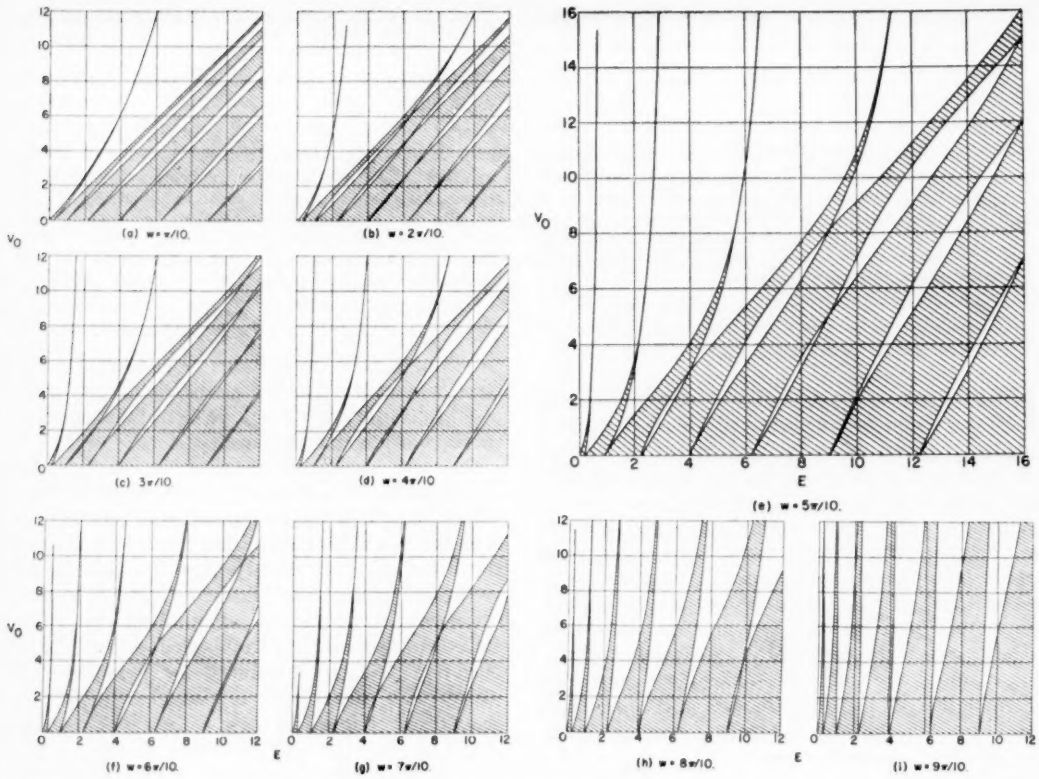

FIG. 2. Band structure as a function of energy and well depth. In (e), note the recrossing of the boundary curves which share the exceptional point $E=6.25$ on the E axis.

one-dimensional calculation analogous to the usual three-dimensional one, it is necessary to find the band structure for a whole range of values of w/h. This corresponds to the usual procedure of varying the lattice spacing in order to determine the most stable configuration of a crystal. For this reason, the restriction $w=h$ is objectionable.

II. THE EIGENSPECTRUM

Without loss of generality we shall confine ourselves to the case where $S(x)$ has the period 2π. Then the bounded solutions of Eq. (1) can always be represented as combinations of functions having the property

$$\psi(x+2n\pi)=e^{ink}\psi(x), \tag{2}$$

k being a real number and n an integer.[10] The value of k can be determined from E and V_0 when $E>V_0$ by the relation,[11]

$$\cos(2u)\cos(2v) - \left[\frac{w^2u^2+(\pi-w)^2v^2}{2(\pi-w)wuv}\right]\sin(2u)\sin(2v)=\cos(nk), \tag{3}$$

where $u=(\pi-w)(E-V_0)^{\frac{1}{2}}$, and $v=wE^{\frac{1}{2}}$.

Equation (3) is valid for all the points (E, V_0) for which $E>V_0$ and for which Eq. (1) has bounded solutions. At the boundary curves, however, $\cos(nk)$ assumes an extreme value, that is ± 1. In these cases, Eq. (3) is factorable and the equations for the boundary curves may be written

$$u\tan u=-[(\pi-w)/w]v\tan v, \tag{4a}$$

$$u\cot u=-[(\pi-w)/w]v\cot v, \tag{4b}$$

$$u\cot u=[(\pi-w)/w]v\tan v, \tag{4c}$$

$$u\tan u=[(\pi-w)/w]v\cot v, \tag{4d}$$

where Eqs. (4a) and (4b) are the factors of Eq. (3) when $\cos(nk)=+1$, and Eqs. (4c) and (4d) are the factors when $\cos(nk)=-1$. An equation similar to Eq. (3) results for $E<V_0$, and the equations for the boundary curves are then identical with Eqs. (4) with u replaced

[10] F. Block, Z. Physik **52**, 555 (1928).
[11] F. Seitz, *The Modern Theory of Solids* (McGraw-Hill Book Company, Inc., New York, 1940), p. 282.

by iu so that hyperbolic functions replace the trigonometric ones.

Equations (4) and the corresponding set for $E<V_0$ were used to obtain the plots of Figs. 2(a) to 2(i). In these graphs the shaded regions represent allowed regions, and the white ones, the unallowed regions. For each interior point of the shaded (allowed) regions, Eq. (1) has two linearly indeperdent bounded solutions. Along the boundary curves separating allowed from unallowed regions, Eq. (1) has, in general, a unique bounded solution. However, there exists a discrete set of exceptional points for each of which Eq. (1) has two linearly independent solutions corresponding to two different boundary curves which, therefore, have such points in common. In the standard treatment of Hill's equation, it is shown that any two such curves having one or more points in common in the finite plane must both bound the same unallowed region, so that the widths of the allowed bands there never vanish. Those exceptional points which occur in the interior in the finite part of the $E-V_0$ plane correspond to a crossing of the boundary curves. In addition to these, there are junctions in which pairs of curves meet on the E axis and at infinity. In the latter case, the curves meeting at infinity both bound the same allowed band.

III. LOCATION OF THE EXCEPTIONAL POINTS

A. Crossings

The exact location of the crossings may be found by considering Eqs. (4). Any values of u and v, such that any two of these equations are satisfied simultaneously, determine a crossing. The crossings are found to occur at the points

$$\begin{pmatrix} E=n^2\pi^2/4w^2, \\ V_0=n^2\pi^2/4w^2-[m^2\pi^2/4(\pi-w)^2] \end{pmatrix}, \quad V_0\neq 0, \quad n\neq 0, \quad (5)$$

where n and m are integers.

A similar consideration of the equations analogous to Eqs. (4), when $E<V_0$, shows that no pair of these equations can be satisfied simultaneously for finite u's and v's. Hence, we conclude that crossings of the type previously described can occur only when $E>V_0$, and the location of these is given by Eq. (5).

B. Junctions on the E Axis

When $V_0=0$, Eq. (1) becomes

$$d^2\psi/dx^2+E\psi=0,$$

which has bounded solutions for all positive values of E. Hence, there are no forbidden regions along the E axis and each boundary curve ends in an exceptional point. The location of these junctions is readily found from Eq. (4). They are at the points

$$(E=n^2/4, \ V_0=0), \quad n\neq 0, \quad (6)$$

where n is an integer.

C. Asymptotic Junctions

Although no crossings occur in the finite plane when $E<V_0$, it may be shown that pairs of boundary curves share the vertical asymptotes

$$E_\infty=n^2\pi^2/4w^2, \quad n=1, 2, 3, \cdots. \quad (7)$$

These junctions are all between pairs of curves bounding allowed regions.

IV. THE NUMBER OF EXCEPTIONAL POINTS

The number of junctions is clearly equal to the number of boundary curves. We shall now establish that, given any prescribed integer N, there exists for any value of w a set of boundary curves which crosses more than N times.

We first find the number of crossings in a right triangle bounded by the E axis, the line $E=V_0$, and a vertical line $E=n_{\max}{}^2\pi^2/4\pi^2$, where $n_{\max}$ is an integer. Every crossing within the triangle is located at the intersection of a vertical line, $E=n^2\pi^2/4w^2$, and a line of slope one, $V_0=E-m^2\pi^2/4(\pi-w)^2$. The number of crossings is thus equal to the number of such intersections of diagonal lines with vertical lines. There will obviously be $n_{\max}$ such vertical lines if we include the boundary of the triangle as one of the lines. For large $n_{\max}$, to a good approximation, the number of crossings ν will be given by

$$\nu=[(\pi-w)/2w]n_{\max}{}^2. \quad (8)$$

We next find the number of pairs of boundary curves among which these double points are distributed. We know that a pair of boundary lines passes through the base of the triangle at the points $E=n^2/4$. Therefore, there are at most $n_{\max}$ such boundary pairs. Since (as can be shown) the slope of these curves is always positive, no boundary curve which starts at $V_0=0$ outside the triangle will enter it. Thus, the ratio of the number of double points to the number of boundary curves is directly proportional to $n_{\max}$ for large $n_{\max}$.

Now if there are p double points to be distributed among q boundary pairs, there must be at least one boundary pair having at least p/q double points along it. Since p/q is a linear function of $n_{\max}$, a pair of boundary curves can be found with any given number of crossings.

Note that the preceding discussion does not exclude the possibility that between two pairs of boundary curves having a large number of crossings there are sandwiched pairs of boundary curves having a smaller number or, perhaps, no crossings at all.

ACKNOWLEDGMENTS

The author is indebted to Dr. Rolf W. Landauer, now at International Business Machines Corporation, Poughkeepsie, New York, for proposing this problem and for stimulating discussions and valuable suggestions. He would also like to thank Miss Laura Holden and Miss Janet Kohl who performed the computations.

Photoemission from Silver into AgCl, KBr, NaCl, and New Bands of Photosensitivity in AgCl*

M. A. GILLEO†
Laboratory for Insulation Research, Massachusetts Institute of Technology, Cambridge, Massachusetts
(Received April 20, 1953)

The work required to move an electron from a metal into an insulator has been investigated photoelectrically. The work function thus found was about 4.3 ev for Ag evaporated in vacuum on KBr (Fowler plot) as well as on NaCl (threshold wavelength). The photoelectrons become trapped in these crystals at vacant anion sites and may be released by *F*-band illumination. For Ag on AgCl a work function of 1.1 ev is measured at the low temperatures used to freeze out ionic conductivity.

In AgCl seven new bands of photosensitivity were found; the corresponding optical absorption was too small to be measured directly. These bands have a half-width of *ca* 0.2 ev at 90°K and are bleached by irradiation. The 4400, 5000, 5700, 6600, and 7500A bands increase in intensity with an increasing supply of electrons provided by photoelectric emission. These bands are identified, by their location and behavior, with the *F*, *E*, *D*, *C*, and *G* bands (Petroff's notation) in the alkali halides. The 4800A (*A* band) and 9200A bands are favored by a scarcity of electrons and may correspond to trapped holes. Photosensitivity in all these bands can be created by irradiation in the intrinsic optical-absorption edge of AgCl at low temperature. They may not be characteristic of a perfect crystal.

The intrinsic band-like photoconductive response of AgCl and the absorption edge on which it occurs shift toward shorter wavelengths with decreasing temperature. The maximum of response which appears with decreasing wavelength may arise from a bimolecular recombination of charge carriers released by light. The absorption edge steepens as it shifts toward shorter wavelength with decreasing temperature.

THE mechanisms by which electrons may be released in an insulator and their modes of migration in an electric field are included in the range of interests of this laboratory. The alkali and silver halides are especially favorable test objects because of their simple atomic structure and the fact that they may be obtained as good single crystals. Electronic effects in these crystals may be conveniently studied through their electrical, optical, and photoelectrical properties as has been amply demonstrated at low field strength by Pohl and his co-workers and near breakdown by von Hippel and his associates.

Mott and Gurney[1] found evidence in the experiments of Gyulai[2] of photoelectric emission from colloidal sodium in sodium chloride. The threshold energy for this emission is about 0.5 ev less than that into vacuum from a clean sodium surface. They attribute this depression of the metal work function to the presence of the insulator.

From data on the Herschel effect they have deduced the threshold for photoelectric emission from colloidal silver in silver chloride. The Herschel effect is the bleaching of a latent image in a photographic plate by exposure to red light; it has been studied by several investigators.[3] According to the elementary theory of Mott and Gurney[1] based on the work of Hilsch and Pohl[4,5] for the photographic process, the latent image consists of colloidal silver specks. Illumination of such a speck with a photoelectrically active wavelength causes it to become positively charged. For every electron lost one silver ion migrates from this speck into the crystal. Thus the size of the colloidal particles is gradually reduced and the latent image destroyed. The threshold for this effect is *ca* 1.2 ev, corresponding to a reduction of 3.5 ev in the *ca* 4.7-ev work function from silver[6] into a vacuum.

Electrons do not long remain free in KBr and NaCl. Flechsig[7] observed an electron range of less than 3×10^{-7} cm/(v/cm) for NaCl and Witt[8] a range of 4.8×10^{-8} cm/(v/cm). Vacant anion sites in the lattice are surrounded by a Coulomb-like field in which electrons may be trapped to form an *F* center[9] and an absorption (*F* band) characteristic of the crystal. Absorption of light in the *F* band leads to destruction of the *F* center and to photoconductivity.[9]

In silver chloride the electron range may be 5×10^{-4} cm/(v/cm) in carefully annealed crystals.[10] Accordingly, for a given crystal thickness appreciably greater than the electron range the currents observed in silver chloride are about 10^4 times greater than in sodium chloride if the same number of electrons is involved.

There is ample evidence that electrons can be trapped in silver chloride in the experiments reported by Hecht,[11]

* Sponsored by the U. S. Office of Naval Research, the Army Signal Corps, and the Air Force.
† Present address: Bell Telephone Laboratories, Inc., Murray Hill, New Jersey.
[1] N. F. Mott and R. W. Gurney, *Electronic Processes in Ionic Crystals* (Clarendon Press, Oxford, 1940).
[2] Z. Gyulai, Z. Physik **35**, 411 (1926).
[3] W. F. Berg, Trans. Faraday Soc. **35**, 445 (1939); H. Tollert, Z. physik. Chem. **140**, 355 (1929); O. Bartelt and H. Klug, Z. Physik **89**, 779 (1934); B. H. Carroll and C. M. Kretchmann, J. Research Natl. Bur. Standards **10**, 449 (1933).
[4] R. Hilsch and R. W. Pohl, Z. Physik **64**, 606 (1930).
[5] R. Hilsch and R. W. Pohl, Z. Physik **77**, 421 (1932).
[6] C. Herring and M. H. Nichols, Revs. Modern Phys. **21**, 185 (1949); E. W. J. Mitchell and J. W. Mitchell, Proc. Roy. Soc. (London) **210**, 70 (1950); H. E. Farnsworth and R. P. Winch, Phys. Rev. **58**, 812 (1940).
[7] W. Flechsig, Z. Physik **46**, 788 (1928).
[8] H. Witt, Z. Physik **128**, 442 (1950).
[9] R. W. Pohl, Proc. Phys. Soc. (London) **49**, E3 (1937); F. Seitz, Revs. Modern Phys. **18**, 384 (1946); reference 1, Chap. IV.
[10] W. Lehfeldt, Nachr. Ges. Wiss. Göttingen. Math.-physik. Kl, Fachgruppen II. **1**, 171 (1935); J. R. Haynes and W. Shockley, Phys. Rev. **82**, 935 (1951).
[11] K. Hecht, Z. Physik **77**, 235 (1932).

Haynes and Shockley,[12] and Smith.[13] Hecht showed that at −170°C electrons were released by light of 4050A wavelength. Smith reports that at −70°C mobile holes as well as electrons were produced by electron bombardment.

An *F* band analogous to that found in the alkali halides has long been sought in silver chloride and bromide. Hilsch and Pohl[4] found instead only a broad absorption band at 5400A for silver chloride, which they attributed to colloidal silver. Nevertheless, the theories of the photographic process set forth by Mott and Gurney[1] and by Mitchell[14] postulate the existence of a trapping mechanism analogous to that leading to *F*-center formation in the alkali halides.

The research reported here was initiated with the purpose of measuring the work required to move an electron photoelectrically from silver into an alkali or silver halide crystal. At the same time evidence was sought for the existence of *F*-center-like traps in silver chloride.[15]

I. EXPERIMENTAL

A. Preparation of Samples[16]

The NaCl and KBr crystals were cleaved to a size of 18×18×1 mm, outgassed at *ca* 200°C in a vacuum of 10^{-5} mm of Hg, and then silver was evaporated in the vacuum on one face at room temperature.

AgCl crystals were ground to 20×20×5 mm and then polished on a beeswax lap with No. 303½ emery[17] in water. Subsequently, they were annealed in air by heating in the dark to 400°C for two hours and cooling to room temperature over a period of two days. This type of annealing was found by Lehfeldt[10] and Haynes[18] to be effective in increasing the electron range by removing internal strain. After annealing, one surface was coated with silver by vacuum deposition.

When a guarded electrode with a window was needed on AgCl, it was produced by painting the required areas with a colloidal graphite dispersion[19] in alcohol.

All work on AgCl was done under a light covered by a Wratten Series "0" filter.

B. Photoelectric Measurements

For the measurement of photoelectric emission from metallic silver into NaCl and KBr, the quartz double-monochromator of a Cary Recording Spectrophotometer[20] was used. A high-pressure xenon arc,[21] which provides an intense ultraviolet continuum in the 2200 to 4000A region, served as a light source. Measurements on AgCl were made between 3400 and 12 000A with a tungsten lamp as a light source and the same monochromator.

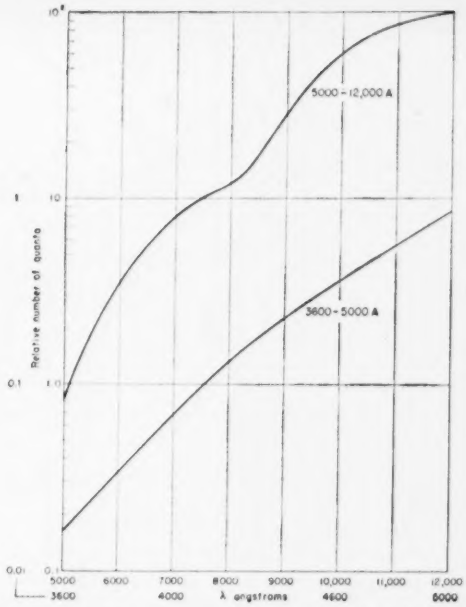

FIG. 1. Relative number of quanta *vs* wavelength for Cary spectrophotometer (tungsten lamp, 0.30 mm slit width, units of *ca* 7.4×10¹¹ quanta).

The power output of the monochromator was measured by a special, compensated radiation thermocouple[22] with a calcium fluoride window. In the 2300 to 4000A region the monochromator slits were adjusted at each wavelength for the same power. In the 3400 to 12 000A region the slit width was constant for each run. Consequently, the number of quanta varies with wavelength (Fig. 1) and nearly as the square of the slit width.

For a field of 200 v/cm in an NaCl crystal and an electron range of 5×10^{-8} cm/(v/cm) the electrons move only about 10^{-5} cm before being trapped again. Consequently, the emission current in the external circuit for a crystal thickness of 1 mm and the nickel screen spaced 1 mm in front of the crystal is only about 2×10^{-6} of the current at the silver surface. This reduction factor is much less serious for AgCl since the electron range is 10^4 times greater.

Currents as small as 4×10^{-17} amp were measured with a vibrating-reed electrometer[23] by the rate-of-charge

[12] J. R. Haynes and W. Shockley, *Report on 1947 Strength of Solids Conference* (Physical Society, London, 1948), p. 151.

[13] L. P. Smith, in *Semi-Conducting Materials*, Proc. Conf. at Univ. of Reading, July, 1950 (Butterworths Scientific Publications, London, 1951), pp. 114–121.

[14] J. W. Mitchell, in *Photographic Sensitivity*, Proc. Symp. Univ. of Bristol, March, 1950 (Butterworths Scientific Publications, London, 1951), pp. 242–258.

[15] A detailed review of the properties of the silver halides has been given by F. Seitz, Revs. Modern Phys. **23**, 328 (1951).

[16] The crystals of NaCl, KBr, and AgCl were grown by the Harshaw Chemical Company, Cleveland, Ohio.

[17] American Optical Company, Buffalo, New York.

[18] J. R. Haynes, Rev. Sci. Instr. **19**, 51 (1948).

[19] Dag Dispersion No. 154, Acheson Colloids Corporation, Port Huron, Michigan.

[20] Model 12M, Applied Physics Corporation, Pasadena, California.

[21] Type XBO-250, Osram Gmbh., Berlin, Germany.

[22] The Perkin-Elmer Corporation, Norwalk, Connecticut.

[23] Model 30S, Applied Physics Corporation, Pasadena, California.

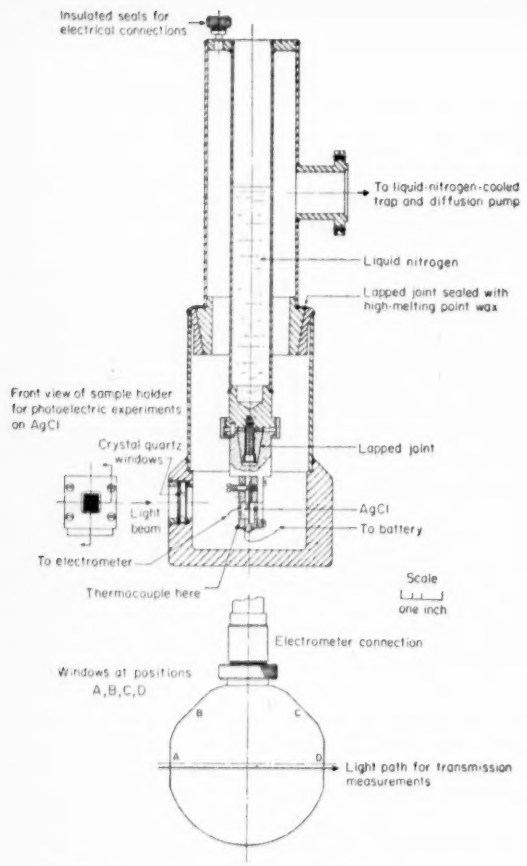

FIG. 2. Low-temperature sample holder in cross section.

method. When the current to be measured was greater than 10^{-14} amp, a 10^{11}-ohm shunt resistance was used.

Photoelectric measurements were made with the sample mounted in an evacuated metal case (Fig. 2) provided with crystal-quartz windows. The sample could be cooled to liquid nitrogen temperature. The holder was evacuated to prevent deterioration of the alkali halide crystals by water vapor, and, in the case of AgCl in which the ionic conductivity must be frozen out, to improve the thermal insulation and prevent condensation on the sample.

C. Optical Absorption

Measurements of optical absorption were made with the Cary Recording Spectrophotometer. This instrument records optical density[24] *vs* wavelength on linear scales.

It was necessary to cool the AgCl for the photoelectric measurements, hence also the optical absorption measurements were made at low temperatures. When the sample holder (Fig. 2) served for absorption measurements, the AgCl crystal was clamped between recessed silver plates covered with a thin layer of silicone grease which promoted good thermal contact in the vacuum. The temperature of the AgCl was determined by that of the silver plates to which a copper-constantan thermocouple was attached.

[24] Optical density is defined by $D=\log_{10}(I_0/I)$, where I_0 is the intensity of the incident light and I the intensity of the transmitted light.

II. EXPERIMENTAL RESULTS

A. Photoelectric Emission

If we assume that the only effect of placing an insulator at the metal surface is to change its work function from the vacuum value ϕ to an apparent value ϕ', then we may determine ϕ' from a Fowler plot[25] (I *vs* x, $x=h\nu/kT$) of the experimental data. This assumption is not strictly justifiable. An electron is removed from a quantized state in the metal to another quantized state in the conduction band of the insulator. Therefore the transition probabilities may be a function of x, a possibility which we neglect in making a Fowler plot.

The threshold for photoelectric emission from silver into KBr was observed to fall between 2800 and 2900A at room temperature. At 2700A the power in the monochromatic light beam was 0.47 μwatt and the photocurrent 4.9×10^{-17} amp in one instance; the currents increased with decreasing wavelength.

When plotted on Fowler co-ordinates the data (Fig. 3) fit a Fowler curve well for a work function ϕ of 4.28 ev. The work function for a clean silver surface is about

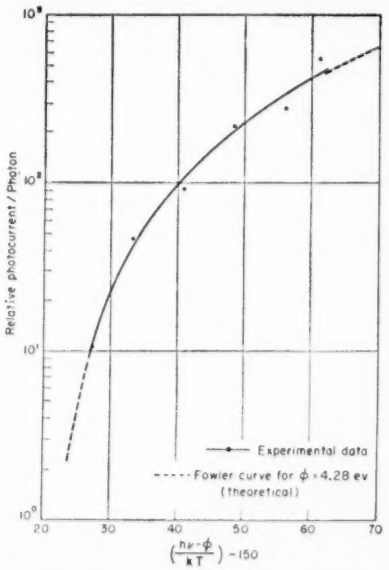

FIG. 3. Fowler plot of photoelectric emission data for Ag on KBr ($1/kT=40$).

[25] R. H. Fowler, Phys. Rev. **38**, 45 (1931); Fowler plot data from A. L. Hughes and L. A. DuBridge, *Photoelectric Phenomena* (McGraw-Hill Book Company, Inc., New York, 1932).

4.7 ev.[6] Consequently, the insulator seems to be responsible for a reduction of the work function of about 0.4 ev.

That the observed current must be a photoelectric emission current was shown in several ways. (a) With the field direction reversed the flow of current ceases. Hence it cannot be a photoconductive effect in the volume of the insulator because it would be independent of the field direction. (b) When the photoemission current is allowed to flow for a few minutes and the photoelectrically active radiation is then cut off, illumination at a wavelength of the F band (*ca* 6400A for KBr) produces a sudden release of charge. Hence the photoelectrons were apparently trapped to form F centers. The quantity of charge thus released is about the same as the integrated photoelectric current. (c) When a piece of fused quartz, coated with silver on one side, was mounted in place of the KBr sample no photocurrent was observed in the wavelength range previously used for determination of the threshold.

For silver on NaCl the threshold wavelength at 90°K was 2850A (4.3 ev). With decreasing wavelength the yield increased. The photoemission current increased linearly with the voltage, as it should for electron motion in a crystal with a small mean range. At room temperature the photoemission current produced by light of short wavelength ($\lambda < 2900$A) could be enhanced by simultaneous irradiation in the F band (*ca* 4700A for NaCl).[26]

The measurements of photoelectric emission from silver into AgCl were carried out in a similar way, but the crystal was cooled to 170°K or below in order to eliminate ionic conductivity. With one crystal[27] photoelectric emission was observed with the silver both positive and negative and dag as the counter electrode. With silver positive the current must have come from the dag electrode which was illuminated by reflected light.

The data for silver negative are closely fitted by a Fowler curve (Fig. 4) for a work function of 1.1 ev; with silver positive the fit is poor.

After the photoemission current has continued for some time a negative space charge builds up in front of the emitting surface. The field there is reduced and the emission current decreases.

The photocurrent at long wavelength ($\lambda > 7000$A) is initially small or undetectable in a "silver-on-silver chloride" specimen cooled in the dark. After the crystal has been illuminated with weakly absorbed light of the photoconductively active region (*ca* 3900A), the response at long wavelength greatly increases. During this illumination about 10^{-10} coulomb may pass in the external circuit (illuminated area about $\frac{1}{2}$ mm^2; silver negative). The field at the silver surface has apparently been increased by the illumination because the quantum yield may be greater in photoconductivity than in photoemission. Hence more electrons are removed from the space in front of the silver than are emitted by it.

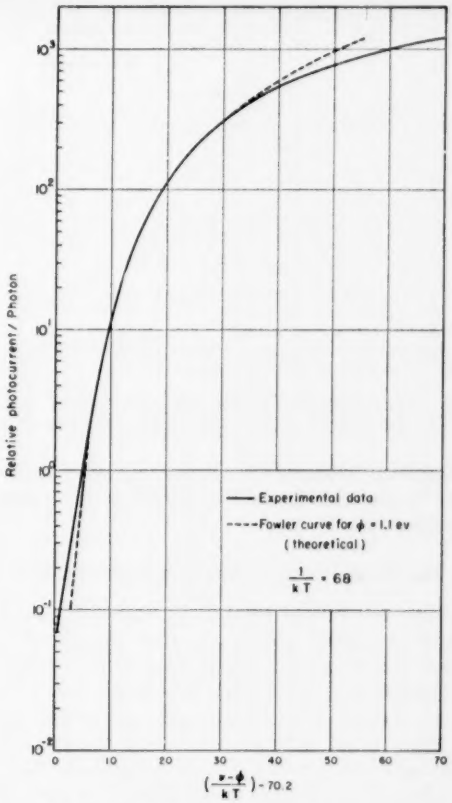

FIG. 4. Fowler plot of photoelectric emission for Ag on AgCl.

At room temperature the theoretical thermionic emission current from a surface of 1 ev work function is 5×10^{-14} amp/cm^2. Accordingly, we can expect that emission from the silver may fill traps in the AgCl in front of the electrode. The retarding field of the resulting space charge eventually stops emission unless it is neutralized by photoconductivity, as described.

In order to observe the influence of freshly deposited electrolytic silver on the photoelectric work function, a current was passed through a crystal (silver negative) at room temperature. The time of flow was sufficient to allow a deposit of an amount of silver equivalent to one monolayer on the silver electrode. A Fowler plot made afterward showed that the surface had changed. The photoemission data no longer can be represented by a Fowler curve for a single work function; patches of different work function may now be present.

[26] An interference filter (Baird Associates, Cambridge, Massachusetts) with transmission bands at 4700 and 7000A was used with a tungsten lamp. Illumination in the F' band also is an accidental consequence of the 7000A transmission of this filter.

[27] Dr. C. D. West of the Polaroid Corporation, Cambridge, Massachusetts, supplied this crystal and useful information on the handling of it. The crystal was machined from a boule purchased by Polaroid from Harshaw.

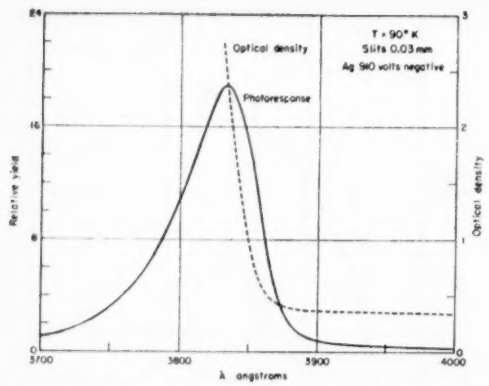

FIG. 5. Photoconductive response and optical density *vs* wavelength for Ag on AgCl (yield unit *ca* 8.4×10^{-6} electron/photon).

Additional evidence for electron emission from the silver was found in the investigation of bands of photosensitivity.

B. Bands of Photosensitivity in Silver Chloride

In the detection of trapped electrons which can be released by light absorption, the photoconductive method is much more sensitive than optical absorption measurements. However, the photoconductive method leads to results which require more careful interpretation than those obtained in optical absorption. An absorbing center causes the same reduction of intensity regardless of its location in the crystal. In the photoconductive effect the migration distance of the electrons determines the current and this distance depends on the field distribution (including space-charge effects) in the crystal.

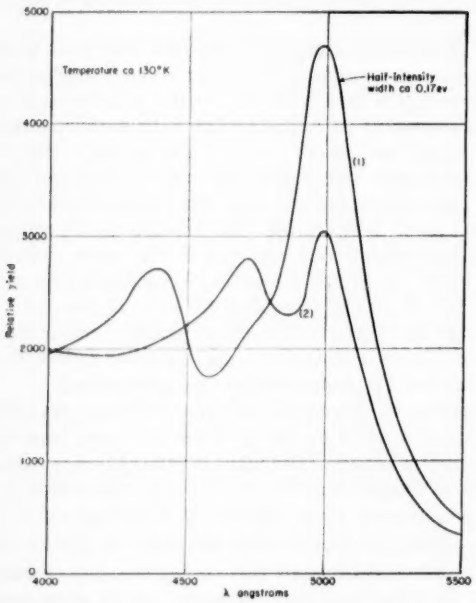

FIG. 6. Yield *vs* wavelength for photosensitivity bands in AgCl (space-charge field only; yield unit *ca* 8.4×10^{-10} electron/photon).

At low temperature in AgCl a characteristic photoconductivity is observed at about 3900A in the form of a narrow band. The optical absorption of the crystal begins to rise steeply (absorption edge) near the maximum of response. With decrease of temperature this maximum and the absorption edge shift simultaneously toward shorter wavelengths (Fig. 5). The observed quantum yield in this band is of the order of one percent. The true yield may be higher since the electrode geometry is unfavorable to the photoconductive effect.

This association with the absorption edge and the moderately large quantum yield speak for an intrinsic photoconductive effect. An electron is lifted by light absorption from the filled band into the conduction band of the crystal. We believe that the band-like nature of the photoresponse may be interpreted in terms of a bimolecular recombination of electrons and holes released by light. At long wavelength the response is small because the absorption of light is small. For shorter wavelength at which absorption of light takes place within a thin surface layer, the density of holes and electrons becomes high. In the case of a bimolecular process the rate of recombination rises as the square of the charge-carrier density. For a fixed number of charge carriers released per unit of time the equilibrium density will accordingly decrease as the concentration increases. Hence a maximum is observed at some optical density for a bimolecular process, while a monomolecular process does not yield this behavior.

In addition to the intrinsic photoconductive response, several other bands of photosensitivity can be produced in AgCl. They were observed at temperatures between 90° and 130°K in crystals purchased directly from Harshaw. A crystal with a silver and a nickel screen electrode was illuminated with silver positive and negative at various times. After the wavelength had been scanned through the region of intrinsic photoconductivity several times, the external field was removed. The current flow in the space-charge field was recorded while the wavelength was scanned from 12 000 to 4000A. The use of the space-charge field alone eliminated some noise troubles.

Three bands of photosensitivity appeared at 4400, 4800, and 5000A with a half-width of *ca* 0.2 ev (Fig. 6). The 5000 and 4400A bands were demonstrated to be independent of one another by scanning the 4000 to 6000A region several times with fixed slit width (see Fig. 1). The number of quanta at 4400A is smaller than at 5000A. Accordingly, the 5000A band is bleached rapidly and the previously invisible 4400A band is uncovered (Fig. 7).

The contribution made to the intensity of these bands by electron emission from the silver was revealed

by two experiments. In the first the crystal was illuminated at 3850A with the silver 1200 v positive, so that electron emission from the silver was excluded; the front electrode was again a nickel screen. After 6×10^{-5} coulomb passed in the external circuit the external field was removed and the photoresponse was measured in the space-charge field (Fig. 8). Bands at 4800 and 9200A stand out prominently. A repetition of this procedure with silver negative leads to a much higher response (Fig. 9; note the decreased slit width); similar currents were observed, although about ten times less power was in the light beam. In this case

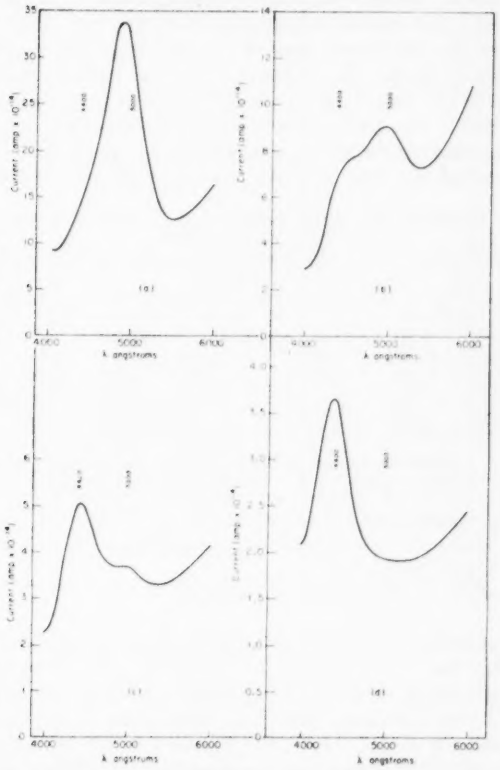

FIG. 7. Bleaching of the 5000 and 4400A bands in AgCl by successive scanning (temp. *ca* 130°K; slit width 0.15 mm).

the main response occurs at 6600A with some response at 4400, 5000, and 9200A. Obviously, the response has been increased by the additional electron supply made available from the silver cathode.

In a second experiment a crystal without evaporated electrodes was used. The photoconductivity which could be induced in the photosensitive bands by 3850A radiation was small for either field direction because no electrons were supplied from the cathode (platinum foil).

When a silver cathode was evaporated on the same crystal, a high response was found again in these bands,

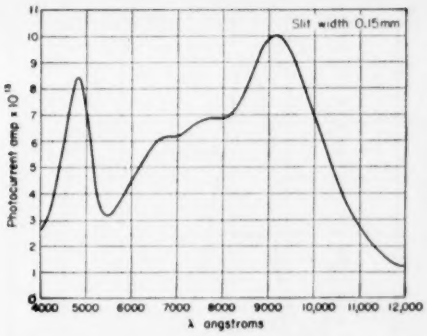

FIG. 8. Photocurrent *vs* wavelength for space-charge field; current flow toward Ag (prior excitation; Ag+1200 v, 3850A, temp. *ca* 130°K).

as expected (a guarded dag electrode with a window was used on the other face). With silver negative larger currents were observed at long wavelengths and the photosensitive bands were more prominent than with silver positive[28] (Fig. 10). In addition, a new band can be seen (Fig. 10) at 5700A with silver negative.

Summarizing: With silver negative the 4400, 5000, 5700, and 6600A bands have consistently appeared together. A band also seems to be present at 7500A. One has also been observed near 11 000A in the crystal which showed mostly photoemission currents, as well as with the others. With silver positive the 4800 and 9200A bands have been more prominent, apparently favored by a scarcity of electrons. Possibly they could be ascribed to trapped holes.

These bands appear to be completely analogous to the *F* band and the subsidiary long-wavelength bands observed by Molnar[29] in the alkali halides. In these crystals the product νd^n for each band (ν is the frequency of the peak, d the lattice constant, and n an empirical constant) is nearly constant.[30] In AgCl the

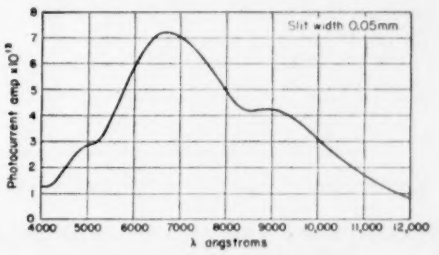

FIG. 9. Photocurrent *vs* wavelength for space-charge field; current flow away from Ag (prior excitation; Ag−1200 v, 3850A, temp. *ca* 130°K).

[28] Careful focusing of the light on the window in the dag electrode reduced the amount of light reflected to it from the silver. This was an improvement over the previous experiment.

[29] J. P. Molnar, Ph.D. thesis, Massachusetts Institute of Technology, October, 1940 (unpublished).

[30] Mollwo [E. Mollwo, Nachr. Ges. Wiss., Göttingen, Math.-physik. Kl. **97** (1931), Vol. I] observed that νd^2 was nearly constant for the *F* bands in the alkali halides. Later Fröhlich [H. Fröhlich, Z. Physik **80**, 819 (1933)] gave simple theoretical derivation of

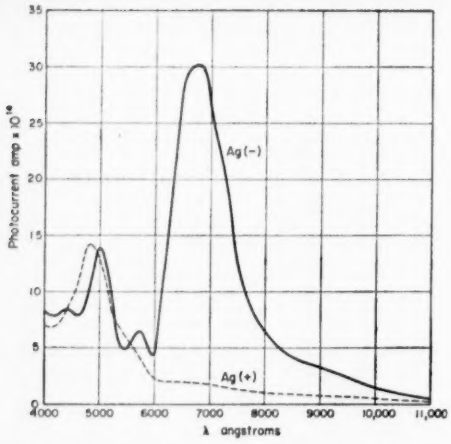

FIG. 10. Photocurrent *vs* wavelength: photosensitive bands and electron emission for Ag on AgCl (applied voltage 910 V, crystal thickness 5 mm, slit width 0.15 mm, temp. 90°K).

values of νd^n computed from the photosensitivity bands agree well, for example, with those computed from Petroff's[31] data for KCl (Table I), as was expected. The data of Stasiw[32] on optical absorption bands in AgBr containing 0.02 mole percent Ag_2S also confirm this expectation.[33] Thus the original convictions of Hilsch and Pohl[4,5] regarding the parallelism of the photochemical processes in the alkali and silver halides appear to be substantiated.

Additional evidence for the above conclusions is found in the behavior of the response in the photosensitivity bands as a function of excitation. The *C* band is the most prominent and appears early, while the *D* band builds up more slowly as found by Petroff[31] in KCl. However, the behavior of the bands in AgCl as observed here may be somewhat different from that found in the alkali halides since electrons have been supplied by the intrinsic photoconductive effect or photoelectric emission instead of a photoeffect in the *F* band as is customary for alkali halide crystals.

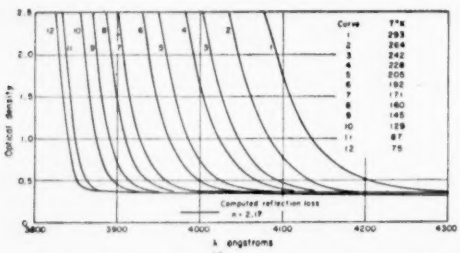

FIG. 11. Optical density *vs* wavelength at constant temperature (cooling curve, AgCl 5 mm thick).

this relation. Ivey [H. F. Ivey, Phys. Rev. **72**, 341 (1947)] obtained better agreement with the data for the *F* and longer-wavelength bands by using νd^n, where $n = 1.84$ for the *F*, *E* (or R_1), *D* (or R_2), and $n = 1.56$ for the *C* (or *M*) band.

[31] S. Petroff, Z. Physik **127**, 443 (1950); see also R. W. Pohl, in *Photographic Sensitivity*, Proc. Symp. Univ. of Bristol, March, 1950 (Butterworths Scientific Publications, London, 1951), pp. 4–8.

[32] O. Stasiw, Z. Physik **134**, 106 (1952).

[33] The Ag_2S is here assumed to enhance existing absorption bands by increasing crystal imperfection rather than to introduce new absorption bands in the region in question.

C. The Optical Absorption of Silver Chloride

The optical absorption of a crystal 5 mm thick was measured in the 3800 to 8000A region over the temperature range 300 to 75°K. The lowest temperature was reached by reducing the pressure above the liquid nitrogen.

Optical density was measured as a function of wavelength at a series of successively lower temperatures by pouring small quantities of liquid nitrogen into the sample holder. The absorption curve was recorded while the temperature passed through a minimum. In another run the optical density was recorded as a function of time at constant wavelength as the sample warmed up. The warming time from 90° to 290°K amounted to two hours. Consequently thermal equilibrium was certainly maintained in this run. The temperatures for the curves recorded while cooling were adjusted to give agreement with the data taken during the warming run. At 129°K the difference was 15°K, while at the 87°K (atmospheric-pressure) and 75°K (reduced-pressure) boiling points of nitrogen the difference was zero since thermal equilibrium was reached.

TABLE I. Values of νd^n for the *F*, *A*, *E*, *D*, *C*, and *G* bands in KCl, AgCl, and AgBr.

Band	n	KCl[a] (103°K)	AgCl (90°K)	AgBr[b] (103°K)
F	1.84	1.63 cm^n/sec	1.59 (4400A)	1.56
A	(1.84)	1.46	1.46 (4800A)	···
E	1.84	1.36	1.40 (5000A)	1.39
D	1.84	1.22	1.23 (5700A)	1.19
C	1.56	0.663	0.650(6600A)	0.640
G	(1.84)	0.907	0.933(7500A)	···

Room-temperature values of d: KCl, 6.28A; AgCl, 5.54A; AgBr, 5.76A. The band designation is that of Petroff (reference 31). Values of n enclosed in parentheses have been assumed.

[a] From reference 31.
[b] From reference 32 (bands corresponding to *A* and *G* were missing but probably can be found with suitable technique).

With decreasing temperature the absorption edge of AgCl steepens and moves toward shorter wavelengths (Fig. 11). At constant wavelength the absorption rises gradually at first and then with increasing rapidity (Fig. 12). Small humps have been observed in these curves (Fig. 12, 4050A). At the lowest temperatures the wavelength at which a given density is reached approaches a constant value asymptotically (Fig. 13). We may interpret this behavior in terms of the thermal expansion of the lattice. The band separation is a function of the lattice constant. The thermal coefficient of expansion approaches zero with the temperature.

Consequently, the lattice spacing and band separation approach a constant value asymptotically.

The optical modes of vibration may be expected to set up fluctuating electric fields in the lattice which will perturb the band edges. The thermal excitation of these modes will vary exponentially with temperature. The observation (Fig. 14) that at longer wavelengths the optical density is more strongly temperature dependent may be understood as follows: at these wavelengths the perturbing effect of the higher energy modes of vibration for which the temperature dependence is largest is chiefly responsible for the absorption.[34] At shorter wavelengths the slower shift of the band edge with lattice constant change predominates. This effect has been observed before by the author[35] in selenium, and by Cronemeyer[36] in co-operation with the author for TiO_2. Cheesman[37] has recently treated the theory of this problem.

The optical absorption in the photosensitive absorption bands was too weak to be recorded (Fig. 15).

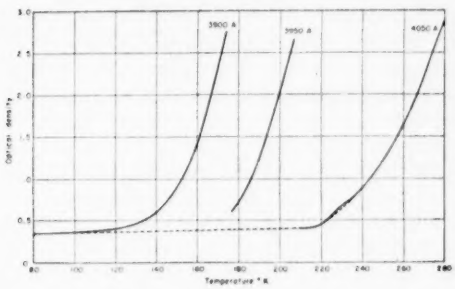

FIG. 12. Optical density *vs* temperature at constant wavelength (warming curve, AgCl 5 mm thick).

D. Conduction Effects

The conductivity of two AgCl crystals was measured as a function of temperature. The crystal which proved best for photoemission measurements showed at room temperature a thermal activation energy of about 0.8 ev according to a resistance *vs* $1/T$ plot. At lower temperatures the activation energy became about 0.34 ev. One of the crystals with prominent bands of photosensitivity had a resistivity about 100 times lower than the above crystal. Its thermal activation energy between room temperature and 160°K was also 0.34 ev. Below 160°K it seemed to decrease to 0.3 ev (Fig. 16). Consequently, it appears that the crystals with more response in the photosensitive bands may have been the less perfect ones (larger impurity content, more lattice defects, etc.).

[34] The measurements of Fesefeldt [H. Fesefeldt, Z. Physik **64**, 741 (1930)], Hecht (reference 11) and Hilsch and Pohl (reference 4) are much less extensive than those reported here, but imply the same conclusion.

[35] M. A. Gilleo, J. Chem. Phys. **19**, 1291 (1951).

[36] D. C. Cronemeyer, Phys. Rev. **87**, 876 (1952).

[37] I. C. Cheesman, Proc. Phys. Soc. (London) **A65**, 25 (1952).

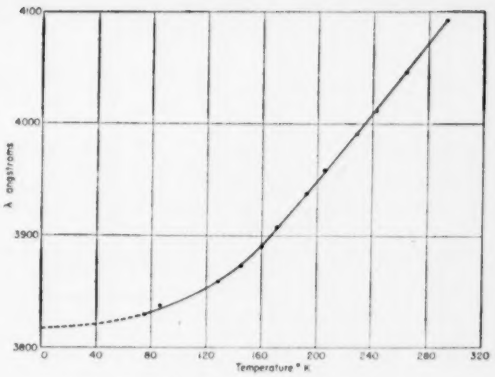

FIG. 13. Wavelength *vs* temperature for a constant optical density of 2 (AgCl 5 mm thick).

The existence of two modes of conduction with different activation energies is also revealed by the thermal release of space charge. A crystal was cooled to liquid nitrogen temperature, then a voltage applied and the crystal exposed to light of 3850A (intrinsically photoconductive region). The current flow creates a space charge within the crystal which remains after the illumination and removal of the external field. If the crystal is then slowly warmed, a current flows as a

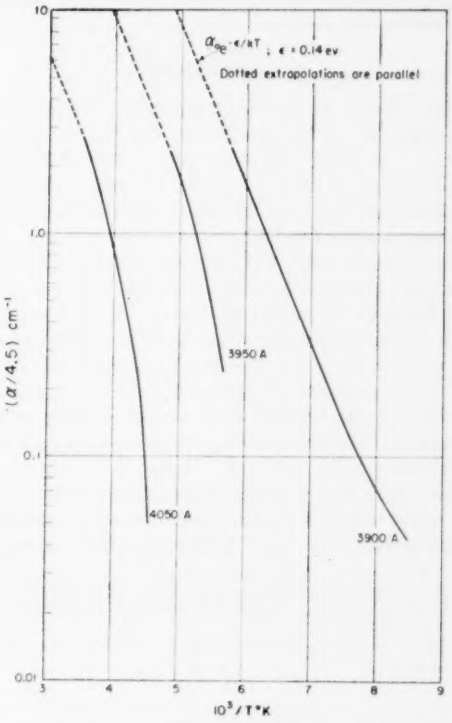

FIG. 14. Log (absorption coefficient) *vs* $1/T$ at constant wavelength.

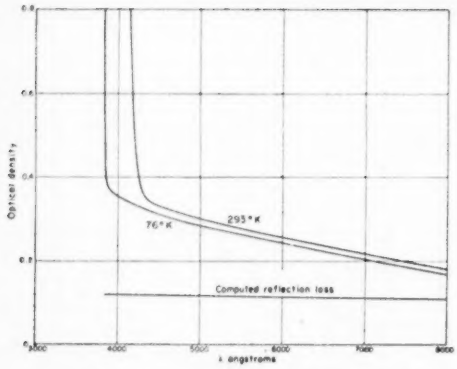

FIG. 15. Optical density *vs* wavelength at constant temperature (AgCl 5 mm thick).

function of time. The current *vs* time curve shows two peaks at 134° and 183°K corresponding to two activation energies for conductivity in the 0.3 to 0.4 ev range.[38] These peaks may be associated with those of the optical absorption observed previously (Fig. 12).

A spectroscopic analysis[39] of the two crystals for which resistivity was measured as a function of temperature revealed no significant differences in impurity content. Traces of Al, Ca, Cr, Cu, Fe, Hg, Mg, Mn, Mo, Na, Ni, Pb, Si, and Zn were found. Impurities such as S cannot be detected by this analysis, but may be important nevertheless.

III. DISCUSSION

Photoelectric emission has been observed from silver into KBr and NaCl with a work function ϕ' of about 4.3 ev; from silver into AgCl ϕ' is *ca* 1.1 ev. The effect of the insulator thus has been to reduce the silver-vacuum work function by 0.4 ev for the alkali halide crystals and by about 3.5 ev for AgCl.

We must consider the energy-band structure of the insulators in order to understand this reduction. Mott and Gurney[1] attempted to do this by estimating the value $-\chi$ of the energy of an electron in the bottom of the conduction band. For NaCl and KBr they found $-\chi$ to be *ca* 0.5 and 0.7 ev, respectively. The metal-insulator work function ϕ' is $\phi-\chi$ according to their reasoning. The results reported here support this conclusion.

The existence of optical absorption bands in AgCl analogous to the *F* band and its long wavelength subsidiaries of the alkali halides, has been established through their photosensitivity. These bands apparently vary greatly in strength in different crystals and were nearly absent in one specimen.

The interpretation of these bands may involve impurities, lattice defects, ionic diffusion, and possibly aggregates of *F* centers, as postulated by Mitchell.[14]

The photoconductivity of AgCl near the absorption edge appears to be intrinsic. Caldwell[40] suggested that it might correspond to an *F*-band absorption because chlorination (to reduce anion-vacancy concentration) reduced its magnitude as well as that of the fluorescence which can be excited by ultraviolet light. Farnell and Burton,[41] in contrast, found that chlorination increased

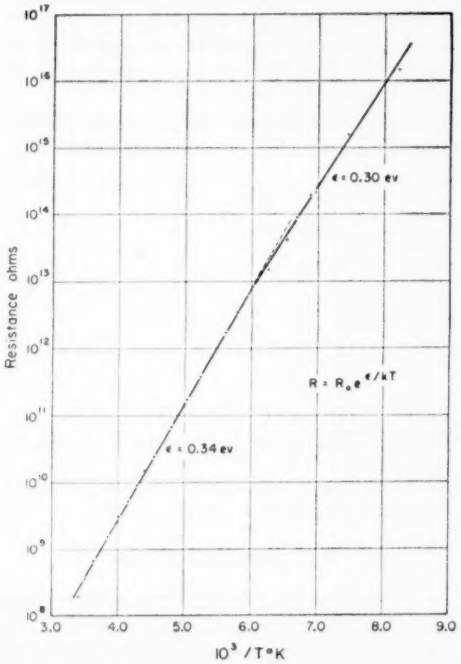

FIG. 16. Resistance *vs* reciprocal temperature for AgCl (multiply by 1.6 for resistivity in ohm-cm).

the fluorescence. We believe that our evidence favors the "intrinsic" interpretation.

ACKNOWLEDGMENT

The writer wishes to acknowledge his indebtedness to Professor A. von Hippel for his suggestions, advice, and discussions during his supervision of this research.

[38] See the analysis of an analogous effect, thermoluminescence, by G. F. J. Garlick, *Luminescent Materials* (Clarendon Press, Oxford, 1949).

[39] New England Spectrochemical Laboratories, Ipswich, Massachusetts.

[40] W. C. Caldwell, Ph.D. thesis, Cornell University, April, 1948 (unpublished).

[41] G. C. Farnell and P. C. Burton, in *Photographic Sensitivity*, Proc. Symp. Univ. of Bristol, March, 1950 (Butterworths Scientific Publications, London, 1951), pp. 61–73.

Electron Ejection from Ta by He^+, He^{++}, and He_2^+

HOMER D. HAGSTRUM
Bell Telephone Laboratories, Murray Hill, New Jersey
(Received April 2, 1953)

Measurements of total yield (γ_i) and kinetic energy distribution are reported for electrons ejected from tantalum by the ions He^+, He^{++}, and He_2^+ in the kinetic energy range 10 to 1000 ev. The evidence presented indicates that the electrons are released by a collision of the second kind of the ion with the metal surface (potential ejection). One internal secondary electron is produced per incident ion. The probability of this electron escaping is reduced by the possibility of internal reflection at the image barrier at the metal surface. γ_i for the slowest ions is observed to be 0.14, 0.52, and 0.10 for He^+, He^{++}, and He_2^+, respectively. The data presented must be considered representative of gas-covered tantalum, since no gas was observed to desorb from the target on heating to 1750°K. γ_i was found not to vary with time after cooling the target indicating rapid re-establishment of the equilibrium gas layer on the surface from within the metal. The work function of the covered Ta surface is found to be *ca* 4.9 ev, some 0.8 ev higher than that of atomically clean Ta. Considerations based on a theory which includes variation of energy levels near the metal surface show resonance neutralization of He^+ at the covered Ta surface not to be possible. Thus only the so-called direct process of potential ejection occurs, with which conclusion the measured energy limits of ejected electrons are in agreement.

I. INTRODUCTION

THE work reported in this paper is part of a program of study of electron ejection from the refractory metals by noble gas ions. Reports of work on electron ejection from Mo by He^+, He^{++}, and He_2^+ ions[1] and of the instrumentation and method[2] have been published. In these papers experimental apparatus and procedure, as well as the theoretical predictions concerning the so-called potential ejection of electrons by ions based on published theoretical treatments, have been discussed in some detail. Frequent reference to these discussions are made throughout this paper.

Measurements reported here include those of total electron yield (γ_i) *versus* incident ion kinetic energy in the range 10 to 1000 ev for He^+, He^{++}, and He_2^+, and of electron energy distributions for incident He^+ and He^{++} ions (Sec. III). It has been a primary goal in the present series of studies of electron ejection by ions to make these measurements with atomically clean target surfaces. Tantalum presents an interesting problem in this regard. The evidence is that, on heating the tantalum to 1750°K, the equilibrium adsorbed gas layer is absorbed into the lattice, and that the surface layer is re-established from within the metal rapidly on cooling. The work function of the cold tantalum appears to be some 0.8 ev higher than that of the hot tantalum. These conclusions are demanded by the observations of contact potential, energy limits of ejected electrons, electron yield as a function of time after cooling the target, and the adsorption rate of molecules from the surrounding residual gases in the apparatus (Sec. IV).

A brief sketch of an extension of the theory of potential ejection is given in this paper (Sec. V). In this theory an attempt is made to include the energies of interaction between the metal and the atomic particle (ion, metastable atom, normal atom) outside its surface. Electronic transitions which can occur as the ion approaches the metal surface are then described as transitions, obeying the Franck-Condon principle, between suitable potential energy curves. Only those aspects peculiar to the tantalum case are discussed in any detail here. A complete presentation of the theory is in preparation for separate publication. It should also be mentioned that these theoretical ideas and hence their application in the case of tantalum are strongly supported by experimental work with singly and multiply charged ions from all the noble gases (He, Ne, Ar, Kr, Xe) on atomically clean tungsten. This work has also been completed and is in preparation for publication.

In view of previous publications,[1,2] only a brief statement concerning apparatus and general procedure is included here (Sec. II). Notation used in this paper is defined in Table I in which numerical values used are also specified.

II. EXPERIMENTAL APPARATUS AND PROCEDURE

The experiment was performed with an apparatus in which ions, formed by electron impact, are (m/e)-analyzed and focused by suitable ion lenses on the front surface of a ribbon target situated in the center of a spherical electron collector. This instrument is that used in the molybdenum work[1] and is the first of the series discussed in the report on instrumentation and procedure.[2] The experimental method and evacuation procedure were the same as those used in the study of molybdenum[1] with the modifications noted below.

A conventional ionization manometer (the D.P.I. Model VG-1A) was used.[3] It read 1 to 2×10^{-8} mm Hg during the experiment. This is now recognized to be the lowest apparent pressure reading attainable with such a gauge, the plate current then actually resulting primarily from the release of photoelectrons by soft x-rays generated at the grid. That the pressure conditions were comparable to those of the molybdenum

[1] H. D. Hagstrum, Phys. Rev. **89**, 244 (1953).
[2] H. D. Hagstrum, submitted for publication in *The Review of Scientific Instruments*.
[3] The Bayard-Alpert ionization manometer [R. T. Bayard and D. Alpert, Rev. Sci. Instr. **21**, 571 (1950)] was disclosed during the course of the present experiments.

TABLE I. Notation and numerical values used.

e^-	electron
$e^-_{Ta}(-\alpha)$	electron in conduction band of Ta, α ev below top of surface barrier
e	electronic charge
He	normal helium atom
He^*	excited helium atom
He^m	^2S metastable helium atom
He^+, He^{++}	atomic helium ions
He_2^+	diatomic molecular helium ion
$E_{i1}(He)$, E_{i}, E_{i1}	first ionization energy of He ($\rightarrow He^+$; $=24.58$ ev)[a]
$E_{i2}(He)$, E_{i2}	second ionization energy of He ($\rightarrow He^{++}$; $=E_{i1}(He)+E_{i1}(He^+)=78.98$ ev)[a]
$E_i^v(He_2)$, E_i^v	vertical ionization energy of He_2 ($\rightarrow He^+$; $\cong 16.8$ ev)[b]
$E_x(He^m)$	electronic excitation energy of He^m ($=19.81$ ev)[a]
ϵ	ionization energy of He^m ($\rightarrow He^+$; $=E_i(He^m)=E_i(He)-E_x(He)=4.77$ ev)
$E_k(e^-)$, $E_k(He^+)$	kinetic energy of e^- and He^+, respectively
$\varphi(Ta)$, φ	work function of atomically clean tantalum ($=4.12$ ev)[c]
φ_h	work function of hot target during contact potential determination (taken in this work to be $\varphi(Ta)=4.12$ ev)
φ_c	work function of target at room temperature
$W_i(Ta)$, W_i	width of filled portion of conduction band in tantalum ($\cong 5.4$ ev)[d]
$W_a(Ta)$, W_a	$W_i+\varphi$ (for the cold target $W_i+\varphi_c$ should be used)
$E(He^+-Ta)$	energy of interaction of He^+ with the Ta target
$E(He^m-Ta)$	energy of interaction of He^m with the Ta target
α_n	static polarizability of He (2.16×10^{-25} cm^3)[e]
α_m	static polarizability of He^m (ca 57×10^{-25} cm^3)[f]
k_{max}	wave number of an electron in the highest occupied state in the metal (ca 10^8 cm^{-1})[g]
S, T	electrode designations for electron collector and target, respectively
V_{ST}	voltage between S and T (positive when T is positive with respect to S; in this work corrected for contact potential with respect to the hot target)
V_r	true retarding potential V_{ST}, corrected for contact potential with respect to the cold target
I_S, I_T	positive currents to electrodes S and T, respectively
I^i	primary ion current entering electrode S
I_r	current flowing between S and T when electron current ejected from T is suppressed, i.e., total current which flows as a result of reflection at T of incident ions as ions or metastable atoms and electron ejection by these particles at S. (See Fig. 4 of reference 1)
γ_i	number of electrons ejected at T per incident ion
ρ	$I_S/(I_T+I_S)$ ($=-\gamma_i$ for $V_r\ll 0$)
R	ρ at $V_r\gg 0$ ($=I_r/I^i$)
z	number of electronic charges per ion
$zd\rho/dV_r$	electron energy distribution function
p	pressure in mm Hg
Δt_c	target cold interval (measured from instant target is cooled after a flash)
Δt_h	target hot interval (measured from instant heating current is turned on)
Δt_m	monolayer adsorption time (Δt_c required to reach the surface condition at which the adsorption rate is observed to decrease from a relatively high to a relatively low value)
$(\Delta p)_1$	pressure rise observed at $\Delta t_h\cong 1$ sec resulting from desorption at the target
$(\Delta p)_2$	pressure rise observed at $\Delta t_h\cong 30$ sec resulting from desorption at the target supporting leads

[a] C. E. Moore, *Atomic Energy Levels*, National Bureau of Standards Circular 467 (U. S. Government Printing Office, Washington, D. C., 1949), Vol. I. Note that ionization energies are designated E_i rather than I, as in reference 1, to avoid confusion with currents. Excitation energy is denoted by E_x rather than E_e.

[b] This is taken to be the energy liberated accompanying neutralization by transition from the stable He_2^+ state to the repulsive He_2 state at constant nuclear separation. The value given here is that quoted by R. Meyerott, Phys. Rev. **70**, 671 (1946), based on observations of O. S. Duffendack and H. L. Smith, Phys. Rev. **34**, 68 (1929) of spectral enhancement in the $A^2\Pi\rightarrow X^2\Sigma$ system of CO^+ by the molecular ion He_2^+.

[c] H. B. Michaelson, J. Appl. Phys. **21**, 536 (1950).

[d] M. F. Manning and M. I. Chodorow, Phys. Rev. **56**, 787 (1939).

[e] *Landolt-Börnstein Tables* (Verlag Julius Springer, Berlin, 1950), Vol. I, Part I, p. 401.

[f] This value has been estimated on the basis of the one-term formula for the static polarizability given by H. Margenau, Revs. Modern Phys. **11**, 1 (1939), Eq. (C9). The f values for He and He^m are taken to be equal and the Δ values as equal to the corresponding E_i. Thus,

$$\alpha_m\cong[E_i(He)/E_i(He^m)]^2\cdot\alpha_n=57\times10^{25}\text{ cm}^3.$$

[g] This value is estimated from Fig. 3 of Manning and Chodorow (footnote d) for an electron at the highest occupied level in the metal Ta, 5.4 ev above the bottom of the conduction band.

experiment can be judged from the measurement of the rate of adsorption by the target support leads (see Sec. IV and Fig. 9). The 20 percent increase in initial slope of the $(\Delta p)_2$ *vs* Δt_c curve of Fig. 9, observed when He gas was admitted to the apparatus, indicates the admission of only a very small amount of adsorbable impurity with the He.[1]

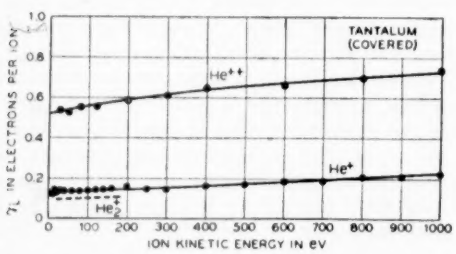

FIG. 1. Plots of total electron yield γ_i, as a function of ion kinetic energy for He^+, He^{++}, and He_2^+. The data must be taken as representative of gas-covered tantalum, as is discussed in the text.

III. RESULTS OF ELECTRON EJECTION EXPERIMENTS

The variation of total yield (γ_i) with ion kinetic energy has been determined for each of the ions He^+, He^{++}, and He_2^+. Results are plotted in Fig. 1. The He_2^+ ions were formed in the ionization chamber at relatively high gas pressure by the two-stage process: $He+e^-\rightarrow He^*+e^-$, followed by: $He^*+He\rightarrow He_2^++e^-$.[4] Beam currents of this ion were small; the data scatter is about ± 30 percent about the He_2^+ line in Fig. 4. Measurements for He^+ and He^{++} are believed to be accurate to 5 percent.

It will be noted that the data of Fig. 1 are attributed to "covered" tantalum. This is meant to call attention to the fact that the tantalum surface is not atomically

[4] J. A. Hornbeck and J. P. Molnar, Phys. Rev. **84**, 621 (1951).

clean in this work. The dependence of $\gamma_i(He^+)$ on ion energy observed here is seen to resemble that observed for gas-covered Mo (Fig. 6 of reference 1) and not that for atomically clean Mo. This is the first of several pieces of evidence relating to the state of the target surface.

Retarding potential curves from which electron energy distributions are determined are plotted in Fig. 2. The quantity $\rho=I_S/(I_T+I_S)$ is plotted against the voltage V_{ST} between target and electron collector, corrected for the measured contact potential between the collector and the target. The contact potential measurement[5] is made with the target hot enough to emit electrons thermally and thus strictly gives the correction relative to the *hot* target only. Barring

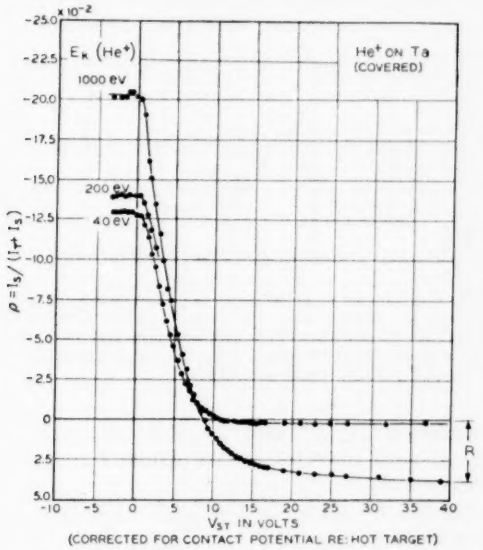

FIG. 2. Retarding potential curves for electrons ejected by He^+ ions of 40-, 200-, and 1000-ev kinetic energy. Note that the abscissa scale is not true retarding potential V_r for the cold target.

extraordinary circumstances, this may also be taken as the contact potential between electron collector and the target immediately after cooling, before an appreciable fraction of a monolayer has been adsorbed upon the surface. Extraordinary circumstances prevail in the case of tantalum, however, a second evidence of which is to be noted in the curves of Fig. 2. The downward break from the value of ρ at $V_{ST}<0$ $(=\gamma_i)$ is seen to occur nearly a volt to the right of the zero axis. This is observed at each ion energy used and represents a behavior at variance with that observed for clean Mo.

In Fig. 3 are plotted the initial portions of retarding potential curves for covered Ta and atomically clean Mo determined with He^+ ions of 200-ev energy. Both are plotted against V_{ST} corrected by the contact

[5] See Sec. VIII of reference 2.

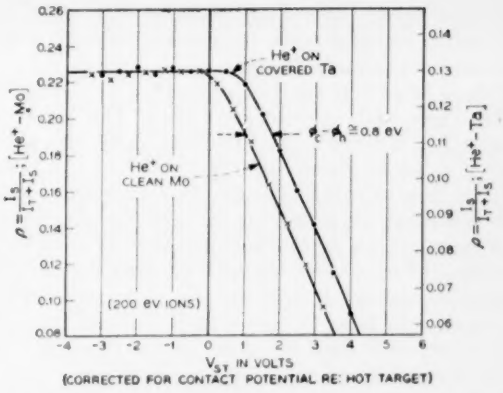
He⁺ ON COVERED Ta
He⁺ ON CLEAN Mo
(200 eV IONS)
ρ = I_S/(I_T+I_S); [He⁺-Mo]
ρ = I_S/(I_T+I_S); [He⁺-Ta]
V_ST IN VOLTS
(CORRECTED FOR CONTACT POTENTIAL RE: HOT TARGET)

FIG. 3. "Initial" portions of ρ *vs* V_{ST} curves for He^+ ions of 200 ev incident on atomically clean Mo and gas-covered Ta. The abscissa scale has been corrected for contact potential relative to the hot target and represents the true V_r scale for the Mo only. The shift of the Ta curve is caused by the increase of work function of the Ta on cooling as discussed in the text. The ordinate scales have been adjusted in extension to make the slopes of the curves at positive V_{ST} about equal and have been adjusted relative to one another so as to make the horizontal portions at negative V_{ST} colinear.

potential measured relative to the hot target. It is unthinkable that the tantalum curve indicates a measured minimum electron energy in the distribution greater than zero. The finite size of the target relative to the electron collector makes electrons of apparently zero energy appear in the measured distribution, even though, in fact, the actual distribution does not extend

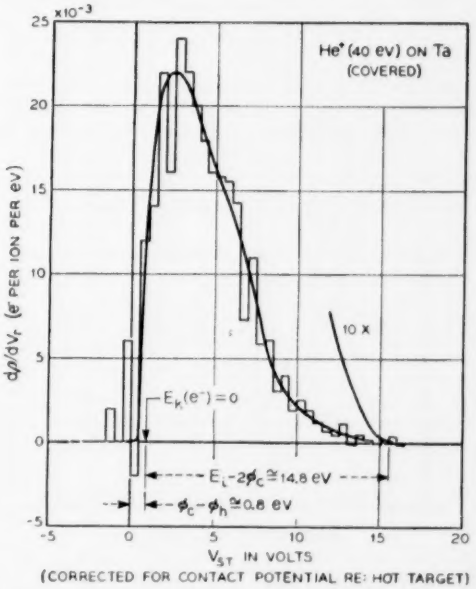

FIG. 4. Plot of $\Delta\rho/\Delta V_r$ obtained from the retarding potential data for electrons ejected by 40-ev He^+ ions. A smoothed $d\rho/dV_r$ curve is drawn through the stepped curve.

to zero energy. One must conclude that since the retarding potential curve is measured with the target at room temperature, the shift of the curve on the V_{ST} scale to be seen in Fig. 3 is the result of an increase in the target work function on cooling. The curve for clean Mo is taken to represent the curve obtainable with a metal whose work function does not alter appreciably on cooling. None of the evidences presented in this paper which indicate the rapid covering of the tantalum on cooling with a surface layer of atoms from within the metal were observed for molybdenum. The small dependence of work function on temperature for a clean metal is not taken into account specifically here. If it were the same for clean Ta and clean Mo, its effect would cancel out of these measurements.

The relative positions on the abscissa scale of the two curves of Fig. 3 is taken to indicate that the work function of the tantalum at room temperature φ_c is *ca* 0.8 ev greater than that of the hot tantalum φ_h. Whether φ_h is the work function φ of atomically clean Ta or not has not been demonstrated. φ_h is probably equal to φ, but if not, is most likely greater than φ. The true retarding potential (V_r), when the tantalum target is at room temperature, is to be obtained by subtracting 0.8 volt from the V_{ST} scale which has already been corrected by the *measured* contact potential.

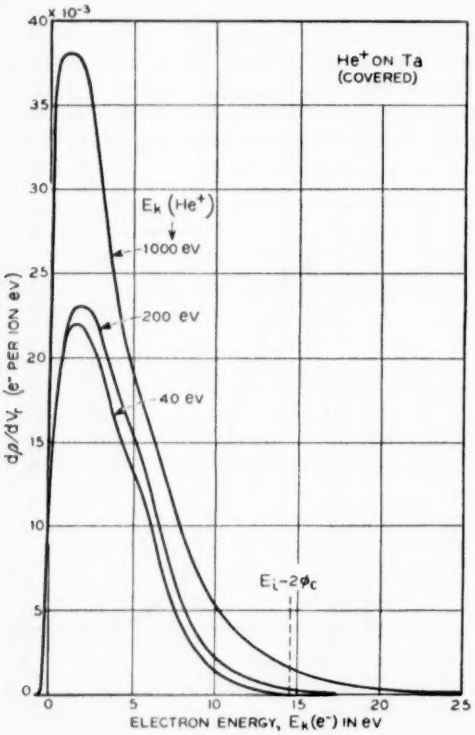

FIG. 5. Kinetic energy distributions of electrons ejected by He^+ ions of 40-, 200-, and 1000-ev kinetic energy. Note that the abscissa scale here has been corrected by contact potential *to the cold target* and is thus shifted by 0.8 volt from those of Figs. 2, 3, and 4.

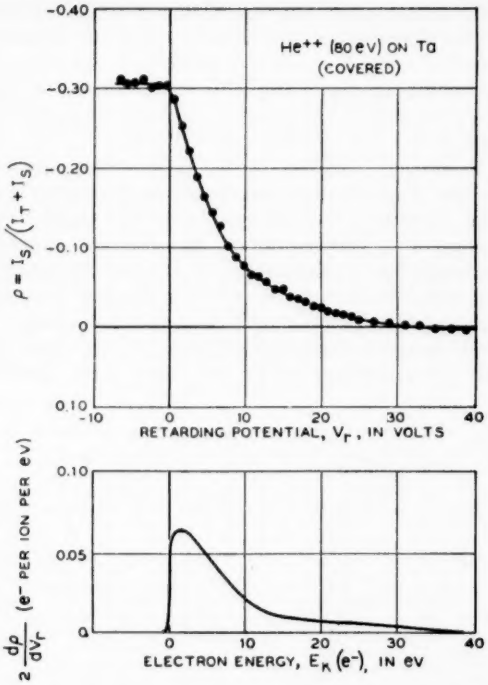

FIG. 6. Retarding potential curve (top) and energy distribution (bottom) for electrons from He^{++} ions of 80-ev energy incident on gas-covered tantalum. Note that for both of these curves the abscissa scale used is the true V_r scale, i.e., the V_{ST} scale corrected by contact potential to the *cold* target.

The electron energy distribution function is obtained from the ρ *vs* V_{ST} curve by differentiation. This has been done in this work by plotting the $\Delta\rho/\Delta V_r$ curve calculated from the data (the step curve in Fig. 4) and drawing through this a smooth curve (also to be seen in Fig. 4). $d\rho/dV_r$ curves obtained in this manner for each of the energies of He^+ used are shown in Fig. 5 plotted to the true V_r scale, as defined above. The reasons for the small extension of these curves to negative V_r has been discussed in Sec. VI of reference 1. Here again the resemblance of these curves to those for gas-covered Mo is to be noted. Attention is called to the fact that the distribution for $E_k(He^+)=40$ ev contains no electrons of energies greater than the limit $(E_i-2\varphi_c)$ and that the distribution for $E_k(He^+)=1000$ ev does. These facts will be discussed in Sec. V.

In Fig. 6 retarding potential data and electron energy distribution for ejection by He^{++} are plotted.

Many of the conclusions to be drawn from the data presented here are the same as those already drawn in the case of He ions on Mo. They will be only briefly summarized here. Nine points may be made, as follows.

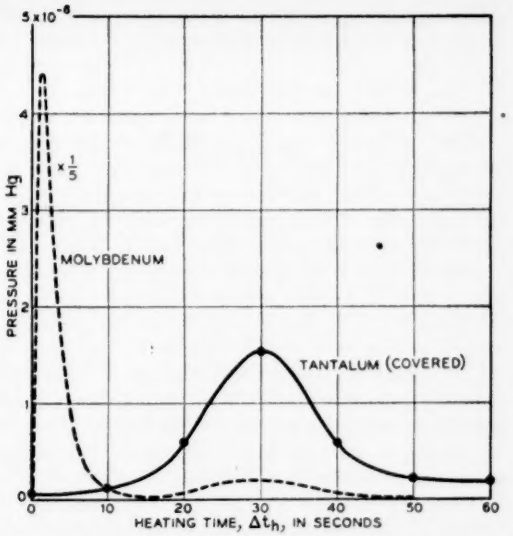

FIG. 7. Plots of pressure *versus* heating time Δt_h, observed for tantalum and molybdenum targets heated to 1750°K. The curve for the molybdenum target is schematic. The maxima in the pressure rise at $\Delta t_h \cong 1$ and 30 sec are designated $(\Delta p)_1$ and $(\Delta p)_2$, respectively. Note that $(\Delta p)_1 = 0$ for the tantalum target.

1. γ_i is remarkably independent of ion kinetic energy (Fig. 1). This is taken to indicate a *potential* ejection mechanism.

2. The quantity $R = I_r/I^i$ (the value of ρ at $V_r \gg 0$) is found to be small relative to γ_i, at least at low ion energy (Fig. 2). I_r specifies the secondary ionic and tertiary electronic currents which flow between target and electron collector as the result of reflection of ions as ions or metastable atoms at the target surface. Thus the smallness of R indicates that essentially every ion decays to the normal atom at the metal surface.

3. The measured value of γ_i is considerably less than 0.5, despite the fact that every ion decays. This is taken to indicate refraction and partial internal reflection at the image barrier of the internal secondary electrons as they attempt to leave the metal.[6] The observed value of γ_i is then determined principally by the probability of the electrons escaping from the metal rather than by the probability of excitation of electrons which is near unity.

4. The electron yields for He^{++}, He^+, and He_2^+ are roughly in the ratio of energy available after neutralization, that is: $\gamma_i(He^{++}):\gamma_i(He^+):\gamma_i(He_2^+) \cong [E_{i2}(He) - 2\varphi_e]:[E_{i1}(He) - \varphi_e]:[E_i^v(He_2) - \varphi_e]$.[7] This result is consistent with the observation that the average energy of electrons ejected by He^+ and He^{++} are roughly equal (see item 9 below).

5. The maximum kinetic energy in the distribution of electrons ejected by slow He^+ ions (40 ev) is, if anything, less than the limit $E_i - 2\varphi_e$ predicted for the direct Auger process (Fig. 2 of reference 1) without any account being taken of energy level shifts when the atomic particle is near the metal surface. This point is discussed again in Sec. V below.

6. Both the γ_i *vs* $E_k(He^+)$ and the $d\rho/dV_r$ *vs* $E_k(e^-)$ curves found here resemble in form those observed for gas-covered tantalum. γ_i is found to rise steadily with $E_k(He^+)$, not to drop first and rise again with increasing $E_k(He^+)$, as was observed with clean Mo. The electron energy distributions are found to be deficient in faster electrons as was found for covered Mo with respect to clean Mo.

7. The quantity R is observed to increase with kinetic energy of the incoming ion indicating greater chance of reflection as an ion or metastable atom as the ion approach velocity increases.

8. Electrons are found to be ejected with velocities in excess of the limit $E_i - 2\varphi_e$, when the incident ion energy is 1000 ev. Here is further evidence of the deficiencies of the published theories in that they neglect energy level shifts near the metal surface.

9. Electrons ejected by He^{++} possess, on the average, little more energy than those ejected by He^+. This is taken to indicate a stepwise decay of He^{++} to normal He, one electron being excited inside the metal per jump. The γ-ratios mentioned in item 4 may also be taken as evidence supporting this view.

Further discussion of the tantalum results as they relate to the state of the target surface is included in Sec. IV, and as they relate to present and proposed theory in Sec. V. There have been published no other studies of electron ejection from Ta by noble gas ions with which the present results may be compared.

IV. STATE OF THE TANTALUM SURFACE

In the results of the electron ejection experiments, we have seen two evidences that the tantalum surface at room temperature is not atomically clean. These are: (1) that the forms of the γ_i *vs* E_k and $d\rho/dV_r$ curves resemble those for gas-covered molybdenum and (2) that the work function of the cold surface appears to be

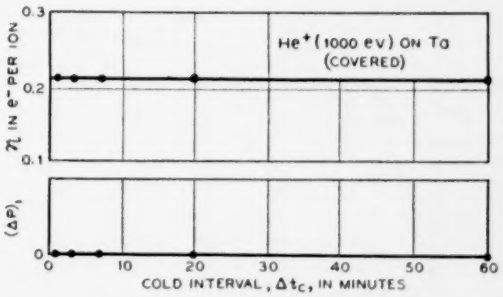

FIG. 8. Plots of γ_i, the electron yield per incident ion, and $(\Delta p)_1$, the pressure rise observed when the tantalum target is heated, as functions of target cold interval. The γ_i-measurements were made with He^+ ions of 1000-ev kinetic energy at the target. Note specific definition of $(\Delta p)_1$ in Fig. 1.

[6] Sec. V and Fig. 7 of reference 1.
[7] This is further discussed in Sec. V of reference 1.

ca 0.8 ev greater than that of the hot surface. Two further results concerned with the state of the tantalum surface are the following: (3) No gas could be removed from the tantalum by heating to 1750°K, and (4) γ_i was observed to be independent of time after cooling from 1750°K.

In the experiment with molybdenum, it was possible to measure the rate of adsorption of residual gases on the target and thus to determine the so-called monolayer adsorption time. This time interval turned out to be sufficiently great to show the molybdenum to be atomically clean to within a few percent for secondary electron emission measurements made within a few minutes after a target flash. This was not possible in the case of tantalum. Although the Ta target was heated to 1750°K as was the Mo, at no time was a pressure rise observed on heating. This result is to be seen in Fig. 7. Despite the fact that the target comes up to temperature in 1 to 2 seconds, it is seen that the pressure begins to rise only after a considerably greater time has elapsed, reaching a peak some 30 seconds after heating commenced. This later pressure rise is the result of evolution of gas from the heavy molybdenum leads to which the thin target ribbon is attached. After passing through the maximum at 30 seconds the pressure drops to a value below 2×10^{-7} mm Hg, where it has been observed to remain with the target hot for as long as 20 minutes. The dashed curve of Fig. 7 represents schematically the p *vs* Δt_h dependence characteristic of a Mo target. Note the large pressure rise in about 1 second as gas is desorbed from the target itself as well as the desorption of gas from the target leads at longer times.

The evidence concerning the variation of γ_i with target cold interval Δt_c is to be found in Fig. 8, in which both γ_i and $(\Delta p)_1$ are plotted as functions of Δt_c. Neither is observed to vary with Δt_c, in remarkable contrast to what was observed with Mo (Fig. 5 of reference 1). γ_i at other ion energies was also found to be independent of target cold interval.

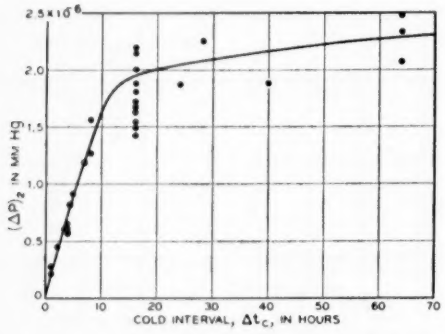

FIG. 9. Plot of $(\Delta p)_2$ *versus* Δt_c for release of adsorbed gas from the target support leads. All the data taken over a period of several weeks are plotted here.

What we now know and are driven to conclude about the state of the tantalum surface is the following. It has a work function when cold *ca* 0.8 ev greater than when hot. Clearly the cold surface differs from the hot surface and must be covered with adsorbed atoms. However, no gas is observed to flash off the surface. Hence, the surface layer must be "swallowed" into the lattice on heating. But the surface condition of the tantalum, when cold, reestablishes itself in less than one minute, the Δt_c value of the first reading of the γ_i-curve of Fig. 8. It is true that one depends here upon a γ_i-measurement which could conceivably be insensitive to the surface condition. This is considered unlikely in view of the observations of changes in γ_i with the adsorption of gas on Mo[1] and on W.[8] Furthermore, one cannot attribute the rapid restoration of the equilibrium surface condition to adsorption from the surrounding residual gas in the apparatus. The arrival rate of gas molecules at the surface is too small. The experimental evidence for this last statement is the $(\Delta p)_2$ *vs* Δt_c-curve of Fig. 9, which shows the adsorption rate on the target supporting leads to correspond to a monolayer adsorption time close to 10 hours.

The evidences from several directions thus appear to point to the following conclusion with respect to the state of the tantalum surface. When cold, it is covered with an equilibrium gas layer. This layer is absorbed into the body of the metal on heating to 1750°K reducing the surface work function by *ca* 0.8 ev. The surface layer is re-established rapidly on cooling by the "squeezing out" of the absorbed gas onto the surface again. Presumably the continued periodic heating has brought about a state of equilibrium such that no further gas need be adsorbed from the surroundings. If φ_h is taken as equal to $\varphi(\text{Ta})=4.12$ ev, φ_c is approximately 4.9 ev.

The behavior of tantalum observed in this work is in accord with what is known of the reaction of gases with incandescent tantalum. Andrews,[9] for example, reports that N_2 is readily absorbed by Ta at 2100°K, slowly below 1600°K. O_2 is taken up readily at 1000°K and with extreme rapidity at 1800°K. H_2O, on the other hand, is decomposed above 1400°K, according to Andrews, the O_2 being absorbed and the H_2 evolved. The residual gas in the present apparatus consists predominantly of CO, which may presumably be taken to behave with respect to adsorption much like N_2. O_2 has never been observed with the mass spectrometer. From the fact that no gas is evolved when the Ta is heated and Andrews' result that H_2 is evolved when H_2O decomposes, it may be concluded that little H_2O is present in the background gas, although it was observed in the early stages of the evacuation procedure.

[8] Work done on the adsorption of the common gases, including N_2 and CO, on *W* and its effect on the electron ejection by ions is to be published soon. See H. D. Hagstrum, Phys. Rev. **89**, 338 (1953).

[9] M. R. Andrews, J. Am. Chem. Soc. **54**, 1845 (1932).

V. DISCUSSION OF THEORY

In the published literature there are wave mechanical theories which deal with two types of possible potential ejection processes.[10] These processes are (1) the direct neutralization of the ion to the normal state of the atom accompanied by the excitation of an internal secondary electron (called here the direct process) and (2) the resonance neutralization of the ion to the metastable state followed by the decay of the metastable atom with excitation of an internal secondary electron (called here the two-stage process). The calculations of the transition probabilities involved have all neglected shifts of atomic energy levels near the metal surface. In the present work and the earlier molybdenum work,[1] there are definite violations for fast ions of the electron kinetic energy limits expected on the basis of no energy level variation.

The treatment of electronic transitions in diatomic molecules is suggestive of a manner of description in the present case which lends itself to the inclusion of the energies of interaction between the metal and the atomic particles involved. One calculates, or estimates where necessary, the potential energy of the ion, metastable atom, and normal atom as a function of distance outside the metal surface. Such potential energy curves are placed properly with respect to each other on an energy-distance plot by consideration of the energy transformations in isoelectronic systems necessary to go from one state to another with the atomic particle removed to an infinite distance. The electronic transitions involved in potential ejection processes are then described as jumps between these potential curves which obey the Franck-Condon principle. The probability of a transition at a given distance from the metal may be considered to be given, to order of magnitude at least, by the wave mechanical theories which neglect level shifts. This approach is most useful in determining whether a process (resonance neutralization, for example) can or cannot occur at a certain atom-metal distance and what are the energy limits to be expected for electrons ejected by the Auger processes listed above.[11]

The forces considered in drawing potential energy curves are (1) the image force of attraction for ions, (2) the van der Waals forces of attraction between the metastable atom or the normal atom and the metal, and (3) the repulsive forces which set in at close approach. The image force can be calculated exactly. The van der Waals attractions have been calculated by the formula of Prosen and Sachs.[12] The repulsive forces must be estimated. The reasonable assumption has been made, however, that these forces *may* become appreciable at distances from the metal which increase with the diameter of the atomic particle in question. This assumption has been found adequate to indicate significant differences between the energy limits to be expected for electrons ejected by the direct *versus* the two-stage ejection mechanisms.

The conclusions with respect to the energy limits of electrons resulting from the direct and the two-stage ejection processes are the following, stated here without proof. The direct process is expected to yield electrons which for sufficiently slow ions have energies outside the metal which cannot exceed the limit $E_i-2\varphi$. The two-stage process, on the other hand, is expected to yield electrons whose energies do exceed the limit $E_z-\phi$ calculated for this process neglecting level shifts. It may be stated that in the work on noble gas ions on W, mentioned in Sec. I of this paper as being in preparation for publication, there are to be found examples of both of the cases listed. As the approach velocity of the ion is increased, an increasing proportion of the electronic transitions resulting in secondary electron emission occur very close to the metal surface where the energy levels are most likely quite diffuse. This possibility is called upon to account, at least in part, for electrons ejected by faster ions (1000 ev) which possess energies in excess of the limits given in either case.

In the light of the theory sketched above there are two points of interest in the case of He^+ on Ta. These are: (1) Can He^+ be neutralized to the metastable level He^m, making the two-stage ejection process possible, and (2) are the observed energy limits for slow ions (40 ev) consistent with the result of point (1) and the theoretical conclusions with regard to the energy limits to be expected from the two types of ejection processes? Interest in the answers to these questions is heightened because they are intimately bound up with the value of the work function of the tantalum surface and must be consistent with the conclusions concerning the state of the tantalum surface already indicated (Sec. IV).

We consider first the possibility of resonance neutralization to the metastable level. This process may be written thus:

$$He^+ + \epsilon^-_{Ta}(-\alpha) \rightarrow He^m, \qquad (1)$$

where $-\alpha$ is an energy below the vacuum level which puts ϵ^-_{Ta} in the conduction band, i.e., $\varphi<\alpha<W_a$. In addition, α must have the value which makes the energies represented on the two sides of Eq. (1) equal. Neglecting the energies of interaction of He^+ and He^m with Ta, it is apparent that $\alpha=\epsilon$ is the value which meets this criterion. Thus, on this simple picture the process of Eq. (1) can occur if $\varphi<\epsilon<W_a$ and cannot if $\epsilon<\varphi$.

Including the energies of interaction of the atomic particles with the metal surface, the energy balance demanded by Eq. (1) and the Franck-Condon principle, taking the energy level of the system $He^+ + \epsilon^-_{Ta}(-\varphi)$

[10] The results of these theories have been summarized in Sec. II of reference 1.

[11] Results of this potential curve theory were mentioned briefly in Sec. VII of reference 1.

[12] Equation (20) of E. J. R. Prosen and R. G. Sachs, Phys. Rev. **61**, 65 (1942).

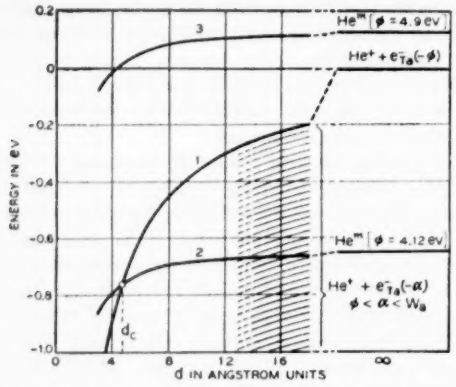

FIG. 10. Potential energy diagram for the case of resonance neutralization of He^+ to He^m at a tantalum surface. Curves are drawn representing the situation for atomically clean Ta ($\varphi = 4.12$ ev) and for the covered Ta encountered in the experimental work ($\varphi = \varphi_c \cong 4.9$ ev). Discussion of the conclusions drawn is to be found in Sec. V of this paper.

as zero, is the following:

$$E(\mathrm{He}^+ - \mathrm{Ta}) - (\alpha - \varphi) = E(\mathrm{He}^m - \mathrm{Ta}) - (\epsilon - \varphi), \quad (2)$$

or

$$\alpha = E(\mathrm{He}^+ - \mathrm{Ta}) - E(\mathrm{He}^m - \mathrm{Ta}) + \epsilon. \quad (3)$$

The Franck-Condon principle must be applied here, because the interaction energies involved are functions of the metal-atom distance d. The Franck-Condon principle, in this case, states that the position and momentum of the atomic particle relative to the metal are essentially unaltered during the electronic transition represented by Eq. (1). Only if this is true can one insert expressions for $E(\mathrm{He}^+ - \mathrm{Ta})$ which involve the distance d and calculate α on a quasi-equilibrium basis as a function of d.

For $E(\mathrm{He}^+ - \mathrm{Ta})$ we use the image potential energy $-e^2/4d$, and for $E(\mathrm{He}^m - \mathrm{Ta})$, the van der Waals interaction energy, $-[\alpha_m e^2 \pi k_{\max}{}^2 \ln(2k_{\max} d)]/(2\pi)^3 d^2$, calculated by Prosen and Sachs.[12] Numerical values used are specified in Table I. Insertion of these expressions into Eq. (3) yields

$$\alpha = -\frac{e^2}{4d} + \frac{\alpha_m e^2 \pi k_{\max}{}^2 \ln(2k_{\max} d)}{(2\pi)^3 d^2} + \epsilon. \quad (4)$$

As d decreases from large values toward zero, α decreases since the image potential term $-e^2/4d$ predominates. When α reaches the value φ, the work function of the metal, the neutralizing electron is removed from the top of the conduction band. The distance d_c at which this takes place represents a critical distance beyond which resonance neutralization is possible and within which it is not. For $d < d_c$, $\alpha < \varphi$ in which region the energy levels are not populated (neglecting the small population above the Fermi level at temperatures above absolute zero). If the resonance neutralization has occurred at $d > d_c$, it is possible, however, for the metastable atom so formed to be ionized at $d < d_c$.[13]

The relationships discussed above are conveniently shown in the potential energy diagram of Fig. 10. Here the potential energies of the isoelectronic systems represented on each side of Eq. (1) are plotted against the distance, d, between the metal surface and the atomic particle. These potential energies are specified in Eq. (2). Curve 1 represents the energy of the system $\mathrm{He}^+ + e^-_{\mathrm{Ta}}(-\varphi)$ as a function of d. This level lies below that of $\mathrm{He}^+ + e^-_{\mathrm{Ta}}(-\varphi)$ at $d = \infty$, taken as zero, by the image potential $-e^2/4d$. Below curve 1 there lies a continuum of potential curves representing the levels $\mathrm{He}^+ + e^-_{\mathrm{Ta}}(-\alpha)$, $\varphi < \alpha < W_a$, which extends to a level W_i below curve 1. Curve 2 represents the level of the metastable atom He^m relative to $\mathrm{He}^+ + e^-_{\mathrm{Ta}}(-\varphi)$ at $d = \infty$. Its variation with distance is given relative to the assumed zero level by $E(\mathrm{He}^m - \mathrm{Ta}) - (\epsilon - \varphi)$. Curve 2 is drawn for $\varphi = \varphi(\mathrm{Ta}) = 4.12$ ev, curve 3 for $\varphi = \varphi_c = 4.9$ ev.

The Franck-Condon principle permits transitions from $\mathrm{He}^+ + e^-_{\mathrm{Ta}}(-\alpha)$ to He^m only at crossing points of the corresponding potential curves. It is clear from Fig. 10 that curve 2 crosses some curve in the continuum below curve 1 at all $d > d_c$. Curve 3 crosses no curve belonging to the family of states $\mathrm{He}^+ + e^-_{\mathrm{Ta}}(-\alpha)$, $\varphi < \alpha < W_a$. Thus, if the conclusions concerning the work function of the tantalum already arrived at are correct, $\varphi = \varphi_c$ and the resonance neutralization process cannot occur at any distance d. Hence, the only potential ejection process possible for covered tantalum is the direct process for which, at low incoming ion velocity, the electron energies should not exceed $E_i - 2\varphi_c$. That this is true is to be seen in Fig. 5 [$E_k(\mathrm{He}^+) = 40$ ev].

It should be noted that the resonance neutralization of He^+ to He^m at an atomically clean Ta surface would be possible only if the transition probability has become appreciable before the ion crosses the critical distance d_c. Sternberg[14] has recently calculated 4 to 5A as the distance at which it becomes highly probable that a 10-ev He^+ ion will be neutralized. Thus resonance neutralization of He^+ at an atomically clean Ta surface should just be possible. However, the uncertainties in the van der Waals interaction term used here should not be forgotten.

Finally, it should be remarked that the direct process predicts a minimum electron energy of $E_i - 2W_a \cong 4.0$ ev on the basis of no energy level shifts near the metal surface. Consideration of the process in more detail shows this limit to be reduced by energy level shifts

[13] L. J. Varnerin, Jr. (private communication) has found independently that inclusion of the image potential in the consideration of the resonance neutralization process yields the critical atom-metal distance, with respect to which the process may or may not proceed as described here.

[14] D. Sternberg (private communication).

near the metal. Furthermore, the finite size of the target precludes observation of a minimum energy greater than zero on geometrical grounds.

The discussion of theory included here is admittedly sketchy. It is meant to show the consistency of the theoretical results with the conclusions concerning the state of the tantalum surface and its work function demanded by the experiment. A detailed account of the theory, including conclusions stated here without proof, is forthcoming.

The author wishes to acknowledge with thanks the discussions with his colleagues, J. A. Hornbeck, K. G. McKay, J. P. Molnar, and A. H. White, the efforts of H. W. Weinhart in design and supervision of construction of the experimental apparatus, and the technical assistance of F. J. Koch.

PHYSICAL REVIEW VOLUME 91, NUMBER 3 AUGUST 1, 1953

Reversible Bleaching of a Band in the Absorption Spectrum of Diamond

PETER PRINGSHEIM
Chemistry Division, Argonne National Laboratory, Lemont, Illinois
(Received April 13, 1953)

When diamonds which show the absorption band in the near ultraviolet, characteristic of blue fluorescing samples, are exposed to neutron bombardment, a continuous absorption slowly rising toward shorter wavelength is superimposed upon the band. Heating such a diamond to temperatures between 300° and 600°C decreases the continuous absorption and the structure of the band becomes appreciably sharper. Subsequent exposure to light greatly reduces the height of individual peaks in the band, while the continuous absorption at shorter wavelengths is increased. Renewed heating restores the sharp structure of the band and the cycle can be repeated at will. Heating the crystal to 750°C brings the crystal very nearly back into the state before neutron bombardment in which the reversible bleaching cannot be observed. A similar band accompanies the sharp line at 503 mμ that is produced in the absorption spectrum of diamonds by neutron bombardment and heat. The structure of this band is also altered by heating to various temperatures but is not affected by absorption of light.

MOST diamonds of the so-called type I show in their absorption spectra a sharp line at 415.2 mμ and an adjoining band with a number of peaks in the range from 405 to 350 mμ. It has been mentioned in a preceding paper[1] that under certain conditions the intensity distribution within this band can be altered appreciably and reversibly by heating a diamond in the dark to temperatures between 300 and 500°C and then exposing it to violet or near ultraviolet radiation. The phenomenon had been observed only with a diamond which had previously been subjected to neutron bombardment in the Argonne heavy water pile. However, since the band was present in the absorption spectrum before this treatment, it seemed probable that even then it would have exhibited the same behavior which might be connected with the well-known thermoluminescence properties of many diamonds.

In more recent experiments, several diamonds were investigated in which the line and band in the neighborhood of 400 mμ in the absorption spectra before irradiation had a much greater intensity than in the earlier sample. Moreover, the spectra were recorded at the temperature of liquid nitrogen at which temperature the structure of the band is much better resolved than at room temperature. Figure 1, curve a represents the absorption spectrum from 800 to 300 mμ of one of the new diamonds (D46) before any treatment. The line at 415.2 mμ is somewhat distorted on the curves of Fig. 1 because the scanning speed of the recording spectrophotometer was too great for the high intensity and sharpness of the line. Curve a in Fig. 2 represents the region from 420 to 300 mμ of the same spectrum with a tenfold slower scanning speed. The relative intensities of the line and the various band peaks are shown with much better accuracy in this figure.[2] Repeated heating of the diamond to temperatures between 300 and 650°C and subsequent exposure to light did not alter the spectrum in the least. The same result was obtained with another sample (D52). Curves b in Figs. 1 and 2 represent the absorption spectrum of the diamond D46 after 20 hours exposure to neutron bombardment. The absorption spectrum is characterized by a broad band in the orange and a strong increase of absorption below 500 mμ. Since the maximum transmission is located in the neighborhood of 500 mμ, the crystal acquired the well-known blue-green color in transmitted light. The nearly straight line c, obtained as the difference between curves b and a in Fig. 2, proves that, at least in this spectral region, the effect of the pile exposure consists only in the super-

[1] P. Pringsheim and R. Voreck, Z. Physik **133**, 2 (1952).

[2] On spectrograms obtained by several investigators with spectrographs of higher resolving power, additional fine structure appears in the band, of which only a trace can be recognized in the curves of Figs. 2 and 3. [See P. G. N. Nayar, Proc. Indian Acad. Sci. **A15**, 293 (1942); A. Mani, Proc. Indian Acad. Sci. **A19**, 231 (1944).]

position upon the original band of a continuous and continuously rising absorption without any selectivity. As shown by comparison of curve b of Fig. 2 with curve a of Fig. 3 this continuum is not uniformly reduced by a certain amount when the diamond is heated at 540°C, but simultaneously the band peaks beginning with the one at 393 mμ are relatively enhanced and some of them at least become much sharper, while the line at 415.2 mμ and the first band peak remain essentially unaltered. This is demonstrated very clearly by curve d of Fig. 3, which was obtained as the difference between curve b of Fig. 2 (before heating) and curve a of Fig. 3 (after heating). At the peak wavelengths, 393, 384, 375, and 366 mμ, the decrease in optical density is much smaller than in the other parts of the spectrum. If the crystal, which so far had been kept in the dark, was now exposed for an hour to the radiation of a mercury-H4 lamp,[3] the intensity distribution in the absorption band is altered as indicated in curve b of Fig. 3. Curve c in the same figure, which is almost exactly complementary to curve d, is drawn as the difference between curves a and b of Fig. 3. Curve e of Fig. 3, which represents the difference between curve b of Fig. 2 and curve b of Fig. 3, is again very nearly a straight line. Thus, a part of the continuum produced by neutron bombardment is bleached out by heating and irradiating with light while by heat alone, in addition to the general bleaching, the band peaks below 403 mμ are enhanced. The relatively larger intensity loss which heating produces in the continuum below 340 mμ is recovered in the light bleaching process.

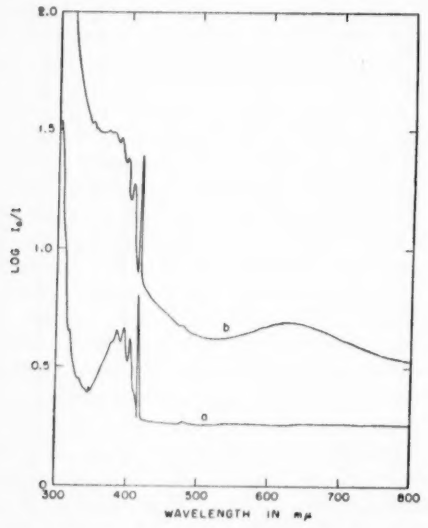

FIG. 1. Absorption spectrum of diamond D46 recorded at −190°C. a. Before treatment; b. after exposure in the pile

[3] It has been shown that the green-yellow lines of the mercury arc are ineffective and that the violet and near ultraviolet lines are responsible for the bleaching. (See reference 1.)

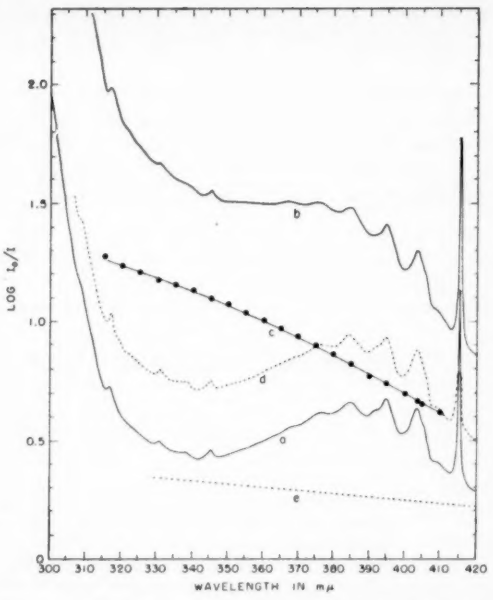

FIG. 2. Absorption band of diamond D46 below 420 mμ recorded at −190°C. a. Before treatment; b. after exposure in pile; c. difference b−a; d. after 20 hours at 750°C; e. difference d−a.

The temperature range in which this effect is produced lies between 300 and 650°C, with an optimum between 450 and 550°C. The case represented in Fig. 3 relates to heating at 540°C. Almost identical sets of curves were obtained with another irradiated diamond (D44) after heating it to 450°C. A second heat treatment at the same temperature reproduced exactly the same behavior. A third diamond (D19) underwent the entire cycle of treatments five times: heating to 350°C, bleaching with light and reheating, every time with identical results. It thus appears that when a pile-irradiated diamond has been heated for one hour to a certain temperature, additional heating at the same temperature does not alter its optical properties any further, except to enhance the various band peaks, and this effect disappears again under exposure to light. The bleaching is quite as effective when the crystal is kept at the temperature of liquid nitrogen as it is at room temperature. Heating to temperatures as low as 300°C or as high as 650°C produces the same phenomenon, but the sharpening and enhancement of the band peaks are less pronounced. This is no longer true, when the diamond is heated to 750°C. In this case the crystal is converted directly into the state represented by curve d of Fig. 2. The difference between this curve and curve a is given by the slowly rising straight line e in Fig. 2 which represents the small remainder of the continuum produced by the neutron bombardment. Exposure to light does not alter this state further.

The line at 415.2 mμ and the first main band peak at 403 mμ are practically unaffected by the treatment

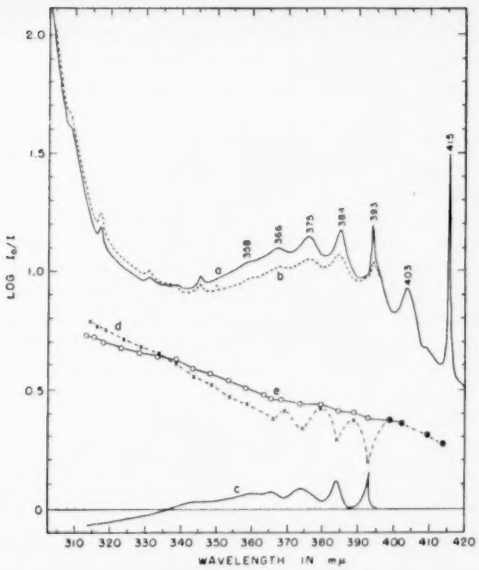

FIG. 3. Absorption band of diamond D46 below 420 mμ recorded at −190°C. a. After 20 hours in pile and 1 hour at 540°C in the dark; b. after 1-hour exposure to Hg arc light; c. difference a−b; d. difference between b of Fig. 2 (after pile exposure) and a of Fig. 3 (after heating in dark); e. difference between b of Fig. 2 (after pile exposure) and b of Fig. 3 (after heating and light bleaching).

described above. The line corresponds almost certainly to a purely electronic transition and the adjoining band originates from transitions to various vibrational levels of the excited electronic state. The spacing of the peaks is of the order of magnitude occurring also in the infrared and Raman spectra of diamond. An exact coincidence is not to be expected because these vibrational frequencies belong to different electronic states. Moreover, the peaks are not characteristic of transitions to a single series of vibrational levels but to several overlapping series. Even the incompletely resolved spectra represented by Figs. 2 and 3 show this. The sharpening of the peak at 393 mμ is clearly due to the disappearance of a weaker component forming a shoulder on the long wavelength side of the main peak. The complex formed by the line and the band is always weak. Even in the spectra of samples which show it with relatively great intensity the absorption at the center of the band seldom exceeds 10 cm^{-1}, with a half-width of about 0.5 ev. This means that either the corresponding electronic transition occurs in all atoms of the diamond lattice with an oscillator strength of about 10^{-8} or that a relatively small number of "centers" with an appreciably greater oscillator strength are responsible for the absorption. The fact that the intensity of the band differs so widely in various samples is definitely in favor of the second assumption.

This does not mean necessarily that the line and band are due to the presence of impurities. It might quite as well be possible that local irregularities in the lattice make possible an electronic transition in the carbon atom which otherwise is strictly forbidden.[4] However this may be, it seems reasonable to assume that the absorption of the line and band is localized in certain "centers" which may be called 415-centers.

The optical properties of diamond are altered in several respects by neutron bombardment. Among other phenomena, a continuous and continuously rising absorption band is produced in the violet and near ultraviolet. This must be due to the creation of some sort of perturbations, such as interstitial atoms, vacancies, etc., which, macroscopically, are uniformly distributed throughout the crystal. There is no reason to suppose that these perturbations are directly connected with the existence of the 415-centers, since they are formed with equal intensity in diamonds which have little or no intensity in the 415-mμ line and band. Nevertheless, the presence of these perturbations in the vicinity of the 415-centers alters their reaction to the influence of heat.

The increase in the relative intensity of certain peaks in an absorption band reveals the fact that the transitions to certain vibrational levels of the excited electronic state have become more probable, while others—and in our case also transitions into a nonquantized continuum—have become less probable. This can be the consequence of a small shift in the relative position of the configurational potential curves due to changes in the arrangement of the neighboring perturbations. The normal arrangement of the perturbations is restored by irradiation with light. It is not possible to ascertain whether the light absorption occurs in the 415-centers or in the perturbation continuum, because the latter is superimposed on the former. However,

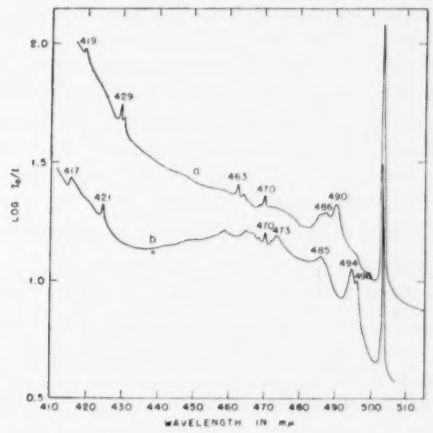

FIG. 4. Absorption band of diamond D14 below 510 mμ recorded at −190°C. a. After prolonged pile exposure and heating at 540°C; b. after 1 hour at 775°C.

[4] G. N. Ramachandran and V. Chandrasekhar, Proc. Indian Acad. Sci. **A24**, 176 (1946).

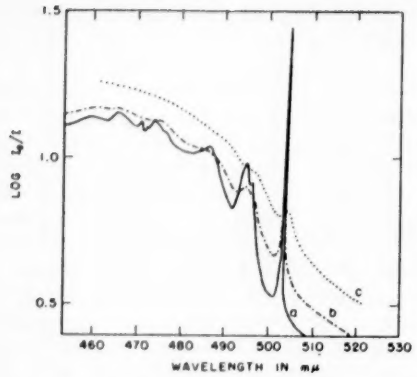

FIG. 5. Absorption band of diamond D14 after additional heating at 450°C. a. Recorded at −190°C; b. recorded at −78°C; c. recorded at +25°C.

since the effect is only observed in the neutron bombarded crystals and vanishes when the continuum has practically disappeared after heating to 750°C, the second assumption is probably correct.

The absorption spectra of some diamonds are known to contain a second sharp line at 503 mμ, and this line too is accompanied by a band at its short wavelength side. None of the 52 industrial diamonds investigated in this laboratory[5] exhibited this line before undergiong neutron bombardment. As observed first by Dugdale,[6] however, a line of apparently the same wavelength arises in the absorption spectrum of diamonds which have been exposed to neutron bombardment and subsequently heated at temperatures of about 300°C. Although the line could be produced by suitable treatment in the spectra of all diamonds investigated so far, it appears that samples of the type I variety with a low intensity 415-mμ line and adjacent band show the strongest response in the production of the line at 503 mμ. Since the region around 500 mμ in the diamond absorption spectrum is least affected by pile exposure, appreciably longer exposures are necessary in this case than were used in the experiments described in the first part of this paper. On the other hand, after such a strong neutron bombardment the crystals withstand heating to much higher temperatures before being completely bleached. When produced by heating a pile-irradiated diamond to temperatures between 300 and 350°C, the line at 503 mμ, accompanied by only one weak broad band peak at 490 mμ, is clearly visible on a continuous background in spectra recorded at room temperature, as shown in Figs. 3 and 4 of the earlier paper.[1] After heating to 400°C or more the line is practically invisible if the spectrum is again recorded at room temperature, but it reappears with great intensity and great sharpness in the spectrum recorded at −190°C. In addition to its main peak which is still located at 490 mμ, the band now exhibits a number of secondary peaks. This is shown in curve a of Fig. 4 which represents the spectrum of diamond D14 after repeated pile exposure and heating to temperatures below 600°C. Curve b of Fig. 4 reproduces the spectrum of the same sample after it had been heated for an hour to 775°C. The intensity of the line and the background is reduced by about 20 percent, and the structure of the band is altered appreciably. The most striking alteration in the band structure is the appearance of a new double peak at 495 mμ and the almost complete disappearance of the peak at 490 mμ. This change in the intensity distribution is not reversed when the diamond is exposed to light. Curve a of Fig. 5 is very nearly a repetition of curve b in Fig. 4. It was obtained with the same diamond after heating it once more for one hour at 450°C. Curves b and c of Fig. 5 illustrate how the line and band are almost totally submerged under the continuum when the temperature at which the spectrum is recorded is raised to −78° and −25°C, respectively.[7]

The intensity of the line at 503 mμ can be enhanced appreciably by successive periods of neutron bombardment and heat treatment, but even the highest intensities obtained so far do not exceed the order of magnitude mentioned in connection with the line at 415 mμ. Thus the line at 503 mμ must probably be ascribed also to a normally forbidden transition in relatively few centers which, in this instance, are not present in the crystal before exposure in the pile. An interpretation of the various observations concerning the 503-mμ line and the adjoining band would require the introduction of numerous arbitrary assumptions with respect to the perturbations produced in the lattice and their influence on the centers responsible for the line. Such a tentative interpretation would practically be merely a repetition of the description of the observed facts with other words.

[5] Most of these diamonds were returned to Super-Cut, Inc., after a cursory inspection of their absorption spectra, while only seven samples were selected because of their specific qualities for further treatment. I want once more to thank D. A. Trescott of Super-Cut, Inc., for his kind help in this matter.

[6] R. A. Dugdale, Harwell Report AERE-N/*PC*-15, 1950 (unpublished); P. Pringsheim, Argonne National Laboratory Report ANL-4797, 1951 (unpublished).

[7] Almost identical behavior is shown by a line which can be produced in the absorption spectrum of lithium fluoride by exposure to x-rays and subsequent irradiation with short wavelength ultraviolet light [C. F. Delbecq and P. Pringsheim, J. Chem. Phys. **21**, 794 (1953)].

Diffusion Currents in the Semiconductor Hall Effect

ROLF LANDAUER AND JOHN SWANSON
International Business Machines Corporation, Poughkeepsie, New York
(Received April 2, 1953)

The usual Hall effect equation for semiconductors applies if the concentration of carriers is undisturbed. In a magnetic field, however, holes and electrons are swept to the same side of the conductor. A gradient of carrier concentrations is thereby established, giving rise to diffusion currents across the sample. The magnitude of the diffusion currents depends on the recombination velocity at the surface and on the lifetime of excess carriers in the interior.

Partial differential equations governing the electric field and the variation of the carrier concentrations across the transverse cross section of the Hall sample are obtained. These are applied to rectangular and circular transverse cross sections. Equations for the Hall voltage as a function of both bulk lifetime and surface recombination velocity are derived and discussed. The analysis considers only disturbances which are linear in the applied magnetic field.

I. INTRODUCTION

IN semiconductors two current carriers are present in variable proportions: electrons having energies in the conduction band, acting as negative carriers; and vacant states or "holes" in the valence band, acting as positive carriers. When a current flows, electrons and holes move in opposite directions; however, a magnetic field tends to deflect the oppositely moving and oppositely charged carriers in the same direction. A counteracting electric field, such as is usually set up in the presence of a magnetic field by an initial movement of charge, cannot simultaneously balance the magnetic deflections of both carriers in view of the opposite forces exerted by the electric field on the two particles. Consequently, in the steady state, holes and electrons will flow in equal numbers in the direction of magnetic deflection. The equality of the two currents is required in order that the net transverse current be zero, in accordance with the principle of charge conservation. The Hall field is then that electric field which insures the necessary equality of transverse hole and electron flow.

Since the currents for the individual carriers perpendicular to the imposed direction of net steady-state current do not vanish, the particles themselves are not conserved. In fact, hole-electron pairs must be continuously generated in the region or on the surfaces from which the transverse current flows and must recombine in the region or on the surfaces to which it flows. If the processes of recombination and generation are slow, requiring large deviations of the carrier concentrations from their equilibrium values in order to be effective, holes and electrons will tend to accumulate on that side of the sample toward which they are deflected by the magnetic field. Since they are deflected in equal numbers, no space charge will result from this accumulation. However, once a gradient in carrier concentration is set up across the sample, further accumulation will be opposed by the resulting diffusion currents. The diffusion currents constitute a second means by which the effects of magnetic deflection may be balanced under steady-state conditions. In particular, when there is no generation or recombination of carriers whatever, the existence of diffusion currents makes possible the simultaneous vanishing of both the hole and the electron transverse currents.

The formula for the Hall constant usually quoted in the literature is appropriate for the case of zero lifetime, i.e., for the case in which any desired rate of generation or recombination can be maintained without an appreciable change in the carrier concentrations. This restriction upon the validity of the formula in question is usually not explicitly stated. The derivation of the formula is much simpler than that for the general case since no concentration gradients, and hence no diffusion currents, can exist when the lifetime is zero. Fowler[1] has given a discussion for the extreme case of infinite lifetime, and Welker[2] has, in addition, treated the intermediate case for intrinsic semiconductors. Welker's treatment neglects the surface recombination on two of the four long surfaces of the usual rectangular Hall specimen. It is the purpose of this paper to derive and discuss the more general equations needed for the interpretation of Hall experiments. It is instructive to compare the formulas for zero lifetime and infinite lifetime (no recombination). In Gaussian units they are

$$R=\frac{3\pi}{8ec}\frac{p-b^2n}{(p+bn)^2} \quad \text{(zero lifetime)}, \tag{1}$$

and

$$R=\frac{3\pi}{8ec}\frac{p-bn}{(p+bn)(p+n)} \quad \text{(infinite lifetime)}. \tag{2}$$

Here e is the magnitude of the electronic charge, c the velocity of light; p and n are, respectively, the concentrations of holes and electrons, and b is the ratio of electron mobility to hole mobility. Equations (1) and (2) assume that the energy band surfaces are spherical and that holes and electrons are scattered by lattice

[1] R. H. Fowler, *Statistical Mechanics* (Cambridge University Press, Cambridge, 1936), p. 428.
[2] H. Welker, Z. Naturforsch. **6a**, 184 (1951).

vibrations. Other cases are discussed by Shockley[3] and Klahr.[4]

When the concentration of one carrier very greatly exceeds that of the other, Eqs. (1) and (2) become identical. However, the distinction becomes quite important in the near-intrinsic region. In particular, the point at which the Hall constant is zero is quite different in the two cases. It is well known that the Hall coefficient for a P-type germanium or silicon sample reverses sign when the temperature is raised sufficiently, because the sample eventually becomes intrinsic; and when p is equal to n, the Hall constant must be negative, since b is greater than unity for silicon and germanium. The above two formulas show that the temperature at which this reversal occurs will be influenced by the lifetime of excess carriers in the particular sample measured. Considerations such as these indicate the possibility that the lifetimes of excess carriers might be measured on the basis of Hall effect experiments alone, without the necessity of observing the decay times of injected carriers. This possibility has in part motivated the following derivation of the Hall constant for the general case in which neither the bulk lifetime nor the surface recombination velocity is assumed to have an extreme value.

II. FUNDAMENTAL EQUATIONS

The total current density, i, is the sum of the current densities due to the magnetic deflection, to the concentration gradients, and to the electric fields present. Symbolically, we may write

$$\mathbf{i}=\mathbf{i}_H+\mathbf{i}_D+\mathbf{i}_C, \tag{3}$$

where $\mathbf{i}_H$ is the deflection current, $\mathbf{i}_D$ is the diffusion current, and $\mathbf{i}_C$ is the conduction current. The direction in which the net steady-state current flows will be called the "longitudinal direction," and will be designated by the subscript "l." Similarly, the subscript "t," standing for "transverse," will designate the directions contained in a plane perpendicular to the longitudinal direction. It is not necessary that all transverse currents lie along the direction of magnetic deflection; consequently, equations to which the subscript "t" are applied are two-dimensional vector equations.

Under steady-state conditions the transverse current must be zero. It follows that

$$\mathbf{i}_{Ht}+\mathbf{i}_{Dt}+\mathbf{i}_{Ct}=0, \tag{4}$$

$$\mathbf{i}_{Ct}=\mathbf{i}. \tag{5}$$

Before proceeding, it will be necessary to define a coordinate system. Let the magnetic field be oriented at right angles to the longitudinal direction, and let a right-handed Cartesian coordinate system be chosen such that the x axis lies along the longitudinal current direction, and the negative z axis along the direction of the magnetic field (i.e., $|H|=-H_z$). Then both holes and electrons will be deflected in the direction of the positive y axis. The deflection currents are given by

$$\mathbf{i}_{Hp}=(\mu_{Hp}i_{lp}H/c)\mathbf{y}_1, \tag{6}$$

$$\mathbf{i}_{Hn}=-(\mu_{Hn}i_{ln}H/c)\mathbf{y}_1, \tag{7}$$

where $\mathbf{y}_1$ is a unit vector along the y axis. In Eqs. (6) (6) and (7), as throughout the paper, the subscripts "p" and "n" refer to holes and electrons, respectively, so that $\mathbf{i}_{Hp}$ and $\mathbf{i}_{Hn}$ are the deflection currents for the two carriers, and i_{lp} and i_{ln} are the longitudinal currents. The constants of proportionality μ_{Hp} and μ_{Hn} are the Hall mobilities defined by Shockley.[5] If the energy surfaces at the top of the valence band and the bottom of the conduction band are spherical, if Boltzmann statistics apply, and if the scattering is primarily due to the lattice vibrations, then the Hall mobilities are related to the drift mobilities, μ_p and μ_n, in the following way:

$$\mu_{Hp}=3\pi\mu_p/8, \tag{8}$$

$$\mu_{Hn}=3\pi\mu_n/8. \tag{9}$$

However, these relations are not always valid, so that no use of Eqs. (8) and (9) will be made in the subsequent derivations.

The longitudinal currents are conduction currents, and hence

$$\mathbf{i}_{lp}=e\mu_p p\mathbf{E}_l, \tag{10}$$

$$\mathbf{i}_{ln}=e\mu_n n\mathbf{E}_l, \tag{11}$$

where $\mathbf{E}_l$ is the longitudinal electric field, which is constant both across and along the specimen, and p and n are the actual hole and electron concentrations as distinguished from the equilibrium concentrations, to be represented by p_0 and n_0. Thus (6) and (7) become

$$\mathbf{i}_{Hp}=e\mu_{Hp}\mu_p E_l H p\mathbf{y}_1/c, \tag{12}$$

$$\mathbf{i}_{Hn}=e\mu_{Hn}\mu_n E_l H n\mathbf{y}_1/c. \tag{13}$$

In materials that are not excessively P type or N type, both carriers obey Boltzmann statistics, so that the diffusion currents are

$$\mathbf{i}_{Dp}=-kT\mu_p\nabla p=-kT\mu_p\nabla_t p_1, \tag{14}$$

$$\mathbf{i}_{Dn}=kT\mu_n\nabla n=kT\mu_n\nabla_t p_1, \tag{15}$$

where k is Boltzmann's constant. In the right-hand terms of these equations, p_1 is the deviation from equilibrium of the two carriers:

$$p_1=p-p_0=n-n_0=n_1. \tag{16}$$

The deviations in n and p must be the same in order to

[3] W. Shockley, *Electrons and Holes in Semiconductors* (D. Van Nostrand Company, Inc., New York, 1950), p. 277.

[4] C. N. Klahr, Phys. Rev. **82**, 109 (1951), Scattering due to sources other than lattice vibrations is considered by Klahr. Even more serious modifications are required by the nonspherical energy surfaces resulting from the calculations of Herman and Callaway, Phys. Rev. **89**, 518 (1953).

[5] Reference 3, p. 209, 270.

preserve space charge neutrality. The subscript "t" on the inverted delta signifies that only the transverse components of the gradient need be considered.

Formulas for the transverse conduction currents are written similarly to (10) and (11), with $\mathbf{E}_t$, the transverse electric field, replacing $\mathbf{E}_t$:

$$\mathbf{i}_{Cpt}=e\mu_p p\mathbf{E}_t, \tag{17}$$

$$\mathbf{i}_{Cnt}=e\mu_n n\mathbf{E}_t. \tag{18}$$

The consequences of Eqs. (12) to (18) are now summed up in three equations:

$$\mathbf{i}_{pt}=e\mu_p[\mu_{Hp}E_t H p_0\mathbf{y}_1/c-(kT/e)\nabla_t p_1+p_0\mathbf{E}_t], \tag{19}$$

$$\mathbf{i}_{nt}=e\mu_n[-\mu_{Hn}E_t H n_0\mathbf{y}_1/c+(kT/e)\nabla_t p_1+n_0\mathbf{E}_t], \tag{20}$$

$$\mathbf{i}_{pt}=-\mathbf{i}_{nt}. \tag{21}$$

Equations (19) and (20) express the total transverse hole and electron currents in terms of the applied electric and magnetic fields, and the resultant transverse electric field and concentration gradient. Except in the diffusion current term, the hole and electron concentrations have been given their equilibrium values, since the neglected products $p_1 H$ and $p_1\mathbf{E}_t$ are of second order in the applied magnetic field. Throughout this paper we shall be concerned only with quantities which are of first order in the magnetic field. The discussion will, therefore, apply to the Hall effect in the limit of small fields, and will not reveal anything about the variation of the Hall constant with magnetic field.

III. PARTIAL DIFFERENTIAL EQUATIONS FOR TRANSVERSE VARIATION

The flow of excess carriers obeys the continuity equations

$$\mathrm{div}\mathbf{i}_p+ep_1/\tau=0, \tag{22}$$

$$\mathrm{div}\mathbf{i}_n-en_1/\tau=0, \tag{23}$$

where τ is the lifetime of excess carriers in the body of semiconductor. If Eqs. (19) and (20) are substituted in Eqs. (22) and (23), we find

$$\mathrm{div}\mathbf{E}_t-(kT/ep_0)\nabla_t^2 p_1+p_1/(\tau\mu_p p_0)=0, \tag{24}$$

$$\mathrm{div}\mathbf{E}_t+(kT/en_0)\nabla_t^2 p_1-p_1/(\tau\mu_n n_0)=0. \tag{25}$$

$\mathbf{E}_t$ can be eliminated by subtracting Eq. (25) from Eq. (24) leaving

$$\nabla_t^2 p_1-\beta^2 p_1=0, \tag{26}$$

where β and another quantity,[6] D, which we shall need later, are defined by

$$\beta^2=\frac{1}{\tau D}=\frac{1}{\tau}\frac{e}{kT}\frac{\mu_n n_0+\mu_p p_0}{\mu_n\mu_p(n_0+p_0)}. \tag{27}$$

Equation (26) will determine the variation of p_1 in the interior of the transverse cross section, if we have boundary conditions available along the surface of the sample. These boundary conditions are determined by the rate of recombination at the surface and are given by[7]

$$\mathbf{i}_p\cdot\mathbf{n}_1=sep_1, \tag{28}$$

$$\mathbf{i}_n\cdot\mathbf{n}_1=-sep_1, \tag{29}$$

where $\mathbf{n}_1$ is the unit outward normal along the surface, and s is a quantity characteristic of the surface called the surface recombination velocity. If we substitute Eqs. (19) and (20) in Eqs. (28) and (29), the resulting equations can be combined to give a boundary condition involving p_1 only

$$(\mu_{Hp}+\mu_{Hn})\frac{H}{c}E_t(\mathbf{n}_1\cdot\mathbf{y}_1)-\left(\frac{kT}{ep_0}+\frac{kT}{en_0}\right)\frac{dp_1}{d\mathbf{n}}=sp_1\left(\frac{1}{\mu_p p_0}+\frac{1}{\mu_n n_0}\right). \tag{30}$$

This boundary condition, in addition to Eq. (26), serves to determine p_1.

To find $\mathbf{E}_t$, once we have found p_1, either Eq. (24) or Eq. (25) can be used, which can be written with the use of Eq. (26) as

$$\mathrm{div}\mathbf{E}_t=-\frac{kT}{e}\left(\frac{\mu_n-\mu_p}{n_0\mu_n+p_0\mu_p}\right)\nabla_t^2 p_1. \tag{31}$$

Now the potential V has the same variation in each transverse cross section, while its longitudinal variation is defined by E_t, so that we can write

$$V=-E_t x+V_t, \tag{32}$$

where $\mathbf{E}_t=-\nabla_t V_t$, and hence

$$\mathrm{div}\mathbf{E}_t=-\nabla^2 V_t. \tag{33}$$

Together with Eq. (31) this gives

$$\nabla_t^2 V_t=\frac{kT}{e}\left(\frac{\mu_n-\mu_p}{n_0\mu_n+p_0\mu_p}\right)\nabla_t^2 p_1, \tag{34}$$

or

$$V_t=\frac{kT}{e}\left(\frac{\mu_n-\mu_p}{n_0\mu_n+p_0\mu_p}\right)p_1+V_L, \tag{35}$$

where V_L is a solution of Laplace's equation (in the transverse coordinates). The boundary condition on V_t may be obtained by adding Eqs. (28) and (29) and substituting for the currents from (19) and (20) giving

$$\frac{\partial V_t}{\partial\mathbf{n}}=\frac{kT}{e'}\left(\frac{\mu_n-\mu_p}{n_0\mu_n+p_0\mu_p}\right)\frac{\partial p_1}{\partial\mathbf{n}}+\frac{\mu_{Hp}\mu_p p_0-\mu_{Hn}\mu_n n_0}{(n_0\mu_n+p_0\mu_p)}\times\frac{H}{c}E_t\mathbf{y}_1\cdot\mathbf{n}_1. \tag{36}$$

[6] This is the same diffusion coefficient defined by Harvey Brooks, Phys. Rev. **90**, 336 (1951).

[7] Reference 3, p. 321.

Substituting (35) in (36) leaves

$$\frac{\partial V_L}{\partial \mathfrak{n}}=\frac{\mu_{Hp}\mu_p p_0-\mu_{Hn}\mu_n n_0}{n_0\mu_n+p_0\mu_p}\frac{H}{c}E_l\mathbf{y}_1\cdot\mathfrak{n}_1. \tag{37}$$

A solution of Laplace's equation which satisfies (37) is given by

$$\mathbf{E}_{Ll}=-\nabla_l V_L=-\frac{\mu_{Hp}\mu_p p_0-\mu_{Hn}\mu_n n_0}{(n_0\mu_n+p_0\mu_p)^2}\frac{Hi}{ce}\mathbf{y}_1. \tag{38}$$

Here E_l has been replaced by

$$E_l=\frac{i}{e(n_0\mu_n+p_0\mu_p)}. \tag{39}$$

The field given by Eq. (38) is the one given by the usual Hall formula for zero lifetime. Hence V_l can be written as

$$V_l=V_D+V_L, \tag{40}$$

where

$$V_D=\frac{kT}{e}\left(\frac{\mu_n-\mu_p}{n_0\mu_n+p_0\mu_p}\right)p_1. \tag{41}$$

V_D is the part of V_l which depends on surface and volume recombination.

The general procedure that has been discussed has been applied to circular and rectangular cross sections, and the results will be described. In the limiting cases in which the excess carrier lifetime is zero (representing either zero bulk lifetime, or else an infinite surface recombination velocity) or infinite (representing infinite bulk lifetime accompanied by zero surface recombination velocity), a transverse electric field is set up which is independent of the shape of the transverse cross section. This transverse electric field has only a y component and is constant across the transverse cross section. The field established in the case of zero carrier lifetime is given by Eq. (38). The field established in the case of infinite carrier lifetime is

$$\mathbf{E}_l=\frac{(\mu_{Hp}p_0-\mu_{Hn}n_0)}{(n_0\mu_n+p_0\mu_p)(n_0+p_0)}\frac{iH}{ec}\mathbf{y}_1. \tag{42}$$

Equations (38) and (42) lead to Eqs. (1) and (2) under the assumptions of Eqs. (8) and (9).

IV. CIRCULAR CROSS SECTION

The voltage distribution around the circumference of the transverse cross section turns out to be of the form $V_l=V_0\cos\theta$, where θ is the angle that the radius makes with positive y-axis. A definition of the Hall constant R, which is consistent with Eqs. (1) and (2), is

$$V_0=RHia, \tag{43}$$

where a is the radius of the cylinder. R can best be written in the form

$$R=R_D+R_L, \tag{44}$$

where R_D is a measure of V_D and R_L is a measure of V_L. We then have

$$R_L=\frac{1}{ce}\frac{(\mu_{Hp}\mu_p p_0-\mu_{Hn}\mu_n n_0)}{(n_0\mu_n+p_0\mu_p)^2}, \tag{45}$$

and

$$R_D=\frac{I_1(\beta a)}{(s/D)aI_1(\beta a)+\beta aI_1'(\beta a)}\Re, \tag{46}$$

where

$$\Re=\frac{(\mu_n-\mu_p)(\mu_{Hp}+\mu_{Hn})n_0p_0}{(n_0\mu_n+p_0\mu_p)^2(n_0+p_0)}\frac{1}{ec}, \tag{47}$$

and $I_1(x)=-iJ_1(ix)$ is a Bessel function of an imaginary argument, whose values can be found in tables.[8] In the case of zero carrier lifetime ($s=\infty$ or $\tau=0$) we find $R_D=0$. In the case of infinite carrier lifetime ($s=0$ and $\tau=\infty$) we find $R_D=\Re$. For intermediate cases:

$$0<R_D/\Re<1. \tag{48}$$

It should be noted that the Hall measurement on a cylindrical conductor yields only one constant: the value of V_0. If all the mobilities and carrier densities are known and if one of the two quantities, s and τ, is known, the other one can be found directly from a Hall measurement. If both s and τ are unknown, their values cannot be found from Hall measurements on a single specimen. In actual practice it is likely that s is not uniform over the surface of the sample. This will be revealed by deviations from $V_l=V_0\cos\theta$.

V. RECTANGULAR CROSS SECTION

General Discussion

We shall assume that the Hall sample is oriented with respect to the magnetic field as shown in Fig. 1. Before discussing the detailed equations it will be in order to point out that the voltage distribution over the surface of the cross section depends on s and τ in different ways. If $s=0$, all the transverse currents are in the y direction, and the surfaces at $y=\pm w/2$ are equipotentials. If s is different from zero, diffusion currents flow toward all surfaces, and most of the quantities we are concerned with will show a variation

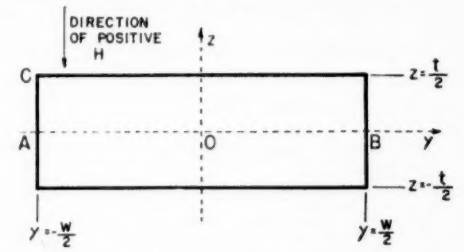

FIG. 1. Transverse cross section of rectangular Hall specimen. The longitudinal current is considered positive if directed out of paper.

[8] E. Jahnke and F. Emde, *Tables of Functions* (Dover Publications, New York, 1945).

with z as well as with y. Naturally, we still cannot find both s and τ from one Hall measurement. If, however, two potential differences are measured, on the same cross section, it will be possible to find both s and τ, providing all the mobilities and carrier concentrations are already known. This could be done, for instance, by measuring the potential between points A and C shown in Fig. 1, as well as the potential between A and B.

Detailed Equations

The field distribution due to V_L is specified by Eq. (38). This gives a potential difference between $y=w/2$ and $y=-w/2$:

$$V_L\left(\frac{w}{2}\right)-V_L\left(-\frac{w}{2}\right)=\frac{\mu_{Hp}\mu_p p_0-\mu_{Hn}\mu_n n_0}{(\mu_p p_0+\mu_n n_0)^2}\frac{wHi}{ec}. \quad (49)$$

In addition to this, there is a potential distribution of the form

$$V_D=Hig(z,y)\mathcal{R}, \quad (50)$$

where $\mathcal{R}$ is given by Eq. (47) and $g(z,y)$ is still to be defined. It is a quantity which satisfies

$$0<g(z,w/2)-g(z,-w/2)<w, \quad (51)$$

so that the Hall constant measured in the normal manner by probes at A and B will be between R_L and $R_L+\mathcal{R}$, as in the cylindrical case.

In order to exhibit $g(z,y)$, it is necessary to define a set of numbers γ_n which are positive roots of the equation

$$\gamma_n\tan(\gamma_n t/2)=s/D. \quad (52)$$

The roots are numbered in order of size; the lowest one is labelled $n=0$. The roots then satisfy

$$2n\pi<\gamma_n t<(2n+1)\pi. \quad (53)$$

Furthermore, for each γ_n we shall define an α_n:

$$\alpha_n=+(\beta^2+\gamma_n^2)^{\frac{1}{2}}. \quad (54)$$

Then, $g(z,y)$ is given by

$$g(z,y)=\sum_{n=0}^{\infty}g_n\sinh\alpha_n y\cos\gamma_n z, \quad (55)$$

with

$$g_n=\frac{4\sin(\gamma_n t/2)}{[(s/D)\sinh(\alpha_n w/2)+\alpha_n\cosh(\alpha_n w/2)]\times(\sin\gamma_n t+\gamma_n t)}. \quad (56)$$

Special Situations

The series given by (55) will be discussed in further detail for a number of special situations. If $s=0$, only the term for $n=0$ is present. Furthermore, $\gamma_0=0$, so that only variation along the y-axis exists. In that case the Hall coefficient, determined in the usual way from the potential difference between A and B in Fig. 1, will be given by[9]

$$R=R_L+\mathcal{R}\frac{2}{\beta w}\tanh\left(\frac{\beta w}{2}\right). \quad (57)$$

If we consider lifetime as a variable, Eq. (57) shows that R makes the transition from R_L to $R_L+\mathcal{R}$ when the diffusion length, $1/\beta$, is comparable to the width, w, of the specimen.

In order that the concentration of carriers across the thickness, t, of the sample (i.e., along the z direction) be constant, it is not necessary that s vanish. If s is small enough, diffusion can maintain equilibrium across the sample. The condition for this is $st\ll D$. Under this condition only the term for $n=0$ in (55) is important. In this case,

$$\alpha_0=(1/D\tau_e)^{\frac{1}{2}}, \quad (58)$$

where τ_e is an effective lifetime given by

$$1/\tau_e=1/\tau_s+1/\tau \quad (59)$$

and where τ_s is the lifetime which would be measured if the surfaces at $z=\pm t/2$ were the only place where recombination occurs. τ_s is in turn equal to $t/2s$.

The case in which one value of surface recombination velocity, s_w, applies for the surfaces at $y=\pm w/2$ and another value, s_t, applies at $z=\pm t/2$, is treated almost as easily as the case leading to (55) and (56). If $s_t\neq s_w$, (55) still holds, but instead of (56) we have

$$g_n=\frac{4\sin(\gamma_n t/2)}{[(s_w/D)\sinh(\alpha_n w/2)+\alpha_n\cosh(\alpha_n w/2)]\times(\sin\gamma_n t+\gamma_n t)}, \quad (60)$$

where

$$\alpha_n=+(\beta^2+\gamma_n^2)^{\frac{1}{2}}, \quad (61)$$

and instead of Eq. (52),

$$\gamma_n\tan(\gamma_n t/2)=s_t/D. \quad (62)$$

It is interesting to note that g can be made arbitrarily small by making s_w large enough. The value of g cannot be made arbitrarily small by increasing s_t without limit. Physically this comes from the fact that for very large values of s_t the rate at which recombination occurs at $y=\pm t/2$ is not determined by s_t but is limited by the time it takes the holes to diffuse to $y=\pm t/2$ from the interior of the specimen. Diffusion will determine the rate of recombination at $y=\pm t/2$, if $s_t t\gg D$. (For room temperature germanium mobilities, st is comparable to D if $s=750$ cm/sec and $t=1$ mm.) If $s_t t\gg D$, and if, furthermore, $s_w\geq s_t$, $w\geq t$, and $\tau=\infty$, then it is only the recombination at the surfaces at $y=\pm w$ that counts. In this case the series given by Eq. (55) can easily be summed, and the Hall coefficient,

[9] A formally very similar expression has been derived by H. Welker, L'Onde Electrique **30**, 309 (1950). Welker's equation (33) applies to a semiconductor with no recombination, but with an alternating longitudinal current.

determined in the usual way from the potential difference between A and B in Fig. 1, will be

$$R=R_L+\frac{2D}{sw}\mathfrak{R}. \tag{63}$$

Another case of interest occurs if s_t is zero. Then all terms of the series but the first vanish, and we find

$$R=R_L+\frac{1}{s_w w/2D+(\beta w/2)\coth(\beta w/2)}\mathfrak{R}. \tag{64}$$

It should be pointed out that an experimental arrangement in which the voltage between two points on the same surface at $z=t/2$ is measured allows one to dispense with all terms of the series given by Eq. (56) except the first one, even if s_t is not zero. In such arrangements we rely on the fact that the hyperbolic functions with larger values of α_n decay more rapidly with y as we move away from $y=\pm w/2$.

VI. CONCLUDING REMARKS

In conclusion we wish to point out that a complete interpretation of the experimental Hall effect in near-intrinsic semiconductors requires a knowledge of the precise nature of the probes used to detect the Hall voltage. The voltage of a metal probe placed on the surface of a semiconductor is not a direct indication of the electrostatic potential of the underlying semiconductor unless the carrier concentrations have their equilibrium values. This is because a metal contact acts as a recombination center for excess carriers; and if there is a barrier to holes or electrons associated with the contact (as is usually the case), a potential change across the barrier is required to equalize the flow of holes and electrons toward the contact.[10] In the first approximation this extra contribution to the probe voltage will be proportional to the excess carrier concentration. Since V_b [see Eq. (41)] is also proportional to the excess carrier concentration, one may take the extra probe voltage into account by replacing the constant $\mathfrak{R}$, defined by Eq. (47), by an effective constant $\mathfrak{R}'$ in the subsequent equations. If one writes

$$\mathfrak{R}'=\mathfrak{R}(1+\alpha), \tag{65}$$

then α will be a constant depending on the nature of the probe. The maximum value of α is $(n_0\mu_n+p_0\mu_p)/p_0(\mu_n-\mu_p)$, corresponding to an infinitely high barrier to electrons. The minimum value of α is $-(n_0\mu_n+p_0\mu_p)/n_0(\mu_n-\mu_p)$, corresponding to an infinitely high contact barrier to holes. The special case $\alpha=-1$ corresponds to a contact having no barrier. Over the surface of such a contact the recombination velocity is equal to thermal velocity (10^7 cm/sec), and hence no appreciable deviation of the carrier concentrations in the immediate vicinity is possible.

The authors wish to thank L. P. Hunter for pointing out that the usual interpretation of Hall effect data leads to inconsistencies and also for many discussions.

[10] J. Bardeen, Bell System Tech. J. **29**, 469 (1950).

The Photoemission of Tungsten in the Region of Predicted Schottky Deviations*

E. E. Buder, J. J. Ruddick, and A. H. Weber
Physics Department, Saint Louis University, Saint Louis, Missouri

(Received January 26, 1953)

Experimental evidence for the existence of deviations from the photoelectric Schottky line theoretically predicted by Guth-Mullin has been obtained. In the phase of the periodic deviations an averaging of data yields for example a maximum at 219±18 (v/cm)$^{\frac{1}{2}}$ and a minimum at 278±16, in agreement with theoretical values of 215 and 285, respectively. The amplitudes of the deviations are 0.3–1.5 the predicted values with smaller than theoretical values predominating.

A noted difference between data from ac and dc heated filamentary cathodes is considered in relation to the effect of emission surface roughness on electric field strength calculations. Also, patch theory has been applied to the photoelectric data, supplying evidence of patches of about 6 microns in extent for dc heated wires. An electron microscope study of the tungsten filament emission surfaces supports the conclusions.

The influence of more recent theory on the interpretation of the experimental results is briefly discussed in an appendix.

I. INTRODUCTION

GUTH and Mullin,[1] employing an electric-field-dependent electron transmission coefficient, theoretically predicted a photoelectric analog of the well established[2–6] deviations of thermionic electron emission from the straight Schottky line. For photoemission, their field dependent photocurrent i is, to a good approximation,

$$i \propto a+bE^{\frac{1}{2}}+cE-\frac{(d+fE^{\frac{1}{2}})\cos u}{(g+jE^{-\frac{1}{2}}+pE^{-\frac{3}{2}})^{\frac{1}{2}}}, \qquad (1)$$

where

$$a=(\pi kT)^2/6+h^2(\nu-\nu_0)^2/2,$$
$$b=h(\nu-\nu_0)e^{\frac{1}{2}},$$
$$c=e^3/2,$$
$$d=W_a{}^{\frac{1}{2}}h(\nu-\nu_0)/2,$$
$$f=W_a{}^{\frac{1}{2}}e^{\frac{1}{2}}/2,$$
$$g=(kT)^{-2}$$
$$j=(300e)^{\frac{1}{2}}[\pi^2+(\gamma+2\ln 2)^2]/16q^3,$$
$$p=\pi(300e)^{\frac{1}{2}}/2kTq^{\frac{1}{2}},$$
$$q=h^2/me^2,$$
$$u=(4/3q^{\frac{1}{2}})(300e)^{\frac{1}{2}}E^{-\frac{1}{4}}-2W_a{}^{-\frac{1}{4}}$$
$$+\tan^{-1}\left[\frac{W_a{}^{\frac{1}{2}}}{4}\right]-\tan^{-1}\left[\frac{(\gamma+2\ln 2)(300e/q^2)^{\frac{1}{2}}E^{-\frac{1}{2}}}{\pi(300e/q^2)^{\frac{1}{2}}E^{-\frac{1}{2}}+(kT)^{-1}}\right],$$

e = electronic charge,
E = applied electrostatic field,
γ = Euler's constant (0.5772),
ν = incident frequency,
ν_0 = threshold frequency, and
W_a is the barrier height, which for the assumption of one free electron per metal atom is 10.33 ev for tungsten.

For a field-independent transmission coefficient (normal Schottky effect) the theory shows that the last term of Eq. (1) is zero, yielding

$$i_0 \propto a+bE^{\frac{1}{2}}+cE. \qquad (2)$$

The experimental investigation of Eq. (1) for tungsten is the subject of the present paper, which appears to be the first experimental study of this effect for a metallic element. Carroll and Coomes[7] have done similar work on BaO, finding qualitative agreement with the Guth-Mullin theory.

To interpret the experimental results it is convenient to plot $\Delta i/i_0$, where Δi is the last term of Eq. (1) and i_0 is given by Eq. (2). The reference photocurrent i_0 as a function of $E^{\frac{1}{2}}$ is shown by Fig. 1 for two important incident light frequencies. For the present experimental conditions the parabola of Eq. (2) is practically a straight line for the fields plotted.

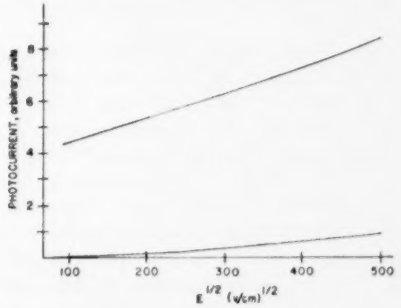

FIG. 1. Photoemission vs the half-power of the applied electric field according to Eq. (2). The upper plot is for the present experimental conditions ($T=293°$K and $h(\nu-\nu_0)=0.368$ ev), with the proportionality constant of the theory taken as 10^4. The lower curve is for $\nu=\nu_0$. The transmission coefficient of the barrier is considered constant.

* Assisted by the U. S. Office of Naval Research.

[1] E. Guth and C. J. Mullin, Phys. Rev. **59**, 575 (1941); **59**, 867 (1941); **61**, 339 (1942); **60**, 535 (1941).

[2] R. L. Seifert and T. E. Phipps, Phys. Rev. **56**, 652 (1939).

[3] D. Turnbull and T. E. Phipps, Phys. Rev. **56**, 663 (1939).

[4] W. B. Nottingham, Phys. Rev. **57**, 935 (1940). See also the last reference of footnote 1.

[5] Munick, LaBerge, and Coomes, Phys. Rev. **80**, 887 (1950).

[6] E. A. Coomes, Phys. Rev. **85**, 392 (1952).

[7] P. E. Carroll and E. A. Coomes, Phys. Rev. **85**, 389 (1952).

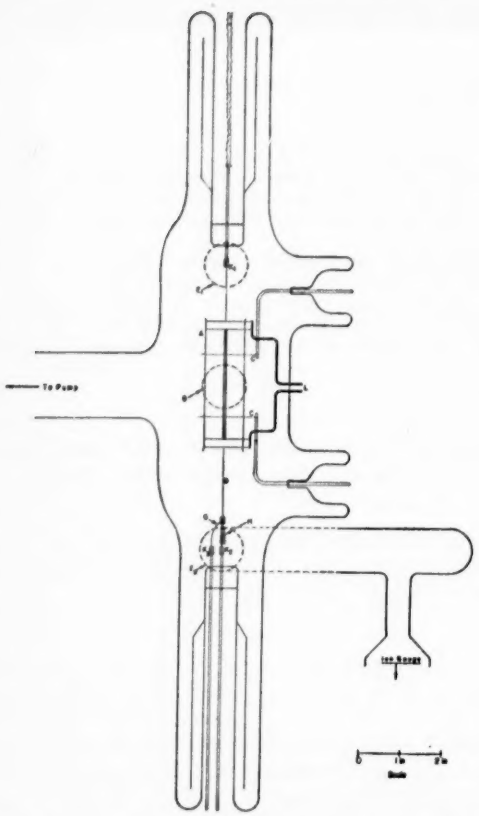

FIG. 2. Phototube. *A*, 3-in. tantalum cylindrical anode of internal diameter 0.75 in. with 1-mm slit in wall; *B*, quartz window in wall of main glass tubing; *C*, 0.015-in. tungsten filaments (for outgassing *A* by electron bombardment) welded to two-wire presses; *D*, 0.004-in. tungsten filamentary cathode; E_1 and E_2, access tubes for changing filament *D*, with E_2 connected to ionization gauge; *G*, 0.020-in. nickel wire for by-passing spring *H* during cathode (filament) outgassing; *H*, 0.015-in. coiled tungsten spring for filament tautness; K_1, K_2, K_3, nickel chucks for fastening wires to press leads.

The Guth-Mullin theory involves several assumptions: (1) The Fowler theory of the photoeffect, the basis of the work of Guth and Mullin, relies on the assumption that the incident frequency is near the threshold frequency. The frequency used in the present work (λ, 2537A) differs from the threshold frequency by only 8 percent, well within the range allowed by Fowler.[8] (2) The problem is considered as one-dimensional. This is a considerable assumption in view of the periodic structure of the metal surface. However, Herring and Nichols[9] indicate that the assumption is at least reasonable. (3) The zero-field threshold energy difference $h(\nu-\nu_0)$ is replaced simply by the field dependent threshold energy difference $h(\nu-\nu_0)+e^{\frac{1}{2}}E^{\frac{1}{2}}$. This change, corresponding to the Schottky lowering of the potential barrier at the metal surface, is amply justified by the experimental confirmation of the thermionic Schottky effect and by the photoelectric study of Lawrence and Linford.[10] (4) The surface is considered to have a constant work function.[11]

[8] R. H. Fowler, Phys. Rev. **38**, 45 (1931).
[9] C. Herring and M. H. Nichols, Revs. Modern Phys. **21**, 185 (1949).

II. EXPERIMENTAL

The evacuation and outgassing procedure used on the several phototubes was standard. The earlier tubes were sealed off containing Kemet Laboratories KIC barium core getters. However, on a suggestion of W. B. Nottingham the later tubes were sealed off without getters to avoid introducing foreign substances into the tube. After seal-off further lowering of the pressure was obtained by continuous operation of the ionization gauge.[12]

Pressures were measured with either VG-1A or Bayard-Alpert[13] ionization gauges.

The phototube design is shown by Fig. 2. The quartz window opposite the slit in the anode enables the incident radiation (from a narrow slit) to enter the tube without appreciable scattering. Although the light is incident predominantly on one portion of the central wire filament, emission also occurs from the other areas of the cathode surface due to reflections of the radiation from the inner surface of the anode. The electric field at the surface of the central filament is calculated from the assumed ideal cylindrical geometry of the tube. For the 0.004-in. wire used, E is 37.7 V v/cm, where V is the magnitude of the applied voltage. It can be shown that the centering of the filament is not critical for the dimensions actually used.

The light source was a Hanovia *SC*-2537 low pressure mercury arc which is practically a monochromatic ultraviolet source of 2537A radiation.[14]

For most of the work the phototube potential was provided by a bank of 45-v *B* batteries which with a specially constructed voltage divider provided a continuously variable voltage from 0 to 4500 v. The batteries gave a very steady voltage when new and well cared for but developed leakage paths to ground with the passage of time. To overcome the inconvenience of the batteries, an electronic power supply was constructed. It was a simple half-wave rectifier with a 2-μf output capacitor and a 20-megohm filter resistor.

The photocurrent amplifier was a DuBridge-Brown dc amplifier using an *FP*-54 electrometer tetrode.[15] It was stable (zero drift of about 0.3 percent of the usual photocurrent per hour) and, over the range of input voltages used (0–0.25 v), quite linear. The output

[10] E. O. Lawrence and L. B. Linford, Phys. Rev. **36**, 482 (1930).
[11] Deviations were studied only for regions where patch effects could be neglected.
[12] W. v. Meyern, Z. Physik **84**, 531 (1933).
[13] R. T. Bayard and D. Alpert, Rev. Sci. Instr. **21**, 571 (1950).
[14] A. H. Weber, Phys. Rev. **53**, 895 (1938). See also manufacturer's data.
[15] L. A. DuBridge and H. Brown, Rev. Sci. Instr. **4**, 283 (1933).

current of the amplifier was measured either by a Leeds and Northrup wall galvanometer of sensitivity 4×10^{-9} amp/mm or by a Minneapolis-Honeywell Brown recording potentiometer. Leakage currents, mechanical vibrations, and variations of arc intensity were minimized. Arc current fluctuations were not more than 0.25 percent, with resultant photocurrent changes of less than 0.13 percent.

When the galvanometer was used for readings the method of observation was to wait for about 10 minutes after changing the voltage to obtain a practically constant background of low magnitude and then to take 7 readings of photocurrent in succession. The average of these is the value plotted on the curves. When the recording potentiometer was used it was found possible to decrease the waiting period since accurate readings could be taken from the record obtained.

III. RESULTS

Graphical analysis is the most convenient method of examining the experimental data. Figure 3 presents the essential results of the Guth-Mullin theory. The principal difficulty of working the experimental data into the form of Fig. 3 was in determining the correct Schottky line representing the theory for constant transmission coefficient, analytically expressed by Eq. (2). Since the actual experimental currents represented the sum of undeviated currents and corresponding deviations, the observed currents could not yield a unique undeviated line.

The method of analysis was to represent the data by a straight line, visually adjusted to give a good fit over the significant portion of the curve. This could be done more accurately for those curves of larger abscissa ranges than for those of limited extent. In any case the line was somewhat arbitrary. Since Eq. (2) involves an undetermined proportionality constant, the slope of the experimental line cannot be compared to the theory. After determination of the line for the undeviated current i_0 the difference Δi between the measured and the undeviated currents for a given field value was obtained. The experimental $\Delta i/i_0$ can then be compared with the theoretical curve of Fig. 3.

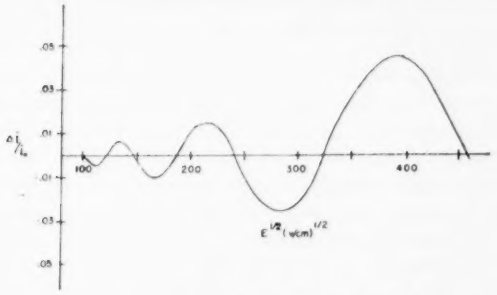

FIG. 3. Deviations, calculated by the Guth-Mullin theory Eqs. (1) and (2), from the photoelectric Schottky effect. The ordinates are the fractional magnitudes of the deviations from the constant transmission coefficient theory. The calculations have been made for 293°K and an incident wavelength of 2537A.

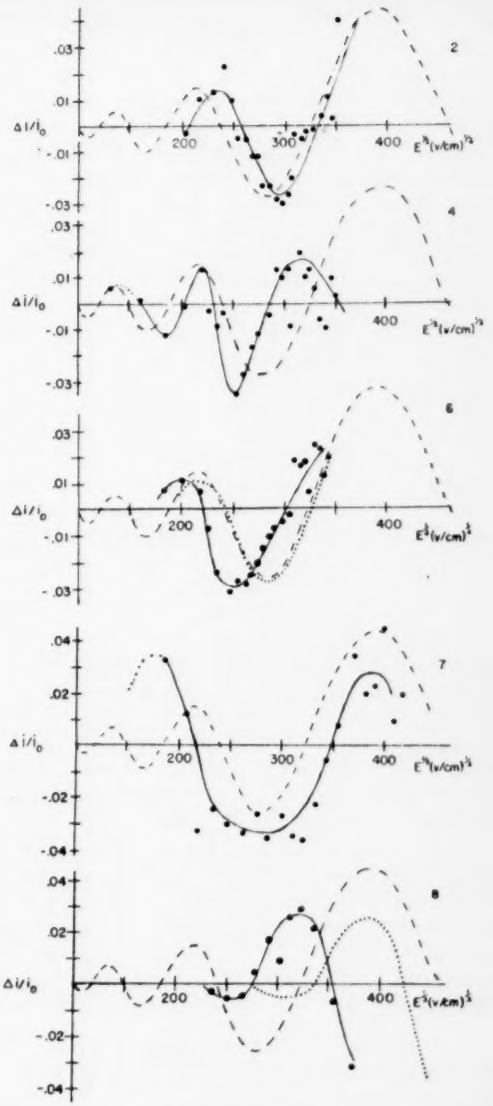

FIG. 4. Experimental results for dc-heated wires and unpolished tungsten. The *dashed* lines are the theoretical predictions; the *dotted* lines in Curves 4 and 7 are extensions of the experimental curves in ambiguous regions; the dotted lines of Curves 6 and 8 are the experimental curves obtained when the surface field is increased 1.2 and 1.5 times, respectively, to allow for surface roughness. The curves are numbered in the order in which the data were obtained, with the first three sets of data obtained from one tube and the other two from another tube.

The essential results of the present investigation are shown in Figs. 4 and 5. The curves of Fig. 4 are for filaments that were not polished and were outgassed with dc. Curve 2 was obtained from a tube at a pressure

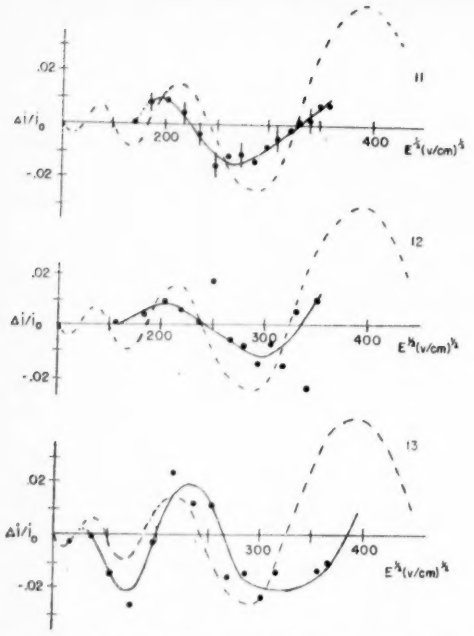

FIG. 5. Experimental results for ac-heated wires. The dashed lines are the theory; the dotted extensions of Curves 11 and 13 are for ambiguous regions. Standard deviations of the current readings are given for some of the points of Curve 11. Curve 13 is the only curve for the electronic power supply and recording potentionmeter.

of 10^{-7} mm Hg or less; 4, 6, 7, and 8 were obtained from tubes at about 5×10^{-7} mm Hg.

Figure 5 shows three curves for wires manually polished and outgassed with ac. Curve 11 was obtained from a phototube at a pressure of 3×10^{-7} mm Hg, while the other two curves were taken at about 2×10^{-8} mm Hg. To indicate the accuracy of the deviation amplitudes, the fractional magnitudes of the standard deviations of important points are shown on Curve 11.

TABLE I. Observed and predicted deviations.[a]

Curve[b]	0	Max	0	Min	0	Max	0	Min	0	Max	0	Agreement with theory[c]
Accurate field measurements (ac heating)												
9 ns							200	260	325			F
10 ns							200	260	305			F
11					170	195	225	270	330			G
12					160	205	245	295	335			G
13	120	127	135	170	200	230	265	315	385			G
Inaccurate field measurements (dc heating)												
2					205	235	255	295	335			G
3 ns					255	270	280	315	345			F
4			160	185	205	220	230	250	285	315	350	P
5 ns					200	240	280	300	320			P
6					170	200	225	250	300			G
7						175	215	280	350	390	445	F
8							225	250	275	320	355	F
Theory	120	135	150	165	185	215	240	285	325	390	460	

[a] All measurements are in $(v/cm^{\frac{1}{2}})$.
[b] ns, not shown in Figs. 4 and 5.
[c] G, good; F, fair; P, poor.

It is seen that the amplitudes of the Schottky deviation are greater than the usual standard deviations of the individual points and this is generally true of all the curves obtained.

Table I gives a summary of the experimental data and the corresponding theoretical positions of maxima, minima and intercepts. The data for four runs not plotted in Figs. 4 and 5 are included. These four runs show less favorable agreement in general between theory and experiment than is indicated by the eight runs of Figs. 4 and 5. Table II contains the results of averaging the values of Table I.

The amplitudes of the deviations are not uniquely established but appear usually to be somewhat smaller than theory predicts, varying from 0.3 to 1.5 the corresponding calculated values.

IV. DISCUSSION

A. Surface Roughness

A factor of importance is the roughness of the emitting surface. In addition to changing the effective area for photoemission and gas adsorption, roughness affects the magnitude of the applied electric field. Since the field strength is inversely proportional to the radius of the filamentary cathode any sharp irregularity will increase the local field.

TABLE II. Phase relationships of observed to predicted deviations.[a]

	Experiment	Theory	
	Average of Table I values	Guth-Mullin	Juenker *et al.*
First zero	120[b]	120	108
First maximum	133±4[b]	135	120
Second zero	148±8[b]	150	130
First minimum	178±5[b]	165	145
Third zero	196±19	185	160
Second maximum	219±18	215	180
Fourth zero	237±18	240	204
Second minimum	278±16	285	235
Fifth zero	324±19	325	266
Third maximum	342±23[b]	390	315
Sixth zero	383±29[b]	460	360

[a] All data in $(v/cm^{\frac{1}{2}})$.
[b] Not reliable due to insufficient data.

The first sets of data (Fig. 4) obtained in this study were for filaments that were rough due both to lack of polishing and to the etching effect of dc heating.[16] Later filaments (Fig. 5) were polished and heated with ac to avoid the roughness. An electron microscope study of the filaments used in this research (Callite No. 200-*H*) has shown that unpolished, dc heated wires are rougher than polished wires comparably heated with ac. The notable differences between the curves of Fig. 4 and those of Fig. 5 are probably due to the smoother filament surfaces of the latter. The dc roughness is ap-

[16] See reference 9, pp. 202, 261.

parently time dependent for runs taken before and after heating are not consistent in the phase locations of the deviations. The electron microscope study also indicated that even moderate dc heating can change filament surfaces. Hence if the filament is dc heated between runs, the values of the applied fields for given voltages will generally be different due to the changes in the surface structure.

As an example of how this dc roughness may affect the experimental data, it is interesting to examine Curve 6 of Fig. 4. If a multiplying factor of 1.2 for the field is assumed as a correction for the roughness of the emitter, the experimental curve becomes that shown by the *dotted* line. The improved agreement with theory over a complete cycle may mean that surface roughness for dc heated filaments is a source of experimental error.

The evidence indicates that ac heated filaments are not rough enough to have surface fields materially larger than calculated.

B. Patch Effects

The tungsten filament wire used is polycrystalline. Before heating in a vacuum, its crystals are of the order of half a wire diameter or less in length, as determined by inspection under polarized light. Heating recrystallizes the wire, for examination after the heat treatment showed crystals in a wire diameter or more in length.

The crystal structure of the wire leads to the problem of patch effects.[9] Since the various crystal planes of tungsten differ in their work functions, the presence of different planes at the surface of the metal produces patches of different work functions.[17] Furthermore, the roughness of the surface affects the size of the patches exposed at any place.

Application of the theory of Herring and Nichols[18] yields the result that the empirical slope of the straight line approximation for the normal Schottky effect [Eq. (2) with the cE term dropped] should be smaller than the calculated slope in the weak field region and larger in the strong field region.

Of interest in the present investigation is the location of the breaks in slope in the region between intermediate and large fields. Many of the photocurrent *versus* (applied field)$^{\frac{1}{2}}$ curves obtained (from which the deviation curves of Figs. 4 and 5 are derived) have a sharp change in slope near 180 (v/cm)$^{\frac{1}{2}}$. If such a break occurs where the field satisfies the strong field criterion δ to the extent that $2E=100(\delta\phi/\Delta y)$, and if $\delta\phi$ be taken as 0.4 v, the indicated patch diameter would be of the order of six microns.[19] This agrees reasonably with the patch size indications given by the electron microscope study of the filament surfaces.

[17] M. H. Nicols, Phys. Rev. **78**, 158 (1950).
[18] See reference 9, pp. 204–205, 214.
[19] Writing the inequality $E\gg\delta\phi/\Delta y$ (reference 9, p. 204, II.5.4) as the equality $2E=100(\delta\phi/\Delta y)$.

V. CONCLUSIONS

The present investigation has produced good evidence for the existence of the quasi-periodic deviations of the photoemission of tungsten from the Schottky effect for a constant transmission coefficient. Errors were carefully considered and the usual causes of current fluctuations were systematically eliminated. The main dependence for the conclusions is on the statistical nature of the data. Of especial importance is the fact that the standard deviations of the current readings for the individual points near practically all of the maxima and minima are appreciably less than the amplitudes of the deviations.

The amplitude of the measured deviations is 0.3–1.5 the theoretical value, being generally smaller than theory predicts, while the phase locations averaged from the curves of Figs. 4 and 5 are in closer agreement with the theory. Thus, a maximum (average) at 219 $\pm$18 (v/cm)$^{\frac{1}{2}}$ and a minimum (average) at 278$\pm$16 correspond to calculated values of 215 and 285 (v/cm)$^{\frac{1}{2}}$ and intercepts at 196$\pm$19, 237$\pm$18 and 324$\pm$19 (v/cm)$^{\frac{1}{2}}$ correspond to calculated values of 185, 240 and 325 (v/cm)$^{\frac{1}{2}}$.

It is particularly noted that: (1) dc heating of filaments may cause sufficient surface roughness to make the actual applied field noticeably larger than ideally calculated and to cause patch breaks in the region of fields of interest; (2) since all readings were taken for filaments with one or more layers of adsorbed gas the presence of such layers does not completely inhibit the Guth-Mullin deviation effect,[5] though it may be a contributing cause to the small amplitudes of a number of deviation curves.

The authors are indebted to Harry U. Rhoads, Research Associate in Physics, for the electron microscopy. They also acknowledge with thanks the helpful comments of J. A. Becker and Conyers Herring of the Bell Telephone Laboratories who read a preliminary draft of this paper.

VI. APPENDIX

A subsequent consideration of the experimental results presented above in light of the recent theoretical modifications of Juenker *et al.*[20] of the original theory[1] of Schottky deviations yields these conclusions. (1) The present photoelectric experiments agree somewhat better in average with the original Guth-Mullin[1] theory in the phase of the deviations, although several individual curves (such as Fig. 4, curve 8 and Fig. 5, curves 11 and 12) suggest deviation phases rather close to those of the Juenker theory which are shifted about a quarter-period relative to the older theory. Hence there remains the possibility that the proposed dc roughness factor suggested (Fig. 4, dotted curve 6 and 8) may be invalid with the correct explanation of the out-of-phase character of the experimental and

[20] Juenker, Colladay, and Coomes, Phys. Rev. **89**, 894 (1953); **90**, 772 (1953); and private communication.

theoretical results lying in the incorrectness as to phase locations of the old theory. (2) The present photoelectric experiments agree approximately in amplitude of the deviations with the Guth-Mullin theory with, as has been pointed out, the experimental amplitudes coming out somewhat smaller usually. The experimental amplitudes therefore are smaller than predicted by the old theory and larger than by the Juenker theory. (3) The present photoelectric experiments agree quite closely with the Juenker theory in the magnitude of the difference between positions of successive zero deviation points; 0.9π comes out of the experiments as the average value of the half-period of the appropriate parameter as against π in the theory.

PHYSICAL REVIEW VOLUME 91, NUMBER 3 AUGUST 1, 1953

The Storage of Energy in Silver Activated Potassium Chloride*

C. E. MANDEVILLE AND H. O. ALBRECHT
Bartol Research Foundation of The Franklin Institute, Swarthmore, Pennsylvania
(Received February 2, 1953; revised copy received April 20, 1953)

Crystals of KCl-Ag and NaCl-Ag have been excited by x-ray irradiation. The photostimulated light yield of the ultraviolet emission band has been observed simultaneously with application of the stimulating near-ultraviolet light. The decay with time of the stored energy in the two phosphors is compared.

THE energy storage properties of some silver activated alkali halides have been discussed in several recent publications.[1,2] The procedure outlined in references 1 and 2 has been to irradiate an excited phosphor with long wave light and observe in a phototube (RCA-1P28) what may be described as a "post-stimulation phosphorescence" of the ultraviolet emission band after the stimulating long wave light has been extinguished. In using the 1P28 as a detector, difficulties are encountered if attempts are made to measure the stimulated emission while the stimulating light is on, because the phototube's spectral response is such as to respond to the stimulating light as well. The stimulated light emitted while the stimulating light is on might be called "co-stimulation phosphorescence." To avoid this problem, the writers have employed photosensitive Geiger counters to detect the stimulated emission. It has long been known[3] that photosensitive Geiger counters can be produced which have an excellent sensitivity at 2500A but no response to near-ultraviolet or visible radiations. Accordingly, in the present investigation, photosensitive Geiger counters have been employed to detect the photostimulated emission of the ultraviolet bands of KCl-Ag and NaCl-Ag, the ultraviolet band of KCl-Ag being centered at 2800A and that of NaCl-Ag at 2500A. Irradiation, storage, and measurements relating to all phosphor samples were carried out at toom temperature (25°C).

To study the photostimulated emission from NaCl-Ag and KCl-Ag, a polycrystalline mass of KCl-Ag (AgCl concentration 0.10 ± 0.02 percent by weight) and a single crystal of NaCl-Ag prepared by The Harshaw Chemical Company (AgCl concentration 0.37 ± 0.06 percent by weight) were irradiated by x-rays of maximum energy 25 kev for ten minutes to receive a dosage of three roentgens. The irradiations were carried out in total darkness, and the materials were stored for twenty-four hours in light-tight containers. At the end of that time, the crystals were each stimulated by a one-watt tungsten lamp at a distance of seven centimeters for a period of one minute. The counting rates of NaCl-Ag and KCl-Ag before, during, and after the one-minute period of photostimulation are shown in Fig. 1. A time of one minute before the stimulating light was turned on was taken arbitrarily as time zero. Prior to stimulation, the slow normal unphotostimulated phosphorescence of NaCl-Ag was ~35 counts per minute, rising immediately to ~50 000 counts per minute in the form of co-stimulation phosphorescence. After one minute of photostimulation, the stimulating tungsten lamp was extinguished, and the luminescence from NaCl-Ag dropped immediately to a post-stimulation phosphorescence count of about 9000 per minute. Thus, photostimulation with the one-watt bulb of NaCl-Ag twenty-four hours after receipt of a dosage of three roentgens gave rise to a co-stimulation phosphorescence 1400 times greater than the residual unphotostimulated phosphorescence (35 counts per minute) existing prior to stimulation, and to a post-stimulation phosphorescence greater than the same quantity by a factor of 257. The similarly exposed KCl-Ag gave no evidence of slow unphotostimulated phosphorescence at 25°C, twenty-four hours after excitation. The counting rate in the photosensitive Geiger counter was only the natural background count. However, upon photostimulation, the

* Assisted by the joint program of the U. S. Office of Naval Research and the U. S. Atomic Energy Commission.
[1] M. Furst and H. G. Kallmann, Phys. Rev. **82**, 964 (1951); **83**, 674 (1951); Kallmann, Furst, and Sidran, Nucleonics **10**, No. 9, 15 (1952).
[2] Bittman, Furst, and Kallmann, Phys. Rev. **87**, 83 (1952).
[3] P. B. Weisz, Electronics **19**, No. 7, 106 (1946); H. Friedman and C. P. Glover, Nucleonics **10**, No. 6, 24 (1952); C. E. Mandeville and H. O. Albrecht, Phys. Rev. **79**, 1010 (1950).

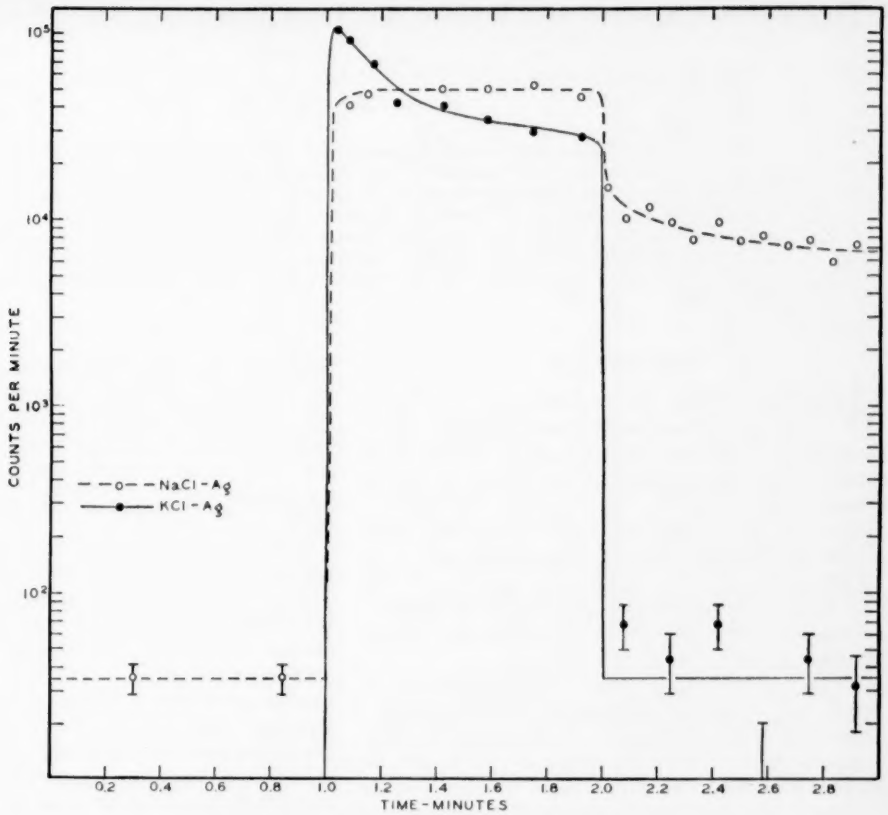

FIG. 1. Photostimulation for one minute of NaCl-Ag and KCl-Ag twenty-four hours after irradiation by three roentgens of x-rays.

counting rate rose to $\sim 10^5$ counts per minute, decreased to 2.5×10^4 counts per minute during one minute of photostimulation, and dropped very nearly to zero when the stimulating light was turned off.

Thirty seconds after the one-minute period of photostimulation, the counting rate arising from NaCl-Ag was 7600 counts per minute, whereas that of KCl-Ag was ~ 35 counts per minute. The large difference in the two curves at $t = 2.5$ min explains why Bittman, Furst, and Kallmann[4] reported the post-stimulation photophorescence of KCl-Ag to be essentially zero which led to the conclusion that only NaCl-Ag exhibits good storage properties. The fact is that KCl-Ag exhibits light storage which can be measured by co-stimulation phosphorescence, but not by poststimulation phosphorescence.

In Fig. 2 is shown a comparison of the co-stimulation phosphorescence of NaCl-Ag and KCl-Ag, the AgCl concentrations being the same as previously given. To obtain the data of Fig. 2, equal volumes of the two materials were irradiated in an x-ray field of intensity twenty roentgens per hour for a period of ten minutes. The irradiated materials were immediately stored in darkness and subsequently stimulated by the one-watt tungsten lamp for a period of six seconds every twenty-four hours. The counting rate during the six-second period of photostimulation is recorded.

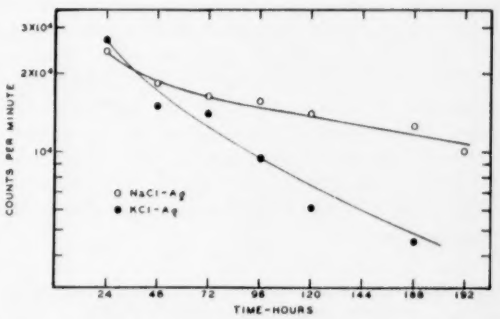

FIG. 2. Decay of co-stimulation phosphorescence of KCl-Ag and NaCl-Ag. The sample of NaCl-Ag was a single crystal (Harshaw).

Note added in proof:—Particular attention should be called to the papers of Mikao Kato, Sci. Papers Inst. Phys. and Chem. Research (Tokyo) **41**, 113 (1944); **41**, 135 (1944); **42**, 35 (1944); **42**, 95 (1944). In the fourth publication of the series, he describes many of the storage properties of KCl-Ag and comments on the spectral response of the Geiger counter and its importance in photostimulation studies. Kato's measurements differ from those of the writers in that his means of primary excitation were limited to ultraviolet light. Copies of Kato's papers have been difficult to obtain in the United States and were not available to the writers until after this manuscript had been submitted for publication.

[4] Bittman, Furst, and Kallmann, Phys. Rev. **87**, 83 (1952).

Photocurrent, Space-Charge Buildup, and Field Emission in Alkali Halide Crystals*

A. VON HIPPEL, E. P. GROSS, J. G. JELATIS, AND M. GELLER
Laboratory for Insulation Research, Massachusetts Institute of Technology, Cambridge, Massachusetts

(Received March 18, 1953)

Additively colored alkali halide crystals represent, in a first approximation, a transparent solid with frozen-in electrons which can be mobilized by light absorption. When moving towards the anode, these electrons leave a positive space charge behind, and an adjustable cathode fall results which can be steepened until electrons are released by field emission. The steady-state and transient solutions for the charging and discharging cycle are calculated, the effects of light intensity, wavelength, and field emission discussed, and KBr crystals investigated experimentally as function of time, voltage, light intensity, and color-center density. Field emission has been produced with voltages as low as 1 volt, and a field-emission photocell has been realized.

INTRODUCTION

WHILE studying the mechanisms of electric breakdown, we have become increasingly interested in the formation of space charges, the release of electrons from the cathode, and their transconductance through the dielectric.[1] Space-charge phenomena, furthermore, are the key problem for the understanding of interfacial polarization and electret formation, and for the operation of dry rectifiers and transitors. If the field distortion could be observed in a transparent system and controlled at will, much useful insight would be gained.

Alkali halide crystals, permanently colored by F centers, can fulfill the prerequisites for such a system. Under the proper conditions they represent a transparent solid with frozen-in electrons which can be mobilized by light absorption. When moving towards the anode, these electrons leave behind halogen defects as positive countercharges. An adjustable voltage gradient results that can be steepened at the cathode until electrons are released from the metal electrode into the crystal. Space charges of any desired distribution may be created by selective, localized illumination, thus permitting the formation of rectifying boundaries and the reproduction of a variety of electret effects which, in opaque solids, puzzle the observer.

The present paper reports the first stages of this research project.

1. SPACE-CHARGE BUILD-UP BY PHOTOEFFECT UNDER IDEALIZED CONDITIONS

An alkali halide crystal, permanently and not too deeply colored in alkali vapor or by the release of electrons from the cathode at high temperature, fulfills, in a first approximation, the following conditions:

(1) The principal electron traps are uniformly dispersed anion vacancies; (2) only a small fraction of these traps is occupied; (3) the essential release mechanism is light absorption in the F band; thermal liberation of electrons from their traps may be neglected; (4) the charge-carrier density depends only on the distance x between cathode ($x=0$) and anode ($x=l$) as long as the light absorption of the crystal, illuminated perpendicularly to the field, is small; (5) electrons may leave at the anode but not re-enter from the cathode; (6) conduction by ions and holes may be neglected.

In this situation our crystal represents a box containing, at the start, an electron cloud of uniform density, frozen into a compensating positive matrix. When a dc field is applied in the x direction, the voltage gradient is constant throughout, until, at $t=0$, a uniform illumination is switched on. Electrons now become mobilized, equal in number to the quanta absorbed times the quantum yield, and drift toward the anode until they are discharged or retrapped by anion vacancies. This motion of the electron cloud towards the anode leaves a bleached region of positive space charge behind. If the initial concentration of color centers is sufficiently small and the applied voltage sufficiently high, the final state will be a completely bleached crystal. For higher concentrations or lower voltages, the crystal in the end stage will consist of two distinct sections; a completely bleached positive region I in front of the cathode absorbing the total voltage drop, and a field-free, unbleached, neutral region II with the original color-center concentration (Fig. 1). Diffusion blurring the boundary between the regions I and II will be neglected for the present.

This final steady state of the field distribution can be calculated easily. If N_0 denotes the number of F centers per unit volume and e the elementary charge, we have in bleached region I a constant positive space-charge density

$$\rho_0 = N_0 e, \tag{1}$$

i.e., according to Poisson's equation, a constant field strength gradient[2]

$$(dE/dx)_1 = \rho_0/\epsilon', \tag{2}$$

where ϵ' is the dielectric constant of the crystal. The field strength,

$$E_1 = (\rho_0/\epsilon')(x - d_\infty), \tag{3}$$

* Sponsored by the U. S. Office of Naval Research, the U. S. Army Signal Corps, and the U. S. Air Force.

[1] A. von Hippel and R. S. Alger, Phys. Rev. **76**, 127 (1949).

[2] We use the rationalized mks system where the dielectric constant of vacuum is $\epsilon_0 = 8.854 \times 10^{-12}$ [farad m^{-1}].

decreases linearly with the distance x from the cathode and is concentrated in a cathode fall of the length d_∞. Region II, unbleached, is free of space charge and of field,

$$(dE/dx)_2=0, \quad E_2=\text{const}=0. \tag{4}$$

The total voltage V_0, applied initially across the geometrical length l of the crystal, has contracted across d_∞ in front of the cathode as

$$V_0=-\int^{l} Edx=-\int_0^{\infty}\frac{\rho_0}{\epsilon'}(x-d_\infty)dx=\frac{\rho_0}{2\epsilon'}d_\infty^2. \tag{5}$$

Thus a cathode fall has formed of length

$$d_\infty=(2\epsilon' V_0/\rho_0)^{\frac{1}{2}}\ [\text{m}], \tag{6}$$

in which the field strength reaches its maximum value,

$$E_c=-(\rho_0/\epsilon')d_\infty\ [\text{volt m}^{-1}], \tag{7}$$

directly in front of the cathode.

An F-center concentration, $N_0=1\times10^{22}$ [m^{-3}], may be a reasonable upper limit in view of conditions (2) and (4), and a static permittivity $\epsilon'=6\epsilon_0$, a representative value for the alkali halides. By applying 1000 v across a crystal of 1-cm length, we contract, by illumination, the original field of uniform strength $E_0=1\times10^5$ [volt m^{-1}] into a cathode fall of length

$$d_\infty\simeq8\times10^{-6}\ [\text{m}],$$

and raise the field strength in front of the cathode to

$$E_c\simeq2.5\times10^8\ [\text{volt m}^{-1}].$$

This field strength exceeds the intrinsic breakdown strength of most alkali halide crystals;[3] hence field emission is likely to set in and to arrest the further rise of the field before the breakdown strength is reached.[1] But obviously the simple expedient of creating a high-voltage gradient internally by controlled space-charge buildup instead of applying a comparable external field gives a new access to the "physics of high-field strength" without the difficulties usually encountered in high-voltage investigations.

2. TRANSIENT RESPONSE

The steady state produced by illumination leaves the crystal divided into two sections, a completely bleached cathodic region I and an unbleached anodic region II, abutting in a sharp boundary. We will assume that this division prevails also during the transient stage, i.e., that a "shock front" $x=d(t)$ separating regions I and II advances from the cathode and, slowing down, comes to rest at the distance $x=d_\infty$. This presupposes that we can lump summarily the photoelectric release of the electrons, their motion through the lattice and retrapping by halogen defects into an *effective mobility* b. Thus we have the model of an electron cloud of the density ρ and mobility b, moving through a stationary cloud of positive charges of the density ρ_0.

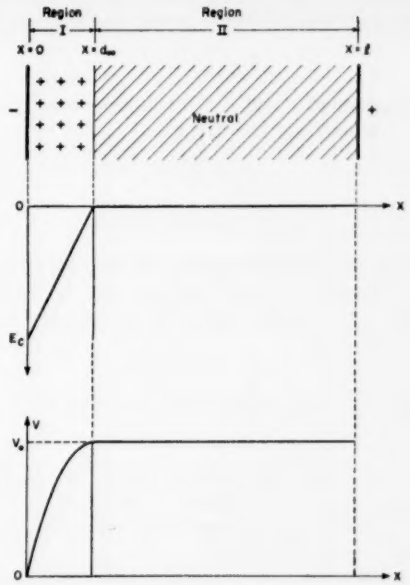

FIG. 1. Space charge, field strength, and voltage distribution in colored alkali halide crystal after charging (theoretical).

The electron cloud, according to Stokes' law, carries a current density

$$J=\rho bE; \tag{8}$$

the field-strength gradient, according to Poisson's equation, is

$$\partial E/\partial x=(\rho+\rho_0)/\epsilon' \tag{9}$$

with ρ negative; the condition of current continuity demands furthermore that

$$\partial\rho/\partial t=-\partial J/\partial x. \tag{10}$$

Substituting J from Eq. (8) we obtain the continuity condition in the form of the nonlinear differential equation

$$\partial\rho/\partial t+b\partial(\rho E)/\partial x=0, \tag{11}$$

with the boundary conditions

$$\begin{aligned}&\text{for } t=0: \quad \rho=-\rho_0, \quad E=\text{const}=-V_0/l,\\ &\text{for } t>0: \quad \rho(\text{at } x=0)=0, \quad \int_0^{l} Edx=-V_0.\end{aligned} \tag{12}$$

Region I, extending from $x=0$ to $x=d(t)$, has been vacated by the electron cloud [$\rho(x)=0$ for $x<d(t)$]; according to Eq. (9) the field strength is here

$$E_1=(\rho_0/\epsilon')x+C(t). \tag{13}$$

In the unbleached region II the space-charge densities of electron cloud and positive background cancel

[3] See A. von Hippel, J. Appl. Phys. **8**, 815 (1937).

$[\rho(x)=-\rho_0]$; hence the field strength in this section,

$$E_2=D(t), \tag{14}$$

is independent of x and is a function of time only. At the shock front itself $[x=d(t)]$,

$$E_1=E_2. \tag{15}$$

Hence

$$(\rho_0/\epsilon')d(t)+C(t)=D(t). \tag{16}$$

The boundary condition for $t>0$ (Eq. 12) leads to a second equation between the position of the shock front $d(t)$ and the time-dependent voltage gradients in regions I and II:

$$\int_0^{d(t)}\left[\frac{\rho_0}{\epsilon'}x+C(t)\right]dx+D(t)[l-d(t)]=-V_0. \tag{17}$$

A third equation is obtained from the continuity condition, Eq. (11). Region I, stripped of moving charge carriers, is traversed only by a displacement current of density

$$\epsilon'\partial E_1/\partial t=\epsilon'\partial C(t)/\partial t. \tag{18}$$

Region II carries a conduction and a displacement current:

$$-\rho_0 bE_2+\epsilon'\partial E_2/\partial t=-\rho_0 bD(t)+\epsilon'\partial D(t)/\partial t. \tag{19}$$

Current continuity requires that the total current passing through region I equals that through region II, or

$$\epsilon'\partial C(t)/\partial t=-\rho_0 bD(t)+\epsilon'\partial D(t)/\partial t\equiv J'. \tag{20}$$

Substituting $D(t)$ from Eq. (16) into Eqs. (17) and (20), we arrive at the two equations for $d(t)$ and $C(t)$:

$$\begin{aligned}\frac{\rho_0}{\epsilon'}ld(t)+lC(t)-\frac{\rho_0}{2\epsilon'}[d(t)]^2&=-V_0,\\ -\frac{\rho_0 b}{\epsilon'}d(t)+\frac{\partial d(t)}{\partial t}&=bC(t).\end{aligned} \tag{21}$$

By eliminating $C(t)$ we finally obtain the differential equation for the motion of the shock front:

$$\frac{\partial d(t)}{\partial t}-\frac{\rho_0 b}{2l\epsilon'}[d(t)]^2=-\frac{b}{l}V_0. \tag{22}$$

Its solution is

$$d(t)=\left(\frac{2\epsilon'}{\rho_0}V_0\right)^{\frac{1}{2}}\frac{1-\exp[-(2\rho_0 b^2V_0/\epsilon' l^2)^{\frac{1}{2}}t]}{1+\exp[-(2\rho_0 b^2V_0/\epsilon' l^2)^{\frac{1}{2}}t]}. \tag{23}$$

For $t=0$, $d(t)=0$ as prescribed, i.e., the crystal is colored uniformly. For $t=\infty$,

$$d(t)=(2\epsilon' V_0/\rho_0)^{\frac{1}{2}}\equiv d_\infty, \tag{24}$$

in accordance with Eq. (6). The motion of the shock front itself is regulated by a relaxation time

$$\tau\equiv(2\rho_0 b^2V_0/\epsilon' l^2)^{-\frac{1}{2}}, \tag{25}$$

which has a simple physical interpretation. By introducing d_∞ from Eq. (24), the relaxation time may be written

$$\tau=d_\infty/2bE_0\equiv d_\infty/2v_0. \tag{26}$$

Hence τ represents the time required for an electron to move with the drift velocity v_0 in the undistorted field E_0 through half the distance of the final cathode fall d_∞. By introducing d_∞ and τ, Eq. (23) for the shock-front position becomes

$$d(t)=d_\infty\frac{1-e^{-t/\tau}}{1+e^{-t/\tau}}=d_\infty\tanh\left(\frac{t}{2\tau}\right). \tag{27}$$

The motion of the shock front may be determined visually by observing $d(t)$, if the cathode fall is of macroscopic length. Alternatively, it can be measured by the current $I(t)$ or the charge $Q(t)$ that traverses the external circuit. For a crystal of cross section A, the current is, according to Eqs. (20) and (21):

$$I(t)\equiv AJ'(t)=\frac{A\epsilon'}{b}\left\{\frac{\partial^2 d(t)}{\partial t^2}-\frac{\rho_0 b}{\epsilon'}\frac{\partial d(t)}{\partial t}\right\}, \tag{28}$$

or, by introducing $d(t)$ from Eq. (27), it is

$$I(t)=\frac{-2A\rho_0 d_\infty}{\tau}e^{-t/\tau}\left\{\frac{(1-e^{-t/\tau})d_\infty/l+(1+e^{-t/\tau})}{(1+e^{-t/\tau})^3}\right\}. \tag{29}$$

At $t=0$, when the illumination has just been switched on, the current is at its maximum,

$$I(0)=-A\rho_0 d_\infty/2\tau=-A\rho_0 v_0, \tag{30}$$

and equal to the conduction current traversing the crystal in the undistorted field.

Since, for our experiments, $d_\infty/l\ll 1$, Eq. (29) simplifies to

$$I(t)\simeq I(0)/\cosh^2(t/2\tau). \tag{29a}$$

Plotted as $\log I(t)$ *vs* $\zeta\equiv t/2\tau$, the characteristic deviates from a straight line only for $\zeta<1$, where the slope curves towards zero (Fig. 2).

The charge transferred during the time t is [see Eq. (20)]:

$$Q(t)=\int_0^t I(t)=A\epsilon'\{C(t)-C(0)\}. \tag{31}$$

Since, according to Eq. (21),

$$C(t)-C(0)=-\frac{\rho_0}{\epsilon'}d(t)+\frac{\rho_0}{2\epsilon' l}[d(t)]^2, \tag{32}$$

Eq. (31) may be rewritten

$$Q(t)=A\rho_0 d(t)\{-1+(1/2l)d(t)\}; \tag{33}$$

and the total charge transported through the crystal for $t\to\infty$ becomes

$$Q(\infty)=-(A\rho_0 d_\infty/l)\{l-\tfrac{1}{2}d_\infty\}. \tag{34}$$

This result has again a simple meaning. If the whole crystal had been bleached ($d_\infty=l$), $Q(\infty)=A\rho_0 l/2$, i.e., the total charge of the electron cloud would have been moved in effect across half the crystal length. Vice versa, for a very short cathode fall ($d_\infty\ll l$), $Q(\infty)\simeq A\rho_0 d_\infty$, i.e., the electron cloud has moved the distance of the cathode fall.

The field distribution in region I [$x\leqslant d(t)$], according to Eqs. (13) and (21), is

$$E_1=-\frac{V_0}{l}+\frac{\rho_0}{\epsilon'}\left\{(x-d(t)+\frac{1}{2l}[d(t)]^2\right\}. \tag{35}$$

For $t=\infty$, since

$$\rho_0 d_\infty^2/\epsilon' 2l=V_0/l, \tag{36}$$

the field in the cathode fall becomes

$$E_1(\infty)=(\rho_0/\epsilon')(x-d_\infty), \tag{37}$$

as Eq. (3) of the steady-state solution prescribes. The field strength in region II, according to Eqs. (14) and (16), is

$$E_2=-(V_0/l)\{1-(d(t))^2/d_\infty^2\}; \tag{38}$$

it is independent of x and falls to zero at $t=\infty$. For $t=0$, both fields are identical and equal to the undistorted field $E=-V_0/l$.

3. DISCHARGING AND RECHARGING

The preceding calculation describes the *initial* charging of a crystal. Any *subsequent* discharging and later recharging to the same voltage proceeds under altered conditions since only the first application of the field discharges electrons at the anode. From here on, as long as electrons may not re-enter from the cathode and the ions are frozen in, the space charge in the crystal adjusts itself to shorting and reapplication of the voltage V by a backward or forward motion of the electron cloud without charge transfer to the electrodes.

Let us illustrate the situation graphically. The charging process terminates in the steady-state condition shown in Fig. 1:

$$\begin{aligned}&\text{for } x\leqslant d_x \quad \text{(region I)} \begin{cases} E_1(x)=(\rho_0/\epsilon')(x-d_x), \\ V_1(x)=-\int_0^x E_1 dx=(\rho_0/\epsilon')(d_x x-\tfrac{1}{2}x^2), \end{cases}\\ &\text{for } d_x\leqslant x\leqslant l \quad \text{(region II)} \begin{cases} E_2(x)=0, \\ V_2(x)=\rho_0 d_x^2/\epsilon'^2=V_0. \end{cases}\end{aligned} \tag{39}$$

When, at the start of a discharging experiment, the external voltage is removed at $t=0$ by short-circuiting the electrodes, we have to subtract from $E(x)$ the external field $-V_0/l$ and from $V(x)$ the external voltage $V_0 x/l$. Hence

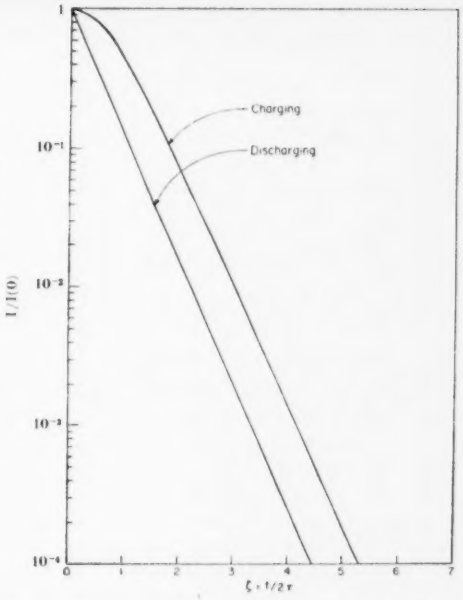

FIG. 2. Time dependence of photocurrent through colored alkali halide crystal (theoretical).

$$\begin{aligned}&\text{region I} \begin{cases} E_1(x)=(\rho_0/\epsilon')(x-d_x)+V_0/l \\ V_1(x)=(\rho_0/\epsilon')(d_x x-\tfrac{1}{2}x^2)-V_0 x/l, \end{cases}\\ &\text{region II} \begin{cases} E_2(x)=V_0/l \\ V_2(x)=V_0(1-x/l) \end{cases}\end{aligned} \tag{40}$$

(see Fig. 3). The voltage now reaches a maximum in the bleached region at the location

$$x_0=d_\infty-V_0\epsilon'/l\rho_0=d_\infty(1-d_\infty/2l) \tag{41}$$

of the value

$$V_{1\,\max}=(\rho_0/2\epsilon')x_0^2, \tag{42}$$

and drops on both sides towards zero.

This situation is obviously not a stable one. When mobilized by illumination, the electron cloud will be pulled back by the space-charge field into a symmetrical position between the electrodes (Fig. 4). Region II again will become field free, and two unbleached regions I and III in front of the electrodes and of equal thickness $d_x/2$, will contain the voltage drop produced by the positive space charge. The steady state must be (for $t=\infty$)

$$\begin{aligned}&E_1(x)=(\rho_0/\epsilon')(x-\tfrac{1}{2}d_x), \quad && V_1(x)=(\rho_0/\epsilon')(\tfrac{1}{2}d_x x-\tfrac{1}{2}x^2),\\ &E_2(x)=0, && V_2(x)=\tfrac{1}{4}V_0,\\ &E_3(x)=-E_1(l-x), && V_3(x)=+V_1(l-x).\end{aligned} \tag{43}$$

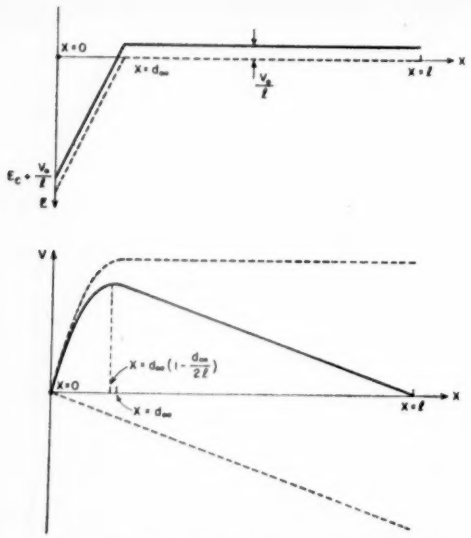

FIG. 3. Field and voltage distribution at beginning of discharge (theoretical).

The calculation of the transient response follows the pattern set in the preceding section. In analogy to Eqs. (13) to (15), we specify for the three fields:

$$\begin{aligned} E_1&=(\rho/\epsilon')x+C(t) \quad [\text{for } x\leqslant d(t)],\\ E_2&=D(t) \quad [\text{for } d(t)\leqslant x\leqslant l-d_\infty+d(t)],\\ E_3&=(\rho/\epsilon')x+F(t) \quad [\text{for } l-d_\infty+d(t)\leqslant x\leqslant l], \end{aligned} \tag{44}$$

with the matching conditions

$$\begin{aligned} E_1(d(t))&=E_2(d(t)),\\ E_2(l-d_\infty+d(t))&=E_3(l-d_\infty+d(t)). \end{aligned} \tag{45}$$

Current continuity demands [see Eqs. (18) to (20)]

$$\epsilon'\partial C(t)/\partial t=\rho_c bD(t)+\epsilon'\partial D(t)/\partial t=\epsilon'\partial F(t)/\partial t. \tag{46}$$

Furthermore, replacing Eq. (17), we require that the total voltage must be zero:

$$\begin{aligned} \{(\rho_0/2\epsilon')[d(t)]^2+C(t)d(t)\}+D(t)(l-d_\infty)\\ +\{(\rho_0/2\epsilon')(l^2-[l-d_\infty+d(t)]^2)\}\\ +F(t)[d_\infty-d(t)]=0. \end{aligned} \tag{47}$$

Eliminating $C(t)$ and $D(t)$ we arrive at the differential equation for the shock front,

$$\partial d(t)/\partial t+d(t)d_\infty b\rho_0/l\epsilon'=(b/l)V_0, \tag{48}$$

with the solution

$$d(t)=\tfrac{1}{2}d_\infty(1+e^{-t/\tau}). \tag{49}$$

In contrast to the first charging, the displacement of the electron cloud follows now a simple exponential decay law (see Fig. 2) with the previous time constant [see Eq. (26)]:

$$\tau=d_\infty l/2bV_0. \tag{50}$$

In consequence, the short-circuit current caused by the motion of the electron cloud [see Eq. (28)],

$$\begin{aligned} I(t)=A\epsilon'\frac{dC(t)}{dt}&=-\frac{A\epsilon'}{b}\left\{\frac{\partial^2 d(t)}{\partial t^2}-\frac{\rho_0 b}{\epsilon'}\frac{\partial(t)}{\partial t}\right\}\\ &=A\frac{\rho_0 d_\infty}{2t}\left(1-\frac{d_\infty}{l}\right)e^{-t/\tau}, \end{aligned} \tag{51}$$

also shows a simple exponential decay. Its initial value, for $t=0$ and $d_\infty\ll l$, is identical with the maximum charging current of Eq. (30).

After the equilibrium situation of Fig. 4 is established, a reapplication of the voltage V_0 causes a transient described by the same equations as above, only the voltage $-V_0$ has to be introduced on the right side of Eq. (47). The shock front moves to the right again according to the exponential decay law

$$d(t)=d_\infty(1-\tfrac{1}{2}e^{-t/\tau}), \tag{52}$$

with an identical current flow

$$I(t)=-A(\rho_0 d_\infty/2\tau)(1-d_\infty/l)e^{-t/\tau} \tag{53}$$

in the opposite direction. Hence, by applying an alternating field of the amplitude V_0, biased with a dc voltage $V_0/2$, we should observe, as function of frequency, a simple relaxation spectrum caused by the space-charge motion in the crystal capacitor.

4. DEPENDENCE ON LIGHT INTENSITY AND WAVELENGTH

Since we specified that the electron cloud may be mobilized by light only (condition 3, Sec. 1), we have

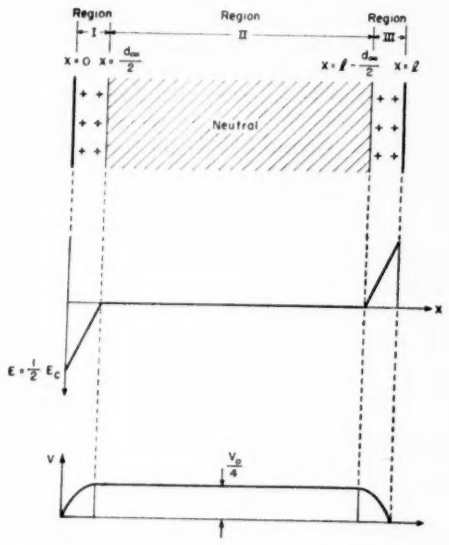

FIG. 4. Space-charge, field-strength, and voltage distribution after discharge (theoretical).

the unusual situation that the mobility b, and with it the time constant τ of the space-charge buildup, can be controlled from the outside by the color and intensity L_0 of the illumination.

The photoelectrons in the alkali halides, as Pohl and his co-workers[4,5] found, travel, after release, an average distance $\bar{w}$ towards the anode before they are retrapped. This drift distance increases proportionally to the driving-field strength, decreases with the concentration of color centers, and depends on the temperature, composition and prehistory of the sample. The drift distance per unit field strength, $\bar{w}_0$, is short and of the order 10^{-11} [m/v]. If t_b and t_f designate the average time intervals during which an electron is bound or travels freely, the drift velocity may be written

$$\bar{v}=bE=[\bar{w}_0/(t_b+t_f)]E. \tag{54}$$

Obviously, for our model, the time an electron stays bound is inversely proportional to the intensity of the releasing light,

$$t_b=1/\beta L_0. \tag{55}$$

If this time is long compared with the time of free travel ($t_b \gg t_f$), as is normally the case, the mobility

$$b\simeq\bar{w}_0/t_b\simeq\bar{w}_0\beta L_0 \tag{56}$$

is proportional to the intensity of illumination.

The introduction of a mobility b into Eq. (54) presupposes that the internal field strength across the drift distance $\bar{w}$ is constant. Since the drift distance $\bar{w}_0$ is very small and the field strength in region II does not exceed the applied field V_0/l, the assumption should be valid in this region. Difficulties may arise if the shock front is not the sharp boundary of our model, but diffuse because electrons have been left behind in the cathode fall. However, such stragglers, when liberated, find themselves in a much steeper field and tend to catch up with the main front speedily. Thus one may expect, just as in the Stasiw experiment on the thermal mobilization of electrons at high temperature,[6] that the shock is sharply defined towards the cathode.

Real difficulties will arise for our simple model from other causes. Until now we have assumed the existence of only one type of trap, that characterized by the F-band absorption. Actually, we know that a variety of traps exist, starting with the F band of Pohl and co-workers[7] and the M and R bands found by Molnar[8] in this laboratory, to the broad, continuous absorptions of colloidal aggregates that form by irradiation with with white light[5,9] or during long-time storage of additively colored crystals. If the F centers are caused by Schottky defects and correspond, as de Boer suggested,[10] to *one* electron attached to a negative ion vacancy, the F' centers, according to Pick's quantum efficiency measurements,[7] may represent *two* electrons attached to such vacancy. The R and M centers, as Seitz proposed,[11] may correspond to two F centers side by side and to the combination of an F center with an anion-cation vacancy pair. Thus, while starting our experiment with a crystal containing only the F-band absorption, we are bound to produce, by illumination in this band, new trapping centers absorbing at longer wavelengths.[9,11]

In consequence, if we mobilize the electron cloud by F-band illumination, we will leave electrons behind in other trapping centers as the shock front progresses. The effective space-charge density begins to fall below ρ_0, and the relaxation time τ increases [see Eq. (25)]. Illumination at low temperature may delay the formation of these additional centers, as the yield characteristics of Pick indicate.[7] This is understandable if the motion of Schottky defects and of vacancy pairs is a prerequisite for their formation.[11]

White-light illumination will obviate some of these difficulties by remobilizing electrons trapped outside the F-band range. However, since the quantum yield from the R centers and from the colloidal centers is very low, we are found to lose electrons[12] as the experiment progresses.

5. FIELD EMISSION

When the field strength at the cathode builds up beyond some critical value, the probability rapidly increases that electrons enter by field emission. This effect will keep the gradient at the cathode lower than Eq. (7) prescribes, and a final current will flow; this requires that the field E_2 across the electron cloud does not drop to zero.

Field emission tends to take place at sensitive spots; and the distribution and efficiency of such spots is apt to alter as time goes on and to be affected in our case by the discharging of alkali metal.[13] Neglecting this complication at present, we assume that the field-current density is prescribed by the field strength at the cathode as $J=J(E_c)$ and that it is carried through the crystal according to Stokes' law as

$$J(E_c)=\rho bE, \tag{57}$$

with the field gradient prescribed by Poisson's equation

$$\partial E/\partial x=(\rho+\rho_0)/\epsilon' \tag{58}$$

[4] B. Gudden and R. Pohl, Z. Physik **31**, 651 (1925); W. Flechsig, Z. Physik **33**, 372 (1925); **46**, 788 (1928); K. Hecht, Z. Physik **77**, 235 (1932).

[5] G. Glaser and W. Lehfeldt, Nachr. Ges. Wiss. Göttingen, Math-physik. Kl. Fachgruppen II **2**, 91 (1936).

[6] O. Stasiw, Nachr. Ges. Wiss. Göttingen, Math.-physik. Kl. 261 (1932).

[7] Cf. H. Pick, Ann. phys. **31**, 365 (1938).

[8] J. P. Molnar, Ph.D. thesis, MIT, 1940; Phys. Rev. **59**, 944 (1941).

[9] G. Glaser, Nachr. Ges. Wiss. Göttingen, Math.-physik. Kl. Fachgruppen II, **3**, No. 2, 31 (1937).

[10] J. H. de Boer, Rec. trav. chim. **56**, 301 (1937).

[11] F. Seitz, Revs. Modern Phys. **18**, 384 (1946).

[12] See in this connection the interesting observations of J. J. Oberly, Phys. Rev. **84**, 1257 (1951); and of D. B. Dutton, Ph.D. thesis, University of Illinois, 1952 (unpublished).

[13] A. von Hippel, Z. Physik **98**, 580 (1936).

[see Eqs. (8) and (9)]. The initial current density at $t=0$ in the undistorted field is given [see Eq. (12)] as

$$J_0=\rho_0 bV_0/l; \tag{59}$$

hence the ratio of final current caused by field emission to initial current may be written

$$J(E_c)/J_0=J(E_c)l/\rho_0 bV_0\equiv -K. \tag{60}$$

We note that K is a negative number. By referring to the *relative* field strength, space-charge density, and distance,

$$E'=El/V_0, \quad \rho'=-\rho/\rho_0, \quad x'=x/l, \tag{61}$$

we may rewrite Eq. (58) for the discussion of the steady state

$$dE'/dx'=\alpha(1-\rho'), \tag{62}$$

where [see Eq. (6)]

$$\alpha=l^2\rho_0/\epsilon' V_0=2l^2/{d_\infty}^2\gg 1. \tag{63}$$

Since, according to Eqs. (57) and (60),

$$\rho'=K/E', \tag{64}$$

the Poisson equation becomes

$$\frac{dE'}{dx'}=\frac{d}{dx'}\left(-\frac{dV'}{dx'}\right)=\alpha\left(1-\frac{K}{E'}\right), \tag{65}$$

with the boundary conditions:

$$\begin{aligned} &\text{for } x'=0, \quad E'=E_c/(V_0/l);\\ &\text{for } x'=1, \quad V'=-\int_0^1 E'dx'=1. \end{aligned} \tag{66}$$

Integrating Eq. (65) we obtain

$$\tfrac{1}{2}E'^2=-\alpha(V'+Kx')+A; \tag{67}$$

since the voltage $V'=0$ at $x'=0$,

$$A=\tfrac{1}{2}E_c'^2. \tag{68}$$

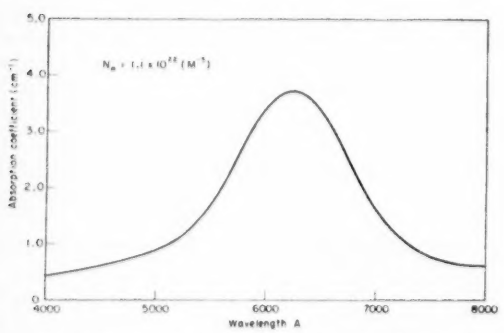

FIG. 5. Typical F-band absorption in colored crystal before experiment.

Rewriting Eq. (67) as

$$(1/\sqrt{2})(dV'/dx')=[A-\alpha(V'+Kx')]^{\frac{1}{2}},$$

or

$$(2\alpha)^{\frac{1}{2}}dx'=\frac{dV'}{(A/\alpha-V'-Kx')^{\frac{1}{2}}}, \tag{69}$$

and integrating once more we obtain the voltage distribution V' as $f(x')$ in the somewhat involved form,

$$-\frac{(2\alpha)^{\frac{1}{2}}}{2}x'=\left[\left(\frac{A}{\alpha}-V'-Kx'\right)^{\frac{1}{2}}-\left(\frac{A}{\alpha}\right)^{\frac{1}{2}}\right]-\frac{K}{(2\alpha)^{\frac{1}{2}}}\times\log\left[\frac{K/(2\alpha)^{\frac{1}{2}}+(A/\alpha-V'-Kx')^{\frac{1}{2}}}{K/(2\alpha)^{\frac{1}{2}}+(A/\alpha)^{\frac{1}{2}}}\right]. \tag{70}$$

By invoking the boundary condition [Eq. (66)], i.e., for $x'=1$, $V'=1$, we arrive at a relation between K, A and α as

$$-\frac{(2\alpha)^{\frac{1}{2}}}{2}=\left[\left(\frac{A}{\alpha}-1-K\right)^{\frac{1}{2}}-\left(\frac{A}{\alpha}\right)^{\frac{1}{2}}\right]-\frac{K}{(2\alpha)^{\frac{1}{2}}}\log\left[\frac{K/(2\alpha)^{\frac{1}{2}}+(A/\alpha-1-K)^{\frac{1}{2}}}{K/(2\alpha)^{\frac{1}{2}}+(A/\alpha)^{\frac{1}{2}}}\right]. \tag{71}$$

This expression can be reduced by approximation to an equation for the determination of the field gradient E_c at the cathode from a measurement of K, the ratio of final to initial current. In the case of no field emission, Eqs. (6), (7), and (63) specify that

$$(A/\alpha)^{\frac{1}{2}}=(E_c'^2/2\alpha)^{\frac{1}{2}}=1, \tag{72}$$

or

$$E_c'(K=0)=(2\alpha)^{\frac{1}{2}}. \tag{73}$$

When field emission occurs, $(A/\alpha)^{\frac{1}{2}}<1$ and $0>K>-1$, and, since $\alpha\gg 1$, $|K|/(2\alpha)^{\frac{1}{2}}\ll 1$. The left side of Eq. (71) is large and negative; hence the argument of the logarithm on the right side must be positive and very close to zero, i.e.,

$$K/(2\alpha)^{\frac{1}{2}}+(A/\alpha-1-K)^{\frac{1}{2}}\ll 1,$$

or

$$A/\alpha-1-K\simeq K^2/2\alpha. \tag{74}$$

Since $K^2/2\alpha\ll 1$, Eq. (74) approximates to $2A\simeq(1+K)2\alpha$ or $E_c'\simeq(1+K)^{\frac{1}{2}}(2\alpha)^{\frac{1}{2}}$, that is,

$$E_c\simeq(1+K)^{\frac{1}{2}}E_c(K=0). \tag{75}$$

The field E_c of the cathode fall drops initially very slowly with K. For $K=-\frac{1}{2}$ it decreases to $0.71E_c(K=0)$. However, as K approaches -1, i.e., when the final current approaches the initial current, the cathode fall begins to disappear, and for $K=-1$ the space-charge-free situation exists. Hence, by observing K and calculating $E_c(K=0)$ for no field emission, the gradient E_c at the cathode in the case of field emission may be obtained, and by plotting the final current $J(E_c)$ against E_c, the law of electron emission can be found.

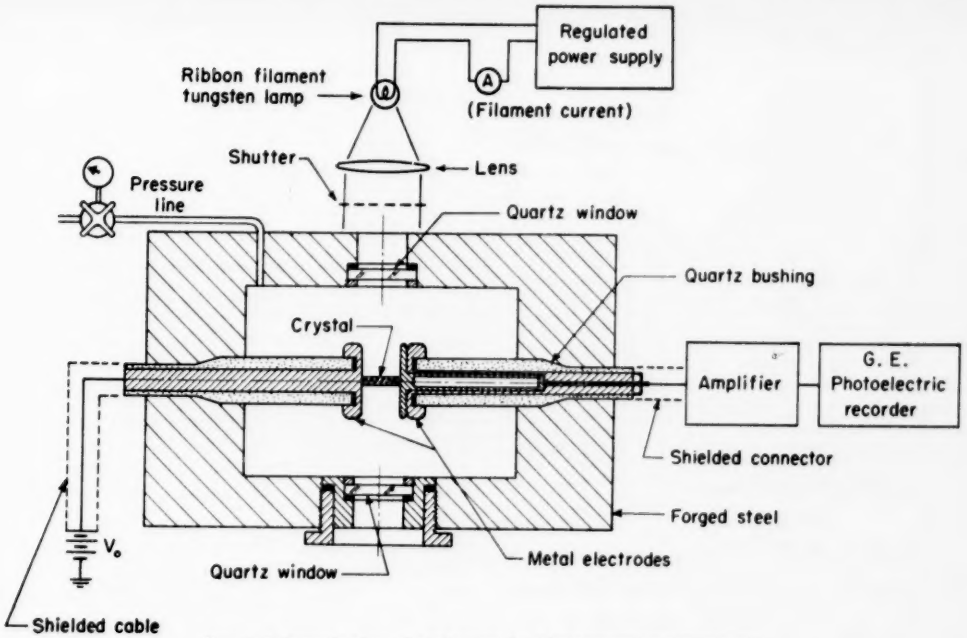

FIG. 6. Schematic view of equipment for photocurrent measurements.

6. EXPLORATORY EXPERIMENTS

To test the validity of our box model of the frozen-in electron gas, and to check on the field emission situation, a number of exploratory experiments were made at room temperature.

Samples and Equipment

As samples KBr crystals in the shape of rectangular bars were used, and colored either by the immigration of electrons at about 500°C or additively colored in alkali metal vapor. The vapor treatment was carried out in an iron tube placed in a two-stage furnace. The crystal was kept at high temperature (625°C) to reach equilibrium rapidly by diffusion, while the alkali metal in the low-temperature section determined, by its vapor pressure, the density of the color centers, N_0 [see Eq. (1)]. Rapid cooling by an air blast kept the electrons in their F-center traps, as a check of the optical absorption with a recording Cary spectrophotometer confirmed (Fig. 5). The density of F centers was calculated from the half-width of the F band according to Smakula's procedure;[14] it was adjusted for our experiments from *ca* 10^{20} to 10^{24} [m^{-3}].

Gold electrodes were applied to the end surfaces of the samples by vacuum evaporation; and the crystals were inserted in a sample holder that allowed illumination from both sides and the application of gas pressure to suppress corona discharges (Fig. 6).

Three types of illumination were provided: (a) constant over-all illumination by a tungsten ribbon-filament lamp; (b) a narrow light probe that could be focused on any part of the crystal and was modulated at 90 cps by a mechanical chopper; (c) a third light source that could project a slit of adjustable width on the crystal for any partial illumination desired.

The photocurrent as a function of time was measured with a feedback micromicroammeter (maximum sensitivity, *ca* 10^{-13} amp full scale, noise level 10 percent of this value) connected to a G-E recorder. The ac system consisted of an electrometer tube amplifier, followed by a high-gain ac amplifier, tuned filter and output meter (maximum sensitivity about the same as that of the dc system). Batteries served as the voltage supply for the crystal current.

In the experiments reported here, the tungsten ribbon filament lamp (G-E 6 v, 18 amp) was used as the only light source. It has not yet been calibrated in absolute units as function of the lamp current; a relative intensity characteristic is included in Fig. 11. In the measurements reported in the subsequent section, the lamp current served as a measure of the light intensity.

Measurements and Results

A KBr crystal of medium color-center density ($N_0 \simeq 10^{22}$ [m^{-3}]), connected to a voltage of about 500 v and weakly illuminated by white light (8 amp), shows a current-time response, as indicated in curve (1) Fig. 7. Contrary to the expectations of our simple model (see Fig. 2), no straight line portion manifesting an exponential current decrease can be discerned, but only a rapidly arrested slope leading to a slightly

[14] A. Smakula, Z. Physik **59**, 603 (1930).

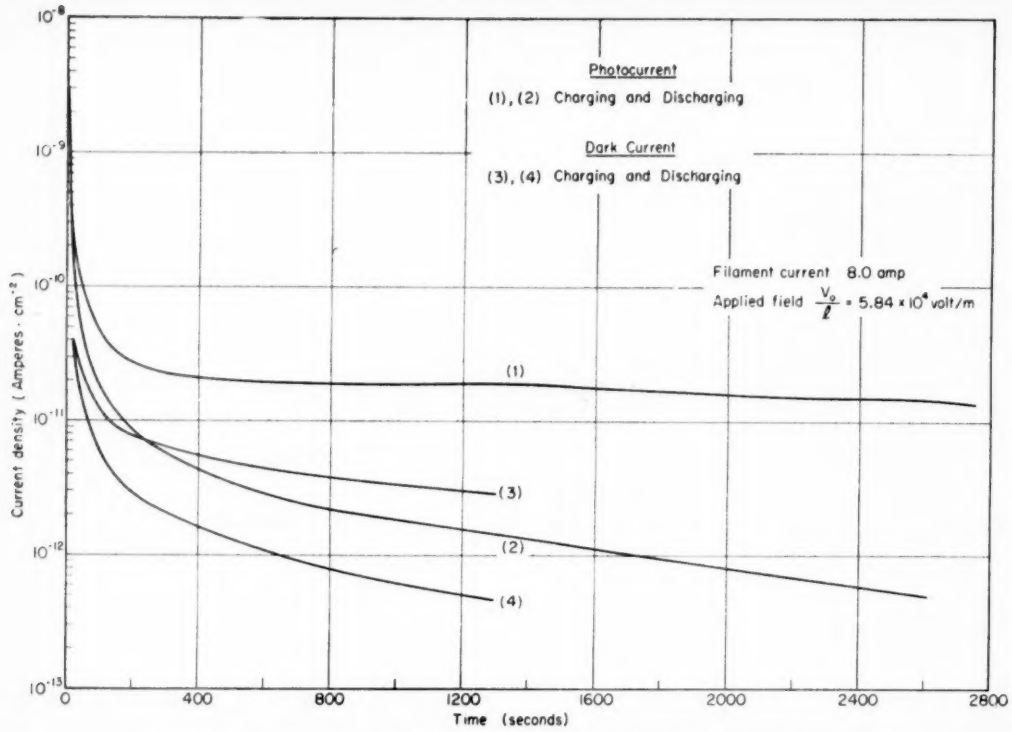

FIG. 7. Current density *vs* time for charging and discharging with and without illumination.

undulating final value. Repetition of the charging experiment produces similar curves with somewhat faster decay and lower final currents. The discharging characteristic (2) shows a still faster initial fall, followed by a long, sloping decrease over hours. Charging and discharging without illumination produces the same type of curves (3 and 4), displaced by about an order of magnitude to lower current values. The relatively large dark current in these first experiments is due to traces of moisture; in later measurements on freshly split crystals it is reduced by a factor of *ca* 100.

The situation is clarified when the charging and discharging curves are observed on a crystal of lower color-center density ($N_0 \simeq 5\times10^{21}$ [m^{-3}]) over a wide range of voltages (Fig. 8). For low voltage, the charging and discharging characteristics are really straight lines of nearly identical slope. For higher voltages the linear part of the charging curve systematically shortens and steepens, and the characteristic bends over rapidly to some constant current value. Simultaneously the discharging characteristic drops rapidly below that of the charging current.

The deviation from a straight line relation and the existence of a final current are factors indicating field emission. At a first glance, this explanation seems unlikely in view of the low voltages applied. However, according to our model [see Eqs. (6) and (7)], 22.5 volts across the crystal of Fig. 7 contract to a cathode fall of $d \simeq 1.2\times10^{-6}$ [v·m] with a field gradient $E_c \simeq 3.7\times10^{7}$ [v·m^{-1}] in front of the electrode. We know from experience[15] that such fields, not far below the breakdown strength, produce field emission. In charging, the emission sets in *after* the cathode fall has contracted sufficiently; a final state then is approached in which the emission from the cathode is balanced by the transconductance through the electron-cloud region II. In discharging, the electron cloud is pushed backwards, the gradient at the previous cathode is lowered rapidly, and the gradient at the previous anode is built up until field emission sets in also at that electrode. Zero current results when the gradient and field emission at both electrodes have become equal. The emission at the electrodes is expected to follow the law[16]

$$J = aE_c^2 e^{-b/E_c}. \tag{76}$$

The indirect evidence for field emission just discussed can be confirmed by direct experimental proof. When field emission exists, electrons are drawn into the crystal even in the dark. They accumulate in front of the cathode, and are released in a current pulse when the light is suddenly switched on. Figure 9 gives an example

[15] A. von Hippel, Phys. Rev. **54**, 1096 (1938).
[16] R. H. Fowler and L. Nordheim, Proc. Roy. Soc. (London) **A119**, 173 (1928).

TABLE I. Time constant *vs* light intensity at 22.5 v.

Filament current (amp)	τ (sec)	J_0 (amp/cm²)	$J_0\tau$ (coulomb/cm²)
8	128	4.4×10^{-13}	5.6×10^{-11}
9	70	10^{-12}	7×10^{-11}
10	35	2.3×10^{-12}	8.1×10^{-11}
11	19	4.4×10^{-12}	8.3×10^{-11}
12	13	7.6×10^{-12}	9.9×10^{-11}
13	8	1.3×10^{-11}	10.4×10^{-11}
14	6	1.7×10^{-11}	10.2×10^{-11}

of such current pulses, measured as a function of dark-time interval and voltage. For the crystal shown, field emission can thus be clearly demonstrated at 4.5 v; for higher color-center densities we could establish field emission even below 1 v. When a crystal has been charged with sufficient voltage, such current pulses can be produced in discharge for many days and give, in their height, a good measure of the remaining field gradient.

Returning to the initial current density J_0 and the relaxation time τ of the space-charge buildup, we would expect that τ is inversely proportional to the light intensity [see Eqs. (26) and (56)], but that the product $J_0\tau$ is constant for a given crystal and charging voltage. Table I confirms that this is the case within our limits of accuracy. Table II shows, in addition, that the initial current increases proportionally to the applied voltage, as predicted; the time-constant measurements for higher voltages are relatively inaccurate since the linear slopes are very short, hence the expected decrease of τ, as $(V_0)^{-\frac{1}{2}}$ can only be surmised. Similarly Table III, for the same reason, cannot confirm accurately that τ varies proportionally to $(N_0)^{-\frac{1}{2}}$, but shows the expected trend. The pen recorder is being replaced presently by a cathode-ray oscillograph for more accurate slope measurements.

TABLE II. Variation of time constants with voltage, Crystal 12A, at 10 amp.

Volts	τ (sec)	I_0 (amp)
4.5	33.5	2×10^{-12}
22.5	21	1.1×10^{-11}
90	14	4.5×10^{-11}
300	9	1.5×10^{-10}

Seen from the standpoint of photoelectric response, our crystals represent a *new type of photocell*. Ordinarily,

TABLE III. Variation of time constant with color density at 22.5 v and 10 amp.

Crystal	N_0/cm³	τ (sec)
13B	2×10^{14}	35
12A	8.6×10^{14}	21
10A	4.3×10^{15}	7

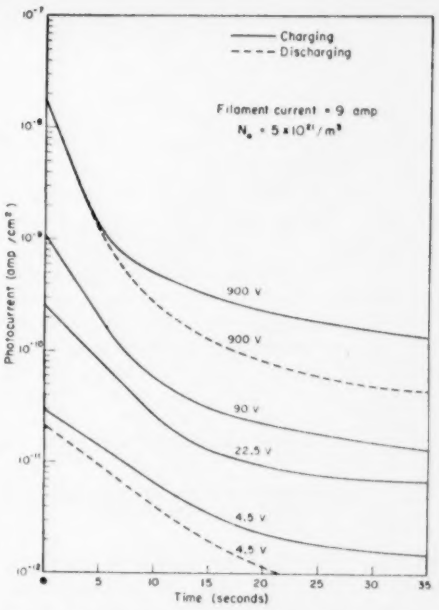

FIG. 8. Photocurrent curves at different voltages for constant light intensity.

the photoeffect in solids is either composed of the electrons directly liberated by the absorbed quanta (*primary photoeffect*) or results from a change in the conductivity of the dielectric induced by the light absorption (*secondary photoeffect*). A distinction between these two effects, based on the speed and yield of the response, was made by Gudden and Pohl[17] at an early date. The primary photoeffect, represented, for example, by the *F*-center electrons mobilized by light absorption, responds instantaneously and can usually

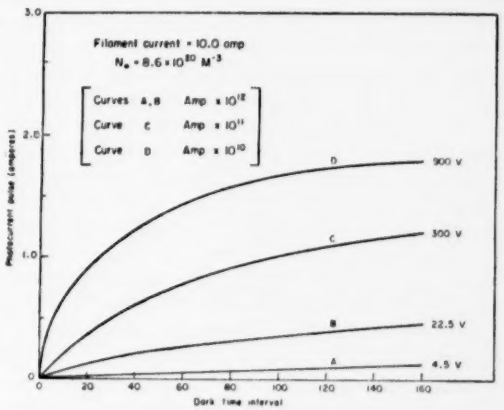

FIG. 9. Photocurrent pulse as function of dark-time interval and voltage.

[17] See B. Gudden, *Lichtelektrische Erscheinungen* (Verlag. Julius Springer, Berlin, 1928).

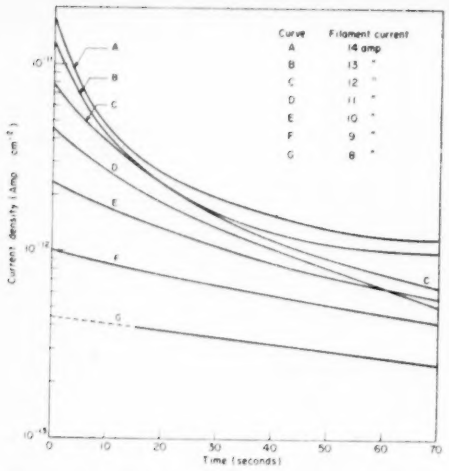

FIG. 10. Charging characteristics for different light intensities ($V_0=22.5$ v, $N_0=2\times10^{20}/m^3$).

not exceed one electron per absorbed quantum. The secondary photocurrent, exemplified, for instance, by the thallous sulfide photocell,[18] responds sluggishly, but can reach much larger quantum yields.

In our experiments of controlled space-charge build-up, first a normal primary photoeffect occurs. When the stationary state is reached without field emission, the bleached cathode fall (region I of Fig. 1) is free of F centers, and the colored region II of the electron cloud, free of field. Hence, while photoelectrons are still being liberated in region II, they acquire no drift velocity towards the anode, and the current ceases.

The situation changes when electrons are taken in at the cathode. This may be accomplished by the normal *external photoeffect*, well known from gas and vacuum photocells. The energy required to transfer an electron from silver into KBr photoelectrically has been investigated recently by Gilleo[19] in this laboratory and amounts to about 4.3 ev. This external photoeffect actually occurs in our experiments under strong white-light illumination, as Fig. 10 indicates. If a crystal of very low color-center density is illuminated by the tungsten lamp raised only to yellow heat (curve G, 8 amp), a straight, exponential, current decay is observed at low voltage indicating no emission. As the temperature of the light source is increased, the characteristics bend over systematically to higher and higher constant values. Simultaneously, the initial slopes steepen as predicted by our model, because the mobility b of the F electrons in the crystal increases proportionally to the light intensity [see Eq. (56)], hence the time constant shortens. These curves are similar to those obtained by field emission, but that they originate from external photoeffect can be established beyond doubt. The photoresponse is greatly reduced when the blue part of the light beyond the F-band region is cut out by filters;[20] furthermore, no electrons accumulate in dark-time intervals which could be released as current pulses.

In the region of field emission, this external photocurrent is overshadowed by the field current; the strong photosensitivity now appearing (Fig. 11) is due to the delicate balance between the field strength at the cathode, regulating the emission, and the voltage gradient in the electron cloud (region II), providing for the electron transport to the anode. With increasing light intensity, the mobility of the electrons in this region rises; the voltage gradient required for the current transport diminishes, and field can be retracted to the cathode, until the increasing emission establishes a new balance at a higher current value.

This new photocell type, that responds to illumination changes by changes in field distribution and thus in

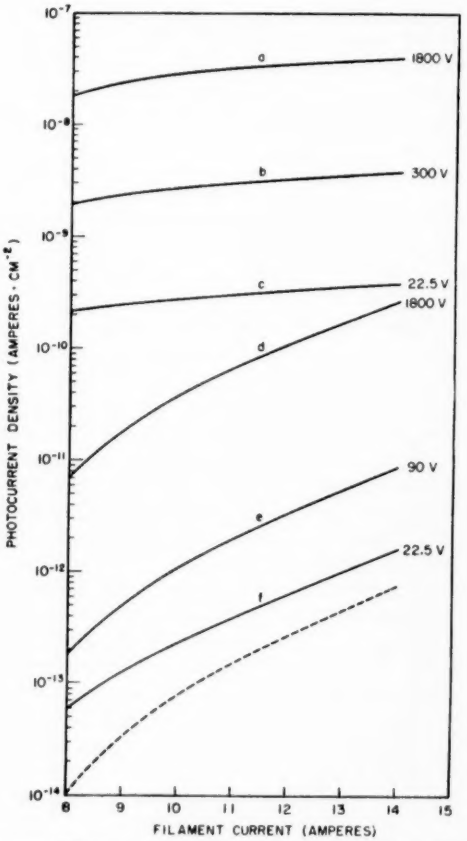

FIG. 11. Photocurrent as function of light intensity. Curves a, b, c: $N_0=1.1\times10^{23}$ m^{-3}; curves d, e, f: $N_0=2\times20^{20}$ m^{-3}; - - - intensity of light source in F-band region (arbitrary units).

[18] A. von Hippel and E. S. Rittner, J. Chem. Phys. **14**, 370 (1946).

[19] M. A. Gilleo, this issue [Phys. Rev. **91**, 534 (1953)].

[20] In our crystals some potassium is deposited at the cathode by ionic migration as the experiment continues, hence some sensitivity to larger wavelengths remains.

field emission, may properly be called a "field-emission photocell." It has some peculiar properties. Since the relaxation time τ is inversely proportional to the mobility [see Eq. (25)], the cell becomes sensitive to higher frequencies as the light intensity increases. Furthermore, since the voltage gradient required for the transport of current is inversely proportional to the color-center density, a lighter colored crystal is more sensitive to illumination changes, because more voltage can be reflected towards the cathode. Finally, we have observed that the photosensitivity can be extended by building in new absorption centers in other spectral regions, for example, in the infrared.

In Eq. (75) we show how the true field gradient E_c at the cathode may be found from the ratio of initial-to-final current. The law of electron emission can thus be established. No quantitative comparison has been made at the present time because the emission experimentally observed is not uniformly distributed over the cathode surface but takes place from sensitive spots. If we could observe it visually, it would resemble a scintillation phenomenon, with spots becoming active and inactive, changing shape and emissivity as time goes on. The field emission current is therefore noisy, but the noise diminishes as the cathode becomes conditioned. We believe that this is the noise observed in pre-breakdown currents by Haworth and Bozorth,[21] by us,[15] and recently again by Kawamura and Omuki,[22] and that it should probably not be interpreted as the sign of pre-breakdown avalanches.

The authors are greatly indebted to D. A. Powers for the design of the micromicroammeter, to L. B. Smith for the design of the high-pressure sample holder, and to J. Kalnajs for the preparation of the colored crystals.

[21] R. M. Bozorth and F. E. Haworth, Phys. Rev. **39**, 845 (1932).
[22] H. Kawamura and M. Omuki, J. Phys. Soc. Japan **6**, 283 (1951).

PHYSICAL REVIEW VOLUME 91, NUMBER 3 AUGUST 1, 1953

Current Carrier Mobility Ratio in Semiconductors

L. P. HUNTER
International Business Machines Corporation, Poughkeepsie, New York
(Received April 3, 1953)

The ratio of the electronic mobility to the hole mobility in germanium has been reported by many workers. The ratio reported is usually obtained by measurements on two different samples of different conductivity types. The method suggested here deduces the mobility ratio from resistivity measurements made on a single sample. An accurate plot of resistivity as a function of temperature is made. The extrinsic and intrinsic branches of this curve are extrapolated to their intersection. If r is defined as the ratio of the resistivity of this intersection point to the measured resistivity at the same temperature, the quantity $[1/(r-1)-r]$ gives the mobility ratio for P type samples, and its reciprocal for N type samples.

IN the past few years a great many measurements of current carrier mobility in semiconductors have been reported.[1–5] The values reported show considerable disagreement, especially between values deduced from Hall effect measurements and those obtained from measurement of the drift velocity of injected carriers. This discrepancy has been noted and several mechanisms[1] suggested to account for it.

The ratio of the mobility of electrons to the mobility of holes in germanium may be computed from these various mobility values reported, and the best data presently available seems to give a value of about 2.1 for drift measurements[1] and a value of about 1.5 for Hall effect measurements.[3] In all of these measurements the mobility values for electrons and holes were obtained on different samples, of different conductivity types, at different times. Because of their nature, no direct measurements of the mobility ratio were made on a single sample under a single set of conditions.[6]

The purpose of this paper is to suggest a method of measuring the mobility ratio directly using a single sample of either conductivity type. In Fig. 1 is shown a typical curve of the logarithm of resistivity *versus* the reciprocal of the absolute temperature. The two branches of this curve are extrapolated to their intersection point. This intersection point determines a resistivity value, ρ_e, and a temperature, T_0. At the temperature T_0 the resistivity value of the measured curve ρ_0 is determined. If the ratio, $r=\rho_e/\rho_0$, is formed, it will be shown that for P type samples the mobility

[1] J. R. Haynes and W. Shockley, Phys. Rev. **81**, 835 (1951).
[2] Lark Horovitz, Middleton, Miller, and Walerstein, Phys. Rev. **69**, 258 (1946).
[3] W. C. Dunlap, Phys. Rev. **79**, 286 (1950).
[4] Esther M. Conwell, Proc. Inst. Radio Engrs. **40**, 1327 (1952).
[5] G. L. Pearson and J. Bardeen, Phys. Rev. **75**, 865 (1949).

[6] W. Shockley, *Electrons and Holes in Semiconductors* (D. Van Nostrand Company, Inc., New York, 1950), p. 218, problem 7 suggests a method of determining the mobility ratio for P type samples under the assumptions of equal Hall and drift mobility ratios and zero carrier lifetime. These assumptions are, in general, invalid [see R. Landauer and J. Swanson this issue, Phys. Rev. 555 (1953)].

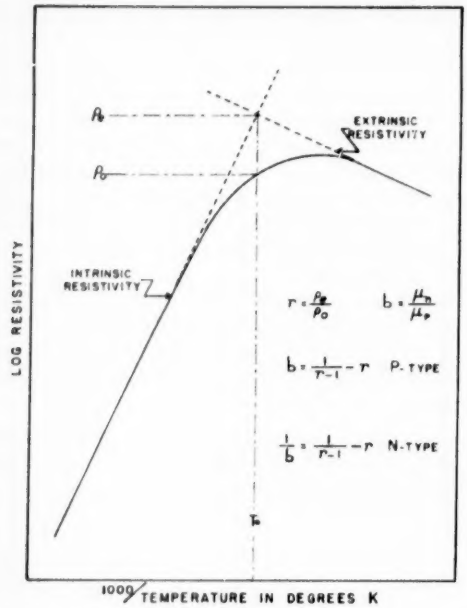
EXTRINSIC RESISTIVITY
INTRINSIC RESISTIVITY
LOG RESISTIVITY
$r = \frac{\rho_e}{\rho_0}$ $b = \frac{\mu_n}{\mu_p}$
$b = \frac{1}{r-1} - r$ P-TYPE
$\frac{1}{b} = \frac{1}{r-1} - r$ N-TYPE
1000/TEMPERATURE IN DEGREES K

FIG. 1. Definition of quantities determining the mobility ratio b.

ratio is given by

$$b=1/(r-1)-r \tag{1}$$

(where $b=\mu_n/\mu_p$, and μ_n=electron mobility, μ_p=hole mobility). For N type samples

$$1/b=1/(r-1)-r. \tag{2}$$

To prove these relations we will consider the intrinsic resistivity line given by the equation

$$\rho_i=1/[n_i e(\mu_n+\mu_p)], \tag{3}$$

and the extrinsic resistivity line by

$$\rho=1/(p_e e\mu_p), \tag{4}$$

where p_e is the density of acceptor levels in the P type material, and n_i is the density of either electrons or holes in the intrinsic material. At the intersection point we have

$$\rho_e=\rho_i=\rho \quad \text{or} \quad p_e/n_i=1+b. \tag{5}$$

At the intersection temperature T_0 we have

$$\rho_0=1/[ne\mu_n+(n+p_e)e\mu_p], \tag{6}$$

where n is the density of electrons at the intersection temperature. Using Eqs. (4) and (6) to define the ratio r, we find

$$r=\rho_e/\rho_0=(nb+n+p_e)/p_e. \tag{7}$$

At any given temperature the mass action law gives the following relation between the intrinsic carrier concentration and the concentration present in an impurity semiconductor at that temperature

$$n_i^2=n(p_e+n). \tag{8}$$

By dividing the numerator and denominator of the fraction on the right-hand side of Eq. (7) by n_i, we obtain

$$r=\left[\frac{n}{n_i}(b+1)+\frac{p_e}{n_i}\right]\Big/\frac{p_e}{n_i}, \tag{7'}$$

and dividing Eq. (8) through by nn_i, we find

$$n_i/n=p_e/n_i+n/n_i. \tag{8'}$$

By proper algebraic manipulation p_e/n_i and n/n_i can be eliminated between Eqs. (5), (7'), and (8') giving Eq. (1). Equation (2) follows from Eq. (1) by symmetry and the definition of b.

From Eqs. (1) and (2) it can be calculated that $1.0<r<1.62$ for all positive values of b. The accuracy required in determining r must be an order of magnitude greater than that required of the resulting value of b. For example, to distinguish between the mobility ratios 1.5 and 2.0 we must distinguish between r values of 1.47 and 1.50 for N type samples. Experience has shown that with reasonable care resistivity curves are capable of determining r to about 0.5 percent and with elaborate precautions r could be fixed to about 0.1 percent.

In Fig. 2 are shown typical resistivity curves for N and P type samples. These samples show the characteristic behavior predicted by theory. The resistivity ratios shown (1.5 for the N type sample and 1.3 for the P type sample) correspond to the mobility ratio 2.0. It is interesting to note that N and P type germanium can be distinguished from the resistivity curve alone. Since the mobility of electrons is greater than that of holes, the resistivity curve for a P type sample crosses over the intrinsic line before joining it. This is seen to be reasonable since a small deviation from the intrinsic condition, produced by lowering the temperature, tends to replace electrons with slower moving holes thus increasing the resistivity. At still lower temperatures the

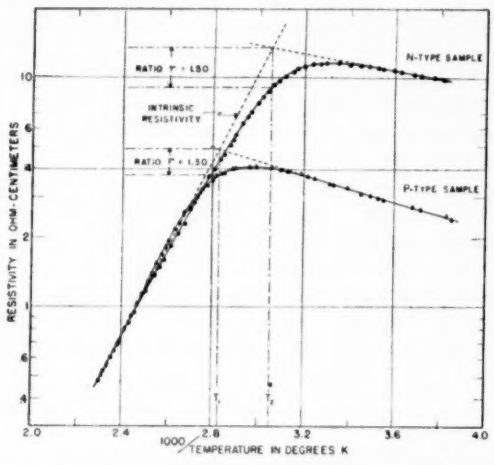

FIG. 2. Typical experimental results for N and P type samples.

resistivity levels off as the extrinsic range is entered and there must be a crossover of the resistivity curve and the intrinsic line. Simple theory gives $p=nb^2$ as the condition at the crossover point, and $p=nb$ as the condition for the point of maximum overshoot.

The method of extrapolation will now be discussed. In the intrinsic range the resistivity has primarily an exponential temperature dependence. However, the amplitude constant[7] contains the factor

$$1/[T^{3/2}(b+1)\mu_p].$$

On the basis of the usual theory μ_p should have a $T^{-3/2}$ temperature dependence and b should be independent of temperature. Under these conditions the extrapolation of the intrinsic line should be strictly linear on a semilog plot. It turns out experimentally, however, that μ_p has a temperature dependence for many samples which is more nearly $T^{-2.2}$, while μ_n comes close to the theoretical dependence of $T^{-3/2}$. A simple computation shows that for the ranges of temperature over which extrapolation is necessary the deviation of the intrinsic line from linearity is negligible. Linear extrapolation was, therefore, used for the intrinsic resistivity line. After several samples of different impurity content have been measured, the intrinsic line is sufficiently well determined so that with succeeding samples it is unnecessary to remeasure and extrapolate in this region.

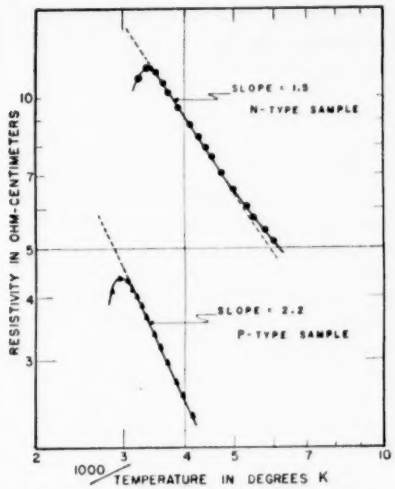

FIG. 3. Method of extrapolation in the extrinsic region.

[7] Reference 6, Chap. II.

TABLE I. Intrinsic resistivity of germanium.

$1/T°K$	Resistivity Ω cm	$T°K$
0.00333	47.0 ±0.5	300
0.00300	11.0 ±0.1	333
0.00250	1.23±0.01	400

The extrapolation of the extrinsic branch of the curve is best made on a log-log plot as shown in Fig. 3. From this figure it is apparent that the temperature variation of the mobility of either electrons or holes is essentially a power law. The two samples plotted here are the same two samples shown in Fig. 2. Linear extrapolations of the straight line regions of the curves of Fig. 3 were used to plot the extrinsic extrapolations shown in Fig. 2. Using this method, values of the ratio r can be determined to better than 0.5 percent from reasonably good data.

The difference in the slope of the extrinsic curve shown in Fig. 3 is typical of N and P type samples. The purest P type sample measured gave a slope of about 2.5. This ranged down to values as low as 2.0 for the more impure samples. All N type samples, regardless of their purity, gave slopes very close to 1.5. Since the Hall coefficient of all of these samples was constant over the range for which the slopes were determined, these slopes presumably represent the temperature dependence of the mobility of holes and electrons. Considering the data of the purest samples, the mobility ratio b should vary directly as T in the temperature range 150° to 350°K. The average value of the mobility ratio determined from the resistivity curves of these samples was 2.0±0.2 in the neighborhood of 300°K. The accuracy of this determination was not sufficient to be certain of the temperature dependence of b over the limited range of temperatures represented by the extrapolated intersection points of these samples. There seems to be a trend in agreement with the above mentioned direct dependence of b on temperature, but it cannot be said to be independently established by the mobility ratio measurements.

As a by-product of this investigation the intrinsic resistivity line for pure germanium was determined quite accurately. The best averages are listed in Table I.

The author wishes to acknowledge the assistance of Dr. E. J. Huibregtse, Mr. R. L. Anderson, Miss B. E. Montgomery, and Miss V. M. Palmer for compiling the large amount of accurate data upon which this analysis is based.

Secondary Electron Emission of Crystalline MgO

J. B. JOHNSON* AND K. G. MCKAY
Bell Telephone Laboratories, Murray Hill, New Jersey
(Received March 13, 1953)

Secondary emission is measured from single crystals of MgO cleaved along the (.00) plane. The maximum ratio of secondary to primary current, δ_{max}, is about 7 at about 1 000 volts and room temperature. The cross-overs are at 33 volts and far above 5 000 volts. Most probable energy of emission is 1 ev or less. A definite effect of temperature is established, δ decreasing with increasing temperature, in accord with expectations for an insulator.

OBJECT

THIN insulating films made in a variety of ways have long been used as "dynodes" in devices operating on the basis of secondary emission, and the emission properties of many of these films have been studied, particularly those of MgO. The results have varied widely with the methods of production and treatment. There often appears the abnormal emission associated with the Malter effect. Because of experimental difficulties, however, work on insulators in bulk form has not been extensive.[1]

The purpose of the present work was to obtain data on the secondary electron emission evoked by electron bombardment of a simple massive insulator of known structure and properties, for elucidating the mechanism of secondary emission from insulators. Magnesium oxide in the form of single crystals was chosen as the material studied. It has the advantages of having simple body-centered cubic structure and good cleavage and of being very inert and refractory so that it can withstand the severe heat treatment in vacuum needed to insure the cleanness of its surface. Besides this, many of its physical properties are well known.

METHOD AND APPARATUS

The method employed here is essentially the one used earlier in the measurements on the oxide cathode,[2] with differences in detail. The primary electrons bombard the uncharged target in short pulses. By applying to the nearby collector electrode a steady negative or positive potential, the current in the target circuit becomes either the primary electron current alone, or the difference between the secondary and primary current, so that the ratio δ of secondary to primary current can be established. The problem with the insulating target is to obtain the measurement with the target initially neutral and before appreciable charge is accumulated during the measurement. The essentials of the present method are that the target is heated to about 600°C before each measurement to relax surface or volume charge by conduction, and that then the single measurement is made at room or other temperature with a pulse of primary electrons of low current density and short duration.

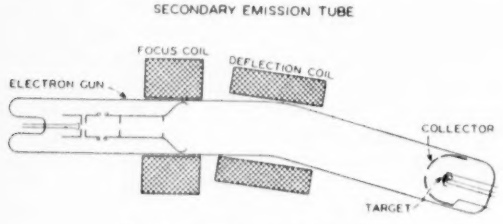

FIG. 1. Secondary emission tube.

EXPERIMENTAL TUBE

The experimental tube is shown schematically in Fig. 1, with details of the target structure in Fig. 2. At one end of the tube is an electron gun of conventional design for electrostatic control. The cathode is a flat ribbon of tungsten and all other metal parts are of tantalum. The electron beam is focused principally by a magnetic focus coil and is positioned on the target by a magnetic deflection yoke, as shown in Fig. 1. The tube is bent at an angle of 15° in order to protect the target from negative ion bombardment and from the direct light of the filament.

The target assembly is located at the other end of the tube. The target is a thin plate of the MgO mounted on the flat end of a cup-shaped base of tantalum $\frac{5}{16}$ in. in diameter. It is held in place by hooks of thin molybdenum wires. Within the cup is a coil of tungsten wire for

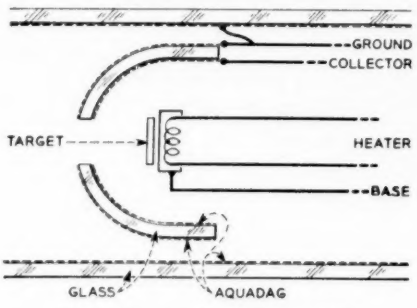

FIG. 2. Target and collector assembly.

* Now with Edison Laboratory, Thomas A. Edison, Inc., West Orange, New Jersey.

[1] For a review of this field see K. G. McKay in *Advances in Electronics* (Academic Press, Inc., New York, 1948), Vol. 1, p. 65.

[2] J. B. Johnson, Phys. Rev. **73**, 1058 (1948) and **83**, 49 (1951).

heating the base and target. The collector is a graphite coating on a hemispherical glass dome of one in. diameter with the target at its radial center. A $\frac{1}{4}$ in. hole at the apex admits the electron beam. The outside of the dome and the inside of the main tube are covered with colloidal graphite, serving as an electrostatic shield and as a connection to ground for the second anode. The tube was constructed with great attention to cleanliness. Before assembly of the tube the graphite coatings were baked at 500°C in flowing CO_2 or air. The metal parts of the tube were vacuum pre-glowed, as far as possible. Welds were freed from copper by chemical treatment. The electron gun was degassed at high temperature in a separate tube before assembly. The tube was exhausted on a clean vacuum system with mercury vapor pumps, with extended baking and outgassing. It was sealed off, without getter, at a pressure of about 10^{-8} mm Hg. Each target was mounted in a separate tube.

The target specimens were cleaved along the (100) plane from a clear single crystal of MgO, grown by Rochow[3] some years ago. Details are given in Table I. Spectro-chemical analysis of the present crystal revealed the following impurities: Ca<0.3 percent (probably substitutional in the lattice); very slight trace, <0.001 percent, Ag, Al, Cr, Cu, Fe, Na, Si. No analysis is available on the Pt used on target *A*. The Pd used on target D is thought to have impurities Mg, Al, Fe, Au, to a total of 0.1 percent. The colloidal graphite contained the following impurities: Fe 0.1–3 percent; Ca, Mg, Mn, Si, 0.01–0.03 percent; Al, Cu, Na, Pb, Sn, Ti, <0.03 percent.

TABLE I. Thicknesses and electrode elements used on MgO targets.

Sample identification	Thickness cm	Backing element for contact with base plate
A	0.165	platinum
B	0.127	colloidal graphite
C	0.025	colloidal graphite
D	0.035	palladium

CIRCUIT AND OPERATION

The circuit is indicated in Fig. 3. The electron beam is turned on by a pulsing circuit with variable amplitude (microamperes), duration (microseconds), and repetition rate (single pulse, 4 pulses per second, 60 pps geared to the power frequency, etc.).

The current in the target circuit flows to ground through the input resistance of an amplifier which has a frequency band-width of about 10 megacycles and drives the beam of a 5XP11 C.R.O. operated at 10 kv. Deflections in a single sweep of 20-μsec duration can be observed visually or photographed against a fine line reticle.

[3] E. G. Rochow, J. Appl. Phys. **9**, 664 (1938).

Except for the lowest values of V_p the collector was usually held at −40 or +40 volts. The −40 is set by the fact that by far the larger fraction of secondary electrons leave the target with energy less than 40 ev, so that the current in the target circuit is then essentially the primary current. The +40 volts is set to keep down the effect of charging of the target. When the collector is positive and when $\delta>1$, then the target surface accumulates a positive charge until its potential approaches that of the collector or even exceeds it by a few volts so that the sum of incoming primary current and escaping secondary current is eventually zero. Before this condition is reached the secondary current begins sharply to decrease when the target potential passes the collector potential and the slower secondary electrons cannot escape to the collector against the opposing field. Arrival at this condition is delayed by making the positive collector potential large, the beam current small, the beam area large, and the target thin so that the electrostatic capacity of the bombarded area is large.

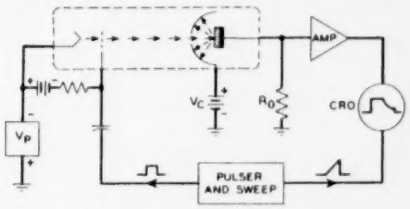

FIG. 3. Block diagram of circuit.

A photograph of some pulses will make these considerations clearer. In Fig. 4 are shown four pairs of primary and secondary pulses, the primary pulse downward and the secondary pulse up, *a* and *b* single traces, *c* and *d*, 30 repetitions in 0.5 second. In Fig. 4(a) conditions were such that there was no visible effect of charging during the period of 10 μsec; in (b) and (c) the point where the target potential passes the collector potential is marked by a break in the line; in (d), where the beam was sharply focused and the collector voltage low, the break came in less than the resolving time of the system.[4] In this work the conditions were always

FIG. 4. Primary and secondary pulses. Target *D*, room temperature. Downward pulse, primary current; upward pulse, secondary current. V_c lowered in order *a*, *c*, *b*, *d*. *a* and *b* are single traces; *c* and *d* show 30 repetitions in 0.5 sec.

[4] Proposals for using the break and the subsequent curve shape for analysis of initial energy distribution of secondaries from insulators have been made by K. G. McKay, J. Appl. Phys. **22**, 89 (1951) and R. Barthelemy, Compt. rend. **232**, 20 (1951).

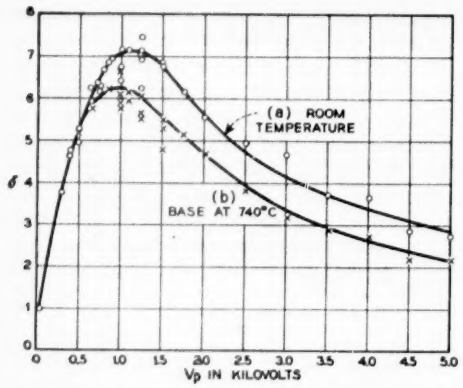

FIG. 5. Yield δ *versus* bombarding voltage V_p. Target *C*.

adjusted so that readings could be made before the break in the flat top of the curve.

The temperatures quoted are the optical pyrometer temperatures of the base plate. The temperature of the crystal was presumably somewhat lower.

EXPERIMENTAL RESULTS

δ *vs* V_p

The yield curves for specimen *C* are shown in Fig. 5, and these are typical of the curves for the other specimens. At room temperature, curve (a), the yield δ reaches a maximum of about 7, when V_p is about 1200 v.[6] The first crossover, $V_p{}^I$, where $\delta=1.00$, is at very low primary energy, and the curve suggests that the second crossover is far above 5 kv.

The results for the other specimens of MgO were qualitatively similar, but nevertheless disclosed some quantitative differences. At room temperature, for example, the maximum yield δ_{max} was 5.5 for specimen *A* and 6.8 for specimen *D*. It seems unlikely that the treatment of these similar crystals could have introduced lattice distortions sufficient to cause such differences. Rather it must be the surface that in either physical structure or in work function was altered by the treatment after cleavage. A fresh surface of MgO tarnishes slowly on exposure to moist air, and the products of this tarnish might well persist after the heat treatment and affect the work function of the surface.

δ *vs* Temperature

With the base plate at 740°C the yield is substantially reduced, as shown by curve (b) Fig. 5, in the range of high V_p. In the lower range the yield is little changed by temperature. The primary energy of maximum yield V_{pmax}, is lowered slightly but definitely as the temperature increases. Figure 6 gives the variation of yield with heater setting and temperature for this specimen, in the region of V_{pmax}. Such curves are reproducible, and there is no doubt of this temperature effect. This is in striking contrast to the behavior of clean metals which show no variation of yield with temperature.[1] This temperature sensitivity at higher V_p, and the shift of V_{pmax} has a clear meaning. Temperature cannot appreciably affect the collisions and depth of penetration of the primary electrons, especially the higher energy ones. What is involved must be rather the probability of escape of the internal secondaries. The escape process can change either by variation of the work function at the surface or by changes in the rate of energy loss of the internal secondaries. Change in work function would alter the whole curve because it would affect all escaping secondaries alike, whether liberated by low energy primaries near the surface, or at greater depths by high energy primaries. It is assumed that, as with metals, the energy distribution of the emitted secondaries is essentially independent of V_p. Lattice disturbance by temperature, on the other hand, would hinder the escape of the internal secondaries, the more so the greater the depth from which they come. The yield at low V_p and low penetration of the primaries would be little affected by elevated temperature except for possible changes in work function. In the region of high V_p, however, the increased lattice interaction at higher temperatures would decrease the yield and thus shift V_{pmax} to lower values. The observed lowering of yield and of V_{pmax} is then undoubtedly caused by the increased temperature vibration of the lattice.

FIRST CROSSOVER

The primary energy $V_p{}^I$ at which the yield is unity can be determined quite accurately, because at this point the net current in the target circuit is zero, even though the primary current may be large. The value of $V_p{}^I$ is remarkably independent of temperature, as shown by Fig. 7 for specimen *C*, and is here 32.8 ± 0.2 volts over the temperature range.

At this low energy the range of the primary electrons must be not over two or three atom layers, and the escape of the secondaries depends more on the work function than on the lattice. The constancy of $V_p{}^I$ therefore suggests that the work function is relatively

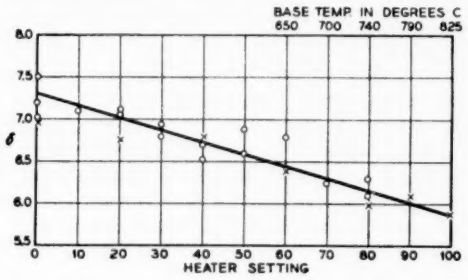

FIG. 6. Yield δ *versus* heater setting and temperature. Target *C*. V_p near V_{pmax}.

[6] This is in general agreement with work on MgO recently reported by K. C. Nomura, Phys. Rev. **89**, 894 (1953).

insensitive to temperature change and that lattice vibrations are responsible for the change in yield at higher V_p.

SURFACE CHARGE AND INTERNAL FIELD

When an insulating target is bombarded by electrons whose energy lies between the two crossovers, positive charge collects on the surface so as to make the potential eventually slightly more positive than that of the collector. An electric field is then set up through the target. There is a question as to whether such a field can change the secondary yield.

The simplest approach is merely to calculate the field uniformly distributed through the thickness of the sample that is developed when the target surface is at collector potential. For a collector potential of 40 volts and a crystal thickness of 0.025 cm, this gives a field of 1600 volts/cm which is far too low to affect the secondary yield. However, a more stringent limit is set by the transient behavior. From pulses such as those shown in Fig. 4(a) we know that the yield remains constant for at least 10 μsec following its rise time of 0.1 μsec. Thus, if field enhancement plays a role, it must set in and reach a final constant value during the rise time with a field which is then no more than 16 volts/cm. If we assume that all the positive charge resulting from the charging-up process resides on the surface, then the internal field will depend solely on the net positive charge and thus will be independent of the sample thickness by Gauss' theorem. Specifically, this means that even if the entire target voltage drop is concentrated across a layer that lies within a few hundred angstroms of the surface, the field will still be no more than 16 v/cm at 0.1 μsec. Any distribution in depth of the net positive charge will reduce this subsurface field. Moreover, the mobility and finite lifetime of the internally produced electrons and positive holes result in a local conductivity which opposes the formation of a field in this subsurface region.

If there are no strong local fields built up in the process, it should then be possible to remove the surface charge of the target and restore the potential to a desired uniform value after a measurement by bombarding the target with the collector potential at a value near zero instead of by our customary heat treatment. That this may not happen is shown by the two curves

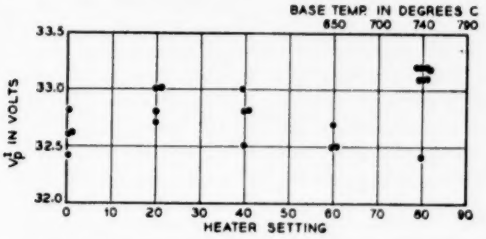

FIG. 7. First crossover V_p^1 *versus* heater setting and temperature. Target *C*.

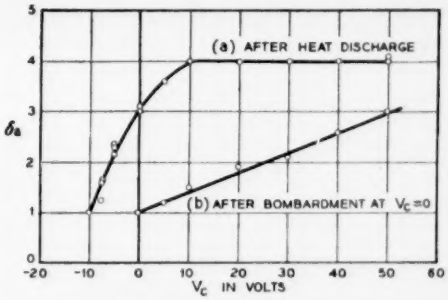

FIG. 8. Effect of surface charge. Apparent δ *versus* collector voltage. Target *A*. V_p=300 volts.

of Fig. 8, displaying apparent secondary yield as a function of collector potential. In both curves the yield was obtained at room temperature for specimen *A*. In curve (a) the target was heated and cooled down after each reading, while in curve (b) the surface was bombarded at V_c=0 after each reading. The latter curve lies considerably below the former, showing that bombardment discharge is not equivalent to heat discharge. The difference is probably ascribable to a patch-field effect rather than the formation of internal dipole layers. At the bombarded area primary electrons arrive and slower secondary electrons leave, and this area takes nearly the potential of the collector. The surrounding area receives slow electrons—secondaries that come from the bombarded area, or tertiaries from the collector—for which δ is usually less than unity. It can therefore become more negative than the collector and the bombarded area.[6] The field set up by this negative charge acts in a grid-like manner to suppress the emission from the bombarded area when the collector is positive. There seems to be nothing in Fig. 8 that cannot be ascribed to this process rather than to dipole layers in the target.[7]

ENERGY DISTRIBUTION

The distribution in energy of the secondary electrons was observed roughly by the retarding-potential method, the potential of the collector being varied in successive bombardments by a fixed primary current. A retarding-potential curve for specimen *D* is shown in Fig. 9. Like the δ measurements, the curve is based on the slightly erroneous assumption that no secondary electrons have energy higher than 40 ev. Differentiating a smooth line drawn through the points of Fig. 9 gives the curve of Fig. 10 which is the distribution-in-energy of the secondary electrons from this target. The most probable energy comes at the right of the zero axis, which indicates a difference in contact potential between the MgO and the carbon film. The work

[6] F. C. Williams, Proc. Inst. Elec. Engrs. (London) **96**, 81 (1949).

[7] The results of H. Hintenberger may involve such an effect of patch-fields [Z. Physik **114**, 98 (1939)].

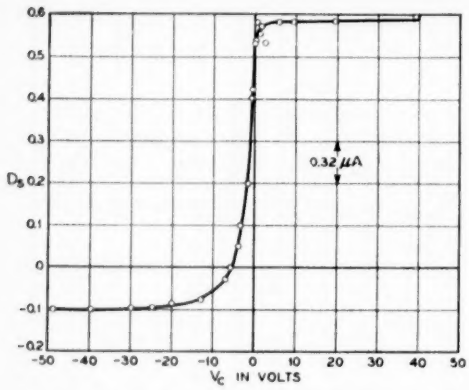

FIG. 9. Retarding potential curve. Target *D*. $V_p = 1000$ volts. Room temperature.

function of MgO is thought to be about 3.0,[8] and that of carbon about 4.7. The collector would then be over 1.5 volt negative with respect to the target, and the curve should be shifted to the left by this amount. The most probable energy of emission is therefore approximately 1 ev.

DISCUSSION

Insulators generally have higher secondary yields than metals. This difference is usually ascribed primarily to two sources: (1) the energy required of a free electron to escape from the solid, (2) the rate of loss of energy of the internal secondaries as they approach the surface. These two factors do not act independently, for, if the rate of energy loss is high for all energies of the internal secondaries which lie between their initial energy and that required for escape, the yield should be low. This represents the situation in metals where there are many free and bound electrons with which the secondaries can make allowable collisions involving either large or small transfers of energy. This process quite overshadows the effects of electron-phonon interaction, and it continues until the secondaries approach thermal equilibrium. This concept fits well with the universally low secondary yield of the pure metals and is in accord with the observation that the yield from clean metals is quite insensitive to change in temperature of the target over a wide range.

In a similar way, in insulators the rate at which high energy internal secondaries lose energy is large, through interaction with the bound electrons of the valence band. However, neglecting collisions with impurities, the minimum energy that can be lost in this process is equal to the forbidden energy gap E_G. In MgO ultraviolet absorption measurements suggest that E_G must be at least 5.6 ev,[9] and the energy required for escape is less than 3 ev.[8] Thus for electrons with kinetic energy lying between about 3 and 6 volts, the only available mechanism for energy loss is through interaction with the phonon field.[10] Although the collisions be frequent, the energy lost per collision is very small. These electrons have, therefore, a higher probability of reaching the surface from a considerable depth with sufficient energy to escape. This implies a high yield with δ_{max} occurring at a large value of bombarding voltage and also an energy distribution with a large preponderence of electrons of less than about 3 ev energy. Moreover, the rate of energy loss by electron-phonon interaction should increase with the temperature, thus reducing the yield. Our experiments agree with these expectations.

The specimens studied showed a wide range of resistance. If this is attributed to a volume effect, the observed resistivities varied from about 10^{10} ohm cm to about 10^{16} ohm cm. This must involve lattice disturbances by either impurity atoms or stoichiometric excess of one of the component elements. Weber[9] and Nomura[5] have studied the effect of these disturbances on the properties of the crystal. In the present case the crystals were relatively pure to begin with. There is a question whether with some of the specimens impurities were added in the preparation. It is fairly certain, for instance, that at the temperatures used carbon would tend to reduce the MgO, leaving excess Mg in the lattice. Other impurities in the graphite or Pd backing might migrate into the lattice and create mobile holes or electrons in the lattice to contribute to the conductivity. Tantalum would reduce MgO, but the Ta plate was not in direct contact with the crystals.

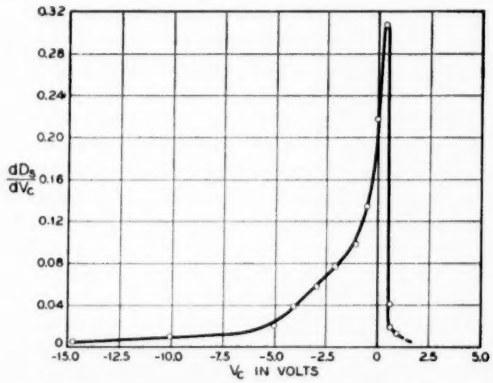

FIG. 10. Energy distribution curve from Fig. 9.

If this impurity content is responsible for the conductivity of some of the crystals, there is no evidence that it reduced the yield. In fact, specimen A with the lowest conductivity had also the lowest yield. Conductivity increased by impurity content would probably have less effect on the yield than a similar increase by

[8] A. Eisenstein, private communication.
[9] H. Weber, Z. Physik **130**, 392 (1951).
[10] This may also be true for somewhat more energetic electrons. The probability of ionization by an electron with energy between E_G and $2E_G$ depends on the role played by the lattice in such an interaction, and at present this is not known.

heat, since the heat vibrations involve all of the atoms in the lattice, the impurity content relatively few.

SUMMARY

We can sum up our results as follows:

(1) The high secondary yield from large single crystals of MgO is in accord with current band theory. Specifically, it implies that the high yields observed from thin film MgO targets that are used commercially, are not merely a consequence of thin film behavior but are related to body properties of the MgO.

(2) The temperature dependence of the yield can be used to obtain data on the interaction between the lattice and the internal secondaries which have several electron volts of energy.

(3) Field enhanced emission is not observed in these experiments.

(4) Neutralization of surface charge by bombardment must be approached with care because a lack of uniformity may easily produce highly erroneous results.

(5) No correlation was found between conductivity and yield. However, the causes of the observed conductivity have not been determined.

We are indebted to Conyers Herring for many valuable discussions of the interpretation of the data presented. The MgO crystal used was supplied by E. G. Rochow through the good offices of A. J. Ahearn, and the individual specimens were prepared by J. Andrus. The spectrochemical analyses were performed by E. K. Jaycox. Finally we wish to express our thanks to the group working under the direction of H. W. Weinhart who constructed the various experimental tubes.

PHYSICAL REVIEW VOLUME 91, NUMBER 3 AUGUST 1, 1953

Theory of Alpha Decay. I*

JOSEPH J. DEVANEY†
Los Alamos Scientific Laboratory, University of California, Los Alamos, New Mexico
(Received March 30, 1953)

A preliminary report on the application of the perturbation of boundary conditions theory of Feshbach, Weisskopf, and Peaslee to the problem of the decay of a virtual state is presented. In particular, the formulas for alpha decay are derived. The derivation assumes no model of the nucleus nor of nuclear forces. It contains the slope of the logarithmic derivative of the wave function *versus* energy as the only factor related to the nuclear structure; therefore, it includes earlier theories of alpha decay as special cases.

1. INTRODUCTION

IN 1928 Gamow and, independently, Condon and Gurney[1] made use of quantum mechanics to explain the tremendous variation of alpha-decay half-lives with small variations in alpha-particle energy (from 1.4×10^{10} years to 3×10^{-7} second, for alpha-particle energies of 4 to 9 Mev, respectively). The foregoing theories correctly accounted for the exponential-type behavior of the half-life as a function of energy, but solved only the Coulomb barrier penetration problem. This paper presents a preliminary attack upon internal alpha-decay theory. The most frequent assumption of older theories for the internal problem was that of a single particle in a square well ground state. In fact, the spontaneous decay of an alpha particle from a square well bounded by a Coulomb barrier has been rigorously solved as an eigenvalue problem by Preston.[2] Another,[3] admittedly approximate, attack postulated that the intrinsic alpha-decay probability (the decay probability without Coulomb barrier) is roughly the same as that of a neutron of the same energy. The application of the WKJB approximation to the model of a single particle in a square well surrounded by a Coulomb barrier is widely used, but sometimes incorrectly. Sufficient care is not always taken at the joining point R (defined as the edge of the square well and considered in actuality to include the "naked" nuclear radius, the range of alpha-nucleus forces, and the "naked" alpha-particle radius), where Kramers type joining formulas are not applicable even when the drop in potential from Coulomb to the nuclear is gradual through a distance of the order of the nuclear force range. If this drop is taken to be vertical, the wave equation then has a singular point and no Taylor expansion whatever is possible, so that joining of the solutions in this manner completely breaks down.

Although our treatment assumes no model of the nucleus nor of nuclear forces, it does postulate that the alpha particle is an entity at the radius R and thereafter. In addition, this paper asks for a certain smoothness, to be defined below, in the nuclear wave function at the nuclear surface. Because of the generality of this

* Work performed under the auspices of the U. S. Atomic Energy Commission.

† This report is based on a thesis submitted by the author to the Massachusetts Institute of Technology, 1950 (unpublished).

[1] G. Gamow, Z. Physik **51**, 204 (1928); G. Gamow and F. Houtermans, Z. Physik **52**, 495 (1928); R. W. Gurney and E. U. Condon, Nature **122**, 439 (1928); and Phys. Rev. **33**, 127 (1929).

[2] M. A. Preston, Phys. Rev. **69**, 535 (1946); **71**, 865 (1947).

[3] H. A. Bethe, Revs. Modern Phys. **9**, 69 (1937). See also B. L. Cohen, Phys. Rev. **80**, 105 (1950).

assumption the present theory includes prior theories as special cases. However, we feel this treatment to be incomplete, and we present it only in the hope that it is useful even in its preliminary form.

2. THE THEORY OF CHARGED PARTICLE DECAY

Following a suggestion of Weisskopf,[4] it is possible to extend the theory of Feshbach, Peaslee, and Weisskopf[5] to the decay of virtual nuclear states. This can be done in the following way.[6]

We discuss the decay of a nucleus, atomic number Z; mass number A; through charged-particle emission (charge z) with orbital angular momentum l, z component m; in a half-life $T_{\frac{1}{2}}$; with a decay constant, $\gamma/\hbar$ sec^{-1}; and with decay energy E. Let r be the distance from the center of mass of the daughter nucleus to that of the emitted-particle. R is the largest value of r for which the potential energy V is appreciably different from $Zze^2/\epsilon_0 r$, the Coulomb potential. With the foregoing notation, then, the substitution $\psi=\Phi^{(l)}(r)r^{-1}Y_l^m(\theta,\phi)$ into Schrödinger's (center-of-mass) equation yields the following for Φ:

$$d^2\Phi^{(l)}/dr^2-U_l(r)\Phi^{(l)}=-(2\mu E/\hbar^2)\Phi^{(l)}, \quad (2.1)$$

with

$$U_l(r)\equiv l(l+1)/r^2+(2\mu/\hbar^2)V(r) \quad \text{for} \quad r>R.$$

The assumption $V=V(r)$ and the separation of variables is made only for $r\geqslant R$. The general solution of (2.1) can be written in the form

$$\Phi^{(l)}=au_l(r)+bv_l(r),$$

with $u_l\equiv v_l^*$ (the asterisk means complex conjugate), a and b constants, and with asymptotic behaviors

$$u_l \underset{r\to\infty}{\longrightarrow} \exp[-ikr+i(\pi l/2)-i\alpha\ln(2kr)+i\eta_l], \quad (2.2a)$$

$$v_l \underset{r\to\infty}{\longrightarrow} \exp[+ikr-i(\pi l/2)+i\alpha\ln(2kr)-i\eta_l], \quad (2.2b)$$

where $\alpha\equiv 2\pi ZZ'\mathbb{P}/h$(velocity) and η_l are the usual Coulomb field type corrections to the asymptotic forms,[7] $k=1/\lambda=(2\mu E)^{\frac{1}{2}}/\hbar$. A decaying state is defined by having outgoing waves only at $r=\infty$; thus, $\Phi^{(l)}=v_l$ for $r\geqslant R$. The other boundary condition of the problem occurs at the nuclear surface, that is at $r=R$. Of interest is the ratio of derivative to value of the radial wave function at R. Define this quantity as f/R, which must equal $(1/v)(dv/dr)$ evaluated at R. We shall leave the subscript l to be understood. If, following FPW, we set $v(r=R)\equiv|v|_R\exp(i\delta)$,

$$x\equiv kR, \text{ and } v'\equiv dv/dx=(1/k)\,|dv/dr|_{r=R}\exp(i\delta_1); \quad (2.3)$$

then

$$f/R=[(1/v)(dv/dr)]_R$$

or

$$f=x|v'/v|\exp[i(\delta_1-\delta)] \quad (2.4)$$

is the boundary condition on the solution at $r=R$.

The Wronskian of two independent solutions of a canonical second-order differential equation is a constant; hence

$$k\begin{vmatrix} u' & v' \\ u & v \end{vmatrix}=\begin{vmatrix} du/dr & dv/dr \\ u & v \end{vmatrix}_{\substack{\text{evaluated}\\ \text{at } r=\infty}}=-2ik; \quad (2.5)$$

whence, using $u=v^*$, we get

$$|vv'|\sin(\delta_1-\delta)=1. \quad (2.6)$$

If we write

$$f=\Delta+is, \quad (2.7)$$

which is the boundary condition, with Δ and s real and defined by (2.4) and (2.6),

$$\Delta\equiv x|v'/v|\cos(\delta_1-\delta), \quad (2.8a)$$

$$s\equiv x/|v|^2. \quad (2.8b)$$

It is well known that the time variation of the wave function is of the form $\exp(-iWt/\hbar)$ and that a complex W is a description of a decaying state.

We therefore write for the decaying state s of energy E_s,

$$W_s=E_s-i(\gamma_s/2), \quad (2.9)$$

where the decay probability λ_s, of the state s, is simply $\gamma_s/\hbar$, per second, per nucleus.

f is a function of W, so we can expand f in the series

$$f(W_s)=f(E_s)-i(\gamma_s/2)\partial f/\partial E_s+\cdots, \quad (2.10)$$

and use only the linear term, since for charged particle decay $\gamma_s\ll E_s$.

The nuclear boundary condition for decay is expected to be of the same form for each decaying state s, so we are led (FPW) to expect simplification by writing f as a periodic function; $f=X\cot\mathbf{Z}$. $\mathbf{Z}=\mathbf{Z}(E)$ is a quite arbitrary function of E, and $X\equiv KR$, where K is the propagation vector magnitude of the escaping particle just within the nucleus. For example, the nuclear boundary condition for a square well is $f=X\cot[X-(e\pi/2)]$.

Now as we vary E we can expect decaying states only when (2.7) holds, or when (from 2.10)

$$\Delta(E_s)=X_s\cot\mathbf{Z}(E_s), \quad (2.11)$$

and

$$-(\gamma_s/2)\partial f/\partial E|_{E_s}=S. \quad (2.12)$$

We shall later show that for decaying states $(\Delta(E_s)/X_s)$ is a slowly varying function of E_s, so that we can with good accuracy put

$$\mathbf{Z}(E_{s+1})=\mathbf{Z}(E_s)+\pi, \quad (2.13)$$

---

[4] V. F. Weisskopf (private communication, 1949).

[5] Feshbach, Peaslee, and Weisskopf, Phys. Rev. **71**, 145 (1947), which we refer to as FPW.

[6] See also J. M. Blatt and V. F. Weisskopf, *Theoretical Nuclear Physics* (John Wiley and Sons, Inc., New York, 1952), which we refer to as BW.

[7] See N. F. Mott and H. S. W. Massey, *Theory of Atomic Collisions* (Oxford University Press, London, 1949), second edition.

since the cotangent is π-periodic, and since the slope of the cotangent is always greater than or equal to one in magnitude, thus is insensitive to small changes in $(\Delta(E_s)/X_s)$. The proof of these statements must await specific calculation of v and v'. We can, however, point out *a priori*, that in the case of charged particle decay with kinetic energies definitely below the top of the Coulomb and centripetal barriers, the magnitudes of v and of v' are large compared to one. This conclusion follows from the fact that the particle probability density in such a case is much greater within the nucleus ($\sim|v|^2$) than at infinity (1).

In the foregoing case, therefore, (2.6) yields

$$\sin(\delta_1-\delta)=|vv'|^{-1}.$$

Thus

$$\Delta=x|v'/v|\,(1-|vv'|^{-2})^{\frac{1}{2}}\approx x|v'/v|, \tag{2.14}$$

thus the quantity,

$$\Delta(E_s)/X_s\approx(x/X)|v'/v|, \tag{2.15}$$

is what we shall have to show is weakly energy dependent. [See (2.32) and thereafter.]

We shall need $\partial f/\partial E|_{E_s}$ in order to get γ_s in (2.12):

$$\partial f/\partial E|_{E_s}=X'\cot\mathbf{Z}(E)|_{E_s}-X\mathbf{Z}'(E)/\sin^2\mathbf{Z}|_{E_s}. \tag{2.16}$$

The fundamental postulate of this treatment is that the slope of $\mathbf{Z}$ at the energy E_s at which decay occurs can be approximately given by the average slope in the region of E_s, that is, that

$$\mathbf{Z}'|_{E_s}\approx\pi/D, \tag{2.17}$$

where D is the energy level spacing.[8] ($\mathbf{Z}$ is π-periodic.) This assumption is not meant to be more than a rough approximation.

(2.11) gives

$$(\sin\mathbf{Z})^{-2}=[(\Delta^2/X^2)+1] \text{ at } E=E_s. \tag{2.18}$$

Substituting Eqs. (2.17), (2.18), and (2.11) into (2.16) gives

$$\left.\frac{\partial f}{\partial E}\right|_{E_s}\sim X'\frac{\Delta}{X}-\frac{X\pi}{D}\left(\frac{\Delta^2}{X^2}+1\right), \quad E=E_s. \tag{2.18a}$$

Using (2.12), (2.8b), and (2.18a), we obtain

$$\gamma_s\approx\frac{2}{\pi}\frac{xX}{|v|^2}\cdot\frac{D}{[\Delta^2+X^2]-(1/\pi)X'\Delta D}, \quad E=E_s. \tag{2.19}$$

With the aid of (2.14), Eq. (2.19) becomes

$$\gamma_s\approx\frac{D}{2\pi}\cdot\frac{4xX}{x^2|v_l'|^2+X^2|v_l|^2-(1/\pi)xX'|v_l'v_l|D}, \quad E=E_s. \tag{2.20}$$

The last term in the denominator will be shown [see (2.34)] to be small compared to the other two, so so we can neglect it and find

$$\gamma_s\approx\frac{D}{2\pi}\cdot\frac{4xX}{x^2|v_l'|^2+X^2|v_l|^2}, \quad E=E_s. \tag{2.21}$$

The $D/2\pi$ is interpreted as $1/\hbar$ times the intrinsic (nonbarrier) decay probability of the nucleus and the other factor as the discontinuity and barrier transmission probabilities (see interpretation below). Equation (2.21) is the fundamental equation for decay of a charged particle from a nucleus through the Coulomb and centripetal barriers. Approximations (2.20) to (2.21) and (2.15) must yet be verified.

In order to estimate the correction (2.20) to (2.21) it is necessary to assign an energy dependence to K. The usual, and indeed most reasonable, premise is that the kinetic energy of the charged particle should vary linearly with the decaying state energy E. We therefore put

$$K^2=(2\mu/\hbar^2)(E_0+E), \tag{2.22}$$

where E_0 is a constant. Therefore

$$X_s=(2\mu R^2/\hbar^2)^{\frac{1}{2}}(E_0+E_s)^{\frac{1}{2}}, \tag{2.23}$$

and

$$X'=\mu R^2/\hbar^2 X, \tag{2.24}$$

so that

$$\gamma_s\approx\frac{D}{2\pi}\cdot\frac{4xX}{x^2|v_l'|^2+X^2|v_l|^2-(\mu R^2/\pi\hbar^2)(x/X)|v_l'v_l|D} \tag{2.25}$$

is Eq. (2.21) corrected by substituting the assumption (2.22) into (2.20). We shall, however, find that (2.21) is sufficiently accurate for our purposes.

We next calculate v and v' for $l=0$, using the WKBJ approximation.[9] From (2.1) we must solve

$$(d^2v/dr^2)+k^2(r)v=0, \tag{2.26}$$

where $k^2(r)\equiv(2\mu E/\hbar^2)-(2\mu Zze^2/\hbar^2 r)\equiv A-(B/r)$. This equation defines A and B; note that $k\equiv k(\infty)$. The WKBJ solution is

$$v=\frac{1}{[k(r)]^{\frac{1}{2}}}\exp\left[\pm i\int_a^r k(r)dr\right], \quad \alpha=\text{constant}, \tag{2.27}$$

which is valid when

$$-\frac{d}{dr}\left(\frac{1}{k(r)}\right)\ll 1,$$

or[10] when

$$F(r)\equiv\frac{(B/r^2)}{2[(B/r)-A]^{\frac{1}{2}}}\ll 1. \tag{2.28}$$

[8] This is the same postulate as in FPW; see also the discussion there. We shall discuss the type levels D refers to in Sec. 3.

[9] See, for example L. I. Schiff, *Quantum Mechanics* (McGraw-Hill Book Company, Inc., New York, 1949). This barrier penetration solution is well known from the very earliest attacks on the problem. We outline our method for convenience.

[10] In alpha decay B is about $0.559\times10^{13}\,Z$ cm^{-1}, with A equal to $1.96\times10^{26}\,E$ cm^{-2}, E in Mev, so that the outer turning point $r_1=B/A$ is roughly $2.85\times10^{-13}\,Z/E$ cm.

It is clear that (2.28) holds in the classically allowed region, $r>r_1$; the validity must be examined in the classically forbidden

Using the boundary condition

$$v \underset{r\to\infty}{\longrightarrow} \exp(ikr)$$

and the Kramers joining formulas[9] through the point $r=r_1$, we obtain for $r<r_1$

$$v=y^{\frac{1}{4}}(1-y)^{-\frac{1}{4}}\exp\left[-i\frac{\pi}{4}+\int_R^{r_1}\kappa dr\right], \quad (2.29)$$

where $\kappa\equiv[(B/r)-A]^{\frac{1}{2}}$, and $y\equiv ER/Zze^2=AR/B$, that is, the ratio of the Coulomb barrier height at $r=R$ to the kinetic energy at $r=\infty$.

Integration of (2.29) for $l=0$ and a Coulomb barrier yields

$$v(r)=y^{\frac{1}{4}}(1-y)^{-\frac{1}{4}}\exp\left[-i\frac{\pi}{4}+\left(\frac{2\mu}{\hbar^2}Zze^2R\right)^{\frac{1}{2}}\gamma(y)\right], \quad (2.30)$$

where[11]

$$\gamma(y)\equiv y^{-\frac{1}{2}}(\arccos y^{\frac{1}{2}})-(1-y)^{\frac{1}{2}}.$$

The quantity $|v|^{-2}$ gives the Coulomb penetration factor. Differentiation yields

$$v'(x)=\frac{v(x)}{2k}\left\{\frac{1}{2(1-y)R}-2\left(\frac{2\mu Zze^2}{\hbar^2R}\right)^{\frac{1}{2}}\cdot(1-y)^{\frac{1}{2}}\right\}. \quad (2.31)$$

Equations (2.31), (2.30), and (2.21) give the computational formulas for $l=0$, charged particle decay which we shall later display for alpha decay.

Discussion of Approximations

We are now able to examine our approximations. We shall do so for the special case of alpha decay in which we are primarily interested. The first is that $(x/X)|v'/v|$ is a weak function of the decay energy. [This is necessary for (2.13); see (2.15).]

From (2.31),

$$\frac{x}{X}\left|\frac{v'}{v}\right|=\frac{1}{2X}\left\{\frac{1}{2(1-y)}-2\left(\frac{2\mu Zze^2R}{\hbar^2}\right)^{\frac{1}{2}}(1-y)^{\frac{1}{2}}\right\}, \quad (2.32)$$

where y ranges from 0.19 to 0.35 for alpha decayers (including those in the upper middle of the periodic table).

X is given by (2.23), so that indeed (2.32) is weakly energy dependent.[12]

We must next show that

$$H\equiv\left[\left(\frac{\mu R^2}{\pi\hbar^2}\right)D\left(\frac{x}{X}\right)\left|\frac{v'}{v}\right|\right]\Big/\left[x^2\left|\frac{v'}{v}\right|^2+X^2\right]\ll 1, \quad (2.33)$$

in order that (2.21) be valid. For kinetic energies within the nucleus of 1 to 16 Mev, $D\leqslant 1$ Mev, $R\sim 10^{-12}$ cm, and for nuclei in the alpha-decay region,

$$H\lesssim 0.01\ll 1. \quad (2.34)$$

Interpretation

Under the assumption of equidistant nuclear energy levels it has been shown[13] that the nuclear period is $2\pi\hbar/D$. The period of a particle in a one-dimensional square well of quantum number n is $T_n=(2\pi\hbar/D)\times(1+1/2n)$, and that of a harmonic oscillator is of course $T=2\pi\hbar/D$ (equally spaced levels). Thus the factor $D/2\pi$ of formula (2.21) may be considered as $\hbar$ multiplied by the time rate of appearance of an outgoing alpha particle at the nuclear radius. The remaining term is easily shown to be exactly the barrier penetration factor of a particle whose wavelength is large compared to the rise of the (Coulomb) barrier at $r=R$. It is therefore asserted that this theory includes the single charged particle in a square well as a special case. It should be recognized that the barrier penetration includes not only the penetration of the body of the Coulomb barrier ($1/|v|^2$), but also the very real discontinuity barrier at $r=R$, [which may be likened to the neutron penetration, $4kK/(k+K)^2$].

3. THE THEORY OF ALPHA DECAY, CONTINUED, ORBITAL ANGULAR MOMENTUM

The general formula (2.21) is applicable to nonzero angular momenta as well; we must, however, make quite clear what we mean by the energy level spacing D, and further we must verify that the approximations of Sec. 2 are still valid in this case. That D shall be between energy levels in the parent nucleus of the same spin and parity follows immediately from the definition of D ($\mathbf{Z}'|_{E_s}\approx\pi/D$); we vary the energy of the system and postulate that the slope at the decay energy, E_s, will be roughly given by the average slope. No continuous variation of the parameter E from resonance s to $s+1$ can cause a discontinuous change in spin or parity. Nuclei of different spins are, so to speak, "different" nuclei. This can be seen in another way from the interpretation of the nuclear period $T\approx 2\pi\hbar/D$. The period of a nucleus with spin J is determined by the level system of such a nucleus (with spin J).

region, however, since (2.28) fails both for small r and for r close to r_1, the turning point. In the worst case, that of $_{62}Sm^{148}$, we have

$F(r)$:	$\propto$	$0.059E^{\frac{1}{2}}$	$0.026E^{\frac{1}{2}}$	$0.019E^{\frac{1}{2}}$	$0.024E^{\frac{1}{2}}$
$r\times10^{12}$ (cm):	$r_1=177/E$	$133/E$	$89/E$	$45/E$	$17.5/E$

with E the alpha-decay energy in Mev.

It appears then that the WKBJ approximation is applicable; however, Eq. (2.28) gives no indication of the accuracy of joining at $r=r_1$.

A check upon the accuracy of the *entire* approximation is obtained by comparison with the exact calculations of Preston and of Tyson [M. A. Preston, Phys. Rev. **71**, 865 (1947); James K. Tyson, Ph.D. thesis, Massachusetts Institute of Technology, 1948 (unpublished)]. This comparison shows that the terms of our WKBJ solution (to be derived below) are accurate for alpha decay to one part in 220, which is fantastically good since we have reason to believe that errors in D are 100 percent to 1000 percent.

[11] Compare Bethe, reference 3, p. 161 ff.

[12] Actually we need the value of K only to an order of magnitude, so that we can neglect even its linear variation in the square and will later assign the same wave number, K, to all outgoing alpha particles within the nucleus regardless of the nucleus or of the alpha-decay energy.

[13] V. F. Weisskopf, Helv. Phys. Acta **23**, 187 (1950).

Now let us ask for the dependence of D on the orbital angular momentum l of the outgoing alpha particle. There are the following possibilities for l, if i_p is the parent spin and i_d the daughter spin:

$$|i_p+i_d|,\quad |i_p+i_d-1|,\quad \cdots,\quad |i_p-i_d|;$$

a total of the smaller of $(2i_p+1)$ and $(2i_d+1)$ in all. Parity conservation allows a total of $i+1$ or i (i is the smaller of i_p and i_d), only, of these. We assert that the boundary condition of $f_l=X\cot\mathbf{Z}_l(E)$ differs for each value l of the outgoing orbital momenta. This assertion immediately follows from the factor $Y_{lm}(\theta,\phi)$ governing the distribution in angles of the complete wave function. Thus we have different Z's and hence separate D's for each l. D must stand for the level spacing between alpha energy levels of equal outgoing orbital angular momentum. In this paper we shall not attempt to distinguish between different D's that are between levels of the same spin and parity.[14] Indeed we shall be forced to take for D the first energy level spacing because of the paucity in data.

The effect of angular momenta in the external barrier penetration is small for small l, as Table I shows. (The centripetal barrier height at $r=R$ is $0.054l(l+1)$ Mev and the Coulomb is 25 Mev.) These values were computed from the data of ${}_{88}\mathrm{Ra}^{226}$ using the method exhibited below.

It should be noted that large spins, because of the possibility of many-channel decay,[14] can lead to barrier penetration greater than a single $l=0$ penetration. For example, in Table I, spin 2 decaying to a spin-2 residual nucleus with even parity would be listed as 1.407 (>1), if one weights all possible channels equally.

TABLE I. Ratio λ_l/λ of the alpha-decay probability for angular momentum l to that for angular momentum zero.

Orbital angular momentum quantum number, l	λ_l/λ
0	1
1	0.7
2	0.37
3	0.137
4	0.0368
5	7.11×10^{-3}
8	9.95×10^{-6}

We now proceed to solve the barrier penetration for $l\neq0$. Our equation is again

$$d^2v_l/dr^2+k_l^2(r)v_l=0, \tag{3.1}$$

but now

$$\begin{aligned}k_l^2(r)&\equiv(2\mu E/\hbar^2)-(2\mu Zze^2)/\hbar^2r-(l(l+1)/r^2)\\&\equiv A-(B/r)-(l(l+1)/r^2),\end{aligned} \tag{3.2}$$

which defines the constant A and B.

The WKBJ solution is

$$v_l(R)=A^{\frac14}\left[\frac{l(l+1)}{R^2}+\frac{B}{R}-A\right]^{-\frac14}\left[\exp\left(-i\frac{\pi}{4}+\int_R^{r_1'}\kappa dr\right)\right]$$

with

$$\begin{aligned}\kappa&\equiv[(l(l+1)/r^2)+(B/r)-A]^{\frac12},\\ r_1'&\equiv(B/2A)\{1+[1+(4A/B^2)l(l+1)]^{\frac12}\}.\end{aligned} \tag{3.3}$$

Evaluation of the integral yields

$$\begin{aligned}\int_R^{r_1'}\kappa dr=&-R[l(l+1)/R^2+B/R-A]^{\frac12}\\&+[l(l+1)]^{\frac12}\ln\left|\frac{(2l(l+1)/R)+B+2[l(l+1)]^{\frac12}[l(l+1)/R^2+B/R-A]^{\frac12}}{\{B^2+4l(l+1)A+B[B^2+4Al(l+1)]^{\frac12}\}/\{B+[B^2+4Al(l+1)]^{\frac12}\}}\right|\\&+(B/2A^{\frac12})\cdot\{\arcsin(1)-\arcsin[(2AR-B)/(B^2+4Al(l+1))^{\frac12}]\}.\end{aligned} \tag{3.4}$$

Formula (3.4)[15] reduces to the exponent of (2.30) by setting $l=0$ if one remembers that

$$\arccos(2u-1)=2\arccos u^{\frac12}.$$

Defining

$$w\equiv l(l+1)A/B^2, \tag{3.5}$$

$$\begin{aligned}v_l(x)=&\,y^{\frac14}(w+y-y^2)^{-\frac14}\\&\times[1+2y^{-1}[w+w^{\frac12}(w+y-y^2)^{\frac12}]/(1+4w)^{\frac12}]^{\sqrt{l(l+1)}}\\&\cdot\exp[-\tfrac14 i\pi+\Gamma(y)],\end{aligned} \tag{3.6}$$

with

$$\begin{aligned}\Gamma(y)\equiv(B/A^{\frac12})\cdot\{&\tfrac12\arccos[(2y-1)/(1+4w)^{\frac12}]\\&-(w+y-y^2)^{\frac12}\}.\end{aligned}$$

Differentiation gives

$$\begin{aligned}v_l'(x)=[v_l(x)/x]\{&[(2w+y)/4(w+y-y^2)]\\&+[[y(y-1)BA^{-1}-w^{\frac12}(l(l+1))^{\frac12}]/\\&(w+y-y^2)^{\frac12}]\}.\end{aligned} \tag{3.7}$$

Equations (3.6), (3.7), and (2.21) give the computational formula for alpha decay in the case $l\neq0$.

Validity of $l\neq0$ Calculations

The energy variation of $(x/X)|v_l'/v_l|$, which we must show to be weak in order that (2.13) may be valid, is easily shown by neglecting the small quantity w in comparison to $y-y^2$ in (3.7), so that $(x/X)|v_l'/v_l|$

[14] Use must here be made of the fact that our problem is a many-body one in order to admit the *a priori* possibility of many orbital angular momentum decay channels for the same energy, E_x. In a one-body potential well, for example, the decaying state energy is different for different decay orbital angular momenta so that for a given energy state, decay is possible for only one orbital angular momenta, l.

[15] Equation (3.4) is identical to Bethe, reference 3, Formula (631), and the first terms of Tyson's asymptotic expansion (see reference 10).

has approximately the energy dependence of $l=0$ for $l \lesssim 10$. Because of the smallness of w the arguments of (2.33) and (2.34) follow verbatim for $l \neq 0$ so that (2.20)→(2.21) is still valid. The situation is not so obvious for the external (barrier) problem, however, since one might expect $-(d/dr)(1/k(r))=k'(r)/k^2(r)$ to become of the order of, or larger than, unity for small r. A short numerical calculation shows that this is not the case and that, in fact, $F(r)$ [defined in (2.28)] is still the same as for $l=0$ unless $l \gtrsim 10$. These last remarks can be directly seen by recognizing that $k_{l=0}^2(r) \approx k_{l\neq 0}^2(r)$ and comparing the derivative of $k(r)$ in the two cases. This last ratio, from (3.1), is

$$1+2l(l+1)/RB \approx 1 \text{ for alpha decay,} \qquad (3.8)$$

with $B=0.559\times 10^{13} Z/\text{cm}$, R ranges from 8 to 11×10^{-13} cm. The accuracy of joining is the same in this case because the r dependence is essentially that of the Coulomb field at $r=r_1'$.

4. THE EFFECTIVE RADIUS R

In this section we use the formulas derived in the preceding sections to give a computational formula for the nuclear radius R, as defined in Sec. 2. The "effective" radius R can be thought of as including the "naked" radius of the nucleus, the "naked" alpha-particle radius, and the range of nuclear forces between them. Further, the calculations are made for zero angular momentum. Thus in the case of a single channel large angular momentum, the R thus calculated will be too small, and in the case of many channel decay with small-to-zero orbital angular momenta possible, the R will be slightly larger. The effects of angular momenta are negligible for $l=0$, 1, and 2 regardless of the number of channels open, since our accuracy, because of the assumption connected with D, is not good enough to distinguish these cases. However, for $l=3$ and above, the calculation for $l=0$ is misleading. We are forced to calculate for $l=0$, regardless of other considerations, however, because there does not exist one case where the spin of both daughter and parent nucleus in the alpha decay is known.[16] In fact, we know only very few cases where the spin of one member is known. We do not wholly leave the problem of (external) angular momentum with these remarks; we shall take up the problem again in connection with explaining anomalous radii.

The Energy Level Spacing D

We will not be able to get D between levels of equal spin and parity for the simple reason that few spins and parities of the various levels are known.[17] We must therefore estimate the energy and level spacing. It will turn out that the radius R depends weakly on D, so that our estimates may be off by large factors without appreciably altering the nuclear radius; a factor of five in D alters R by at most 5 percent and usually ~2.5 percent. We will therefore, arbitrarily, choose the lowest-lying energy level spacing (obtained from any experiment whatever) in the parent nucleus to be D, and in the case where no experimental evidence exists for the parent in question, we shall estimate the spacing from surrounding nuclei of the same type (i.e., even-odd, etc.). This choice we make for the purpose of consistency. If the experiments truly give the lowest spacing, we shall expect our D to be larger,[18] (for it is unlikely that the ground state and the first excited state are so kind to us as to be of the same spin and parity). On the other hand, there is still the possibility that the low-lying levels have not yet been detected; this leads to a smaller D than we use.

In summary, the requirements that D shall be between alpha-forming levels of the same spin and parity tends to make our choice of D too small, and uncertainty in measurement tends too give to large a D.

Kinetic Energy of an Alpha Particle in the Nucleus

We must determine the propagation constant K or, alternatively, the internal kinetic energy of an alpha particle just within the nuclear radius. A lower bound for this energy is the lowest momentum state of an Einstein-Bose particle in the alpha nuclear-volume, which we take to be given by a radius of $1.57A^{\frac{1}{3}}\times 10^{-13}$ cm. This "alpha nuclear-volume" is larger than the true nuclear volume; it is the "trial" nuclear volume of an escaping alpha particle. Thus it includes the range of nuclear forces as well as the alpha particle radius.

The kinetic energy lower bounds are then: 0.76 Mev for mass number $A=150$, 0.63 for 200, and 0.53 for 250, respectively.

An even numbered conglomerate of Fermi-Dirac particles (for example, an alpha particle) can only be considered to obey Einstein-Bose statistics when the perturbations on its constituent particles are smaller than the binding of the particles in the conglomerate. Such is *not* the case for an alpha particle in a nucleus, where the perturbations are indeed of the order of the nucleon binding energy. Therefore, we may *not* consider the conglomerate of two protons and two neutrons, each pair with opposing spins, to be a true Bose particle. We shall call it a four-particle.

This four-particle, in fact, must obey the exclusion principle to some extent because of its Fermi-Dirac constituents. (For example, two alpha particles cannot occupy the same configuration state.) If it were a

[16] Except of course for the presumption that all even-Z and even-A spins are zero and are of the same parity.

[17] Again except for the presumption of zero spin and even parity for the ground states of even-even nuclei.

[18] The mounting evidence that the first excited states of even-even nuclei are spin 2, positive parity, indicates that D is probably larger for even-even nuclei. See, for example, the paper of Gertrude Scharff-Goldhaber, Phys. Rev. **90**, 587 (1953).

complete Fermi-Dirac particle, we can use

$$N = V_c V_p / h^3, \tag{4.1}$$

where N is the number of equal particles, V_c the volume in configuration space, and V_p the volume in momentum space, to arrive at a figure of 5.02 Mev for the kinetic energy of the highest energy Fermi-Dirac four-particle (when formed) in the nucleus. This figure is independent of A. We, therefore, suggest that the true kinetic energy of an alpha particle in the nucleus lies between 5 and 0.5 Mev.

The foregoing remarks lead to a best guess of the kinetic energy of a four-particle in the nucleus of the order of 3 Mev. K shall, therefore, be chosen to correspond to 3 Mev for ground-state transitions, less for transitions to excited states, and more for transitions from excited states ("long range"). Fortunately the theory is even more weakly dependent on the choice of the internal kinetic energy of the alpha particle than on the choice of D, so that a factor of five change in this energy is not significant, (a factor of $\frac{1}{5}$ times the internal kinetic energy chosen changes the radius by less than 2 percent, a factor of five by less than 0.6 percent).

Electron Screening Correction

The electron shell about the nucleus weakens the positive potential barrier. Using the Thomas-Fermi approximation,[19] the first-order atomic electron correction to the Coulomb potential is a constant. We choose to add this correction to the decay energy as follows:

$$E_t = E_d + 72.8\times 10^{-6}(Z_d)^{4/3} \text{ Mev}, \tag{4.2}$$

where E_t is the total energy, which is utilized in the foregoing formalism, E_d is the measured decay energy (energy of alpha+recoil nucleus), and Z_d is the charge of the daughter nucleus.[20]

Calculation of the Radius R

We take formulas (2.21), (2.30), (2.31) together with the preceding work of this section and obtain

$$\gamma_\alpha \sim \frac{2D_0}{\pi}\left(\frac{3}{E_t}\right)^{\frac{1}{2}}\cdot\left(\frac{1-y}{y}\right)^{\frac{1}{2}} \times\left\{\exp\left[-2\left(\frac{2\mu}{\hbar^2}Zze^2R\right)^{\frac{1}{2}}\cdot\gamma(y)\right]\right\} \cdot\left\{\frac{3}{E_t}+\frac{1}{4k^2}\left[\frac{1}{2(1-y)R} -2\left(\frac{2\mu}{R\hbar^2}Zze^2\right)^{\frac{1}{2}}\cdot(1-y)^{\frac{1}{2}}\right]^2\right\}. \tag{4.3}$$

The inaccuracy in D and in K permits rough approximations for factors not of the exponential in (4.3). Thus for such terms we put $R = 1.57\times 10^{-13}A^{\frac{1}{3}}$ cm² and thus $y \approx \chi \equiv 0.545E_tA^{\frac{1}{3}}Z^{-1}$. The term $1/[2(1-y)R]$ turns out not only to be negligible but to give a better approximation (according to the formulas of Tyson, reference 10) if neglected. So that (4.3) becomes

$$y^{\frac{1}{2}}\gamma(y) = \frac{E_t^{\frac{1}{2}}(1+4/A_d)^{\frac{1}{2}}}{2.520Z_d}\ln\left\{\frac{D_0}{\gamma_\alpha}\cdot 0.367\frac{Y^{\frac{1}{2}}}{1+\frac{1}{3}Y}\right\} \tag{4.4}$$

with

$$Y \equiv (Z_d/0.545A_d^{\frac{1}{3}}) - E_t, \tag{4.5}$$

$$E_t = E_d + 72.8\times 10^{-6}Z_d^{4/3}, \tag{4.2}$$

$$R = 2.879\times 10^{-13}yZ_d/E_t, \tag{4.6}$$

where E_t, E_d, γ_α, D_0 are in Mev. Z_d and A_d refer to the daughter nucleus.

Equations (4.4), (4.5), (4.2), and (4.6) comprise the computational formulas for alpha decay. These formulas are good only for normal alpha decay and make no pretense of giving proper radii from anomalous fine structure [*viz.*, the most energetic lines of Am^{241}; see Asaro, Reynolds, and Perlman, Phys. Rev. **87**, 277 (1952)]. We have not changed K for different energies E_t, neither among different nuclei, nor in fine structure of the same nucleus. The effect of the variations is negligible, and we do not know K well anyway.

The radii calculated on the basis of the foregoing theory will be presented and discussed critically in Part II, to be submitted shortly for publication in *The Physical Review*.

The writer is grateful to Professor V. F. Weisskopf for suggesting the problem and to many colleagues and friends, particularly Dr. Frederick Reines, for their criticism. He acknowledges his indebtedness to the U. S. Atomic Energy Commission for a fellowship, 1948–1950.

[19] E. Thomas, Proc. Cambridge Phil. Soc. **23**, 542 (1927); E. Fermi, Z. Physik **48**, 73 (1928); E. B. Baker, Phys. Rev. **36**, 630 (1930).

[20] The importance of this correction was emphasized by G. Ambrosino and H. Piatier, Compt. rend. **232**, 400 (1951). We use Z_d because the inner shells can rearrange to the daughter Coulomb field. See P. Benoist-Guental, J. phys. et radium **13**, 486 (1952). We have made use of the work of Rasmussen, Thompson, and Ghiorso, University of California Radiation Laboratory Report UCRL-1473, 1952 (unpublished) and their references to older work.

Long-Lived Delayed Neutrons from Fission

J. W. KUNSTADTER,* J. J. FLOYD, AND L. B. BORST†
Brookhaven National Laboratory, Upton, New York

(Received April 13, 1953)

Low-intensity delayed neutrons from uranium have been observed with half-lives of 3, 12, and 125 minutes and yields per fission of 5.8×10^{-4}, 5.6×10^{-10}, and 2.9×10^{-10}, respectively.

INTRODUCTION

DELAYED neutrons have been recognized as a minor product of fission since 1939. Quantitative evaluation has led to the acceptance of five well-defined species having half-lives of 0.4 to 55 seconds.[1] Observations by Jordon at Oak Ridge in 1948 using BF_3 counters gave evidence of small time-dependent effects after hours and days. A repetition of these measurements with the Brookhaven reactor gave identical curves.

To confirm these data, further work was done using foil activation techniques. Neutrons were found with characteristic times which are long compared to the known delayed neutrons. These activation data did not correspond at all well with the previous BF_3 data, which were therefore ascribed to beta- or gamma-ray sensitivity of the counters.

OBSERVATIONS

Foils of both rhodium and indium were irradiated under carefully controlled conditions within the uranium-bearing lattice of the Brookhaven reactor, removed and counted by a conventional thin-wall counter (Fig. 1). Rhodium exposures were carried to saturation of the 44-second activity. Indium exposures ranged from 30 seconds to many hours. Control experiments demonstrated that errors caused by foil placement were less than one percent, well within the statistical accuracy. Under normal irradiation conditions, the foils were 10 cm from the nearest uranium. The foil position used had a neutron flux about 60 percent of maximum.

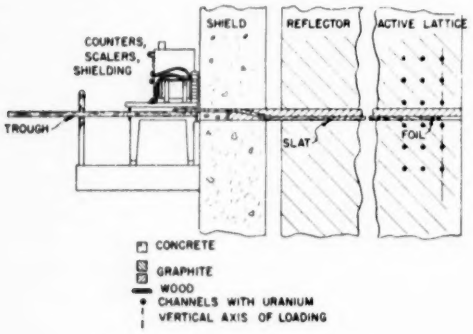

FIG. 1. Experimental arrangement.

The schedule of reactor operation for the experiment required the reactor to be in a rested condition, i.e., shut down for a period long enough to permit virtually complete decay of the delayed neutron emitters under study. The reactor was rapidly brought to a predetermined power level and held for a given time. After rapid shutdown, observations were started. The control rod pattern was specified both during operation and after shutdown to minimize the perturbation of the neutron flux at the position of measurement.

The observed foil counts were corrected for resolving time losses, foil background, irradiation, and counting intervals to give standardized saturated activities. Since the neutron flux was time-dependent during foil irradiation, an additional correction was made where necessary.

Rhodium foils showed effects identical to indium, but the difficulty of working with the 44-second activity mitigated against its general use. All data quoted are based upon the 54-minute activity of In^{116}.

Decay curves were prepared using the corrected foil activities as an index of the neutron flux (Fig. 2). Observations were continued in each run until a time-independent activity could be evaluated. This activity is produced by spontaneous neutrons from the spontaneous fission of U^{238} in the lattice. No variation of this activity was observed as a function of reactor history, comparing 2, 15, and 80 hours of operation. After subtracting this constant term, a clean exponential tail was found, having a half-life of 125 minutes. This component was then subtracted. Observations were made, in each case, within a few minutes of shutdown when the known 55-second emitter predominated. This component was also subtracted. The residue was fit in each case satisfactorily by two components having half-lives of 3 and 12 minutes. These were identified early in the study and were found to satisfy all subsequent observations.

The intensity at zero time of each component of each run was normalized in terms of the 55-second activity and the data plotted as a function of irradiation time in Figs. 3(a)–3(c). The continuous curve is the saturation curve with the designated time constant, normalized to the observed value for long irradiation. While

* Present address: The Formfit Company, Chicago, Illinois.
† Present address: University of Utah, Salt Lake City, Utah.

[1] Snell, Nedzel, Ibser, Levinger, Wilkinson, and Sampson, Phys. Rev. **72**, 541 (1947); Hughes, Dabbs, Cahn, and Hall, Phys. Rev. **73**, 111 (1948); Sun, Charpie, Pecjak, Jennings, Nechaj, and Allen, Phys. Rev. **79**, 3 (1950).

the data do not fall uniformly on this curve, the fit is such as to preclude the possibility of a precursor of half-life comparable to that of the delayed neutron emitter.

Since these observations were all made within the reactor lattice, it seemed appropriate to check the data in the absence of a lattice. Foils were therefore irradiated in the graphite reflector at a distance of 50 cm from the closest uranium. All components were found.

To eliminate all possibility of the observed effects being due in some unknown way to the reproducing medium, a graphite block more than a meter on an edge was constructed outside the reactor shield. 3.5 kg of uranium metal was irradiated at maximum flux for 40 minutes, after which it was withdrawn through the shield into the graphite block. Foils were irradiated in close proximity to this metal and counted in the normal manner. The 55-second and 3-minute components may be easily evaluated. A long period tail undoubtedly exists but is difficult to evaluate because of poor statistics (Fig. 4).

A further check was made to eliminate the possible effect of graphite. A block was constructed by fitting large quartzite boulders together similar to the external graphite block. 3.5 kg of uranium was irradiated and studied in an analogous fashion. The intensities are low, but a long period tail is again evident (Fig. 4).

EVALUATION

The data taken within the reactor are summarized in Table I in terms of neutron yield per fission. (The previous data of Hughes were expressed as delayed neutrons per prompt neutron.) The external graphite block or "small pile" experiment gave quantitative data on the three-minute period which is compared.

The twofold difference may be understood if the three-minute neutron is less energetic than the 55-second neutron. The lattice experiments were carried out with a local reproduction factor near unity, so that

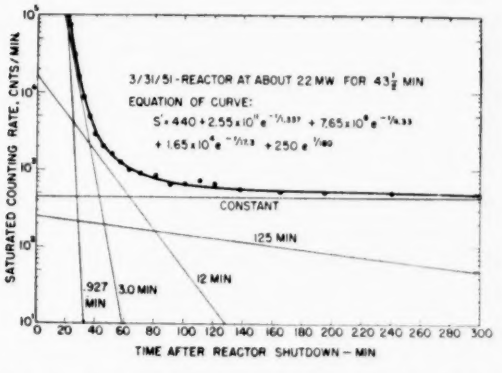

FIG. 2. Decay curve for neutron density after reactor shutdown. The saturated counting rate of indium foils is plotted as a function of time after reactor shutdown.

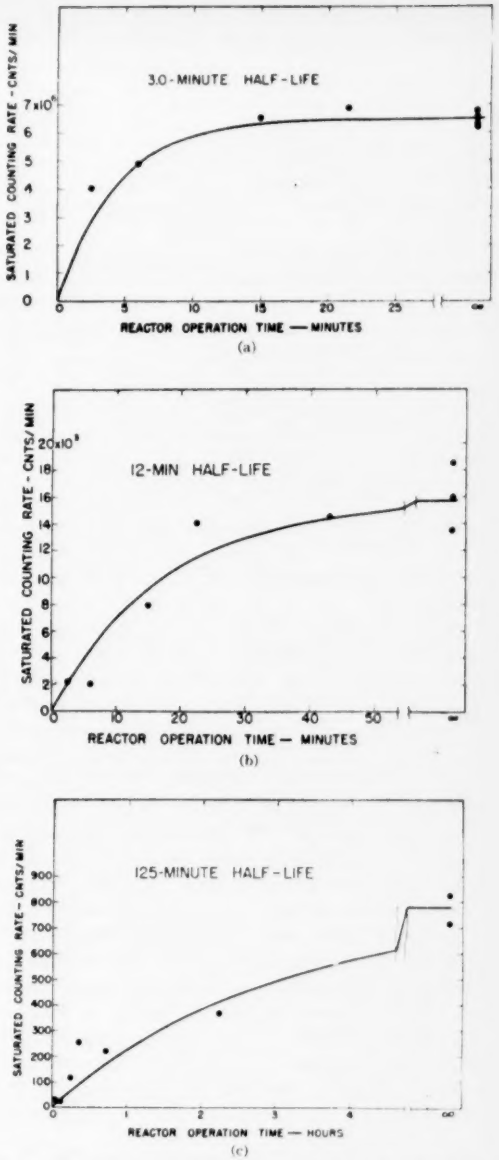

FIG. 3. Growth curves for (a) 3-minute, (b) 12-minute, and (c) 125-minute components. The initial activity is plotted as a function of reactor operating time.

the neutrons observed were probably more than 99 percent prompt neutrons from the convergent series of fissions triggered by the delayed neutron. The lattice data should therefore indicate source strengths. In the external experiment, however, there is no reproduction, and the activation ratios for the 55-second and 3-minute neutrons will only be independent of position if the energies are identical. Since the foils were very close to the uranium, a low-energy 3-minute neutron

TABLE I. Experimental results, long period delayed neutrons.

Half-life minutes	Yield probability per fission	
	Reactor	Graphite block
0.927	6.25×10^{-4}	6.25×10^{-4}
3.0±0.5	$(5.8\pm0.6)\times10^{-8}$	$(12\pm)\times10^{-8}$
12±3	$(5.6\pm0.6)\times10^{-10}$	...
125±15	$(2.9\pm0.6)\times10^{-10}$	...

TABLE II. Possible delayed neutron emitters.

	$T_{\frac{1}{2}}$ min	Product	Proton number	Neutron number
Br^{85}	3	Kr^{84}	36	48
Nb^{99}	2.5	Mo^{98}	42	56
Rb^{89}	15.4	Sr^{88}	38	50
Y^{95}	10.5	Zr^{94}	40	48
Cs^{139}	9.5	Ba^{138}	56	82
Pm^{157}	12	Sm^{150}	62	88
Br^{83}	140	Kr^{82}	36	46

with its short range would tend to enhance this component.

The interpretation of these data as supporting true delayed neutron emission as a consequence of fission is favored because of the following considerations: (a) long period neutrons are detected using both rhodium and indium foils, (b) they are found in the reflector as well as the reproducing lattice, (c) they are found using a single uranium element in carbon and silicon dioxide moderators, (d) they show normal growth and decay.

The only possibility not excluded is photoneutron emission in deuterium by fission product gamma-rays. A quantitative evaluation excludes this even if one part per million of deuterium is assumed when compared to the published photoneutron data of Bernstein.[2] A comparison of the shapes of either his beryllium or deuterium curves with the present data shows qualitatively that the same mechanism cannot be involved.

The extremely low yield and the consequent large scale of the experiments render further characterization extremely difficult. Chemical identification can only be accomplished by expending a major effort because of the magnitude of the fission sources required. Neutron energy measurements, while in principle feasible, would require an extended effort. It appears that identification must be based on theory, if it can be accomplished at all.

Table II shows the possible known fission activities which have the right characteristics, i.e., approximate half-life without a long-lived precursor, and having odd charge and odd mass. Considering the extremely small yield involved, it is quite possible as yet undiscovered fission chains are responsible. Among the chains cited, Rb^{89} and Cs^{139} produce shell closure on neutron numbers 50 and 82. These would therefore be the preferred choices for the 12-minute delayed neutron.

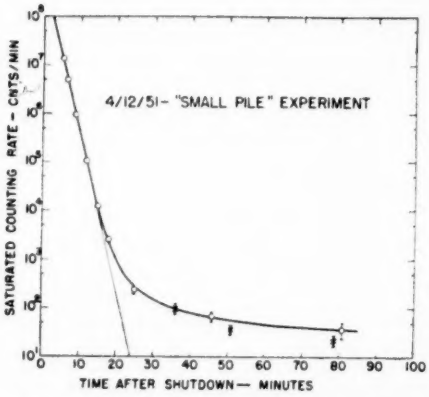

FIG. 4. Decay curve for neutron density in external experiments. *O*-Graphite blocks; *X*-SiO_2 block. The saturated activity of indium foils is plotted as a function of time after reactor shutdown.

Since Br^{83} is the only specie corresponding to the 125-minute delayed neutron among known fission chains, tentative assignment must be made. This raises to three the number of bromine isotopes thought to emit delayed neutrons. The existence of a fourth isotope Br^{85} as one of two known alternatives for the 3-minute delayed neutron renders this coincidence even more remarkable. $Br^{83,85,87,89}$ then all have properties corresponding to delayed neutron emitters. If these do, in fact, all lead to delayed neutron emission, the energy difference between $Z=35$ and $Z=36$ must be unusually large.

[2] Bernstein, Preston, Wolfe, and Slattery, Phys. Rev. **71**, 573 (1947).

Slow Neutron Scattering Cross Sections for Rare Earth Nuclides

W. C. KOEHLER* AND E. O. WOLLAN
Oak Ridge National Laboratory, Oak Ridge, Tennessee
(Received April 23, 1953)

Coherent neutron scattering amplitudes and total scattering cross sections have been determined for a number of elements and separated isotopes of the rare earth series. One nuclide, Sm^{152}, was found to scatter with negative phase.

ALTHOUGH neutron scattering cross sections for over sixty elements and nuclides, as determined by neutron diffraction methods, have been reported by Shull and Wollan,[1] relatively few coherent scattering cross sections in the rare earth region have heretofore been measured.

As an essential part of an investigation of the magnetic scattering of neutrons by rare earth oxides,[2] as well as for their intrinsic interest, nuclear scattering properties of twelve elements or nuclides in the rare earth region have been determined, and these results are listed in Table I.

The coherent scattering data in the table have been obtained from the interpretation of the Bragg reflections from the oxides of the nuclides listed by methods which have been previously described,[1] and the total scattering cross sections were evaluated from transmission measurements at near thermal energy corrected for capture. The capture cross sections were obtained by Pomerance,[3,4] and in most cases he measured the sample on which the scattering measurements were made. The total scattering cross sections have been corrected as far as possible for magnetic scattering so that they represent only the nuclear scattering cross sections. The potential scattering cross sections have been computed from the relation $R=1.53\times10^{-13}A^{\frac{1}{3}}$.

La^{139}

The total cross section of lanthanum obtained from transmission measurements at 0.07 ev was 14.3b, from which the total scattering cross section was found to be 9.3b. This value is close to the coherent scattering cross section of 8.7b, and is in reasonable agreement with that of Harris, Muehlhause, and Thomas[5] but is somewhat lower than the total scattering cross section of 10.5b reported by Brockhouse.[6]

Ce, Ce^{140}, and Ce^{142}

The two major isotopic constituents of cerium are Ce^{140} and Ce^{142}, which together account for 99.55 percent of the normal mixture. The scattering amplitudes of Ce^{140} and Ce^{142} were obtained from neutron diffraction patterns of isotopically enriched samples of CeO_2. Both nuclides are even-even isotopes so that no spin effects are expected, and Ce^{++++} has zero magnetic moment. Transmission measurements, corrected for capture, led to total scattering cross sections equal to the coherent scattering cross sections.

TABLE I. Nuclear scattering properties of rare earth nuclides.

Nucleus	Coherent scattering amplitude (10^{-12} cm)	Coherent scattering cross section barns	Total scattering cross section[a] barns	Potential scattering cross section barns
La^{139}	0.83	8.7±0.3	9.3±0.7	7.90
Ce	0.46	2.7±0.2	2.7±0.2	...
Ce^{140}	0.47	2.8±0.1	2.8±0.1	7.94
Ce^{142}	0.45	2.6±0.2	2.6±0.2	8.00
Pr^{141}	0.44	2.4±0.2	4.0±1.0	7.96
Nd	0.72	6.5±0.4	16±3	...
Nd^{142}	0.77	7.5±0.6	7.5±0.6	8.00
Nd^{144}	0.28	1.0±0.2	1.0±0.2	8.08
Nd^{146}	0.87	9.5±0.4	9.5±0.4	8.16
Sm^{152}	−0.5	3±1	...	8.38
Sm^{154}	0.8	8±2	...	8.44
Er	0.79	7.8±0.4	15±4	...

[a] For the even-even nuclides the total bound scattering cross sections have been taken equal to the coherent scattering cross sections.

* Portions of this work were presented in partial fulfillment of the requirements for the degree of Doctor of Philosophy at the University of Tennessee, Knoxville, Tennessee.

[1] C. G. Shull and E. O. Wollan, Phys. Rev. **81**, 527 (1951).
[2] W. C. Koehler and E. O. Wollan (to be published).
[3] H. Pomerance, Phys. Rev. **88**, 412 (1952).
[4] H. Pomerance, Phys. Rev. **83**, 641 (1951).
[5] Harris, Muehlhause, and Thomas, Phys. Rev. **79**, 11 (1950).
[6] B. N. Brockhouse (private communication).

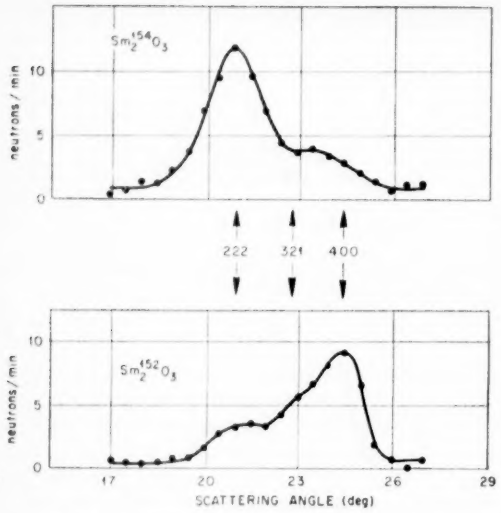

FIG. 1. Neutron diffraction patterns of isotopically enriched samarium oxides.

Both isotopes have cross sections low compared to potential scattering and so also does normal cerium. These results indicate the existence of positive energy resonances in both the major isotopes of cerium. Hibden and Muehlhause,[7] however, using Co and Mn detected neutrons were unable to find resonance effects at these energies.

A sample of normal CeO_2 was prepared from reagent grade cerium nitrate, and the analysis of the neutron pattern for the sample suggested a coherent scattering cross section of 2.2 barns. From the isotopic amplitudes the calculated value for the normal element is 2.7b. This discrepancy is well outside of experimental error and may be due to impurities in the normal cerium oxide which were indicated by the anomalously high total cross section of the sample. The better value is undoubtedly the calculated one and this value appears in the table.

A measurement of the scattering amplitude of cerium from transmission through CeO_2 was reported by Verdaguer, del Rio, Keller, and Kind.[8] These authors give as the scattering amplitude $f_{Ce}=+0.22\pm0.02 \times 10^{-12}$ cm, and this amplitude corresponds to a cross section of 0.61b, which is nearly a factor of four smaller than the result quoted here.

Nd, Nd^{142}, Nd^{144}, Nd^{146}

Two samples of normal Nd_2O_3 were studied. Pomerance measured the thermal absorption cross sections of the two samples and found 100b for one sample and 42b for the other. The transmission cross section was measured for the high-capture sample at 0.07 ev and also at 1.44 ev,[9] and these values were found to be about 10 percent higher than those of Sturm and Arnold.[10] Both sets of data suggest a total scattering cross section of about 16b. The low-capture sample, after correction for capture on a $1/v$ law indicated a total scattering cross section of 20b. The application of a $1/v$ correction law is probably somewhat questionable. A more reliable estimate of 16 ± 3b has been obtained from the analysis of the diffuse scattering in the diffraction pattern of Nd_2O_3.

The cross sections listed for the separated isotopes of neodymium are strictly correct only for the sample studied and must be corrected for isotopic analysis. However, these cross sections are approximately correct for the individual nuclides because the isotopic enrichment was in each case approximately 95 percent. The three cases studied are all examples of zero spin nuclei so that no spin effects are to be expected. The low-scattering cross section of Nd^{144} indicates the effects of a resonance at positive energies.

The three isotopes, Nd^{142}, Nd^{144}, Nd^{146}, together make up 65 percent of the normal element, the remainder being Nd^{143} (13.0 percent), Nd^{145} (9.2 percent), Nd^{148} (6.8 percent) and Nd^{150} (5.95 percent). The contribution of the three even-even isotopes to the coherent scattering amplitude of normal neodymium is $+0.32 \times 10^{-12}$ cm as compared to $+0.72\times10^{-12}$ cm. The effective weighted scattered amplitude of the remaining isotopes must therefore be positive and equal to 0.40×10^{-12} cm. The contribution of these three isotopes to the total scattering cross section is only 3.8b. The effective weighted total cross section of the remaining isotopes must hence be of the order of 12b. It is therefore indicated that one or more of the remaining isotopes has a large coherent scattering amplitude and probably exhibits pronounced spin-dependent scattering.

Pr^{141}

The relative magnitude of the coherent and total scattering cross sections of praseodymium indicate a strong spin dependence of scattering. Harris, Muehlhause, and Thomas[5] suggest a scattering resonance in praseodymium at 10 ev. The total scattering cross section of praseodymium has been measured by Brockhouse[6] at Chalk River to be 4.0 barns in exact agreement with our value.

Sm^{152}, Sm^{154}

An attempt was made to evaluate the scattering properties of Sm^{152} and Sm^{154} from samples of isotopically enriched samarium oxide. Both samples contained approximately 3 percent of Sm^{149} which is responsible for the large capture cross section of samarium, and Sm^{152} has a thermal capture cross section of 200b in its

[7] C. T. Hibden and Muehlhause, Phys. Rev. **76**, 100 (1949).
[8] Verdaguer, del Rio, Keller, and Kind, Helv. Phys. Acta **25**, 80 (1952).
[9] We are indebted to Mr. L. A. Rayburn for this measurement.
[10] W. J. Sturm and G. Arnold, Phys. Rev. **71**, 556 (1947).

own right.[11] The measured total cross section at 1.163A was 880b/molecule for the Sm^{152} sample and 396b/molecule for the Sm^{154} sample.

The diffraction peaks in both these samples were extremely weak due to the strong absorption, but rough values for the coherent cross sections were obtained. In Fig. 1 portions of the patterns obtained are illustrated. From a consideration of the relative intensities of the reflections shown, it can be deduced that Sm^{152} has a negative scattering amplitude, and from the absolute intensities approximate cross sections were evaluated. No effort has been made to extract total scattering cross sections from the transmission data.

Er

Erbium has six stable isotopes all of which except Er^{167} (22.9 percent) are even-even nuclei. Bernstein *et al.*[12] have measured the total cross section of Er in Er_2O_3 over the near thermal energy range and they find capture resonances at 0.45 ev and 0.58 ev. The total cross section which was obtained at $\lambda = 1.163$A (0.06 ev) for Er was 138b and this compares favorably with 135b taken from the curve of Bernstein and coworkers. Pomerance found the thermal absorption cross section to be 166±17b. The contribution of the magnetic scattering of Er at 0.06 ev to the total scattering cross section is 5b based on the experimentally determined form factor. From the diffuse scattering in the diffraction pattern a value of 15±4b was obtained which is not inconsistent with the less precise value of 26±11b from the transmission data.

The cooperation of Dr. F. H. Spedding of the Ames Laboratory, and of Dr. G. E. Boyd of the Chemistry Division of the Oak Ridge National Laboratory in making these samples available to us is gratefully acknowledged. For the loan of the isotopically enriched samples we are indebted to the Stable Isotopes Division of the Laboratory, and for x-ray analyses of all the samples to Mr. B. S. Borie and Mr. R. M. Steele.

[11] Lapp, Van Horn, and Dempster, Phys. Rev. **71**, 745 (1947).
[12] Bernstein, Borst, Stanford, Stephenson, and Dial, Phys. Rev. **87**, 487 (1952).

PHYSICAL REVIEW VOLUME 91, NUMBER 3 AUGUST 1, 1953

The Gamma Radiation from B^{11} Bombarded by Protons*

TORBEN HUUS† AND ROBERT B. DAY‡
Kellogg Radiation Laboratory, California Institute of Technology, Pasadena, California
(Received April 20, 1953)

The spectrum of gamma radiation emitted when B^{11} is bombarded by protons has been investigated with a NaI scintillation counter. Capture gamma rays have been found which occur in a direct transition to the ground state of C^{12} and a cascade transition through a level in C^{12} at 4.45 Mev. Yield curves for these gamma rays have been obtained for proton energies up to 2.8 Mev, and the cross sections for emission of the various gamma rays are given. In addition to the well-known resonance at 0.163 Mev, new resonances have been found at 0.675 Mev with $\Gamma = 0.33$ Mev and 1.388 Mev with $\Gamma = 1.27$ Mev. Spin and parity assignments for these states which are deduced from the results of this and the $B^{11}(p, \alpha)Be^8$ reactions are 2^- (or 3^+) and 1^-, respectively. A 2.13-Mev gamma ray has also been observed, which is produced in an inelastic scattering reaction involving the first excited state of B^{11}. This reaction exhibits a resonance at 2.664 Mev with a width of 48 kev. The cross section at resonance is 3.1×10^{-26} cm².

I. INTRODUCTION

IN the bombardment of boron by protons a number of gamma rays have been found by various investigators, but the variation of their yield with energy is known only in a rough way or over a limited energy region. The purpose of this investigation was to determine the energies of the gamma rays from proton reactions with B^{11} and their yields for proton bombarding energies up to about 3 Mev.

Previous work on gamma rays from B^{11} reactions has been confined to the reaction

$$B^{11} + H^1 \rightarrow (C^{12}) \rightarrow C^{12} + \gamma_0$$
$$\searrow C^{12*} + \gamma_1 \rightarrow C^{12} + \gamma_1 + \gamma_2.$$

The yield curve for this capture radiation in the region up to 500-kev bombarding energy was investigated by Tangen,[1] who found the position of the well-known low-energy resonance to be 162 kev, with a width of 5.3 kev. From measurements of the absorption of secondary electrons he concluded that the radiation is harder off resonance than at 162 kev. Excitation curves at higher energies have been made by Herb, Kerst,

* This work was assisted by the joint program of the U. S. Office of Naval Research and the U. S. Atomic Energy Commission.
† Now at the Institute for Theoretical Physics, Copenhagen, Denmark.
‡ Now at Los Alamos Scientific Laboratory, Los Alamos, New Mexico.

[1] R. Tangen, Kgl. Norske Videnskab. Selskabs, Skrifter No. 1 (1946).

and McKibben[2] and by Curran, Dee, and Petrzilka.[3] The former found a resonance at 820 kev, while the latter reported resonances at 650, 850, and 950 kev. From the position of these resonances and also from work done at this laboratory (see Sec. II), it seems likely that these were actually produced by fluorine contamination in the targets. The rise at higher energies in the curve of Herb *et al.* is probably due to the reaction $B^{10}(p, \alpha\gamma)Be^7$. Recently Cochran *et al.*[4] have reported a broad resonance at 670 kev with a width of 390 kev.

The energies of the gamma rays produced in this reaction have been measured by several investigators. Using a cloud chamber to measure the energy of secondary electrons, Fowler, Gaerttner, and Lauritsen[5] found gamma-ray lines at 4.3, 11.8, and 16.6 Mev, with relative intensities of 7:7:1. The measurements were taken with a peak bombarding voltage of 850–900 kev and a thick boron target. Walker[6] has measured the gamma-ray energies with a magnetic pair spectrometer. Bombarding a thick B_4C target with 1.2 Mev protons he found $E_\gamma = 16.70$, 12.12, and 4.41 Mev. The relative intensity of the 16.7- and 12.12-Mev lines was 1:2.1, while the intensity of the 4.41-Mev line was of the same order of magnitude. At a bombarding energy of 0.52 Mev, gamma-ray lines were found at 16.34 and 11.76 Mev with a relative intensity of 1:4. Carver and Wilkinson[7] have also found a gamma ray of 12.5 Mev at a proton bombarding energy of 0.85 Mev. This measurement was made by determining the spectrum of recoil protons from the photodisintegration of the deutron.

A number of experiments have been conducted on the angular distribution and angular correlation of the gamma rays at low bombarding energies. Although earlier work indicated that the angular distribution was isotropic, more recent work has revealed an anisotropy in both the 12- and 16-Mev gamma rays. There is also a definite angular correlation between the 12- and 4-Mev gamma rays. The recent work on these phases of the reaction is summarized by Ajzenberg and Lauritsen[8] in their review article.

Another reaction for which gamma radiation is energetically possible is

$$B^{11}+H^1 \rightarrow (C^{12}) \rightarrow B^{11*}+H^1 \searrow B^{11}+\gamma.$$

The low-energy levels of B^{11} have been located quite precisely by Van Patter, Buechner, and Sperduto[9] by a magnetic analysis of the proton groups occurring in the reaction $B^{10}(d, p)B^{11}$. The only level they found with an excitation energy less than 3 Mev was at 2.138 Mev. An inelastically scattered proton group corresponding to this level has also been found at higher bombarding energies by Fulbright and Bush and by Cowie, Heydenburg, and Phillips,[10] although the gamma-ray has not previously been detected.

The only other reaction which might possibly produce gamma rays is

$$B^{11}+H^1 \rightarrow (C^{12}) \rightarrow Be^{8*}+He^4 \searrow Be^8+\gamma.$$

A gamma-emitting level at 4.9 Mev in Be^8 has been reported[11] in the reaction $Li^7(d, n)Be^{8*}$ but it has not yet been observed in any other reaction. No other low levels in Be^8 have been observed to emit gamma radiation.

We have used a scintillation counter to measure the energy of the gamma radiation produced in these reactions and have also obtained yield curves up to proton bombarding energies of about 2.8 Mev. From these measurements it has been possible to deduce some of the properties of the nuclear energy levels involved in the reactions.

II. EXPERIMENTAL PROCEDURE

The gamma-ray energies were measured by means of a sodium iodide scintillation counter. This counter consisted of a NaI(Tl) crystal $1\frac{1}{2}$ inches long and $1\frac{1}{2}$ inches in diameter mounted in a Lucite container on a selected 5819 photomultiplier. A magnesium oxide reflector surrounding the Lucite container served to improve the optical coupling between the crystal and the photomultiplier. Pulses from the photomultiplier were amplified and then analyzed by a single-channel pulse-height analyzer designed by Professor M. Sands. After a pulse-height distribution had been obtained, the gain of the system was calibrated by introducing artificial pulses, whose height could be measured to an accuracy of a few tenths of a percent, into the input of the preamplifier. This calibration was made in the neighborhood of each peak observed in the pulse-height spectrum and served to eliminate errors due to nonlinearity of the amplifier and analyzer as well as to reduce the effect of any slow drifts in the gain of the equipment.

The calibration of pulse height in terms of energy was performed by analyzing the pulse-height spectrum of some radioactive substance which emits gamma rays of known energy. For this purpose we used a number

[2] Herb, Kerst, and McKibben, Phys. Rev. **51**, 691 (1937).
[3] Curran, Dee, and Petrzilka, Proc. Roy. Soc. (London) **169**, 269 (1939).
[4] Cochran, Ryan, Givin, Kern, and Hahn, Phys. Rev. **87**, 672 (1952).
[5] Fowler, Gaerttner, and Lauritsen, Phys. Rev. **83**, 628 (1938).
[6] R. L. Walker, Phys. Rev. **79**, 172 (1950).
[7] J. H. Carver and D. H. Wilkinson, Proc. Phys. Soc. (London) **64A**, 199 (1951).
[8] F. Ajzenberg and T. Lauritsen, Revs. Modern Phys. **24**, 321 (1952).
[9] Van Patter, Buechner, and Sperduto, Phys. Rev. **82**, 248 (1951).
[10] H. W. Fulbright and R. R. Bush, Phys. Rev. **74**, 1323 (1948); Cowie, Heydenburg, and Phillips, Phys. Rev. **87**, 304 (1952).
[11] Bennett, Bonner, Richards, and Watt, Phys. Rev. **71**, 11 (1947).

of elements, including radiothorium (2.615 Mev) and Na^{22} (0.511 Mev and 1.277 Mev). In these calibrations it was assumed that the pulse height was proportional to energy. This relation had already been verified for energies up to 1.3 Mev,[12] and our work showed that it was valid to within one percent for electron energies up to 12 Mev.

The protons were accelerated in the 3-Mev electrostatic accelerator and analyzed in energy by a 90° electrostatic or magnetic analyzer. These were generally adjusted to give a resolution of 0.1 percent or better. The energy calibration of the analyzers was made in terms of the 873.5-kev resonance in $F^{19}(p, \alpha\gamma)O^{16}$ or the 993.3-kev resonance of $Al^{27}(p, \gamma)Si^{28}$. The beam current incident on the target was measured with a current integrator that has been in use for several years and has proved to be reliable to a few percent. For proton energies below 450 kev the mass-3 beam was used. Above this energy the mass-1 beam was used.

Since boron is not readily obtainable in a pure form and is difficult to evaporate without impurities being carried over from the furnace, we decided to use targets prepared by evaporating B_2O_3 on a thin tantalum backing. This material proved quite easy to evaporate in a vacuum furnace in thin layers whose thickness could be controlled fairly easily. Our first results on the gamma-ray yields with these targets showed peaks at 670, 870, and 940 kev, which seemed to corroborate the earlier work of Curran, Dee, and Petrzilka.[3] However, a closer examination showed that the position and relative yield of these peaks was exactly that to be expected from fluorine contamination. By cleaning the tantalum backing more carefully and evaporating most of the B_2O_3 in the furnace to get rid of volatile impurities before finally evaporating onto the target, we were able to prepare targets in which the fluorine contamination was generally negligible.

The relatively low melting point of B_2O_3 prevented us from using target currents of more than one or two microamperes since the targets tended to deteriorate under excessive heating. Accordingly a method was developed for preparing thin layers of pure boron by decomposing diborane (B_2H_6) on a thin sheet of tantalum.[13] This was accomplished by heating the tantalum in vacuum in an induction furnace and then admitting a small amount of diborane, which decomposed in a fairly uniform layer on the tantalum. By controlling the amount of diborane admitted to the furnace it was possible to obtain the desired target thickness. The development of these targets was not completed until most of the results on the capture radiation reaction had been obtained; consequently they were used only in the work on inelastic scattering.

[12] R. Hofstadter and J. A. McIntyre, Phys. Rev. **79**, 389 (1950).

[13] This method was developed and the targets produced by Dr. James Shoolery. The pure diborane was obtained through the courtesy of Professor Anton Burg of the University of Southern California.

III. EXPERIMENTAL RESULTS

1. $B^{11}(p, \gamma)C^{12}$ $B^{11}(p, \gamma)C^{12*}(\gamma)C^{12}$

Excitation curves for these reactions were obtained by using two scalers in parallel—one biased to count pulses from the scintillation counter larger than 8 Mev and the other set to count pulses larger than 13.5 Mev. Figure 1 shows the results of a run obtained in this manner by bombarding a B_2O_3 target that had a stopping power of 165 kev at an energy of 244 kev. The curves here show two new resonances, at 0.675 Mev and 1.388 Mev, in addition to the previously known resonance at 0.163 Mev.

The gamma radiation at the peak of each resonance was investigated by measuring the pulse-height distribution from the scintillation counter. In Figs. 2–4 are shown the results of spectra obtained at the resonances. Each of these shows the typical pulse-height distribution to be expected of a 4.45-Mev gamma ray as well as those of gamma rays near 12 and 16 Mev. It will be observed that the 16-Mev gamma ray does not show any of the peaks typical of lower-energy gamma rays. In determining the energy of this gamma ray we have arbitrarily assumed that the position of the usual pair peak should correspond to the "knee" of the curve. However, even with this assumption the energies obtained are somewhat low, hence we have placed little confidence in them. Figure 4 also shows peaks at 5.2 and 6.1 Mev which we have attributed to fluorine contamination of the target, since they correspond to two known gamma rays[14] from the reaction $F^{19}(p, \alpha\gamma)O^{16}$.

The averages of a number of energy measurements at each resonance are summarized in Table I, together with the excitation energy E_x of the compound nucleus. These results show that there is a direct gamma-ray transition to the ground state of C^{12} as well as a cascade transition through a level in C^{12} at 4.45 Mev. The fact that the sum of the energies of the two cascade gamma rays is equal to the excitation energy of the compound nucleus is to be interpreted as demonstrating the proportionality of the light output of the NaI crystal for electron energies up to 12 Mev. At higher energies wall effects and energy loss from bremsstrahlung distort the pulse-height spectrum too much for the size of crystal used here to permit accurate energy measurements to be made. A notable characteristic of these pulse-height curves is the flat region below the pair peak of the higher energy gamma rays. This makes it possible to obtain the total number of pulses produced in the crystal by extrapolating horizontally to zero pulse height and then integrating under the curve. The gamma-ray yield can then be obtained in a rather simple way by dividing the number of pulses thus

[14] R. L. Walker and B. D. McDaniel, Phys. Rev. **74**, 315 (1948); Rasmussen, Hornyak, Lauritsen, and Lauritsen, Phys. Rev. **77**, 617 (1950).

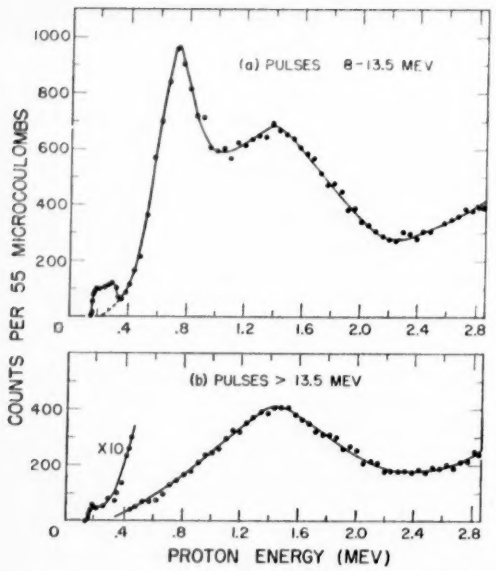

FIG. 1. Variation of yield with bombarding energy. (a) Pulses from the scintillation counter corresponding to secondary electron energies from 8 to 13.5 Mev. (b) Pulses corresponding to energies greater than 13.5 Mev.

obtained by the calculated total absorption of the crystal. This method has been checked with gamma rays of known yield and has given agreement in each case within 10 percent.

The curves shown in Fig. 1 do not represent the true excitation curves for the ground-state and cascade transitions. However, the true curves can be obtained from these in a straightforward manner from a consideration of a typical integral bias curve (Fig. 5). From the properties of the pulse-height distribution mentioned in the last paragraph it is clear that the total yield of pulses from any given gamma ray can be obtained by extrapolating the corresponding straight portion of the integral bias curve linearly to zero bias. In Fig. 5, E_1 and E_2 are the end points for the two

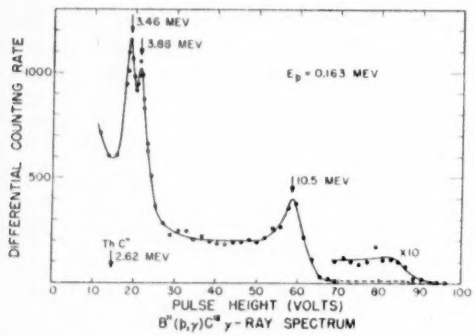

FIG. 2. Typical pulse-height distribution at the 0.163-Mev resonance.

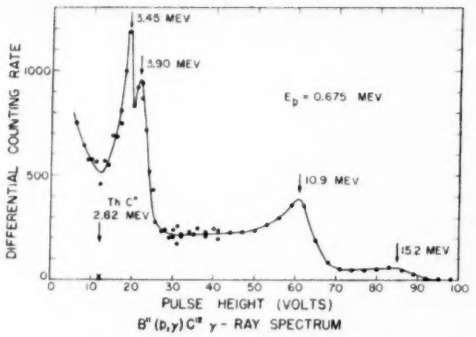

FIG. 3. Pulse-height distribution at the 0.675-Mev resonance.

high-energy gamma rays, B_1 and B_2 the biases at which the scalers were set in obtaining the curves in Fig. 1, Y_1 and Y_2 the total number of pulses from each gamma ray. Knowing B and E, and taking into account the linear variation of E with bombarding energy, which can be calculated from the Q of the reaction and a knowledge of the dynamics involved, one can correct each point of the curves in Fig. 1 to obtain the true yields $Y_{1,2}$. To aid in doing this, integral bias curves were obtained at each of the resonances and at 2 Mev. These gave a check on the positions of the end points $E_{1,2}$ as well as on the yields. The curves finally obtained, which represent the actual excitation curves for the two possible transitions, are given in Fig. 6. The total yield of gamma rays from the target was obtained by dividing the total number of pulses in the crystal by the probability that a gamma ray emitted from the target would be absorbed. Since all measurements were made at an angle of 90° to the beam this procedure actually gave $4\pi \cdot Y(90°)$. When a correction for the target thickness is applied, these curves give for the width at half-maximum and the resonance energy of the two new resonances $\Gamma = 0.33$ Mev at $E_r = 0.675$ Mev and $\Gamma = 1.27$ Mev at $E_r = 1.388$ Mev. The value

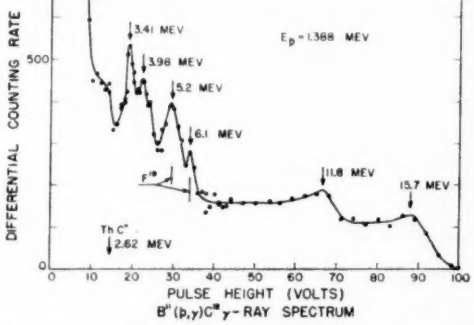

FIG. 4. Pulse-height distribution at the 1.388-Mev resonance. The peaks at 5.2 Mev and 6.1 Mev are probably from the $F^{19}(p, \alpha\gamma)O^{16}$ reaction.

for the width of the lower of these resonances is significantly less than the value of 390 kev reported by Cochran *et al.*[4] This discrepancy probably arises from the fact that they did not measure the excitation curves for the two transitions separately and therefore they were not aware of the existence of the resonance at 1.388 Mev. The distortion of their curve by this resonance would tend to increase the apparent width of the 0.675-Mev level.

The apparent intensity of the 16-Mev gamma ray at the 163-kev resonance was only seven percent of that of the cascade transition. This must be reduced to take into account the case when both the 4.45- and 11.6-Mev gamma rays are emitted in the same direction and absorbed in the crystal simultaneously. To correct for this effect, one must know both the probability of absorption in the crystal and the angular correlation of the two cascade gamma rays. Since the correlation function is not completely known we have assumed it to be isotropic in making the correction. The corrected intensity of the 16-Mev gamma ray is then four percent of the 11.6-Mev gamma ray. If there is a strong correlation for emission of the two gamma rays at 90°, the intensity of the 16-Mev gamma ray may be even lower, although it is not likely that it is zero. Investigations at the Oak Ridge National Laboratory[15] under conditions in which the correction is negligible have showed that the 16-Mev gamma-ray yield is approximately two percent of the 11.6-Mev gamma-ray yield at the resonance.

TABLE I. Gamma-ray energies at the three resonances. E_x is the excitation energy of the compound nucleus.

E_r (Mev)	E_x (Mev)	E_γ (Mev)		
0.163	16.10	4.45	11.6	
0.675	16.58	4.44	12.0	16.4
1.388	17.23	4.45	12.7	16.9

Since it has been suggested[16] that the cascade and ground-state transitions originate in different states of the compound nucleus, a careful examination of the yield curves for the two transitions was made. It showed that both were resonant at 163 kev. If they are indeed resonant at different energies, it would appear that these cannot be more than 2 kev apart. However, this conclusion is rendered somewhat uncertain by the large resonant contribution of the gamma-gamma coincidences.

The target thickness was obtained from the apparent width of the resonance at 163 kev. To obtain the variation of the stopping power with proton energy, a curve of the differential stopping cross section for B_2O_3 was prepared by extrapolation from Bethe's curve[17] for the stopping cross section of air and from the experimental data on beryllium of Warshaw[18] and Madsen and Venkateswarlu.[19] The data for air were extrapolated to oxygen as Z^4 since available stopping powers in this region generally vary in this manner as a function of the atomic number. The data for beryllium were extrapolated as Z since a calculation of the average ionization potential[20] gave the same result for boron as for

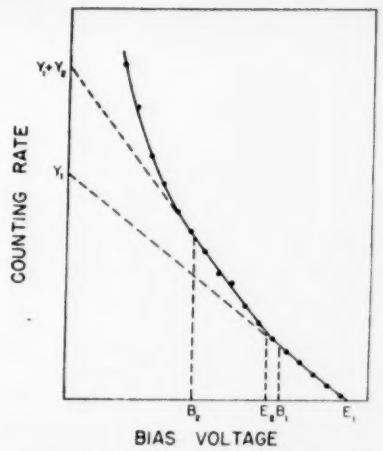

FIG. 5. Typical integral bias curve for $B^{11}(p,\gamma)C^{12}$. E_1 and E_2 are the end points of the two high-energy gamma rays. Y_1 and Y_2, which are the total number of pulses from each gamma ray, are obtained by extrapolating the corresponding straight portion of the curve linearly to zero bias. B_1 and B_2 are the biases used in obtaining the curves in Fig. 1.

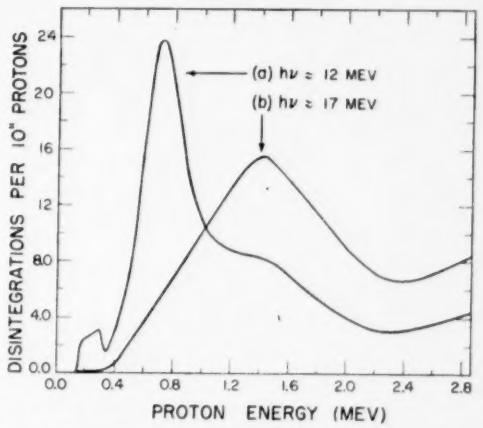

FIG. 6. True yield curve for the capture radiation, obtained from Fig. 1 by applying the corrections described in the text. The target thickness at the three resonances is given in Table II. Except at the lowest-bombarding energies, the distortion of the shape of the curve by the target thickness is small.

[15] C. D. Moak, (private communication).
[16] G. B. Arfken and L. C. Biedenbarn, Phys. Rev. **83**, 238 (1951).
[17] H. A. Bethe, Brookhaven National Laboratory Report BNL-*T*-7, June 1, 1949 (unpublished).
[18] S. D. Warshaw, Phys. Rev. **76**, 1759 (1949).
[19] C. B. Madsen and P. Venkateswarlu, Phys. Rev. **74**, 648 (1948).
[20] This calculation was performed by Dr. R. G. Thomas. We would like to thank Dr. Thomas for making the results of his calculations available to us.

TABLE II. Resonance yields and cross sections for the reactions $B^{11}(p,\gamma)C^{12}$ and $B^{11}(p,\gamma)C^{12*}(\gamma)C^{12}$. The yields (in gamma rays per proton) are given for a B_2O_3 target whose stopping power at the various resonances is given in column 3.

E_r (Mev)	Γ(Mev)	Target thickness (Mev)	$B^{11}(p,\gamma)C^{12}$ Yield (γ/p)	$B^{11}(p,\gamma)C^{12}$ σ(barns)	$B^{11}(p,\gamma)C^{12*}(\gamma)C^{12}$ Yield (γ/p)	$B^{11}(p,\gamma)C^{12*}(\gamma)C^{12}$ σ(barns)
0.163	0.005	0.165	0.098×10^{-11}	5.5×10^{-6}	2.71×10^{-11}	152×10^{-6}
0.675	0.33	0.088	$<1\times10^{-11}$	$<2.3\times10^{-6}$	20.7×10^{-11}	48×10^{-6}
1.388	1.27	0.055	15.5×10^{-11}	35×10^{-6}	8.1×10^{-11}	18×10^{-6}

beryllium. Because of the uncertainties in the method of extrapolation, as well as in the data for beryllium and air, it is expected that the stopping power for B_2O_3 may be in error by possibly 10 percent.

From a knowledge of the gamma-ray yield per proton as well as the target thickness and stopping cross section one can calculate the cross sections for the ground state and cascade transitions. These results are given in Table II. Except for the 11.6-Mev gamma-ray at the 163-kev resonance all the yields and cross sections were calculated for an isotropic angular distribution. For this case, the results of Hubbard, Nelson, and Jacobs[21] that $I(\theta)=1+0.23\cos^2\theta$ were used in correcting the data obtained at 90°. At the 0.675-Mev resonance the values given were obtained after subtracting out the effects of the higher resonance. The upper limit given here for the ground-state transition is our estimate of the maximum contribution to this resonance that would have escaped detection. These cross sections are estimated to have an accuracy of 15 percent.

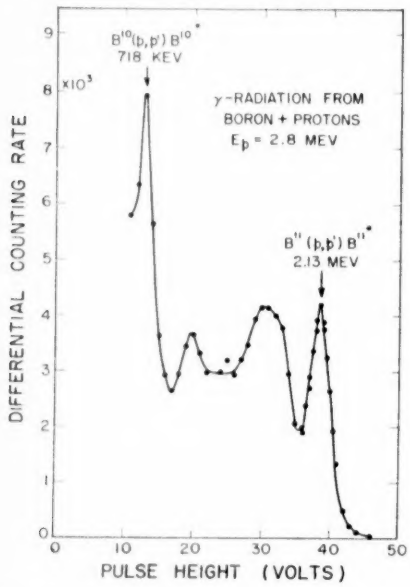

FIG. 7. Pulse-height distribution obtained at a bombarding energy of 2.8 Mev for the gamma radiation resulting from inelastic scattering.

[21] Hubbard, Nelson, and Jacobs, Phys. Rev. **87**, 378 (1952).

The same energy region was also investigated with a B_2O_3 target of a few kilovolts thickness. Several narrow, weak resonances were observed at which gamma-radiation of about 12-Mev energy was emitted. However, a search for these resonances with the improved boron targets developed later failed to reveal them. It seems likely that these originated in some target contamination, possibly sodium.

2. $B^{11}(p,p'\gamma)B^{11}$

At higher energies a new gamma ray was observed which was considerably stronger than the capture radiation. From measurements of the pulse-height distribution the energy of the gamma ray was found to be 2.13 Mev. This agrees very well with the value 2.138 Mev determined by Van Patter, Buechner, and Sperduto[9] for the energy of the first excited state of B^{11}. A typical pulse-height spectrum is shown in Fig. 7. The assignment of this radiation to a B^{11} reaction was checked by bombarding a similar target of enriched B^{10}. The gamma ray was absent then, although the 718-kev gamma ray from inelastic scattering in B^{10} (also evident in Fig. 7) was very strong.

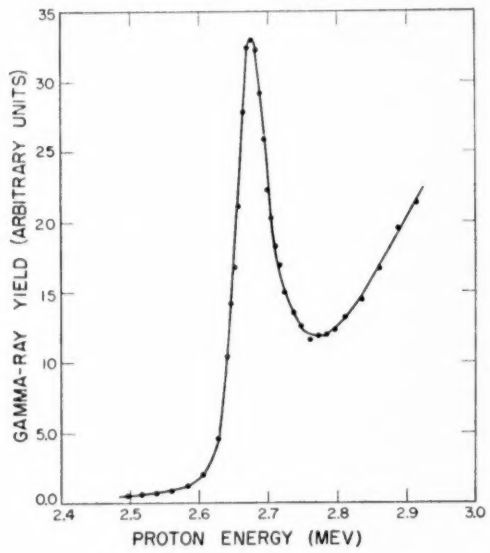

FIG. 8. Excitation curve for the reaction $B^{11}(p,p'\gamma)B^{11}$. $E_\gamma=2.13$ Mev.

The excitation curve for this reaction is shown in Fig. 8. The target used here was a thin film of normal boron whose thickness was measured by comparing the yield of the capture radiation from B^{11} with the yield from the previously calibrated B_2O_3 target. A resonance at 2.664 Mev with a width at half-maximum of $\Gamma=48$ kev was found superposed on a rapidly rising background. The cross section at resonance for this radiation is 3.1×10^{-26} cm^2 assuming an isotropic angular distribution.

Following the discovery of this resonance the excitation curve for the high-energy gamma rays was investigated closely in this region. However, there was no evidence of a resonance here for the capture radiation. A resonance cross section as large as 2×10^{-30} cm^2 would have been detectable.

3. $B^{11}(p, \alpha)Be^{8*}(\gamma)Be^8$

Although a systematic search was not made, no evidence was found for gamma radiation from the reaction $B^{11}(p, \alpha)Be^{8*}(\gamma)Be^8$.

IV. DISCUSSION

A considerable amount of work has been done on the $B^{11}(p, \alpha)$ and $B^{11}(p, \gamma)$ reactions at the 163-kev resonance.[22] The results of these experiments are all consistent with the assignment to this level of spin two and even parity (2^+), hence the nature of this level is fairly well established.

Analysis of the levels at 0.675 Mev and 1.388 Mev is aided considerably by recent results on the excitation curves for the $B^{11}(p, \alpha)$ reaction.[23] Using the (p, α) cross section one can calculate Γ_p, the width for proton emission, and from this the reduced width γ^2 of a state can be obtained. A value of γ^2 greater than $3\hbar^2/(2MR)$ indicates that the assumed orbital angular momentum can be ruled out, but since in general there are two possible solutions for Γ_p one cannot always use this means of excluding a particular angular momentum. However, given Γ_p one can calculate the radiation width Γ_γ of the level and compare this with the upper limits given by Blatt and Weisskopf.[24] Thus, there are two possibilities for limiting the range of values for the spin and parity of the resonances. In this way one can restrict the possible assignments of the 0.675-Mev resonance to $1^\pm$, $2^\pm$, and 3^+. Of these, only the values 2^- and 3^+ can be used to explain readily the fact that the ground-state gamma-ray transition and the high-energy alpha particles (α_0) going to the ground state of Be^8 are not resonant at this energy. For these two assignments the magnetic quadrupole or electric octopole radiation to the ground state of $C^{12}(0^+)$ would be expected to be very much less intense than the electric or magnetic dipole radiation to the 4.45-Mev level (2^+),[25] while the α_0 group would be forbidden since the ground state of Be^8 is 0^+. The results of a recent investigation[26] show that the gamma-ray angular distribution between 300 and 800 kev has a $\cos\theta$ term, which implies the existence of a p wave state. Whether the 0.675-Mev level is that state or whether it is the broad level indicated by the rise in the gamma-ray yield above 2.2 Mev is open to question. More detailed information on the angular distribution is needed to settle this point.

The fact that the α_0 group is resonant at 1.388 Mev shows that this level has either odd spin and parity or even spin and parity. One can further limit the range of spin and parity to 0^+ or 1^- by arguments based on the upper limits for γ^2 and Γ_γ. Finally, we can rule out the possibility of spin zero since 0–0 radiative transitions are forbidden, hence this resonance is clearly a 1^- level. This assignment is supported by the work of Thomsen *et al.*[27] on the angular distribution of the α_0 group at low bombarding energies, which required the existence of a broad 1^- level at higher energies in order to explain the observed interference terms.

To summarize, the considerations outlined above lead us to the conclusion that the resonances at 0.163 Mev, 0.675 Mev, and 1.388 Mev have spin and parity assignments of 2^+, 2^- (or 3^+), and 1^-, respectively.

From the excitation curve for inelastic scattering one can draw no such conclusions concerning the nature of the level at 2.664 Mev. However, from the work of Thirion[28] on the p-γ angular correlation in the reaction $B^{10}(d, p\gamma)B^{11}$ there is evidence that the first excited state of B^{11} has spin $\frac{1}{2}$. The gamma radiation from this state is therefore isotropic, regardless of the way in which the state is formed; hence the assumption of isotropy made in calculating the cross section for inelastic scattering is justified.

We would like to thank Professor T. Lauritsen for suggesting this problem and for his interest and help in this work. To Professor C. C. Lauritsen, Professor W. A. Fowler, and Professor R. F. Christy we would like to express our thanks for their continued interest and for their comments on the manuscript. We are also indebted to Dr. James N. Schoolery for producing the thin targets by the diborane method. One of us (T.H.) is grateful for a research fellowship at the California Institute of Technology.

[22] This work and the conclusions to be drawn from it are summarized by Ajzenberg and Lauritsen, reference 8.

[23] Beckman, Huus, and Zupančič, following paper [Phys. Rev. **91**, 606 (1953)].

[24] J. M. Blatt and V. F. Weisskopf, *Theoretical Nuclear Physics* (John Wiley and Sons, Inc., New York, 1952), p. 627.

[25] The fact that this state of C^{12} is 2^+, as expected from theory, has been quite firmly established by the work of Kraus, French, Fowler, and Lauritsen, Phys. Rev. **89**, 299 (1953).

[26] Jenkins, Cockran, Givin, Ryan, Hahn, and Kern, Bull. Am. Phys. Soc. **28**, No. 2, 12 (1953).

[27] Thomsen, Cohen, French, and Hutchinson, Proc. Phys. Soc. (London) **A65**, 745 (1952).

[28] Thirion, Compt. rend. **232**, 2418 (1951).

Excitation Curves for α Particles from B^{11} Bombarded with Protons

OLOF BECKMAN,* TORBEN HUUS, AND ČRTOMIR ZUPANČIČ†
Institute for Theoretical Physics, Copenhagen, Denmark
(Received March 31, 1953)

The spectra of the α particles emitted from B^{11} under proton bombardment have been investigated by means of a 180° double-focusing magnetic spectrometer. In the range of bombarding energies from 0.3 Mev to 1.8 Mev, the α group leading to the first excited state of Be^8 exhibits the same resonances, at 0.67 Mev and 1.4 Mev, as does the proton capture process, whereas the α group leading to the ground state of Be^8 is resonant only for the higher energy. The approximate values for the cross sections at the maxima, are in the former case, 600 millibarns and 150 millibarns, respectively, and, in the latter, 6 millibarns. Spin and parity assignments of 2^- and 1^- for the two levels, respectively, are compatible with these results.

INTRODUCTION

RECENT investigations of the proton capture processes in B^{11} [1,2] have shown the existence of two new levels in C^{12} corresponding to proton bombarding energies of 0.675 Mev and 1.39 Mev. These resonances give a stronger yield and have a much greater width than the well-known resonance at 0.163 Mev. It is, therefore, most likely that they are excited by s-wave protons, although p-wave protons cannot definitely be excluded. The simplest assumptions fitting the results of these investigations would appear to be that the two levels have odd parity and spin 2 and 1, respectively.

This assignment can be tested by investigating the excitation curves for the $B^{11}(p, \alpha)Be^8$ process in the same range of proton energies. Such measurements have not been reported so far, but the spectrum of the α-particles has been investigated by several authors[3] at various proton energies. It consists of a sharp peak (α_0) at high energy, well separated from a broader peak (α_1), which is superimposed on a continuous background (α_{12}), extending down to low energies. The α_0 peak is due to α particles leaving the Be^8 nuclei in the ground state and corresponds to a Q value of 8.57 Mev. The α_1 peak is related to the first excited level in Be^8, which has an excitation energy of 2.95 Mev and a width of 1.20 Mev.[4] The α_{12} particles come from the break-up in flight of the Be^8 nuclei in this excited state. It is generally believed that the excited state of Be^8 is a 2^+ level and the ground state a 0^+ level. The assignment suggested for the C^{12} states, therefore, implies that the α_0 particles should not be resonant at the 0.67-Mev bombarding energy.

EXPERIMENTAL PROCEDURE

A 2-Mev electrostatic generator[5] equipped with a magnetic beam separator supplied a homogeneous, collimated beam of protons. Reaction products were analyzed with a 6-Mev double-focusing magnetic α spectrometer and detected with a large proportional counter. The spectrometer is of the design described by Snyder *et al.*,[6] except that the coils are wound around the pole shoes. The stabilized current in the coils was used as a measure of the α-particle energy, after careful cycling to avoid hysteresis effects. The scale was calibrated by using the known Q values of the α processes themselves, as well as by means of scattered protons.

The maximum field available in the spectrometer was not high enough for the detection of the α_0-particles at the higher proton energies. In the measurements of the ground-state transition, a 1.2-mg/cm^2 mica foil was, therefore, placed at the entrance to the spectrometer, whereby the particle energy for the α_0 group was decreased by about 650 kev. The foil was placed as close to the target as possible in order to avoid distortion of the lines because of scattering in the foil. The influence of the energy straggling in the foil, however, had to be taken into account. The straggling should be approximately independent of the α energy and correspond to a half-width of about 50 kev. The lower end of the spectrum was limited, in most of the measurements, by the cutoff at about 2.5 Mev of the 0.6-mg/cm^2 mica window of the proportional counter. A few measurements at lower energies were made with a scintillation counter, but unfortunately certain difficulties with background counts precluded precise determinations in this region. The general trend found for the α_{12} spectrum is nevertheless believed to be correct.

The 10-mm aperture of the counter window gave an energy resolution of the spectrometer corresponding to a half-width of 1.3 percent. This large value was chosen in order to get an adequate intensity, especially in the case of the α_0 group. The solid angle of the

* On leave from the University of Uppsala, Uppsala, Sweden.
† On leave from J. Stefan Institute of Physics, Ljubljana, Yugoslavia.
[1] T. Huus and R. B. Day, Phys. Rev. **85**, 761 (1952) and Phys. Rev. **91**, 597 (1953).
[2] Cochran, Ryan, Givin, Kern, and Hahn, Phys. Rev. **87**, 672 (1952).
[3] For references, see F. Ajzenberg and T. Lauritsen, Revs. Modern Phys. **24**, 321 (1952).
[4] Ward Whaling and C. W. Li, Phys. Rev. **81**, 661 (1951).
[5] Bröström, Huus, and Tangen, Phys. Rev. **71**, 661 (1947).
[6] Snyder, Rubin, Fowler, and Lauritsen, Rev. Sci. Instr. **21**, 852 (1950).

spectrometer was $2\times10^{-4}\times4\pi$ steradian, measured by means of the decrease in intensity when a limiting stop corresponding to a known solid angle was placed at the entrance to the spectrometer.

The angle between the beam of the bombarding protons and the direction of the particles observed in the spectrometer was about 97°, and the target was placed so that the surface made angles of 60° and 37°, respectively, with these two directions. For this position the target thickness corresponded to a half-width for the α_0 particles of about twice the spectrometer resolution used. The target was prepared in the isotope separator of the Institute[7] in order to have a pure and stable B^{11} target. The content of B^{11} atoms was determined by comparison with a B_2O_3 target, the thickness of which was found both from the width of the α_0 peak and from the proton scattering profile curve. The B^{11} target proved to be equivalent to a mixed layer of an equal number of B^{11} and Ag atoms on an Ag backing and of a thickness (perpendicular to the surface) of about 22 kev for 1-Mev protons.

RESULTS

The energy spectra of the α particles were obtained from the measured curves by means of the empirical energy-current relation. An example is shown in Fig. 1 for a proton energy of 0.700 Mev, where also the α_0-energy is low enough to be within the range of the spectrometer without use of the extra foil. The positions of the peaks of course agree with the known Q values used for the adjustment, but the agreement in the width of the α_1 peak with the value given by Whaling and Li gives an independent check on their result.

The excitation curves shown in Fig. 2 have been obtained from the measured spectra by calculating the areas of the peaks. In the case of the sharp α_0 lines,

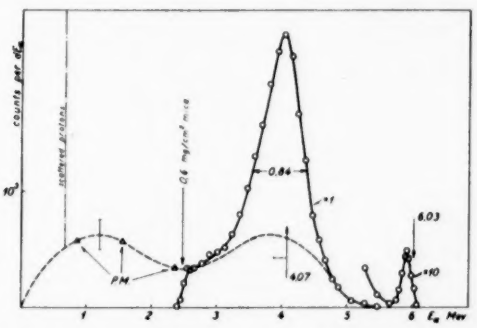

FIG. 1. Energy distribution of α particles from B^{11} bombarded with 0.700-Mev protons. The spectrum is not corrected for the finite experimental resolution. The points plotted as circles are obtained with a proportional counter as detector, whereas the triangle points (marked P.M.) at energies below the cutoff of the counter window correspond to a few less accurate measurements with a scintillation counter. The dashed curve indicates the spectrum assumed for the α particles from the break-up of Be^8. (See text.)

[7] We are grateful to Dr. J. Koch for supplying this target.

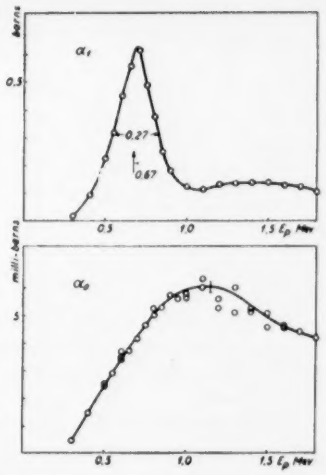

FIG. 2. Excitation curves for the process $B^{11}(p,\alpha)Be^8$ for proton energies in the range from 0.3 Mev to 1.8 Mev. α_1 corresponds to the case where Be^8 is left in the first excited state, whereas α_0 corresponds to the ground-state transition. The curves are not corrected for the influence of target thickness.

however, the areas are not calculated directly for each proton energy, because the accuracy of an individual measurement is limited by the accuracy in the field determination. Instead, the peak values have been used in combination with the average half-width of all the α_0 peaks multiplied by a correction factor, which varies smoothly with the proton energy in accordance with the dependence on the window-, straggling-, and target-widths.

It is evident from the figure that the α_1 excitation curve shows both the broad resonances found also in the capture processes and at energies which are in very good agreement with these measurements. In the case of the α_0 excitation curve, it can be seen from the figure that this process is not resonant at 0.67 Mev but only at the higher energy. There is a clear shift downward of the peak of this resonance compared to the value of 1.39 Mev found for the capture process. This shift, apparently, cannot be due to penetration effects but might be explained by interference with higher-lying levels.

In order to find the absolute yields, the theoretical value for the dispersion of the spectrometer was used in the calculation of the total number of particles in each peak. This procedure is justified, since the spectrometer does, in fact, have the double-focusing properties expected, and the field, therefore, must decrease approximately as the reciprocal of the square root of the radius. As regards the absolute values of the cross sections, it must be borne in mind that, in the case of the α_1 peak, a large contribution of α_{12} particles must be expected. This correction is not easy to apply accurately, but if one assumes that the C^{12} levels in question are formed by s-wave protons, it is obvious that, in any direction in the laboratory system, there

TABLE I. Cross sections in millibarns for proton-induced processes in B^{11}. The values given are 4π times the differential cross sections at about 90°. E_{res} is the resonance energy of the protons in Mev.

E_{res}	0.163	0.67	≃1.4
$\sigma_{p\gamma_0}$	≲0.006	≲0.002	0.035
$\sigma_{p\gamma_1}$	0.15	0.048	0.018
$\sigma_{p\alpha_0}$	0.2[a]	≲0.2	6
$\sigma_{p\alpha_1}$	10[a]	600	150

[a] See reference 8.

must be an equal number of the high and low energy component of the α_{12} pairs, i.e., the α_{12} spectra must be symmetrical around half the energy available, which is the 3-Mev excitation energy of the Be^8 level and the approximately 2-Mev kinetic energy of the Be^8 nuclei. For this reason, one should expect 50 percent of the α_{12} particles to be found in the energy region from about 2.5 Mev to 5 Mev and since the total number of α_{12} particles is twice that of the α_1 particles, it follows that only 50 percent of the particles found in this range are due to the α_1 process. This can only be the case if the α_{12} spectrum also has a peak at approximately 4 Mev, as indicated by the dashed curve in Fig. 1. This means that the low energy component of the α_{12} particles should also give a peak in the spectrum, approximately at 1 Mev. It was in order to check this point that the measurements with the photomultiplier were made. They were not in disagreement with the above considerations, and the cross sections for the α_1 process, therefore, are calculated by using only half the area of the peak between 2.5 Mev and 5 Mev. The values given are 4π times the differential cross section at 97°, both for the α_1 and the α_0 processes.

The cross sections found were expected to be correct within about 30 percent, but a measurement of the yield of protons scattered from a copper target gave a cross section nearly 50 percent smaller than that corresponding to the Rutherford scattering. It was made under the same conditions except for the use of an extra scaler, since the counting rate, even at a considerably lower current, was of the order of 10^3 counts per second. It is, however, not likely that the α-cross sections are a factor 2 too small, since the maximum found for the α_1 process in one case already is close to the highest value possible.

DISCUSSION

It is interesting to compare the measured cross sections for α emission with those for the resonance at 0.163 Mev[8–11] as well as with the capture cross sections for all three resonances.[1] This is done in Table I. Using these values and the approximate values for the total width Γ for the three levels, given in the second line of Table II, one obtains the estimates for the various partial widths Γ_z, given in the rest of the table, by means of the formula for the peak value of the resonance cross section

$$\sigma_{pz}=\omega 4\pi\lambda_p^2\Gamma_{p0}\Gamma_z/\Gamma^2.$$

For the present purpose the value $\omega\simeq\frac{1}{2}$ can be used for the spin weight factor, and as the cross sections $\sigma_{p\alpha_1}$ for all three resonances are considerably larger than the other reaction cross sections, one has, approximately,

$$\sigma_{p\alpha_1}\simeq(1.3/E_{res})y(1-y)\text{barns}$$

and

$$\Gamma_z\simeq(\sigma_{pz}/\sigma_{p\alpha_1})(1-y)\Gamma,$$

where $\Gamma_{p0}=y\Gamma$, $\Gamma_{\alpha_1}\simeq(1-y)\Gamma$, and E_{res} is expressed in Mev. There are, in general, two sets of solutions, corresponding to the cases where the main contribution to Γ comes from the proton width Γ_{p0} or from Γ_{α_1}.

In the case of the resonance at 0.163 Mev, one gets the two solutions $y\simeq1$ and $y\simeq10^{-3}$. The first possibility, however, can be excluded, as the values for the reduced proton width which would correspond to $\Gamma_{p0}=5$ kev for angular momenta of $l\geq1$ are considerably higher than the theoretical upper limit of $\gamma_{\max}\simeq3\hbar^2/2M_0R^2$, and it is known [see (3)] that the level is not formed by s waves, because the reaction products are anisotropically distributed. Taking $y=10^{-3}$, one obtains the values for the partial widths listed in the second column of Table II. If the level is a 2^+ state [see (3)], the strongest transitions should be of the type indicated in the table in the corresponding parentheses. The theoretical estimates[12] for single particle γ-ray transition probabilities agree reasonably well with the experimental radiation widths for the transitions in question. The relative smallness of the α widths as well as the large ratio between Γ_{α_1} and Γ_{α_0} cannot be accounted for theoretically in terms of the listed wave types by the penetration factors alone, since these at the energies involved are of the order unity for s-, p-, and d-wave α particles. This difficulty was pointed out at an early date by Oppenheimer and Serber,[13] who brought

TABLE II. Estimates of the partial widths for proton induced processes in B^{11}. Spin and parity assignments and the corresponding type of transitions are indicated in parentheses.

E_{res}	[a] 0.163	(2^+)	0.67	(2^-)	[b] ≃1.4	(1^-)
Γ	5 kev		0.3 Mev		≃1 Mev	
Γ_{γ_0}	≲3 ev	$(E2)$	≲0.5 ev	$(M2)$	40 ev	$(E1)$
Γ_{γ_1}	70 ev	$(M1)$	15 ev	$(E1)$	20 ev	$(E1)$
Γ_{α_0}	100 ev	(d)	≲50 ev	(no)	7 kev	(p)
Γ_{α_1}	5 kev	(s,d)	150 kev	(p,f)	200 kev	(p,f)
Γ_{p_0}	5 ev	(p)	150 kev	(s)	1 Mev	(s)

[a] $\Gamma_{p_0}:\Gamma\simeq10^{-3}$ or 1; the former value is used.
[b] $\Gamma_{p_0}:\Gamma\simeq0.2$ or 0.8; the latter value is used.

[8] The α-particles from this sharp resonance were barely detectable with the present experimental setup. Estimates for the cross sections can be obtained by comparing the information in references 9–11.
[9] J. D. Cockcroft and W. B. Lewis, Proc. Roy. Soc. (London) **154**, 261 (1936).
[10] Williams, Wells, Tate, and Hill, Phys. Rev. **51**, 434 (1937).
[11] R. B. Bowersox, Phys. Rev. **55**, 323 (1939).
[12] J. M. Blatt and V. F. Weisskopf, *Theoretical Nuclear Physics* (John Wiley and Sons, Inc., New York, 1952).
[13] J. R. Oppenheimer and R. Serber, Phys. Rev. **53**, 636 (1938).

forward the suggestion that an isotopic spin selection rule is involved. It is, in fact, just in this region of C^{12}, from 15.5 Mev and up, that the first states of isotopic spin $T=1$ are expected, and it appears not impossible that the present level, at 16.11 Mev in C^{12}, corresponds to the first excited state, at 0.947 Mev, of B^{12}. The α width would than be expected to be rather small and to depend critically on the purity of the initial and final states. Finally, it should be noted that the value given for the proton width, with the assignment used, is about 50 times smaller than corresponding to γ_{max}.

For the resonance at 0.67 Mev, there is no ambiguity in the estimate of the partial widths, since the cross section $\sigma_{p\alpha_1}$ is close to the maximum value possible ($y=\frac{1}{2}$), but as the maximum is rather insensitive to y, there is an extra uncertainty in the values given here. The value of Γ_{p_0} is, however, so large that the corresponding reduced width is equal to γ_{max} already for p-wave protons, so that it can be concluded that the level is formed by waves with $l\leq 1$, and thus most likely due to s-wave protons. If this is the case, it follows that the state must have odd parity and spin 1 or 2. The absence of α_0 and γ_0 transitions to the respective ground states (both 0^+) can then readily be explained by the assignment 2^-. This means that the γ_1 transition to the 2^+ state at 4.4 Mev in C^{12} should be predominantly of the electric dipole type. The value given for $\Gamma_{\gamma 1}$ in the table is of the same order as found for such transitions in other light nuclei. This would indicate an isotopic spin $T=1$ for the state, considering the forbiddenness of $T=0\rightarrow T=0$ transitions for $E1$ radiation and the assumed value $T=0$ for the first excited level in C^{12}. $T=1$ would also account for the relatively small value of Γ_{α_1} as compared to, for instance, the 1.2-Mev α width of the Be^8 level.

Also for the third resonance, $\sigma_{p\alpha_1}$ is comparatively close to the highest value possible, although the two sets of solutions appear to be somewhat more different than in the previous case. For this reason and because of the higher proton energy, the above argument for $l\leq 1$ is less definite here. Assuming s waves for the protons also in the present case, it follows that the level must be a 1^- state, because of the occurrence of the α_0 transition. This assignment is supported by the results of measurements on the angular distributions of the α_0 particles in the region of the resonance at 0.163 Mev,[14] which are explained in terms of interferences with a broad 1^- level at higher energies. For the calculation of the values of the partial widths listed in the last column of Table II the solution $y=0.8$ has been chosen rather than $y=0.2$, because it gives widths more similar to those of the same transitions for the previous level. As in the case of that level, the strong $E1$ transitions indicate $T=1$, which also helps explain the relatively small α widths.

The shape of the α_{12} spectra might constitute a possible difficulty in ascribing the formation of the two broad states to s-wave protons. With the above assignments, the d_{12} spectra corresponding to p-wave α_1 particles should show a maximum at about 2.5 Mev for the 2^- level and two maxima at about 0 Mev and 5 Mev for the 1^- level. The measurements indicate shapes of the spectra which are similar for both resonances and lie between these two limits, but it appears, nevertheless, possible to account for this discrepancy by a suitable contribution of f-wave α_1 particles. The amplitudes of the f waves are, however, diminished by the penetration factor, which for $l=3$ and $E_\alpha\sim 4$ Mev depends strongly on the value used for the nuclear radius, and the point is therefore left open.

It is of interest to note that the cross-section measurements can also be explained if the resonance at 0.67 Mev corresponded to a 3^+ state formed by p-wave protons. It would, therefore, be of importance to measure the angular distribution of the α_1-particles at this energy. Also measurements of the scattered protons from all the three resonances might be useful in order to check the estimates made here for the proton widths, which, in view of the inaccuracy of the cross-section values, are rather uncertain.

We are very grateful to Mr. A. P. French and Mr. G. A. Dissanaike from the Cavendish Laboratory for informing us about the results of experiments they have recently made on much the same lines as the present investigation. Compared with our results, the main differences are as follows: They find the second resonance at 0.64 Mev by direct comparison with the fluorine resonance at 0.669 Mev and suggest that the discrepancy with the resonance energy here reported might be due to our use of targets prepared by bombardment in the isotope separator. This might be true, although the way in which the boron ions penetrate into the silver target is believed more to resemble a diffusion process and the concentration of boron atoms, thus, to be highest at the surface.§ For the resonance at 0.163 Mev, they have made indirect estimates of $\sigma_{p\alpha_0}$ and $\sigma_{p\alpha_1}$, which are factors of 6 and 2.5, respectively, larger than the values listed in Table II.|| For the two broad resonances their α-emission cross-section estimates are about three times smaller than ours. This emphasizes the uncertainty in the determination of the absolute values.

In conclusion, we want to express our thanks to Professor Niels Bohr for working facilities and constant interest. We are also indebted to Professor Thomas Lauritsen whose visit to the Institute as Fulbright Lecturer has been a source of great stimulation to us. One of us (O.B.) wishes to acknowledge a grant from the Swedish Atomic Committee and another (Č.Z.) a grant from the Rask-Oersted Foundation.

[14] Thomson, Cohen, French, and Hutchinson, Proc. Phys. Soc. (London) **A65**, 745 (1952).

§ *Note added in proof:*—Paul and Clarke (Washington meeting, 1953) have found this α resonance at a proton energy of 0.68 Mev.

|| *Note added in proof:*—In a private communication, Whaling gives estimates which are even larger than those given by French.

The Analysis of Angular Correlation and Angular Distribution Data

M. E. Rose
Oak Ridge National Laboratory, Oak Ridge, Tennessee
(Received March 25, 1953)

Consideration of a number of problems which arise in the analysis of angular correlation and angular distribution data is given. These include corrections for finite angular resolution. For a source of constant strength the questions of determination of most probable counting rates, their associated errors and the determination of the most probable coefficients in the Legendre representation of the data, as well as the errors in the determination of these coefficients, are examined. A brief discussion of the corrections for a decaying source is also presented.

I. INTRODUCTION

THE importance of measurements of angular distributions in nuclear reactions and of angular correlation in nuclear cascades has become more and more evident in recent months. As experimental precision improves, the need for a systematic discussion of methods of evaluating the data becomes more pressing. Certain aspects of some of the problems which arise have been discussed.[1] However, a number of questions arise having to do with angular resolution corrections, determination of counting rates and errors in the coefficients, in terms of which the data are finally represented. The analysis of these problems is presented herewith, and the application of the results to angular correlation measurements has been made and described in an accompanying paper.[2]

In succeeding sections we take up the following problems. The effect of the finite solid angle of the detectors on the correlation function is treated in Sec. II. The results are, of course, also applicable in angular distribution measurements where only a single-counting rate need be determined. In Sec. III the question of determination of counting rates at each angle and assignment of weights to each determination is treated. In Sec. IV a discussion is given of the least squares fit of the data in terms of a series of Legendre polynomials, or if desirable, any other functions of the (scattering) angle ϑ or angle between the two radiations. This includes an account of the statistical errors in the coefficients as well as a method whereby the existence of other types of errors may be detected. Finally, in Sec. V the question of a decaying source is briefly considered.

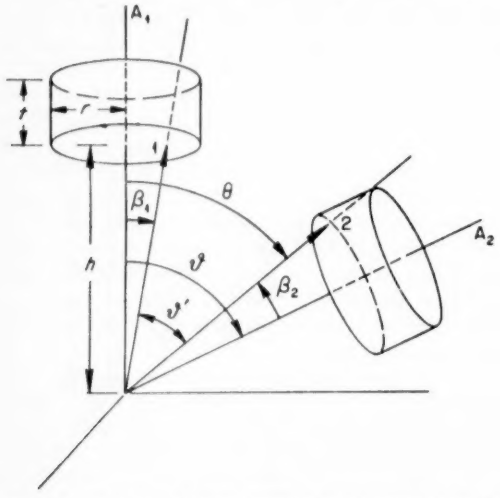

FIG. 1. Geometry for finite resolution in angular correlation. The notation also applies for singles counts as in angular distribution measurements. The azimuth angles φ_1 and φ_2 are measured with respect to the cylinder axes A_1 and A_2, respectively.

II. ANGULAR RESOLUTION CORRECTION

The results of an angular correlation measurement are most conveniently expressed in terms of a Legendre polynomial expansion. That is, the coincidence counting rate per unit solid angle $\sin\vartheta d\vartheta d\varphi$ (where the angles represent the relative orientation of the propagation vectors of the two radiations) is proportional to

$$W(\vartheta)=\sum_{\nu=0}^{\nu_m}\alpha_\nu P_\nu(\cos\vartheta). \tag{1}$$

When the detectors for the two radiations subtend finite solid angles Ω_1 and Ω_2 at the source, it is advisable to modify the theoretical correlation and compare this smeared correlation with the measured one. The geometry envisaged is shown in Fig. 1. The detectors (scintillation counters) are assumed to be crystals cut in the form of right circular cylinders with the base oriented towards the source. The source, at the origin, is on the intersection of the axes of the cylinders. In this case, as the following shows, the form of the correlation function is unchanged[3] and each coefficient α_ν becomes multiplied by an attenuation factor for which one can obtain an exact and very simple expression.

Taking into account the absorption of the radiation

[1] H. Fraunfelder in *Annual Reviews of Nuclear Science* (Annual Reviews, Inc., Stanford, 1953), Vol. 2.

[2] E. Klema and F. McGowan, this issue [Phys. Rev. **91**, 616 (1953)].

[3] This fact, which is *a priori* evident, was also brought out by S. Frankel, Phys. Rev. **83**, 673 (1951) and by E. L. Church and J. J. Kraushaar, Phys. Rev. **88**, 419 (1952). While the geometry considered here is a special one, the results presented below may constitute an incentive for the use of such wherever it is convenient to do so.

in each crystal, we introduce the following notation. The distance from the source to the front face of each crystal is h, the thickness is t, and r is the radius of the crystal. If $x(\beta)$ is the distance traversed by the radiation incident on the crystal at an angle β with the axis, the absorption is proportional to $(1-e^{-\tau x})$. Then the measured correlation function would be

$$\bar{W}(\vartheta)=\frac{\int d\Omega_1 d\Omega_2 W(\vartheta')(1-e^{-\tau x_1})(1-e^{-\tau x_2})}{\int d\Omega_1 d\Omega_2 (1-e^{-\tau x_1})(1-e^{-\tau x_2})}, \quad (2)$$

where x_1 and x_2 refer to the two crystals, $d\Omega_1$ and $d\Omega_2$ are the solid angle elements for each radiation, and ϑ' is the angle between their propagation vectors, while ϑ is the angle between the cylinder axes.

The required integrals are of the form

$$I_l=\int d\Omega_1 d\Omega_2 P_l(\cos\vartheta')(1-e^{-\tau x_1})(1-e^{-\tau x_2}), \quad (3)$$

and

$$x(\beta)=t\sec\beta \quad \text{for} \quad 0\leqslant\beta\leqslant\tan^{-1}[r/(h+t)]=\beta',$$
$$x(\beta)=r\cos\beta-h\sec\beta \quad \text{for} \quad \beta'\leqslant\beta\leqslant\tan^{-1}(r/h)=\gamma,$$

where γ is the half-angle subtended on the front face. Using the addition theorem

$$P_l(\cos\vartheta')=\frac{4\pi}{2l+1}\sum_{-l}^{l} Y_l^{m*}(1)Y_l^m(2),$$

the integration over φ_1, the azimuth of direction of radiation 1 can be carried out since x_1 is independent of φ_1. Then only the $m=0$ term contributes and

$$I_l=2\pi\int_0^{\gamma}\sin\beta_1 d\beta_1 P_l(\cos\beta_1)(1-e^{-\tau x_1})\times\int_{-\gamma}^{+\gamma}\int\sin\theta d\theta d\varphi_2 P_l(\cos\theta)(1-e^{-\tau x_2}).$$

Here θ is the angle between radiation 2 and the axis of detector 1. Applying the addition theorem once more to the spherical triangle formed by the axes of the two detectors and the direction of radiation 2 so that

$$P_l(\cos\theta)=P_l(\cos\beta_2)P_l(\cos\vartheta)+\cdots,$$

the dots indicating azimuth dependent terms, we have on integration over φ_2, for which the azimuth dependent terms do not contribute,

$$I_l=4\pi^2 P_l(\cos\vartheta)J_l(1)J_l(2),$$

where

$$J_l=\int_0^{\gamma}P_l(\cos\beta)(1-e^{-\tau x(\beta)})\sin\beta d\beta. \quad (5)$$

The result (4) confirms the statement made above with regard to the angular dependence of the correlation function. Of course, ϑ represents the angle between detector axes. The attenuation factor is

$$Q_l=(J_l/J_0)^2 \quad (6)$$

for similar detectors and for γ rays with similar absorption coefficients. For a single detector, as would be used in an angular distribution measured, with the data represented by Eq. (1), the attenuation factor would be simply

$$Q_l=J_l/J_0. \quad (6a)$$

For full absorption ($x\tau\to\infty$) we have

$$\frac{J_l}{J_0}=\frac{P_{l-1}(x_0)-x_0P_l(x_0)}{(l+1)(1-x_0)}, \quad (6b)$$

where $x_0=\cos\gamma$.

TABLE I. Attenuation coefficients J_l/J_0 for angular distribution measurements. For angular correlation measurements these coefficients should be squared or a product of two coefficients should be taken.

	$l=2$		$l=4$	
τ (cm^{-1})	$h=7$	$h=10$	$h=7$	$h=10$
0.123	0.95931	0.97823	0.86873	0.92865
0.130	0.95927	0.97821	0.86862	0.92863
0.150	0.95917	0.97818	0.86833	0.92850
0.200	0.95887	0.97808	0.86758	0.92818
0.300	0.95851	0.97790	0.86620	0.92759
1.00	0.95565	0.97672	0.85737	0.92383
2.00	0.95311	0.97567	0.84938	0.92049
3.00	0.95172	0.97510	0.84508	0.91863
5.00	0.95039	0.97457	0.84096	0.91695
10.0	0.94925	0.97410	0.83746	0.91551
40.0	0.94830	0.97373	0.83457	0.91432

In Table I numerical results are given for the case $h=7$ and 10 cm, $t=2.54$ cm and $r=1.9$ cm, for $l=2$ and 4 ($Q_0=1$) and several values of the absorption coefficient τ ranging from 0.123 cm^{-1} to 40 cm^{-1}. These values are pertinent to the experiments of Klema and McGowan.[2] While the individual J_l vary appreciably with absorption coefficient, the ratios J_l/J_0 are much less sensitive.

In the sequel it will be assumed that these angular resolution corrections have been made so that, for the considerations given below, no further reference to this effect need be made.

III. COUNTING RATE DETERMINATION

For both angular distribution and angular correlation measurements one wishes to fit a counting rate μ_i, determined at each angle of observation ϑ_i, by a function of the form exhibited in Eq. (1). There are three main questions: (1) the evaluation of the coefficients α_ν, (2) the evaluation of the errors in these coefficients, and (3) the determination of the maximum order of the Legendre polynomial ν_m, assuming that no *a priori* information on this point is available. The latter question is best discussed after questions (1) and (2) are clearly

explored. The importance of the maximum $\nu(=\nu_m)$ in angular distribution measurements is pointed up by the dependence of ν_m on the angular momentum of the incident beam of particles.[4] Its importance for angular correlations rests on the fact that $\nu_m \leqslant 2j_i,\ 2L_1,\ 2L_2$, where j_i, L_1, L_2 are, respectively, the intermediate state angular momentum and the angular momenta of radiations 1, 2.

For the determination of the counting rate μ_i, at a fixed angle, we consider two possible procedures: (a) The detector(s) is exposed to the radiation(s) for time intervals $t_1, t_2 \cdots t_s$ and the number of counts (singles or coincidences) obtained during each time interval is recorded. (b) The detector records a given number of counts n_j and the time t_j required for this is recorded. For the angular distribution case we clearly deal with a source of constant strength. For certain correlation experiments this assumption may be made with extremely negligible error.[2] Consequently, the fact that the detectors may not have 100 percent efficiency is a trivial effect: the counting rate given below is multiplied by $1/\eta$, where η is the pertinent efficiency. We consider the case of a decaying source in Sec. V. The possible presence of an appreciable background count would alter the results given below. This question is considered elsewhere[2] and will not enter in the following.

(a) Fixed Time of Counting

If the true counting rate for the source of given strength is μ, the probability for n_j counts in a time interval t_j is given by the Poisson law:

$$P_{t_j}(n_j)=\frac{(\mu t_j)^{n_j}}{n_j!}e^{-\mu t_j}, \tag{7}$$

$$\langle n_j\rangle=\mu t_j, \tag{7a}$$

$$\sigma^2(n_j)=\langle(n_j-\langle n_j\rangle)^2\rangle=\mu t_j. \tag{7b}$$

The data, represented by the numbers n_j, t_j are fitted by least squares. That is, μ' is determined so that

$$\sum_j w_j(n_j-\mu' t_j)^2=\text{minimum}. \tag{8}$$

The weights w_j are inversely proportional to $\sigma^2(n_j)$ and here, as well as in the following, the normalization of the weights is irrelevant. We take $w_j=1/\sigma^2(n_j)=1/\mu t_j$. Then (8) gives

$$\mu'=\sum_j w_j t_j n_j/\sum_j w_j t_j^2=\sum n_j/\sum t_j. \tag{9}$$

The weight attached to this determination of the counting rate can be taken to be

$$w(\mu_i')=1/\sigma^2(\mu_i')=N_i/\mu_i'^2, \tag{10}$$

using (7b). Here the index i refers to a particular angle ϑ_i.

[4] C. N. Yang, Phys. Rev. **74**, 764 (1948).

(b) Fixed Number of Counts

At the specified angle one measures the time t_j required to accumulate n_j counts. Let $P_n(t)dt$ be the probability that the nth count is recorded in the time interval t to $t+dt$. Then

$$P_n(t)dt=dt\int_0^t dt' P_{n-1}(t')K(t-t');\quad n\geqslant 1, \tag{11}$$

where the kernel $K(t-t')dt$ is the probability that a single count occurs in the time interval $t-t'$ to $t-t'+dt$. For a constant strength source this is

$$K(t-t')=\mu e^{-\mu(t-t')}. \tag{12}$$

The solution of (11) with the condition $P_1(t)=K(t)$ is

$$P_n(t)=\mu^n t^{n-1}e^{-\mu t}/(n-1)!. \tag{13}$$

Clearly $P_n(t)$ is normalized to unity and

$$\langle t\rangle=n/\mu, \tag{13a}$$

$$\sigma^2(t)=\langle(t-\langle t\rangle)^2\rangle=n/\mu^2. \tag{13b}$$

The least squares fit of the data now takes the form

$$\sum_j w_j(t_j-n_j/\mu')^2=\text{minimum},$$

where $w_j=1/\sigma^2(t_j)$. This gives

$$\mu'=\sum w_j n_j^2/\sum w_j n_j t_j=\sum n_j/\sum t_j. \tag{14}$$

In both cases (a) and (b) the most probable counting rate (for the given finite number of counts) is given by the ratio of total counts to total time.

In order to determine the weight to be associated with this counting rate determination the probability that a sequence of t_i measurements shall give $T=\sum_j t_j = (\sum_j n_j)/\mu'$ in an interval dT must be obtained. This problem is slightly different from that considered in (a) above since now the statistically varying quantities t_j are in the denominator of (14). The required probability is

$$P_{N_i}(T)=\mu^{N_i}\frac{T^{N_i-1}e^{-\mu T}}{(N_i-1)!} \tag{15}$$

from (13), and $N_i=\sum_j n_j$. Then the probability that a measurement of the counting rate gives a value μ' to $\mu'+d\mu'$ is

$$P(\mu')d\mu'=P_{N_i}(T)\,|dT/d\mu'|=(N_i/\mu')^2 P_{N_i}(T), \tag{16}$$

and $T=N_i/\mu'$. For convenience a subscript i is omitted from μ' and μ here and above. From this (normalized) probability function we obtain

$$\langle\mu_i'\rangle=\mu_i N_i/(N_i-1)\approx\mu_i, \tag{16a}$$

$$\sigma^2(\mu_i')=\langle(\mu_i'-\langle\mu_i'\rangle)^2\rangle = \mu_i^2 N_i^2/(N_i-1)^2(N_i-2)\approx\mu_i^2/N_i. \tag{16b}$$

For the weight $w(\mu_i')$ we may take

$$w(\mu_i')=N_i/\mu_i'^2. \tag{16c}$$

In (16b) and (16c) we consider that $N_i \gg 1$ at each angle. Of course, for $N_i \to \infty$ we obtain $\langle \mu' \rangle = \mu$ and $\sigma^2(\mu') = 0$. In fact, $P(\mu')$ is then equal to $\delta(\mu' - \mu)$, as is to be expected. It will be noted that for large N_i there is essentially no difference between procedures (a) and (b).

IV. LEAST SQUARES FIT OF THE DATA

Once the counting rates are determined at each angle, and thereby, the associated weights determined, one may proceed to problems (1) and (2) mentioned at the beginning of the previous section. A discussion of problem (3) can then be given (see end of this section).

The determination of the coefficients α_ν is now to be carried by replacing $W(\vartheta)$ in Eq. (1) by $\mu(\vartheta)$, or more specifically,

$$\mu_i = \mu(\vartheta_i) = \sum_\lambda \alpha_\lambda A_{i\lambda}, \tag{17}$$

where $A_{i\lambda} = \varphi_\lambda(\cos\vartheta_i)$ and φ_λ may be taken to be P_λ or any other function. In (17) the left and right sides are not equal but what is meant is that the right side represents $\mu(\vartheta_i)$ as closely as possible. The prime on the symbol μ' has been dropped. The measurement of ϑ_i, it will be assumed, contains no error.

Let m be the number of angles at which data is taken and l be the number of coefficients α_λ which one assumes. Then $l = \nu_m + 1$ in the angular distribution case and in the angular correlation case, since ν is even, $l = \frac{1}{2}\nu_m + 1$. In any case $m \geqslant l$.

The coefficients α_λ, which are the most probable values for the given data, are determined from

$$\sum_i w_i(\mu_i - \sum_\lambda \alpha_\lambda A_{i\lambda})^2 = \text{minimum},$$

yielding the normal equations

$$\sum_i w_i(\mu_i - \sum_\lambda \alpha_\lambda A_{i\lambda}) A_{i\gamma} = 0. \tag{18}$$

Here w_i is given by (10) or (16c). Equation (18) and subsequent results are more compactly expressed by introducing matrix notation. We define a square $(l \times l)$ matrix C whose elements are

$$C_{\lambda\gamma} = \sum_i w_i A_{i\lambda} A_{i\gamma} = C_{\gamma\lambda}.$$

That is,

$$C = \tilde{A} w A,$$

where w is the diagonal $(m \times m)$ matrix with elements w_i and A is the $m \times l$ matrix (nonsquare, in general). The tilde means transposed. Further let $\boldsymbol{\xi}$ be the l component vector

$$\boldsymbol{\xi} = \tilde{A} w \boldsymbol{\mu},$$

where $\boldsymbol{\mu}$ is the m component vector with components μ_i. Then

$$C\boldsymbol{\alpha} = \boldsymbol{\xi},$$

or, in detail,

$$\alpha_\lambda = \sum_\gamma C_{\lambda\gamma}^{-1} \xi_\gamma. \tag{19}$$

Of course, C^{-1} is constructed by forming a matrix k whose λ, ν element is the cofactor of $C_{\lambda\nu}$ in the determinant $|C|$ and dividing by $|C|$. Note, that k like C is symmetric.

Equation (19) gives the coefficients α_λ. It is seen that the normalization of the weights does not enter; that is, if $w_i = b/\sigma^2(\mu_i)$, the constant b cancels out. From (19) we observe that $\boldsymbol{\alpha}$ is a linear homogeneous function of the counting rates μ_i. Hence, due to the existence of a variation in μ_i, expressed by the mean square deviation $\sigma^2(\mu_i)$, there will be a corresponding mean square deviation in α_λ. Writing

$$\alpha_\lambda = \sum_i B_{\lambda i} w_i \mu_i,$$

where

$$B_{\lambda i} = \sum_\nu C_{\nu\lambda}^{-1} A_{i\nu},$$

we have

$$\begin{aligned}\sigma^2(\alpha_\lambda) &= \sum_i B_{\lambda i}^2 w_i^2 \sigma^2(\mu_i) \\ &= b \sum_{i\nu\gamma} C_{\nu\lambda}^{-1} C_{\gamma\lambda}^{-1} A_{i\nu} A_{i\gamma} w_i \\ &= b C_{\lambda\lambda}^{-1}.\end{aligned}$$

Consequently, if we define a matrix G by

$$G_{\lambda\gamma} = \sum_i A_{i\lambda} A_{i\gamma} / \sigma^2(\mu_i) = G_{\gamma\lambda},$$

then

$$\sigma^2(\alpha_\lambda) = G_{\lambda\lambda}^{-1}. \tag{20}$$

That is, the mean square deviation of the coefficient α_λ is given by the λ, λ diagonal matrix element of the inverse of G and this does not depend on the normalization b.[5] However, $\sigma^2(\alpha_\lambda)$ is linear homogeneous in the $\sigma^2(\mu_i)$ as it should be.

Now the square error given by (20) is a measure of the deviations to be expected on purely statistical grounds. Of course, in an actual experiment other sources of error may exist. A clue to the existence of extraneous errors is provided by comparing (20) with the mean square error defined in a different manner. This mean square error, to which we now turn our attention, is based on a comparison between the true coefficients, which we denote by α_λ^0, and the least squares value α_λ given by (19).

Consider the residuals E_i between the measured values of μ_i and the true values represented by $\sum_\lambda \alpha_\lambda^0 A_{i\lambda}$. For convenience we reduce the equations to the form in which the weights are effectively unity by introducing the notation

$$z_i = w_i^{\frac{1}{2}} \mu_i, \tag{21a}$$

$$a_{i\lambda} = w_i^{\frac{1}{2}} A_{i\lambda}, \quad b_{\lambda i} = w_i^{\frac{1}{2}} B_{\lambda i}. \tag{21b}$$

Then, the residual E_i are given by

$$E_i = \sum_\lambda \alpha_\lambda^0 a_{i\lambda} - z_i. \tag{22a}$$

The residual between the measured values and the least squares curve are

$$\epsilon_i = \sum_\lambda \alpha_\lambda a_{i\lambda} - z_i. \tag{22b}$$

[5] The result expressed by Eq. (20) is not new. However, it has been reproduced here for two reasons. First, it seems not to be widely known and secondly the customary derivations of the result are somewhat beclouded by a cumbersome notation. The same remark applies to the result given in (30) below.

We make use of the following:

$$\sum_i a_{i\gamma} e_i = \sum_\lambda \alpha_\lambda C_{\gamma\lambda} - \xi_\gamma = 0, \tag{23a}$$

$$\sum_i a_{i\lambda} b_{\gamma i} = \sum_i a_{i\lambda} \sum_\nu C_{\nu\gamma}^{-1} a_{i\nu} = \delta_{\lambda\gamma}, \tag{23b}$$

$$\sum_i e_i b_{\gamma i} = \sum_i e_i \sum_\nu C_{\nu\gamma}^{-1} a_{i\nu} = 0, \tag{23c}$$

where the last result follows from (23a).

Then, from (22a) and (22b),

$$\sum_i (E_i e_i - e_i^2) = \sum_{i\lambda} (\alpha_\lambda^0 - \alpha_\lambda) a_{i\lambda} e_i = 0,$$

by (23a). Also, using the above,

$$\sum_i (E_i^2 - e_i E_i) = \sum_i (E_i^2 - e_i^2) = \sum_\lambda (\alpha_\lambda^0 - \alpha_\lambda) \sum_i E_i a_{i\lambda}, \tag{24}$$

and

$$\sum_i (E_i - e_i) b_{\gamma i} = \sum_i E_i b_{\gamma i} = \sum_{i\lambda} (\alpha_\lambda^0 - \alpha_\lambda) a_{i\lambda} b_{\gamma i} = \alpha_\gamma^0 - \alpha_\gamma, \tag{25}$$

by (23c) and (23b).

If a large number of measurements of the coefficients α_γ are carried out and the values of $(\alpha_\gamma^0 - \alpha_\gamma)$ is squared and averaged over this sequence of experiments, we would obtain the following for the mean square difference of true and least squares coefficients

$$\langle (\alpha_\gamma - \alpha_\gamma^0)^2 \rangle_{Av} = \sum_{ij} \langle E_i E_j \rangle_{Av} b_{\gamma i} b_{\gamma j}.$$

Here, and below, $\langle\ \rangle_{Av}$ is used to denote the average over a large number of experiments. Now, since E_i and E_j are uncorrelated (if $i \neq j$)

$$\langle E_i E_j \rangle_{Av} = \langle E_i^2 \rangle_{Av} \delta_{ij} = \epsilon^2 \delta_{ij}.$$

Hence

$$\langle (\alpha_\gamma - \alpha_\gamma^0)^2 \rangle_{Av} = \epsilon^2 \sum_i b_{\gamma i}^2 = \epsilon^2 C_{\gamma\gamma}^{-1}. \tag{26}$$

To calculate the mean square residual ϵ^2, we have from (24) and (25) that

$$\sum_i (E_i^2 - v_i^2) = \sum_{\lambda ij} E_i E_j b_{\lambda i} a_{j\lambda}.$$

Then, taking averages in the above sense,

$$\sum_i \epsilon^2 - \sum_i \langle v_i^2 \rangle_{Av} = \epsilon^2 \sum_{\lambda i} b_{\lambda i} a_{i\lambda} = l\epsilon^2,$$

from (23b). Hence

$$\epsilon^2 = \sum_i \langle v_i^2 \rangle_{Av} / (m - l). \tag{27}$$

Since one does not carry out the large number of experiments envisaged in the averaging process, the mean square $\langle v_i^2 \rangle_{Av}$ is replaced by the sum of squares of the actual residuals:

$$\sum_i \langle v_i^2 \rangle_{Av} \approx \sum_i w_i (\mu_i - \sum_\lambda \alpha_\lambda A_{i\lambda})^2 = \sum_i v_i^2, \tag{28}$$

where α_λ are the most probable (least squares) coefficients from (19). Inserting (19) in (28) we find

$$\sum_i v_i^2 = \sum_i w_i \mu_i^2 - \boldsymbol{\alpha} \cdot \boldsymbol{\xi}. \tag{29}$$

The mean square error in α_λ is then

$$\langle (\alpha_\lambda - \alpha_\lambda^0)^2 \rangle_{Av} \cong [\sum_i v_i^2 / (m - l)] C_{\lambda\lambda}^{-1}, \tag{30}$$

where the result (29) is to be used. Since this result is independent of a normalization constant b, one may use $w_i = 1/\sigma^2(\mu_i)$ throughout. It is clear that for the purpose of quoting mean square errors like that given in (30) one should have an excess of points of observation, i.e., $m > l$.

From the manner in which the result (30) is constructed it would seem that essentially all sources of error are included and not just the statistical errors $\sigma^2(\mu_i)$. In fact $\langle (\alpha_\lambda - \alpha_\lambda^0)^2 \rangle_{Av}$ is independent of the size of the $\sigma^2(\mu_i)$ and depends only on ratios of these mean square deviations. Thus, a comparison of (30) and (20) would serve to indicate the importance of non-statistical errors. A value of ϵ appreciably greater than unity implies that errors other than those due to a finite number of counts, taken in the whole experiment, are of importance. If one can be reasonably sure that systematic errors are eliminated, a value of ϵ much greater than unity would presumably imply that the function used in the least squares fit is incorrect. A possible procedure would be to increase ν_m by one unit, or by two units for the correlation experiment, and reanalyze the results. When $\alpha_{\nu_m} \approx 0$, that is, when $\alpha_{\nu_m}^2 / \sigma^2(\alpha_{\nu_m}) \approx 1$ with the assumed ν_m, one can take the maximum ν to be this value of ν_m decreased by one (or two) units. Of course, for most practical cases of angular correlation it is necessary to distinguish only between $\nu_m = 2$ and 4.

V. MEASUREMENTS WITH A DECAYING SOURCE

In the foregoing it was assumed that for an angular correlation, the lifetime of the source is large compared to the time of measurement. This assumption is well-fulfilled, for example, in the cases studied by Klema and McGowan.[2] If this is not the case corrections must be made for depletion of source strength during the course of the measurements. The explicit problem considered in this section is the optimal procedure for determining the lifetime of the source.

Consider a source which initially has N radioactive nuclei. In most cases N is essentially unknown and is eventually eliminated from the final results. The procedure considered is that one records the time intervals at which n, $2n$, $\cdots rn$ counts are obtained. For a source with N' radioactive nuclei, the probability for a decay between time t to $t+dt$ is

$$p\,dt = N' \mu_0 e^{-N'\mu_0 t} dt. \tag{31}$$

For the moment we assume detector efficiency $\eta = 1$. The probability $P(n, N; t)$ that the nth count occurs in the interval dt at t is obtained from the integro-difference equation (11) with the kernel

$$K(t - t') = (N - n + 1) \mu_0 e^{-(N-n+1)\mu_0 (t-t')}.$$

The solution of (11) is subject to $P(1, N; t) = N \mu_0 e^{-N\mu_0 t}$.

Then the required probability is[6]

$$P(n, N; t)=\frac{N!\mu_0}{(n-1)!(N-n)!}\times[1-e^{-\mu_0 t}]^{n-1}e^{-(N-n+1)\mu_0 t}. \quad (32)$$

For $n\mu_0 t\ll 1$ and $n\ll N$ this reduces to (13) with $\mu=N\mu_0$.

For the sequence of events that n counts are collected in τ_s to $\tau_s+d\tau_s$, $s=1\cdots r$, so that nr is the total number of counts recorded, the probability is $P(\tau_1, \tau_2\cdots\tau_r)d\tau_1 d\tau_2\cdots d\tau_r$ and

$$P(\tau_1, \tau_2\cdots\tau_r)=\prod_{s=1}^{r}P(n, N-sn+n; \tau_s)$$

$$=\frac{N!\mu_0{}^r}{(n-1)!^r(N-nr)!}\exp[-\sum_{s=1}^{r}(N-ns+1)\mu_0\tau_s]\times\prod_{s=1}^{r}[1-e^{-\mu_0\tau_s}]^{n-1}. \quad (33)$$

The most probable counting rate μ_0 is obtained by eliminating N from the equations

$$\partial P/\partial N=0, \quad \partial P/\partial\mu_0=0.$$

These give

$$\sum_{\nu=1}^{nr}\frac{1}{N-\nu+1}=\mu_0\sum_{s=1}^{r}\tau_s=\mu_0 T, \quad (34a)$$

and

$$\Phi\equiv\sum_{s=1}^{r}\frac{\mu_0\tau_s}{e^{\mu_0\tau_s}-1}=\frac{1}{n-1}\{-r+\sum_{s=1}^{r}(N-ns+1)\mu_0\tau_s\}. \quad (34b)$$

Introducing

$$\langle r\rangle=\frac{1}{T}\sum_{s=1}^{r}s\tau_s,$$

the resulting equation, after elimination of N is,

$$\sum_{\nu=1}^{nr}[n\mu_0 T\langle r\rangle+r+(n-1)\Phi-\nu\mu_0 T]^{-1}=1. \quad (35)$$

The given data fix T, $\langle r\rangle$ and Φ as a function of μ_0. Then the root of (35) fixes the most probable counting rate μ_0.

The result (35) may be considered in the case $n=1$. Then we obtain from (34b)

$$(r/\mu_0 T)-(N+1)=-\langle r\rangle. \quad (36a)$$

If in (34a) the sum is replaced by an integral (corresponding to replacing $N!$ by $N\log N-N$), one has

$$(N-nr)/N\cong e^{-\mu_0 T}.$$

Using this result and $n=1$ in (36a) there results

$$\frac{1}{\mu_0 T}-\frac{1}{e^{\mu_0 T}-1}=\frac{1}{r}(r+1-\langle r\rangle). \quad (36b)$$

If we introduce

$$t_s=\sum_{1}^{s}\tau_i,$$

this becomes

$$\frac{1}{\mu_0 T}-\frac{1}{e^{\mu_0 T}-1}=\frac{1}{rT}\sum_{s=1}^{r}t_s. \quad (36c)$$

Equation (36c) is in the form given for this case by Hole[6] and Peierls.[7]

Since nr is usually a very large number compared to unity, the sum involved in (35) is rather difficult to evaluate. Replacement of the sum by an integral is permissible, leading to a comparatively simple result for μ_0, only if the summand never becomes large. This corresponds to values of $N\gg nr$. Then, with $nr\gg 1$,

$$(n-1)\Phi+r+n\mu_0 T\langle r\rangle\cong\mu_0 Tnre^{\mu_0 T}/(e^{\mu_0 T}-1). \quad (37)$$

For counter efficiency $\eta\neq 1$ one must replace the probability function (32) by[6]

$$P(n, N, \eta; t)=\frac{\mu_0 N!\eta^n}{(n-1)!(N-n)!}e^{-\mu_0 t}(1-e^{-\mu_0 t})^{n-1}\times[1-\eta(1-e^{-\mu_0 t})]^{N-n}. \quad (38)$$

For $n\ll N$ and $n\mu_0 t\ll 1$ this reduces to (13) with $\mu=N\mu_0\eta$. The probability of the sequence of events: n counts in τ_1 to $\tau_1+d\tau_1\cdots n$ counts in τ_r to $\tau_r+d\tau_r$ is (per $d\tau_1 d\tau_2\cdots d\tau_r$)

$$P(\tau_1\tau_2\cdots\tau_r)=\prod_{s=1}^{r}P(n, N-sn+n, \eta; \tau_s)$$

$$=\frac{\mu_0{}^r\eta^{nr}N!}{(n-1)!^r(N-nr)!}e^{-\mu_0 t}\prod_{s=1}^{r}(1-e^{-\mu_0\tau_s})^{n-1}\times\prod_{s=1}^{r}[1-\eta(1-e^{-\mu_0\tau_s})]^{N-ns}. \quad (39)$$

Application of the conditions $\partial P/\partial N=0$ and $\partial P/\partial\mu_0=0$ and elimination of N again gives a determining equation for μ_0. While the procedure for obtaining a numerical value for μ_0 from the ensuing result is essentially no more difficult than in the case of unit efficiency, the analytical form is even more cumbersome and we need give no further details. Once μ_0 is found, the source depletion in a time t could be obtained from $1-e^{-\mu_0 t}$.

[6] This result has previously been given by N. Hole, Arkiv. Mat. Astron. Fysik **34B**, No. 12 (1948).

[7] R. Peierls, Proc. Roy. Soc. (London) **149**, 467 (1935).

Gamma-Gamma Angular Correlation in Ni^{60}

E. D. KLEMA AND F. K. MCGOWAN
Oak Ridge National Laboratory, Oak Ridge, Tennessee
(Received March 25, 1953)

The angular correlation of the gamma rays emitted in cascade from the excited states of Ni^{60} has been measured at increments of 10° from 90° to 270° with automatic apparatus using sodium iodide detectors and 5819 photomultipliers. For a dilute $CoCl_2$ source, the correlation obtained is $W(\theta)=1+(0.131\pm0.017)\cos^2\theta+(0.024\pm0.017)\cos^4\theta$. The anisotropy, $(\alpha_2+\alpha_4)/\alpha_0\equiv R$, where $W(\theta)=\alpha_0+\alpha_2\cos^2\theta+\alpha_4\cos^4\theta$, is 0.1557 ±0.0010. The expected value of R, taking the finite angular resolution of the apparatus into account, is 0.1517. A change in the anisotropy to a value of 0.1453±0.0023 due to a chemical change in the source was observed.

I. INTRODUCTION

THE angular correlation of the gamma-rays emitted in cascade from the excited states of Ni^{60} is known from experimental and theoretical considerations.[1] The present investigation was undertaken to find out how accurately the apparatus in use at Oak Ridge can measure the coefficients in the correlation function. This information is of considerable interest at present because of the finding of mixed radiation in parity-unfavored transitions.[2] The precision of the determination of the coefficients determines the limits which can be assigned to the mixing ratios. The Ni^{60} correlation has been measured by several investigators[3] since the pioneer work by Brady and Deutsch. Recently Aeppli *et al.*[4] have measured the anisotropy precisely; and their value, 0.148±0.002, is considerably lower than the expected theoretical value of 0.167.

II. EXPERIMENTAL APPARATUS

The apparatus used in the present experiments is a modification of that described previously.[5] The detectors are sodium iodide crystals $1\frac{1}{2}$ in. in diameter and 1 in. long, and the source is at the intersection of the axes of the cylindrical crystals at a distance of 7 centimeters from the front face of each crystal. The fractional acceptance of the windows of the differential analyzers included only the full-energy peaks of the two gamma rays in the cascade. The electronic equipment is the same as that described previously, but the apparatus has been equipped with a motor to change the angle between the two detectors. In the present experiment, data were taken automatically at 10° increments from 90° to 270°. The apparatus takes the data in sequence from 90° to 270° and then from 270° back to 90°, so that the point at 180° has only about half as much data as the other angles in the least squares fit of the data.

III. EXPERIMENTAL METHOD AND ANALYSIS OF DATA

At any given angle θ_i between the two detectors, the experimental method used was as follows: 4096 coincidence counts between the detectors were counted. The receipt of the 4096th count furnished a signal which started a sequence in which the time required for the collection of the counts was printed on a paper tape by a printing timer and the total number of singles counts of the fixed detector and of the moveable detector were also stamped on paper tapes.

The data for making the correction due to the random coincidences were obtained in a similar manner with the pulses from one detector delayed by 0.5 microsecond. In the present experiments the random rate was about 20 percent of the gross coincidence rate.

The above pieces of information are sufficient to enable one to combine the data for the various passes over a given angle properly, correcting for changes in the gain of the two detectors and of the fractional acceptance of the windows of the differential analyzers. Let us call the total counts for the jth pass over the angle θ_i, M_j and F_j for the moveable and fixed detectors, respectively; the number of coincidence counts observed C_j, and the time required for the collection of the C_j counts t_j. If the disintegration rate of the source is a constant N_0, then the total coincidence rate of the true coincidences plus the random coincidences is given by

$$\mu_j=N_0\epsilon_F\epsilon_M W(\theta_i)+N_0\epsilon_F N_0\epsilon_M 2\tau,$$

where ϵ_M and ϵ_F contain the solid angles of the detectors, the detector efficiencies, and the fractional acceptance of the windows of the differential analyzers,

$$W(\theta_i)=\alpha_0+\alpha_2\cos^2\theta_i+\alpha_4\cos^4\theta_i,$$

and τ is the resolving time of the coincidence circuit.

The singles counting rates in the fixed and moveable channels are $N_{0F}=N_0\epsilon_F$ and $N_{0M}=N_0\epsilon_M$, respectively. Thus the times t_j vary inversely with the product of

[1] E. L. Brady and M. Deutsch, Phys. Rev. **78**, 558 (1950).
[2] Aeppli, Frauenfelder, and Walter, Helv. Phys. Acta **24**, 335 (1951); E. D. Klema and F. K. McGowan, Phys. Rev. **87**, 524 (1952); R. M. Steffen and W. Zobel, Phys. Rev. **88**, 170 (1952); R. M. Steffen, Phys. Rev. **89**, 665 (1953).
[3] J. R. Beyster and M. L. Wiedenbeck, Phys. Rev. **79**, 411 (1950); R. M. Steffen, Phys. Rev. **80**, 115 (1950); H. E. Petch and M. E. Johns, Phys. Rev. **80**, 478 (1950); B. L. Robinson and L. Madansky, Phys. Rev. **84**, 604 (1951).
[4] Aeppli, Frauenfelder, Heer, and Rüetschi, Phys. Rev. **87**, 379 (1952).
[5] McGowan, Klema, and Bell, Phys. Rev. **85**, 152 (1952).

the channel rates, M_jF_j/t_j^2. One may then correct each t_j to an arbitrary fixed product of the channel rates $N_{0F}N_{0M}$ as follows:

$$\text{Corrected } t_j \equiv t_{j0} = \frac{t_j(M_jF_j/t_j^2)}{N_{0F}N_{0M}} = \frac{1}{N_{0F}N_{0M}}\left(\frac{M_jF_j}{t_j}\right).$$

If n passes are made over the angle θ_i, the corrected gross coincidence rate is given by

$$(\mu_{i0})_{\text{gross}} = nC_j \Big/ \sum_{j=1}^{n} t_{j0}.$$

Similarly, if m measurements are made of the random coincidence rate, collecting R_j coincidence counts each time, the corrected random rate is

$$(\mu_0)_{\text{random}} = N_{0F}N_{0M}mR_j \Big/ \sum_{j=1}^{m}\left(\frac{M_{j\text{ random}}F_{j\text{ random}}}{t_{j\text{ random}}}\right).$$

We have finally for the corrected true coincidence rate at the angle θ_i,

$$\mu_{i0} = (\mu_{i0})_{\text{gross}} - (\mu_0)_{\text{random}}.$$

The variance of this rate, $\sigma^2(\mu_{i0})$, is given by

$$\sigma^2(\mu_{i0}) = (\mu_{i0})^2_{\text{gross}}/nC_j + (\mu_0)^2_{\text{random}}/mR_j.$$

The weighting factor, $w(\mu_{i0})$, to be used with μ_{i0} in the least squares fitting of the data is then $w(\mu_{i0}) = 1/[\sigma^2(\mu_{i0})]$.

IV. EXPERIMENTAL RESULTS

The data obtained in the various runs of this experiment are shown in Table I. The individual runs are based on total coincidence counts of from 2×10^5 to 4×10^5. The first data obtained with a dilute solution source were those shown for August 27. This source consisted of 5 microliters of $CoCl_2$ solution in a Lucite holder. After this run a continuous decrease in the anisotropy was noticed for a time, the values obtained being 0.148, 0.145, and 0.141. Then the anisotropy remained constant as is shown by the data in the table for the runs of September 4th through September 12th. It was hypothesized that this change in the anisotropy was caused by the fact that the liquid in the bottom of the Lucite source holder had disappeared, and that the chemical state of the source had changed (probably the cobalt changed from the divalent to the trivalent state). To test this hypothesis, 25 microliters of water were added to the source; and the data shown for the runs from October 3 through October 10 were obtained. Finally a dry source of $CoCl_2$ was prepared, and the anisotropy found with this source for the runs of October 13 and October 15 agreed with that obtained with the dilute solution source.

The standard deviations of the R's shown in Table I have been obtained from those defined in Eq. (30) of the accompanying paper[6] as follows:

TABLE I. Experimental values of the anisotropy, $R=(\alpha_2+\alpha_4)/\alpha_0$, and the coefficients of the expansion $W(\theta)=\alpha_0+\alpha_2\cos^2\theta+\alpha_4\cos^4\theta$ obtained for the various runs. The $\sigma(R)$ is the standard deviation of R in each case. The ϵ^2 is a figure of merit for each experiment; it is defined in the accompanying paper (see reference 6).

Date	R	$\sigma(R)$	ϵ^2	α_2/α_0	α_4/α_0
August 27	0.1564	0.0072	0.898	0.201	−0.045
October 3	0.1554	0.0059	0.875	0.0936	0.62
October 6	0.1526	0.0082	1.088	0.156	−0.0032
October 8	0.1572	0.0091	1.564	0.125	0.032
October 10	0.1300	0.0071	1.124	0.0840	0.046
October 13	0.1533	0.0058	0.656	0.115	0.038
October 15	0.1592	0.0070	0.957	0.0972	0.062
September 4	0.1406	0.0078	0.691	0.109	0.032
September 8	0.1484	0.0034	0.234	0.113	0.035
September 10	0.1500	0.0058	0.679	0.132	0.018
September 12	0.1423	0.0047	0.688	0.106	0.036

$$\text{variance}\left(\frac{\alpha_2+\alpha_4}{\alpha_0}\right) \equiv V\left(\frac{\alpha_2+\alpha_4}{\alpha_0}\right) \cong \left(\frac{\alpha_2+\alpha_4}{\alpha_0}\right)^2 \times\left[\frac{V(\alpha_2)+V(\alpha_4)+2\,\text{Cov}(\alpha_2,\alpha_4)}{(\alpha_2+\alpha_4)^2} + \frac{V(\alpha_0)}{\alpha_0^2} - 2\frac{\text{Cov}(\alpha_0,\alpha_2)+\text{Cov}(\alpha_2,\alpha_4)}{\alpha_0(\alpha_2+\alpha_4)}\right],$$

where

$$V(\alpha_\lambda) = \epsilon^2\sigma^2(\alpha_\lambda),$$

and

$$\text{covariance}(\alpha_\lambda,\alpha_{\lambda'}) \equiv \text{Cov}(\alpha_\lambda,\alpha_{\lambda'}) = \langle(\alpha_\lambda-\alpha_\lambda{}^0)(\alpha_{\lambda'}-\alpha_{\lambda'}{}^0)\rangle_{Av} = [\Sigma_i v_i^2/(m-l)]C^{-1}{}_{\lambda\lambda'}, \quad \lambda\neq\lambda'.$$

On evidence obtained from an unpublished investigation[7] of the accuracy of the approximate formula for the variance of a ratio, the variance estimate from the above equation for $V((\alpha_2+\alpha_4)/\alpha_0)$ is probably within 2 percent of the true variance.

The ϵ^2 for each measurement is shown in column 4. Since the values of ϵ cluster about unity, it has been concluded that the various runs have a single statistical distribution; and in each case of the final results of the experiment as shown in Table II, the standard deviation of the mean has been calculated from the mean square deviation of the individual runs from the average.

The means obtained have been calculated both without and with the run of October 10. If one applies a range criterion to see if the October 10 run can safely be omitted from the group of runs on the argument that it does not belong in the same statistical distribution which is represented by the other members,[8] one

[6] M. E. Rose, (preceding article) Phys. Rev. **91**, 609 (1953).
[7] A. W. Kimball, private communication.
[8] J. Moshman and G. J. Atta, Oak Ridge National Laboratory Report ORNL 1020 (unpublished).

TABLE II. Mean values of the quantities listed in Table I. The errors are standard deviations.

	Dilute solution and dried $CoCl_2$ sources	Chemically changed source
Without October 10 run	$\bar{R}=0.1557\pm0.0010$	$\bar{R}=0.1453\pm0.0023$
With October 10 run	$\bar{R}=0.1520\pm0.0038$	
Without October 10 run	$W(\theta)=1+(0.131\pm0.017)\cos^2\theta+(0.024\pm0.017)\cos^4\theta$	$W(\theta)=1+(0.1149\pm0.0058)\cos^2\theta$ $(0.0304\pm0.0042)\cos^4\theta$
With October 10 run	$W(\theta)=1+(0.124\pm0.016)\cos^2\theta+(0.028\pm0.015)\cos^4\theta$	

finds that he can do so with less than a 1 percent probability of being in error.

In order to determine whether a real effect exists for the different source conditions, a "Student" t-test has been performed on the two sets of data. The test is used as a check on the consistency between the sample and the hypothesis that the two means in question are equal. If the computed t is large, as indicated by its level of significance, the hypothesis of equality of true means is rejected as incompatible with the differences in the observed means. When one considers the results without the October 10th run, he finds that if there were in fact no difference between the two sets of experiments, the chances of getting as large a difference of the means of the two sets of data as was observed are less than 1 out of 1000. The corresponding value with the October 10 run included is 12 chances in 100.

V. DISCUSSION

The theoretical correlation function for two quadrupole transitions between levels of angular momenta 4, 2, and 0, when allowance is made for the finite angular resolution of the detectors,[6] is

$$W(\theta)=1+0.1203\cos^2\theta+0.0314\cos^4\theta,$$

which yields a value of 0.1517 for the anisotropy. This calculated anisotropy is unaffected by the 3 percent uncertainty in the absorption cross section of sodium iodide for the gamma-rays of the Ni^{60} cascade. The theoretical correlation function is modified to allow for finite angular resolution before comparing with the measured anisotropy because the anisotropy is measured more accurately than the individual coefficients.

We can summarize the results of the present experiments as follows: the measured effect on the anisotropy of the chemical state of the source seems to be a real one with some degree of certainty. This observed change is surprising since the first measurement of the lifetime of the intermediate state in the cascade is $<10^{-10}$ second.[9] With this short lifetime one would expect that the correlation would be unperturbed by external fields. The explanation of the deviation of four times the standard error of our measurements from the expected value of the anisotropy is probably to be found in imperfection in the experimental apparatus, even though the ϵ^2 tests of the data show that the nonstatistical errors are small. However, it does seem that with a dilute source of $CoCl_2$, the anisotropy of the cascade is not attenuated by external effects.

Since the above experiments were completed, it was necessary to dismantle and reassemble the apparatus. The detectors have been changed to use a different light reflector around the sodium iodide crystals, and the coincidence circuit has been replaced by a new one of improved design. This apparatus has been checked by measuring the Ni^{60} cascade with a dilute solution source in a fluorothene holder. The results obtained for the anisotropy are 0.1501 ± 0.0054 and 0.1532 ± 0.0027. The average of these measurements agrees with the expected anisotropy of 0.1517. If these results are combined with those of the previously described experiments, the discrepancy between the experimental and theoretical values is reduced to three times the standard deviation of the measurements.

It is a pleasure to express our appreciation to George Kelley and P. R. Bell for stimulating discussions during the course of these experiments. We also wish to acknowledge the aid which we have received in the statistical analysis of the data from Dr. M. E. Rose, Dr. A. W. Kimball, and Jack Moshman. We should like to express our appreciation to Buford Carter, who carried out the I.B.M. calculations in the analysis of our data.

[9] Bay, Henri, and McLernon, Phys. Rev. **90**, 371 (1953).

The Hyperfine Structure and Nuclear Moments of Pr^{141}†

HIN LEW
Division of Physics, National Research Council, Ottawa, Canada
(Received April 20, 1953)

The hyperfine structure of the ground state of Pr^{141} has been studied by the atomic beam magnetic resonance method. It has been established that the electronic ground state of Pr is $4f^36s^2$, $^4I_{9/2}$. Of the five hyperfine intervals arising from this electronic state and a nuclear spin of 5/2, the lowest two have been observed. They are $W(F=4)-W(F=3)=3708.05$ Mc/sec and $W(F=3)-W(F=2)=2782.25$ Mc/sec. If the hfs is assumed to be entirely due to an interaction between the $^4I_{9/2}$ state and the nucleus, the observed intervals may be expressed in terms of a magnetic dipole interaction constant A and a nuclear electric quadrupole interaction constant B. It is found that $A=926.03\pm0.1$ Mc/sec and $B=-13.9\pm1.0$ Mc/sec. From these constants, the nuclear moments have been evaluated by means of approximate methods. The values obtained are

$$\mu=+3.8 \text{ nm}, \qquad Q=-0.054\times10^{-24} \text{ cm}^2.$$

I. INTRODUCTION

THE experiment to be described in this paper represents the beginning of a program for the study of the rare earths by the atomic beam magnetic resonance method. The rare earths are of interest both on account of their atomic ground states and on account of their nuclear moments. For some of these elements the atomic ground states are not yet known. A determination of this characteristic through an investigation of the Zeeman effect should be of considerable assistance to spectroscopists in their analysis of the very complex spectra of these elements. Although the spin values of most of the rare earth nuclides have been reported, much remains to be done in the determination of their magnetic dipole moments and electric quadrupole moments. In view of the lack of success of the nuclear induction method in the case of the rare earths and in view of the difficulty of evaluating crystalline fields in the paramagnetic resonance method, it has been considered worth while to supplement and extend existing data by precise measurements of atomic hyperfine structures by the atomic beam method.

In 1929, White[1] observed that many of the lines of Pr II consisted of six hyperfine components. He was able to account for this observation on the basis that the Pr^{141} nucleus had a spin of $(5/2)h/2\pi$. Later, Rosen, Harrison, and MacNally[2] studied the Zeeman effect of Pr II and succeeded in classifying many lines. They found that the lowest terms of Pr II were f^3s, $^{5,3}I$. From this result, it has been suggested[3] that the ground state of Pr I is probably f^3s^2, $^4I_{9/2}$. Thus, the present investigation started with a certain knowledge of the nuclear spin and a probable knowledge of the atomic ground state.

II. THEORY

In the atomic beam magnetic resonance method, one studies the Zeeman effect of the hyperfine structure of the ground state or of low-lying metastable states of atoms. In a magnetic field an atom possessing an electronic angular momentum J and a nuclear spin I is usually described by a Hamiltonian of the form[4–6]

$$\mathcal{H}=A\mathbf{I}\cdot\mathbf{J}+BQ_{\text{op}}+g_J\mu_0\mathbf{J}\cdot\mathbf{H}+g_I\mu_0\mathbf{I}\cdot\mathbf{H}, \qquad (1)$$

where Q_{op} stands for the operator

$$Q_{\text{op}}=\frac{3(\mathbf{I}\cdot\mathbf{J})^2+\frac{3}{2}(\mathbf{I}\cdot\mathbf{J})-IJ(I+1)(J+1)}{2IJ(2I-1)(2J-1)}.$$

A and B are interaction constants, and the respective terms in Eq. (1) represent the energy of interaction between the nuclear magnetic dipole moment and the magnetic field of the electrons and the energy of interaction between the nuclear electric quadrupole moment and the electric field of the electrons. The last two terms in the Hamiltonian represent the energy of the magnetic dipole moment of the electrons and of the nucleus, respectively, in the external field. The g factors g_J and g_I are defined as the negative ratios of the electronic and nuclear magnetic dipole moments, respectively, in units of the Bohr magneton μ_0 to the corresponding angular momenta in units of $h/2\pi$.

Theoretical expressions for the constants A and B in terms of fundamental atomic and nuclear quantities have been given by various authors. They will be considered later when we come to the evaluation of the nuclear quantities from the experimental results.

† Contribution No. 3038 from the National Research Council of Canada.

[1] H. E. White, Phys. Rev. **34**, 1397 (1929).

[2] Rosen, Harrison, and MacNally, Phys. Rev. **60**, 722 (1941).

[3] P. Schuurmanns, Physica **12**, 589 (1946); W. F. Meggers, Science **105**, 514 (1947).

[4] H. B. G. Casmir, *Interaction between Atomic Nuclei and Electrons* (Teyler's Tweede Genootschap, Haarlem, 1936).

[5] H. Kopfermann, *Kernmomente* (Akademische Verlagsgesellschaft, Leipzig, 1940; reprinted in U. S. by J. W. Edwards, Ann Arbor, 1945).

[6] Davis, Feld, Zabel, and Zacharias, Phys. Rev. **76**, 1076 (1949). Our notation differs from that of these authors in that we have used capital letters instead of small letters for the interaction constants A and B. Capital letters have been used because they refer to the $^4I_{9/2}$ term arising from several electrons. The contributions of the individual electrons will be denoted by small letters.

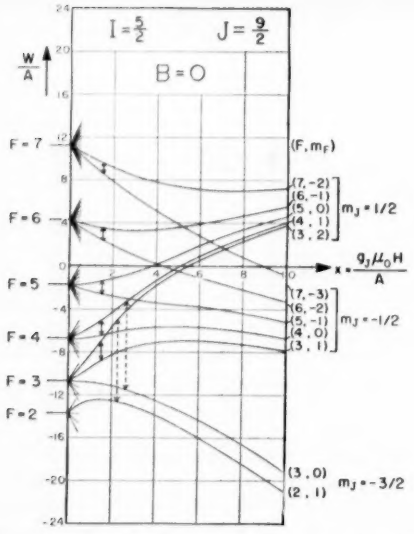

FIG. 1. Energy levels of an atom with $I=5/2$, $J=9/2$ in an external magnetic field, calculated for zero quadrupole interaction. Only those levels which have been observed in the present experiment are shown over the entire range of the parameter x.

The energy levels of an atom with the above Hamiltonian are simply the characteristic values of the matrix of the Hamiltonian. The matrix elements of the operators in the Hamiltonian may be found in many places in the literature.[7] In the (I, J, F, m_F) representation, the matrix elements of $\mathbf{I}\cdot\mathbf{J}$ are particularly simple. They are independent of m_F and are equal to $C/2$, where[8]

$$C=F(F+1)-J(J+1)-I(I+1).$$

Thus, in the absence of an external field, the characteristic values of the Hamiltonian are

$$W=A\frac{C}{2}+B\frac{\frac{3}{8}C(C+1)-\frac{1}{2}I(I+1)J(J+1)}{I(2I-1)J(2J-1)}. \qquad (2)$$

These are the familiar hyperfine structure levels, each level being characterized by a given F, with the possible values of F ranging from $I+J$ to $|I-J|$. If B is zero, the spacings between these levels obey the interval rule.

In the presence of an external field, the energy levels cannot, in general, be expressed explicitly in terms of the various parameters. The secular determinant, in general, gives rise to equations which are of higher degree than the second. However, for very weak fields, first- or second-order perturbation theory may be applied to obtain approximate solutions. The first-order solution yields the result that each hyperfine level with quantum number F splits up into $2F+1$ equally spaced magnetic levels with separations given by

$$\nu_F=g_J\frac{F(F+1)+J(J+1)-I(I+1)}{2F(F+1)}\mu_0 H. \qquad (3)$$

Transitions between adjacent magnetic levels belonging to a given value of F are observable in the atomic beam magnetic resonance method and are called low-frequency (l.f.) transitions. It is obvious from Eq. (3) that if the J and g_J values of the electronic state are known, the spin I may be determined by the observation of the low-frequency transitions. Conversely, if I is already known, J and g_J may be determined. This will be illustrated below for the case of Pr. It is even possible to determine all three quantities I, J, and g_J, provided there is a sufficient number of F's and therefore ν_F's.

In the present experiments, J was not known initially. Various values of J were assumed, and energy level diagrams of the corresponding hyperfine structures constructed in order to see what levels satisfied the refocusing conditions of the experiment and were therefore observable. In Fig. 1 is shown such a diagram for $I=5/2$ and $J=9/2$, this value of J being the one eventually found for Pr. To avoid unnecessary confusion, only some of the levels have been shown over the entire range of the parameter of the abscissa. These levels have been determined by numerical solution of the secular determinant of the Hamiltonian, Eq. (1), with B and g_I set equal to zero and the whole expression divided through by A. In other words, they are the characteristic values of

$$\mathcal{H}'=\mathcal{H}/A=\mathbf{I}\cdot\mathbf{J}+xJ_z, \qquad (4)$$

where $x=g_J\mu_0 H/A$ and $J_z H=\mathbf{J}\cdot\mathbf{H}$ if $\mathbf{H}$ is in the z direction.

At weak fields, the low frequency lines are, by Eq. (3),

$$\begin{aligned}&\nu_7=(9/14)g_J\mu_0 H, \quad \nu_4=(9/10)g_J\mu_0 H,\\ &\nu_6=(29/42)g_J\mu_0 H, \quad \nu_3=(7/6)g_J\mu_0 H,\\ &\nu_5=(23/30)g_J\mu_0 H, \quad \nu_2=(11/6)g_J\mu_0 H.\end{aligned} \qquad (5)$$

The ratios of these low frequency lines depend only on I and J and not on g_J or the term type. It can be easily verified that for $I=5/2$, no value of J other than $9/2$ will give rise to a set of low frequency lines which are related in the above proportions. Thus, by observing the relative frequencies of a set of low frequency lines, one may determine J uniquely. From the absolute frequencies, one may then calculate g_J, the Landé g factor of the electronic state. The association of a term type with a given g_J will, of course, depend on the electronic coupling assumed and, even with a given coupling, may not be unique. Thus, other considerations will, in general, need to be brought in for a unique identification of the term type.

[7] See E. U. Condon and G. H. Shortley, *Theory of Atomic Spectra* (Cambridge University Press, Cambridge, 1935).

[8] Authors are divided between the symbols K and C for this expression, and we have chosen C to conform with the usage in molecular spectroscopy.

III. EXPERIMENTAL PROCEDURE AND APPARATUS

(a) The Over-All System

The present atomic beam magnetic resonance apparatus is patterned after those of the Molecular Beam Laboratory of the Massachusetts Institute of Technology.[9,10] The essential dimensions and the locations of the various components are shown in Fig. 2. There are the usual two inhomogeneous deflecting fields A and B on either side of a homogeneous field C where transitions take place. The magnetic field gradients in the A and B regions are parallel to each other and in the same direction, an arrangement first used by Zacharias[11] in the study of K^{40}. Atoms which do not undergo transitions in traversing the magnetic fields are swept away from the detector which lies on the neutral axis of the beam. Only those atoms are redeflected back on to the detector which undergo transitions between states with effective magnetic moments of the opposite sign in the A and B fields. This special "refocusing" condition restricts the number of observable transitions to considerably less than that permitted by the selection rules. This apparent disadvantage, however, is outweighed by the advantage that there is no large background of atoms striking the detector when there is no transition.

The loop in the C field through which radio-frequency power is sent for the inducement of transitions is a vertical hairpin about 1.5 inches high which produces an oscillating magnetic field directed mainly parallel to the atomic beam and about $\frac{3}{8}$ inch in extent in this direction. Another loop of wire mounted close to this one but out of the way of the beam is used to pick up the field radiated by the first loop. By rectifying the rf energy with a crystal rectifier and measuring the resultant current in a microammeter, some indication is obtained of the power that is in the transition region.

Caesium atoms are used to measure the field strength in the C region. The particular line used is $(F=4, m_F=-3)\rightarrow(F=4, m_F=-4)$ which, at weak fields, is related to the field strength through the first-order approximation.

$$\nu=0.35H \text{ Mc/sec}, \tag{6}$$

where H is in gauss.

The widths of the various slits are as follows: oven 0.004 inch, collimator 0.006 inch, ionizer or detector 0.015 inch. The first obstacle wire is 0.010 inch in diameter and the second 0.008 inch in diameter. The presence of two obstacle wires instead of the usual one will be explained below in connection with the determination of the sign of the magnetic dipole interaction constant.

The electron multiplier for the detection of ions is a 15-stage secondary electron emission multiplier with

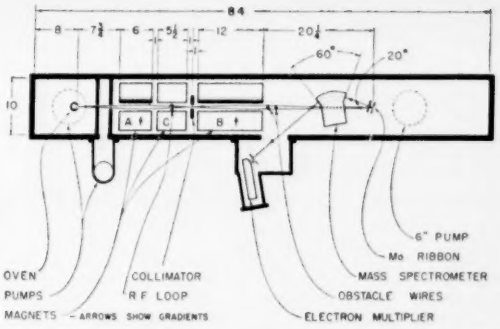

FIG. 2. Diagram of atomic beam magnetic resonance apparatus showing locations of components. All dimensions are in inches.

dynodes of beryllium-copper. The shapes of the electrodes and their preparation are exactly as described by Allen.[12]

(b) The Vacuum System

The vacuum housing is a box of square cross section 10 in.×10 in. inside dimensions and 84 in. long. The walls are of rolled brass plate, 1 in. thick on top and $\frac{3}{4}$ in. thick on the other three sides. The joints between the plates are grooved, screwed together, and soft soldered. The top plate is planed smooth and flat after assembly, since it is used as the reference plane for the components which go into the vacuum system. As is the case with the instruments at the Massachusetts Institute of Technology, all the components are suspended from brass plates which lie over rectangular ports in the reference plane. The vacuum seal between these brass mounting plates and the reference surface is accomplished by vacuum grease and Apiezon Q wax. The ends of the box are closed by flat brass plates and again made vacuum tight with Apiezon Q wax. All windows and pump connections to the box are made through O-ring gaskets.

The three chambers of the vacuum housing are individually evacuated, the oven and detector chambers by 6-in. diameter oil diffusion pumps and the isolation chamber by a 4-in. diameter pump. Gate valves and water-cooled baffles are provided in the connections between the pumps and the box. Furthermore, a small gate valve is provided between the oven chamber and the isolation chamber to permit air to be let into the oven chamber without affecting the vacuum in the rest of the system. The diffusion pumps are backed by two oil booster pumps and these in turn by two mechanical pumps. In operation, one small mechanical pump is sufficient to back the boosters. When pumping the system down from atmospheric pressure, however, the other larger mechanical pump is brought into play, first for roughing out the system and then for backing the diffusion pumps until a high degree of vacuum is reached. Liquid air traps are introduced into the three

[9] Davis, Nagle, and Zacharias, Phys. Rev. **76**, 1068 (1949).
[10] Eisinger, Bederson, and Feld, Phys. Rev. **86**, 73 (1952).
[11] J. R. Zacharias, Phys. Rev. **61**, 270 (1942).
[12] J. S. Allen, Rev. Sci. Instr. **18**, 739 (1947).

TABLE I. Data on magnets.

A and *B* magnets	*A*	*B*	
Length	6	12	inches
Separation of equivalent 2-wire system	0.250	0.750	inch
Gap at apex	0.0937	0.125	inch
Number of turns	39.5	28	
Field *H*	208	111	gauss/amp
Gradient	3.15 *H*	1.05 *H*	gauss/cm
C magnet			
Length	5½ inches		
Gap	0.250 inch		
Number of turns	36		
Field	67 gauss/amp		
Mass spectrometer magnet			
Radius of curvature	5 inches		
Angle of sector	60 degrees		
Gap	½ inch		
Number of turns	40		

chambers through side ports. A vacuum of better than 10^{-6} mm Hg is easily obtainable in the detector chamber. The pressure in the oven chamber depends on the evolution of gas from the oven and is usually 10^{-5} mm Hg or less. The pressure in the isolation chamber is usually around 10^{-6} mm Hg.

(c) The Magnets

All the magnets are made of Armco magnet iron with windings of copper tubing insulated with Fiberglas sleeving. Their essential dimensions and characteristics are given in Table I.

The *A* and *B* magnets are of conventional design,[12] the pole pieces being shaped to give a field distribution in the gap which is equivalent to that of two parallel wires carrying equal currents in opposite directions. The pole pieces are reversible without disturbing the yokes so that the gradients in the *A* and *B* fields may be made parallel or antiparallel. With the geometry as shown in Fig. 2 and magnet characteristics as given in Table I, the refocusing condition for atoms with equal and opposite effective magnetic moments in the *A* and *B* fields is that the gradient in the *B* field shall be 0.32 times that in the *A* field. Typical energizing currents for achieving this are 30 amperes in *A* and 55 amperes in *B*.

The *C* magnet is of the simplest possible construction being composed entirely of rectangular pieces bolted together. The gap faces are ground smooth and flat and separated by precision spacers. For the present experiment, no attempt had been made to homogenize the field through shimming.

The mass spectrometer magnet is of the familiar 60° sector type.

(d) The Ovens

Two ovens are used in the present experiment, one for the generation of a beam of Pr atoms and the other one for a beam of Cs atoms. The two ovens are mounted in such a way that either one may be brought into the proper operating position simply and accurately without disturbing the vacuum in the oven chamber. The arrangement is shown in Fig. 3. The two ovens are mounted on the underside of a rotatable platform which is made vacuum tight with respect to its mounting plate by means of an O-ring. The angular position of the platform is accurately located through micrometer stops, and it has been found that the positions of the ovens may be set to about 0.001 inch.

The cell used for the vaporization of Pr is essentially a thin-walled molybdenum cylinder with a slit cut longitudinally in the wall. The unit is machined from ⅜-inch solid molybdenum rod into the form shown in the figure. The thin-walled section is ¼ inch in inside diameter and $\frac{5}{16}$ inch in outside diameter, and the slit in it is 0.004 inch by ⅛ inch. The unit is clamped by its lower stem between two blocks of copper which are in thermal and electrical contact with the bottom of the water-cooled radiation shield surrounding the unit. The top end of the cell, i.e., the stem of the cap that closes the cylindrical chamber, protrudes through the radiation shield and makes contact with a water-cooled copper block which is electrically insulated from the rest of the oven assembly. Electrical power is applied between this electrode and the radiation shield by way of the tubes which lead cooling water to these parts. The praseodymium metal to be vaporized, instead of being placed in direct contact with the molybdenum, is contained in a ThO_2 crucible. This greatly reduces the chances of the oven slit being clogged by the molten metal. A current of about 240 amperes at 10 volts is required to bring the oven to the operating temperature of 2000°K (1570°C brightness temperature at a wavelength of 0.65μ).

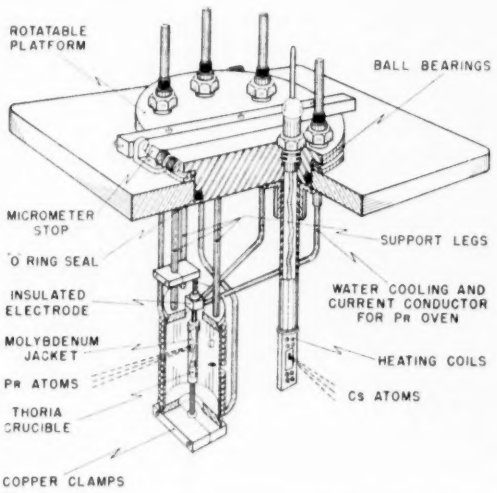

FIG. 3. The Pr and Cs ovens shown mounted on rotatable platform for simple and accurate interchange of positions.

[12] Millman, Rabi, and Zacharias, Phys. Rev. **53**, 384 (1938).

The oven for the production of a Cs beam consists of an iron cell of square cross section $\frac{1}{4}$ in.$\times\frac{1}{4}$ in.$\times\frac{7}{8}$ in. with a longitudinal slit in one face 0.004 in.$\times\frac{1}{8}$ in. This fits into a rectangular hole in a block of iron in which are imbedded some molybdenum heating coils. A charge of Na metal and CsCl in the cell yields a very steady beam of Cs atoms when the oven is raised to a temperature of about 200°C.

(e) The Ionizer

For the detection of the neutral atoms of an atomic beam, the atoms may be ionized by the familiar surface ionization method. Because of its low ionization potential of 3.9 volts, Cs can be ionized by any of a large number of metals by this process. However, considerable difficulty was experienced in finding a suitable ionizer for Pr. Of the various refractory elements tried, including Pt, W, Cb, and Mo, molybdenum was found to be the best, even though it suffered from two serious limitations. The first limitation is its low efficiency.The work function ϕ of Mo is 4.27 ev,[14] while the ionization potential I of Pr is approximately 5.76 ev.[15] With the Mo ribbon at a temperature of 2070°K, which is experimentally found to be the temperature of best compromise between ionization efficiency and long life, the probability of ionization, as given by $\exp[(\phi-I)/kT]$ is 2×10^{-4}. This low efficiency is still usable, however, by using a high enough incident beam intensity and measuring the ion intensity with an electron multiplier and a pulse counting system. The more serious defect of Mo as a surface ionizer is that the re-emission of Pr from its surface as ions does not take place instantaneously. The delay between the striking of the neutral atom on the surface and its re-emission as an ion varies from one or two seconds when the Mo ribbon is at 2160°K to about 30 seconds at 1870°K. At the higher temperatures, the ribbon, which is under slight tension to keep it taut, easily breaks and also diminishes in size rapidly through evaporation. The most practical operating temperature has been found to be about 2070°K, at which temperature the time delay is about 3 seconds. It is obvious that, with this time constant, the search for narrow transition lines over a wide frequency range can become extremely tedious.

The molybdenum ribbon used in the present experiments measured 0.015 inch wide by 0.002 inch thick and is of commercial purity. Before such a ribbon can be used as a detector of Pr, it must be cleaned by prolonged heating in vacuum. It seems that the Mo is contaminated by many oxides including those of the rare earths. When a new ribbon is first installed in the ionizer assembly and brought up to about 2070°K, it emits ions copiously over a wide range of masses. One of these masses is of mass number 157 and is probably PrO. As long as this impurity is present, it is found that a Pr atom striking the surface is not re-emitted as Pr^+ but as an ion of mass 157 which presumably is PrO^+. This behavior itself would not be objectionable, for the atomic beam would be detected thereby anyway, if it were not for the fact that the background from the wire itself at this same mass number is unsteady, and its magnitude prevents the observation of weak transitions that would otherwise be observed. In order to remove this impurity, it has been found sufficient to maintain the ribbon at a temperature of about 2000°K for about 12 hours. The ribbon then re-emits Pr atoms as Pr^+ with a reasonably steady and tolerably low background.

Of the other materials that were tried as ionizers, tungsten was found to have a time delay several times greater than that of Mo. Columbium, on the other hand, had a shorter delay, but its ionization efficiency was lower because of its lower work function (3.99 ev). Platinum with its high work function of 5.1 ev would probably have made an efficient ionizer if it had not been for the fact that, because of its low melting point, it broke too easily at the temperatures necessary for the re-evaporation of Pr.

(f) Oscillators and Frequency Meters

A variety of oscillators was used to cover the wide range of frequencies encountered in the present study. For the $\Delta F=0$ lines, the following oscillators were used: General Radio Type 1001-A (5 kc/sec–50 Mc/sec), General Radio Type 1208-A (65 Mc/sec–500 Mc/sec), Airborne Instruments Laboratory Type 124A Power Oscillator (300 Mc/sec–2500 Mc/sec). For the $\Delta F=1$ lines, Sperry reflex klystrons were used, the 2K41 for the 2782 Mc/sec line, and the 2K42 for the 3708 Mc/sec line. Higher frequency lines of the hyperfine structure were searched for unsuccessfully with the 2K43 and 2K44.

Frequencies below 100 Mc/sec were measured with a General Radio Type 620-A Heterodyne Frequency Meter and Calibrator. The accuracy of this instrument is 1 part in 10^4 or better. Frequencies above 100 Mc/sec were measured with a General Radio Type 720A Heterodyne Frequency Meter in conjunction with a General Radio Type 1110-A Interpolating Frequency Standard. The crystal oscillator in the latter has been checked against standard transmissions from station WWV and found to be correct to 1 part in 10^5 or better.

IV. RESULTS

(a) $\Delta F=0$, $\Delta m_F=\pm1$ Transitions

At the outset of the present experiments, when the atomic ground state of Pr was not known, a general search was made for transitions between magnetic levels belonging to the same F. These transitions were sought at low fields of a few tens of gauss, i.e., in the Zeeman region where linear relations of the type Eq. (3) held to a percent or better. The C field was held

[14] H. B. Michaelson, J. Appl. Phys. **21**, 536 (1950).
[15] L. Rolla and G. Piccardi, Phil. Mag. **7**, 286 (1929).

TABLE II. Low frequency lines.

Observed Pr lines						Theoretical lines for $I=5/2$, $J=9/2$		
At 28.37 gauss		At 56.31 gauss		At 83.85 gauss				
Freq., Mc/sec	Rel. freq.	Freq., Mc/sec	Rel. freq.	Freq., Mc/sec	Rel. freq.	Frequency in units $g_J\mu_0 H$		Relative to $(F=6)$
18.67	0.932	37.08	0.930	55.19	0.931	$F=7$	9/14	0.9310
20.03	1.000	39.88	1.000	59.28	1.000	$F=6$	29/42	1.0000
22.26	1.111	44.26	1.110	65.88	1.111	$F=5$	23/30	1.1103
26.06	1.301	51.90	1.301	77.23	1.303	$F=4$	9/10	1.3034
33.65	1.679	67.09	1.682	99.58	1.680	$F=3$	7/6	1.6896
						$F=2$	11/6	2.6552

constant, while the frequency in the rf loop was varied over a reasonably wide range, say 50 kc/sec to 50 Mc/sec. The magnitude of the C field was determined by the low frequency transition of Cs^{133}. After the proper experimental conditions (oven temperature, ionizer material, and rf field strength) had been found for the detection of transitions, five $\Delta F=0$, $\Delta m_F=\pm 1$ transitions were observed in Pr at a given value of the C field. A series of readings at C fields of 28.37 gauss, 56.31 gauss, and 83.85 gauss are shown in Table II. These magnetic fields correspond to low frequency transitions in Cs^{133} of 10.0 Mc/sec, 20.0 Mc/sec, and 30.0 Mc/sec, respectively. Each reading represents a single setting of the oscillator on the estimated peak of the line. The width of each line is about 0.2 Mc/sec, and, therefore, the peaks are probably no more accurately located than to 0.05 Mc/sec. At each field strength, the observed frequencies are reduced to a set of relative values, as shown in the table. The line with the second lowest frequency was chosen as the reference line in this relative scale, because it was found to be the strongest and, therefore, the most accurately measurable.

Assuming that these $\Delta F=0$, $\Delta m_F=\pm 1$ transitions all belonged to the same hyperfine multiplet, various values of the electronic angular momentum J were assumed and, with $I=5/2$, the theoretical relative frequencies of the possible low frequency lines calculated by Eq. (3). Only for $J=9/2$ was any agreement found between the calculated relative frequencies and the observed relative frequencies. This agreement is seen in Table II where the calculated values are shown in the last two columns. Within the accuracy of the measurements and the validity of the first-order approximation, the agreement may be considered to be exact. We may conclude that the J value of the electronic state under study is almost certainly 9/2. All subsequent observations are in agreement with this J value. We shall, therefore, in our discussions consider this J value as being correct.

From Fig. 1 we may identify the magnetic quantum numbers of the levels involved in the observed transitions. The gradients of the A and B fields were set, in the observations, to refocus equal and opposite magnetic moments. Assuming that the strength of these fields are sufficiently high so that the Pr atoms are in the Paschen Back region while going through the deflecting fields, then, remembering that the magnetic quantum number m_F may change by unity only, the only observable transitions are those between levels with strong field quantum number $m_J=\frac{1}{2}$ and $m_J=-\frac{1}{2}$. This allows us to deduce immediately that the observed transitions were $(7,-2)\rightarrow(7,-3)$, $(6,-1)\rightarrow(6,-2)$, $(5,0)\rightarrow(5,-1)$, $(4,1)\rightarrow(4,0)$, $(3,2)\rightarrow(3,1)$. These are shown by the solid arrows in the figure. The reason why no l.f. transition belonging to $F=2$ was observed is simply that the magnetic levels of $F=2$ all have negative m_J, while at least one positive m_J is necessary for refocusing.

As mentioned above, the $(6,-1)\rightarrow(6,-2)$ line was found to be considerably stronger than the others. The reason for this was not understood until the hyperfine structure interval factor A had been found. It was then realized that the magnetic fields of 5500 gauss used in the A and B regions corresponded to $x=g_J\mu_0 H/A=6$ and that, at this value of x, the Pr atoms were not in the Paschen-Back region where their effective magnetic moments assumed the limiting values $-m_J g_J \mu_0$. As may be seen from Fig. 1, the effective magnetic moments at $x=6$ may be greater or less than those in the Paschen-Back region. The initial and final levels of all the observed low frequency transitions except $(6,-1)\rightarrow(6,-2)$ do not have equal and opposite slopes in this intermediate field region. Since the A and B fields were set to refocus equal and opposite magnetic moments, only the line belonging to $F=6$ was properly refocused. The others were improperly refocused and hence were of lower intensity.

Once J has been found from the relative frequencies of the observed transitions and the identification of the latter has been accomplished, the Landé g factor of the fine structure state may be calculated from the absolute frequencies. Using the observations at 28.37 gauss shown in Table II and observations at lower fields not shown, we find from Eq. (5) $g_J=0.731\pm 0.004$.[16] The large error in this value is partly due to the inaccuracy

[16] The value of 0.727 ± 0.005 quoted in a preliminary note [H. Lew, Phys. Rev. **89**, 530 (1953)] differs from this value, because in the previous value the magnetic field H was calculated from the Cs frequency by means of the first-order relation, Eq. (6). In the present case, H has been calculated by means of the exact Breit-Rabi formula, using the Cs constants given by P. Kusch and H. Taub [Phys. Rev. **75**, 1477 (1949)].

on the measurements and partly due to the inaccuracy of the first-order expressions, Eq. (5). A better value may be found by using second-order expressions for the low-frequency lines which contain the magnetic dipole interaction constant A determined later in the experiment. With this little refinement, we find, on simply averaging the results of the five levels, $g_J=0.731 \pm 0.002$, i.e., the average value is unchanged but the limits of error are reduced. The effect of g_I has been neglected in these calculations for the limited accuracy of the measurements does not warrant its inclusion.

Knowing J and g_J for the state under study, we may search the tables for likely term types. If we assume that Russell-Saunders coupling holds for the state, we find that the term type with $J=9/2$, and g_J nearest 0.731 is $^4I_{9/2}$. For pure Russell-Saunders coupling, this term type has a g value of 0.727. The observed deviation of $\frac{1}{2}$ percent from the extreme Russell-Saunders value is not surprising, considering the complexity of atomic spectra in the rare earth region of the periodic system. A $^4I_{9/2}$ ground term implies, according to Hund's rules, an f^3 or f^3s^2 electron configuration. An f^3s^2, $^4I_{9/2}$ ground term is very plausible in view of the known ground terms, f^3s, $^{3,5}I$, of Pr II, as mentioned in the introduction.

Further evidence that the state under study is $^4I_{9/2}$ comes from our observation of low-frequency lines which may be ascribed to $^4I_{11/2}$. If the state under investigation is indeed $^4I_{9/2}$ and is the ground state, then there should exist metastable states $^4I_{11/2}$, $^4I_{13/2}$, $^4I_{15/2}$. The low-frequency lines belonging to the hfs of $^4I_{11/2}$ may be calculated by means of Eq. (3), using $g_J(^4I_{11/2})=0.965$, the value corresponding to extreme Russell-Saunders coupling. Such lines were sought and found, except that a g_J of 0.970 fitted the observations better than 0.965. The intensities of these lines were about 40 percent of those belonging to $^4I_{9/2}$. This is in agreement with the relative populations of the two states at 2000°K, if the two states are separated by the 1450 cm^{-1} which we have estimated below.

(b) $\Delta F=1$, $\Delta m_F=\pm 1$ Transitions

When the magnitudes of the hfs intervals are completely unknown, it is generally impractical to search for them with a continuous sweep over a wide rf spectrum. It is customary to make an estimate of the hfs constant A through the low-frequency lines. Explicit expressions for the dependence of the observable low frequency transitions on A are not obtainable in cases where I, $J>\frac{1}{2}$. One must resort to approximate perturbation expressions or to numerically computed detailed plots of the energy levels, such as those shown in Fig. 1. We have followed the latter method. It will be noticed that A enters into both the ordinate and the abscissa. Only for the correct choice of A will an observed low frequency line fit into the energy level diagram at the value of x calculated for the assumed A and for the observed magnetic field H. For our low-frequency line, we chose $(6, -1)\rightarrow(6, -2)$, since it was the strongest for reasons already mentioned. It was measured accurately at 1000 gauss, and its frequency was found to be 723.9 Mc/sec. Using $g_J=0.727$, the theoretical Landé g value for $^4I_{9/2}$, we found a value for A of approximately 830 Mc/sec. This turned out to be about 12 percent lower than the correct value which was eventually found. On examining our original calculations, we discovered that if we had taken for g_J the value 0.731 which was contained in our low frequency observations, we would have come to within 2 or 3 percent of the correct value of A. We were fortunate in finding a $\Delta F=\pm 1$ transition, despite the poor estimate.

The first high-frequency line was found at around 3320 Mc/sec at a C field of approximately 570 gauss. This was followed down to as low a field as possible, the last measurement taken being at appromately 1 gauss. The measurements between zero and 30 gauss are shown in Fig. 4. The sizes of the circles in the figure do not represent the probable errors in the measurements. These are less than 0.1 Mc/sec and cannot be shown in the scale of the figure. By plotting the observations on a large scale and extrapolating graphically to zero field, we find a frequency of 2782.25 ± 0.05 Mc/sec. Furthermore, the field dependence of this line at zero field is 0.51 ± 0.01 Mc/sec-gauss. This slope enables us to identify the line unambiguously as the $(F=3, m_F=2)\rightarrow(F=2, m_F=1)$ transition (assuming A positive, as shown below). The theoretical slopes of the energy levels at zero field are given rigorously by the first-order expressions, and, for the $(3, 2)\rightarrow(2, 1)$ transition, the theoretical slope is $0.500\ g_J\mu_0$ or, using $g_J=0.731$ and $\mu_0=1.400$ Mc/sec-gauss, it is 0.512 Mc/sec-gauss. There is no other transition between $F=3$ and $F=2$ which has a theoretical slope within 33 percent of this

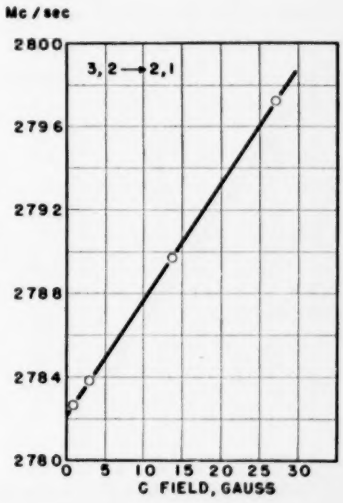

FIG. 4. $(3,2)\rightarrow(2,1)$ transition in Pr plotted against C field.

value. The closest is $(3, -1)\rightarrow(2, -1)$ which has a theoretical slope of 0.67 $g_J\mu_0$ or 0.685 Mc/sec-gauss. This line can be safely excluded, not only because of its slope but also because of its unobservability in the apparatus. The possibility of the observed line belonging to the hyperfine interval $(F=4)\rightarrow(F=3)$ may also be excluded by slope considerations.

Assuming that the interval rule held approximately for the hfs of Pr, a search was next made for transitions between $F=4$ and $F=3$ at frequencies in the vicinity of 4/3 of 2782 Mc/sec. One was duly found at 3730 Mc/sec at a C field of about 23 gauss. This was followed down to 1 gauss and extrapolated to zero field. The zero field frequency was 3708.05±0.05 Mc/sec. From its field dependence at zero field, the line was positively identified as $(4, 1)\rightarrow(3, 0)$. The results are shown in Fig. 5.

Search for further lines belonging to the same hyperfine intervals as the above two and for lines belonging to higher intervals was unsuccessful. The lack of success in the latter aspect may be explained on the basis of insufficient microwave power in the transition region. For a $F=5\rightarrow F=4$ transition, for instance, rf power of frequencies around 4635 Mc/sec or wavelengths around 6.57 cm was needed. The output of a 2K43 klystron was coupled to the rf loop in the C field through a coaxial line and a single tuning stub. The energy picked up by the monitoring loop in the C region indicated very little power there. This was probably due to the crudeness of the electrical matching system. Unfortunately, there was no equipment on hand to permit an attempt at better matching. Aside from the indication provided by the monitoring loop, another indication that our rf system was inefficient at higher frequencies was the fact that the 3708-Mc/sec transition was several times weaker than the 2782-Mc/sec transition.

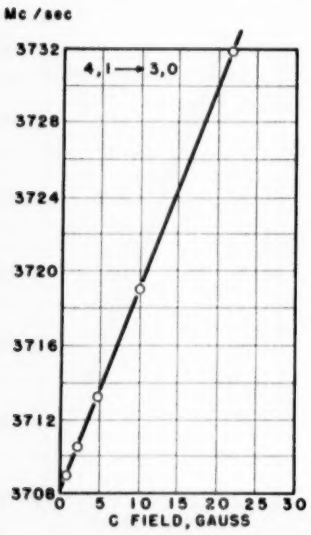

FIG. 5. (4,1)→(3,0) transition in Pr plotted against C field.

With regard to the question why no other transitions between $F=4$ and $F=3$ and between $F=3$ and $F=2$ were found, a detailed examination of the energy levels showed that no other transitions were favored either by the selection rules or by the refocusing condition. Between $F=3$ and $F=2$, the only transitions which are allowed by the selection rules and by the refocusing condition that m_J must change in sign are $(3, 3)\rightarrow(2, 2)$, $(3, 2)\rightarrow(2, 2)$, and $(3, 2)\rightarrow(2, 1)$. The last one has been observed. The first one is not favorable to refocusing because the $(2, 2)$ level has an effective magnetic moment of nearly zero at $x=6$. The second one has the same unfavorable characteristic. In addition, it is a $\Delta m_F=0$ transition and would have required a polarization of the rf field perpendicular to that actually used. The same arguments apply to $(4, 2)\rightarrow(3, 1)$, $(4, 1)\rightarrow(3, 1)$, and $(4, 1)\rightarrow(3, 0)$. Thus, we observed all the lines which were allowed by the selection rules and the experimental conditions.

If the hyperfine structure of the $^4I_{9/2}$ state under study is not appreciably perturbed by higher levels of the same multiplet, we may express our observations in terms of the two constants A and B appearing in Eq. (2):

$$4A-(17B/60)=3708.05\pm0.05 \text{ Mc/sec},$$

$$3A-(3B/10)=2782.25\pm0.05 \text{ Mc/sec}.$$

Hence,

$$A=926.03\pm0.10 \text{ Mc/sec}, \quad B=-13.9\pm1 \text{ Mc/sec},$$

$$B/A=-0.0150.$$

(c) The Sign of A

So far in the interpretation of our observations, we have tacitly assumed that the magnetic dipole interaction constant A is positive. An internally consistent interpretation could just as well have been obtained for a negative A. To determine the sign of A, we have examined the trajectories of the atoms under special refocusing conditions in the manner outlined by Davis, Feld, Zabel, and Zacharias.[6] When the gradients in the A and B deflecting regions are such as to refocus equal and opposite magnetic moments, atoms which have undergone transitions either through the absorption of a quantum of energy or through the stimulated emission of a quantum of energy strike the detector in equal numbers. Their trajectories, however, are different. One group follows a sigmoid path which takes them around one side of the obstacle wire, and the other group follows a path which takes them around the other side of the obstacle wire. This symmetry is lost, however, when the A and B fields are set to refocus atoms which have effective magnetic moments in the two regions differing not only in sign but also in magnitude. In Fig. 6(a), we show the energy levels involved

in the 2782-Mc/sec line for A assumed positive and in Fig. 6(b) the corresponding levels for A assumed negative. The vertical dotted lines indicate the magnetic fields which existed in the A and B deflecting regions in the trajectory exploration. Under these conditions, the gradients are such that only the transition indicated by the solid arrow in either case is refocused. The accompanying transition indicated by the dotted arrow is not refocused, because the effective magnetic moments of the initial and final levels are not correct. The refocused beams trace out the trajectories shown in the diagram below the energy levels. It is seen that, for A positive, the refocused beam goes around the obstacle wire on that side of the neutral axis which is closer to the convex pole piece of the B magnet (i.e., with a transverse acceleration which is opposite in direction to the gradient in the B field). The opposite is true in the case of A negative. By moving the second obstacle wire to one side or the other of the neutral position, we have found that Fig. 6(a) holds, i.e., that A is positive.

The use of two obstacle wires instead of the usual one is necessitated by the fact that there are in the beam many atoms of low effective magnetic moment or high velocity or both which are only slightly deflected by the A and B fields. If we tried to explore the trajectory of the atoms by the use of only one obstacle wire, we would find that these slightly deflected atoms would obscure the observations completely.

V. EVALUATION OF THE NUCLEAR MOMENTS

(a) Possibility of Magnetic Perturbation

The observed deviation from the interval rule has been ascribed to the existence of a nuclear electric quadrupole interaction. It is of interest to see whether such a deviation could arise from a magnetic perturbation by a neighboring fine structure level. Casimir[4] has calculated the effects of such a magnetic interaction. His conclusions are: that only levels with the same J or with J's differing by one perturb each other, that levels with the same F repel each other, and that the repulsion between two levels with the total quantum number F and electronic angular momenta J and $J+1$ is given by

$$W=\frac{|(n,J;F|T|n',J+1;F)|^2}{W(n',J+1;F)-W(n,J;F)}, \tag{7}$$

where the denominator is the separation between the two hyperfine levels concerned (usually replaceable by the fine structure separation) and the numerator is given by

$$(n,J,F|T|n',J+1,F)$$
$$=-\gamma\frac{(n,J|H_z|n',J+1)_{m_J=J}}{(2J+1)^{\frac{1}{2}}}\tfrac{1}{2}[(F+J+I+2)$$
$$\times(F+J-I+1)(J+I+1-F)(F-J+1)]^{\frac{1}{2}}$$
$$\times 1.585\times10^{-3}\ \text{cm}^{-1}. \tag{8}$$

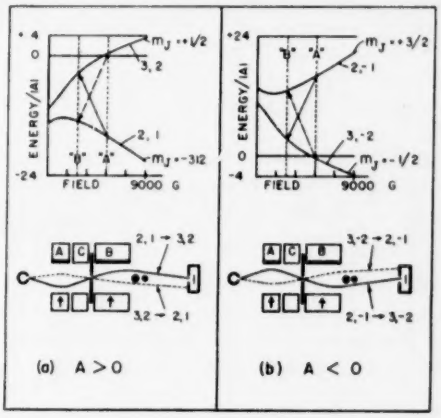

FIG. 6. Diagrams of energy levels used in the determination of the sign of A and the trajectories of the atoms for A positive and A negative. The energy levels are taken from Fig. 1.

γ is the positive ratio of the nuclear magnetic moment in nuclear magnetons to the nuclear spin in units of $h/2\pi$. In order to evaluate the matrix element of H_z connecting the two perturbing states, it is necessary to know the eigenfunctions of the states. However, it is possible to find the relative displacements of levels of different F belonging to the same fine structure multiplet without such knowledge.

An approximate picture of the ^4I fine structure multiplet of the $4f^36s^2$ ground configuration of Pr I may be deduced from the known ground levels of Pr II. According to Rosen, Harrison, and McNally,[2] the lowest terms of Pr II arise from a $4f^36s$ configuration and consist of four pairs of levels as shown in Fig. 7. This pattern is indicative of a strong Jj coupling between the s electron and the f^3 core. It can be shown on theoretical grounds that the lowest levels of the configuration f^3 or f^3s^2 would then consist of levels with spacings corresponding to the spacings of the centers of gravity of these pairs. This picture has been borne out in the f^4s^2, ^5I and f^4s, $^{6,4}I$ terms of NdI and NdII, respectively.[3] Thus, we find that the $^4I_{11/2}$ level of Pr I should lie at approximately 1450 cm^{-1} above the $^4I_{9/2}$ level.

The hyperfine structure of $^4I_{11/2}$ consists of six levels with $F=8, 7, 6, 5, 4, 3$. All of these levels, except $F=8$, will repel the corresponding ones of $^4I_{9/2}$. Since our observations concern only the $F=4$ and $F=3$ levels, we shall consider only their relative displacements. Since the fine structure separation, by our estimate above, is about 1600 times the total hfs of $^4I_{9/2}$, we may replace the actual separation between the hyperfine levels required in Eq. (8) by the fine structure separation. Then, by Eqs. (7) and (8), the relative displacements are

$$\delta W(F=4)/\delta W(F=3)=91/45\simeq 2.$$

Calling the displacement downwards of the $F=3$ level

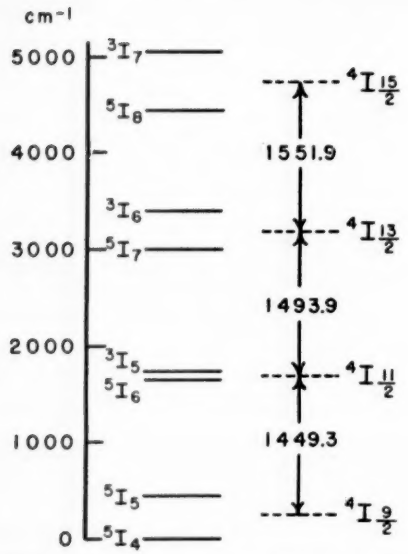

FIG. 7. The fine structure of the ground state of Pr II according to Rosen, Harrison, and MacNally. The separations between the centers of gravity of the pairs of lines give an estimate of the fine structure of the ground state of Pr I.

δ, the displacement of the $F=4$ level is then 2δ, also downwards. If we assume that, without perturbation, the interval rule holds with the interval factor A', we may write

$$4A'-\delta=3708.05, \quad 3A'-\delta=2782.25.$$

Solving for δ, we obtain $\delta=-4.85$ Mc/sec. A negative value for δ, however, means that the levels have been displaced upwards in contradiction to the original assumption of a mutual repulsion. An upward displacement would be consistent with a repulsion only if the $^4I_{11/2}$ level were below the $^4I_{9/2}$ level. Such an inverted fine structure cannot be the case, for otherwise we would have seen low frequency transitions in the hfs of $^4I_{15/2}$. Furthermore, it should not occur on theoretical grounds from the known structure of Pr II. We conclude then that the observed deviation cannot be entirely due to a perturbation and assume that, in the absence of further data, it is caused by a nuclear electric quadrupole moment. The magnetic dipole interaction constant A and the nuclear electric quadrupole interaction constant B are then as we have given them above.

(b) The Nuclear Magnetic Dipole Moment

The interaction constant $A=926.03$ Mc/sec represents the resultant interaction of three equivalent $4f$ electrons with the nucleus. Since relativity can be neglected for $4f$ electrons, the contribution resulting from a single $4f$ electron may be calculated by a method attributable to Goudsmit.[17] We find

$$a_{4f}=+0.7626A\,(f^3, {}^4I_{9/2})=706.2 \text{ Mc/sec}.$$

There are a number of theoretical relations connecting this quantity with the gyromagnetic ratio of the nucleus, relations which involve varying assumptions about the field in which the electron moves. For simplicity, we have chosen the relation which assumes that the $4f$ electron moves in a hydrogen-like field. It is

$$a_{4f}=\frac{\gamma}{1836}\frac{R\alpha^2(Z-\sigma)^3}{n^3l(l+\frac{1}{2})(l+1)},$$

where γ is as defined previously and σ is a screening constant. A reasonable value of σ may be obtained from the known fine structure of the $4f^46s^2\ {}^5I$ ground state of Nd I (see P. Schuurmanns[8]). The measured total width of this fine structure is 5048 cm^{-1}. Assuming that Russell-Saunders coupling applies, this width is also equal to 26ζ, where ζ is the Landé interval factor. Thus, $\zeta=194.15$ cm^{-1}. According to a relation in Condon and Shortley,[7] the contribution to $\zeta(4f^4, {}^5I)$ by a single $4f$ electron is $\zeta_{4f}=4\zeta$. Hence, $\zeta_{4f}=776.6$ cm^{-1}. If we again assume hydrogen-like wave functions for this electron, we may write

$$\zeta_{4f}=\frac{R\alpha^2(Z-\sigma)^4}{n^3l(l+\frac{1}{2})(l+1)}.$$

Substituting for the various quantities in this relation, we obtain $\sigma=35.5$. A value of 35.25 is obtained for σ, when we apply the same method to the estimated fine structure of Pr I. Using $\sigma=35.5$ in the expression for a_{4f}, we find the nuclear gyromagnetic ratio $\gamma=+1.53$. With $I=5/2$, the nuclear magnetic moment is

$$\mu=+3.8 \text{ nm}.$$

In view of the very approximate nature of the formulas which we have used in the evaluation of μ, it would be desirable to have an independent estimate of the reliability of the procedure. To this end, we have applied our crude method to Sc^{45}, V^{51}, and Cu^{63}, the nuclear moments of which are known with high precision. The configurations $3d4s^2$, $3d^34s^2$ and $3d^94s^2$, respectively, of these elements are similar to that of Pr in that there is an s^2 closed shell outside of an incompletely filled shell. The terms we have used are the lowest ones of these configurations, namely, ^2D, ^4F, and ^2D, respectively, with values taken from the National Bureau of Standards Atomic Energy Levels.[18] The hyperfine structure data are taken from the article of Brix and Kopfermann in Landolt-Börnstein.[19] We find by our method a value of μ for Sc which is 14 percent

[17] S. Goudsmit, Phys. Rev. **37**, 663 (1931).
[18] U. S. Department of Commerce, National Bureau of Standards Circular No. 467, Vol. I (1949) and Vol. II (1952).
[19] Landolt-Börnstein, *Zahlenwerte und Funktionen* (Verlag. Julius Springer, Berlin, 1952), sixth edition, Vol. I, Part 5.

too low, for V one 16 percent too high, and for Cu one 10 percent too high. Since the wave functions for the $3d$ electrons of these elements are probably not so hydrogen-like as that of the $4f$ electron of Pr, we take the lowest of the above errors, ± 10 percent, as the estimated error of our value of μ.

(c) The Nuclear Electric Quadrupole Moment

According to Casimir, the interaction constant B, in $\sec^{-1}$, is related to the nuclear electric quadrupole moment Q through the relation

$$hB = -e^2Q\left\langle \frac{3\cos^2\theta_e - 1}{r_e^3} \right\rangle_{J,J}.$$

In this relation, h is Planck's constant, e the electronic charge, θ_e and r_e the coordinates of an element of charge in the electronic charge distribution. The expression in the angular brackets is to be averaged over the electronic state for which $m_J = J$. If we assume a central field approximation for the electronic state, we may separate the radial and angular parts of the wave function and write for the quadrupole moment

$$Q = -\frac{hB}{e^2\langle 3\cos^2\theta_e - 1\rangle_{J,J}\langle 1/r_e^3\rangle_{J,J}}.$$

As in our evaluation of the magnetic dipole moment, we shall again assume hydrogenic wave functions and use the same $\langle 1/r_e^3\rangle$ as before, i.e.,

$$\left\langle \frac{1}{r_e^3} \right\rangle = \frac{(Z-\sigma)^3}{a_0^3 n^3 l(l+\frac{1}{2})(l+1)},$$

where a_0 is the radius of the first Bohr orbit in hydrogen.

To evaluate $\langle 3\cos^2\theta_e - 1\rangle$ for the ${}^4I_{9/2}$, $m_J = 9/2$ state, we adopt the procedure followed by Schmidt[20] in the calculation of the quadrupole moment of Ta. The wave function of ${}^4I_{9/2}$, $m_J = 9/2$ is expressed as a sum of products of wave functions of the individual electrons. The matrix elements of $(3\cos^2\theta - 1)$ for the individual electrons are evaluated by means of the Pauli wave functions for the electron. The details of the calculations are shown in the Appendix. The quantity finally obtained is

$$\langle {}^4I_{9/2}|\, 3\cos^2\theta - 1\,|{}^4I_{9/2}\rangle_{m_J=9/2} = -0.2314.$$

Using this and the above-mentioned substitution for $\langle 1/r^3\rangle$, we find for the nuclear quadrupole moment

$$Q = -0.054\times 10^{-24}\ \text{cm}^2.$$

(d) Remarks on Nuclear Moments

In the calculation of the electronic quantities $\langle r_e^{-3}\rangle$ and $\langle 3\cos^2\theta_e - 1\rangle$, we have assumed that Russell-Saunders coupling holds for the three f electrons. Since, however, the exact coupling is not known, it is difficult to say how reliable the nuclear moments we have calculated are. The best indication we have is that our value of μ agrees well with the value of 3.9 nm obtained by Brix[21] from hfs spectra arising essentially from an s-electron. Since, in this case, the uncertainties concerning couplings between electrons are not present, we may conclude that the procedure we have followed is essentially correct and that our value of the magnetic moment of Pr is probably quite reliable. This value lies well within the Schmidt limits of magnetic moments calculated on the basis of an individual particle model of the nucleus and, in fact, lies on one of the "B" limits calculated by Bohr[22] on the assumption of a single particle moving in a nonspherically symmetric field.

A theoretical value for the quadrupole moment of Pr has been given by Van Wageningen and de Boer[23] who also used a spheroidal nuclear model. Their value of -0.86×10^{-24} cm^2 agrees with ours in sign but is an order of magnitude greater. The negative sign of the experimental value tends to confirm the view that the moments of Pr arise mainly from a single proton outside of completed shells and subshells. As to the magnitude of the experimental value, it is difficult to estimate its accuracy. However, it may be pointed out that Schmidt[20] and Brown and Tamboulian,[24] using the same procedure, have obtained consistent values of the quadrupole moment of Ta^{181} from different terms.

The atomic beam laboratory in which the present experiment was done is part of the Spectroscopy Laboratory of the Physics Division of the National Research Council of Canada. To Dr. G. Herzberg and Dr. A. E. Douglas of this laboratory the writer is very grateful for their continued encouragement and assistance throughout the construction of the atomic beam apparatus and the course of the experiment. The writer is also pleased to thank Dr. P. Brix for stimulating discussions on the evaluation of the nuclear moments.

APPENDIX

Evaluation of $(3\cos^2\theta - 1)_{J,J}$

To evaluate the average value of $(3\cos^2\theta - 1)$ for the ${}^4I_{9/2}$ state with $m_J = 9/2$, we first seek an expression for the wave function of this state in terms of single electron wave functions. Let us denote the wave function of a state characterized by the weak-field quantum numbers S, L, J, m_J by the spectroscopic symbol for the state itself, with the addition of a superscript for the value of m_J; thus, ${}^4I_{9/2}{}^{9/2}$ will denote the wave function of the state with $S = 3/2$, $L = 6$, $J = 9/2$, $m_J = 9/2$. Similarly, let us denote a wave function in the strong field or

[20] T. Schmidt, Z. Physik **121**, 63 (1943).

[21] P. Brix, Phys. Rev. **89**, 1245 (1953).

[22] A. Bohr, Phys. Rev. **81**, 134 (1951).

[23] R. Van Wageningen and J. de Boer, Physica **18**, *369* (1952).

[24] B. M. Brown and D. H. Tamboulian, Phys. Rev. **88**, 1158 (1952).

(S, L, m_L, m_S)-representation by the spectroscopic symbol for S and L, followed by two subscripts giving m_L and m_S; thus, ${}^4I_{6,-3/2}$ will denote the wave function of a state with $S=3/2$, $L=6$, $m_L=6$, $m_S=-3/2$. We may then expand ${}^4I_{9/2}{}^{9/2}$ in terms of strong field wave functions thus:

$$
\begin{aligned}
{}^4I_{9/2}{}^{9/2} = {} & (10/13)^{\frac{1}{2}}\,{}^4I_{6,-3/2} - \tfrac{1}{2}(10/13)^{\frac{1}{2}}\,{}^4I_{5,-1/2} \\
& + (5/11\cdot 13)^{\frac{1}{2}}\,{}^4I_{4,1/2} - (1/2\cdot 11\cdot 13)^{\frac{1}{2}}\,{}^4I_{3,3/2}, \qquad \text{(A1)}
\end{aligned}
$$

where the coefficients of the expansion may be found by the use of Table III[3] of Condon and Shortley.[7] The strong field wave functions are expressible by the method of Gray and Wills[25] in terms of products of wave functions of the individual f electrons which give rise to these terms. We find, in the notation of Condon and Shortley,

$$
\begin{aligned}
{}^4I_{6,-3/2} &= (3^-2^-1^-), \\
{}^4I_{5,-1/2} &= [(3^+2^-0^-) + (3^-2^+0^-) + (3^-2^-0^+)]/\sqrt{3}, \\
{}^4I_{4,1/2} &= [\sqrt{5}(3^+1^+0^-) + \sqrt{5}(3^+1^-0^+) + \sqrt{5}(3^-1^+0^+) \\
&\quad + \sqrt{6}(3^+2^+ - 1^-) + \sqrt{6}(3^+2^- - 1^+) \qquad \text{(A2)} \\
&\quad + \sqrt{6}(3^-2^+ - 1^+)]/\sqrt{(3\cdot 11)}, \\
{}^4I_{3,3/2} &= [(2^+1^+0^+) + 2\sqrt{2}(3^+1^+ - 1^+) \\
&\quad + \sqrt{2}(3^+2^+ - 2^+)]/\sqrt{11}.
\end{aligned}
$$

Combining Eqs. (A1) and (A2), we have an expression for ${}^4I_{9/2}{}^{9/2}$ in terms of single electron wave functions.

In order to evaluate $\langle {}^4I_{9/2}{}^{9/2} | 3\cos^2\theta - 1 | {}^4I_{9/2}{}^{9/2} \rangle$, using the above expansion, we need to know the matrix elements of $(3\cos^2\theta - 1)$ for strong field single electron wave functions, i.e., we need to know the value of such expressions as $\langle 2^+ | \alpha | 3^- \rangle$, where $\alpha \equiv 3\cos^2\theta - 1$. By the use of Pauli wave functions for the electron, we may write down the matrix elements of α in the (s, l, j, m) or weak field representation. The desired matrix elements of α in the (s, l, m_s, m_l) or strong field representation will then be obtained by applying the standard transformation between these two representations.

Denoting the wave function of an electron with quantum numbers s, l, j, m by $l_j{}^m$, the following expressions can easily be derived using Pauli wave functions:

$$
\langle l_{j=l\pm\frac{1}{2}}{}^m | \alpha | l_{j=l\pm\frac{1}{2}}{}^m \rangle = -\frac{1}{2}\,\frac{3m^2 - j(j+1)}{j(j+1)},
$$

$$
\langle l_{j=l+\frac{1}{2}}{}^m | \alpha | l_{j=l-\frac{1}{2}}{}^m \rangle = \frac{12m[(l+\frac{1}{2}+m)(l+\frac{1}{2}-m)]^{\frac{1}{2}}}{(2l-1)(2l+1)(2l+3)}.
$$

Into these expressions may be introduced the relativistic correction factors given in Casimir,[4] R' in the diagonal matrix elements with $j=l+\frac{1}{2}$, R'' in the diagonal matrix elements with $j=l-\frac{1}{2}$, and S in the nondiagonal matrix elements. Thus, for an f electron, we have the following weak field matrix elements:

$$
\begin{aligned}
&\langle f_{7/2}{}^{\pm 7/2} | \alpha | f_{7/2}{}^{\pm 7/2} \rangle = -\tfrac{2}{3}R', \\
&\langle f_{5/2}{}^{\pm 5/2} | \alpha | f_{5/2}{}^{\pm 5/2} \rangle = -4R''/7, \\
&\langle f_{7/2}{}^{\pm 5/2} | \alpha | f_{7/2}{}^{\pm 5/2} \rangle = -2R'/21, \\
&\langle f_{5/2}{}^{\pm 3/2} | \alpha | f_{5/2}{}^{\pm 3/2} \rangle = 4R''/35, \\
&\langle f_{7/2}{}^{\pm 3/2} | \alpha | f_{7/2}{}^{\pm 3/2} \rangle = +2R'/7, \\
&\langle f_{5/2}{}^{\pm 1/2} | \alpha | f_{5/2}{}^{\pm 1/2} \rangle = 16R''/35, \\
&\langle f_{7/2}{}^{\pm 1/2} | \alpha | f_{7/2}{}^{\pm 1/2} \rangle = +10R'/21, \\
&\langle f_{7/2}{}^{5/2} | \alpha | f_{5/2}{}^{5/2} \rangle = -\langle f_{7/2}{}^{-5/2} | \alpha | f_{5/2}{}^{-5/2} \rangle = 2(6)^{\frac{1}{2}}S/21, \\
&\langle f_{7/2}{}^{3/2} | \alpha | f_{5/2}{}^{3/2} \rangle = -\langle f_{7/2}{}^{-3/2} | \alpha | f_{5/2}{}^{-3/2} \rangle = 2(10)^{\frac{1}{2}}S/35, \\
&\langle f_{7/2}{}^{1/2} | \alpha | f_{5/2}{}^{1/2} \rangle = -\langle f_{7/2}{}^{-1/2} | \alpha | f_{5/2}{}^{-1/2} \rangle = 4(3)^{\frac{1}{2}}S/105.
\end{aligned}
$$

The transformation of these matrix elements to the (m_l, m_s) scheme is done in a straightforward manner following the choice of phase factors specified on page 123 of Condon and Shortley. We find:

$$
\begin{aligned}
&\langle 3^+ | \alpha | 3^+ \rangle = \langle -3^- | \alpha | -3^- \rangle = -\tfrac{2}{3}R', \\
&\langle 3^- | \alpha | 3^- \rangle = \langle -3^+ | \alpha | -3^+ \rangle \\
&\qquad = -(2/147)(R' + 36R'' + 12S), \\
&\langle 2^+ | \alpha | 2^+ \rangle = \langle -2^- | \alpha | -2^- \rangle = -(12/147)(R' + R'' - 2S), \\
&\langle 2^- | \alpha | 2^- \rangle = \langle -2^+ | \alpha | -2^+ \rangle = (20/245)(R' + R'' - 2S), \\
&\langle 1^+ | \alpha | 1^+ \rangle = \langle -1^- | \alpha | -1^- \rangle \\
&\qquad = (2/245)(25R' + 4R'' + 20S), \\
&\langle 1^- | \alpha | 1^- \rangle = \langle -1^+ | \alpha | -1^+ \rangle \\
&\qquad = (2/245)(25R' + 32R'' - 8S), \\
&\langle 0^+ | \alpha | 0^+ \rangle = \langle 0^- | \alpha | 0^- \rangle = (8/735)(25R' + 18R'' + 6S), \\
&\langle 3^- | \alpha | 2^+ \rangle = \langle -2^- | \alpha | -3^+ \rangle \\
&\qquad = -(2\sqrt{6}/147)(R' - 6R'' + 5S), \\
&\langle 2^- | \alpha | 1^+ \rangle = \langle -1^- | \alpha | -2^+ \rangle \\
&\qquad = (2\sqrt{10}/245)(5R' - 2R'' - 3S), \\
&\langle 1^- | \alpha | 0^+ \rangle = \langle 0^- | \alpha | -1^+ \rangle = (4\sqrt{3}/735)(25R' - 24R'' - S).
\end{aligned}
$$

These matrix elements are now substituted into the expanded form of $\langle {}^4I_{9/2}{}^{9/2} | 3\cos^2\theta - 1 | {}^4I_{9/2}{}^{9/2} \rangle$. The evaluation of the expansion is facilitated by the application of the results of section 6[8] of Condon and Shortley. The final expression obtained is

$$
\begin{aligned}
&\langle {}^4I_{9/2}{}^{9/2} | 3\cos^2\theta - 1 | {}^4I_{9/2}{}^{9/2} \rangle \\
&\qquad = (92\,820R' - 6552R'' - 353\,808S)/1\,156\,155.
\end{aligned}
$$

If we let $R' = R'' = S = 1$, thus neglecting relativistic corrections, we get

$$
\langle 3\cos^2\theta - 1 \rangle_{J,J} = -0.2314.
$$

[25] N. M. Gray and L. A. Wills Phys. Rev. **38**, 248 (1931).

Nuclear Magnetic Resonance in Solid Hydrogen*

F. REIF† and E. M. PURCELL
Lyman Laboratory of Physics, Harvard University, Cambridge, Massachusetts
(Received April 13, 1953)

The fine structure of the nuclear magnetic resonance line in solid hydrogen at low temperatures (1.15°K) was studied experimentally using a recording meter technique. The observed line shape can be explained quantitatively by the magnetic dipole interaction of the two protons in a hydrogen molecule, provided one takes into consideration the effect of the crystalline potential responsible for lifting the rotational degeneracy of the *ortho*-molecules in the solid. Extremely general assumptions concerning the nature of this crystalline potential are sufficient to account for the nuclear resonance data; in particular, one can treat the case where this potential, by virtue of the random mixture of *ortho*- and *para*-molecules in the solid, is not symmetric and not the same at the positions of different *ortho*-molecules. An apparent hysteresis effect in solid hydrogen was observed and some experiments were also performed on solid HD and D_2. The general theory developed in connection with the foregoing experiments also predicts the detectability in solid hydrogen of a resonance line in zero external magnetic field, this line constituting a direct measure of the dipole interaction responsible for the fine structure of the resonance line in high fields. Despite experimental difficulties peculiar to the zero-field experiment, this resonance line was found at the expected frequency of about 165 kc/sec.

I. INTRODUCTION AND EXPERIMENTAL DETAILS

IT is well known that the methods of nuclear magnetic resonance absorption can, under favorable circumstances, yield information useful in the study of the solid state.[1–3] A few years ago Hatton and Rollin[4] investigated the proton resonance line in solid hydrogen as a function of temperature. They observed in particular that the line exhibits at temperatures close to 1°K a fine structure which, however, they were unable to explain quantitivately. The work to be reported in this paper[5] was undertaken with the aim of studying this fine structure as well as other line shapes more carefully both experimentally and theoretically. It was hoped that the relative simplicity of the hydrogen molecule and of the solid to which it gives rise might permit a detailed interpretation of the data and that the results might possibly also help to throw some light on the nature of the specific heat anomaly found in *ortho-para* mixtures of solid hydrogen.[6,7]

The liquid helium cryostat used in our experiments was of all metal construction[8] and terminated at its lower end in a "tail" of 2 inch diameter, small enough to fit between the poles of our magnet. A pump of 60-cubic ft/min capacity was used to reduce the vapor pressure over the liquid helium and thus to reach temperatures in the vicinity of 1.15°K. The sample assembly proper consisted essentially of a glass bulb connected to a tube terminating at its lower end in a glass tip. The glass bulb was filled with hydrogen gas at atmospheric pressure so that, when the lower end of the sample assembly was immersed into the liquid helium, the gas condensed as a solid in the sample tip. The rf coil was wound on the outside of this tip and was connected electrically to a point outside the cryostat by a specially constructed coaxial cable about 3 feet long. The temperature of the sample was determined by measuring the vapor pressure of the surrounding liquid helium bath.[9] This procedure was perhaps not wholly satisfactory because of the low thermal conductivity of glass at these low temperatures and the existence of a few sources of heat influx into the sample. Of these the heat liberated in the *ortho-para* conversion of the solid hydrogen was probably the most important and it is estimated that it may have resulted in a sample temperature higher than that of the helium bath by a few hundredths of a degree.

The permanent magnet used in these experiments provided a field of 3500 gauss. The radiofrequency spectrometer was of the type originally designed by Pound[10] and subsequently improved by Watkins,[11] the rf coil and coaxial cable described in the preceding paragraph forming part of the tank circuit of the oscillator. The output of the rf spectrometer could be displayed directly on an oscilloscope. Alternatively a clock motor followed by a set of reducing gears could be made to rotate the tuning condenser of the oscillator, changing its frequency very slowly. The output of the spectrom-

* This work was partially supported by the joint program of the U. S. Office of Naval Research and the U. S. Atomic Energy Commission.
† Present address: Institute for the Study of Medals, the University of Chicago, Chicago, Illinois.
[1] Bloembergen, Purcell, and Pound, Phys. Rev. **73**, 679 (1948).
[2] G. E. Pake, J. Chem. Phys. **16**, 327 (1948).
[3] H. S. Gutowsky and G. E. Pake, J. Chem. Phys. **18**, 162 (1950).
[4] J. Hatton and B. V. Rollin, Proc. Roy. Soc. (London) **A199**, 222 (1949).
[5] Previously described by F. Reif, thesis, Harvard University, 1953 (unpublished).
[6] Mendelssohn, Ruhemann, and Simon, Naturwiss. **18**, 34 (1930); Z. Phys. Chem. **B15**, 121 (1931).
[7] R. W. Hill, *Proceedings of the International Conference on Low Temperature Physics* (Oxford University Press, London, 1951), p. 8.
[8] The design of the cryostat was largely based on that described by W. E. Henry and R. L. Dolecek, Rev. Sci. Instr. **21**, 496 (1950).
[9] Royal Society Mond Laboratory, *Helium Vapor Pressure Tables, 1949 Scale* (Cambridge University Press, Cambridge, 1949).
[10] R. V. Pound and W. D. Knight, Rev. Sci. Instr. **21**, 219 (1950).
[11] G. D. Watkins, thesis, Harvard University, 1952 (unpublished).

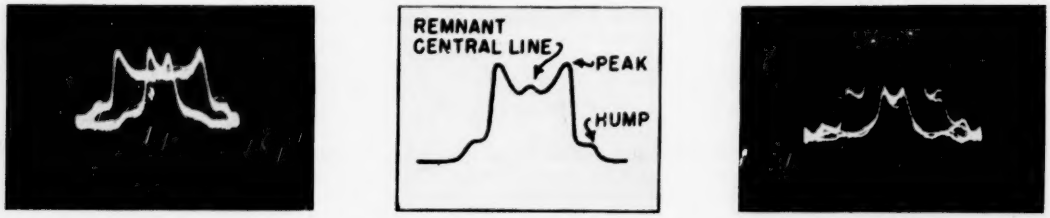

FIG. 1. Nuclear resonance lines in solid hydrogen. The photographs were taken with a sinusoidal (60-cps) magnetic field modulation of about 130-gauss peak-to-peak amplitude and with a sinusoidal sweep on the X axis of the oscilloscope. (a) The line at 1.16°K. (b) Schematic representation of the line shape. (c) The line at about 1.35°K (or at 1.16°K after irreversible transition).

eter was then fed, via amplifiers and a phase-sensitive detector, onto a recording meter. The latter plotted the *derivative* of the absorption line when the sinusoidal magnetic field modulation was small. A secondary frequency standard and associated rf measuring equipment permitted accurate frequency measurements to be made.

II. EXPERIMENTAL RESULTS—HIGH FIELD

The solid hydrogen resonance line is intense enough to be observed on the oscilloscope. At 4.2°K the line is a simple one of a width (measured between points of maximum and minimum slopes) of about 18 kc/sec. As the temperature is reduced the line at first increases in intensity as one would expect. Below 1.5°K it becomes flanked by two side peaks which, as the temperature is reduced further, grow in intensity at the expense of the central line. The resulting line shape at 1.16°K is shown in the photograph of Fig. 1(a) and is portrayed schematically in Fig. 1(b). It exhibits the fine structure first reported by Hatton and Rollin[4] and shows, in addition to the two peaks, a vestige of the central line. In addition it reveals a noteworthy feature made apparent in the photograph only by virtue of the very large magnetic field modulation used, namely, the existence of two "humps" accompanying the outer parts of the two peaks. The detailed quantitative study of this line shape was made with the recording meter technique which yields a plot of the derivative of the line. This plot has the general form shown in Fig. 2 where we have also indicated the experimental values of certain parameters characterizing the line shape.

As the temperature is slowly raised, between 1.30°K and 1.35°K, the resonance line shows a rather rapid transition from the shape of Fig. 1(a) to that of Fig. 1(c). The latter shape is of course reminiscent of the shape obtained at some stage of the original cooling down of the hydrogen sample to the lowest temperature. An apparent irreversibility or hysteresis is also observed; that is, as the temperature is again reduced from 1.35°K to 1.16°K, the line seems to persist in the shape of Fig. 1(c). In one of our runs it showed no indication of reverting to the low-temperature shape of Fig. 1(a) after being kept at 1.16°K for five hours. At this temperature study with the recording meter of line shapes such as that of Fig. 1(c) shows that: (1) the central line has definitely grown in intensity at the expense of the two peaks; (2) the rest of the line shape, and in particular the values of the parameters mentioned in Fig. 2, remain unchanged irrespective of the intensity of the central line; (3) as the rf level is increased, the peak amplitudes labeled M_1 and M_2 in Fig. 2 saturate quite readily (the ratio M_1/M_2 staying constant) while M_0 decreases in intensity only slightly. In these respects the central line behaves in a manner quite distinct from the rest of the line.

We also performed one experiment to study the proton resonance line in solid HD. The line at 4.2°K is a simple one of a width between points of maximum slope of about 18.5 kc/sec. As the temperature is reduced to 1.16°K the line simply grows in intensity by a factor of 3.6[12] (as one would expect if the line shows no splitting) while its width remains unchanged; nor does a search with the recording meter reveal any evidence of a fine structure. The width of the line, incidentally, shows the rather unexpected behavior of *de*creasing as the rf field is *in*creased beyond 0.05-gauss rms, the point where saturation begins to set in. A similar phenomenon was also observed in the case of the H_2 line at 4.2°K, but we have no wholly satisfactory explanation for it.[13]

Finally we also made one experimental run with solid D_2. At 1.16°K we observed only a single deuteron line and could not find any evidence of a fine structure. This experiment was, however, not performed under optimum conditions and ought to be repeated.

III. THEORETICAL CONSIDERATIONS

(a) General Remarks on Solid Hydrogen

The hydrogen molecule is a diatomic one with an internuclear separation of 0.75A. The small moment of

[12] Intensity comparisons are made by means of the calibrator which is part of the rf spectrometer; see reference 11.

[13] A numerical estimate shows readily that the effect cannot be due simply to a rise in temperature of the sample caused by the absorption of rf power. The phenomenon might be understandable *if* one could assume that different regions in the sample differ both in relaxation time and line width. We were interested to find a similar "line-narrowing" phenomenon mentioned in connection with quite a different class of experiments in a recent paper by A. H. Cooke and L. E. Drain, Proc. Phys. Soc. (London) **A65**, 894 (1952).

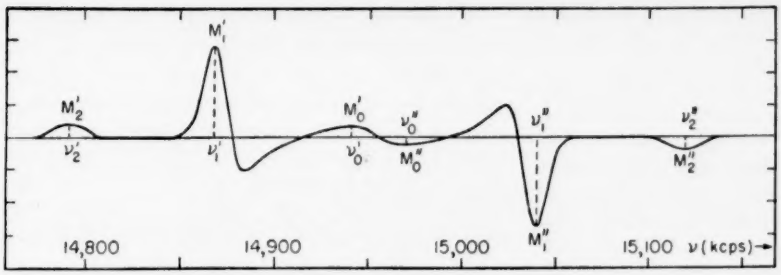

FIG. 2. The derivative of the line of Fig. 1(a) as obtained from a recording meter plot. We have indicated the several maximum amplitudes of this derivative curve by the letters M, the frequencies at which they occur by the letters ν. The maximum M_0 correspond to the remnant central line, M_1 to the peaks, M_2 to the humps. The experimental values quoted are the averages of four meter plots taken in two different liquid helium runs and with different oscillation levels and modulation amplitudes. The indicated errors are intended to be merely a measure of the consistency of the data so averaged.

inertia of the molecule leads to a wide separation of its rotational energy levels, the latter being given by $E_J=BJ(J+1)$, with $B/k=86°$K when measured in terms of degrees. Thus the molecular rotation cannot be treated classically at the lower temperatures. Furthermore it is well known that the Pauli exclusion principle—which here requires the antisymmetry of the molecular wave function under interchange of the two nuclei of spin $\frac{1}{2}$—leads to the conclusion that molecules with total spin quantum number $I=1$ (*ortho*-hydrogen—symmetric in spin) have only antisymmetric rotational wave functions for which J is odd; while conversely molecules with $I=0$ (*para*-hydrogen—antisymmetric in spin) have only symmetric rotational wave functions for which J is even. Since at normal or low temperatures a molecule has only a very small probability of making a transition from an *ortho*- to a *para*-state[14] or vice versa, ordinary hydrogen consists of a mixture of two essentially distinct gases, *ortho*-H_2 and *para*-H_2. The state of metastable equilibrium between these two species persists in the molecular solid which then normally consists of 75 percent *ortho*-molecules in the state $J=1$ and 25 percent *para*-molecules in the state $J=0$.[15] Since for the latter $I=0$, the *ortho*-molecules alone are responsible for the nuclear resonance absorption in solid hydrogen.

The forces between hydrogen molecules in the solid are quite weak. One indication of this fact is the low heat of fusion from which Pauling[16] infers that molecules in the solid should be able to rotate almost freely. Another indication is the existence in *liquid* hydrogen of rotational Raman lines at frequencies in close agreement with those predicted from the rotational energy levels of the free H_2 molecule.[17]

[14] A. Farkas, *Orthohydrogen, Parahydrogen, and Heavy Hydrogen* (Cambridge University Press, Cambridge, 1935).

[15] The 3:1 ratio for ordinary hydrogen corresponds to the equilibrium distribution between the two kinds of molecules at room temperature or above, i.e., to the ratio of the statistical weights of the two spin states. The *ortho-para* conversion rate in the solid is temperature-independent; it amounts initially to about 1 percent per hour and decreases as time goes on. See reference 14, p. 78; also E. Cremer, Z. Physik. Chem. **B39**, 445 (1938).

[16] L. Pauling, Phys. Rev. **36**, 430 (1930).

[17] J. C. McLennan and J. H. McLeod, Nature **123**, 160 (1929).

The crystal structure of solid *para*-hydrogen is known from x-ray diffraction studies to be hexagonal close-packed,[18] each molecule in the solid having 12 nearest neighbors at a distance $R=3.75$A.

(b) The Crystalline Potential

In solid hydrogen, at temperatures not too far below the melting point of 14°K, an *ortho*-molecule has essentially equal probability of being found in any of the three degenerate states associated with $J=1$ and in this sense the average electron distribution of an *ortho*-molecule is then spherically symmetric like that of a paramolecule. The solid consists of a random mixture of *ortho*- and *para*-molecules and may be assumed to have the same crystal structure as pure *para*-hydrogen. At sufficiently low temperatures the nonspherical nature of the *ortho*-molecules must assert itself and the potential—due to neighboring molecules—in which a given molecule finds itself can be expected to depart from spherical symmetry. The orientation dependent part $V(\vartheta, \varphi)$ of this potential is small compared to the binding energy of the molecule in the solid and very small compared to B. It can thus be treated as a small perturbation upon the free rotation of the molecule and its effect is to lift the rotational degeneracy of the *ortho*-molecule in the solid.

Because *ortho*- and *para*-molecules are randomly mixed in the solid, the local surroundings of different *ortho*-molecules are not the same and are likely to be devoid of any particular symmetry properties. We shall therefore make no specializing assumptions about the functional form of V, nor shall we need to assume that V is the same at the position of each *ortho*-molecule. The most general $V(\vartheta, \varphi)$ at the position of a given *ortho*-molecule can be written as an expansion in spherical harmonics,

$$V(\vartheta, \varphi)=\sum_{J \text{ even}} C_{J,m} Y_{J,m}(\vartheta, \varphi). \qquad (1)$$

[18] Keesom, de Smedt, and Mooy, Proc. Koninkl. Akad. Wetenschap, Amsterdam **33**, 814 (1930); also Communs. Phys. Lab. Univ. Leiden **19**, No. 209d, 35 (1931).

Here the restriction to even values of J is due to the fact that V must be invariant under inversion because of the symmetry of the H_2 molecule. Since in our first-order perturbation calculation we shall be only interested in calculating matrix elements for the state $J=1$, all terms with $J>2$ yield vanishing results. The constant $J=0$ term is of no interest and thus V can be expressed solely in terms of spherical harmonics of order $J=2$, or equivalently as a general quadratic form of the $J=1$ harmonics,

$$\lambda_\xi=\sin\vartheta\cos\varphi,\quad \lambda_\eta=\sin\vartheta\sin\varphi,\quad \lambda_\zeta=\cos\vartheta. \tag{2}$$

This quadratic form can always be reduced to diagonal form by transforming to new axes ξ, η, ζ with respect to which the most general V assumes the form

$$V=A_\xi\lambda_\xi^2+A_\eta\lambda_\eta^2+A_\zeta\lambda_\zeta^2, \tag{3}$$

where the A's are constants with $A_\xi\neq A_\eta\neq A_\zeta$ in general. The effect of V upon the $J=1$ state is to split the latter into three states characterized by the wave functions and corresponding energies:

$$\psi_\zeta\sim\lambda_\zeta,\quad E_\zeta=\langle\psi_\zeta|V|\psi_\zeta\rangle=\tfrac{1}{5}(A_\xi+A_\eta+3A_\zeta), \tag{4}$$

with the other two states obtained by cyclic permutation of subscripts.

For the sake of comparison we also want to discuss briefly the case where V is axially symmetric. This case is the one sometimes discussed in the literature[19] and would indeed be likely to represent the situation in a (hypothetical) crystal of pure *ortho*-hydrogen. Here two of the coefficients in (3) are equal, and one can write V without loss of generality in the form

$$V_S=V_0(1-\lambda_\zeta^2)=V_0\sin^2\vartheta, \tag{5}$$

where the ζ axis is chosen along the axis of symmetry. If we consider the angular momentum quantized along this axis, then the effect of V_S upon the $J=1$ state is to split the latter into two distinct states, labeled by

$$\begin{aligned}&\bar{m}_J=0: \quad \psi_0\sim\cos\vartheta,\quad E_0=\tfrac{2}{5}V_0,\\ &\bar{m}_J=\pm1: \quad \psi_{\pm1}\sim\sin\vartheta e^{\pm i\varphi},\quad E_{\pm1}=\tfrac{4}{5}V_0,\end{aligned} \tag{6}$$

where the latter state is doubly degenerate. Here the notation $\bar{m}$ has been introduced to denote quantum numbers referred to the ξ, η, ζ axes.

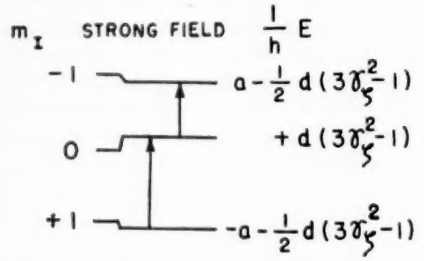

FIG. 3. Energy level diagram for solid hydrogen in strong magnetic field. Energy levels for the state ψ_ζ.

[19] See, for example, R. B. Scott and F. G. Brickwedde, J. Chem. Phys. **5**, 736 (1937).

(c) Energy Levels in Strong Magnetic Field

The magnetic interactions of a hydrogen molecule are very small compared to V (of the order of 0.001°K compared to 1°K) and can be described with sufficient accuracy for our purpose by the Hamiltonian $\mathcal{H}=\mathcal{H}_{ab}+\mathcal{H}_{cd}$, where

$$\left.\begin{aligned}h^{-1}\mathcal{H}_{ab}&=-aI_z-bJ_z,\\ h^{-1}\mathcal{H}_{cd}&=-c\mathbf{I}\cdot\mathbf{J}-5d\left[3(\mathbf{I}^{(1)}\cdot\mathbf{r}/r)(\mathbf{I}^{(2)}\cdot\mathbf{r}/r)-\mathbf{I}^{(1)}\cdot\mathbf{I}^{(2)}\right].\end{aligned}\right\} \tag{7}$$

$$\left.\begin{aligned}a&=(2\mu_i/h)H_0=4.258H_0\ \text{kc/sec},\\ b&=(\mu_J/hJ)H_0=0.6717H_0\ \text{kc/sec},\\ c&=(2\mu_i/h)H'=113.8\ \text{kc/sec},\\ d&=\tfrac{4}{5}(\mu_i^2/h)\langle r^{-3}\rangle=57.68\ \text{kc/sec}\quad(\text{for } J=1).\end{aligned}\right\} \tag{8}$$

Here we have used Ramsey's notation[20] to facilitate comparison with his discussion of the free H_2 molecule. $\mathbf{I}=\mathbf{I}^{(1)}+\mathbf{I}^{(2)}$ is the total nuclear spin in units of h; μ_i denotes the magnetic moment of the proton, μ_J the rotational magnetic moment of the molecule in state J. The terms in a and b represent, respectively, the interactions of the nuclear magnetic moments and of the rotational magnetic moment of the molecule with the external magnetic field of H_0 gauss in the z direction. The terms in c and d express, respectively, the interaction of the nuclear moments with the magnetic field H' produced by the molecular rotation, and the magnetic dipole-dipole interaction of the two protons in the molecule. r denotes the internuclear distance, $\mathbf{r}/r$ a unit vector along the line joining the two nuclei; $\langle r^{-3}\rangle$ is the expectation value of r^{-3} in the particular vibrational and rotational state under consideration. The numerical values in (8) are the ones given by Ramsey[20] for the *free* H_2 molecule studied in molecular beam experiments.

The three sublevels of (4) which result from the crystalline splitting of the $J=1$ state can be considered nondegenerate provided they are split by amounts large compared to b—a very modest requirement. Proceeding by simple perturbation theory we note first that, since the wave functions (4) are real, the expectation value of $\mathbf{J}$ vanishes in each of the three states of (4). The crystalline field has quenched the rotational magnetic moment of the molecule and the interactions b and c in (7) vanish. In a strong magnetic field $\mathcal{H}_{ab}\gg\mathcal{H}_{cd}$; we thus consider $\mathbf{I}$ quantized along the z axis and get for the perturbation energy of an *ortho*-molecule (with $J=1$, $I=1$) in the state ψ_ζ,

$$\begin{aligned}h^{-1}E_\zeta&=-am_I-5d\langle m_I\psi_\zeta|\tfrac{1}{2}(3\cos^2\theta-1)\\ &\qquad\times(3I_z^{(1)}I_z^{(2)}-\mathbf{I}^{(1)}\cdot\mathbf{I}^{(2)})|m_I\psi_\zeta\rangle\\ &=-am_I-(5/2)d(\tfrac{3}{2}m_I^2-1)\\ &\qquad\times\int(3\cos^2\theta-1)|\psi_\zeta|^2d\Omega.\end{aligned} \tag{9}$$

[20] N. F. Ramsey, Phys. Rev. **85**, 60 (1952).

Here θ is the angle between $\mathbf{r}$ and $\mathbf{H}_0$, and it is of interest to note that the integral represents simply Pake's[2] dipole-dipole interaction factor for fixed protons, here averaged over the probability distribution of the molecular quantum state under consideration.

The integral in (9) is readily evaluated if one expresses $\mathbf{r}/r$ in terms of its components λ_ξ, λ_η, λ_ζ with respect to the ξ, η, ζ axes. Denoting the direction cosines of $\mathbf{H}_0$ with respect to these axes by γ_ξ, γ_η, γ_ζ, one has $\cos\theta=\gamma_\xi\lambda_\xi+\gamma_\eta\lambda_\eta+\gamma_\zeta\lambda_\zeta$ and

$$\langle\psi_\xi|\cos^2\theta|\psi_\xi\rangle=\langle\psi_\xi|\gamma_\xi^2\lambda_\xi^2+\gamma_\eta^2\lambda_\eta^2+\gamma_\zeta^2\lambda_\zeta^2|\psi_\xi\rangle,$$

since cross-terms vanish. The last matrix element is of the same form as (3) and was thus already evaluated in (4). The integral in (9) is then simply

$$\langle\psi_\xi|3\cos^2\theta-1|\psi_\xi\rangle=\tfrac{3}{5}(\gamma_\xi^2+\gamma_\eta^2+3\gamma_\zeta^2)-1=\tfrac{2}{5}(3\gamma_\zeta^2-1), \tag{10}$$

and (9) becomes

$$h^{-1}E_\xi=-am_I+d(3\gamma_\zeta^2-1)(1-\tfrac{3}{2}m_I^2), \tag{11}$$

with similar expressions for E_ξ and E_η obtainable by interchange of subscripts. The energy level diagram corresponding to (11) is shown in Fig. 3.

(d) Line Shape

The interaction of the molecule with the rf magnetic field $\mathbf{H}_1$ is given by

$$\mathcal{H}_{\text{rad}}=-(2\mu_i\mathbf{I}+\mu_J\mathbf{J}/J)\cdot\mathbf{H}_1. \tag{12}$$

If one disregards the very high-frequency transitions between the sublevels (4), then (12) implies, for $\mathbf{H}_1$ perpendicular to $\mathbf{H}_0$, the selection rule $\Delta m_I=\pm1$. Each of the three sublevels of (4) thus gives rise to two resonance lines. For the state ψ_ξ their frequencies are given by

$$\nu_\xi=a\pm\tfrac{3}{2}d(3\gamma_\zeta^2-1) \tag{13}$$

(with corresponding expressions for the frequencies arising in the other two states). Equation (13) depends on the orientation of the ξ, η, ζ axes at the position of the *ortho*-molecule under consideration with respect to the external field $\mathbf{H}_0$. Since this orientation is different for different *ortho*-molecules in a crystal and also for the different crystals in the polycrystalline hydrogen sample, it is necessary to average (13) over the angular factors γ in order to find the intensity distribution function $p(\nu)$ of the resulting line.

Consider transitions labeled by r between energy levels E_r and $E_{r'}$ ($E_r<E_{r'}$) and with transition probabilities per unit time W_r. These levels and the resulting frequencies $\nu_r=E_{r'}-E_r$ as well as W_r may all depend on the parameter γ_r which has probability $w_r(\gamma_r)d\gamma_r$ of assuming a value between γ_r and $\gamma_r+d\gamma_r$. Then

$$\begin{aligned}p(\nu)d\nu&\sim\sum_r\int_\nu^{\nu+d\nu}(W_re^{-E_r/kT}-W_re^{-E_{r'}/kT})w_r(\gamma_r)d\gamma_r\\&=\sum_r\int_\nu^{\nu+d\nu}W_re^{-E_r/kT}(1-e^{-h\nu_r/kT})\\&\qquad\times w_r(\gamma_r)\left|\frac{d\gamma_r}{d\nu_r}\right|d\nu_r,\end{aligned} \tag{14}$$

where the summation $\sum_r$ is carried over all frequencies ν_r having possible values in the range ν, $\nu+\Delta\nu$. For $h\nu/kT\ll1$ (14) yields

$$p(\nu)\sim\frac{h\nu}{kT}\sum_r\left[e^{-E_r/kT}W_rw_r(\gamma_r)\left|\frac{d\nu_r}{d\gamma_r}\right|^{-1}\right]_{\nu_r=\nu}. \tag{15}$$

In our present case, since $h\nu/kT\ll1$, $\exp(-E_r/kT)$ is the same for the two lines (13) arising in the state ψ_ξ; further, since $d\ll a$, the factor $h\nu/kT\approx ha/kT$. Also by (12),

$$W(m_I+1\leftarrow m_I)\sim|\langle m_I+1|I_x|m_I\rangle|^2\sim(1-m_I)(2+m_I),$$

so that $W(0\leftarrow-1)=W(-1\leftarrow0)$. For random orientations $w_r(\gamma_r)$ is proportional to the solid angle, i.e., $w_r(\gamma_r)d\gamma_r\sim d\gamma_r$. Hence the resulting line shape arising from the two lines (13) is given by $p(\nu)\sim\gamma^{-1}(\nu)$ or, writing $\tilde\nu=\nu-a$,

$$\begin{aligned}p(\tilde\nu)&=0 && \text{if } \tilde\nu<-3d,\\&\sim(-\tilde\nu+\tfrac{3}{2}d)^{-\frac{1}{2}} && \text{if } -3d<\tilde\nu<-\tfrac{3}{2}d,\\&\sim(-\tilde\nu+\tfrac{3}{2}d)^{-\frac{1}{2}}+(\tilde\nu+\tfrac{3}{2}d)^{-\frac{1}{2}} && \text{if } -\tfrac{3}{2}d<\tilde\nu<0,\end{aligned} \tag{16}$$

with $p(\tilde\nu)=p(-\tilde\nu)$. A plot of (16) is shown in Fig. 4(a). By (13) the lines arising in states ψ_ξ and ψ_η also give rise to the same shape function (16) so that the superposition of all the lines still yields the shape of Fig. 4(a). The latter is identical with that calculated by Pake[2] for the case of interacting pairs of protons rigidly fixed in position. The only difference is that in Fig. 4(a) the separation between the two peaks is $3d=\frac{2}{5}(6\mu_i^2/\text{hr}^3)$, i.e., as a result of the averaging process of (10), only $\frac{2}{5}$ as large as in Pake's case.

For the sake of completeness, one still needs to examine the effect of the small correction terms (of order V/B and consisting of spherical harmonics with $J=3, 5, 7, \cdots$) which, in a more accurate perturbation calculation, become admixed to the simple rotational wave functions (2) used in our discussion up to this point. The presence of these correction terms does not affect the line shape of Fig. 4(a) appreciably. In particular, it can be shown that, quite irrespective of the exact form of V, the shape function $p(\tilde\nu)$ in the wings of the line (i.e., near $|\tilde\nu|=3d$) is still given by Eq. (16) with d replaced by τd, where τ is a correction factor

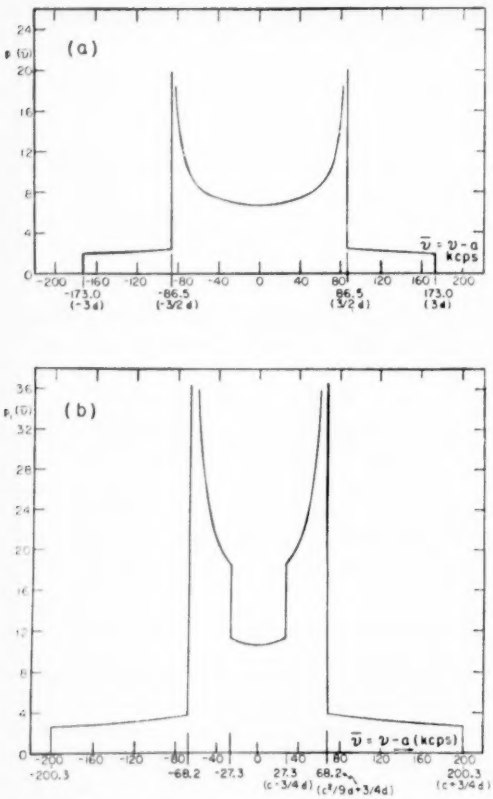

FIG. 4. Theoretical line shapes for a polycrystalline sample of solid hydrogen in strong magnetic field. (a) Calculated line shape corresponding to Eq. (16). This is also the shape arising from the two lines in the state $\bar{m}_J=0$ (case of axially symmetric V_S). (b) Shape arising from the four lines in the state $\bar{m}_J=\pm 1$ (case of axially symmetric V_S). Broadening which is due to neighboring molecules is not taken into account. The numerical values used are those based upon the parameters c and d for the free molecule. The normalization of the curves is arbitrary but their relative intensities are correctly indicated.

which, for an assumed separation between the sublevels (4) of about 5°K, has the value[21]

$$\tau d \approx 1.01 d. \tag{17}$$

This result is of some importance for the subsequent interpretation of the data.

Parenthetically we remark that the calculation for the axially symmetric potential V_S is slightly more complex because of the degeneracy of the $\bar{m}_J=\pm 1$ state. The energy levels can be computed either by wave mechanical or by purely matrix methods[5] and are given by

$$E_{\bar{m}_J} = -am_I - b\gamma\bar{m}_J - c\gamma\bar{m}_J m_I + d(3\gamma^2-1)(1-\tfrac{3}{2}\bar{m}_J^2)(1-\tfrac{3}{2}m_I^2), \tag{18}$$

where γ is the cosine of the angle between $\mathbf{H}_0$ and the symmetry axis ζ. The energy level diagram for the nondegenerate $\bar{m}_J=0$ state is thus the same as that for (11). In the $\bar{m}_J=\pm 1$ state, however, the ζ component of the rotational angular momentum of the molecule is a constant of the motion and one thus gets a finite spin-rotational moment interaction. The energy-level diagram for this state is therefore more complicated and involves the constants b and c. The nondegenerate $\bar{m}_J=0$ state again gives rise to the line shape of Fig. 4(a). On the other hand, the 4 lines arising in the $\bar{m}_J=\pm 1$ state yield the shape function shown in Fig. 4(b). The resultant line shape then consists predominantly of the shape characterizing the state lying lower in energy and superimposed upon it the shape of the higher-lying state weighted by $\exp(-\Delta E/kT)$, where ΔE is the energy difference between the two states of Eq. (6).

Finally we must take into account the fact that the absorption lines (13) are not infinitely sharp but are broadened by the interaction of the magnetic moment of the molecule under consideration with the magnetic moments of neighboring molecules. If $g(\nu-\nu_0)$ is the intensity distribution function of one of these lines, then its second moment $\langle(\Delta\nu)^2\rangle = \int g(\nu-\nu_0)(\nu-\nu_0)^2 d\nu$ (where ν_0 is the central frequency or frequency of the unbroadened line) is calculable by the method of diagonal sums.[22] Considering each *ortho*-molecule to be in the lowest of its rotational sublevels (4), the complete Hamiltonian for all the molecules in a crystal can be written in the form ($\mathbf{r}_{kl}$ are intermolecular distances and the summations extend over all molecules)

$$\mathcal{H}_{\text{tot}} = \mathcal{H}_0 + \mathcal{H}_{\text{dip}} = \sum_k [-2\mu_i H_0 I_{zk} - \delta_k I_{zk}^2 + 2/3\delta_k] + \sum_{k<l}(2\mu_i)^2 r_{kl}^{-3}[\mathbf{I}_k\cdot\mathbf{I}_l - 3(\mathbf{I}_k\cdot\mathbf{r}_{kl})(\mathbf{I}_l\cdot\mathbf{r}_{kl})r_{kl}^{-2}], \tag{19}$$

where the terms in $\delta_k = \frac{3}{2}d(3\gamma_k^2-1)$ are introduced to give the proper energy levels for a single molecule. For large splittings between the lines (13) (i.e., $\delta_k \gg \langle(\Delta\nu)^2\rangle^{\frac{1}{2}}$) these terms make $\mathcal{H}_{\text{tot}}$ similar to a Hamiltonian discussed by Ishiguro *et al.*[23] whose result, averaged over all angular factors, is

$$\langle(\Delta\nu)^2\rangle = (2\mu_i)^4 h^{-2}\sum_l r_{kl}^{-6}. \tag{20}$$

This expression is smaller by a factor $\frac{5}{6}$ than that obtained by Van Vleck[22] since here the effect of the terms in δ_k is to make a smaller part of $\mathcal{H}_{\text{dip}}$ commute with $\mathcal{H}_{\text{tot}}$ and thus to reduce the width of each of the split lines (13) to a value less than that of the unsplit line. Numerically (20) becomes for the close-packed crystal

[21] The fact that τ is greater than unity can be understood qualitatively by noting that if, for example, the potential V is lowest along the ζ axis [i.e., if A_ξ is the smallest coefficient in (1)], then the correction terms will tend to make the probability distribution more concentrated along the ζ axis than the wave function ψ_ξ of (4) would indicate. Hence the averaging process (9) yields a result closer to that obtained for rigidly fixed nuclei, i.e., a splitting larger than in (13).

[22] J. H. Van Vleck, Phys. Rev. **74**, 1168 (1948).

[23] Ishiguro, Kambe, and Usui, Physica **17**, 310 (1951); also J. F. Ollom, thesis, Harvard University, 1948 (unpublished).

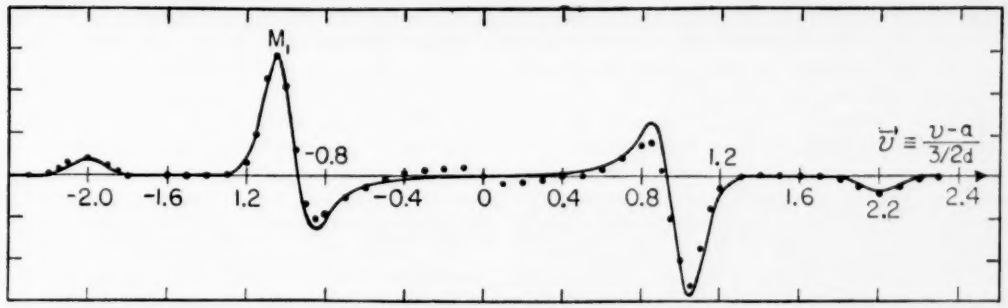

FIG. 5. Solid hydrogen line in strong magnetic field: comparison of theory and experiment. Solid curve: Derivative of the theoretical line shape calculated by Eq. (24) with $\sigma/\frac{3}{2}d=0.086$. (For free molecules $d=57.68$ kc/sec so that $\sigma=7.4$ kc/sec.) Dots: Experimental points taken from a typical recording meter plot and fitted to the theoretical curve by taking $a=14\,953.6$ kc/sec, $d=54.55$ kc/sec, and normalizing to agree with the amplitude of peak M_1.

structure discussed in (a),

$$(\Delta\nu)^2=(2\mu_s)^4\hbar^{-2}\times\tfrac{3}{4}\{12R^{-6}+6(\sqrt{2}R)^{-6}+\cdots\}, \quad (21)$$

where the factor $\frac{3}{4}$ is the probability of a molecule being *ortho* and takes into account the fact that the *para*-molecules with $I=0$ do not contribute to the broadening. Here R is the separation between nearest neighbor molecules, in this case $R=3.75\cdot10^{-8}$ cm. One thus gets

$$\sigma\equiv\langle(\Delta\nu)^2\rangle^{\frac{1}{2}}=7.25 \text{ kc/sec}. \quad (22)$$

If the effect of intermolecular broadening is taken into account, one gets instead of the shape function $p(\nu)$ of (16) the modified function

$$P(\nu)=\int_{-\infty}^{\infty}g(\nu-\nu_0)p(\nu_0)d\nu_0=-\int_{-\infty}^{\infty}p(\nu+x)g(x)dx, \quad (23)$$

where $x=\nu_0-\nu$. More directly, the derivative of the absorption line, which is the quantity measured in our experiments, is

$$\frac{dP(\nu)}{d\nu}=\int_{-\infty}^{\infty}\frac{dg(\nu-\nu_0)}{d\nu}p(\nu_0)d\nu_0 =-\int_{-\infty}^{\infty}p(\nu+x)\frac{dg}{dx}dx. \quad (24)$$

For g we shall in the following assume a Gaussian:

$$g(x)=(2\pi)^{-\frac{1}{2}}\sigma^{-1}\exp(-x^2/2\sigma^2). \quad (25)$$

The integral (24) can then be evaluated numerically; the result is plotted in Fig. 5.

IV. DISCUSSION OF RESULTS

In Fig. 5 we have also indicated the experimental points derived from a typical recording meter plot. In order to fit these points to the theoretical curve we have adjusted only one significant parameter, namely d. If, for the time being, we disregard the existence of the small remnant central line, then the agreement between the theoretical curve and the experimental points is seen to be satisfactory. We note also that, if we had assumed the crystalline potential to be axially symmetric, then the same agreement could be obtained provided that the $m_J=0$ state were to lie lower than the $m_J=\pm1$ state by a sufficient amount so that the latter's contribution to the line shape were less than 20 percent; for otherwise the admixture of the shape of Fig. 4(b) to that of Fig. 4(a) would have been observable.

In terms of the notation of Fig. 2, the theoretical curve calculated by (24) yields $\Delta_2/\Delta_1=1.90$ and $M_1/M_2=7.9$, in fair agreement with the experimental values listed in Fig. 2. Both these ratios depend on σ; but ν_2, the position of the maximum M_2, does not (to a very good approximation). For, since $p(\nu)$ behaves in the vicinity of $\nu=3d$ like a step function, (24) reduces there (provided $\sigma\ll3/2d$) to

$$\frac{dP}{d\bar{\nu}}\sim-\int_{-\infty}^{3d-\bar{\nu}}\frac{dg}{dx}dx\sim g(\bar{\nu}-3d).$$

Hence, irrespective of the exact form of $g(x)$ (as long as it is symmetric), the maxima M_2 occur essentially at $\bar{\nu}=\pm3d$. Thus the separation Δ_2 between the peaks M_2 of the derivative curve provides a direct measure of the quantity d. One has, including a very small correction term which refines the preceding argument, and taking into account the correction factor τ of Eq. (17),

$$6\tau d=\Delta_2[1+(4/3)(\sigma/\Delta_2)^2], \quad (26)$$

from which one gets for the value of d in solid hydrogen

$$\tau d_s=54.71\pm0.25 \text{ kc/sec}, \quad (27)$$

or

$$d_s=54.2\pm0.5 \text{ kc/sec},$$

where the probable error includes an allowance for systematic error. Equation (27) is to be compared with the value d_f for the free molecule; by (8),

$$d_s/d_f=\langle r^{-3}\rangle_s/\langle r^{-3}\rangle_f=0.94.$$

The ratio $\langle r_s\rangle/\langle r_f\rangle$ cannot be inferred directly from this

result since the ground-state vibrational wave function of the molecule in the solid may differ somewhat from that of the free molecule. It seems safe to say only that, if the above interpretation of the fine structure is correct, the internuclear separation in a molecule in the solid slightly exceeds that in a free molecule.

There remains, however, an important question which bears on the preceding argument and on other inferences one might try to draw from the experimental results. It concerns the rate at which transitions occur among the sublevels (4) into which the state $J=1$ is split by the crystalline field. If the average rate of such transitions per molecule were very small compared to the frequency d, then the existence of the central line would be hard to understand.[24] There exists, however, at least one mechanism rather effective in inducing transitions, namely, the thermal vibrations of the lattice. For this process one can arrive at an order-of-magnitude estimate of the transition probability W between two of the sublevels of (4), say those labeled by ξ and ζ, separated in energy by an amount $kT_{\xi\zeta}=E_\xi-E_\zeta$. A rather crude calculation shows that

$$W=10^9\epsilon^2T^3[\exp(T_{\xi\zeta}/T)-1]^{-1}\,\text{sec}^{-1}, \qquad (28)$$

where the numerical factor involves the elastic constants of solid hydrogen and measures the effectiveness of the lattice vibrations in reorienting the ellipsoidal *ortho*-molecule of eccentricity ϵ. For reasonable values of the parameters involved ($\epsilon\approx 0.03$ and $T_{\xi\zeta}$ in the range from 1°K to 5°K), (28) yields, for temperatures above 1°K, $W>d$. In this case of large transition probabilities the dipole-dipole interaction in a molecule, instead of being averaged over the probability distribution of a single sublevel as was done in Eq. (9), must be averaged over the probability distributions of all the sublevels (4) with each weighted according to its respective Boltzmann factor. The resulting line shape is then altered in a complicated way, but the outermost parts of the line profile remain step-like with an over-all separation Δ_2 decreased from that given in Eq. (26) by the factor

$$\rho\equiv\tfrac{1}{2}[3\{1+\exp(-T_{\xi\zeta}/T)+\exp(-T_{\eta\zeta}/T)\}^{-1}-1], \qquad (28a)$$

where we have considered the state labeled by ζ to be lowest in energy and have used the same notation as in Eq. (28). If we again assume that the sublevel separations $T_{\xi\zeta}$ have values in the range from 1°K to 5°K, then at sufficiently high temperatures, say above 4°K, one expects only a central line to be observed. At lower temperatures, however, (e.g., close to 2°K) there will be, because of the differing local surroundings of the *ortho*-molecules, some among them for which $T_{\xi\zeta}\ll T$, while for other molecules $T_{\xi\zeta}\gg T$. The former class of molecules thus again gives rise to a central line only, while the latter class yields the line shape of Fig. 4(a). There are presumably also molecules for which $T_{\xi\zeta}$ and T are comparable. But the contributions to the line due to these molecules would be smeared out over the whole range between the two extremes just discussed and might well, because of its weakness and lack of salient features, escape detection. According to this interpretation the remnant central line and the rest of the line are due to different classes of molecules in the solid and it is therefore not surprising that they should experimentally exhibit rather different behavior.

The weight of the evidence thus seems to favor the assumption that the transition probability W, for most of the molecules at least, is large compared to d. The measured value of Δ_2 at the lowest temperatures we reached may therefore not yet have attained the limiting value given by Eq. (26). For example, if the maximum separation between sublevels is of the order $T_{\xi\zeta}=4$°K, then at a temperature of 1°K the factor ρ equals approximately 0.94. Thus, if ρ is taken into account in calculating d from Δ_2 by Eq. (26), then $d_s\approx d_f$. The effect of lattice vibrations alone might therefore be sufficient to account for the apparent discrepancy, mentioned in connection with Eq. (27), between the values of d_s and d_f; though a detailed knowledge of the level splittings or measurements of Δ_2 at lower temperatures would be required to settle this point. On the other hand, the general agreement between the observed line shape and our interpretation thereof is evidence that the admixture of higher sublevels is rather small and hence that, for a large number of *ortho*-molecules in the solid, the $J=1$ sublevels are split by amounts larger than about 4°K.

Turning now to the case of solid HD we note that, since this molecule is not homonuclear, there exist no particular symmetry requirements on the molecular wave function. Thus all the molecules in the solid can be expected to be in the lowest rotational state, $J=0$. Since this state is spherically symmetric, the dipole-dipole interaction [integral similar to that in (9)] averages to zero. Consequently the proton resonance line should show no fine structure even at the lowest temperatures, in agreement with our experimental findings.[25] In the case of D_2 the molecular wave function must be symmetric under interchange of the two nuclei since the D spin is 1. Two-thirds of the molecules are *ortho*-D_2 in the state $J=0$ and of these $\frac{5}{6}$ (those with $I=2$) give rise to a central line without fine structure since the $J=0$ state is spherically symmetric. One-third of the molecules are *para*-D_2 with $J=1$, $I=1$, and these should give rise to the same line shape as that shown in Fig. 4(a). This follows from the fact that the Hamiltonian for the D_2 molecule has the same form as that for the H_2 molecule. The presence of the additional deuteron nuclear quadrupole interaction has simply the

[24] It should be remembered that even a perfectly free molecule does not give rise to a central line.

[25] If the crystalline potential V were sufficiently large to make the ground state of the HD molecule differ appreciably from a pure $J=0$ state, a fine structure might be possible. The experiment thus shows again how very nearly free the molecules in the solid are.

effect of modifying the constant d.[20] For the *free* D_2 molecule Ramsey[20] gives the value $d=25.24$ kc/sec so that the separation between the peaks in Fig. 4(a) should be $3d\approx 76$ kc/sec. This absorption line is, however, expected to have much weaker intensity than in the case of H_2 and, as we pointed out in Sec. II, we did not succeed in observing this fine structure in our one experimental run.

V. SOLID HYDROGEN RESONANCE IN ZERO FIELD

(a) Theory

The foregoing experiments suggest the possibility of measuring directly, in the absence of external magnetic field, the dipole-dipole interaction responsible for the fine structure of the hydrogen resonance line in high field. Though, in principle, the detection of zero-field resonance lines of this kind would also be possible in other cases [such as in Pake's[2] experiments on $CaSO_4\cdot 2H_2O$], solid hydrogen represents a particularly favorable situation in which the signal-to-noise ratio is not prohibitively low thanks to the large dipole-dipole interaction (small r), the small intermolecular broadening (large R), and the low temperatures involved. The detection of a zero-field line in solid H_2 is also of interest in providing additional experimental data against which to test the theoretical considerations upon which we base the interpretation of the high-field experiments.

In zero magnetic field we need to consider only the Hamiltonian $\mathcal{H}_{cd}$ in (7). In the general case corresponding to Eq. (4) the spin-rotational interaction term c again vanishes. We then have for the perturbation energy in the state ψ_ξ, if we quantize $\mathbf{I}$ along the ζ axis,

$$h^{-1}E_\xi^{(0)}=-5d\langle\psi_\xi\bar{m}_I|\tfrac{1}{2}(3\lambda_\xi^2-1)\times(3I_\xi^{(1)}I_\xi^{(2)}-\mathbf{I}^{(1)}\cdot\mathbf{I}^{(2)})|\psi_\xi\bar{m}_I\rangle$$
$$=-(5/2)d(\tfrac{3}{2}\bar{m}_I^2-1)\int(3\lambda_\xi^2-1)|\psi_\xi|^2d\Omega. \quad (29)$$

Here again λ_ξ is the component of $\mathbf{r}/r$ along the ζ axis. The integration is immediate and yields

$$h^{-1}E_\xi^{(0)}=2d(1-3/2\bar{m}_I^2). \quad (30)$$

In weak magnetic field $\mathcal{H}_{ab}\ll\mathcal{H}_{cd}$ and one gets

$$h^{-1}E_\xi=2d(1-3/2\bar{m}_I^2)-a\gamma_\xi, \quad (31)$$

with similar expressions for the states ψ_ξ and ψ_η. The corresponding energy level diagram is shown in Fig. 6. Equation (12) then implies the selection rule $\Delta\bar{m}_I=0,\pm1$. Thus in zero field one expects an absorption line of frequency $3d$ (about 170 kc/sec). Upon application of a weak magnetic field this line then splits into two lines of frequencies[26]

$$\nu_\xi=3d\pm a\gamma_\xi. \quad (32)$$

[26] If higher-order corrections are taken into account, d in this equation must again be replaced by τd, with τ given by Eq. (17).

For the corresponding transition probabilities (12) gives

$$W(\bar{m}_I+1\leftarrow\bar{m}_I)\sim\mu_\xi^2|\langle\bar{m}_I+1|H_{1\xi}I_\xi+H_{1\eta}I_\eta+H_{1\xi}I_\xi|\bar{m}_I\rangle|^2\sim\mu_\xi^2H_1^2(1-\bar{m}_I)(2+\bar{m}_I)(1-H_{1\xi}^2/H_1^2)$$

so that $W(0\leftarrow1)=W(0\leftarrow-1)$ and the intensities of the lines (32) depend on the orientation of the ζ-axis in space. Specifying this orientation by the polar and azimuthal angles α and β of ζ with respect to the z axis, one has, for $\mathbf{H}_1$ along the x axis, $W\sim(1-\sin^2\alpha\cos^2\beta)$. For given ν determined by (32) one can integrate over the irrelevant angle β to get

$$W\sim(1-\tfrac{1}{2}\sin^2\alpha)=\tfrac{1}{2}(1+\cos^2\alpha)$$

or

$$W_\zeta\sim1+\gamma_\zeta^2. \quad (33)$$

We again need to examine the effect of the random orientations of the ξ, η, ζ axes of the *ortho*-molecules in our hydrogen sample. For the zero-field line the effect, by (33), consists simply in reducing its intensity to $\frac{2}{3}$ of what could be obtained for optimum alignment of all the molecules. For the lines in weak field the effect is to produce an intensity distribution function $p(\nu)$

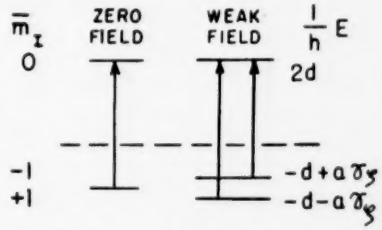

FIG. 6. Energy level diagram for solid hydrogen in weak magnetic field. Energy levels for the state ψ_ξ.

calculable from the general relation (15). For the state ψ_ξ, $\exp(-E_r/kT)$ is the same for both lines (32) since $h\nu/kT\ll1$; also the first factor $h\nu/kT\approx3dh/kT$ to a sufficient approximation since we assumed $a\ll3d$ in our perturbation calculation. Hence by (32) and (33), Eq. (15) reduces to

$$\left.\begin{aligned}p(\bar{\nu})&=\tfrac{3}{8}a[1+(\bar{\nu}/a)^2] \quad \text{for } |\bar{\nu}|<a\\ &=0 \quad \text{for } |\bar{\nu}|>a\end{aligned}\right\}, \quad (34)$$

where $\bar{\nu}=\nu-3d$ and p has been normalized so that

$$\int_{-\infty}^{\infty}p(\bar{\nu})d\bar{\nu}=1.$$

Of course the lines arising in states ψ_ξ and ψ_η have the same shape so that the superposition of all these lines still yields the shape (34) shown in Fig. 7(a).

The effect of intermolecular broadening upon (34) can be taken into account by (23) and (24) with σ still given approximately by (22). The resulting curve for $P(\nu)$ is shown in Fig. 7(a). The width of the line in zero field can be expected to be larger than that of the

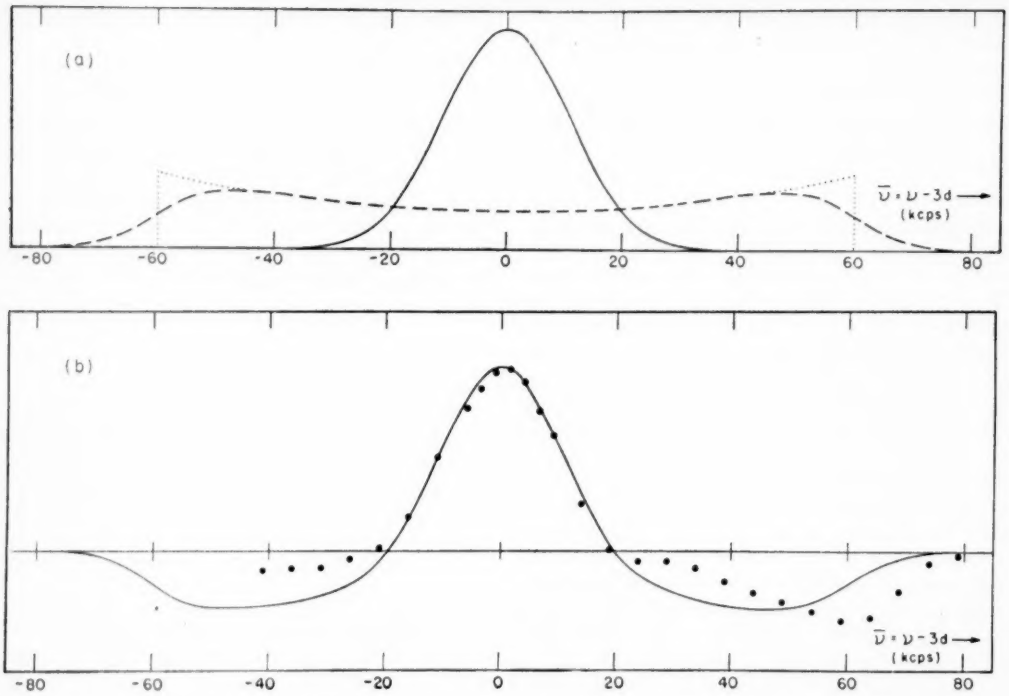

FIG. 7. Solid hydrogen line in zero field. (a) Solid curve: Zero-field line, assumed Gaussian with $\sigma_0 = 10.8$ kc/sec. Dotted curve: Line in dc magnetic field of 14 gauss, intermolecular broadening neglected. Dashed curve: The same line but with intermolecular broadening taken into account (by Gaussian with $\sigma = 7.25$ kc/sec). (b) Solid curve: Theoretical plot of zero-field line as it should appear on the recording meter as a result of square-wave modulation of 14-gauss amplitude. Dots: Experimental points fitted to the above curve by taking $3d = 166$ kc/sec and normalizing so as to agree with the height of the central peak.

resonance line in high field, since the total Hamiltonian can be written in a form similar to (19) with $\delta_k = 3d$ and $H_0 = 0$, and since the absence in $\mathcal{H}_0$ of terms in I_{kz} then results in a much larger part of $\mathcal{H}_{dip}$ commuting with $\mathcal{H}_0$. The second moment of this line was calculated by Kambe and Abragam[37] for the case of an axially symmetric potential V_S and their result can still be expected to yield the right order of magnitude in our more general case. It is sufficiently accurate, by virtue of the symmetry of the crystal structure, to average their result over the angular factors; one then gets $\langle(\Delta\nu)^2\rangle = (2\mu_i)^4\hbar^{-2}\sum_l (11/5) r_{kl}^{-6}$, so that for the zero-field line one has by (19) and (21),

$$\sigma_0 \equiv \langle(\Delta\nu)^2\rangle^{\frac{1}{2}} = (11/5)^{\frac{1}{2}}\sigma = 10.75 \text{ kc/sec}. \quad (35)$$

Assuming a Gaussian shape (25) for the zero-field line, its half-width is then estimated to be

$$(\Delta\nu)_{\frac{1}{2}} = 2.35\sigma_0 = 25.3 \text{ kc/sec}. \quad (36)$$

Finally we remark that, in the case of a symmetric potential V_S, the nondegenerate $\bar{m}_J = 0$ state would lead to results identical with those discussed in this section. The $\bar{m}_J = \pm 1$ state, however, would give rise to a more complex energy level diagram leading to absorption lines with frequencies in the vicinity of 30 and 350 kc/sec.

[37] K. Kambe and A. Abragam, Phys. Rev. **90**, 348 (1953).

(b) Experiment

The magnet was removed and replaced by a pair of modulation coils. The sample assembly was modified to permit the use of large samples of solid hydrogen (up to 8 cm³ as compared to 0.2 cm³ in the high-field experiments). The rf spectrometer had to be adapted for use at these low frequencies by winding a rf coil of about 800 turns around the sample tip and by increasing some resistors and bypass condensers in the spectrometer proper and in the calibrator. The method of modulation was suggested by the theoretical discussion of the last section and consisted in applying a 30-cps square-wave magnetic field to the sample. The resonance line is then present when the field is off and essentially erased when the field is on; the detecting equipment tuned to 30 cps should then plot on the recording meter the difference between the two curves in Fig. 7(a), i.e., the curve of Fig. 7(b). The experimental difficulty in the use of such a square wave is that a 30-cps modulation pick-up signal is induced in the rf coil and then passed on to the detecting equipment. To obviate this difficulty we built an electronic

circuit generating instead of the ordinary square wave of Fig. 8(a) the antisymmetric square wave of modulation current shown in Fig. 8(b). It is to be noted that in the latter case the field is still off 30 times a second and its effect on the resonance line is the same as before. On the other hand the wave shape of Fig. 8(b) has a fundamental periodicity of 15 cps and, because of its antisymmetry, lacks all even harmonics thereof. It should therefore not give rise to any modulation pickup at the frequency of 30 cps to which the detecting equipment is tuned; and in practice it constitutes indeed a very great improvement.

Three experimental difficulties deserve further mention. (A) It is necessary at these low frequencies to search over a comparatively large frequency range and the sensitivity of the rf spectrometer is then effectively frequency dependent. (B) Because of eddy currents in the walls of our metal cryostat the magnetic modulation field at the sample deviates from the ideal square form of Fig. 8(b). (C) At low temperatures *only*, a strong signal is indicated on the recording meter whenever the modulation field is turned on. This phenomenon is affected by the presence of small dc magnetic fields and we believe it to be due to some kind of magnetoresistive effect in the rf coil. Needless to say, the effect constitutes a "background" signal which makes the detection of the nuclear resonance line rather difficult.

Nevertheless the latter is intense enough to show up quite clearly superimposed upon the background. We made five experimental runs, some of them with the sample assembly empty so as to study the background by itself; in these cases introducing hydrogen into the sample assembly in the middle of the run results in the appearance of the zero-field H_2 line. This line also behaves as expected; for example, the two "backswings" [negative portions of the curve in Fig. 7(b)] move toward the center of the line as the modulation amplitude is reduced. Also the line can be saturated as the rf level is increased; this permits an order of magnitude estimate of the relaxation time, yielding $T_1 \approx 0.5$ sec. To obtain more quantitative data, we first subtracted the background from the experimental curve and then corrected for the changing sensitivity of the rf spectrometer [difficulty (A)] by means of the calibrator. Experimental points obtained in this way are indicated in Fig. 7(b). Again the only important parameter adjusted to fit these points to the theoretical curve is d. Though the agreement between theory and the experimental points is less good than it was in the high-field experiment, it can be considered satisfactory in view of the uncertainties involved in subtracting the background[28] and those caused by difficulty (B). The measured half-width of the line is 23 kc/sec. This number is affected by the same uncertainties as those just mentioned and is to be compared with the theoretical value of 25.3 kc/sec given by Eq. (36). A more reliable number is the central frequency ν_0 of the zero-field line. The experimental average value for ν_0 is 165.7 ± 1 kc/sec from which, using (32) and including the correction factor τ of Eq. (17), one gets

FIG. 8. Modulation field wave shapes. (a) Ordinary square wave. (b) Antisymmetric square wave.

$$\tau d_s = \nu_0/3 = 55.2 \pm 0.5 \text{ kc/sec}$$

or

$$d_s = 54.7 \pm 0.7 \text{ kc/sec}, \tag{37}$$

where we have included some allowance for systematic error. This value for d is again smaller than that for the free H_2 molecule but is in good agreement with that obtained in (27) from the high-field data.

VI. CONCLUDING REMARKS

We have shown that the nuclear resonance line shapes in solid hydrogen can be explained quantitatively on the basis of very general assumptions concerning the crystalline potential responsible for lifting the rotational degeneracy of the *ortho*-molecules. In particular we have envisaged the situation in which the crystalline potential (and hence the resulting splittings of the $J=1$ energy levels) may be different at the position of each *ortho*-molecule in the solid as a result of the fact that in a random mixture of *ortho*- and *para*-molecules in the crystal lattice, the local surroundings of different *ortho*-molecules are not the same. This general picture may help to explain the simultaneous existence of both the remnant central line and of the line with fine structure at the same temperature. It also leads, as we hope to show elsewhere, to some suggestive conclusions concerning the experimentally observed anomalous specific-heat curves for *ortho-para* mixtures of solid hydrogen. The hysteresis effect described in Part II still lacks a satisfactory explanation, and further experiments on this effect would seem desirable, as would further experiments on solid deuterium and on solid hydrogen samples with different *ortho*-concentrations.

We would like to express our gratitude to Dr. C. A. Swenson for his help with the low-temperature aspects of this work and to Dr. G. D. Watkins for his advice on the nuclear resonance equipment. We would also like to thank Dr. A. Abragam and Professor H. Brooks for several interesting discussions. One of the authors (F.R.) is indebted to the Socony-Vacuum Oil Company for a predoctoral fellowship.

[28] This uncertainty is particularly large at the high-frequency end of the curve where the background to be subtracted is largest.

New Nuclides Produced in Chlorine Spallation*

MANFRED LINDNER
California Research and Development Company, Livermore, California
(Received April 2, 1953)

The radiation properties of the beta-emitting nuclides Si^{32} and Mg^{28} are described. Si^{32} was found to have a maximum probable half-life of 710 years, emitting beta-particles of $E_{max} \sim 100$ kev. Absence of gamma radiation with this nuclide is indicated.

INTRODUCTION

THE formation of Mg^{28} in bombardments of sodium chloride with 340-Mev protons,[1] in bombardments of magnesium with 40-Mev helium ions, and of silicon with high-energy gamma rays[2,3] and with high-energy protons[4,5] has been reported. Sheline[3] has proposed a decay scheme for this nuclide based upon the gamma rays detected in a scintillation counter. Marquez[4] studied the beta spectra for the pair Mg^{28}-Al^{28}. Both were found to have "allowed" shapes. The present paper describes experiments with Mg^{28} and the characterization of the nuclide Si^{32}.

EXPERIMENTAL PROCEDURE

Samples of sodium chloride weighing about five grams were wrapped in aluminum foil and bombarded in the Berkeley 184-inch cyclotron with 340-Mev protons. The Mg^{28} was isolated in a carrier-free state for beta-spectrum determination, while the Si^{32} was isolated with about one milligram of added silicon carrier.

CHEMICAL SEPARATIONS

The irradiated sodium chloride was dissolved in water, about one milligram of iron carrier added to the solution, and the solution made alkaline with NaOH. The ferric hydroxide was centrifuged, washed and dissolved in 6*N* hydrochloric acid. One milligram of phosphoric acid and an amount of zirconium in slight excess of that required to cause complete precipitation of the phosphate was added. The supernatant from this precipitation was made 10*N* in HCl, then passed through a Dowex-A2 anion exchange resin column. This removed all the iron and excess zirconium. The HCl eluate, containing only the magnesium tracer, was was evaporated to dryness, taken up in water, and the solution passed through a Dowex-50 cation exchange resin column. The Mg^{28} remained on the column, was then removed by elution with 0.5*N* HCl. This eluate was evaporated to dryness leaving only a very slightly visible residue containing the Mg^{28}. This residue may have been due to the presence of a small amount of magnesium chloride present in the original sodium chloride target. Extraordinary precautions had been taken to avoid possible introduction of carrier magnesium through the use of reagents made only from conductivity water.

To the supernatant solution from the original carrying of Mg^{28} on ferric hydroxide was added about one milligram of silicon as $(NH_4)_2SiF_6$. About 10 ml of concentrated H_2SO_4 was added, the resultant solution brought to fuming, cooled, and diluted to about 10*N* H_2SO_4. A small gelatinous precipitate was centrifuged, washed, and dissolved in 6*N* NaOH. After several ferric hydroxide precipitations were made from this solution and discarded, the solution was made 6*N* in HCl, one milligram of phosphorus (as H_3PO_4) and excess zirconium added (as described above). After removal of the zirconium phosphate, the supernatant was heated to fuming with sulfuric acid and the resultant precipitate of SiO_2 separated, washed with acetone, mounted, and counted.

It was found that the zirconium phosphate precipitation step was essential, since P^{32} formed by the reaction $Cl^{37}(p,p\alpha n)P^{32}$ was found to be a major contaminant in silica precipitates, even when the SiO_2 precipitations were made in the presence of phosphoric acid.

EXPERIMENTAL RESULTS

Mg^{28}

About 10^8 disintegrations per minute of Mg^{28} were mounted for a beta-spectrum analysis. The gamma rays associated with the Mg^{28}-Al^{28} pair were determined with a thallium-activated NaI scintillation crystal coupled with a 50-channel pulse-height analyzer. The results of these investigations essentially reproduced those reported by Sheline[3] and by Marquez[4] and, therefore, need little further discussion. The 0.03-Mev gamma rays reported by Sheline were determined in this laboratory as 27 kilovolts on a proportional counter.

The decay of Mg^{28} was followed for ten half-lives before evidence of contamination was observed. Together with experiments using magnesium carrier in which the decay could be followed for thirteen half-lives, it was possible to set a value of 21.2 ± 0.2 hours for the half-life of Mg^{28}. This is in agreement with Sheline's value of 21.3 ± 0.2 hours[3] but measurably different

* This work was performed under contract with the U. S. Atomic Energy Commission.
[1] M. Lindner, Phys. Rev. **89**, 1150 (1953).
[2] R. K. Sheline and N. R. Johnson, Phys. Rev. **89**, 520 (1953).
[3] R. K. Sheline, Phys. Rev. (to be published).
[4] L. Marquez, Phys. Rev. **90**, 330 (1953).
[5] J. W. Jones and T. P. Kohman, Phys. Rev. **90**, 495 (1953).

from the values of 22.1±0.3 hours reported by Jones and Kohman.[5]

The cross section for the reaction $Cl^{37}(p,2\alpha 2p)Mg^{28}$ with 340-Mev protons on NaCl was calculated to be approximately 3×10^{-27} cm^2. Contribution from the reaction $Cl^{35}(p,\alpha 4p)Mg^{28}$ was considered negligible. This conclusion is justified on the basis of spallation yields of other light elements,[6,7] in which it has been shown that the probability for neutron and for proton emission at very high energies become approximately equal for the light elements. Furthermore, Jones and Kohman[5] estimate a cross section of about 10^{-28} cm^2 for the reaction $Si^{30}(p,3p)Mg^{28}$, this being about three percent of the value found in chlorine spallation for the formation of Mg^{28}. Thus, with proton beams of approximately several tenths of a microampere available on the 184-inch Berkeley cyclotron, activities of the order of a millicurie of Mg^{28} could be produced with targets weighing several grams.

Si^{32}

The decay curve found for the silicon chemical fraction followed on a chlorine-filled Amperex argon counter is shown in Fig. 1. This shows the exponential decay of Si^{31} over twenty half-lives, followed by the growth of a fifteen-day daughter.

An absorption curve was obtained with aluminum absorbers in a nucleometer at the minimum of the decay curve in Fig. 1. Care was taken that there could be no contribution from the beta particles of Si^{31}. This curve is shown in Fig. 2. It is seen that beta particles

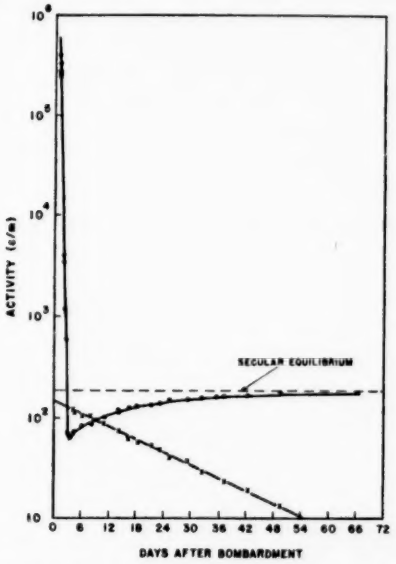

FIG. 1. Radioactive decay of silicon fraction. ●—Gross decay; ×—15-day line from resolution of curve at secular equilibrium.

[6] Batzel, Miller, and Seaborg, Phys. Rev. **84**, 671 (1951).
[7] Rudstam, Stevenson, and Folger, Phys. Rev. **87**, 358 (1952).

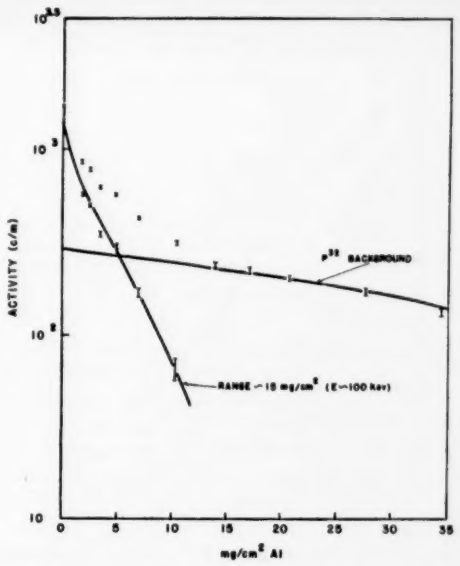

FIG. 2. Absorption curve of silicon fraction through aluminum showing some background of the P^{32} daughter. Curve obtained in a methane flow-type proportional counter of about fifty percent geometry.

of range approximately 15 mg cm^{-2} (corresponding to $E_{max}\sim100$ kev) and a lesser intensity of harder background radiation are present. Presumably the harder radiations are due to P^{32} daughter, which had grown into the sample during the several days, which had to be allowed for the Si^{31} decay. The ratio of the intensities of these two beta groups is approximately correct for the amount of P^{32} which is calculated to grow into a sample of Si^{32} during this period of time.

The entire growth curve of Fig. 2 also indicates that the counting efficiency of the parent activity on the argon-chlorine counter, as a result of the low energy, is only about half that of the fifteen-day daughter. Finally, corroboration of this observation is found in Fig. 3, an aluminum absorption curve of the silicon sample when daughter growth was essentially complete. It is seen that, although the activity of the sample was very low, beta particles of range about 800 mg cm^{-2} are present, in addition to beta particles of much shorter range. The range of the harder radiation corresponds to 1.7 Mev, this being the E_{max} value for the beta particles of P^{32}.

Finally, a tentative observation from Fig. 3 is the probable lack of gamma radiation accompanying the beta decay. The counting rate at 800 mg/cm^2 of absorber was actually determined under conditions of geometry threefold greater than the rest of the curve, the value being adjusted accordingly.

These data, therefore, establish the existence of the long-lived Si^{32}, which emits beta particles of about 100 kev and apparently no gamma radiation.

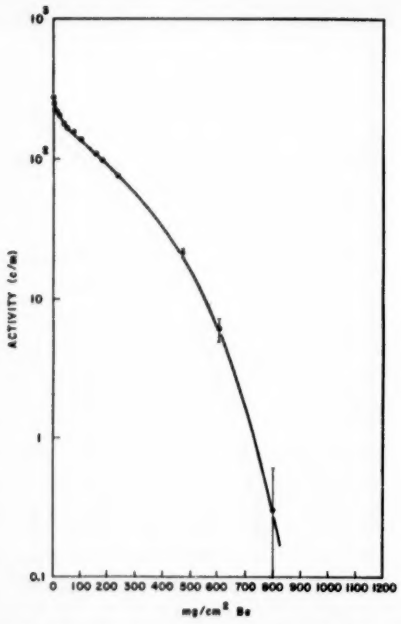

FIG. 3. Beryllium absorption curve of silicon fraction at secular equilibrium. Curve taken on an end-window type argon-filled counter under conditions of about five percent geometry.

The half-life of this isotope could be reasonably well estimated by comparing the activity of Si^{31} obtained from the reaction $Cl^{37}(p,\alpha 2pn)Si^{31}$ with the Si^{32} activity obtained in the same sample by the reaction $Cl^{37}(p,\alpha 2p)Si^{32}$. The half-life may then be calculated from

$$T_{32}=0.693\frac{A_{31}}{A_{32}}\cdot\frac{\sigma_{32}}{\sigma_{31}}\cdot\frac{t}{1-e^{-\lambda_{31}t}}. \quad (1)$$

In this equation, A refers to the activities of the two isotopes, σ to the formation cross sections, λ is the decay constant, and t the duration of the proton bombardment.

The measurement of the relative activities of Si^{31} and Si^{32} was comparatively simple, since this could be done in one sample of silicon if obtained in high chemical purity. Furthermore, although the radiation associated with Si^{32} was inconveniently soft, the equilibrium level of P^{32} daughter was easily determined, as shown in Fig. 1, and could be substituted for the parent Si^{32}. Since Si^{31} and P^{32} have almost identical radiation characteristics, the ratio A_{31}/A_{32}, if determined in the same sample, was independent of chemical yield, self-absorption, backscattering, etc. and could be obtained from Fig. 1.

The quantity σ_{32}/σ_{31}, in Eq. (1), could only be estimated. Information is meager concerning the relative yields of the $(p,\alpha 2p)$ and $(p,\alpha 2pn)$ reactions in light elements. Rudstam *et al.*[7] have established cross-section contours for spallation products of iron with 340-Mev protons which would, on the basis of approximately equal probability of neutron and proton emission from a highly excited light nucleus, permit one to estimate that the ratio for the $(p,\alpha 2p)(p,\alpha 2pn)$ reactions in iron would be about 0.2. However, because of the uncertainties in this estimation and in the extrapolation of this effect to Cl^{37} as a target nucleus, the ratio σ_{32}/σ_{31} has, for purposes of this calculation, been taken as unity. On the basis of this assumption and from the ratio of the activities shown in Fig. 1, a half-life of 710 years was calculated for Si^{32}. It is unlikely that the half-life is as low as 100 years.

Using the rapid method described by Moszkowski,[8] the (ft) value for this nuclide becomes about 5×10^6. This probably represents a first forbidden transition. A similar determination for P^{32} yields an ft value of about 15×10^6, thus indicating that both Si^{32} and P^{32} represent first forbidden transitions.

The author wishes to express his thanks to the crew of the 184-inch cyclotron of the University of California Radiation Laboratory, to Dr. Harry Hicks for many helpful suggestions, and to Mrs. M. Nervick for technical assistance.

[8] S. A. Moszkowski, Phys. Rev. **82**, 35 (1951).

Theory of (d,p) and (d,n) Reactions*

E. GERJUOY
Physics Department, University of Pittsburgh, Pittsburgh, Pennsylvania
(Received April 13, 1953)

The theory of angular distributions in (d,p) and (d,n) reactions is developed by means of standard Green's function techniques, thereby yielding a straightforward derivation of a formula originally deduced by Butler. To minimize formal complications the particles are assumed spinless, and the nucleus replaced by a center of force. It is shown that Butler's theory involves an approximation equivalent to Born approximation, which elucidates the agreement between the Butler and Born approximation derivations of the stripping formula. A discussion relating to the success of the theory is appended.

I. INTRODUCTION

THE theory of (d,p) and (d,n) reactions given by Butler[1] has been the subject of a number of theoretical papers.[2–6] Butler's original deduction of the angular distribution in stripping involved fitting together at the nuclear radius the solutions interior and exterior to the nucleus; it is fair to call complicated the procedure by which Butler obtained the cross section from his solution. Succeeding theoretical studies have been of two kinds: (*a*) attempts to simplify and clarify Butler's calculation of the cross section, but retaining his basic idea of fitting together the interior and exterior solutions[4,6] and (*b*) assuming the Born approximation matrix element for the reaction after which Butler's formula is obtained by more or less direct integration.[2,3] Since Butler's calculation does not seem equivalent to the Born approximation, it is somewhat surprising that the Born approximation gives Butler's result.[3] Austern[5] has attempted to explain this agreement.

In subsequent sections we shall rederive Butler's result by means of standard Green's function techniques, thereby automatically and obviously satisfying the boundary conditions at infinity and at the nuclear radius. To minimize formal complications we consider the following idealization of the stripping problem: A deuteron, spinless, composed of spinless neutron and proton, impinges on a fixed center of force which is the initial nucleus.[3] At infinity the solution Ψ must be of the form

$$\Psi=\psi_D+\Phi, \tag{1}$$

where ψ_D is the incident plane wave of deuterons on the initial nucleus, and Φ is everywhere outgoing. In the problem at hand this means: let the energy have a positive imaginary part; then Φ is everywhere outgoing if it remains bounded as r_N or r_P or both approach infinity. We have been careful to obtain the cross section by a mathematical procedure which corresponds evidently to the experimental situation. To amplify this remark, denote the wave function of the final nucleus in a (d,p) reaction, in which the neutron is captured into a bound state, by $\varphi(\mathbf{r}_N)$. Then the probability of finding the proton at $\mathbf{r}_P$, with the neutron bound in its final state, is $|\int d\mathbf{r}_N\varphi^*(\mathbf{r}_N)\Psi(\mathbf{r}_N,\mathbf{r}_P)|^2$. The experiment measures the flux at infinity of protons whose energy corresponds to leaving the neutron in state $\varphi(\mathbf{r}_N)$, which flux per unit solid angle is $(\hbar k/M)|A(\mathbf{n})|^2$, where the scattering amplitude $A(\mathbf{n})$ in the direction $\mathbf{n}$ is given by

$$A(\mathbf{n})\frac{e^{ikr_P}}{r_P}=\lim_{r_P\to\infty}\int d\mathbf{r}_N\varphi^*\Psi, \tag{2}$$

and r_P approaches infinity along $\mathbf{n}$. We always employ the definition Eq. (2) of $A(\mathbf{n})$ to evaluate the cross section.

Using Eq. (2) in the integral equation for the problem leads in a very straightforward way to the Born approximation matrix element, for which no satisfactory justification has been given previously. In so doing we illuminate the reason for the agreement between the two seemingly different methods (a) and (b) above. Our integral equation is the same as that obtained by Austern,[5] but his not using the definition (2) for the scattering amplitude caused him to overlook the fact that not all the terms in his equation yield protons at infinity, in (d,p) reactions. This statement will be further amplified below. Finally we append some discussion concerning the success of the theory.

II. THE INTEGRAL EQUATION

We fix our attention on (d,p) reactions, i.e., we seek outgoing protons whose energy corresponds to leaving the neutron bound to the center of force. The Hamiltonian is

$$H=T_N+T_P+V_P+V_N+V_{NP}, \tag{3}$$

where T represents kinetic energy, V_N and V_P are the interaction of neutron and proton, respectively, with the fixed center of force, and V_{NP} is the neutron proton

* Work done in part at the Sarah Mellon Scaife Radiation Laboratory and assisted by the joint program of the U. S. Office of Naval Research and the U. S. Atomic Energy Commision.

[1] S. T. Butler, Proc. Roy. Soc. (London) **A208**, 559 (1951).
[2] A. B. Bhatia *et al.*, Phil. Mag. **43**, 485 (1952).
[3] P. B. Daitch and J. A. French, Phys. Rev. **87**, 900 (1952).
[4] R. Huby, Proc. Roy. Soc. (London) **A215**, 385 (1952).
[5] N. Austern, Phys. Rev. **89**, 318 (1953).
[6] F. Friedman and W. Tobocman (to be published).

interaction.[7] The solution satisfies

$$(H-E)\Psi=0, \tag{4}$$

with Ψ of the form given in Eq. (1) and

$$\psi_D=e^{i\mathbf{K}\cdot(\mathbf{r}_P+\mathbf{r}_N)/2}w(\mathbf{r}_P-\mathbf{r}_N). \tag{5}$$

w is the ground state of the deuteron, and ψ_D satisfies

$$(T_N+T_P+V_{NP}-E)\psi_D=0. \tag{6}$$

Using an obvious symbolic notation, the solution satisfies the integral equation:

$$\Psi=\psi_0-G(V_P+V_{NP})\Psi, \tag{7}$$

where

$$(T_N+T_P+V_N-E)\psi_0=0, \tag{8}$$

$$(T_N+T_P+V_N-E)G=1=\delta(\mathbf{r}_P-\mathbf{r}_P')\delta(\mathbf{r}_N-\mathbf{r}_N'). \tag{9}$$

The solution to Eq. (7) satisfies the boundary conditions at the nuclear radius, and satisfies the boundary condition at infinity if G is the outgoing Green's function, which is [8]

$$G(\mathbf{r}_P,\mathbf{r}_P';\mathbf{r}_N,\mathbf{r}_N')=\sum_\lambda g(E-\lambda)\varphi(\mathbf{r}_N,\lambda)\varphi^*(\mathbf{r}_N',\lambda). \tag{10}$$

In Eq. (10) the sum over λ includes an integration in the continuum $\lambda>0$. $\varphi(\lambda)$ are the complete set of eigenfunctions of the neutrons in the field of the initial nucleus:

$$(T_N+V_N-\lambda)\varphi(\lambda)=0. \tag{11}$$

$g(E-\lambda)$ is the outgoing free space Green's function for the proton,[9] i.e.,

$$(T_P-E+\lambda)g(E-\lambda)=\delta(\mathbf{r}_P-\mathbf{r}_P'), \tag{12}$$

$$g(\mathbf{r}_P-\mathbf{r}_P')=\frac{1}{4\pi}\frac{2M}{\hbar^2}\frac{\exp[i(E-\lambda)^{\frac{1}{2}}|\mathbf{r}_P-\mathbf{r}_P'|]}{|\mathbf{r}_P-\mathbf{r}_P'|}. \tag{13}$$

In Eq. (13), M is the mass of proton or neutron and $\mathrm{Re}(E-\lambda)^{\frac{1}{2}}>0$ when E is imaginary.

Equations (1) and (7) imply that the difference between ψ_0 and ψ_D is everywhere outgoing. Rewriting Eq. (6) as

$$(T_N+T_P+V_N-E)\psi_D=(V_N-V_{NP})\psi_D, \tag{14}$$

it follows that[7]

$$\psi_D=\psi_0+G(V_N-V_{NP})\psi_D, \tag{15}$$

so that Eq. (7) becomes

$$\Psi=\psi_D-G(V_N-V_{NP})\psi_D-G(V_P+V_{NP})\Psi. \tag{16}$$

Equation (16) is identical with Austern's integral equation.[5]

Since V_{NP} does not appear in Eq. (8), ψ_0 may be said to represent a combination of free space proton functions and of neutron functions $\varphi(\mathbf{r}_N,\lambda)$, which at infinity looks like an incoming plane wave of free deuterons, but in which the neutrons and protons propagate independently of each other. In order that a neutron be captured it is necessary that the proton remove the excess neutron energy. But Eq. (8) contains no neutron-proton coupling. Consequently it is to be expected that ψ_0 makes a vanishing contribution to the scattering amplitude, in (d,p) reactions.

This plausible argument can be made rigorous. Substitute Eq. (16) in Eq. (2). Using Eq. (5) it is seen that the term in ψ_D vanishes exponentially as $r_P\to\infty$, since both φ and w are bound states. The terms in G simplify with the aid of Eq. (10) and the orthonormality of the set $\varphi(\lambda)$. Letting $r_P\to\infty$, there results

$$A(\mathbf{n})=A_1(\mathbf{n})+A_2(\mathbf{n}), \tag{17}$$

$$A_1(\mathbf{n})=-\frac{1}{4\pi}\frac{2M}{\hbar^2}\int d\mathbf{r}_P d\mathbf{r}_N e^{-i\mathbf{k}\cdot\mathbf{r}_P}\times\varphi^*(\mathbf{r}_N,\lambda_f)(V_N-V_{NP})\psi_D, \tag{18}$$

$$A_2(\mathbf{n})=-\frac{1}{4\pi}\frac{2M}{\hbar^2}\int d\mathbf{r}_P d\mathbf{r}_N e^{-i\mathbf{k}\cdot\mathbf{r}_P}\times\varphi^*(\mathbf{r}_N,\lambda_f)(V_P+V_{NP})\Psi. \tag{19}$$

In Eqs. (18) and (19), λ_f is the energy of the neutron in its final bound state, $\mathbf{k}=k\mathbf{n}$, and

$$\frac{\hbar^2k^2}{2M}+\lambda_f=E=\frac{\hbar^2K^2}{4M}+\epsilon, \tag{20}$$

where, referring to Eq. (5), ϵ is the energy of the deuteron in its ground state.

It can be shown that[7]

$$A_1(\mathbf{n})=0. \tag{21}$$

The demonstration is trivial, involves merely elimination of V_{NP} and V_N by Eqs. (6) and (11), followed by an integration by parts. Equation (21) remains valid when the particles are not assumed spinless, and when w is

[7] The discussion and notation of this section parallels that in E. Gerjuoy, University of Pittsburgh Precision Scattering Project Report No. 3 (unpublished).

[8] It is apparent that G, given in Eq. (10), satisfies Eq. (9) and is outgoing in the protons, in the sense which has been explained in the previous section. It is possible to prove that G is also outgoing in the neutrons, despite the fact that it seems to contain, through $\varphi(\mathbf{r}_N)$, both incoming and outgoing spherical waves in $\mathbf{r}_N$. It must be granted that some mathematical questions concerning the proof are not altogether settled, but its essential correctness seems established. The proof is contained in a report in preparation by B. Friedman and E. Gerjuoy, on the subject of many-particle scattering problems. Related problems are discussed in B. Friedman and E. Gerjuoy, Research Report No. CX-4 (unpublished) and in Harry E. Moses, Research Report No. CX-5 (unpublished) both issued by New York University, Washington Square College of Arts and Science Mathematics Research Group.

[9] In order that Eqs. (10) and (12) yield a convergent result in Eq. (7), Coulomb forces must be neglected or replaced by screened fields. We are also ignoring some formal difficulties connected with the fact that V_{NP} is a function of $\mathbf{r}_P-\mathbf{r}_N$ only, and does not approach zero along all radii of an infinite sphere in the six-dimensional $\mathbf{r}_N$, $\mathbf{r}_P$ space.

not spherically symmetric, i.e., when V_{NP} is noncentral and spin-dependent.[7]

Equation (21) means that, as asserted previously, $\psi_0=\psi_D-G(V_N-V_{NP})\psi_D$ makes no contribution to the scattering amplitude. In Born approximation we replace Ψ by ψ_D in Eq. (19). In this approximation, by virtue of Eq. (18), we may replace V_{NP} by V_N, without additional error. This yields the starting point[2,3] for the Born approximation deductions of the (d,p) angular distribution. Our derivation may be compared with that of Austern.[5] It will be noted that the valid use[2,3] of the Born approximation matrix element depends on the plausible but not obvious circumstance that ψ_0 makes no contribution to the scattering amplitude.

III. BUTLER'S THEORY

Equation (16) remains valid whatever the forms of V_P, V_N and V_{NP}, subject to the remark in reference 9. The special assumptions made by Butler[1] may, for (d,p) reactions, be summarized as follows:[4] (*a*) $V_P=0$; (*b*) within the nucleus, $r_N<a$, neglect V_{NP} in the Schrödinger equation for Ψ; (*c*) exterior to the nucleus, $r_N>a$, assume $V_N=0$; (*d*) for $r_N>a$, Ψ is of the form given in Eq. (1), where Φ is composed of free particles only, i.e., Φ satisfies, when $r_N>a$,

$$(T_N+T_P-E)\Phi=0. \tag{22}$$

We shall see that assumptions (*c*) and (*d*) are not entirely consistent. Assumptions (*a*), (*b*), and (*c*) mean the Schrödinger equation for the problem is

$$r_N<a: \qquad (T_N+T_P+V_N-E)\Psi=0, \tag{23a}$$

$$r_N>a: \qquad (T_N+T_P+V_{NP}-E)\Psi=0. \tag{23b}$$

Equations (23a) and (23b) may be expressed in the form, valid for all $\mathbf{r}_N$, $\mathbf{r}_P$:

$$(T_N+T_P+V_N-E)\Psi=P_>(V_N-V_{NP})\Psi, \tag{24}$$

where we have introduced the projection operator $P_>$:

$$P_>=0, \quad r_N<a; \quad P_>=1, \quad r_N>a. \tag{25}$$

The integral equation equivalent to Eq. (24) is

$$\Psi=\psi_0+GP_>(V_N-V_{NP})\Psi=\psi_0-GP_>V_{NP}\Psi. \tag{26}$$

since $V_N=0$ for $r_N>a$. As in the preceding section Eq. (26) leads to the scattering amplitude:

$$A(\mathbf{n})=-\frac{1}{4\pi}\frac{2M}{\hbar^2}\int d\mathbf{r}_P\int_{r_N>a} d\mathbf{r}_N e^{-i\mathbf{k}\cdot\mathbf{r}_P} \times\varphi^*(\mathbf{r}_N,\lambda_f)V_{NP}\Psi. \tag{27}$$

In Born approximation Ψ is replaced by ψ_D in Eq. (27). Since the right side of Eq. (24) can be interpreted as a source term, the Born approximation in the theory of this section, i.e., the Born approximation in Eq. (24), amounts to neglecting as a source of scattered proton waves at infinity the term $V_{NP}\Phi$ exterior to the nucleus. But this is exactly the approximation which is implied by Eq. (22), in which $V_{NP}\Phi$ is neglected for $r_N>a$. Consequently, the fact that Butler's solution[1] is equivalent to the Born approximation theory of this section is no longer surprising. In fact Eq. (22) implies, using Eqs. (1) and (6),

$$r_N>a: \quad (T_N+T_P-E)\Psi=(T_N+T_P-E)\psi_D =-V_{NP}\psi_D. \tag{28}$$

Equation (28) may be rewritten as

$$r_N>a: \quad (T_N+T_P+V_{NP}-E)\Psi =V_{NP}(\Psi-\psi_D)=V_{NP}\Phi. \tag{29}$$

Equation (29) is not identical with Eq. (23b).

It has been Eqs. (23a) and (28) whose solutions have been fitted at the nuclear radius,[1,4,6] not Eqs. (23a) and (23b). Recalling $V_N=0$ for $r_N>a$, Eqs. (23a) and (28) are equivalent to

$$(T_N+T_P+V_N-E)\Psi=-P_>V_{NP}\psi_D. \tag{30}$$

Equation (30) is an inhomogeneous differential equation, whose solution, satisfying the boundary conditions, is

$$\Psi=\psi_0-GP_>V_{NP}\psi_D. \tag{31}$$

Equation (31) is presumably the solution which is obtained by fitting the exterior and interior solutions at the nuclear radius. Comparing Eqs. (26), (27), and (31), it is at once seen that the scattering amplitude in Butler's theory is the same as the Born approximation in Eq. (27), namely

$$A(\mathbf{n})=-\frac{1}{4\pi}\frac{2M}{\hbar^2}\int d\mathbf{r}_P\int_{r_N>a} d\mathbf{r}_N e^{-i\mathbf{k}\cdot\mathbf{r}_P} \times\varphi^*(\mathbf{r}_N,\lambda_f)V_{NP}\psi_D. \tag{32}$$

The Born approximation in Eq. (19) reduces of course to Eq. (32) if the additional assumptions involved in obtaining Eq. (27) are included in Eq. (19), namely, $V_P=0$ and V_{NP} neglected for $r_N<a$.

IV. EVALUATION OF SCATTERING AMPLITUDE

Equation (32) must be integrated over the region $r_N>a$, and cannot be replaced by an integral over all space, even though we seemingly derived Eq. (32) by neglecting V_{NP} for $r_N<a$. V_{NP} was neglected for $r_N<a$ in Eq. (23a) only, which combined with Eq. (28) led without further approximation to Eq. (32). In Eq. (6) for ψ_D no such assumption about V_{NP} is made. Including in Eq. (32) the region $r_N<a$ would amount to going back to the Born approximation of Sec. II, but with $V_P=0$.

As a consequence, it is not legitimate, in Eq. (32), to replace V_{NP} by V_N, since this substitution is justified only by Eqs. (18) and (21) in which the integrals are extended over all space. That Eq. (32) involves V_{NP}

rather than V_N is desirable, as it enables us to avoid such difficulties as those of Daitch and French[3] who obtain the angular distribution by neglecting the contribution from $r_N<a$ to the overlap integral between $\varphi^*(\mathbf{r}_N, \lambda_f)$ and a spherical Bessel function. Because $\varphi(\mathbf{r}_N, \lambda_f)$ is a bound state, decreasing exponentially for $r_N>a$, it is hard to justify their approximation.

We proceed now to evaluate $A(\mathbf{n})$ from Eq. (32), to satisfy ourselves that it leads without further assumptions to Butler's angular distribution. The evaluation is straightforward and doubtless can be done in a number of ways. We have found it convenient to introduce in Eq. (32) replacing $\mathbf{r}_P$, the new variable $\mathbf{r}=\mathbf{r}_P-\mathbf{r}_N$, and to make use of Eq. (5) and the fact that V_{NP} is a function of r only. Then

$$A(\mathbf{n})=-\frac{1}{4\pi}\frac{2M}{\hbar^2}\int d\mathbf{r}V_{NP}(r)w(r)e^{i\mathbf{r}\cdot(\mathbf{K}/2-\mathbf{k})}$$

$$\times\int_{r_N>a} d\mathbf{r}_N e^{i\mathbf{r}_N\cdot(\mathbf{K}-\mathbf{k})}\varphi^*(\mathbf{r}_N,\lambda_f). \quad (33)$$

In the integral over $\mathbf{r}$ in Eq. (33), we use

$$[-(\hbar^2/M)\Delta_r+V_{NP}(\mathbf{r})]w(\mathbf{r})=\epsilon w(\mathbf{r}) \quad (34)$$

to eliminate V_{NP}, integrate by parts (justified because w is a bound state), and employ Eq. (20), obtaining

$$\int d\mathbf{r}V_{NP}we^{i\mathbf{r}\cdot(\mathbf{K}/2-\mathbf{k})}$$

$$=\left[\lambda_f-\frac{\hbar^2}{2M}(\mathbf{K}-\mathbf{k})^2\right]\int d\mathbf{r}we^{i\mathbf{r}\cdot(\mathbf{K}/2-\mathbf{k})}. \quad (35)$$

From Eq. (11), for $r_N>a$, where $V_N=0$, we find

$$\left[\lambda_f-\frac{\hbar^2}{2M}(\mathbf{K}-\mathbf{k})^2\right]e^{i\mathbf{r}_N\cdot(\mathbf{K}-\mathbf{k})}\varphi^*(\mathbf{r}_N,\lambda_f)$$

$$=-\frac{\hbar^2}{2M}[e^{i\mathbf{r}_N\cdot(\mathbf{K}-\mathbf{k})}\Delta\varphi^*-\varphi^*\Delta e^{i\mathbf{r}_N\cdot(\mathbf{K}-\mathbf{k})}]. \quad (36)$$

Hence, using Green's theorem in the integral over $\mathbf{r}_N$, expanding $\exp[i\mathbf{r}_N\cdot(\mathbf{K}-\mathbf{k})]$ in spherical harmonics with $\mathbf{K}-\mathbf{k}$ as the polar axis, and writing

$$\varphi=R_l(r_N)Y_l^m(\theta_N,\varphi_N),$$

Eqs. (33)–(36) imply

$$A(\mathbf{n})=-i^l\frac{(2l+1)^{\frac{1}{2}}}{(4\pi)^{\frac{1}{2}}}a^2\left[j_l(|\mathbf{K}-\mathbf{k}|r_N)\frac{\partial R_l}{\partial r_N}\right.$$

$$\left.-R_l\frac{\partial}{\partial r_N}j_l(|\mathbf{K}-\mathbf{k}|r_N)\right]_{r_N=a}\int d\mathbf{r}w(r)e^{i\mathbf{r}\cdot(\mathbf{K}/2-\mathbf{k})}. \quad (37)$$

Equation (37) is valid for $m=0$, with $Y_l^m(\theta_N,\varphi_N)$ quantized along $\mathbf{K}-\mathbf{k}$. The integral vanishes for the other values of the magnetic quantum number. Equation (37) yields Butler's angular distribution, as has been previously[3] pointed out.

V. SUCCESS OF THE THEORY

It appears to be established that Butler's theory accounts for the observed angular distributions in (d,p) reactions. The success of the theory remains surprising, in view of the relatively low energy deuterons which have been used in the experiments. We have seen that Butler's assumption (*d*), Sec. III, is equivalent to neglecting as a source of proton waves the term $V_{NP}\Phi$ exterior to the nucleus, and that this neglect is identical with the Born approximation. It is well known that the Born approximation is often much better than expected; the theory of angular distributions in (d,p) reactions seems to be another such case, and we offer no explanation.

Assumption (*b*), Sec. III, led to Eq. (32) being integrated over $r_N>a$ rather than over all space, as in Eq. (19). In a sense neglect of V_{NP} for $r_N<a$ can be thought of as an an impulse approximation, i.e., the neutron-proton forces do not have time to act in the interval that the deuteron overlaps the nucleus. But this interpretation is hard to justify, since V_{NP} is not smaller than V_N, and since the deuterons are slow. In any event it is difficult to see why neglect of V_{NP} for $r_N<a$ should lead to a better result than including it. Integrating over all r_N in Eq. (32) permits V_{NP} to be replaced by V_N, as we have seen, and leads to a modified angular distribution[3] which, however, is generally not very different from Butler's original form. It is doubtful that the available data are accurate enough to choose between the two possibilities: integrating over $r_N>a$ and integrating over all r_N. With better data on selected nuclei in which the differences between the two forms are emphasized, together with comparisons of absolute cross sections with the theory, a decision between the two alternatives may be feasible.

An alternative means (to that in Sec. III) of converting the Schrödinger equation of the problem to an inhomogeneous differential equation is to replace the assumptions (*a*)–(*d*) of Sec. III by: (*a'*) $V_P=0$; (*b'*) assume $V_N=0$ for $r_N>a$; (*c'*) for $r_N<a$ Ψ satisfies

$$r_N<a: \quad (T_N+T_P+V_{NP}-E)\Psi=-V_N\psi_D. \quad (38)$$

With these assumptions, V_{NP} is nowhere neglected. If ψ_D is replaced by Ψ on the right side of Eq. (38), we obtain the presumably correct Eq. (4), with of course $V_P=0$. Thus Eq. (38) amounts to neglecting $V_N\Phi$ as a source term, in the region $r_N<a$.

Without going into as many details as previously, assumptions (*a'*)–(*c'*) imply the solution Ψ is

$$\Psi=\psi_D-G_1V_N\psi_D, \quad (39)$$

where G_1 is the outgoing Green's function satisfying

$$(T_N+T_P+V_{NP}-E)G_1=1. \quad (40)$$

To determine the scattering amplitude in closed form we must express G_1 in terms of G, Eq. (9), enabling us to employ the orthonormality of the set $\varphi(\lambda)$. From Eq. (40) the integral equation for G_1 is

$$G_1=G+G(V_N-V_{NP})G_1. \tag{41}$$

Substituting Eq. (41) in Eq. (39), the scattering amplitude $A(\mathbf{n})$ is seen to be

$$A(\mathbf{n})=-\frac{1}{4\pi}\frac{2M}{h^2}\int d\mathbf{r}_N d\mathbf{r}_P e^{-i\mathbf{k}\cdot\mathbf{r}_P}\varphi^*(\mathbf{r}_N,\lambda_f)V_N\psi_D$$

$$-\frac{1}{4\pi}\frac{2M}{h^2}\int d\mathbf{r}_N d\mathbf{r}_P d\mathbf{r}_N' d\mathbf{r}_P' e^{-i\mathbf{k}\cdot\mathbf{r}_P}$$

$$\times\varphi^*(r_N,\lambda_f)[V_N(r_N)-V_{NP}(\mathbf{r}_P-\mathbf{r}_N)]$$

$$\times G_1(\mathbf{r}_N,\mathbf{r}_N';\mathbf{r}_P,\mathbf{r}_P')V_N(r_N')\psi_D(\mathbf{r}_N',\mathbf{r}_P'). \tag{42}$$

Equation (42) can be approximated by ignoring the term in $G_1V_N\psi_D=\psi_D-\Psi$, Eq. (39), which vanishes in the Born approximation $\Psi=\psi_D$. In first approximation therefore $A(\mathbf{n})$ of Eq. (42) is identical with the Born approximation to Eq. (19) with $V_P=0$. Other equally reasonable ways of estimating Eq. (42) lead to the same conclusion.

The above discussion demonstrates that a variety of different approaches can lead to angular distributions resembling Butler's. This helps to make understandable the success of this theory in accounting for observed angular distributions. As a corollary, the success of Butler's theory with presently available data does not strongly support his particular model.

We consider the physics of the (d,p) reaction still somewhat obscure, and until this is elucidated we see no good reason why Butler's original formula Eq. (32) should be superior to, say, the Born approximation in Eq. (19) or to Eq. (42) including the second correction term.

We add that it seems possible to carry through the calculations of this paper including spin without making the approximation that the nucleus is a center of force. By this means we would arrive at the selection rules,[1] but would not otherwise add enough to the simpler theory we have presented to warrant the extra formal complications. The chief desideratum of a more careful discussion would be to arrive at an improved estimate of the magnitude of the cross section,[1,2,4,6] but this we are not yet prepared to do.

PHYSICAL REVIEW VOLUME 91, NUMBER 3 AUGUST 1, 1953

The Correction for Finite Angular Resolution in Directional Correlation Measurements*

J. S. Lawson, Jr., and H. Frauenfelder
University of Illinois, Urbana, Illinois

(Received March 30, 1953)

The correction of a measured directional correlation function for the finite angular resolution of the radiation detectors (scintillation counters) has been investigated experimentally in the case of the Ni^{60} $\gamma-\gamma$ cascade. The results show that the correction factors depend upon the pulse-height selection. The significance of this result for precision measurements is discussed.

INTRODUCTION

RECENT developments in the measurement of directional correlations, such as the investigation of mixed multipole transitions and the influence of external fields, have revealed the need for higher precision. Because the obtainable accuracy is in most cases limited by statistical errors, one tries to increase the number of measured events (coincidences) by using radiation detectors with high counting efficiency and large solid angles. The measured data then have to be corrected for all deviations from an ideal arrangement,[1] especially for the finite angular resolution of the radiation detectors (*solid angle correction*).

The present paper is confined to the discussion of this correction and its experimental investigation. The work originated from a precision measurement of the directional correlation of the Ni^{60} $\gamma-\gamma$ cascade.[2] We found there that the measured directional correlation function depended strongly on the settings of the pulse-height discriminators in the counting system. In order to explain this result, we assumed tentatively that the effective solid angle depends on the pulse-height selection and started measuring directly the angular resolution curve of the radiation detectors. Once the effective angular resolution curves were known, the calculation of the correction (for our very small source) was straightforward. It showed that the discrepancy actually was due to different solid angles. This result proves that a solid angle correction without experimental de-

* Assisted by the joint program of the U. S. Office of Naval Research and the U. S. Atomic Energy Commission.

[1] H. Frauenfelder, *Annual Review of Nuclear Science* (Annual Reviews, Inc., Stanford, 1953), Vol. 2, p. 145.

[2] Steffen, Lawson, Frauenfelder, and Jentschke (to be published).

termination of the angular resolution of the counters for the radiation to be investigated may lead to serious errors.

We give in the present paper first the main formulas for the solid angle correction and then proceed to the description and discussion of our experimental results.

FORMULAS FOR THE SOLID ANGLE CORRECTION

The solid angle correction has been treated in various approximations by Walter,[3,4] Frankel,[5,6] Church and Kraushaar,[7] and Rose.[8] The papers of these authors provide a sufficient theoretical background for the treatment of almost all experimental arrangements. We use in slightly modified form the results of Frankel and Rose. The complete derivation of the formulas may be found in their papers.

We assume that we are measuring the directional correlation $W(\theta)$ of successive γ rays, γ_1 and γ_2. The experimental arrangement (Fig. 1) shall consist of a point source in the center of the counting system, and of two circular (cylindrically symmetric) scintillation counters I and II.

The axes of the two counters subtend the angle ϑ at the source, the directions of emission of the two γ rays include the angle θ. The efficiency of a counter for a γ ray emitted at an angle α with respect to the counter axis shall be denoted by $\epsilon(\alpha)$. The efficiency $\epsilon(\alpha)$ is clearly also a function of the source-to-counter distance. This distance has to be kept the same for the measurement of the directional correlation and of the angular resolution.

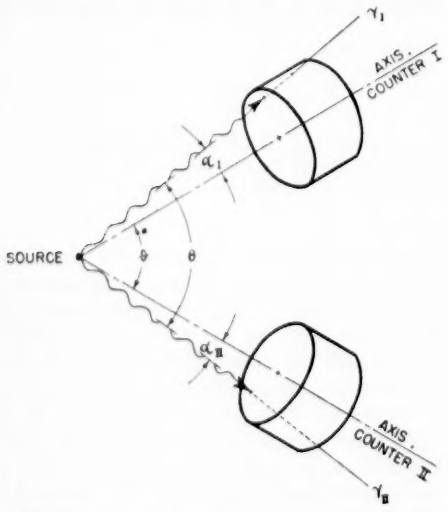

FIG. 1. Geometry of the detecting system for the measurement of the directional correlation between γ_1 and γ_2.

The theoretical directional correlation function $W(\theta)$ may be written as an expansion in Legendre polynomials

$$W(\theta)=1+\sum_{k=1}^{k_m} A_{2k}P_{2k}(\cos\theta). \tag{1}$$

It was first shown by Frankel[5] that the experimentally measured ("smeared out") directional correlation $\langle W(\vartheta)\rangle_{Av}$, where ϑ denotes the angle between the counter axes, then can be written as

$$\langle W(\vartheta)\rangle_{Av}=Q_0+\sum_{k=1}^{k_m} Q_{2k}A_{2k}P_{2k}(\cos\vartheta). \tag{2}$$

The coefficients A_{2k} of the theoretical function simply are multiplied by appropriate attenuation factors Q_{2k}. This procedure is valid, however, only for centered point sources and circular detectors. As has been shown by Walter,[3,4] a mixing of the different A_{2k} occurs if these conditions are not met.

For γ rays of nearly the same energies [i.e., $\epsilon(\alpha,\gamma_1)\cong\epsilon(\alpha,\gamma_2)$], the attenuation factors can be written as

$$Q_{2k}=J_{2k}{}^{I}J_{2k}{}^{II}, \tag{3}$$

with

$$J_{2k}=\int P_{2k}(\cos\alpha)\epsilon(\alpha)|\sin\alpha|\,d\alpha, \tag{4}$$

and where the integrals $J_{2k}{}^{I}$ and $J_{2k}{}^{II}$ are evaluated, respectively, for the first and second counter.

In the case of essentially different γ-ray energies, expression (3) has to be replaced by

$$Q_{2k}=\tfrac{1}{2}\{J_{2k}{}^{I}(\gamma_1)J_{2k}{}^{II}(\gamma_2)+J_{2k}{}^{I}(\gamma_2)J_{2k}{}^{II}(\gamma_1)\}. \tag{5}$$

The procedure of correcting a measured correlation is now straightforward.

(a) The angular efficiencies $\epsilon^{I}(\alpha)$ and $\epsilon^{II}(\alpha)$ of the counters have to be measured by means of a well-collimated beam of γ rays of the substance to be investigated. If γ_1 and γ_2 differ considerably in energy, two different γ sources with suitable energies have to be used to determine $\epsilon(\alpha,\gamma_1)$ and $\epsilon(\alpha,\gamma_2)$.

(b) The correction factors Q_{2k} are obtained by numerically carrying out the integrations (4), using the experimentally determined angular efficiencies.

(c) A least square fit of the experimentally measured correlation $\langle W(\vartheta)\rangle_{Av}$ using the function

$$\langle W(\vartheta)\rangle_{Av}=\text{const}\{1+A_2{}^{*}P_2(\cos\vartheta)+A_4{}^{*}P_4(\cos\vartheta)\} \tag{6}$$

determines the coefficients $A_2{}^{*}$ and $A_4{}^{*}$. Higher terms are usually not necessary. An exhaustive treatment of the method of obtaining a least square fit has been given by Rose.[8]

(d) The corrected coefficients are then given by

$$A_{2k}=(Q_0/Q_{2k})A_{2k}{}^{*}. \tag{7}$$

[3] Walter, Huber, and Zünti, Helv. Phys. Acta **23**, 697 (1950).
[4] M. Walter, formula given in reference 1, page 148.
[5] S. Frankel, Phys. Rev. **83**, 673 (1951).
[6] S. Frankel (to be published).
[7] E. L. Church and J. J. Kraushaar, Phys. Rev. **88**, 419 (1952).
[8] M. E. Rose (to be published).

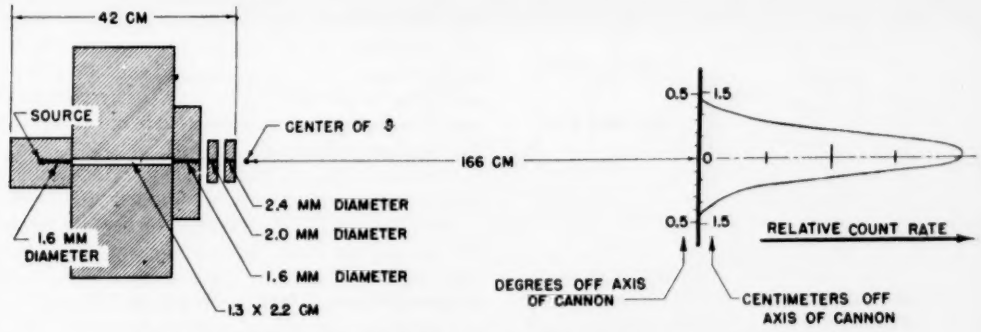

FIG. 2. Collimating system and shape of the γ-ray beam used for the determination of the angular resolution of the scintillation counters.

If the energies of the γ rays γ_1 and γ_2 are not very different from the energy of annihilation radiation, the method of Church and Kraushaar[7] can be used. The angular resolution $F(\alpha)$ of the counter system for a source emitting annihilation radiation has to be measured. Q_{2k} is then directly given by the expression (4) with $\epsilon(\alpha)$ replaced by $F(\alpha)$ and not by the product of two such integrals.

These methods hold only for centered point sources. The correction becomes much more complicated for extended sources. No general formula has yet been developed. But a useful estimate of the correction can be obtained by generalizing Walter's treatment.[4] Despite the fact that we do not use this generalization in the present work (because our source was extremely small), we will outline its derivation.

Walter has carried out his calculations for the case of a linear source (length L, source-to-counter distance D), placed symmetrically on the axis of rotation of the counter system, with counters of constant efficiency over their whole area. For circular detectors with solid angles $\Omega=2\pi\omega$ (steradian), Walter's correction formula can be transformed into the following form:

$$\begin{aligned}\text{const}\times\langle W(\vartheta)\rangle_{Av}=1&+(1-3\omega)A_2P_2(\cos\vartheta)\\&+(1-10\omega)A_4P_4(\cos\vartheta)+\tfrac{1}{4}(L/D)^2[1-P_1(\cos\vartheta)]\\&\times\{A_2P_1(\cos\vartheta)+A_4[P_1(\cos\vartheta)+(7/3)P_3(\cos\vartheta)]\}.\quad(8)\end{aligned}$$

This expression, which is valid for $\omega\ll1$ and $(L/D)^2\ll1$, shows that the corrections for solid angle and for source length then occur independently. A comparison of (8) and (2) shows immediately that Walter's formula can be extended to account for variable counter efficiencies $\epsilon(\alpha)$ by replacing $(1-3\omega)$ by Q_2/Q_0, and $(1-10\omega)$ by Q_4/Q_0. In this form, Eq. (8) may be useful for approximately linear sources.

EXPERIMENTAL RESULTS AND DISCUSSION

As we have mentioned in the introduction, the experimental investigation of the solid angle correction originated through the results of our measurements of the Ni^{60} $\gamma-\gamma$ correlation.[2] In this work, the source consisted of a small piece of pile-irradiated metallic cobalt, with linear dimensions smaller than 0.05 cm. The condition of having a point source was therefore well fulfilled. NaI scintillation counters were used as radiation detectors. The NaI(Tl) crystals were cut in the form of right circular cylinders (diameter 3.5 cm, length 4.0 cm) and immersed in mineral oil in an aluminum pot. The pot was closed airtight by means of a glass plate. The glass was shaped so as to give good optical contact between the scintillation crystal and the surface of the photomultiplier (5819). The counters were laterally shielded against scattered γ rays by lead (minimum thickness 1.5 cm). The discrimination against counter-to-counter scattering at angles near $\vartheta=180°$ was achieved by two different methods: by using heavy front lead shields (*abs*) or by accepting only pulses corresponding to γ rays of at least 0.55 Mev (*disc*). The characteristics of the two methods are given in Table I.

It was found that the measured anisotropy A^* $(A^*=\langle W(180°)\rangle_{Av}/\langle W(90°)\rangle_{Av}-1)$ was markedly different in the two cases *abs* and *disc*. Additional experiments showed that the difference could not be attributed to scattered γ radiation. We then assumed that the two cases *abs* and *disc* had different effective solid angles and measured the angular resolution curves $\epsilon(\alpha)$.

The two γ-rays of Ni^{60} have nearly the same energy $[E(\gamma_1)=1.33$ Mev, $E(\gamma_2)=1.17$ Mev$]$, so that the application of the simple formula (3) instead of (5) is justified. Therefore we used a well-collimated beam of Ni^{60} γ rays to determine the angular efficiency curves $\epsilon^I(\alpha)$ and $\epsilon^{II}(\alpha)$. The shape of the beam was measured in turn with a small scintillation crystal, (0.2-cm width) at a distance of 166 cm from the center of the counter

TABLE I. Characteristics of the two methods for eliminating scattered γ rays.

Method	Front absorber	Discriminator level. Pulses accepted above
abs	0.2 cm Al, 0.7 cm Pb	0.15 Mev
disc (0.55 Mev)	0.2 cm Al	0.55 Mev

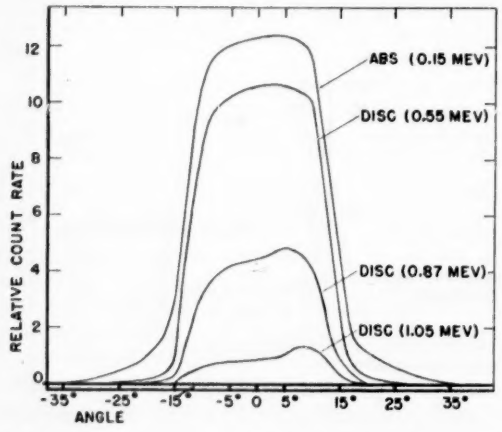

FIG. 3. The experimentally determined angular efficiency curves $\epsilon(\alpha)$ for discriminator levels of 0.15, 0.55, 0.87, and 1.05 Mev. For the measurement of the curve denoted with *abs* (0.15 Mev), a lead front absorber of 0.7-cm thickness was used.

system. Beam shape and collimating system are shown in Fig. 2. The γ-ray beam was found to have a total width of less than 0.8°, so that no correction of the measured angular resolution curves $\epsilon(\alpha)$ for its shape was necessary. Resolution curves were determined for the two different cases *abs* and *disc* of Table I, and for two arrangements with different distances between source and counters. (The two arrangements with different source-to-counter distances shall be characterized by the width α_0 of the efficiency curve at half-maximum.) In order to investigate further the effect of the discriminator level, we measured the resolution curve for two additional level settings, corresponding to energies of 0.87 and 1.05 Mev. Figure 3 represents the resulting curves for counter *I* and $\alpha_0 = 25°$.

The different shapes of the curves in Fig. 3 are caused by differences in fluorescence efficiency and light collection from different parts of the crystal and by low-energy γ rays, scattered into the crystal by the lead absorber around the counter.

The measured angular resolution curves, of which Fig. 3 represents a typical example, now show clearly that the correction factors Q_{2k} will depend upon the lead shielding around the counters, upon the pulse-height selection, and upon the light collection. We have calculated the factors Q_0, Q_2, and Q_4, by numerical integration for the various cases used in our investigation. The results are shown in Table II.

TABLE II. Solid angle correction factors, determined by numerical integration of the measured angular resolution curves.

	Method	(Q_2/Q_0)	(Q_4/Q_0)
14°	*abs* (0.15 Mev)	0.96	0.88
	disc (0.55 Mev)	0.97	0.91
25°	*abs* (0.15 Mev)	0.847	0.577
	disc (0.55 Mev)	0.908	0.721
25°	*disc* (0.87 Mev)	0.914	0.740
	disc (1.05 Mev)	0.912	0.729

In order to test the assumption of cylindrically symmetric counter efficiency, we rotated the crystal of counter I by 90° and remeasured the angular resolution for the case *abs* (0.15 Mev). The curve shape changed slightly, but the correction factors remained unaltered. It should, however, be noted from Fig. 3 that the curves are no longer symmetric at high discriminator levels. The formulas (2)–(5) are then only approximately valid.

The directional correlation of the Ni^{60} $\gamma-\gamma$ cascade has been measured for four of the six cases listed in Table II. The experimental data and the resulting anisotropy values corrected by means of the factors from Table II are given in Table III. All errors are mean statistical deviations; they do not take into account the errors introduced through the solid angle correction.

TABLE III. Measured and corrected values of the anisotropy of the Ni^{60} $\gamma-\gamma$ cascade.

	Method	A^*	A	Theoretical value
14°	*abs* (0.15 Mev)	0.159	0.166±0.002	
	disc (0.55 Mev)	0.163	0.168±0.003	
25°	*abs* (0.15 Mev)	0.139	0.167±0.001	
	disc (0.55 Mev)	0.150	0.167±0.001	
	Weighted average	···	0.167	0.1667

The main results of the present investigation are contained in Fig. 3 and in Tables II and III, and can be summarized as follows.

The precise correction of a measured directional correlation function for the effect of the finite solid angle of the detectors can best be achieved by using experimentally determined angular resolution curves. Other correction methods, using annihilation radiation or calculated efficiencies, are useful as approximations or for small solid angles. For precise measurements with large solid angles, however, they may lead to errors, unless it is certain that all underlying assumptions are fulfilled.

We wish to thank Dr. W. K. Jentschke for his cooperation and valuable advice, and Dr. M. Walter, Dr. S. Frankel, and Mr. M. Girardeau for discussions and suggestions. We are particularly grateful to Mr. D. H. Fraembs for his continuous help in performing the experiments and reduction of the data. We are greatly indebted also to Professor N. A. Parker for permitting us to use space in the Mechanical Engineering Building.

The Radioactivity of Cu^{67}

HARRY T. EASTERDAY
Radiation Laboratory, Department of Physics, University of California, Berkeley, California
(Received March 4, 1953)

The β spectrum of Cu^{67} is found to contain three groups with maximum energies and relative intensities of 577 kev, 20 percent; 484 kev, 35 percent; 395 kev, 45 percent. Conversion electrons from 92- and 182-kev transitions were observed. These results and the absence of the 296-kev γ ray indicate that the β transitions go to the ground and first two excited states of the known Zn^{67} levels.

THE level scheme for Zn^{67} has been derived independently by two groups[1,2] by investigating the K capture decay of Ga^{67}. Their results are indicated in Fig. 1, showing the transitions involved. The purpose of this report is to show the fit of the Cu^{67} β activity to this scheme.

The Cu^{67} activity was produced by two reactions, (α,p) on Ni using 40-Mev α's and $(d,2p)$ on Zn using 195-Mev deuterons. The half-life was found to be 61 ± 1 hours followed over ten half-lives. Since thin samples are essential for the analysis of a β spectrum, chemical separations were made carrier free, employing ion-exchange columns. The β spectrometer used was a thick lens type of two percent transmission and four percent resolution and was equipped with a helical baffle which allowed either positrons or electrons to be transmitted. The baffle was used to check samples for the 12.8-hour Cu^{64} activity which if present could distort the Fermi plot. Figure 2 shows the β and conversion electron spectra and Fig. 3 is the Fermi analysis. Table I gives the end-point energies, relative intensities, and ft values for the β spectra, and the γ-ray energies.

In order to verify the lack of β transitions to the upper levels, a careful search was made for conversion electrons with the β spectrometer and γ rays with crystals[3] from the 296-kev transitions, but none were found to occur. A branching of greater than five percent to the higher levels would produce observable coincidences between the 92- and 296-kev transitions even though the 92-kev level has a lifetime longer than the resolving time of the coincidence apparatus. Coincidences between these transitions were not detected.

In order to attempt to make spin assignments for Zn^{67} levels, the multipole order of the γ rays were determined by measuring the conversion coefficients and comparing them with the theoretical values given in Rose's tables.[4] The photoelectron converter was a 7.5-mg/cm² Ag foil whose conversion efficiency had been determined from the In^{113} lines. The conversion coefficient for the 29-kev transition is 0.5 ± 0.2 which makes the transition an $E2$ by comparing the extrapolated values from Rose's table. A possible mixture of $M1+E2$ can be ruled out since, according to Goldhaber and Sunyar's curves,[5] the half-life given by the Weisskopf formula for an $M1$ transition of this energy in $A=67$ would be roughly 5×10^{-10} second, whereas an $E2$ would be 2.5×10^{-6} second. A similar type of $M1$ transition with 80-kev energy in Xe^{131} has a half-life of 5×10^{-10} second.[6] Therefore, the spin and parity of the first excited state are $\frac{1}{2}$ and odd. This agrees with the assignment of Meyerhof, Mann, and West.[7] The conversion

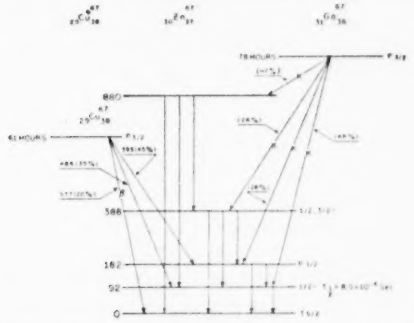

FIG. 1. Zn^{67} energy levels. In the figure, (24%) should read (26%), (48%) should read (41%), and (28%) should read (32%).

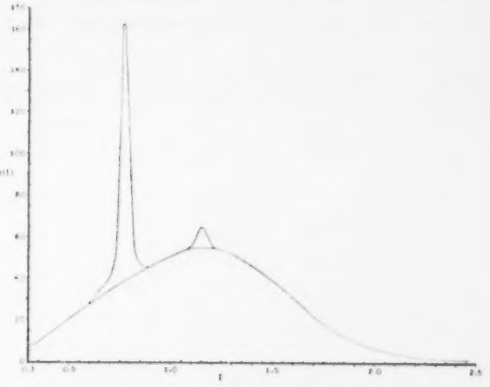

FIG. 2. Cu^{67} β^- and conversion electron spectrum.

[1] A. Mukerji and P. Preiswerk, Helv. Phys. Acta **25**, 387 (1950).
[2] Ketelle, Brosi, and Porter, Phys. Rev. **90**, 567 (1953).
[3] The crystal work was done in the Chemistry Division of the Radiation Laboratory by H. G. Hicks and P. C. Stevenson.
[4] The conversion coefficients have also been measured by Mukerji and Preiswerk (reference 1); the two determinations agree within experimental error.
[5] M. Goldhaber and A. W. Sunyar, Phys. Rev. **83**, 906 (1951).
[6] R. L. Graham and R. E. Bell, Phys. Rev. **84**, 380 (1951).
[7] Meyerhof, Mann, and West, Bull. Am. Phys. Soc. **27**, No. 6, 18 (1952).

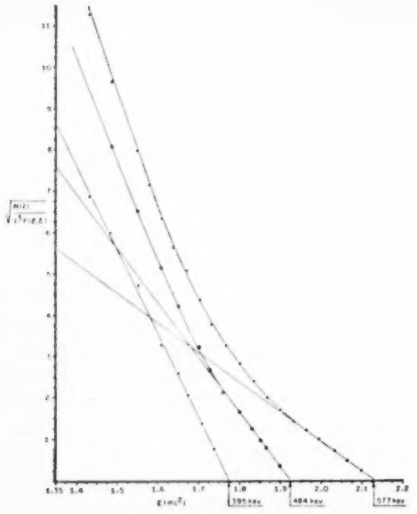

FIG. 3. Cu^{67} Fermi analysis of β spectrum.

coefficient of $12\pm2\times10^{-3}$ for the 182-kev transition lies closest to the value for an $M1$, so the second excited level is a $p_{\frac{1}{2}}$ state. The experimental error in the measurements for the weaker lines was large enough to make it impossible to decide between $M1$ and $E1$ transitions. The spin assignments shown in Fig. 1 are made on the basis of these multipole order determinations and the states available in this region by the one-particle model.[8] The ground-state configurations beyond 28 nucleons of the nuclei involved[9] and the basis for the choice are as follows:

Cu^{67} $(\pi_{\frac{1}{2}})^1{}_{\frac{1}{2}}(f_{\frac{1}{2}})^6(p_{\frac{1}{2}})^4$ (Cu^{63} and Cu^{65} have $I=\frac{3}{2}$ with μ value closest to $l+\frac{1}{2}$ Schmidt line and $Q<0$).

Zn^{67} $(\pi_{\frac{1}{2}})^2(f_{\frac{1}{2}})^5{}_{\frac{1}{2}}(p_{\frac{1}{2}})^4$ (Zn^{67} has a measured $I=5/2$ with μ value closest to $l-\frac{1}{2}$ Schmidt line and $Q>0$).

Ga^{67} $(\pi_{\frac{1}{2}})^3{}_{\frac{1}{2}}(f_{\frac{1}{2}})^6(p_{\frac{1}{2}})^2$ (Ga^{69} and Ga^{71} have $I=\frac{3}{2}$ with μ value closest to $l+\frac{1}{2}$ Schmidt line and $Q>0$).

β-transitions from Cu^{67} to the ground state of Zn^{67} are $f_{\frac{1}{2}}\rightarrow\pi_{\frac{1}{2}}$ which are l forbidden, whereas transitions to the ground state from Ga^{67} would involve a two-particle change which is forbidden.

As indicated in Fig. 1, the spin values of the first and second excited states are $\frac{1}{2}-$ and $p_{\frac{1}{2}}$, respectively. If a $p_{\frac{1}{2}}$ neutron is excited to a $f_{\frac{5}{2}}$ state to form a completed f shell and the two $\pi_{\frac{1}{2}}$ protons couple to give zero spin as expected from the shell model, a $p_{\frac{1}{2}}$ state results from the closed shell minus one-praticle configuration of the neutrons. Since both protons and neutrons exist in incomplete p shells, it is possible that they can interact so the two $\pi_{\frac{1}{2}}$ protons can also couple to give spin two (spin one is excluded) with a $\frac{1}{2}-$ state resulting for the level. The first two excited states then have the configuration:

$$\{(\pi_{\frac{1}{2}})^2{}_{0,2}(p_{\frac{1}{2}})^3{}_{\frac{1}{2}}\}_{\frac{1}{2},\frac{1}{2}}(f_{\frac{5}{2}})^6.$$

K capture and β-transitions to these states would involve $\frac{3}{2}-$ to $\frac{3}{2}-$ or $\frac{1}{2}-$ changes which are allowed in agreement with the decay scheme.

TABLE I. Beta and gamma rays of Cu^{67}.

Transition energy (kev)		Relative intensity (percent)	ft values
Beta	577	20	6.26 (l-forbidden)
	484	35	5.73
	395	45	5.35
Gamma	92		
	182		

The author wishes to thank Professor A. C. Helmholz for his guidance during the course of the study and Professor J. H. D. Jensen for discussions on the spin assignments. Thanks are due to H. G. Hicks and P. C. Stevenson for the chemical separations on the Zn targets.

[8] M. G. Mayer, Phys. Rev. **78**, 16 (1950).

[9] Greek letters indicate proton states; Roman letters indicate neutrons.

Fission Cross Section of Uranium-234

R. W. LAMPHERE
Oak Ridge National Laboratory, Oak Ridge, Tennessee
(Received March 2, 1953)

The neutron-induced fission cross section of U^{234} has been measured from threshold to 4-Mev neutron energy, using the $T(p,n)$ reaction with a tritium gas target, and the Oak Ridge 5-Mev Van de Graaff. The curve rises from threshold at 350 kev to 1.3 barns at 4 Mev. There is a minimum at 1.08 Mev and another at 2.30 Mev. These dips are about 13 percent and 7 percent, respectively, of the cross section at these points. Statistics in these regions are sufficient to establish the fact that the minima are real to a probability of 10^9 relative to a "best fit" curve with no extrema.

RESULTS AND PROCEDURE

THIS paper reports on work done in May, 1952. The results are shown in Fig. 1. Most of the points were taken to 3 percent statistics or better, and the *shape* of the curve is believed to be good to at least 3 percent. However, the ordinate scale factor is in doubt to about 14 percent; this representing the uncertainty in the quantity of uranium deposited on the foils. The curve lies about 8 percent below that obtained by the Los Alamos group from threshold to 1.5 Mev.[1]

Fast fission cross sections of Pa^{231},[1] and Np^{237},[2] show no minima, but that for Th^{232} has a well-defined minimum on the initial rising part of the curve at 1.8 Mev.[1] These observations do not seem to fit in with what one would expect from a purely statistical model. Possibly they are due to shell structure within the nucleus.

A monokinetic neutron beam incident on foils placed back to back in a double ionization chamber served to induce fissions in two foils, one of U^{234} and the other of U^{235}. The ratio of fission pulses together with the known cross section of U^{235} served to establish the cross section of U^{234}. Figure 2 shows the comparison-type fission chamber. The center plate was held at -300 volts with respect to ground by means of a "Minimax" battery. The two foils were mounted back to back on this electrode. The two end plates collected electrons resulting from the fission fragments, and the pulses produced were fed into separate preamplifiers, with gains of about 140. Each preamplifier used a triode-connected 6AK5 input tube, a clipping circuit with an RC constant of 0.38 microsecond after the third stage, and a cathode-follower output that fed positive pulses over a 40-foot doubly-shielded cable to an A-1 amplifier containing a pulse-height discriminator circuit.[3] Over-all gain was about 30 200. All stages were gain stabilized by feedback. With this arrangement, correction for background, and counts from pileup of α pulses in the U^{234} were below 0.01 percent. A switch was provided for inserting a calibrated pulse generator in place of the "Minimax," so that the gains of the two identical channels could be monitored during an experiment.

A mixture of 97 percent argon plus 3 percent carbon dioxide at a pressure of two atmospheres absolute was supplied from a tank of this mixture. No purification was used, but a flow of 0.1 cubic foot per hour was maintained. The chamber was surrounded by a $\frac{1}{32}$-inch thick shield of cadmium to absorb slow neutrons that might otherwise be scattered back into it.

The foils subtended a half-angle of 15° as seen from the tritium target. Figure 3 shows the spread in energy of the neutrons striking the foils *versus* their average energy. The spread is due almost entirely to: (1) target thickness, (2) variation of neutrons energy with angle, (3) proton straggling in the entrance foil. Points were taken at 50-kev intervals.

To promote economical use of the Van de Graaff, a method using relatively thick foils was employed, whereby the fission counting rate was increased about 3.3 times; this reduced by that factor the amount of generator time required. All foils consisted of uranium plated over a one-inch circle on 2-mil thick platinum backing. Two foils were plated for each isotope; one thin foil containing about one milligram of uranium, and one thick foil containing about 4 milligrams. The quantity on the thin foil should be known as accurately as possible, but this is not necessary for the thick one. It is necessary to plate the thick and thin foils for a given isotope from the same batch of source material to

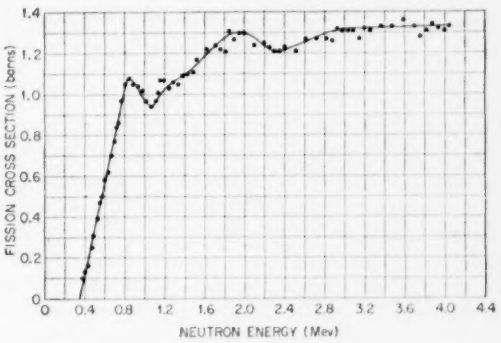

FIG. 1. Neutron-induced fission cross section of U^{234}.

[1] *Neutron Cross Sections*, Atomic Energy Commission Report AECU-2040 (Office of Technical Services, Department of Commerce, Washington, D. C., 1952).
[2] E. D. Klema, Phys. Rev. **72**, 88 (1947).
[3] W. H. Jordan and P. R. Bell, Rev. Sci. Instr. **18**, 703 (1947).

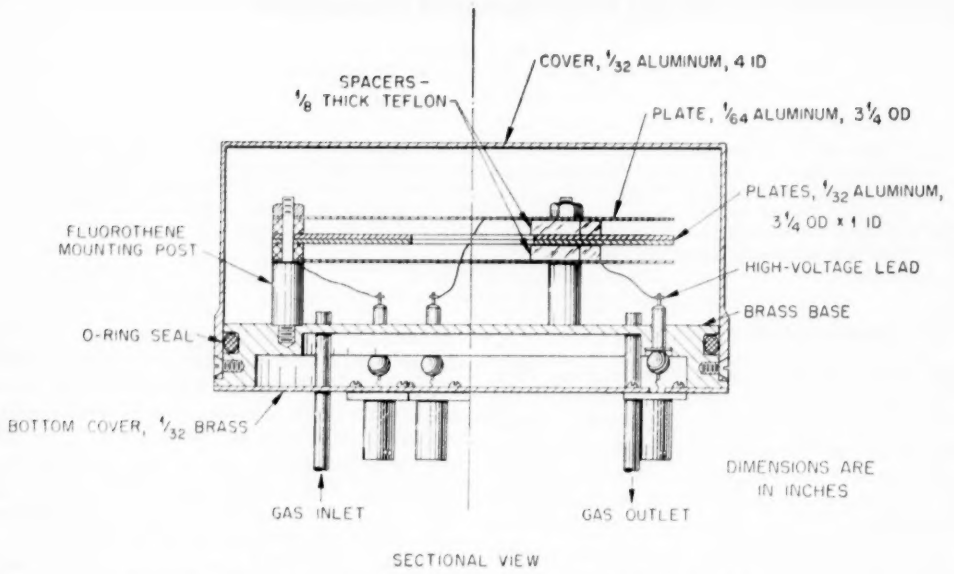

FIG. 2. Double ionization chamber used for comparing fissionability of two foils.

insure that their isotopic composition of fissionable material be precisely the same. The two foils of the *same* isotopic content, one thick and one thin, were placed in the fission chamber back to back, and exposed to neutrons from a Po–Be source for several hours. Thus the ratios of fission yields were found to 0.2 percent for the pair of U^{234} foils and for the pair of U^{235} foils. The thick ones were then used with the Van de Graaff neutrons to find the ratio of the U^{234} cross section to that of the U^{235} as a function of neutron energy.

As a check on the accuracy of the thick-foil technique, several points were taken using the two thin foils, and these points were found to lie on the curve obtained with the thick ones.

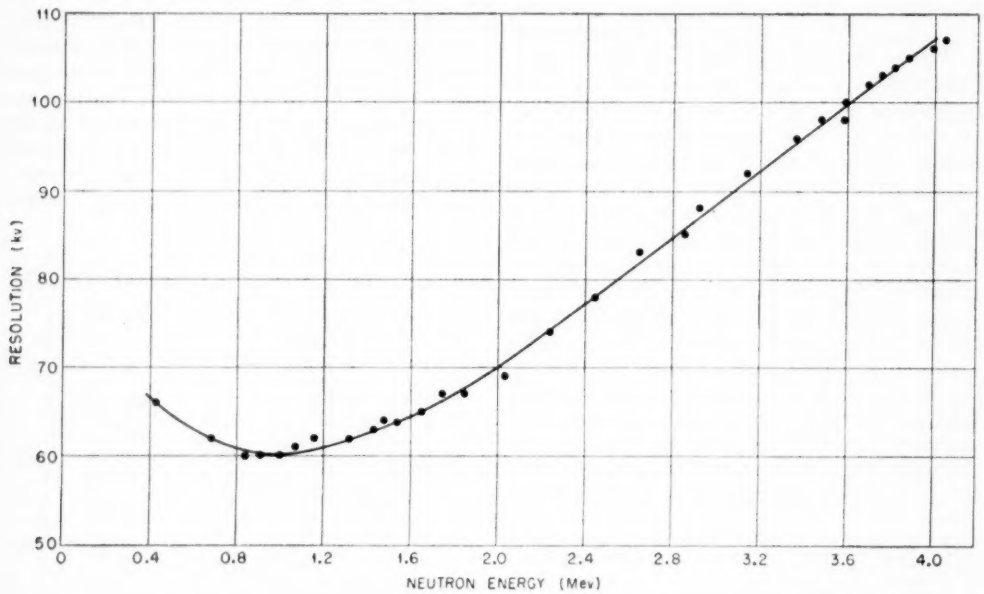

FIG. 3. Energy spread in that portion of the neutron beam incident on fissionable foils.

DISCUSSION OF ERRORS AND CORRECTIONS

A. Foils

These were prepared by the assay laboratory of the Y-12 electromagnetic separation plant, using electrodeposition and a standard assay procedure thought to be good to 0.8 percent. However, for some reaon as yet unknown, successive foils plated from the same batch of isotopic material showed disagreement between weight ratios gotten from the standard assay procedures and ratios of fission counts obtained by placing them back to back in the fission chamber and irradiating for a long time with Po—Be neutrons. This was sufficiently serious to make the ordinate scale of Fig. 1 uncertain to 14 percent but will not affect the shape of the curve.

B. Effect of Amplifier Gain Changes

Figure 4 shows the slopes of the plateaus for thick and thin foils obtained by counting fission pulses for various pulse-height discriminator settings while the foils were being irradiated by Po—Be neutrons. The plateaus for the thick foils have sufficient slope, so that some attention must be paid to the amplifiers to guard against excessive relative gain changes. The pulse generator served as a monitor, and gain changes were compensated for by adjustment of the pulse-height selectors. Relative gain changes were held to 0.2 volt on the pulse-height selector dial, and from Fig. 4 this can be shown to alter the count rate by 0.12 percent for the 4-mg foils. It was easy to hold the relative gains to this degree of precision.

C. Thick Foil Equivalent Weights

These were found to 0.2 percent in terms of the thin foil weights.

D. Scattering

It is inevitable that some neutrons will be scattered from walls and objects in the room, and some of these will find their way back into the fission chamber. The great majority of these will be degraded in energy below the threshold of U^{234} and so will produce fissions only in the U^{235}. This will result in the measured value of the U^{234} cross section being too low by a small amount. From measurements made at two different energies and two different distances between neutron source and fission foils, this correction factor was determined to be 1.01 ± 0.01. This factor has not been applied to the ordinate of Fig. 1.

E. Effect of the Momentum of Incident Neutrons on Absorption Loss

The neutron beam is incident normal to the foil surface. The fission fragments will, therefore, pick up some momentum from the incident neutron that causes the fission to take place. The effect of this is to alter the amount of self-absorption, increasing the absorption loss[4] in the foil facing the neutron source, and decreasing it for the foil facing away from the source. The magnitude of this correction *for each foil* will be about 1 percent at 4 Mev, and will vary as the square root of the energy. This correction is, to first order, independent of foil thickness and of the range of the fragments in the foil. It has been applied to the data in evaluating the cross-section curve; the accuracy of the correction is at least within 10 percent, so the probable error in cross section from this source is not over 0.15 percent. An experimental verification of this factor was made by taking seven points from 2 to 3 Mev with foils "normal" and "reversed" with respect to beam direction. The mean spread in cross-section values are found to be 3.4 percent, and the calculated value is 3.5 percent for 2.5 Mev.

Since one counts all particles in a 2π solid angle, angular asymmetry in the emitted fission particles will not affect the result, providing only that symmetry exists relative to the 90° angle, in c.m. coordinates, with respect to the beam.

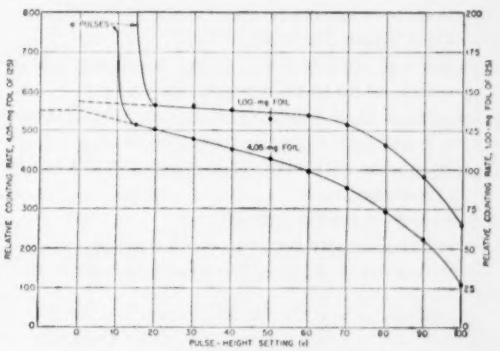

FIG. 4. Relative counting rate for U^{235} foils in fission chamber of Fig. 2 exposed to a constant intensity of thermal neutrons.

SUMMARY

The following summary of errors applied to Fig. 1:

1. Foils	14 percent (scale factor only)
2. Scattering	1 percent
3. Beam momentum	0.15 percent or less
4. Gain changes	0.12 percent
5. Statistics	1.5 to 3 percent

The writer wishes to thank the following members of the High Voltage Laboratory for their help in operating and maintaining the generator during the progress of these measurements: J. K. Bair, F. P. Green, C. H. Johnson, J. D. Kington, and H. B. Willard. Thanks are also due C. H. Johnson for providing the gas target, R. W. Bennett for mechanical design, R. F. Hibbs and his group for preparing the foils, and Dr. J. L. Fowler for his helpful suggestions.

[4] E. Segrè and C. Wiegand, Phys. Rev. **70**, 808 (1946).

APPENDIX

Beam Correction

Notation

$t_1 = 0.20$ mg/cm^2 = actual thickness of the 1-mg foils,
$t_2 = 0.80$ mg/cm^2 = actual thickness of the 4-mg foils,
t' = effective thickness of foil as a result of pulse-height setting on the A-1 amplifier,
$R = 5.0$ mg/cm^2 = mean range of fission fragments in foil,
R_b = component of range imparted by beam—component normal to foil,
z = coordinate normal to foil—taken as zero at surface of foil backing and as t at surface of uranium,
W = weight of thick foil,
W' = equivalent thin-foil weight of thick foil as obtained from polonium-beryllium comparison data,
c = fissions occurring in unit thickness of foil,
N_t = total fission processes in foil,
N_{a0} = fissions not recorded owing to absorption—for case of no beam momentum,
N_{c0} = fissions that would be counted were it not for beam momentum—corrected count,
N_e = fragments extracted from foil as a result of beam momentum,
N_c = fissions actually counted,
$F = N_e/N_{c0}$ (nearly equal to N_e/N_c); then
$N_{c0} = N_c - N_e = N_c[1-(N_e/N_c)] = N_c(1-F)$.

According to Segrè,[4] the self-absorption for the thin foils should be about 2 percent and for the thick foils about 8 percent. That is, for a thin (t less than R), uniformly emitting layer, the fractional loss is $t/2R$.

Since fragments must have some energy after leaving the foil in order to be counted, an effective thickness t' should be used that can be obtained from the slope of the fission plateau. The effective thickness is 0.60 mg/cm^2 for the thin foil and pulse-height settings of 35 to 45 on the A-1 amplifier. Hence, for this work, the loss as a result of foil thickness for the 1-mg foils is 6 percent.

Since the foils are somewhat nonuniform and R is not the same for all fragments, experimental data were used for evaluating t' and N_{a0}/N_{c0} for thick foils:

$$t_2' = 10\frac{N_{a0}}{N_t} = 10\left(1-\frac{0.94W'}{W}\right),$$

where t_2' is for the particular pulse-height setting for which W' is evaluated. The factor 0.94 may need to be altered somewhat for pulse-height settings outside the range 35 to 45:

$$F = \frac{N_e}{N_{c0}} = \frac{N_e}{N_{a0}}\frac{N_{a0}}{N_{c0}} = \left(\frac{N_e}{N_{a0}}\right)_{\text{calc}}\left(\frac{N_{a0}/N_t}{1-N_{a0}/N_t}\right)_{\text{exp}}.$$

The last term is obtained from experimental values of W', as shown previously. The first term is calculated as follows: the number of fragments reaching the end of their range in a thickness dz will equal $czdz(1/R)$, for z less than R. Hence,

$$N_{a0} = \frac{c}{R}\int_0^t zdz = \frac{ct^2}{2R},$$

$$N_e = \frac{c}{R}\int_{t-R_b}^t zdz = \frac{cR_b}{2R}(2t-R_b);$$

therefore,

$$\frac{N_e}{N_{a0}} = \frac{R_b}{t}\left(2-\frac{R_b}{t}\right).$$

Note that the *calculated* value of N_{a0}/N_{c0} is

$$\left(\frac{N_{a0}}{N_{c0}}\right)_{\text{calc}} = \frac{t/2R}{1-t/2R} = \frac{t}{2R-t}.$$

This gives a *calculated* F of

$$F_{\text{calc}} = \frac{R_b}{t}\left(2-\frac{R_b}{t}\right)\left(\frac{t}{2R-t}\right)$$

$$= \frac{R_b}{2R-t}\left(2-\frac{R_b}{t}\right) \cong \frac{R_b}{2R} = 0.0023(E_n)^{\frac{1}{2}} \quad R \gg t \gg R_b.$$

In this work the calculated ratio of N_e/N_{a0} and the experimental ratio of N_{a0}/N_{c0} were used. Thus,

$$F = \frac{2R_b}{t'}\left(1-\frac{R_b}{2t'}\right)\left(\frac{N_{a0}}{N_{c0}}\right)_{\text{exp}}.$$

Hence,

$$R_b = R\left(\frac{E_n}{E_f}\frac{M_n}{M_f}\right)^{\frac{1}{2}} = R\left(\frac{E_n}{200}\frac{1}{235}\right)^{\frac{1}{2}}$$

$$= 0.0046R(E_n)^{\frac{1}{2}} = 0.023(E_n)^{\frac{1}{2}} \text{ mg/cm}^2,$$

where E_n is neutron beam energy in Mev. Therefore,

$$F = \frac{0.046(E_n)^{\frac{1}{2}}}{t'}\left[1-\frac{0.012(E_n)^{\frac{1}{2}}}{t'}\right]\left(\frac{N_{a0}}{N_{c0}}\right)_{\text{exp}}$$

$$= \frac{0.046(E_n)^{\frac{1}{2}}}{t'}\left[1-\frac{0.012(E_n)^{\frac{1}{2}}}{t'}\right]\left(\frac{W}{0.94W'}-1\right)$$

$$= \frac{0.046(E_n)^{\frac{1}{2}}}{10}\frac{W}{0.94W'}\left[1-\frac{0.012(E_n)^{\frac{1}{2}}}{t'}\right]$$

$$= 0.0049\frac{W}{W'}(E_n)^{\frac{1}{2}}\left[1-\frac{0.012(E_n)^{\frac{1}{2}}}{t'}\right],$$

where $t' = 10[1-(0.94W'/W)]$. Note that for thin foils, $W' = W$.

Photoneutron Cross Sections*

R. MONTALBETTI, L. KATZ, AND J. GOLDEMBERG†
University of Saskatchewan, Saskatoon, Saskatchewan, Canada
(Received February 17, 1953)

The neutron yields resulting from photoneutron reactions have been measured as a function of betatron energy from threshold to 23 Mev for 22 elements. These yield curves have been analyzed by the photon difference method to give the total cross section $\sigma=(\sigma_{\gamma,n}+\sigma_{\gamma,np}+2\sigma_{\gamma,2n})$ as a function of photon energy. Whenever possible, this cross section has been resolved into its components using threshold considerations and subsidiary data. Some general conclusions based on the new results are presented regarding the systematics of (γ, n) reactions.

THE study of photoneutron reactions through the detection of the emitted neutrons offers a number of advantages over the usual residual activity method which have been fully appreciated by workers in this field for a long time. For example, in the case of residual activity some of the nuclei resulting from (γ, n) reactions are stable, others have very long half-lives or decay schemes which have not as yet been determined. This is particularly true in the case of $(\gamma, 2n)$ reactions where the product nuclei, except for the light elements, are long lived, emit soft radiation which is difficult to detect, and have decay schemes which are in the main not known. A disadvantage of the neutron detection method is that it only gives the sum of the (γ, n), $(\gamma, 2n)$ and (γ, np) cross sections.[1] However, when the (γ, n) cross section is known from residual activity the other cross sections may be readily obtained by subtraction.[2] Usually threshold considerations are of great assistance in sorting out these cross sections.

The earliest survey of neutron yields from a large number of elements using a betatron was carried out by Price and Kerst.[3] They measured these yields at only two betatron energies, 18 and 22 Mev, using rhodium foil detectors.

Terwilliger[4] and Jones[5] measured the photoneutron cross sections of eleven elements, using the x-rays from synchrotrons, and detecting the emitted neutrons with BF_3 "long counters." Terwilliger's results cover an energy range of 13.5 to 70 Mev, while the measurements of Jones extend from 80 to 320 Mev. Although both of these experiments suffer somewhat from lack of precise energy control of their bremsstrahlung beams and from low intensity in the 20-Mev region, nevertheless they have contributed greatly to our knowledge of the photonuclear cross sections at energies above 30 Mev. Recently, Halpern, Nathans, and Mann[6] have reported the photoneutron cross sections for tantalum and bismuth using a method which detected the emitted neutrons. This was accomplished by thermalizing the emitted neutrons in the vicinity of a BF_3 counter which was surrounded by a paraffin cylinder. The scaler was gated so that only those counts occurring some microseconds after each x-ray burst were registered.

In this paper we report on the photoneutron cross sections of some 22 elements covering the periodic table. These measurements extend from threshold up to an energy of 23 Mev; sufficient to include the giant photoabsorption resonance, characteristic of all high-energy photonuclear reactions. The method which we used is similar to that of Halpern *et al.* The authors would like to thank Dr. J. Halpern for making the design details of his apparatus available to us while his work was still in its initial stages. A complete report of this apparatus has been published by Halpern *et al.*[7]

EXPERIMENTAL TECHNIQUE

Although a BF_3 counter will detect neutrons efficiently, its energy sensitivity follows the 1/v law. In photoneutron reactions the energy of the emitted neutrons range from thermal energies to the order of 10 Mev, depending on the nuclear excitation. As a result it is necessary to make the neutron detector equally

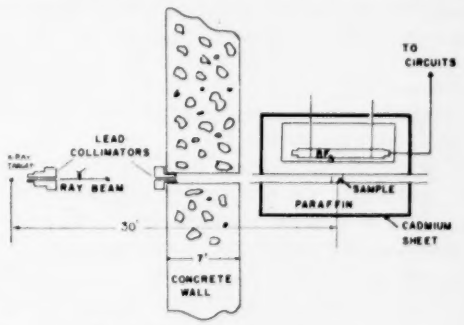

FIG. 1. Experimental arrangement.

* Based on part on a thesis presented for the Ph.D. degree at the University of Saskatchewan by R. Montalbetti.

† On leave of absence from Departamento de Fisica, Universidade de São Paulo, São Paulo, Brazil.

[1] Other neutron emitting cross section are energetically forbidden in the energy region covered in this experiment.

[2] J. Goldemberg and L. Katz, [Phys. Rev. **89**, 1300 (1953)] discuss the validity of such subtractions.

[3] G. A. Price and D. W. Kerst, Phys. Rev. **77**, 806 (1950).

[4] K. M. Terwilliger, Ph.D. thesis, University of California Radiation Laboratory Report UCRL-1917, Aug. 1952 (unpublished).

[5] L. Jones, Ph.D. thesis, University of California Radiation Laboratory Report UCRL-1916, Aug. 1952 (unpublished).

[6] Halpern, Nathans, and Mann, Phys. Rev. **88**, 679 (1952).

[7] Halpern, Mann, and Nathans, Rev. Sci. Instr. **23**, 678 (1952).

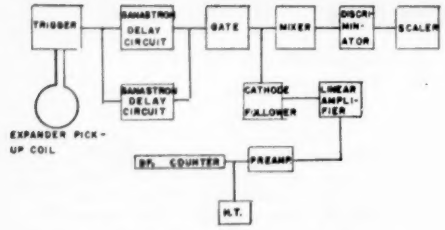

FIG. 2. Block diagram of electronic system.

efficient at all energies. This was accomplished by embedding the BF_3 counter in a paraffin cylinder. The cylinder also served the purpose of confining the neutrons and thermalizing them in the vicinity of the counter. Figure 1 shows the experimental arrangement. The tank was constructed so that the BF_3 counter could be moved up and down in a slot. This slot was necessary in order to determine a position for the counter which gave equal efficiency of counting for all neutron energies. The method of determining this position will be discussed later.

As will be seen from Fig. 1 the sample was placed inside a 1-in. hole at the center of the paraffin block. The x-ray beam which was highly collimated was allowed to strike the sample without hitting any other material.

In order to obtain good counting statistics it was necessary to reduce the neutron background to a very low value. The large neutron flux which accompanied the x-ray burst is sufficient to cause piling-up of counts. These neutrons arise mainly from (γ, n) reactions in the betatron target and the lead shield. It was found that with the equipment in the betatron room, shielded by 8 in. of concrete and approximately 2 ft of water the background was still too high to make an accurate determination of the activation curves.

A solution to this problem was to move the BF_3 detector outside the building where a 7-ft concrete wall could be utilized to considerably reduce this background. The neutrons which did pass through the wall possessed only thermal energies and were captured by the cadmium sheet surrounding the paraffin tank.

A 2-in. hole was drilled through the wall and a lead collimator was inserted. The equipment was aligned photographically so that the x-ray beam had a clear path through the paraffin tank.

The counter experiences a large pile-up of secondary electrons during the x-ray pulse. This was eliminated by means of a gated counting circuit. An electronic system was built so that the photoneutrons which were detected could be counted between the x-ray bursts. These x-ray bursts, of some 4 μsec duration, occur 5500 μsec apart. The electronic system contained a gate which opened 20 μsec after this burst and closed again some 800 μsec later. Neutron pulses were registered on a scaler during the time that this gate is open. Figure 2 shows the electronic system in block diagram. The expander pulse was delayed by two delay circuits which opened and closed a gate at the desired times. The neutron pulses were amplified and fed into a mixer along with the gate signal. The resulting signal was then fed into a discriminator which discriminated the neutron pulses from background.

It was found that by increasing the time beyond 800 μsec gave no appreciable increase in neutron counts. Also by shortening the initial dead time the background rose in greater proportion than the neutron counts so that the values of 20 μsec and 800 μsec were optimum settings.

Samples to be irradiated were placed inside the paraffin tank. It was determined experimentally that for over a region of 10 cm on either side of the center of the BF_3 counter the counting rate remained constant. Beyond this region the counting rate decreased rapidly. Care was taken to locate the samples within this constant counting rate region.

TABLE I. Relative magnitude of background to neutron counting rate for various samples and betatron energies.

Element	Energy	Neutron count (per 10 monitor clicks)	Background (per 10 monitor clicks)
Na	15.4	210	46
(0.55 mole)	19.0	402	78
	22.2	720	98
Cu	15.4	2657	46
(0.27 mole)	19.0	6848	78
	22.2	10 340	98
Bi	15.4	5198	46
(0.086 mole)	10.0	8233	78
	22.2	9530	98

The amount of irradiation a sample received was measured by a Victoreen chamber placed in a 4-cm Lucite block. The Victoreen was placed some 100 cm from the betatron target and aligned so that it "saw" the same portion on the x-ray beam as that "seen" by the sample. Since the activation curves were to be determined relative to copper it was only necessary to calculate the relative dose received by each of the samples.

The procedure for measuring an activation curve was then straightforward. The background for various betatron energies was initially determined with no sample in place. The sample was then inserted and the number of neutrons emitted for a given dose was counted as a function of the betatron energy.

An example of the magnitude of the background count compared to the neutron count is given in Table I.

It is evident that for elements of medium and heavy atomic weight the counting rate necessary for good counting statistics was many times the background. In the region of the light elements however the cross sec-

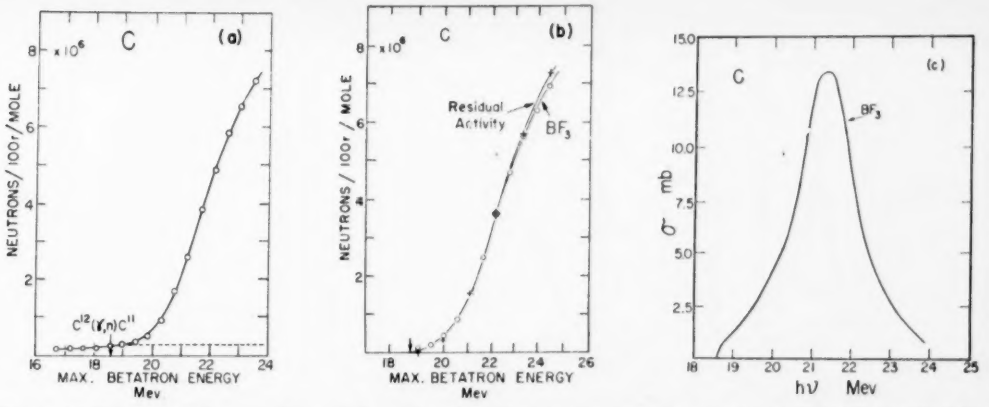

FIG. 3. (a) Neutron yield from a carbon sample as a function of betatron energy. Neutrons below the C^{12} threshold (18.7 Mev) are from the 1.1 percent isotope C^{13} which has a threshold of 4.9 Mev. (b) Neutron yield from $C^{13}(\gamma, n)C^{11}$ reaction as measured by residual activity and direct neutron detection (BF_3) of this experiment. The neutrons from C^{13} shown in Fig. 3(a) have been subtracted. (c) Cross section for the reaction $C^{12}(\gamma, n)C^{11}$ calculated from the neutron yield curve by the photon difference method.

tions are low so that with the size of samples used the neutron counts were only 5 times the background. Nevertheless it was still possible to determine the activation curves quite accurately.

ENERGY SENSITIVITY OF COUNTING SYSTEM

Since calibrated neutron sources were not available to us, it was not possible to determine directly the energy sensitivity of the experimental setup. The method adopted was to compare the shape of the activation curves obtained with the BF_3 counter to that obtained by residual activity, in an element where the (γ, np) and $(\gamma, 2n)$ reactions are energetically forbidden in the energy region examined. One such element available for this comparison is carbon. C^{12} is a 99 percent isotope with thresholds of 28.2 and 32.3 Mev for the (γ, np) and $(\gamma, 2n)$ reactions. Though its activation curve had been previously determined by residual activity,[8] a redetermination was made on the same day as the neutron curve was measured.[9] The position of the BF_3 counter was varied in the slot (Fig. 1) until the activation curve measured by it agreed in shape with that found by residual activity.

As the betatron energy is increased the average nuclear excitation energy increases. This results in an increasing mean energy of the emitted neutrons. The activation curve obtained by residual activity gives a measure of the relative numbers of these neutrons at each betatron energy. Thus when the two activation curves agree in shape, neutrons of different energy are detected with equal efficiency. The results are shown in Figs. 3(a) and (b).

Natural carbon contains 1.1 percent of C^{13} which has a threshold of 4.9 Mev for the (γ, n) reaction. The neutrons in Fig. 3(a) below the $C^{12}(\gamma, n)$ threshold are from this reaction. It is well known that (γ, n) activation curves level off at about 6 Mev above threshold and remains sensibly constant with increasing betatron energy. For this reason the contribution to the neutron flux from C^{13} may be expected to remain sensibly constant above the C^{12} threshold as indicated by the dashed line. Subtracting this contribution gives the activation curve for the C^{12} isotope, which is shown in Fig. 3(b). The curve obtained by residual activity is shown in the same figure for comparison.

It will be seen that the two curves are in excellent agreement up to 4 Mev above threshold and differ by only 4 percent at 6 Mev from threshold. The neutron distribution for a given nuclear excitation in such a light element as carbon has a much higher mean energy than from heavier nuclei. Thus since good agreement was obtained for carbon, the system may be expected to be energy insensitive up to equivalent excitation energies in the heavier elements.

NORMALIZATION

In order to obtain the absolute neutron yield per unit mass of sample per unit of irradiation it is necessary to calibrate our apparatus. The procedure usually followed in this laboratory is to use the (γ, n) reaction in copper as a standard. The absolute cross section for this reaction in both isotopes of copper had been previously measured in this laboratory by residual activity.[10] The cross section for the Cu^{63} isotope has been measured

[8] Haslam, Johns, and Horsley, Phys. Rev. **82**, 270 (1951).

[9] A very disturbing effect was found in this determination. The new activation curve differed considerably from that measured about 2 years ago. The cross-section curve obtained from it is now somewhat more symmetric and peaks at about 0.8 Mev lower than before (21.3 Mev). This change in activation curve shape will be discussed at greater length in a forthcoming paper by Goldemberg and Katz. Intercomparison of activation curves of the lighter elements taken in different laboratories show similar differences. This will be brought out more clearly in our discussion of phosphorus.

[10] Johns, Katz, Douglas, and Haslam, Phys. Rev. **80**, 1602 (1950).

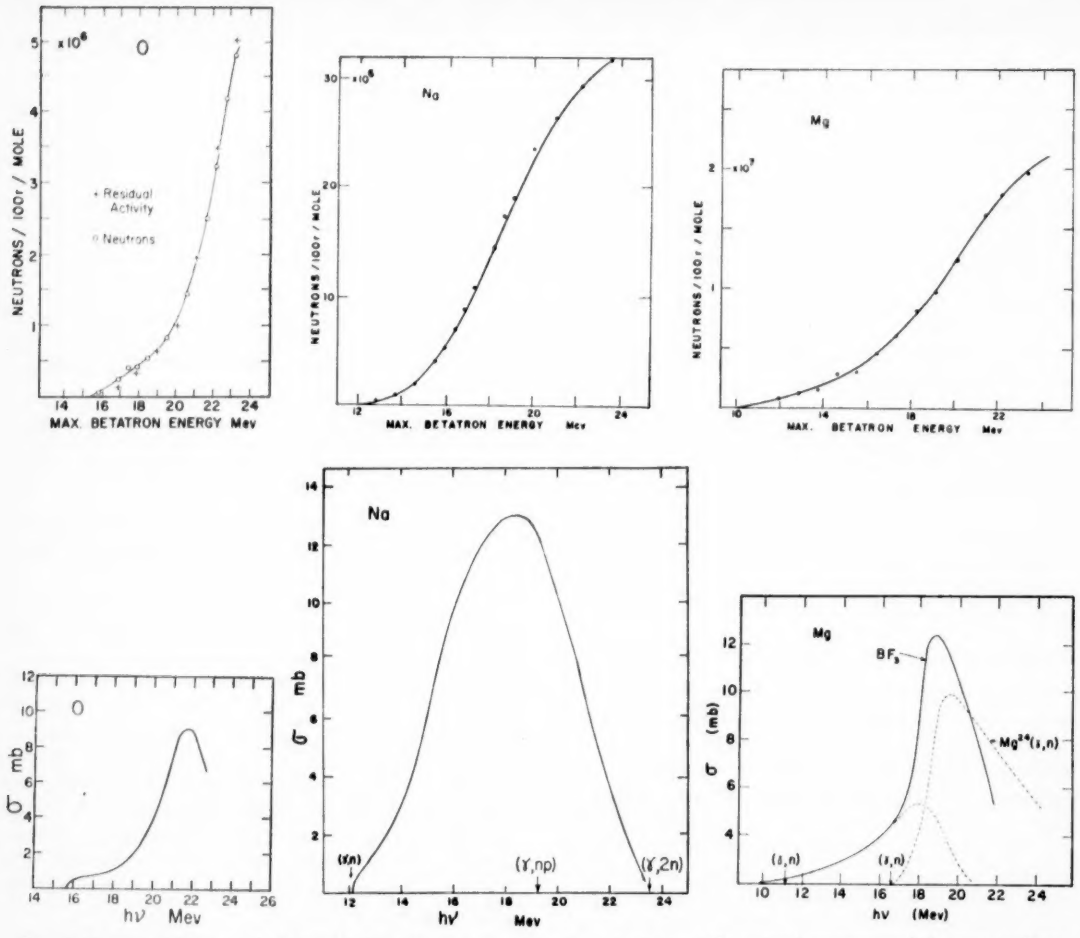

FIG. 4. Neutron yields from the indicated elements as measured by direct detection of the emitted neutrons, and the cross sections calculated from them by the photon difference method. See the more detailed discussion in the contents of the article.

independently in a number of laboratories[11–13] and our value has been well substantiated. The cross section for the Cu^{65} isotope has been measured independently by Byerly and Stephens[12] and is in good agreement with our value. Combining these two cross sections according to the isotopic abundance of Cu^{63} and Cu^{65}, the (γ, n) cross section for the natural element was obtained. The neutron yield for each element in our experiment was compared to that of copper with the betatron energy set at 18 Mev. This allowed us to calculate the absolute neutron yield for these elements at this energy.

The shapes of the yield curves were obtained in a series of experiment extending over a period of five weeks. All curves were then calibrated against copper in one continuous run. The betatron was kept at 18-Mev, samples of the various elements were irradiated one after the other, and the resulting neutron yields were measured. To assure that the energy of the betatron and the sensitivity of the apparatus remained constant, the yield from an aluminum sample was checked periodically.

The normalization point was chosen at 18 Mev since no $(\gamma, 2n)$ is present in copper at this energy. The threshold for $C^{12}(\gamma, n)C^{11}$ is 18.6 Mev and for this reason carbon was normalized against copper at 21 Mev.

Many of the photons which are "absorbed" in the sample only suffer Compton scattering and therefore have a second chance to produce photoneutron reactions, though they have been assumed to be lost in our calculations below. Calculations show that for the size of samples used in this experiment at most 2 percent of all photoneutrons at 24-Mev irradiation could be attributed to this effect.

[11] B. C. Diven and G. M. Almy, Phys. Rev. **80**, 407 (1950).
[12] P. R. Byerly and W. E. Stephens, Phys. Rev. **83**, 54 (1951).
[13] V. E. Krohn, Jr., and E. F. Shrader, Phys. Rev. **87**, 685 (1952).

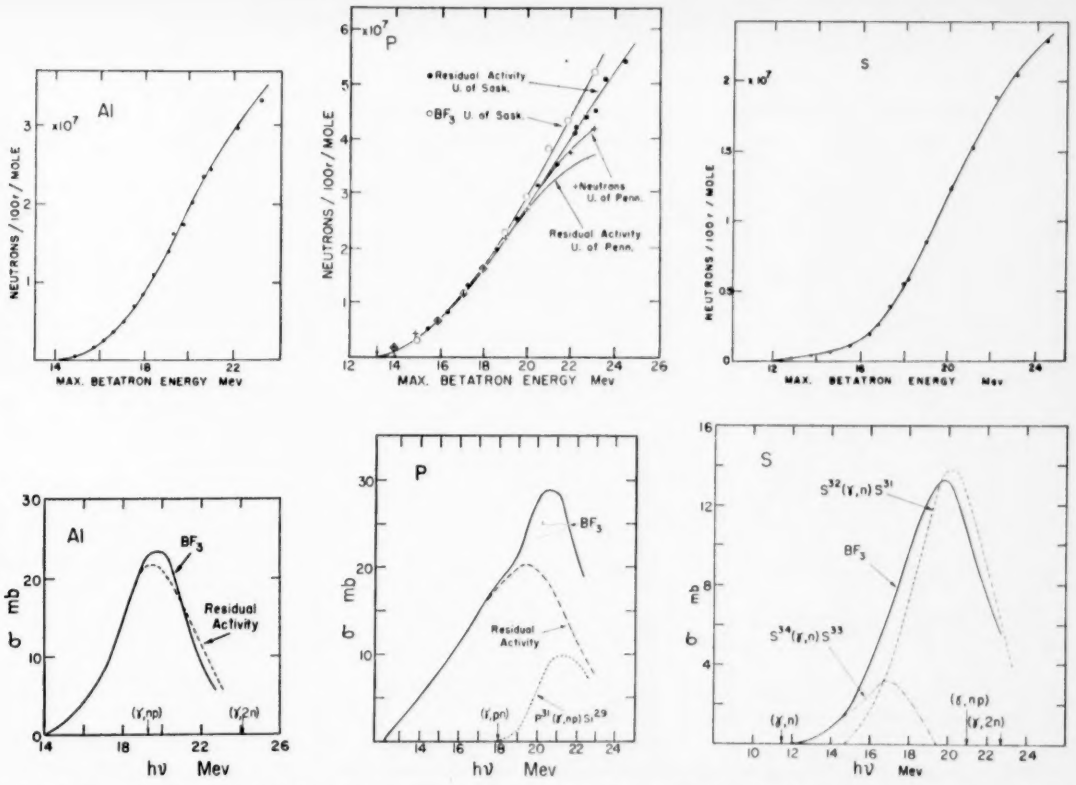

FIG. 5. Neutron yields from the indicated elements as measured by direct detection of the emitted neutrons, and the cross sections calculated from them by the photon difference method. See the more detailed discussion in the contents of the article.

RESULTS

The yield curves which were obtained are shown in Figs. 4 to 10. Before these curves can be analyzed for the photoneutron cross sections, it is necessary to correct for absorption of the bremsstrahlung beam in the sample itself. Small samples are usually used in the residual activity experiments so that this correction is negligible. However, in order to obtain sufficient neutron flux in our experiment with the apparatus situated some 30 feet from the betatron target, considerably larger samples had to be used. This correction is no longer negligible and was applied as follows:

Consider a sample of length l, density ρ and cross-sectional area a, then if α' is the activity from the sample, the activity per mole is:

$$\alpha=\alpha' A/\rho a l.$$

Thus

$$\frac{\alpha' A}{\rho a l}=N\int_0^{E_0}\sigma(E)P(E,E_0)dE\int_0^{l}\frac{e^{-\mu\rho x}}{l}dx,$$

where $\sigma(E)$ is the cross section for the reaction; $P(E, E_0)$ is the number of photons per cm² per 100r/min per Mev interval of energy E when betatron is operating at an energy E_0, μ is the total absorption coefficient in units of cm²/g, and N is Avogadro's number.

Integration with respect to x gives

$$\alpha=N\int_0^{E_0}\sigma(E)P(E,E_0)\left[\frac{1-e^{-\mu\rho l}}{\mu\rho l}\right]dE.$$

The variation with energy of the bracketed term was calculated for the size of samples used. The variation was found to be 1 percent over an energy region of 10 Mev to 22 Mev. For this reason the bracketed term may be taken outside of the integral and the following equation is obtained:

$$N\int_0^{E_0}\sigma(E)P(E,E_0)dE=\frac{\alpha' A\mu}{a(1-e^{-\mu\rho l})}.$$

It is seen from this last equation that after the observed activity is corrected for sample size and photon absorption the basic equation for the photon difference method is obtained. This correction has been applied to the activation curves which are shown in Figs. 3(b) and 4 through 10. These curves were analyzed by the photon difference method and the resulting cross sec-

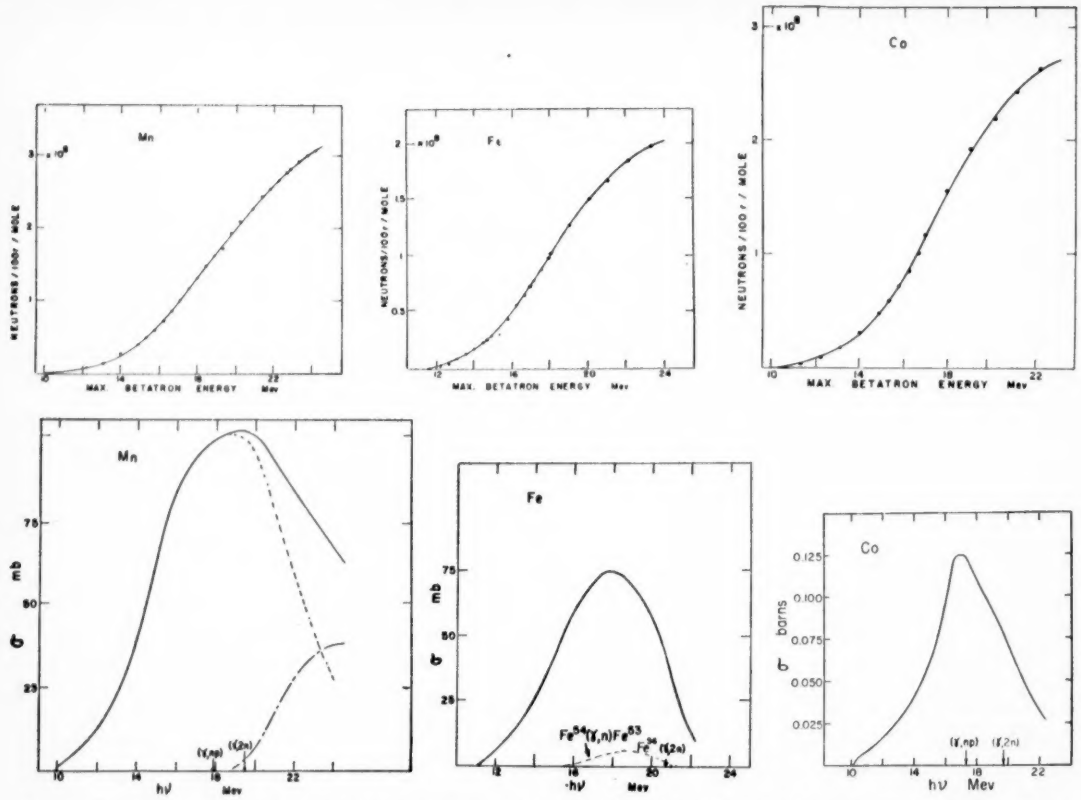

FIG. 6. Neutron yields from the indicated elements as measured by direct detection of the emitted neutrons, and the cross sections calculated from them by the photon difference method. See the more detailed discussion in the contents of the article.

tions[14] are shown in Figs. 3(c) and 4 through 10. As many of the 100 percent isotopes as possible were measured. In these cases the determination of the $(\gamma, 2n)$ contribution is of course much easier to evaluate than when there are several large percentage isotopes present.

The (γ, np) and $(\gamma, 2n)$ thresholds are indicated on the individual cross section curves. These were calculated from mass data whenever those were available. In the lighter elements the data of Li *et al.*[15] and Li[16] were used, the masses of some of the heavier elements were kindly supplied by Duckworth[17] or were taken from the literature.[18] When no mass data were available the thresholds were calculated from the table of atomic masses by Metropolis and Reitwiesner.[19] The (γ, n) thresholds of our activation curves were in good agreement with those published by Sher, Halpern, and Mann.[20] They are not given explicitly since no effort was made to determine them accurately.

The pertinent data obtained for each element have been collected together and are presented in Table II. Previous measurements obtained predominantly by the residual activity method are also given in this table. Each of the curves will now be discussed separately. Heading each of the discussions is a list of the isotopes in the element, their abundance and the (γ, n) threshold (Mev) in each. These data are necessary for a proper interpretation of each of the curves.

Carbon (C^{12} 98.9 Percent, 18.6; C^{13} 1.1 Percent, 4.9)

The cross-section curve obtained by the neutron experiment agrees very well with that obtained using the most recent residual activity measurements. This is of course evident from the excellent agreement between the activation curves. The new curves differ somewhat in shape and area from that found previously in this laboratory by residual activity measurements[8] but the values of the peak cross sections are well within experimental error.

[14] It is to be noted that wherever the cross section includes contributions from the $(\gamma, 2n)$ reaction the cross-section shape is distorted since two neutrons are emitted per absorbed photon.

[15] Li, Whaling, Fowler, and Lauritsen, Phys. Rev. **83**, 512 (1951).

[16] C. W. Li, Phys. Rev. **88**, 1038 (1952).

[17] H. E. Duckworth (private communication).

[18] R. E. Halsted, Phys. Rev. **88**, 666 (1952).

[19] N. Metropolis and G. Reitwiesner, U. S. Atomic Energy Commission Document NP-1980 (unpublished).

[20] Sher, Halpern, and Mann, Phys. Rev. **84**, 387 (1951).

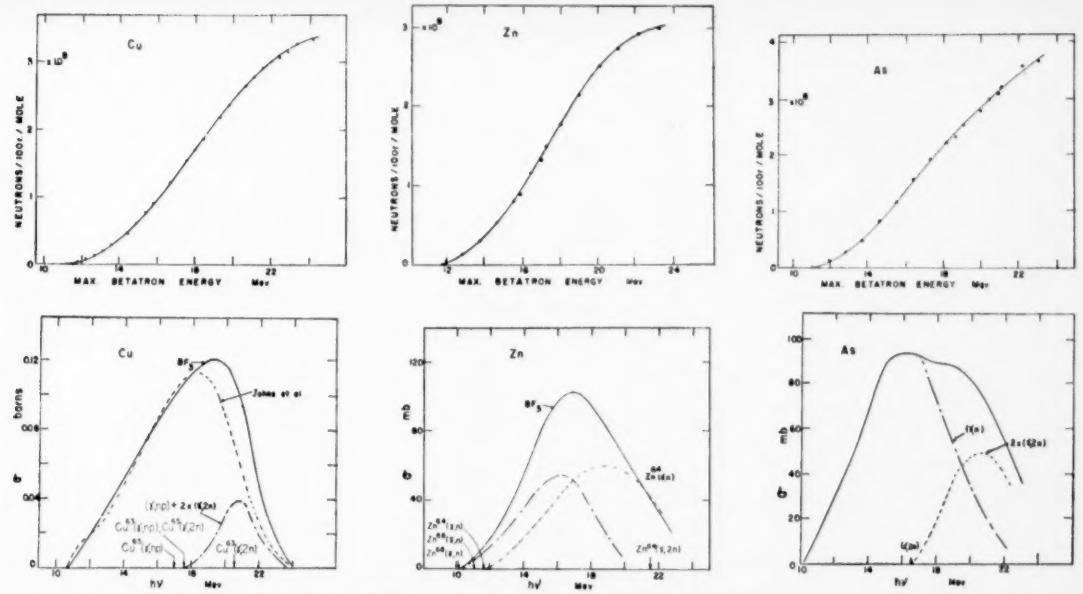

FIG. 7. Neutron yields from the indicated elements as measured by direct detection of the emitted neutrons, and the cross sections calculated from them by the photon difference method. See the more detailed discussion in the contents of the article.

Oxygen (O^{16} 99.8 Percent, 15.6; O^{17} 0.04 Percent, 4.2; O^{18} 0.20 Percent, 8.0)

The agreement between the yield curves obtained from residual activity and direct neutron detection offers further proof that the neutron apparatus is equally sensitive to all neutron energies encountered in this experiment.

The cross-section curve exhibits the initial flat region

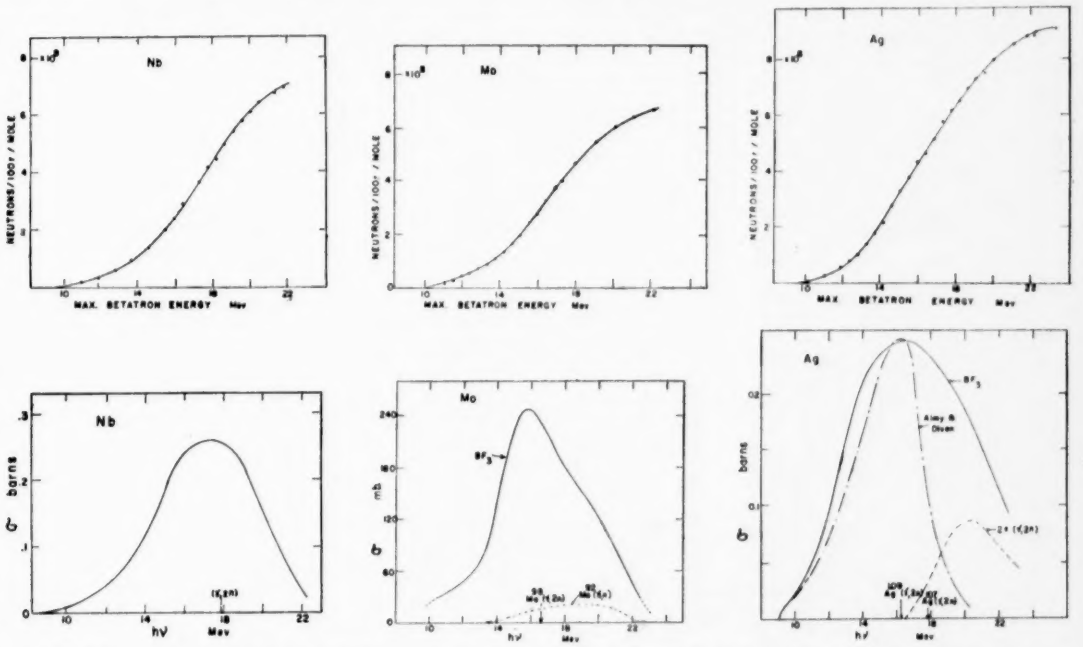

FIG. 8. Neutron yields from the indicated elements as measured by direct detection of the emitted neutrons, and the cross sections calculated from them by the photon difference method. See the more detailed discussion in the contents of the article.

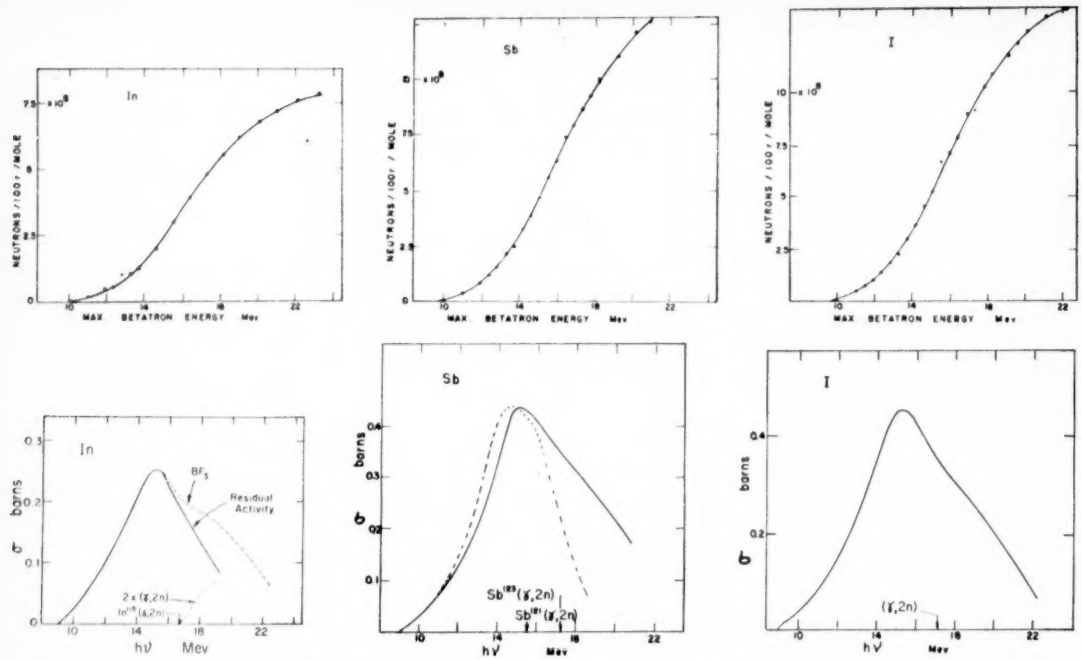

FIG. 9. Neutron yields from the indicated elements as measured by direct detection of the emitted neutrons, and the cross sections calculated from them by the photon difference method. See the more detailed discussion in the contents of the article.

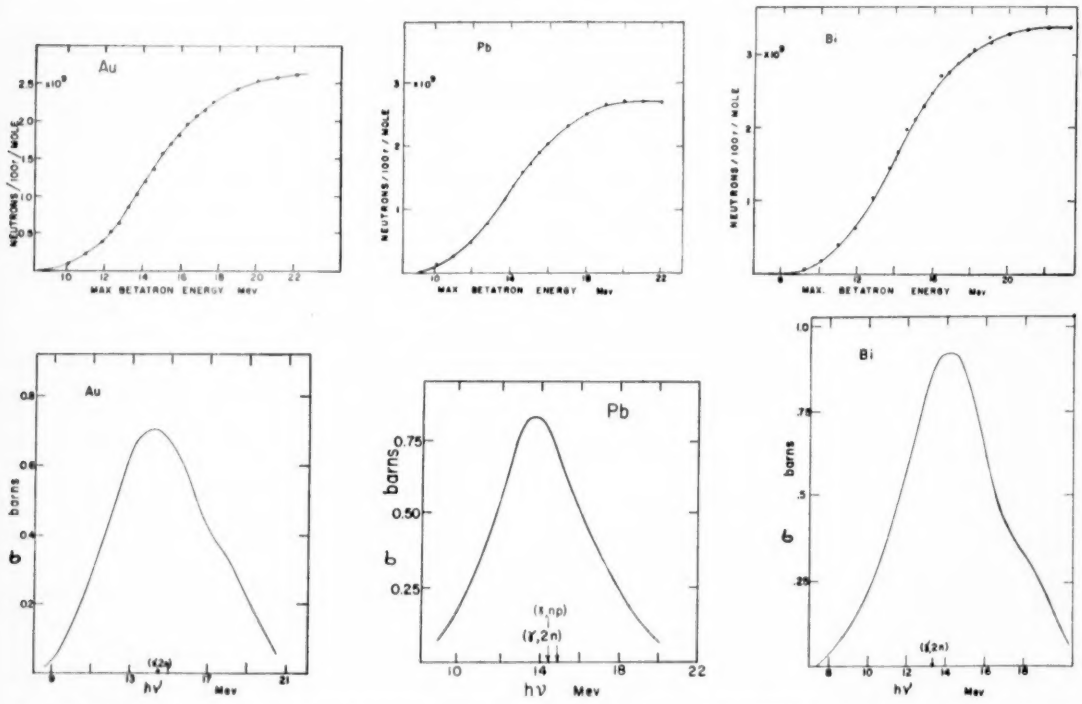

FIG. 10. Neutron yields from the indicated elements as measured by direct detection of the emitted neutrons, and the cross sections calculated from them by the photon difference method. See the more detailed discussion in the contents of the article.

TABLE II. Characteristics of photonuclear cross sections.

Element	Half-width of σ (γ, n)	Half-width of σ for element	E_m (Mev)	σ_m (barns)	Integrated σ (Mev-barn) (γ, n)	(γ, p)	($\gamma, 2n$)	(γ, n)+(γ, np) +2($\gamma, 2n$)	Ref.
Be^{9}	4.7(γ, p)		22.2	0.0027		0.011			*b*
C		2.0	21.4	0.014	0.029				*c*
C^{12}	2.8		22.9	0.013	0.046				*d*
C		1.7(γ, p)	21.5	0.034		0.063			*e*
N^{14}			24.2	0.0028	0.015[a]				*f*
O			21.9	0.0089	0.019[a]				*c*
O^{16}			24.2	0.011	0.031[a]				*f*
F^{19}	~13		~20	0.0035	0.076		0.005		*g*
Na		6.0	18.3	0.013				0.081	*c*
Mg		3.9	18.8	0.011				0.048	*c*
Mg^{24}	5.8		19.4	0.0098	0.057				*h*
Mg^{25+26}		~4.2	17.8	~0.016	~0.065				*c*
Mg^{25}	6.0(γ, p)		21.7	0.015		0.10			*h*
Mg^{26}	3.3(γ, p)		22.6	0.019		0.085			*h*
Al		4.0	19.7	0.023				0.10	*c*
Al^{27}	4.7		19.2	0.008	0.045				*h*
Al		5.4(γ, p)	21.2	0.022		0.12			*e*
Si^{28}	3.5		20.9	0.021	0.070				*i*
P		5.7	20.5	0.029	0.14		0.034(γ, np)	0.17	*c*
P^{31}	6.5		19.5	0.017	0.13				*j*
P^{31}			20	0.017	0.099		0.047(γ, np)	0.15	*k*
S		5.2	19.8	0.013				0.075	*c*
S^{32}	4.5		20.1	0.015	0.069				*i*
S^{32}	1.0(γ, d)		25.6	0.006			0.016(γ, d)		*j, l*
S^{34}	4		~17	~0.060				~0.20	*c*
Ca^{40}	4.2		19.3	0.015	0.065				*i*
Mn		>8	~19	0.10				~0.46[a]	*c*
Fe		6.1	18.0	0.075				0.47	*c*
Fe^{54}	6.3		18.7	0.067	0.48				*d*
Ni^{58}	5.6		18.5	0.054	0.34				*d*
Ni		5.4(γ, p)	18.7	0.058		0.32			*e*
Co		5.4	16.9	0.13				0.75	*c*
Co		5.7(γ, p)	21.5	0.024		0.14			*e*
Cu		7.1	19.5	0.12			0.054	0.87	*c*
Cu^{63}	6.1		18.1	0.10	0.66				*d*
Cu^{65}	7.0		18.6	0.15	1.11				*d*
Zn^{64}	7.9		18.7	0.12	0.99				*d*
As	~6.2	9.4	17	0.093	0.76		0.11	0.98	*c*
Br^{80}	8.0		18.0	0.13	1.08				*m*
Rb^{87}	6.0		17.5	0.23	1.68				*n*
Zr^{90}	5.7		18.0	0.27	1.67				*n*
Mo		6.1	15.7					1.62	*c*
Mo^{92}	6.0		18.7	0.14	0.85				*n*
Nb		6.1	17.3	0.26				1.71	*c*
Nb		6.6(γ, p)	21.3	0.018		0.12			*e*
Ag		9.2	16.3	0.20	2.1		0.22	2.5	*c*
Ag^{109}	4.6		16.5	0.32	1.65				*o*
In	~5.8	8.0	15.2	0.25	~1.6		~0.20	~2.0	*c*
In^{115}	5.5		15.0	0.42	2.7				*p*
In^{115}	~8(γ, γ')		~15	0.05				~0.4(γ, γ')	*p*
Sb		7.2	15.2	0.44				3.1	*c*
Sb^{121}	4.8		14.8	0.68	3.5				*d*
Sb^{123}	4.8		14.8	0.36	1.9				*d*
I	~5.0	6.6	15.2	0.45				3.1	*c*
Ta^{181}	4.6		13.9		>0.47				*d*
Au	~5.6	6.3	14.2	0.70				4.6	*c*
Au^{197}	~10(γ, γ')		15	>0.025				>0.25(γ, γ')	*q*
Pb		5.3	13.7	0.81				4.8	*c*
$Pb^{207+208}$	~6.5(γ, p)		22.0	0.028		~0.17			*r*
Bi	~5.2	5.4	14.2	0.92				4.1	*c*

[a] Integrated cross section to peak position.
[b] Haslam, Katz, Crosby, Summers-Gill, and Cameron, Can. J. Phys. **31**, 210 (1953).
[c] Results from present experiments.
[d] See reference 24.
[e] See reference 34.
[f] Johns, Horsley, Haslam, and Quinton, Phys. Rev. **84**, 856 (1951).
[g] Horsley, Haslam, and Johns, Phys. Rev. **87**, 756 (1952).
[h] See reference 22.
[i] Summers-Gill, Haslam, and Katz, Can. J. Phys. **31**, 70 (1953).
[j] See reference 25.
[k] See reference 23.
[l] L. Katz and A. S. Penfold, Phys. Rev. **83**, 169 (1951).
[m] Katz, Pease, and Moody, Can. J. Phys. **30**, 476 (1952).
[n] Katz, Baker, and Montalbetti, Can. J. Phys. **31**, 250 (1953).
[o] B. C. Diven and G. M. Almy, Phys. Rev. **80**, 407 (1950).
[p] See reference 28.
[q] A. G. W. Cameron and L. Katz, Phys. Rev. **84**, 1264 (1951).
[r] A. G. W. Cameron and L. Katz, Phys. Rev. **83**, 1264 (1951).

followed by the usual resonance curve found previously[21] in residual activity measurements. As in the case of carbon, the activation curve obtained by residual activity in the present experiment differs considerably from that found previously, the general features of the cross-section curves are however not greatly altered.

Sodium (Na^{24} 100 Percent, 12.1)

This is a new cross-section curve since it cannot be measured by residual activity. The (γ, np) threshold was calculated to be 19.2 Mev from the mass data of Li.[16] Thus the high-energy side of the curve may have a contribution from this reaction.

Magnesium (Mg^{24} 78.6 Percent, 16.5; Mg^{25} 10.1 Percent, 7.3; Mg^{26} 11.3 Percent, 11.1)

The solid curve is the cross section for all of the magnesium isotopes. The (γ, n) cross section for the 79 percent isotope as measured by Katz and Cameron[19] is also shown (corrected for isotopic abundance). The difference in the low energy side between these curves may be attributed to the sum of the $Mg^{25}(\gamma, n)$ and $Mg^{26}(\gamma, n)$ reactions. It must be emphasized that since we are subtracting almost equal cross sections the upper part of the difference curve may be greatly in error. We should also note that a change of 20 percent in the residual activity curve would make it coincide with the BF_3 curve at the peak. This is within experimental accuracy.

Aluminum (Al^{27} 100 Percent, 12.8)

The cross-section curve obtained here has the same relative shape as that of Katz and Cameron.[22] Its absolute magnitude is however greater by a factor of 3. There seems to be no reason for this larger discrepancy, it is believed however that the present measurements are more reliable. As previously discussed, the activation curves were standardized in one continuous run and all calculations were carried out in a standardized manner, considerably reducing the chance of relative errors. Good agreement is also obtained between the neutron yields in our activation curves at 18 and 22 Mev and those reported by Price and Kerst.[3]

Phosphorus (P^{31} 100 Percent, 12.1)

Yield curves obtained by Halpern, Mann, and Nathans[23] from residual activity measurements and direct neutron detection are compared in Fig. 5 to those found by us. The curves have been arbitrarily normalized, at 18 Mev since Halpern *et al.* published only relative yields, and our neutron yield curve was somewhat higher at this point than the previous activation curve, though well within experimental accuracy. It will be seen that the shapes of the curves are in excellent agreement below the normalization point, but at greater energies our yields are consistently higher.

The difference between the residual activity yield curve and the direct neutron detection yield above 18 Mev may be caused by the (γ, np) reaction whose threshold is 17.9 Mev. Both sets of data show this effect, with the percent contribution from the (γ, np) reaction being about the same in the two cases.

It would be tempting to attribute the difference between the results taken in the two laboratories to gamma-flux monitoring procedure, however the changes in the carbon and oxygen yield curves taken in our laboratory some three months apart would seem to rule this explanation out, since the same monitor was used in both cases.

An analysis of the "BF_3" yield curve by the photon difference method[24] gave the cross-section curve shown by the solid line of Fig. 5. The cross section for the (γ, n) reaction previously measured in this laboratory[25] was found to be about 15 percent lower at 18 Mev, well within experimental accuracy. If the two curves are then arbitrarily normalized at this energy, dashed curve of Fig. 5, then the difference is attributable to the (γ, np) reaction.

The area under the normalized (γ, n) curve gives an integrated cross section of 0.14 Mev-barn. The integrated cross section for the (γ, np) reaction is estimated to be 0.035 Mev-barn. These values are in fair agreement with those given by Halpern *et al.*,[23] namely 0.099 and 0.047 Mev-barn, respectively.

Sulfur (S^{32} 95 Percent, 14.7; S^{33} 0.74 Percent, 8.6; S^{34} 4.2 Percent, 10.8; S^{36} 0.016 Percent)

The $S^{32}(\gamma, n)S^{31}$ curve as measured by residual activity[26] was subtracted from the total neutron curve. The remaining portion may be attributed to the reaction in the S^{34} isotope. Since this cross section is obtained by subtraction, it is obviously subject to a fairly large error in absolute value. Since S^{34} is only a 4.2 percent isotope its cross section as given by these measurements is about 4 times that of S^{32}. However, before comparing photon absorption cross sections account must be taken of the other modes of de-excitation, particularly (γ, p) which is quite threshold sensitive relative to (γ, n).

Manganese (Mn^{55} 100 Percent, 10.0)

The total photoneutron cross-section curve (solid line) is much broader than expected from our knowledge of other (γ, n) reactions. In this region of the periodic table they are generally found to be 6 Mev wide at half-maximum. An assumed (γ, n) curve (6 Mev wide)

[21] Horsley, Haslam, and Johns, Can. J. Phys. **30**, 159 (1952).
[22] L. Katz and A. G. W. Cameron, Phys. Rev. **84**, 1115 (1951).
[23] Halpern, Mann, and Nathans, Phys. Rev. **88**, 958 (1952).
[24] L. Katz and A. G. W. Cameron, Can. J. Phys. **29**, 518 (1951).
[25] L. Katz and A. S. Penfold, Phys. Rev. **81**, 815 (1951).
[26] The mass data of Li (see reference 16) gives a threshold for this reaction of 14.4 Mev. On the other hand, Haslam, Summers-Gill, and Crosby, (Can. J. Phys. **30**, 257 (1952)) have measured this threshold at 15.0±0.1. We have taken the mean of the values.

has been drawn in as indicated by the dotted line. The difference is made up of twice the $(\gamma, 2n)$ reaction and the (γ, np) reaction. It is not possible to make a separation of the two latter reactions.

Iron (Fe^{54} 5.9 Percent, 13.8; Fe^{56} 91.6 Percent, 11.1; Fe^{57} 2.20 Percent, 7.7; Fe^{58} 0.33 Percent, 10.5)

By subtracting the (γ, n) cross section of the 6 percent isotope (dotted line) as measured by Katz *et al.*[27] from the total curve (solid line) the contributions from the remaining iron isotopes is obtained. Fe^{56} is the major isotope, so it forms the major portion of the total cross section curve. It is not possible to measure the (γ, n) reaction in this isotope by residual activities since the half-life of Fe^{55} is 4 years.

Cobalt (Co^{59} 100 Percent, 10.2)

Not very much can be said about this cross-section curve. When the (γ, n) cross section is determined by residual activity it will be possible to estimate the (γ, np) and $(\gamma, 2n)$ contributions.

Cooper (Cu^{63} 69.0 Percent, 10.9; Cu^{65} 31.0 Percent, 9.8)

Copper was taken as the standard to which all elements were normalized at 18 Mev. The residual activity cross-section curve shown in this figure was obtained by combining the $Cu^{63}(\gamma, n)Cu^{62}$ and $Cu^{65}(\gamma, n)Cu^{64}$ cross sections according to their isotopic abundance. The shape of the experimental curve is in good agreement with that of residual activity measurements except beyond 18.5 Mev; the difference probably being the result of the $(\gamma, 2n)$ and (γ, np) reactions.

Zinc (Zn^{64} 48.9 Percent, 11.6; Zn^{66} 27.8 Percent, 11.1; Zn^{67} 4.1 Percent, 7.0; Zn^{68} 18.6 Percent, 10.1; Zn^{70} 0.63 Percent)

A detailed analysis to determine each cross curve cannot be made since there are four major isotopes. However, taking the difference between the total photoneutron cross-section curve and that obtained from residual activity for the $Zn^{64}(\gamma, n)Zn^{63}$ reaction (properly corrected for isotopic abundance), the contribution from the remaining isotopes is obtained. The threshold for the $(\gamma, 2n)$ reaction in Zn^{64} is 21.6 Mev. The thresholds for the $(\gamma, 2n)$ reactions in the other isotopes are not known.

Arsenic (As^{75} 100 Percent, 10.1)

The shape of the cross-section curve is very odd. In fact it is rather obvious that it is made up of 2 curves, one for the (γ, n) and the other for the $(\gamma, 2n)$ reaction. An analysis of the contribution of $(\gamma, 2n)$ is given in the discussion.

[27] Katz, Johns, Baker, Haslam, and Douglas, Phys. Rev. **82**, 271 (1951).

Niobium (Nb^{93} 100 Percent, 8.7)

The cross-section curve exhibits the usual resonance characteristics. The $(\gamma, 2n)$ reaction is not as evident in this case as for example in arsenic.

Molybdenum (Mo^{92} 15.7 Percent, 13.1; Mo^{94} 9.3 Percent, Mo^{95} 15.7 Percent, Mo^{96} 16.5 Percent, Mo^{97} 9.5 Percent, Mo^{98} 23.9 Percent, Mo^{100} 9.5 Percent)

The large number of high percentage isotopes present in this element with widely different thresholds precludes an analysis of this curve.

Silver (Ag^{107} 51.4 Percent, 9.5; Ag^{109} 48.6 Percent, 9.0)

The total photoneutron cross section is extremely broad. Subtracting the (γ, n) curve as obtained by Almy and Diven[11] using the activity method, the resulting curve is likely attributable to the $(\gamma, 2n)$ process. Following Almy and Diven we assumed that the two isotopes of silver have the same shape since their thresholds are nearly equal.

Indium (In^{115} 95.8 Percent, 9.1; In^{113} 4.2 Percent, 9.7)

Here it seems very likely that the total curve is made up of two separate curves, one attributed to the (γ, n) process and the other to the $(\gamma, 2n)$ reaction. Recently Goldemberg and Katz[28] have measured by residual activity both the (γ, n) and the $(\gamma, 2n)$ reaction in In^{115} in this laboratory. Although the absolute cross sections which they found were somewhat larger (peak cross sections of 0.42 barn for the (γ, n) reaction and about 0.11 barn for the $(\gamma, 2n)$ reaction), the shapes of their curves are almost identical to those shown in the figure. The value reported here would be somewhat depressed, since indium acts as a neutron sink due to its large thermal neutron absorption cross section.

Antimony (Sb^{121} 57.2 Percent, 8.3; Sb^{123} 42.8 Percent, 9.3)

The solid line is the total cross section for all isotopes. The dotted line is that measured by Johns *et al.*[10] for Sb^{123} (43 percent isotope), and has not been corrected for isotopic abundance. This shows that the cross section curves for both isotopes must be very similar in shape. There is obviously a large contribution from the $(\gamma, 2n)$ reactions; the difference between the two curves is, however, not shown explicitly since the (γ, n) cross section in Sb^{121} is not known.

Iodine (I^{127} 100 Percent, 9.1)

This curve exhibits the usual characteristics of all other (γ, n) reactions. This cross section has as yet not been measured by residual activity.

[28] J. Goldemberg and L. Katz, Phys. Rev. **90**, 308 (1953).

Gold (Au^{197} 100 Percent, 7.9)

The $(\gamma, 2n)$ reaction is not readily separated here, as no strong anomaly is present in the total cross section curve.

Lead (Pb^{204} 1.3 Percent, 8.7; Pb^{206} 26 Percent, 10.6; Pb^{207} 21 Percent, 6.9; Pb^{208} 52 Percent, 7.2)

Though there are several high percentage isotopes in lead, the rather smooth over-all cross-section curve is not unexpected since their (γ, n) thresholds are not too different.

Cameron, Harms, and Katz[29] have measured the cross sections for the reactions $Pb^{207}(\gamma, p)Tl^{206}$, $Pb^{208}(\gamma, p)Tl^{207}$ and $Pb^{208}(\gamma, d+np)Tl^{206}$ by detecting the activity of the residual nuclei. Since Tl^{206} and Tl^{207} have almost identical half-lives, the cross section for the individual reactions could not be separated. At 18 Mev, for example, they find the cross section to be about 1 mb, this value being almost wholly the result of the sum of the (γ, p) reactions.

The (γ, n) cross section at the same energy is about 100 mb. Thus we must conclude that at this energy $\sigma_{\gamma,p}/\sigma_{\gamma,n} \simeq 0.01$. On the basis of statistical theory this is rather large considering the height of the potential barrier which the protons must overcome, but is of the correct order of magnitude for a direct photoproton effect. In order to compare this ratio with that predicted by statistical theory we must first calculate the thresholds for these reactions in the various isotopes. The results of such calculations using measured nuclear masses[17] are given in Table III. It will be seen that these are almost equal.

TABLE III. Thresholds for the isotopes of lead.

Isotope	Threshold (Mev) (γ, n)	(γ, p)	(γ, np)	$(\gamma, 2n)$
Pb^{206}	10.6	7.1	14.3	14.5
Pb^{207}	7.2	8.1	14.3	17.9
Pb^{208}	6.9	8.4	15.0	14.2
Natural element (average)	7.9	7.9	14.5	14.9

The average threshold (averaged according to isotopic abundance) is the same for (γ, p) and (γ, n) and the individual values do not deviate very far from these. Taking this average at $\simeq 8$ Mev, the theoretical ratio may be calculated. This ratio is precisely the ratio F_p/F_n at $\epsilon_{bY} = 10$ Mev given by Blatt and Weisskopf.[30] From their graphs we find $F_p/F_n \simeq 10^2/10^8 = 10^{-6}$. Thus the statistical ratio is much lower than that found experimentally; on the other hand there is ample evidence in the literature[11,31] for a small direct photoproton effect.

[29] Cameron, Harms, and Katz, Phys. Rev. **83**, 1264 (1951).
[30] J. M. Blatt and V. F. Weisskopf, *Theoretical Nuclear Physics* (John Wiley and Sons, Inc., New York, 1952), p. 373.
[31] E. D. Courant, Phys. Rev. **82**, 703 (1951).

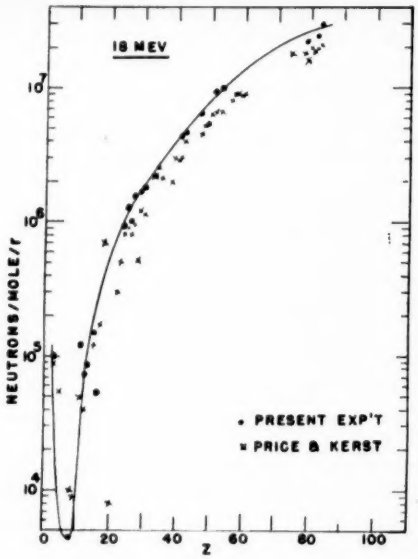

FIG. 11. Neutron yields with betatron operating at 18 Mev compared to the data of Price and Kerst.

Bismuth (Bi^{209} 100 Percent, 7.4)

This cross-section curve exhibits the anomaly on the high-energy side found by Halpern, Nathans, and Mann[6] and attributed by them to the $(\gamma, 2n)$ reaction. The two cross-section curves peak at about the same energy but ours is about twice as large. In view of the excellent agreement between the neutron yields meas-

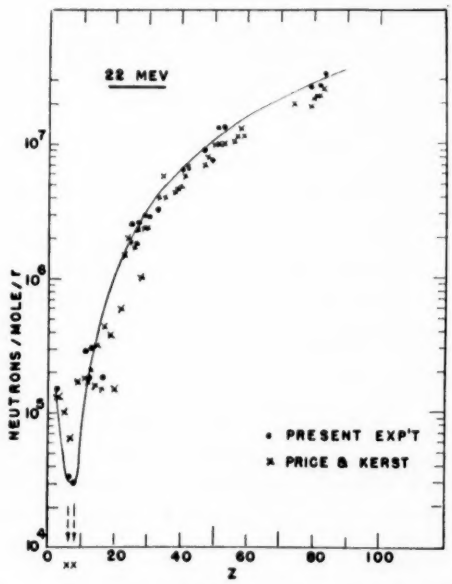

FIG. 12. Neutron yields with betatron operating at 22 Mev compared to the data of Price and Kerst.

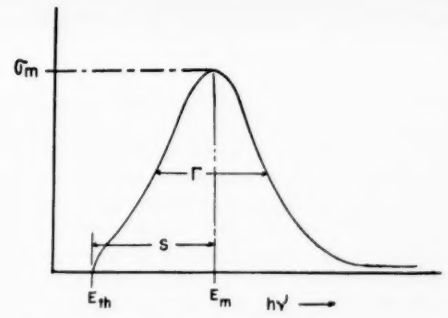

FIG. 13. Figure to illustrate the various parameters used in the discussion.

ured by us and those reported by Price and Kerst,[3] it is felt that the larger cross section is probably correct.

DISCUSSION

The neutron yields at 18 and 22 Mev have been plotted in Figs. 11 and 12, respectively, as functions of Z and are compared to the data of Price and Kerst. Our values are somewhat higher at both energies, though the difference is well within the combined experimental accuracy of both sets of data.

Very few detailed theoretical calculations of photonuclear intereactions have been attempted to date, except for the cases of light nuclei such as beryllium and deuterium. In fact, such calculations are at present not possible with any degree of assurance or accuracy. For this reason a discussion of the photoneutron systematics in the light of our measurements may be of interest to point the way to further research as well as perhaps inspire new theoretical analysis.

The various parameters which we will use to describe the photonuclear cross-section curves are illustrated in Fig. 13. The width Γ is defined by the following equation:

$$\sigma_m\Gamma=\int_0^\infty \sigma_c(\gamma)dE, \qquad (1)$$

where $\sigma_c(\gamma)$ is the cross section for photon capture by the nucleus, and σ_m is the peak cross section for photon absorption. The width Γ is not necessarily equal to the width at half-maximum because of the tail which extends to very high energies. The measurements of Terwilliger and of Jones have however shown that the area under this tail is a small fraction of the area under the giant resonance and for this reason it is expected that Γ is fairly proportional to the width at half-maximum. Terwilliger[4] points out that in the case of tantalum the integrated cross section is 4.20 Mev-barn under the resonance curve (0–27.5 Mev) and only 0.67 Mev-barn under the tail (27.5 to 65 Mev).

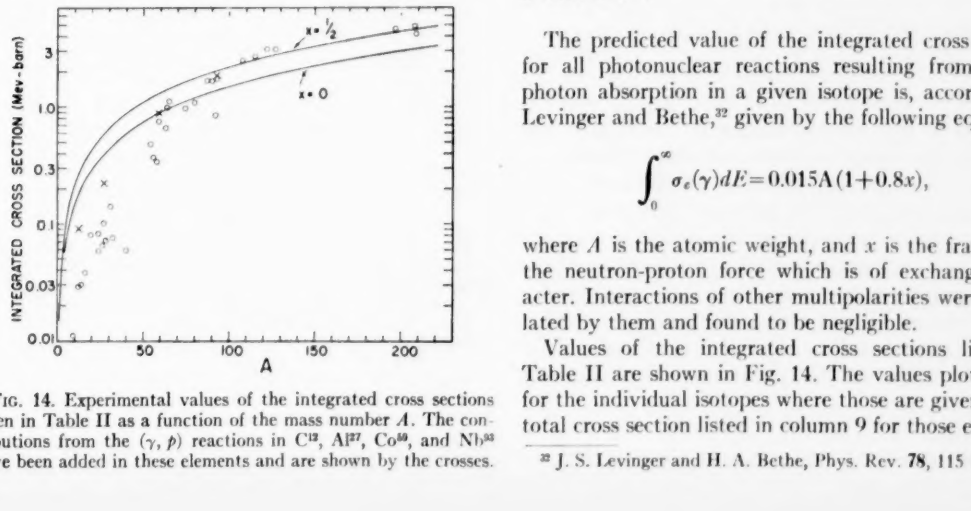

FIG. 14. Experimental values of the integrated cross sections given in Table II as a function of the mass number A. The contributions from the (γ, p) reactions in C^{12}, Al^{27}, Co^{59}, and Nb^{93} have been added in these elements and are shown by the crosses.

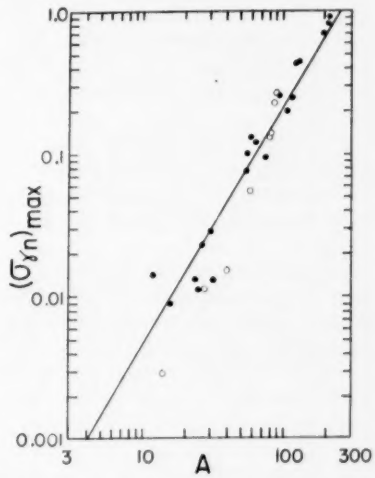

FIG. 15. Experimental values of the peak (γ, n) cross sections as a function of mass number A. The slope of the line shows that it varies as $A^{5/3}$.

The predicted value of the integrated cross section for all photonuclear reactions resulting from dipole photon absorption in a given isotope is, according to Levinger and Bethe,[32] given by the following equation;

$$\int_0^\infty \sigma_c(\gamma)dE=0.015\mathrm{A}(1+0.8x), \qquad (2)$$

where A is the atomic weight, and x is the fraction of the neutron-proton force which is of exchange character. Interactions of other multipolarities were calculated by them and found to be negligible.

Values of the integrated cross sections listed in Table II are shown in Fig. 14. The values plotted are for the individual isotopes where those are given or the total cross section listed in column 9 for those elements

[32] J. S. Levinger and H. A. Bethe, Phys. Rev. **78**, 115 (1950).

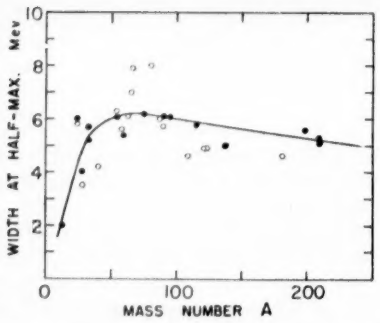

FIG. 16. The measured widths at half cross-section width for the (γ, n) reactions as a function of mass number A.

which are predominantly composed of a single isotope. Since this total cross section contains contributions amounting to twice the $(\gamma, 2n)$ reaction then these points may be overestimated by as much as 10 percent. The two curves on this diagram represent Eq. (2) with $x=0$ and $x=\frac{1}{2}$. This latter value of x is indicated by the neutron-proton scattering experiments[33] of the Berkeley group.

The experimental points fall very close to the $x=\frac{1}{2}$ line for $A\geq 100$, but drop below both lines in the lighter elements. In this region the (γ, p) reactions are expected to be important because of the low Coulomb barrier.

Some (γ, p) reactions have been measured by Halpern and Mann.[34] Taking their results for C^{12}, Al^{27}, Co^{59}, and Nb^{93} (the last 3 being 100 percent isotopes and C^{12} a 99 percent isotope) and adding them to ours we find the sums in the two lighter elements are still below the $x=0$ line, that for Co^{59} falls on this line and that for Nb^{93} approaches the integrated cross section with $x=\frac{1}{2}$. These values are indicated by crosses on Fig. 15.

A plot of the peak values of the (γ, n) cross section $(\sigma_{\gamma, n})_m$ as a function of atomic number A is shown in Fig. 15. The straight line drawn through the points shows that $(\sigma_{\gamma, n})_m$ may be represented as a function of $A^{5/3}$, where the exponent is the slope of the line.

The widths of the cross-section curve at half-maximum were plotted as a function of A and are shown in Fig. 16. Beyond $A=50$ there is a definite trend to narrower widths with increasing A. Terwilliger[4] also came to the same conclusion, though somewhat indirectly. If we assume that Γ is proportional to the width at half-maximum of the photon absorption curve and that this in turn is proportional to the width of the (γ, n) curve, at least for the heavier nuclei then Γ also is a decreasing function of atomic number, changing from a relative value of 1 at $A\simeq 50$ to 0.7 at $A\simeq 200$.

A log-log plot of E_{max} as a function of mass number is shown in Fig. 17. The straight line drawn through these points may be represented by the equation:

$$E_m = 37A^{-0.186}. \tag{3}$$

A similar equation was found by Katz and Cameron[24] to fit data obtained by residual activity. The exponent found by these authors is identical with that of the above equation. The constant preceding A was found by them to be 38.4 instead of 37. The newer results are believed to be more accurate. According to the theory of Goldhaber and Teller[35] one would expect the exponent to be 1/6; on the other hand the computations of Steinwedel, Jensen, and Jensen[36] predict an exponent of 1/3. Our results obviously favor the calculations of Goldhaber and Teller.‡

A similar log-log plot was made of the threshold energy against the mass number. This also is shown in Fig. 17. A best fit straight line drawn through these points is given by the equation:

$$E_{th} = 32A^{-0.270}. \tag{4}$$

The difference between these two equations $\bar{S}_n = E_m - E_{th}$, represents the mean distance between the peak of the photoneutron cross section and the threshold for the (γ, n) reaction. It is interesting to note that this distance is essentially constant, independent of mass number. Thus, according to the above two equations for $A=10$, we find $\bar{S}_n=7$ Mev and for $A=200$, $\bar{S}_n=6.2$ Mev.

Combining Eqs. (1) and (2) we find

$$\sigma_m E_m = 0.015A(1+0.8x)E_m/\Gamma. \tag{5}$$

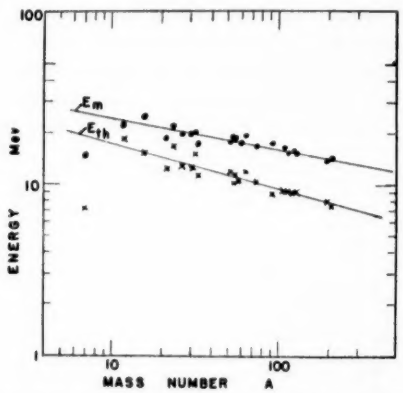

FIG. 17. Plot of E_m for the (γ, n) reaction as a function of mass number. It is well represented by the equation $E_m=37A^{-0.186}$. The lower plot is that of the (γ, n) threshold in the same isotopes for which E_m is given. This line can be represented by $E_{th}=32A^{-0.270}$. The distance between these lines is quite constant independent of A.

[33] Hadley, Kelly, Leith, Segré, Wiegand, and York, Phys. Rev. **75**, 351 (1949).
[34] J. Halpern and A. K. Mann, Phys. Rev. **83**, 370 (1951).
[35] M. Goldhaber and E. Teller, Phys. Rev. **74**, 1046 (1948).
[36] Steinwedel, Jensen, and Jensen, Phys. Rev. **79**, 1019 (1950).
‡ It is not possible to differentiate between these two exponents if only the measurements for nuclei with mass number greater than 100 are used.

Both E_m and Γ are decreasing functions of the mass number A, and the ratio E_m/Γ is quite independent of A for $A \geq 50$. Thus we conclude that

$$\sigma_m E_m \propto A \quad \text{for} \quad A \geq 50. \tag{6}$$

The variation of E_m with A, for the (γ, n) reaction only, is given by Eq. (3) and is probably the same for the photon capture cross section $\sigma_c(\gamma)$. In this case, combining (3) with Eq. (6) we find that σ_m should be expected to vary as $A^{1.186}$. In a recent paper Peaslee[37] has indicated that the peak cross section of the giant resonances should increase roughly with A throughout the periodic table.

In a few cases it was possible to determine unambiguously the $(\gamma, 2n)$ cross section from this experiment. From statistical theory[38] the ratio of $(\gamma, 2n)$ to (γ, n) is given as:

$$\frac{\sigma_{(\gamma, 2n)}}{\sigma_{(\gamma, n)}} = 1 - \left[1 + \left(\frac{a}{E}\right)^{\frac{1}{2}} (E - E_b)\right] \times \exp\left[-\left(\frac{a}{E}\right)^{\frac{1}{2}} (E - E_b)\right],$$

where a is a constant for a given A, E is the photon energy less the threshold energy for the (γ, n) reaction, and E_b is the threshold energy for the $(\gamma, 2n)$ reaction less the threshold energy for the (γ, n) reaction. The cross section has been calculated using this equation for indium and arsenic with the values of a taken from Blatt and Weisskopf[28] and are compared ot the experimental results in Table IV.

TABLE IV. Measured ratio of $\sigma_{(\gamma, 2n)}/\sigma_{(\gamma, n)}$ compared to that calculated from statistical theory.

Photon energy (Mev)	$\sigma_{(\gamma, 2n)}/\sigma_{(\gamma, n)}$ Calculated	Experimental
	Indium	
17	0.12	0.17
18	0.35	0.34
19	0.52	0.8
	Arsenic	
18	0.19	0.15
19	0.40	0.33
20	0.53	0.69
21	0.64	0.90

Considering the difficulty in separating the $(\gamma, 2n)$ cross section accurately from the total cross-section curve the agreement is very good.

In the heavy elements (beyond indium) it was not possible to determine the amount of $(\gamma, 2n)$ present. However when information becomes available on the (γ, n) cross section in heavy nuclei it will be possible to obtain the $(\gamma, 2n)$ contribution. The 100 percent isotopes, iodine, gold, and bismuth should give this contribution with the least ambiguity.

The integrated cross section for the $(\gamma, 2n)$ reaction was determined to be the order of 10 percent of the integrated cross section for the (γ, n) reaction.

The authors would like to thank Dr. A. G. W. Cameron for his assistance during the initial phases of this work and Dr. P. A. Forsyth for his help with some of the circuitry design problems.

[37] D. C. Peaslee, Phys. Rev. **88**, 812 (1952).

[38] Feld, Feshbach, Goldhaber, Goldstein, and Weisskopf, Final Report of the Fast Neutron Data Project, U. S. Atomic Energy Commission NYO-636, January 1951 (unpublished).

Neutrons from the Proton Bombardment of Be^9†

FAY AJZENBERG* AND W. W. BUECHNER
Physics Department and Laboratory for Nuclear Science, Massachusetts Institute of Technology, Cambridge 39, Massachusetts
(Received April 13, 1953)

Be^9 has been bombarded with 6.59-Mev protons. The resultant neutrons, studied by means of nuclear emulsions, indicate an excited state of B^9 at 2.37 ± 0.04 Mev. A continuum of neutrons has also been observed.

I. INTRODUCTION

THE level structure of Be^9 has been investigated by the study of a number of nuclear reactions.[1] In particular, a level at 2.429 Mev has been observed in the inelastic scattering of protons, deuterons, and alpha particles from Be^9 and in the $B^{11}(d, \alpha)Be^9$ reaction.[2] A level at approximately 1.5 Mev in Be^9 postulated by Mullin and Guth[3] has not been confirmed by other observers.[2]

It is of some interest to study the corresponding region in the mirror nucleus B^9 to determine whether a state analogous to the 2.429-Mev level can be found. If such a state were to exist, it would be another link in the overwhelming chain of evidence for the charge symmetry of nuclear forces.

A previous attempt[4] [by means of the $Be^9(p, n)B^9$ reaction] to observe an excited state of B^9 has indicated that there are no narrow levels in the excitation region studied ($E_x < 1.4$ Mev). We decided to repeat this experiment and to study B^9 for $0 < E_x < 3.8$ Mev, using higher-energy protons than were available to the previous experimenters.

II. EXPERIMENTAL PROCEDURE AND RESULTS

The experimental setup is indicated in Fig. 1. A thin foil of beryllium[5] mounted on a 0.03-in. tantalum backing was bombarded by 6.59-Mev protons from the MIT-ONR Van de Graaff generator. The resultant neutron spectrum was observed by means of 200-μ Ilford C-2 nuclear emulsions mounted 10 cm from the target and at a number of angles to the direction of the beam. In addition background plates were exposed at the same angles to protons hitting bare tantalum in the target position. The criteria for the measurements of the recoil proton tracks have been discussed previously.[6] The range-energy relation used

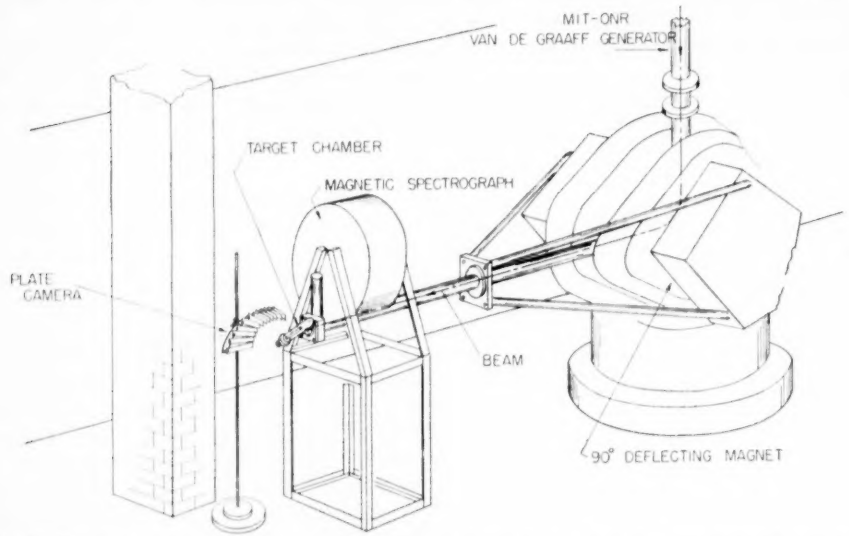

FIG. 1. Experimental setup.

† This work has been supported by the joint program of the U. S. Office of Naval Research and the U. S. Atomic Energy Commission.
* Also at Smith College, Northampton, Massachusetts.
[1] F. Ajzenberg and T. Lauritsen, Revs. Modern Phys. **24**, 321 (1952).
[2] E. H. Rhoderick, Proc. Roy. Soc. (London) **201**, 348 (1950); R. Britten, Phys. Rev. **88**, 283 (1952); Arthur, Allen, Bender, Hausman, and McDole, Phys. Rev. **88**, 1291 (1952); Cowie, Heydenburg, and Phillips, Phys. Rev. **87**, 304 (1952); Browne, Williamson, Craig, and Donahue, Phys. Rev. **83**, 179 (1951); K. Boyer, Massachusetts Institute of Technology Laboratory for Nuclear Science Progress Report (July 1950); McMinn, Sampson, and Rasmussen, Phys Rev. **84**, 963 (1951); Van Patter, Sperduto, Huang, Strait, and Buechner, Phys. Rev. **81**, 233 (1951).
[3] C. J. Mullin and E. Guth, Phys. Rev. **76**, 682 (1949).
[4] Johnson, Ajzenberg, and Laubenstein, Phys. Rev. **79**, 187 (1950).
[5] We are indebted to Dr. H. Bradner for this foil.
[6] Johnson, Laubenstein, and Richards, Phys. Rev. **77**, 413 (1950).

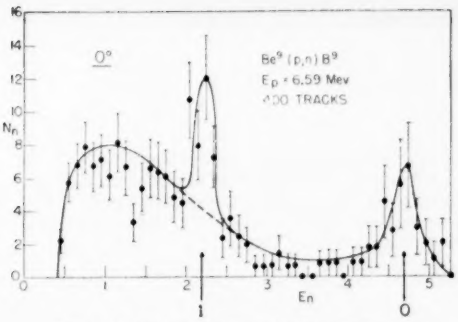

FIG. 2. 0° data. N_n is the relative number of neutrons/100-kev interval.

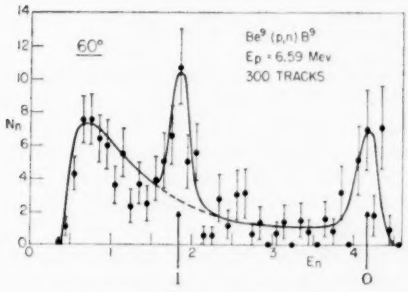

FIG. 3. 60° data. N_n is the relative number of neutrons/100-kev interval.

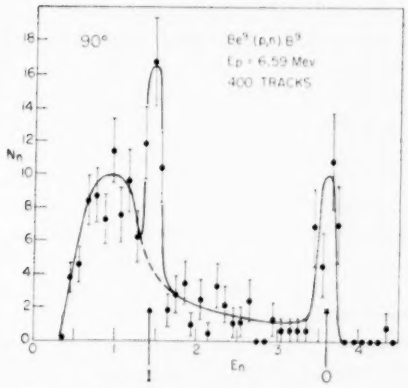

FIG. 4. 90° data. N_n is the relative number of neutrons/100-kev interval.

was that derived by Rotblat.[7] The data shown on Figs. 2–6 have been corrected for geometry[8] and for variation of the n-p scattering cross section.[9]

Only plates exposed at 0, 60, 90, and 135 degrees to the beam have been scanned, since it is felt that sufficiently convincing evidence for the existence of an excited state in B^9 has been derived from the results at these angles. The ground state of B^9 is indicated as 0 on Figs. 2–4 and the excited state as 1. The most convincing evidence for the excited state of B^9 stems from the 0, 60, and 90 degree data, although the corresponding neutron

[7] J. Rotblat, Nature **167**, 550 (1951).
[8] H. T. Richards, Phys. Rev. **59**, 796 (1941).
[9] R. K. Adair, Revs. Modern Phys. **22**, 249 (1950).

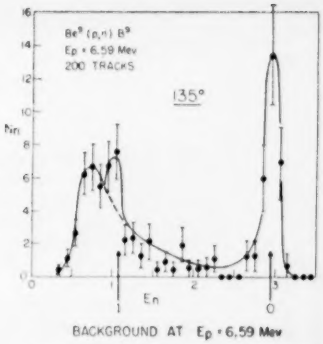

FIG. 5. 135° data. N_n is the relative number of neutrons/100-kev interval.

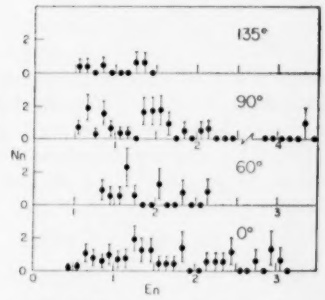

FIG. 6. Background data at 0°, 60°, 90°, and 135°. N_n is the relative number of neutrons/100-kev interval.

group appears fairly meaningfully at 135 degrees. Computing the Q of the first level of B^9 on the basis of the 0, 60, and 90 degree results, we obtain -4.22 ± 0.04 Mev, which yields an excitation energy of 2.37 ± 0.04 Mev above the ground state of B^9. The neutron energies, at which the peaks corresponding to the excited state and to the ground state should occur at each angle, were calculated on the basis of $Q=-4.22$ Mev and $Q=-1.851$ Mev,[1] respectively, and the arrows indicate these expected positions.

The background plate at a given angle has been scanned over the same relative area as the $Be^9(p, n)B^9$ plate at that angle, and the corresponding data have been plotted on the same scale.

The continuous distribution of neutrons, on which the peaks corresponding to the ground state and to the excited state are superimposed, has also been observed in Johnson, Ajzenberg, and Laubenstein's earlier experiment.[4] This continuum is perhaps due to the (p, pn) reaction.

Note added in proof: No particular effort was made to measure tracks caused by recoil protons of $E_p<0.5$ Mev. Thus the sudden cutoff at approximately 0.5 Mev at the various angles is "instrumental."

The 2.37-Mev level is probably the mirror level to the 2.429-Mev state in Be^9. There does not appear to be a state in B^9 with $E_x<2.3$ Mev which would be analogous to the state postulated by Mullin and Guth[3] at $E_x\sim1.5$ Mev in Be^9.

The authors deem it a pleasure to be able to acknowledge their indebtedness to C. M. Braams and to C. K. Bockelman for their generous assistance in the exposure of the plates and to E. W. Nickerson who built the target chamber and the plate "camera."

Energy Levels in Be^8 from the Reaction $Li^6(He^3, p)Be^8$

W. E. Kunz, C. D. Moak, and W. M. Good
Oak Ridge National Laboratory, Oak Ridge, Tennessee

(Received April 13, 1953)

The energy spectrum of protons from the breakup of B^9 following He^3 capture by Li^6 has been obtained by means of a NaI crystal spectrometer. The energy range of the spectrum which corresponds to a range of excitation in Be^8 up to 11 Mev, shows two groups of protons. Because of systematic errors known to be present, the energy determinations are preliminary. With an uncertainty of about 0.25 Mev, the energy difference between proton peaks corresponds to an energy interval in Be^8 of 2.87 Mev.

UP to an excitation energy of 17 Mev the energy levels in Be^8 have been determined principally from α-particle spectra following the breakup of C^{12} and Be^8, from neutron spectra following the capture of deuterons by Li^7, and from γ-ray spectra following proton capture by Li^7. The breakup of B^9 into Be^8 and a proton following He^3 capture by Li^6 releases 16.77 Mev. This reaction therefore provides protons as a means of studying levels in Be^8. The competing reactions in the breakup of B^9 are as follows:

$$He^3+Li^6\rightarrow B^9+\gamma+16.58 \quad \text{(a)}$$
$$Be^8+p+16.77 \quad \text{(b)}$$
$$B^8+n-1.805 \quad \text{(c)}$$
$$Be^7+H^2+0.106 \quad \text{(d)}$$
$$Be^6+H^3-\approx 5 \quad \text{(e)}$$
$$He^4+Li^5+15.06 \quad \text{(f)}$$
$$He^4+He^4+p+10.80. \quad \text{(g)}$$

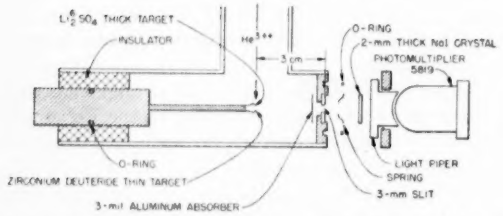

FIG. 1. Schematic diagram of target arrangement for studying the energy spectrum of the decay products accompanying Li^6+He^3.

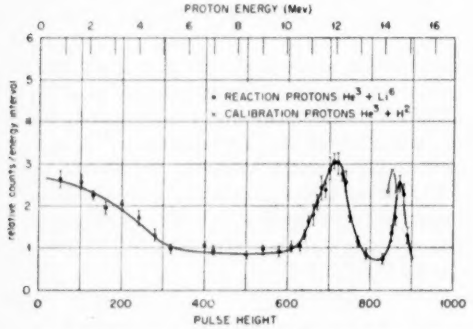

FIG. 2. Pulse spectrum in NaI of protons from the reactions $Li^6(He^3, p)Be^8$ and $Li^6(He^3, p\alpha)\alpha$.

It appears that only α particles and protons will be present at energies above 0.5 Mev. The α particles, having lower energies and being more readily stopped than protons, are easily removed by a few mils of aluminum.

The experimental arrangement is shown schematically in Fig. 1. The accelerator for producing the He^3 ion beam is a 400-kev Cockcroft-Walton. In order to suppress the conflicting $He^3(d, p)He^4$ contamination reaction, the 800-kev He^{3++} beam was used. This beam is present in amount a few parts per thousand. The proton spectrum was obtained by means of a NaI crystal and differential pulse-height selector. The manner of mounting the crystal is illustrated in Fig. 1. Because count rates were small, some rapid means of spectrometer calibration was required. This rapid calibration was achieved by interposing a deuterium target as shown, and checking the pulse height of the reaction protons.

The proton spectrum for 720-kev He^{3++} bombarding energy is shown in Fig. 2. The peak of the ground-state transition corresponds to a Q of 16.60 Mev, agreeing within the present experimental accuracy with 16.77 Mev from mass values.[1] The peak corresponding to the transition to the first excited state in Be^8 gives a Q of 13.73 Mev. The difference in positions of the two proton peaks represents 2.87 Mev energy spacing between ground and first excited states in Be^8. Systematic errors still present in the experiment make this value uncertain by not more than 0.25 Mev. The rise in the spectrum below 5 Mev observed proton energy is caused by breakup of the recoiling Li^5's from channel (f). The experiment is being refined to minimize systematic errors before applying detailed analysis to determine nuclear parameters. The data, however, show evidence for only two levels in Be^8 up to an excitation of about 11 Mev. A recent study of the $B^{10}(d, \alpha)Be^8$ α-particle[2] spectrum shows only two groups of α-particles. Thus, the only experiments indicating more than one level between ground state and 11 Mev in Be^8 are those on the $Li^7(d, n)Be^8$ neutron spectrum.

[1] F. Ajzenburg and T. Lauritsen, Revs. Modern Phys. **24**, 395 (1952).
[2] P. B. Treacy, Phil. Mag. **44**, 326 (1953).

The Production of Positive Pions by 341-Mev Protons on Protons*

W. F. CARTWRIGHT,† C. RICHMAN, M. N. WHITEHEAD, AND H. A. WILCOX‡
Radiation Laboratory, Department of Physics, University of California, Berkeley, California
(Received April 13, 1953)

The production of positive pions by protons on protons has been studied at 0°, 35°, and 58° to the beam of 341-Mev protons produced by the Berkeley synchrocyclotron. In the collision of two protons, two reactions are possible which lead to a π^+ meson: (1) $P+P\rightarrow\pi^++D$ and (2) $P+P\rightarrow\pi^++N+P$. The experimental results at 0° show an energy spectrum from 0 to 70 Mev which is fairly flat except for a large peak at the high-energy end. The flat portion of the spectrum can only be due to reaction (2). A comparison of the shape of the peak with the results of the phenomenological theory of Brueckner and Watson shows that the peak is due solely to reaction (1).

This fact, together with a measurement of the energy of the beam and of the energy of the pions from reaction (1), gives the value 275.1 ± 2.5 electron masses for the mass of the positive pion. The angular distribution in the center-of-mass system for reaction (1) as obtained from the data at the above three angles, is $(3.3\pm1.2)[0.11\pm0.06+\cos^2\theta]\times10^{-29}$ cm² sterad^{-1}, and the total cross section for reaction (1) is $(1.8\pm0.6)\times10^{-28}$ cm².

These results have been compared with the results obtained by Durbin, Loar, and Steinberger and by Clark, Roberts, and Wilson on the inverse reaction, $\pi^++D\rightarrow P+P$. Using the theorem of detailed balancing, these experiments lead to the value zero for the spin of the positive pion with good certainty.

I. INTRODUCTION

THE early investigations of the cross sections for the production of pions by 341-Mev protons, undertaken at the Berkeley 184-inch synchrocyclotron, were made by bombarding various complex nuclei.[1,2]

It is expected that the analysis of the pion production process should be much more incisive for the case of a simple nucleon-nucleon collision than for the earlier experiments. An experiment was therefore undertaken to measure the yield of positive pions produced by 341-Mev protons on hydrogen.

Since the proton beam energy is about 50 Mev above the threshold for the production of pions in this process, $P+P\rightarrow\pi^+$, the pion velocity in the center-of-mass system is comparable to the velocity of the center of mass relative to the laboratory system. Consequently, the pions are emitted primarily in the forward direction in the laboratory; that is, in the direction of the proton beam. It was found possible, by using a magnetic field, to separate the pions produced in the forward direction from the proton beam, and an investigation was made of the energy spectrum of the pions produced at zero degrees.

The initial experiments[3] showed an energy spectrum that was fairly flat except for a large peak at the high-energy end. There are two possible reactions in which the pions may be produced, namely:

$$P+P\rightarrow\pi^++D \quad (1)$$

$$P+P\rightarrow\pi^++N+P. \quad (2)$$

It was suggested[4] that the first reaction is primarily responsible for the peak at the end of the spectrum. A careful measurement was then made of the shape of the spectrum near the maximum energy in order to determine whether this was the case.

Later measurements were also made of the yield of pions at 35° and 58° to the proton beam in order to determine the angular distribution of the pions in the center-of-mass system.

It was pointed out by Johnson,[5] and independently by Marshak and Cheston,[6] that the principle of detailed balance can be applied to reaction (1) and its inverse to obtain the spin of the positive pion. A knowledge of the angular distribution of (1) makes possible the detailed comparison of this experiment with the experiments on the inverse reaction.

II. GENERAL METHOD

For this experiment the electrically deflected 341-Mev proton beam of the Berkeley synchrocyclotron was used. The method of deflection and collimation of the beam has been described previously.[7]

The method used for studying the production from hydrogen is an extension of that developed for meas-

* Preliminary results of this experiment were given in Phys. Rev. **78**, 823 (1950); **79**, 85 (1950); **82**, 460 (1951); and **83**, 855 (1951).

† Now at the University of Rochester, Rochester, New York.

‡ Now at the Naval Ordnance Test Station, China Lake, California.

[1] C. Richman and H. A. Wilcox, Phys. Rev. **78**, 496 (1950).

[2] M. Weissbluth, Ph.D. thesis, University of California, 1950 (unpublished).

[3] Cartwright, Richman, Whitehead, and Wilcox, Phys. Rev. **78**, 823 (1950).

[4] K. A. Brueckner, Phys. Rev. **82**, 598 (1951). (In particular see appendix by Brueckner, Chew, and Hart.)

[5] M. H. Johnson (private communication to R. E. Marshak).

[6] R. E. Marshak, Rochester High Energy Conference, December, 1951 (unpublished); W. B. Cheston, Phys. Rev. **83**, 1118 (1951).

[7] See, e.g., Powell, Henrich, Kerns, Sewell, and Thornton, Rev. Sci. Instr. **19**, 506 (1948) for a description of the deflecting mechanism and Cladis, Hess, and Moyer, Phys. Rev. **87**, 425 (1952) for a description of the collimating system.

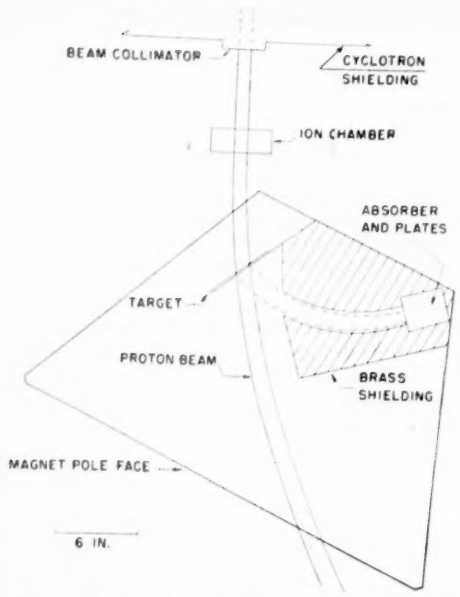

FIG. 1. Schematic diagram of the experimental set-up.

uring the cross section for the production of mesons by protons on heavy nuclei at 90° to the proton beam.[8] It has been modified by the use of a channel and magnetic field to decrease the background of scattered protons which caused difficulty in those experiments.

Figure 1 shows a schematic diagram of the experimental setup. The collimated proton beam passes through an ionization chamber and then strikes either a graphite or polyethylene target which is placed between the pole faces of the magnet.

The pions bend away from the proton beam, and those in the energy interval and angular interval of interest pass through the wide channel cut in the brass shielding and enter the absorber-detector. They are slowed down by ionization in the absorber and the population of stopped pions is sampled by a nuclear emulsion embedded in the absorber. The developed plate is scanned and the positive pions identified by the nature of the pion track and by the characteristic μ-decay track at the end of the range.

The success of this method depends on the fact that a pion with the same momentum as a proton has, as a consequence of the large mass difference, a range approximately one hundred times that of the proton. The protons coming down the channel are therefore stopped in the first part of the absorber and are eliminated as a source of background in the scanned region of the emulsion.

The brass shielding which forms the channel serves only to protect the detector from high-energy protons scattered from the target and to limit the angular spread at the target of the pions detected.

[8] Richman, Weissbluth, and Wilcox, Phys. Rev. **85**, 161 (1952).

One can calculate the number of pions per square centimeter per Mev hitting the face of the absorber from the density of stopped pions in the emulsion. If the solid angle subtended at the target by a unit area at the absorber is known, the cross section can then be calculated in the usual manner.

The calibrated ion chamber placed before the target gives the total number of protons passing through it, making possible the calculation of absolute production cross sections.

Since this arrangement accepts pions produced with a small spread of angles and in a small energy interval, several runs are made to cover the entire energy spectrum at each particular angle.

III. ABSORBER AND DETECTOR

The position of the nuclear plate in the absorber and the type of absorber used are shown in Fig. 2. As can be seen in the figure, the position of a pion's decay in the plate is a measure of the pion's range in the absorber, and therefore of its initial energy upon entering the absorber.

The cross-sectional dimensions of the absorber were made large compared to the mean lateral displacement of the pions due to the multiple Coulomb scattering suffered by them while slowing down. If the pions from the target strike all parts of the absorber face, a condition of "poor geometry" obtains, and it may be assumed that as many pions scatter into that part of the beam which stops in the emulsion as scatter out of it.

The root-mean-square lateral displacement calculated for 70-Mev pions was approximately 8 mm. The width and height of the absorbers were always much larger than this.

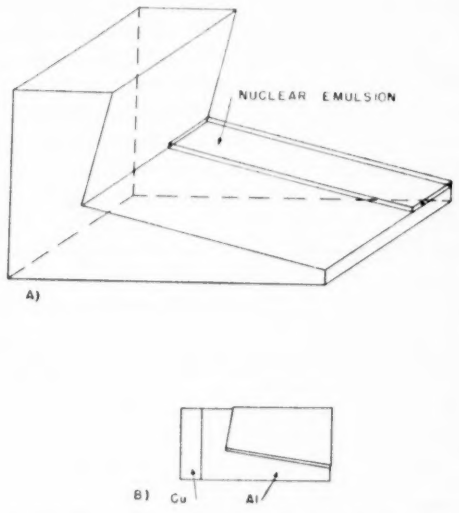

FIG. 2. (A) The position of nuclear emulsion in the absorber. (B) The composite absorber used to obtain the zero degree data.

The number of stopped pions was found by scanning the developed plates under the microscope using a 90× oil immersion objective and 6× eyepieces. The microscopes were equipped with a special stage which was designed and built by Mr. W. M. Brower of the Physics Department machine shop. This stage enables the observer to reset the microscope to an accuracy of about 2 microns and enables him to determine with good accuracy the area which has been scanned. The photographic plates used were Ilford Nuclear Research plates, type C-2 and type C-3, with an emulsion thickness of 200 microns.

An event was counted as a π-μ decay only if either the π or the μ track could be definitely identified as a meson by the usual tests of scattering or of rapid grain density variation. It is estimated that with this procedure the error in the number of pions observed is less than 5 percent.

For the high-energy pions near the peak in the 0° pion spectrum, a copper slab was placed in front of the aluminum absorber holding the emulsion. This is shown in Fig. 2(B). With this arrangement, the pions rapidly lost most of their energy by traveling a short distance in the copper, and the energy spectrum was then spread out along the nuclear plate because of the low stopping power of the aluminum. The range-energy curves of Aron, Hoffman, and Williams,[9] as corrected by the recent work of Mather and Segré,[10] were used to convert the pion range to energy. These latest corrected curves are accurate to about 0.5 percent in energy.

The absorber face was cut so that the pions entered normally. Thus, the variation in depth of penetration with angle of incidence is very small. For the zero degree measurements, with a one-inch diameter target, and with the maximum channel width used, this angle varied between $+3°$ and, $-3°$, depending on the energy of the meson and on its points of origin and decay. This produced an uncertainty in depth of penetration of less than 0.2 percent.

In order to find the density of stopped pions, it is necessary to know the thickness of the emulsion before development. It was possible to calculate this value from the thickness of the processed emulsion by determining the shrinkage factor using either the alpha-particle calibration method of Wilcox,[8] or the similar method of Barkas[11] using x-rays.

IV. CHANNEL

The principal purposes of the channel are to shield the detector from other particles and to insure that the pions enter the detector normally. The energy of the pions is determined by their depth of penetration into the absorber-detector. The minimum width of the channel exit is fixed by the requirement of poor geometry discussed above. The rest of the channel is then designed to allow pions in the desired energy range to reach all points of the absorber face from each part of the target.

For the 0° production experiment the channel accepted a 20-Mev energy interval around the peak. At the other angles it was necessary to use several values of the magnetic field with the same channel in order to cover a comparable energy interval. In these cases the the energy intervals in the different runs were made to overlap.

V. TARGETS

The high cross section of hydrogen in the neighborhood of the peak, relative to that of carbon, made the use of a subtraction method practical. By measuring the pion yield from both polyethylene, $(CH_2)_n$, and carbon, the hydrogen cross section may be calculated with good accuracy.

In the region of the high-energy peak, targets of one-quarter inch thickness were used to obtain good energy resolution. For the slowly varying continuum from hydrogen, and for the carbon data at 0°, one-half inch targets were used to keep the cyclotron bombardment time within reasonable limits. The effective area of the target was that of the proton beam, which was collimated to a one-inch diameter circular area by a 40-inch tube in the cyclotron shielding. The target densities were calculated from the measured weights and volumes.

VI. MAGNETIC FIELD

The magnetic field used to separate the pions from the proton beam was produced by a magnet whose maximum field was about 14 000 gauss over an area sufficiently large to turn a 70-Mev pion trajectory through about 90 degrees. The gap between the pole faces was 3.5 inches. The proton nuclear induction resonance method was used to measure the field to an accuracy of better than one percent. The variation of the field, in time, during any particular run, never exceeded one percent.

VII. BEAM INTEGRATION

The ions produced by the proton beam in the ion chamber were collected on a condenser and the total charge measured by a standard electronic integrating circuit. The ion chamber had previously been calibrated by comparison with the total charge obtained by stopping the proton beam in a Faraday cup. The average beam current was around 10^{-10} ampere. The over-all accuracy of the charge measurement is estimated to be better than ± 5 percent.

VIII. GEOMETRY

From the density of the pions in the emulsion one can obtain the flux of pions of a given energy in the absorber. In order to calculate the differential produc-

[9] Aron, Hoffman, and Williams, U. S. Atomic Energy Commission Report AECU-663 (unpublished).
[10] R. Mather and E. Segré, Phys. Rev. **84**, 191 (1951).
[11] W. H. Barkas (unpublished).

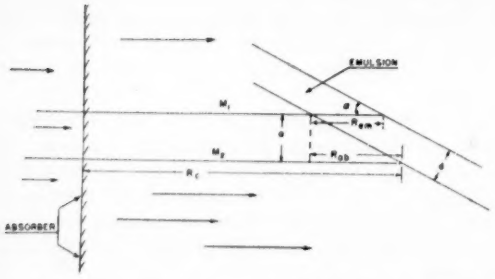

FIG. 3. Diagram used to calculate the flux of pions from the density of stopped pions in the emulsion. (See Section IX.)

tion cross section, it is necessary to know the solid angle subtended at a point in the target by a unit area in the absorber.

If the trajectories lie in a plane perpendicular to the uniform magnetic field, the solid angle subtended by a unit area perpendicular to the trajectories is[12]

$$d\Omega/dA = 1/(\rho^2\phi \sin\phi), \tag{3}$$

where ρ is the radius of curvature of the pion trajectory, and ϕ is the angle through which it turns from the target to the absorber. This formula applies, within 2 percent, even though the field departs from uniformity near the pole boundaries, where ρ remains the radius of curvature in the uniform portion of the field.

A small error is introduced by the use of this formula for pions whose trajectories have a small component along the direction of the magnetic field. For the dimensions used in this experiment, this error was less than 0.1 percent, so no corrections have been made. Also, the finite size of the target and absorber cause some variation in the solid angle ($\sim$7 percent) for pions of different points of origin and termination. The value of $d\Omega/dA$ which was used in the calculations was for a trajectory from the center of the target to the center of the absorber.

IX. CALCULATION OF THE CROSS SECTION

The number of pions in a given energy interval that entered the absorber can be deduced from the number of pions stopped in the emulsion by the following argument. We will make the simplifying approximation that the pions travel in straight lines.

Consider pions of a given energy, E, which enter the absorber normally to and over the entire area of the face of the absorber. Let these pions have a range R_0 in the absorber. Those pions whose trajectories lie between two lines, M_1 and M_2, as shown in Fig. 3, will stop in the emulsion, while pions whose trajectories lie outside of these lines will stop only in the aluminum absorber. It is easy to see that the height, a, between the two trajectories is $d(\sec\alpha)R_{ab}/R_{em}$, where d is the thickness of the emulsion, α is the angle of inclination of the plate as shown in the figure, and R_{em} and R_{ab} are the residual ranges of a meson of residual energy, E_{res}, in emulsion and absorber, respectively. For $\alpha=15°$ and $d=200\mu$, $E_{res}=5.7$ Mev and $R_{ab}/R_{em}=1.20$.

Let the number of pions entering the absorber per unit area in an energy interval ΔE be $N(E)\Delta E$. If then we scan a strip of emulsion of length l, perpendicular to the plane of Fig. 3, the number of pions that have stopped in the emulsion will be $N(E)\Delta E\cdot a\cdot l$.

The spread in pion energies, ΔE, in the beam, corresponding to a distance ΔZ along the plate (in the plane of Fig. 3) is given by: $\Delta E=\Delta Z(\cos\alpha)(-dE/dx)_{ab}$, where $(-dE/dx)_{ab}$ is the rate of energy loss per cm in the absorber at the initial energy of the pions. Thus, the number of mesons that stop in the area $\Delta Z\cdot l$ on the plate is given by $n=N(E)(-dE/dx)_{ab}(\cos\alpha)\cdot a\cdot l\cdot\Delta Z$. If d denotes the thickness of the emulsion and q represents the number of stopped pions found per unit volume of the emulsion, we obtain:

$$N(E)=\frac{n}{(-dE/dx)_{ab}(R_{ab}/R_{em})l\cdot d\cdot\Delta Z} \tag{4}$$

$$=\frac{q}{(-dE/dx)_{ab}R_{ab}/R_{em}}. \tag{5}$$

The number of pions of energy E per Mev per cm^2 in the beam is given by:

$$N(E)=\frac{d\sigma}{dEd\Omega}N_p\frac{tD}{A}A_0\frac{d\Omega}{dA}, \tag{6}$$

where N_p is the total number of protons that have passed through the target, D is the density of the target material, A_0 is Avogadro's number, A is the molecular weight of carbon (or CH_2), t is the target thickness, $d\sigma/(dEd\Omega)$ is the differential cross section for production of mesons by protons on a carbon nucleus (or a CH_2 molecule) per unit solid angle per Mev, and $d\Omega/dA$ is the solid angle per unit area in the emulsion.

Using Eqs. (5) and (6), the differential cross section is therefore found to be as follows:

$$\frac{d\sigma}{dEd\Omega}=\frac{q}{(-dE/dx)_{ab}(R_{ab}/R_{em})N_pDt(A_0/A)(d\Omega/dA)}\times\text{cm}^2\ \text{Mev}^{-1}\ \text{sterad}^{-1}. \tag{7}$$

Three corrections have to be made to Eq. (7). (a) Some of the pions decay in flight before reaching the emulsion. The mean life of the π^+ meson has been found to be $2.65\pm0.12\times10^{-8}$ sec.[13] If the meson moves a distance, dr, in the laboratory with a momentum p_π, the proper time interval that has elapsed is:

$$d\tau=M_\pi dr/(p_\pi c^2),$$

[12] For details, see W. F. Cartwright, University of California Radiation Laboratory Report UCRL-1278 (unpublished).

[13] Chamberlain, Mozley, Steinberger, and Wiegand, Phys. Rev. **79**, 394 (1950).

where M_π is the rest energy of the meson, and c is the velocity of light.

In computing the correction to Eq. (7) due to decay in flight, we neglect energy loss in air, and use, for the absorber, the empirical range energy relation:[14]

$$T_\pi = KR^n, \tag{8}$$

where $n=0.58$, K is a constant of the absorber material, T_π is the meson's kinetic energy, and R is its range. It can then be shown that the cross section as calculated from Eq. (7) should be multiplied by the factor

$$\exp\{0.63\times10^{-3}[x+x^2]^{-\frac{1}{2}}\rho\phi+0.89\times10^{-3}x^{-\frac{1}{2}}R\}, \tag{9}$$

where $x=T_\pi/(2M_\pi)$. This formula is easily extended to the case of a composite absorber.

(b) The pions emerging from the target in a given energy interval, ΔE, are produced at different depths of the target in different energy intervals, $\Delta E'$. When this is averaged over the target, one finds that $(\Delta E/\Delta E')=(-dE/dx)_2\cdot t/(E_1-E_2)$, where $(-dE/dx)_2$ is the specific ionization at the exit side of the target, E_1-E_2 is the energy loss in the target of a pion created at the front face, and t is the target thickness. The pion spectra are plotted as originating from the center of the target and the yields are increased by this factor.

(c) The observed number of pions is decreased from the actual number entering the absorber by large angle nuclear scattering and absorption in the copper and aluminum. A precise measurement of the cross sections for these processes as a function of pion energy is not available, but recent experiments[15] indicate that for the energies involved in our experiment the attenuation cross section is less than nuclear area. We have corrected our data using a total attenuation cross section of 0.8 nuclear area independent of the energy of the pion.

[14] See, e.g., Bradner, Smith, Barkas, and Bishop, Phys. Rev. **77**, 462 (1950).

[15] D. Stork, Bull. Am. Phys. Soc. **27**, No. 6, 16 (1952).

TABLE I. Results at 0°.

Target	Pion energy, Mev	$d\sigma/dEd\Omega\times10^{30}$ (uncorrected), cm² Mev⁻¹ sterad⁻¹	Correction factors: Decay in flight	Thick target	Attenuation in absorber	$d\sigma/dEd\Omega\times10^{30}$ (corrected), cm² Mev⁻¹ sterad⁻¹	Statistical probable error $\times10^{30}$, cm² Mev⁻¹ sterad⁻¹
CH_2	17.5	3.0	1.13	1.11	1.02	3.8	±0.6
Carbon	17.5	1.9	1.13	1.12	1.02	2.5	±0.3
CH_2	34.0	5.3	1.09	1.11	1.05	6.7	±0.7
Carbon	34.0	3.3	1.09	1.12	1.05	4.3	±0.4
CH_2	60.9	13.3	1.08	1.01	1.14	16.5	±0.9
CH_2	63.8	11.8	1.08	1.01	1.16	14.9	±1.4
CH_2	65.7	13.8	1.08	1.01	1.16	17.5	±1.9
CH_2	67.2	22.8	1.08	1.01	1.17	29.1	±2.0
CH_2	68.8	45.4	1.08	1.01	1.18	58.5	±2.4
Carbon	70.0	9.2	1.07	1.02	1.18	11.8	±1.3
CH_2	70.7	50.5	1.07	1.01	1.18	64.4	±2.6
CH_2	72.3	18.7	1.07	1.01	1.19	24.0	±2.1
CH_2	73.7	11.2	1.07	1.01	1.20	14.5	±1.8
CH_2	75.6	10.9	1.07	1.01	1.22	14.4	±1.9

TABLE II. Results at 35°. The correction factor for decay in flight is 1.07. The correction for the thickness of the target is negligible here.

Target	Pion energy, Mev	$d\sigma/dEd\Omega\times10^{30}$ (uncorrected), cm² Mev⁻¹ sterad⁻¹	Attenuation in absorber	$d\sigma/dEd\Omega\times10^{30}$ (corrected) cm² Mev⁻¹ sterad⁻¹	Statistical probable error, cm² Mev⁻¹ sterad⁻¹
CH_2	40.2	7.70	1.08	9.0	±0.62
	42.8	9.97	1.09	11.7	±0.83
	43.8	16.6	1.09	19.7	±1.3
	44.6	19.4	1.09	23.1	±1.6
	45.3	22.8	1.09	27.3	±1.9
	46.0	25.8	1.10	31.2	±2.0
	46.9	26.6	1.10	32.2	±2.1
	47.7	21.3	1.10	25.8	±1.6
	48.3	16.0	1.10	19.4	±1.4
	49.7	8.52	1.10	10.3	±0.94
	50.5	5.31	1.11	6.5	±0.54
C	44.0	5.49	1.08	6.46	±0.45

X. EXPERIMENTAL RESULTS

Tables I, II, and III give the cross sections obtained from CH_2 and C at 0°±3°, 35°±3°, and 58°±3° in the laboratory. The energies given are the production energies of the pions as deduced from the thicknesses of the target, air and absorber traversed. The experimental cross sections, the corrections discussed above, and the final corrected values are listed. The errors shown are the statistical probable errors calculated from the number of pions counted at each energy. The hydrogen spectra are obtained by subtracting the carbon from the CH_2 cross section and dividing by two. Figures 4, 5, and 6 give the resultant spectra at the three angles.

As will be seen in the tables, the CH_2 peaks were examined in detail, but only one point in this energy region was measured for carbon. This is justified since the CH_2 spectrum is so intensely peaked that the exact details of the slowly changing carbon spectrum need not be known in order to get a good subtraction. At zero degrees, where the peak is analyzed in detail, there is good evidence[16] that the carbon spectrum is fairly flat from 60 to 75 Mev.

TABLE III. Results at 58°. The correction factors for decay in flight and for attenuation in the absorber are 1.06 and 1.04, respectively.

Target	Pion energy, Mev	$d\sigma/dEd\Omega\times10^{30}$ (uncorrected), cm² Mev⁻¹ sterad⁻¹	Thick target correction factor	$d\sigma/dEd\Omega\times10^{30}$ (corrected), cm² Mev⁻¹ sterad⁻¹	Probable error $\times10^{30}$, cm² Mev⁻¹ sterad⁻¹
CH_2	20.0	3.03	1.11	3.8	±0.4
	21.0	3.16	1.09	3.8	±0.4
	22.5	3.98	1.08	4.7	±0.4
	24.5	6.81	1.07	8.0	±1.0
	25.0	6.19	1.07	7.3	±0.7
	27.0	4.30	1.07	5.1	±0.7
	28.5	2.70	1.06	3.2	±0.6
C	26.0	3.21	1.08	3.8	±0.3

[16] W. Dudziak (to be published).

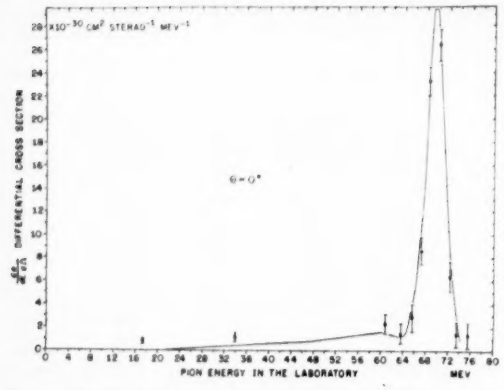

FIG. 4. Differential cross section, as a function of pion energy, for pion production from hydrogen at zero degrees. The solid curve results from folding the experimental resolution into the theoretical spectrum for the final nucleons in a ^3S-state and the pion in a P-state with a $\cos^2\theta$ angular distribution in the c.m. system. (See Section XI.)

The analysis of the zero degree spectrum shows that the peak, from 65.5 to 76 Mev, is a result of deuteron formation. (See Sec. XI.) At the other angles it is assumed that the peaks are also the result of deuteron formation. The pion energy at which the peak occurs is a function of the laboratory angle. (See Appendix I for a discussion of the dynamics of the reaction.) At both 58 and 35 degrees the peaks do not fall at the calculated energy. This fact is not surprising, as the energy is a sensitive function of both the pion mass and the beam energy. The change in maximum pion energy, per Mev change in initial proton energy, varies from 0.9 Mev at zero degrees to 0.6 Mev at 58 degrees. The variation in maximum energy for a change in the pion mass of one electron mass is the same as for one-Mev change in the proton energy. As the pion mass is uncertain by two electron masses, and the external proton beam is known to vary in energy by as much as 3 Mev, the energy of the peaks cannot be predicted exactly unless special precautions are taken as was done at zero degrees.

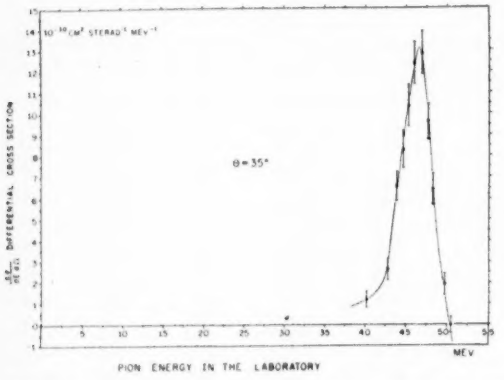

FIG. 5. The differential cross section in the region of the peak for pion production from hydrogen at 35° as a function of the energy.

In order to obtain the cross section per unit solid angle for the formation of pions in the deuteron reaction each experimental spectrum is integrated over the energy interval of the peak. The absolute cross section is assigned a twenty percent error at zero and 35 degrees and 25 percent at the 58-degree point. Table IV shows the cross sections obtained at the different angles in the laboratory and the values after transforming to the center-of-mass system.

Figure 7 shows the cross sections per unit solid angle, $d\sigma/d\Omega$, for $P+P\rightarrow\pi^+ + D$, plotted as a function of the angle of the pion in the center-of-mass system. It is obvious that the cross section varies with angle. The simplest assumption as to the form of the angular distribution is,

$$d\sigma/d\Omega = B(A+\cos^2\theta) \text{ cm}^2 \text{ sterad}^{-1}.$$

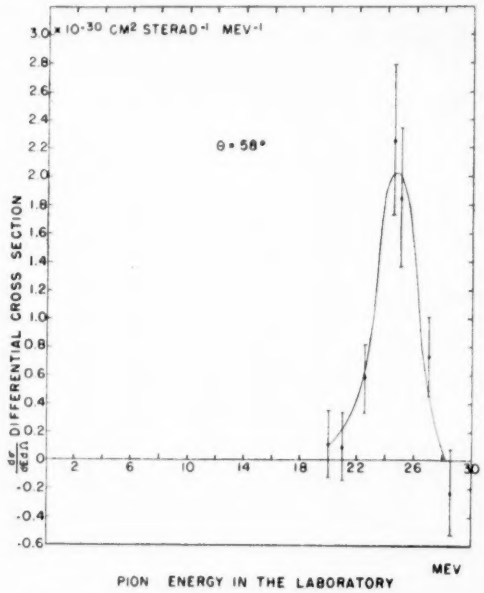

FIG. 6. The differential cross section in the region of the peak for pion production from hydrogen at 58°.

Since the initial particles in the reaction are identical, the distribution must be symmetrical about 90 degrees; therefore, no term in odd powers of the cosine can appear. The constants A and B have been determined by the method of least squares from the data given in Table IV, giving the following result:

$$d\sigma/d\Omega = (3.3\pm1.2)[0.11\pm0.06+\cos^2\theta] \times 10^{-29} \text{ cm}^2 \text{ sterad}^{-1}. \quad (10)$$

The total cross section for $P+P\rightarrow\pi^+ + D$, obtained by integrating Eq. (10), is:

$$\sigma = 1.8\pm0.6\times10^{-28} \text{ cm}^2.$$

The errors given are based on the external consistency between the experimental values and the values calculated from (10). Figure 8 shows the calculated curve and the experimental points as a function of angle in the laboratory system; for comparison a curve for a spherically symmetric distribution in the center-of-mass system is also shown.

An independent measurement at 18 degrees in the laboratory using a liquid hydrogen target has been made by Peterson, Iloff, and Sherman.[17] Their value is also shown in Fig. 8 and is in good agreement with the calculated curve.

The pion energy is also a strong function of the laboratory angle, varying by 0.8 Mev per degree at 58 degrees. The largest possible error in the angle measurement is that at 58 degrees, where it may be as large as three degrees. However, a change in the angle of three degrees changes the constant factor in the angular distribution by only three percent, which is small compared to the uncertainties from other sources of error.

The total cross section at zero degrees, including the contribution from the continuum, is $(1.9\pm0.4)\times10^{-28}$ cm^2 sterad^{-1}.

TABLE IV. Summary of the measured cross sections for the reaction $P+P\rightarrow\pi^++D$.

θ_{lab}	$(d\sigma/d\Omega)_{lab}\times10^{28}$, cm^2 sterad^{-1}	$\theta_{c.m.}$	$(d\sigma/d\Omega)_{c.m.}\times10^{28}$, cm^2 sterad^{-1}
0°	1.2 ±0.25	0°	3.1 ±0.7
35°	0.50±0.10	65°	1.8 ±0.4
58°	0.08±0.02	104°	0.47±0.12

The maximum energy of pions produced in $P-P$ collisions depends on the proton beam energy, the direction of emission of the pions, and on the masses of proton, pion, and product nucleons. (See Appendix I.) In Sec. XI it is shown that the peak in the spectrum is due to deuteron formation and occurs at the maximum pion energy. Thus, knowing proton and deuteron masses, it requires only a measurement of the energy of the pions in the peak, for a given proton beam energy and angle of production of the meson, in order to measure the pion mass.

The data at zero degrees was used to determine the pion mass. At zero degrees, the maximum pion energy is quite insensitive to a small variation in production angle. (See Fig. 10.) The proton beam energy was measured during the zero-degree experiment by Dr. Robert Mather using the Čerenkov radiation of the beam. The energy of the pions in the peak was inferred from their range, taking into account the apparent pion energy spread introduced by the finite resolution of the apparatus. Further details can be found in reference 12.

The positive pion mass determined by this method is 275.1±2.5 electron masses.

[17] Peterson, Iloff, and Sherman, Phys. Rev. **81**, 647 (1951).

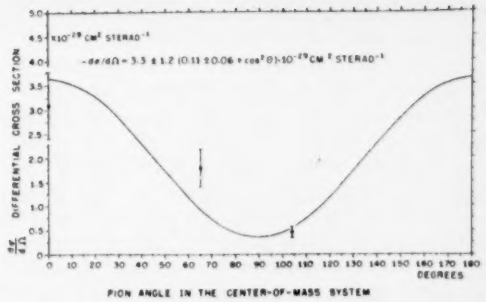

FIG. 7. Angular distribution in the center-of-mass system of the pions in the peak. The solid curve is a least squares fit of the data.

XI. DISCUSSION OF THE EXPERIMENTAL RESULTS AT ZERO DEGREES

It has already been pointed out that two reactions are possible in this experiment: (1) $P+P\rightarrow\pi^++D$ and (2) $P+P\rightarrow\pi^++N+P$.

If only reaction (2) occurs, the pion energy spectrum at any angle will consist of a continuum from zero up to some maximum energy determined by the proton beam energy and the masses of proton, neutron, and pion.

The possibility that the proton and neutron come off as a deuteron was suggested in 1948 by Morand, Cüer, and Maucharafyeh,[18] and in 1949 by Barkas.[19] If a deuteron is formed, the pion spectrum at any angle consists only of a line spectrum at any energy which is, because of the binding energy of the deuteron, a few Mev higher than the maximum energy pion produced by reaction (2).

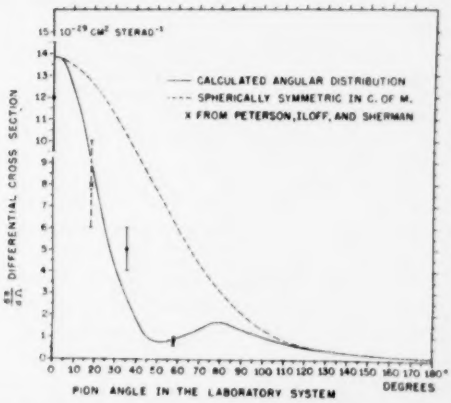
CALCULATED ANGULAR DISTRIBUTION
SPHERICALLY SYMMETRIC IN C. OF M.
X FROM PETERSON, ILOFF, AND SHERMAN
DIFFERENTIAL CROSS SECTION
PION ANGLE IN THE LABORATORY SYSTEM
DEGREES

FIG. 8. Angular distribution of the pions in the peak *vs* laboratory angle. The solid curve comes from a least squares fit of the data in the c.m. system. The dashed curve is the result of transforming to the laboratory a uniform angular distribution in the c.m. system.

[18] Morand, Cüer, and Maucharafyeh, Compt. rend. **226**, 1974 (1948).

[19] W. Barkas, Phys. Rev. **75**, 1109 (1949).

Consider first the pions produced at zero degrees. The energy interval between the upper limit of the continuous spectrum (2) and the line spectrum (1) is then 4 Mev in the laboratory system. If the pion mass were known with great accuracy and if the resolution of the apparatus were sufficiently high, one could tell from the observed maximum pion energy whether or not deuteron formation ever occurred. This approach is very difficult. If, however, the *shape* of the experimental spectrum at zero degrees is compared with some theoretical curves given by Watson and Brueckner,[20] information about the extent to which both reactions occur can be obtained.

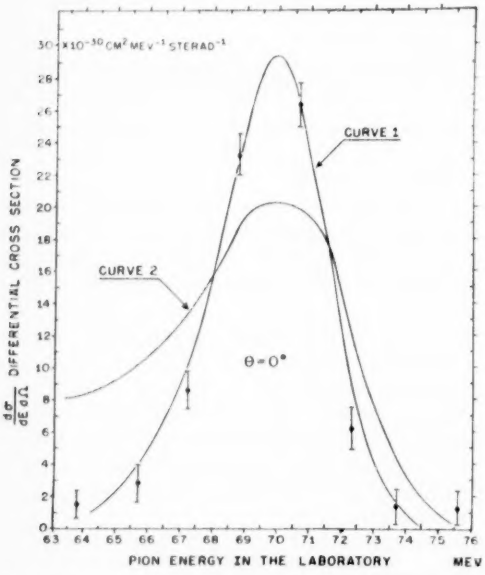

FIG. 9. Experimental points and theoretical curves for the differential cross section for pion production from hydrogen at 0° in the neighborhood of the peak. Curve 1: the nucleons are left in the ^3S-state and the pions are produced in a P-state with a $\cos^2\theta$ distribution in the c.m. system. Curve 2: the nucleons are left in the ^1S-state and the pions are produced in a P-state with a $\cos^2\theta$ distribution in the c.m. system.

It was pointed out by Brueckner, Chew, and Hart that the production of pions in nucleon-nucleon collisions is strongly dependent on the wave state of the product nucleons. This idea was developed by Brueckner and Watson in their phenomenological description of the process. They give pion energy spectra at various angles for the different possibilities of wave states for pion and product nucleons.

The outstanding feature in the experimental spectrum of pions produced at zero degrees by protons on protons is the intense peak near maximum meson energy. The shape of the spectrum near the peak is primarily determined, in the theory, by the wave functions of the nucleons in the final state. It might be expected that for those pions produced with energies near the maximum, the product-nucleons would be in an S-state, since their relative velocity is small. And indeed, the experimental results do not fit any of the theoretical spectra of Brueckner and Watson based on the assumption that the final nucleons are in a P-state.

According to the theory, a strong peak will occur if the nucleons come off in either a triplet S-state or in a singlet S-state. If the product nucleons come off in a ^3S-state, there is a large probability that pion production will be accompanied by deuteron formation. The resulting line spectrum will be intense compared to the continuum, thus giving rise to the peak. If, however, the nucleons are left in the ^1S-state, a strong peak will still arise because of the resonance resulting from the low energy virtual state of the deuteron.

It should be pointed out that deuterons have been detected in coincidence with pions of approximately maximum energy by Crawford, Crowe, and Stevenson.[21]

It can be concluded from the results at zero degrees that the peak in the spectrum is due solely to deuteron formation. This follows from a comparison of the experimental points with the curves derived by folding the resolution of the apparatus (see Appendix II) into the theoretical spectra.

Curve 2, Fig. 9, shows the result of folding the resolution into that theoretical spectrum in which the nucleons are left in the ^1S-state and the pions are produced in a P-state with a $\cos^2\theta$ distribution in the center-of-mass system. As mentioned above, the shape of the spectrum at the peak is primarily determined just by the final state of the nucleons. This choice for the pion wave state, however, gives the best fit of the theoretical spectra based on the ^1S-state to the experimental points in the peak.

Curve 1, of Fig. 9, shows the result of folding the resolution into that spectrum in which the nucleons are left in the ^3S-state, and the pions are again produced in a P-state with a $\cos^2\theta$ distribution. Since the main feature of this spectrum is a line displaced upward by 4 Mev from the continuum, this curve is essentially a plot of the estimated resolution. The resolving power is sufficiently high, as shown in Appendix II, that the apparatus does not appreciably mix the continuum and the line spectrum. The selection of the particular angular momentum and angular distribution of the pions is even *less* critical here than in the ^1S-case, since the intense deuteron peak is the essential feature of all the ^3S-spectra.

Figure 9 also shows the experimental points at zero degrees. Both theoretical curves are normalized so that in each the area from 65.5 to 76.0 Mev agrees with the area under the experimental points in the same energy interval. The close fit of Curve I with the experimental results is strong evidence that the peak corresponds to

[20] K. M. Watson and K. A. Brueckner, Phys. Rev. **83**, 1 (1951). See also K. M. Watson, Phys. Rev. **88**, 1163 (1952).

[21] Crawford, Crowe, and Stevenson, Phys. Rev. **82**, 97 (1951).

deuteron formation. It is clear that the experimental points, on the other hand, are not in agreement with either the half-width or the asymmetric character of Curve II for the ^1S-case.

The experimental results thus establish that the peak is largely due to deuteron formation. There is still the possibility to be examined that the peak contains an appreciable contribution from ^1S final nucleon states. However, the ^1S-peak contribution will occur 4 Mev below the contribution from the ^3S deuteron line. Since, as mentioned above, the resolving power of the apparatus is high enough to distinguish details in the spectrum that are 4 Mev apart, any appreciable ^1S-contribution would have occurred in the experimental results as a separate peak 4 Mev below that of the deuterons. Therefore, it can be concluded that the intense peak is due entirely to deuteron formation.

Since the peak accounts for approximately 70 percent of the total cross section at zero degrees, it is clear that at least 70 percent of the mesons produced at zero degrees are accompanied by nucleons in the ^3S-state.

The observed angular distribution implies that the mesons associated with the $P+P\rightarrow\pi^++D$ reaction are largely in a P-state with, possibly, a small amount of S-state.

Recent experiments suggest that the pion is pseudoscalar.[22] Using the Pauli exclusion principle and conservation of parity and angular momentum, it then follows that if the pion is in an S-state, the nucleons are in a $^1S_0$-state, while if the pion is in a P-state, the nucleons are in a $^3S_1$-state. Thus, the conclusions from the 0° data are consistent with the results from the angular distribution.

That the pions come off largely in a P-state is also consistent with another experimental result. Brueckner and Watson point out that if in the production of neutral pions in proton-proton collisions the pions go off primarily in a P-state, then by conservation of parity and angular momentum one obtains, using the Pauli exclusion principle, a strict selection rule forbidding the reaction if the pion is pseudoscalar. This is in agreement with the experiments of Hales, Hildebrand, Knable, and Moyer,[23] who find an extremely low yield of neutral pions when hydrogen is bombarded by 340-Mev protons.

XII. SPIN OF THE POSITIVE PION

The principal reaction studied in this experiment is $P+P\rightarrow\pi^++D$. In the center-of-mass system the pion energy is 21.4 Mev for an initial proton energy in the laboratory of 341 Mev. If the cross section for the absorption of a 21.4-Mev pion by a deuteron to give two protons is also known, the spin of the pion can be calculated by the principle of detailed balance.[24] Assuming that the initial protons in one case, and the initial pions in the reverse reaction are unpolarized, we can write,

$$\left(\frac{d\sigma}{d\Omega}\right)_P=\frac{(2S_P+1)^2p^2}{(2S_D+1)(2S_\pi+1)q^2}\left(\frac{d\sigma}{d\Omega}\right)_\pi, \qquad (11)$$

where $(d\sigma/d\Omega)_P$ is the cross section for producing a proton in a unit solid angle from the absorption of a pion, S_P, S_D, and S_π are the spins of the proton, deuteron, and pion, respectively, and p and q are the proton momentum and pion momentum, respectively, in the c.m. system.

The pion absorption cross section has been measured by Durbin, Loar, and Steinberger[25] at Columbia University and by Clark, Roberts, and Wilson[26] at the University of Rochester. In the Columbia experiment the cross section has been measured as a function of proton angle at pion energies ranging from 25 to 53 Mev. In the Rochester experiment the angular distribution could not be obtained, but the total cross section was calculated for various values of the constant, A, in the assumed angular distribution, $B(A+\cos^2\theta)$. Their result is an average over pion energies from 0 to 30 Mev.

TABLE V. Comparison of the cross sections for pion absorption by deuterium as obtained by Clark, Roberts, and Wilson at Rochester and Durbin, Loar, and Steinberger at Columbia, with the present results, which have been transformed to give the absorption cross section by the principle of detailed balance.

Experiment	T_π(c.m.) Mev	$(d\sigma/d\Omega)_P\times10^{28}$, cm² sterad⁻¹	$\sigma_{tot}\times10^{27}$, cm²
Berkeley[a]	21.4	$11\pm4(0.11\pm0.06+\cos^2\theta)$	3.0 ± 1.0
Berkeley[b]	21.4	$3.7\pm1.3(0.11\pm0.06+\cos^2\theta)$	1.0 ± 0.3
Rochester	23 (Av)		4.5 ± 0.8[c]
Columbia	25	$9(0.22+\cos^2\theta)$	3.1 ± 0.3

[a] Transformed on the assumption that $S_\pi=0$.
[b] Transformed on the assumption that $S_\pi=1$.
[c] Assuming an angular distribution of $(0.2+\cos^2\theta)$; see reference 26.

The decay scheme of the positive pion and the mode of absorption of the negative pion are good evidence that the pion spin must be integral.[22] Comparison of the experiment at Berkeley by means of the principle of detailed balance with those at Columbia and Rochester makes it possible to choose between the values of zero or one for the spin.

In Table V the cross sections are listed for the process $\pi^++D\rightarrow P+P$. The Berkeley values were calculated using Eq. (11), (a) with the spin of the pion equal to zero, and (b) with the spin equal to one. The total cross section quoted from Rochester is based on the assumed angular distribution, $0.2+\cos^2\theta$. The total

[22] Panofsky, Aamodt, and Hadley, Phys. Rev. **81**, 565 (1951).
[23] Hales, Hildebrand, Knable, and Moyer, Phys. Rev. **85**, 373 (1952).
[24] See, e.g., H. A. Bethe, *Elementary Nuclear Physics* (John Wiley and Sons, Inc., New York, 1947), p. 61.
[25] Durbin, Loar, and Steinberger, Phys. Rev. **83**, 646 (1951) and Phys. Rev. **84**, 581 (1951).
[26] Clark, Roberts, and Wilson, Phys. Rev. **83**, 649 (1951) and Phys. Rev. **85**, 523 (1952).

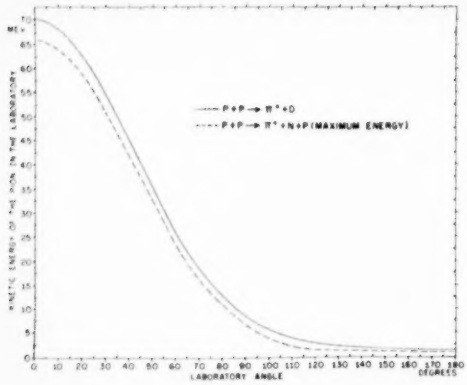

FIG. 10. Kinetic energy of the pion *vs* angle in the laboratory. The solid curve is for the case in which a deuteron comes off. The dashed curve is the maximum energy of the pion when a neutron and proton come off.

cross sections from Berkeley and Columbia are in good agreement for pion spin zero, although the angular distributions differ somewhat. The Rochester cross section, although more than one probable error away from the Berkeley result for spin zero, is in a direction opposite to that expected for spin one. With pion spin equal to unity, the Berkeley measurement yields a $\pi^+ + D \rightarrow P + P$ cross section which is about seven probable errors lower than the direct Columbia measurement, and four probable errors lower than the Rochester measurement.

The excitation function of this reaction is a strong function of energy. The difference in the experimental energies and their uncertainty, thus introduce some ambiguity in the above comparisons. The excitation function at zero degrees has been measured up to a proton energy of 341 Mev by Schulz[27] and in the inverse experiment from a pion energy of 25 to 53 Mev by Durbin *et al.* Using their data it would appear that transforming the Columbia result to the lower pion energy would at most lower it by 30 percent. A change of this magnitude would leave the conclusions as to the spin unchanged.

Thus, on the basis of the experiments done to date one can conclude that the pion spin is very probably zero. The experiments of Panofsky, Aamodt, and Hadley[22] on the pion absorption in deuterium show that if the negative pion has spin zero, it cannot be a scalar particle. Assuming that the positive and negative pions are particles of like character, it can be concluded that the charged pions are pseudoscalar.

It is a great pleasure for us to thank Professor Ernest O. Lawrence, for his interest and encouragement.

Many helpful and stimulating discussions were held with Dr. Kenneth M. Watson and Dr. Miriam Cartwright. We would also like to thank Mr. James Vale and the cyclotron crew for making the bombardments, and Mr. Dan Hamlin and Mr. Otto Heinz for their help in various portions of the experiment which contributed substantially to its successful completion.

[27] A. G. Schulz, Jr., University of California Radiation Laboratory Report UCRL-1756 (unpublished).

APPENDIX I. DYNAMICS

The relativistic calculations for the dynamics of reactions (1) and (2) are easily made. Let T be the kinetic energy of the protons in the laboratory. Then the velocity of the center of mass in units of c, $\beta_{c.m.}$, is given by the formula

$$\beta_{c.m.} = T^{\frac{1}{2}}(2R_P + T)^{-\frac{1}{2}}. \tag{I-1}$$

Let $\gamma_{c.m.} = (1-\beta_{c.m.}^2)^{-\frac{1}{2}}$; then the total energy available in the center-of-mass system, U, is given by

$$U = 2R_P\gamma_{c.m.} = [2R_P(2R_P+T)]^{\frac{1}{2}}. \tag{I-2}$$

In the center-of-mass system, the pions come off in reaction (1) with total energy (rest+kinetic) given by:

$$E_\pi' = \tfrac{1}{2}U - (R_D^2 - R_\pi^2)/2U, \tag{I-3}$$

where R_D and R_π are the rest energies of the deuteron and pion, respectively. The maximum pion energy in reaction (2) is obtained by substituting the rest energy of the neutron plus proton for the rest energy of the deuteron in the last formula. If the pion comes off at an angle θ' to the beam in the c.m. system, then in the laboratory the angle with respect to the beam, θ, is given by the well-known formula:

$$\tan\theta = \frac{\beta_\pi' \sin\theta'}{\gamma_{c.m.}(\beta_\pi' \cos\theta' + \beta_{c.m.})} \tag{I-4}$$

where β_π' is the velocity of the pion, in units of c, in the c.m. system. The total energy of the pion in the laboratory, E_π, is given as a function of θ by the formula:

$$E_\pi = (\gamma_{c.m.}b)^{-1}[E_\pi' + \beta_{c.m.}\cos\theta(E_\pi'^2 - \gamma_{c.m.}^2 b R_\pi^2)^{\frac{1}{2}}], \tag{I-5}$$

where $b = 1-\beta_{c.m.}^2\cos^2\theta$.

Figure 10 is a plot of Eq. (I-5) for the case in which a deuteron is formed and also for the case in which the neutron and proton come off unbound and the pion is emitted with maximum energy.

The relation between the elements of solid angle in the laboratory, $d\Omega$, and the corresponding element of solid angle in the c.m. system, $d\Omega'$, is given by the formula:

$$\frac{d\Omega}{d\Omega'} = \frac{p_\pi'}{p_\pi c^2}(E_\pi E_\pi' - \gamma_{c.m.}R_\pi^2). \tag{I-6}$$

p_π and p_π' are the momenta of the pion in the laboratory and in the c.m. system, respectively.

At zero degrees and for 340-Mev protons and a pion mass of 275.1 electron masses, $dE_\pi/dE_P = 0.9$ and $(dE_\pi/dm_\pi) = 0.8$ Mev per electron mass.

APPENDIX II. RESOLUTION

The experimental energy spectrum of the pions was determined from the density of pion endings found at each depth in the absorber. The density of pions as a function of range was then converted to the density of pions as a function of energy by means of the range-energy curves for pions. This method of detection introduces a finite resolving power into the apparatus. Pions of a particular energy will not have a unique depth of penetration into the absorber because of range straggling and multiple small angle scattering. The first effect is due to the statistical fluctuations in the number of collisions the pion undergoes, and gives an approximately Gaussian distribution in range. The multiple Coulomb scattering gives rise to a distribution in depth of penetration for pions of the same range because the projected range depends on the angles through which each pion has been scattered in the course of its travel through the absorber. Since the energy of a pion was deduced from the position of its

ending in the absorber, the above variation in depth of penetration for a monoenergetic beam of pions will manifest itself as an apparent spread in the energies of the pions coming to the absorber.

Further energy smearing arises because the detector accepts mesons from a small range of angles about zero degrees, and the pion cut-off energy or peak energy, in which we are interested, varies with the angle of production. The geometry of the zero degree experiment allowed a variation in angle, for the maximum energy pions, from $-3°$ to $+3°$. As is shown in Fig. 10 this introduces a spread in energy of less than 0.2 Mev. Therefore, this effect can be neglected in determining the resolving power.

The use of a thick target would also be expected to decrease the resolving power. However, for the pions of maximum energy, this turns out to give only a spread of 0.1 Mev for the thickness of CH_2 used in the experiment. This comes about in the following way: while the pions at the front of the target lose a small amount of their energy in traversing the target, the protons also lose energy in passing through the target, and produce pions of correspondingly lower energy at the back of the target. Thus, the energy loss in the target by the pions tends to be compensated for by the energy loss of the protons.

The main causes of the finite resolving power introduced by the detection method are, therefore, the multiple small angle scattering and the range straggling mentioned above. An additional energy spread is introduced into the experiment by the proton beam, which is itself not monoenergetic. The energy distribution of maximum energy pions arising from each of these three effects has been calculated below. The three distributions are then folded together. The resulting curve, shown in Fig. 11, gives the distribution in energy that maximum energy pions produced in proton-proton collisions will appear to have when produced at 0° and detected with the experimental equipment used.

The resolution has been assumed to be constant over the high energy part of the spectrum in obtaining the curves in Figs. 4 and 9.

The depth of penetration for a monoenergetic beam of pions entering an absorber normally will have a distribution, due to scattering, which is calculated approximately below.

A collimated monoenergetic beam of pions will, after passing through an absorber of thickness dx, possess a Gaussian distribution of angles due to multiple small angle scattering. The mean square angular spread is[28]

$$\langle\theta^2\rangle_{Av}=\frac{16\pi NZ^2e^4dx}{v^2p^2}\ln(181Z^{-\frac{1}{3}})=\frac{Cdx}{v^2p^2}, \qquad \text{(II-1)}$$

where $C=16\pi NZ^2e^4\ln(181Z^{-\frac{1}{3}})$, and where N is the number of atoms per cm³ of the absorber, Ze is the atomic charge of the absorber material, e is the electronic charge, and v and p are the velocity and momentum of the pion, respectively.

Using Eq. (8) we find that a pion following the rms angle of deflection in each thickness dx of the absorber, will have, at a depth x in the absorber, a direction of travel given approximately by $\Theta_{\text{rms}}(x)$, where

$$\langle\Theta^2(x)\rangle_{Av}=\frac{0.31C}{k^2(2n-1)}[(R_0-x)^{1-2n}-R_0^{1-2n}]. \qquad \text{(II-2)}$$

This formula is not applicable at $x=R_0$ where the small angle scattering formula (II-1) does not hold. However, for an aluminum absorber, $[\Theta^2(x)]^{\frac{1}{2}}$ is about 22° at $x=0.99R_0$. The assumption of small angle scattering is therefore valid in the interval $x=0$ to $x=0.99R_0$. Since almost all of the variation in depth of penetration of the pions takes place in this interval, Eq. (II-2) should be accurate, for our purposes, to within about 20 percent.

Now, in order to obtain the distribution in depth from the expression for Θ_{rms}^2, we introduce the assumption that a pion at a depth x' whose trajectory makes an angle $\Theta(x')=k\Theta_{\text{rms}}(x')$ with the forward direction, will at all x, maintain a direction of travel given by $\Theta(x)=k\Theta_{\text{rms}}(x)$. Thus, on this assumption, a pion traveling at an angle equal to twice the rms angle, always travels at twice the rms angle. This assumption is not unreasonable for obtaining a rough idea of the distribution. An exact treatment of the problem seems difficult. On the other hand, the above assumption leads to a distribution in depth of penetration, which, although crude, seems more realistic than assuming, for example, a constant "average" decrease in depth of penetration for each pion.

[28] B. Rossi and K. Greisen, Revs. Modern Phys. **13**, 263 (1941).

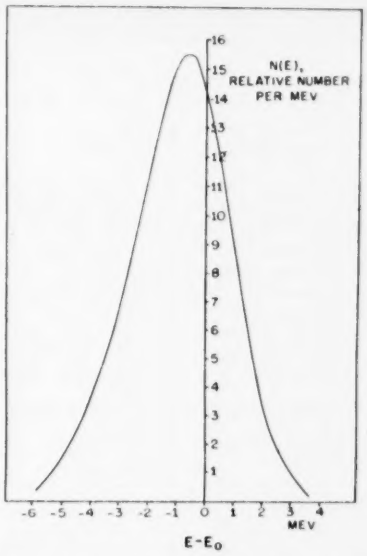

FIG. 11. Resolution of the apparatus for the zero degree experiment.

Since the distribution in $\Theta(x)$ is Gaussian, the distribution in k is also Gaussian, and the fraction of the total number of pions with k in dk is

$$N(k)dk=[2/(2\pi)^{\frac{1}{2}}]\exp(-k^2/2)dk.$$

Knowing, at every depth x, the angle with which each pion travels relative to the original direction, we are able to compute each path.

The path length traversed by a pion is $\int[dx/\cos\Theta(x)]$, and the shortening in the projected path distance is, therefore, given approximately by $\omega=\int_0^R[dx\Theta^2(x)/2]$.

The average shortening that the projected paths undergo is given by the shortening for the pion which maintains the rms angle. Using Eq. (II-2) this average shortening, ω^*, turns out to be $0.08C/(1-n)\cdot R_0^2/T_0^3$, where T_0 is the initial kinetic energy of the pion.

The pion maintaining the direction of travel $k\Theta_{\text{rms}}(x)$ has then a decrease of penetration given by $\omega=k^2\omega^*$. The distribution in ω is found from the distribution in k:

$$N(\omega)d\omega=(2\pi\omega\omega^*)^{-\frac{1}{2}}\exp(-\omega/2\omega^*)d\omega. \qquad \text{(II-3)}$$

With the absorbers used, the total shortening in depth of penetration was, for the "rms" pion, 0.14 cm of aluminum. Since the energy is inferred from the depth of penetration, a pion traveling along the path with the rms angle will appear to have an energy decreased from the true energy by $\omega^*(-dE/dx)_{\text{Al}}\,T_0$. This yields $\Delta E^*=0.88$ Mev. The distribution in ω, [Eq. (II-3)] corresponds to a distribution in E given by:

$$N(E)dE=\frac{e^{-(E_0-E)/[2(0.88)]}}{[2\pi(E_0-E)\times0.88]^{\frac{1}{2}}}dE, \qquad \text{(II-4)}$$

where E_0 is the true pion energy and the energies are in Mev.

Next, the effect on the energy resolution of range straggling due to statistical fluctuations in the number of collisions that the

meson undergoes is computed. Livingston and Bethe[29] give an expression for the mean square width in the Gaussian distribution of distance traveled by monoenergetic particles which lose a given amount of energy by ionization. For pions of high velocity which decrease in energy from E_1 to E_2 this expression yields:

$$\langle \Delta R^2 \rangle_{Av} \cong \int_{E_2}^{E_1} \frac{4\pi e^4 NZ'}{(-dE/dx)^3} dE, \qquad \text{(II-5)}$$

where e is the electronic charge, N is the number of atoms per cubic centimeter of the absorber, Z' is the number of electrons per atom that are effective in the ionization process, and $(-dE/dx)$ is the rate of energy loss of the pion at the energy E. The integration can be carried out by means of Eq. (8). For the experimental absorbers used, the total accumulated straggling in range was calculated as $\Delta R_{rms}=0.15$ cm of Al. If there were no straggling, this Gaussian distribution in range would correspond to a Gaussian distribution in the energy with which the pions enter the absorber. The mean square in this energy distribution is given by:

$$\langle \Delta E^2 \rangle_{Av} = (dE/dx)_{E_0}^2 \cdot \langle \Delta R^2 \rangle_{Av} = 0.92 \text{ Mev}^2.$$

The electrically deflected 341-Mev proton beam has an energy spread estimated to be about 1.5 Mev. Without a detailed analysis of the origin of this spread, we have assumed that the distribution in energies is Gaussian with an rms spread of 1.2 Mev. This value gives the best fit to the experimental points. If, however any value in the vicinity of 1.5 Mev were used for the rms spread, the conclusions reached would remain unchanged.

Protons with a Gaussian energy distribution will produce pions whose maximum energy will also have a Gaussian distribution. Since a change in proton energy of 1 Mev produces a change of 0.9 Mev in the maximum pion energy, the pion energy Gaussian will have an rms width of 0.9×1.2 or 1.08 Mev.

The range straggling and proton beam energy distributions, when folded together, give a Gaussian of rms width 1.44 Mev. The final resolution curve is found from folding the distribution produced by multiple Coulomb scattering into this Gaussian, and is plotted in Fig. 11.

[29] M. S. Livingston and H. A. Bethe, Revs. Modern Phys. **9**, 245 (1937).

PHYSICAL REVIEW VOLUME 91, NUMBER 3 AUGUST 1, 1953

Effects at Godhavn and Lower Latitudes of Changes in Energy and Composition of Solar Cosmic Rays

V. SARABHAI AND R. P. KANE
Physical Research Laboratory, Ahmedabad, India
(Received March 24, 1953)

Time series have been derived for changes of the amplitude and the hour of maximum of the diurnal component of the daily variation of the pressure-corrected meson intensity at Godhavn from Carnegie Institution data. While these series show some features which are strikingly similar to those observed at other stations, the variability at Godhavn is much greater than elsewhere. Comparison of the series at Godhavn with the corresponding series for the mean changes observed at Cheltenham and Christchurch permits information to be derived concerning changes in the mean energy of cosmic-ray primaries responsible for the daily variation, and their "stiffness" in the geomagnetic field. On the basis of an interpretation in terms of continuous emission of cosmic rays from the sun, there is evidence for an increase in the mean energy of solar cosmic rays from 1940 to 1944. Reasons are given for believing that during 1944, the solar cosmic rays became richer in alpha particles as compared to protons.

WE have earlier presented[1] evidence demonstrating world-wide changes in the daily variation of cosmic-ray meson intensity. Time series for the period 1937 to 1946 have been derived for changes in the amplitude M^D and the hour of maximum ϕ^D of the diurnal harmonic component of the daily variation of mesons observed at Huancayo (H), Cheltenham (C), and Christchurch (C'). Similar analysis has now been conducted for the daily variation of meson intensity at Godhavn (G) from data furnished by Lange and Forbush.[2]

Figure 1 shows the time series for changes in absolute magnitude of $M_G{}^D$ and $\phi_G{}^D$ during the years 1939 to 1946. These series at Godhavn (mag. lat. 79.9° N) may be compared with the time series $M_{\langle C \rangle}{}^D$ and $\phi_{\langle C \rangle}{}^D$, which represent the mean of the time series for Cheltenham (mag. lat. 50.1° N) and Christchurch (mag. lat. 48.6° S). Huancayo has not been included in the mean time series because it is a high level station on the magnatic equator and during years of high solar activity, $M_H{}^D$ exhibits a different course of changes compared to $M_C{}^D$ or $M_{C'}{}^D$. Though the changes in the daily variation at G and $\langle C \rangle$ have broad similarities, there are certain important differences.

1. The variability of $M_G{}^D$ and $\phi_G{}^D$ at Godhavn is much greater than the variability of $M_{\langle C \rangle}{}^D$ and $\phi_{\langle C \rangle}{}^D$.

2. For the period 1943 to 1946, the time series for $M_G{}^D$ and $\phi_G{}^D$ are remarkably similar to those for $M_{\langle C \rangle}{}^D$ and $\phi_{\langle C \rangle}{}^D$, respectively. For 1939 to 1942 however, $M_G{}^D$ has a low and almost constant value nearly equal to the minimum reached in 1944, while $M_{\langle C \rangle}{}^D$ steadily decreases from a high to an intermediate value in its total range. During the same period, $\phi_G{}^D$ has a peak at 1940 while $\phi_{\langle C \rangle}{}^D$ has a slowly increasing value.

G and $\langle C \rangle$ refer to sea level stations which lie outside the region where the geomagnetic latitude effect is observed at this depth of the atmosphere. However, if the daily variation is considered to be produced by

[1] V. Sarabhai and R. P. Kane, Phys. Rev. **90**, 204 (1953).
[2] I. Lange and S. E. Forbush, Carnegie Inst. Wash. Pub. **175** (1948).

cosmic rays from the sun, there can still be differences in its form at the two places because, with change of latitude, the sun's mean zenith distance and consequently the mean atmospheric path length for solar rays would alter. The atmospheric path length for the radiation would be greater at Godhavn on account of its higher latitude. This has the following consequences.

1. The $M_G{}^D$ series shows the changes of intensity of the high energy radiation which makes its effect felt at both G and $\langle C\rangle$.

2. The difference curve $M_{\langle C\rangle}{}^D - M_G{}^D$ shown in Fig. 1, reflects the changes of intensity of the low energy solar cosmic radiation which reaches $\langle C\rangle$ but not G.

3. The changes in $M_G{}^D$ and $M_{\langle C\rangle}{}^D - M_G{}^D$ thus give information of the changes of the high and the low energy radiations reaching $\langle C\rangle$. The two taken together indicate changes in the mean energy of the radiation responsible for $M_{\langle C\rangle}{}^D$.

When it is realized that the trajectories of positive particles from the sun would be bent in the geomagnetic field so that they would appear to come from the west and would register a maximum which would be earlier for the more deflected trajectories, we can look upon the $\phi_{\langle C\rangle}{}^D$ and $\phi_G{}^D$ series as indicative of the mean deflections suffered by the solar particles approaching $\langle C\rangle$ and G, respectively. The radius of curvature of a trajectory is proportional to $(mv)/Z$, so that for either protons or alpha particles or a combination of both in a constant proportion, the energy hardening of the radiation would be accompanied by an increase of the radius of curvature and an increase of ϕ^D corresponding to a later hour of maximum. ϕ^D however, should tend to approach a maximum value since for large energies the deflection of the trajectories is negligible.

In terms of the interpretation given above, we can draw certain broad conclusions regarding the changes in intensity and composition of the solar cosmic-ray emission. The increased emission in 1943 appears to be confined to high-energy primaries which make their effect felt at G as well as $\langle C\rangle$. From 1940 to 1944, the $M_{\langle C\rangle}{}^D - M_G{}^D$ series decreases steadily, while $M_G{}^D$ does not decrease likewise. Hence at $\langle C\rangle$, the mean energy of the solar radiation increases from 1940 to the year 1944. Up to 1943, $\phi_{\langle C\rangle}{}^D$ also increases and appears to approach saturation. In 1944 however, there is a rapid and large decrease of $\phi_{\langle C\rangle}{}^D$ although the mean energy of the radiation continues to increase. In early 1945, the radiation at $\langle C\rangle$ again becomes energetically softer, but this is accompanied by a rapid increase of $\phi_{\langle C\rangle}{}^D$. It is possible to reconcile the changes of mean energy of incoming radiation and of ϕ^D during 1944 and 1945 if we postulate an alteration in the proportion of protons and alpha particles in the solar cosmic-ray emission. The present interpretation requires that during 1944, the solar cosmic-ray emission became richer in alpha particles as compared to protons.

The form of the mean daily variation curve for mesons for the period 1939–1946 at G is strikingly different[3] from the corresponding curve at $\langle C\rangle$. At G the amplitude $M_G{}^D = 0.10$ percent is much less than at $\langle C\rangle$ where the amplitude $M_{\langle C\rangle}{}^D = 0.16$ percent. Also, the maximum at G is much flatter than that at $\langle C\rangle$. This is qualitatively in agreement with the view that the difference at the two places is due to differences in the mean value, as well as in relative changes, during the day, of the atmospheric path length for solar cosmic rays. A quantitative analysis is rendered difficult in the absence of knowledge of the true trajectories of solar cosmic rays. Considerable deflection of the trajectories in the geomagnetic field would alter substantially an oversimplified view based on optical paths for particles from the sun.

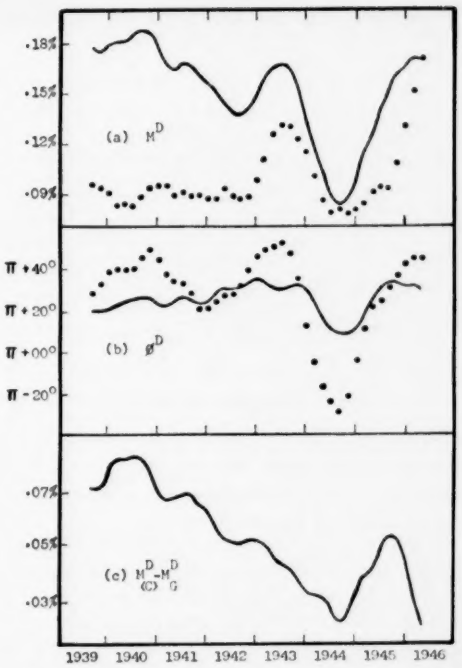

FIG. 1. Time series for annual mean values during period 1939 to 1946 of (a) M^D, meson diurnal amplitude; (b) ϕ^D, meson diurnal hour of maximum expressed in degrees; π corresponds to mid-day and 15° to one solar hour. (c) $M_{\langle C\rangle}{}^D - M_G{}^D$, difference between diurnal amplitudes at $\langle C\rangle$ and G. In (a) and (b), the continuous lines indicate the values for $\langle C\rangle$, and . . the values for G.

While only a very tentative interpretation is possible with the relatively scanty data that are available, the present analysis is indicative of the type of information about the primary radiation which could be obtained from a close study of the changes of meson daily variation at a number of stations on the earth. We are grateful to Professor K. R. Ramanathan and Professor B. Peters for helpful discussions, and to Mr. K. A. Gidwani for computational assistance. Our thanks are due the Indian Atomic Energy Commission for financial assistance.

[3] J. G. Wilson, *Progress in Cosmic Ray Physics* (North-Holland Publishing Company, Amsterdam, 1952), p. 468.

Anisotropic Distribution of Secondaries in Extreme Energy Cosmic-Ray Stars

FRANK C. ROESLER AND C. B. A. MCCUSKER
Dublin Institute for Advanced Studies, Dublin, Ireland
(Received April 6, 1953)

The connection between the conservation law for angular momentum and the anisotropy observed in cosmic-ray stars produced by energetic primaries is investigated. A model is proposed which is probably reasonable for noncentral nucleus-nucleus collisions and may have some meaning for nucleon-nucleon collisions; it is based on assuming that the disk-shaped "interaction volume" consists of many zones acting independently. If equilibrium is reached within individual zones, the particles emerging from one zone ought to be distributed isotropically in its center-of-mass frame. In a noncentral collision these frames will in general, in accordance with the conservation of momentum, be different for different zones. Some anisotropy in the total angular distribution follows, but on this model it could never reach the degree frequently observed.

I. INTRODUCTION

IN Fermi's statistical theory of high-energy processes[1] it is postulated that the outgoing particles correspond to a state of equilibrium within the interaction volume V. Once the particles have left V their coupling is supposed to cease. The number and angular distribution of the particles depends on V and on the energy and angular momentum deposited therein. Fermi took V to be independent of the initial impact parameter, more especially to be a flattened ellipsoid of revolution with its axis, the length of which depends on the collision energy, parallel to the direction of approach of the particles. This simplification seems reasonable in the domain of small impact parameters; but as these approach the transverse radius of the ellipsoid, the predicted measure of anisotropy tends to infinity. This is clearly brought about by the simplifying geometrical assumptions, and one must ask oneself whether, on replacing them by less crude ones, the theory will still account for the considerable anisotropy found in recent experiments.[2,3] One might try to check this by having V depend on the impact parameter (increasing with it) while otherwise taking over Fermi's whole formalism. We are indeed convinced that on doing this and admitting even a rather weak increase of the transverse dimensions of V one would find the peaking predicted for large impact parameters greatly reduced. However, as Fermi has pointed out, it is difficult to specify shape and size of V in a realistic and unambiguous way. Therefore we have tried to find another method, not dependent on precise assumptions concerning V, and which may yet enable us to estimate what *maximum* anisotropy can reasonably be explained from the assumption of a flattened interaction volume and the conservation laws.

To avoid misunderstanding we should here say that we do *not* question Fermi's basic principle: we definitely follow him in asserting that the conservation of angular momentum will, for a flat interaction volume result in some anisotropy of the total angular distribution. However, we think we can show that this anisotropy may be very much weaker than on Fermi's original estimate. Consequently we doubt that an explanation of the observed, strong anisotropy is possible on this basis.

Below we carry out an investigation of a model similar to Fermi's but based on the hypothesis of "local interactions." (This is explained below.) We find that this model gives only negligible "peaking" (even for the largest impact parameters), although all conservation laws are satisfied.

II. EVIDENCE OF ANISOTROPY

We are concerned with the angular distribution in cosmic-ray stars produced by primaries with an energy of a few thousand Bev or greater. The shower or jet part of such a star consists of tracks which do not allow identification of the particles. The only data with direct bearing on the interaction are in most cases the angles between the tracks in the laboratory frame. These are not sufficient to determine the center-of-mass frame (c.m.f.) of the process. For the majority of observed jets there is no Lorentz-frame in which the angular distribution is spatially isotropic. Usually it proves possible to find a Lorentz-frame in which the distribution is more or less symmetric with respect to a plane normal to the path of the primary. It is often thought that this amounts to finding the c.m.f. In most cases, however, it is known that the colliding entities are by no means identical (nucleon-nucleus collision). It is then unlikely, *a priori*, that the angular distribution in the real c.m.f. should exhibit forward-backward symmetry. One could only, *a posteriori*, admit this symmetry if it were found that the distributions are isotropic in the c.m.f. But this is, experimentally, not the case. Therefore this procedure for guessing the c.m.f. and all conclusions based on it should be regarded with some caution.

A convenient measure for the anisotropy has been

[1] E. Fermi, Progr. Theoret. Phys. **5**, 570 (1951); Phys. Rev. **81**, 863 (1951).
[2] M. F. Kaplon and D. M. Ritson, Phys. Rev. **88**, 386 (1952).
[3] Lal, Pal, Peters, and Swami, Proc. Indian Acad. Sci. **36**, 75 (1952).

introduced by Kaplon and Ritson.[2] Let ϕ_n denote the half-angle of the cone in the laboratory frame in which the tracks of nN of all the N particles in the jet are situated. Form the ratio $\phi_{3/4}/\phi_{1/4}$ for the observed distribution and, for comparison, for a distribution isotropic in the same c.m.f. The quantity,

$$X=\frac{(\phi_{3/4}/\phi_{1/4})_{\text{observed}}}{(\phi_{3/4}/\phi_{1/4})_{\text{isotropic}}}, \tag{1}$$

is equal to 1 for distributions for which a Lorentz-frame exists in which they are isotropic. For distributions peaked in forward and backward direction in that Lorentz-frame in which they are symmetrical with respect to the transverse plane, X is greater than 1. A large X manifests itself by the appearance of a "double cone" in the laboratory frame. The wider the outer, diffuse cone and the narrower the superimposed, inner, dense cone is, the larger is X. In the cases of interest the Lorentz-transformation relating the laboratory frame and the so-called c.m.f. is strong ($\gamma\gg1$) so that, e.g., $\phi_{3/4}$ is still a small angle. For a distribution isotropic in the c.m.f. one has under these conditions, as can be proved with the help of Eqs. (5) and (8) below $\phi_n/\phi_{1-n}=n/(1-n)$. (Here n stands for any fraction not too near 0 or 1.) Putting $n=3/4$, one finds $(\phi_{3/4}/\phi_{1/4})_{\text{isotropic}}=3$. Therefore one can in practice evaluate X from

$$X=\phi_{3/4}/3\phi_{1/4}. \tag{2}$$

For the twenty events in copper described by Kaplon and Ritson[2] the quantity X has values varying from 1.17 to 66, and X is in this set of events not significantly correlated with either the energy or the multiplicity. The Lord-Fainberg-Schein star[4] and the very large star with an Mg primary described by Lal *et al.*[3] both show $X\approx3$. Two events in copper with α primaries observed by Kaplon and Ritson[2] give $X=1.17$ and $X=2$. The Bradt-Kaplon-Peters star[5] has $X=2.33$. In Fermi's original paper[1] he obtained for median impact parameter a distribution in agreement with that of the Lord-Fainberg-Schein star, i.e., with an $X\approx3$.

Since nothing is known about the interaction laws, there is no very convincing reason why peaking rather than isotropy should be regarded as surprising and as requiring a *special* explanation. The *a priori* motivation for requiring such an explanation is different for the different authors. Without going into too much detail, we should mention that besides Fermi's argument involving the conservation of angular momentum several other explanations of the anisotropy have been proposed. A number of investigators have put forward the most obvious idea that the double cone may be due to multiple scattering inside the target nucleus; those particles which are scattered more often being deflected more strongly from the direction of the primary. This explanation does away with the assumption that the jet is generated in a single act, and it denies the special role of either the real c.m.f. of the jet or of the frame (probably not identical with the c.m.f.) in which the distribution is most symmetric in backward and forward direction. Arguing from the opposite viewpoint that the peaking is a fundamental feature of interactions at high energies, already present and perhaps most prominent in the results of simple nucleon-nucleon collisions, Heisenberg[6] has pointed out that it might be explained in terms of the coherence of the waves going out from the flat-shaped zone of interaction.

III. MODEL OF THE INTERACTION

Fermi and Heisenberg have pictured "extreme-relativistic" ($E\gg Mc^2$) nucleons as disk-shaped objects, flattened in their direction of motion according to the ratio Mc^2/E. In dealing with the collision of two such disks and the insuing splash of matter they have used a mixture of arguments based on the "particle" and the "wave" picture of quantum processes and have amplified these by certain assumptions about the consequences of the "strong coupling" of the mesonic fields. With Fermi's approach, one difficulty which presumably has occurred to many and is mentioned by Lewis[7] is the clash between the assumption of equilibrium within the whole of V and the velocity of propagation of action within V, which one will be inclined to assume $\leq c$. The interaction volume has no "walls" which hinder the particles to escape; this is inherent in the physical picture and is also implied by Fermi's use of wave functions corresponding to free particle states. Hence the concentration of energy will only exist for a time of the order $(R/c)\cdot(Mc^2/E)$, which is short compared to the time (R/c) approximately required so that action should spread across the disk. Thus, if one assumes that the coupling of the outgoing particles ceases (equilibrium frozen) when they leave the interaction volume, one can hardly avoid assuming at the same time that the processes in different zones of the interaction volume are physically independent if the transverse distance in between such zones is large compared to the depth of the interaction volume along the line of approach of the initial collision. (Whether such a split into independent zones might occur in Heisenberg's model depends on the field law assumed; more specifically on when the nonlinear character of the wave propagation ceases to be important. If this is soon after the waves start to spread out from the initial disk, the split into independent zones will occur.)

One may now consider amplifying the Fermi-Heisenberg disk-model by a postulate of "independent zones." This, in effect, we will do. However, the piling of more assumptions on to a perhaps rather uncertain basis must cease at some stage or be compensated for by

[4] Lord, Fainberg, and Schein, Nuovo cimento **7**, 774 (1950).
[5] Bradt, Kaplon, and Peters, Phys. Rev. **76**, 1735 (1949).
[6] W. Heisenberg, Z. Physik **133**, 65 (1952).
[7] H. W. Lewis, Revs. Modern Phys. **24**, 241 (1952).

establishing a more secure foundation. Since we are not in a position to provide additional support in the shape of theoretical arguments, we will try to get on firmer ground by restricting our claims as to the applicability of the model. We will consider (noncentral) nucleus-nucleus collisions and leave open the question of how far the model may apply to nucleon-nucleon interactions (see Appendix).

For a heavy nucleus, divisibility into subsystems is quite a reasonable assumption, and indeed independent of whether the nucleus is Lorentz-contracted or not. On the other hand, in a noncentral collision between two heavy nuclei the ratio of the initial angular momentum to the total energy and proper mass is even larger than for a noncentral nucleon-nucleon interaction at the same specific energy. Thus Fermi's fundamental idea should apply for complex collision partners at least as well as in the case of the nucleon-nucleon interaction. Finally, it is known from experiment[3] that energetic nucleus-nucleus collisions may give rise to a strongly anisotropic distribution of the outgoing particles. We may therefore expect that the more surveyable nucleus-nucleus process can be used to test the working of Fermi's basic idea. In carrying through the computations and making the comparison with experiment there is, of course, at the back of our minds the hope that this more surveyable problem may tell us something, by analogy, about the nucleon-nucleon case.

We make the following assumptions. The system of the two colliding nuclei consists of many independent zones. For every zone we assume isotropic evaporation, even if the total collision is noncentral. Two reasons can be given for this. First, the zone, in contrast to the whole system, is not essentially flat-shaped. Second, if the zones are small compared to the whole system, the angular momentum deposited in every zone, with respect to an axis through the center of mass of the zone, is negligibly small. (On decreasing in thought the size of the zone the angular momentum deposited in it goes more quickly to zero than the mass of matter in the zone.) Therefore we do not have to worry about conservation of angular momentum when dealing with an individual zone. The angular momentum of the whole system is automatically conserved if the energy-momentum four-vector is conserved for every zone individually.[8] If the total collision is noncentral, the c.m. frames of different zones are, in general, different.

A qualitative understanding of the way in which peaking can come out of these assumptions may be obtained by looking at the picture of a star described by Dainton and Kent.[9] In this event, a very heavy ($Z=13\pm1$) and slow ($\approx0.55c$) primary closely passes a heavy nucleus in the emulsion. The resulting excitation leads to the disintegration of the primary into six α's as well as to the evaporation of particles from the nucleus in the emulsion. Both these processes can be assumed to proceed isotropically in the respective center-of-mass frames. Since the evaporation velocity of the α's is only a few percent of c one observes the six α's from the incident nucleus forming a narrow forward cone in the laboratory frame. The particles from the emulsion nucleus go off in haphazard directions. Because of the low velocity of the primary the geometry of the event is not obscured by relativistic effects.

IV. ANALYSIS OF THE MODEL

We carry out most of the analysis in the laboratory frame and, unless otherwise specified, all quantities used below refer to it. The nucleus initially at rest in this frame will be called the target and the bombarding particle the primary. All our considerations in this section refer to a single zone. Let μ_t and μ_p denote those parts of the mass of target and primary which belong to this zone and put $\mu_p/\mu_t=q$. M shall denote the nucleon mass, and we define $\Gamma=E'/Mc^2$, where E' is the total primary energy. Assuming $\Gamma\gg1$ one finds from a simple application of the relativistic transformation laws that the center-of-mass frame of the zone moves with respect to the laboratory frame with velocity βc such that

$$\beta=\Gamma\mu_p/(\Gamma\mu_p+\mu_t). \tag{3}$$

Under the condition $1/\Gamma\ll q\ll\Gamma$ we get for $\gamma=1/(1-\beta^2)^{\frac{1}{2}}$ the approximation

$$\gamma=(\Gamma\mu_p/2\mu_t)^{\frac{1}{2}}=(\Gamma q/2)^{\frac{1}{2}}. \tag{4}$$

As explained, we assume that the particles originating in a zone are emitted isotropically in its c.m.f. Then their normalized integral distribution law is, in this frame,

$$n(\vartheta)=(1-\cos\vartheta)/2. \tag{5}$$

We have to transform this distribution into the laboratory frame, where the angles will be denoted by ϕ. By vc we denote the velocity of the particles in the c.m.f. of the zone and we put $G=1/(1-v^2)^{\frac{1}{2}}$. We will for the moment proceed as if one could ascribe to all particles the same value of v and G.[10] The velocity four-vector to be transformed is

$$Gv\cos\vartheta,\quad Gv\sin\vartheta,\quad 0,\quad G. \tag{6}$$

The transformation parameters are β, γ and the trans-

[8] This is, in fact, only true if the individual zone is infinitesimally small. Since, physically, this is not allowable, and is not meant here, there is a residual angular momentum to be conserved in every zone. Still, this neglected part is small compared to the part we take into account.

[9] A. D. Dainton and D. W. Kent, Phil. Mag. **41**, 963 (1950).

[10] The average value of G can be estimated from the energy balance of the event if the primary energy is known. In events with large primary energy and large multiplicity $1\ll\langle G\rangle_{Av}\ll\gamma$. We will show later that certain properties of the angular distribution are not sensitive to the individual G's.

formation reads

$$\begin{aligned} G'v' \cos\phi &= \gamma(Gv\cos\vartheta+\beta G),\\ G'v' \sin\phi &= Gv\sin\vartheta,\\ 0 &= 0,\\ G' &= \gamma(G+\beta Gv\cos\vartheta). \end{aligned} \tag{7}$$

Dividing, we find

$$\gamma\frac{\sin\phi}{\cos\phi}=\frac{\sin\vartheta}{\cos\vartheta+\beta/v}. \tag{8}$$

We put $\sin\phi=z$, express $\cos\phi$ by it and express $\sin\vartheta$ by $\cos\vartheta$. We now have a relation between z and $\cos\vartheta$ which we can use to substitute a function of z for $\cos\vartheta$ in (5) and thus obtain the transformed distribution. Actually (8) is a quadratic equation for $\cos\vartheta$, with two roots, say,

$$\cos\vartheta=A(z)\pm\sqrt{B(z)}. \tag{9}$$

The two roots arise in a natural fashion: To a given value of $z=\sin\phi$ must correspond two values of ϕ between 0 and π; and to these, two values of ϑ and of $\cos\vartheta$. In the high-energy stars one has $\beta/v>1$; then the function $B(z)$ is positive and correspondingly the roots are real only for values of z up to a certain $z=z_{\max}<1$. This means that the transformed angular distribution reaches the value 1 ("all particles") at the corresponding angle $\phi=\arcsin z_{\max}$. Two different domains of the $\cos\vartheta$ space are mapped on the domain $0<z<z_{\max}$ such that $\cos\vartheta=1$ and $\cos\vartheta=-1$ both correspond to $z=0$. Therefore the transformed angular distribution reads

$$n(\phi)=\tfrac{1}{2}[1-(A+\sqrt{B})]+\tfrac{1}{2}[1+(A-\sqrt{B})], \tag{10}$$

or

$$n(\phi)=1-\sqrt{B}. \tag{10a}$$

The actual expression for B is found from (8) by simple algebra. We obtain then

$$n(z)=\frac{z^2(\gamma^2-1)+1-(1-z^2)^{\frac{1}{2}}[1-z^2(\gamma^2-1)/(G^2-1)]^{\frac{1}{2}}}{z^2(\gamma^2-1)+1}. \tag{11}$$

All the particles appear within the angular domain

$$z=\sin\phi\leq[(G^2-1)/(\gamma^2-1)]^{\frac{1}{2}}. \tag{12}$$

The relation (11) is cumbersome but exact, that is, it holds for all values of γ and G provided $\gamma\geq G$. For $\gamma\gg1$ it is easily simplified to read

$$n(z)=\frac{z^2\gamma^2+1-[1-z^2\gamma^2/(G^2-1)]^{\frac{1}{2}}}{z^2\gamma^2+1}. \tag{13}$$

If we restrict ourselves to the dense center-part of the distribution, that is, to the angular domain $z\ll(G^2-1)^{\frac{1}{2}}/\gamma$, we can further simplify and obtain

$$n(z)=z^2\gamma^2/(z^2\gamma^2+1). \tag{14}$$

The simple approximation (14) gives $n=1$ only for $z=\infty$, instead of for $z=(G^2-1)^{\frac{1}{2}}/\gamma$. However, the numerical error in the whole region where the exact distribution does not vanish is very small. If we take, e.g., $G=10$ (which is a small-to-moderate value) and γ very large, the limit of the exact distribution defined by $(G^2-1)^{\frac{1}{2}}/\gamma=\sqrt{(99)}/\gamma$ gives, on using (14), $n=0.99$ instead of the exact value $n=1$. It is of interest to note that the approximation (14) conserves the property $\phi_n/\phi_{1-n}=n/(1-n)$, or, more specially, $\phi_{3/4}/\phi_{1/4}=3$, $X=1$ of an isotropic distribution subjected to a strong Lorentz transformation; thus we may use (14) in a treatment of the X measure of anisotropy of Kaplon and Ritson. Finally, after having obtained (14) we may now drop the assumption of a single value of G. The central part of the distribution (13) is approximated by (14) and this evidently does not depend on the G's. Also, since (14) is a small-angle approximation anyhow, we may put $z=\sin\phi\approx\phi$.

V. LIMITS FOR THE ANISOTROPY BY SUPERPOSITION

If we wanted to obtain the total angular distribution of the event in the laboratory frame we would have to sum or integrate over all the zones. Every zone would give a contribution according to (14), with a value of γ depending by (4) on the q of the zone. The contribution from every zone would have to be multiplied by a *weight* equal to that fraction of all the particles in the event which comes from the zone. For a central collision of two nuclei of equal weight all q's are 1 and (14) gives the total distribution, X being equal to 1. The wider the variation in q for the different zones is and the larger the contributions to the total multiplicity (i.e., the weights) of those zones which have extreme values of q the larger an X (the stronger anisotropy) one may expect for the distribution resulting from the summing or integrating procedure. If q varies within a certain range only, from q_1 to $q_2=f^2q_1$ say, the maximum anisotropy formally possible will arise if there are just two zones, of weight $\frac{1}{2}$ each, with values of q as defined by the limits of this range, i.e., q_1 and q_2. The corresponding X is an upper limit for the anisotropy possible on our model in an event where q varies within the range from q_1 to q_2. We will now find such upper limits for X, based on shifting all the weight to the extreme values of q. (We have met, in the Dainton-Kent star, with an event—albeit at much lower energy—where two zones actually suffice for a reasonably exact description.) To the limiting values q_1 and $q_2=f^2q_1$ will from (4) correspond two values γ_1 and γ_2 such that $\gamma_2^2=f^2\gamma_1^2$. The distribution of maximum anisotropy compatible with this range of q or γ is, using (14) and writing γ for γ_1,

$$n(\phi)=\frac{1}{2}\left[\frac{\phi^2\gamma^2}{\phi^2\gamma^2+1}+\frac{\phi^2f^2\gamma^2}{\phi^2f^2\gamma^2+1}\right]. \tag{15}$$

We may now find the value of X corresponding to a certain value of f. We may presuppose that f^2 is fairly

large compared to 1 so that the second term in the bracket will with increasing ϕ tend towards 1 much faster than the first term. The values of ϕ for which $n=\frac{1}{4}$ and for which $n=\frac{3}{4}$ can then be found in close approximation by putting the second term in the bracket and the first term in the bracket equal to $\frac{1}{2}$, respectively. The results are $\phi_{1/4}=1/(\gamma t)$, $\phi_{3/4}=1/\gamma$. Therefore

$$X=\phi_{3/4}/3\phi_{1/4}=t/3. \tag{16}$$

Checking these last approximations shows that the error of (16) is smaller than 1 percent for all $t\geq 6$, $X\geq 2$.

We must now consider what effective range of q is physically reasonable. This depends on the distribution of matter density one chooses to attribute to the disks, and on the dependence of the number of particles produced in a zone on the collision energy and the proper mass initially deposited in it. One can hardly avoid assuming that the number of particles from a zone depends on these quantities in such a manner as to become very small when they do. If this is granted, and furthermore if the matter density in the disks is chosen so as to give the original collision-partners a more or less uniform density inside and a fairly sharp boundary, the effective range of q cannot be large. We estimate on the basis of some graphical work that in a collision with large impact parameter ($r\approx R$)[11] appreciable contributions to the total multiplicity may at most come from zones with q values ranging from $\frac{1}{6}$ to 6. Correspondingly, the upper limit for X is, from (16): $X<2$. (By contrast $X\approx 3$ is, on Fermi's original estimate, the expected value for median impact parameter.) Thus, if we make what seem the most natural assumptions about the weight of the zones as a function of q, we get very little peaking. Turning to the large values of X observed in nucleon-nucleus collisions[2] and considering a value $X=20$ (which is quite frequent), it is evident from (16) that to explain it with our model we would have to require q to vary from a value $q_{\min}<1/60$ to a value $q_{\max}>60$. That the effective range of q should have such a huge span seems quite impossible, however strange and (from our present knowledge) unexpected a law for the weighting of the zones one might choose.

VI. CONCLUSIONS

We have pointed out a model of the extreme energy nucleus-nucleus collision which (a) operates with a flattened interaction volume and (b) satisfies the conservation laws. This model fails to give appreciable peaking, even for the largest impact parameters. Consequently we feel it is doubtful whether conservation of angular momentum is a good explanation for the peaking, even for events which may be nucleon-nucleon collisions. In terms of our model, the origin of the peaking must be in the individual zones: Our initial assumption of isotropy for the particles from one zone must be incorrect. This seems to imply that equilibrium is not even reached within a zone. If this conclusion holds for nucleon-nucleon-collisions, it contradicts the basic assumptions of the statistical theory.

Any theory of the peaking must not only explain the strong anisotropy, but also the large variation in anisotropy which is observed. This was indeed a strong point of the Fermi theory. If we can no longer ascribe the variation in anisotropy to different impact parameters, we must attribute the fluctuations in the angular distribution to the nature of the interaction itself. For this reason we believe that Heisenberg's explanation of anisotropy (wave coherence and a flat interaction zone) is not satisfactory. It does lead to strong anisotropy, but it cannot explain, so far as we can see, strongly varying anisotropy.

It seems to us that the best hope for an explanation of the angular distribution in extreme energy stars lies, after all, in assuming a cascade process and renouncing the idea that the jets are generated in a single act.

We are grateful to Professor W. Heitler for various illuminating discussions on the interpretation of high-energy events. Professor E. Fermi has very kindly sent us some comment on a draft of this work; his remarks have enabled us to clarify, we hope, the issue involved.

Our thanks are due Professor E. Schrödinger for guidance and instruction throughout the work and also for his patient help with the formulation of the paper.

One of us (F.C.R.) is indebted to the Governing Board of the Dublin Institute for Advanced Studies for a scholarship.

APPENDIX

We briefly indicate one of the difficulties the conception of independent zones meets with if applied to nucleons.

The interaction volume has the depth $s=R/\xi$, with $\xi=E/Mc^2$. The volume of one zone must be of order of magnitude s^3. The number of zones must be of order of magnitude ξ^3. Thus, with increasing primary energy the number of zones increases more quickly ($\propto\xi^3$) than the energy itself ($\propto\xi$), and the energy deposited in one zone must *decrease*. Therefore, the higher the energy, the less it seems justified to use statistical arguments if they are to refer to a single zone. For suitably high energies ($\xi\geq 10^3$, $E'\geq 10^{15}ev$), one is led to the picture that in most of the zones nothing at all happens, while in some of them one single outgoing particle appears. Such a picture, while not necessarily wrong, is yet quite different from what one would expect for "strong coupling" interactions.

[11] In Fermi's notation.

The Production of Charged Photomesons from Helium. Hydrogen-Helium Ratios. II

M. J. JAKOBSON,* A. G. SCHULZ,† and R. S. WHITE
Radiation Laboratory, Department of Physics, University of California, Berkeley, California

(Received April 17, 1953)

A study similar to that made by the same authors on hydrogen and deuterium has been made of charged photomesons produced from helium. Measurements were made at the three angles of 45°, 90°, and 135°. π^+ mesons were detected by scintillation counters and delayed coincidence detection. π^+ and π^- mesons were detected with Ilford C2-200μ nuclear emulsions. The π^-/π^+ ratios are 0.99 ± 0.15, 1.07 ± 0.17, and 0.91 ± 0.13 for angles of 45°, 90°, and 135°, respectively. The total cross section for π^+ meson production is $4.8\pm1.0\times10^{-29}$ cm^2 proton^{-1} Q^{-1} for helium as compared to $10.3\pm2.1\times10^{-29}$ for hydrogen. This indicates that a proton in helium is about one half as effective as a free proton for the photoproduction of π^+ mesons. A comparison is made of the π^+ meson production from hydrogen, deuterium, helium, and carbon.

I. INTRODUCTION

PART I[43] presents data for the reactions

$$\gamma+n\rightarrow\pi^-+p \quad (1)$$

$$\gamma+p\rightarrow\pi^++n \quad (2)$$

when the nucleons involved are either free or weakly bound. This paper presents data for reactions (1) and (2) when the production nucleons are strongly bound in the helium nucleus. Experiments on carbon and other elements[1–12,44] have indicated that (1) and (2) decrease as $A^{-\frac{1}{3}}$ for bound nucleons. Experiments on the ratio of (1) to (2) have indicated that the ratio is quite dependent on the nucleus containing the nucleons.[3,8,12,44,45]

The present paper presents the ratio of (1) to (2) for helium as well as the ratios of the cross sections of hydrogen, deuterium, helium, and carbon. The carbon data is that of Peterson, Gilbert, and White.[3]

II. EXPERIMENTAL PROCEDURE

The study was made by bombarding the gas target described in I with the 318 ± 10-Mev bremsstrahlung "spread out" beam from the Berkeley electron synchrotron. The target was filled with helium to a pressure of 140 atmospheres at liquid nitrogen temperature. The density of the gas was calculated from the Beattie-Bridgeman equation of state. The constants in the equation of state have been evaluated by Akin.[46] The error in the number of nuclei/cm^3, as evaluated by this method, is estimated to be less than 5 percent.

The target and collimators were aligned by means of a transit. Photographs of the beam confirmed the fact that the target was aligned. As in the preceding experiment, mesons produced in the gas target were channeled by means of uranium collimators at the nominal angles of 45°, 90°, and 135°. Lead absorbers were used to degrade the energy of the mesons. Those in the proper energy interval stopped and were detected either in nuclear emulsions or in scintillation counters. The emulsions were used to obtain π^-/π^+ ratios, the 45° energy distribution, and the absolute cross sections. The counters were used to obtain the π^+ meson spectra. The minimum meson energy detected was about 30 Mev at 90° and 35 Mev at 135° and 45°. This minimum energy was limited primarily by the energy loss of the mesons in the target.

Operation of the counters has been described in I. The emulsions were exposed and the counter data was taken in one long run. The nuclear emulsions were exposed for 3.8×10^{12} equivalent quanta. The helium-hydrogen ratios were obtained by changing the gasses cyclicly. The cyclic interchange reduced error caused by drift in monitoring and detection.

The uncertainty in the relative photon beam integration is about 2 percent. The absolute beam integration is uncertain to the order of 20 percent.

Bombardment of the empty target indicated that the number of mesons produced by the target chamber and collimator system was negligible. This was verified by the fact that the number of σ endings found in emulsions exposed to hydrogen was less than 2 percent

TABLE I. Minus-plus ratio of π mesons from helium

Angle	π-meson energy (Mev)	Ratio	Ratio (alternate method listed in I)
45°+17°	39±9	1.33±0.33	1.22±0.38
−15°	72±8	0.76±0.18	0.78±0.22
	101±7	1.20±0.34	1.10±0.35
	128±7	0.73±0.30	0.55±0.27
(mean)		0.99±0.15	0.92±0.16
90°±16°	34±10	1.30±0.22	1.36±0.38
	53±8	0.89±0.20	0.99±0.27
(mean)		1.07±0.17	1.21±0.24
135°+15°	57±7	0.90±0.14	0.90±0.17
−17°	72±6	0.93±0.31	0.85±0.34
(mean)		0.91±0.13	0.88±0.14
All angles (mean)		0.98±0.08	0.96±0.10

* Now at the Department of Physics, University of Washington, Seattle, Washington.

† Now at the Applied Physics Laboratory, John Hopkins University, Silver Spring, Maryland.

[43] White, Jakobson, and Schulz, Phys. Rev. **88**, 836 (1952); hereafter referred to as I. *Note*: Reference numbers 1 through 42 refer to references listed in Part I.

[44] R. M. Littauer and D. Walker, Phys. Rev. **86**, 838 (1952).

[45] J. C. Carrothers, Ph.D. thesis, University of California, 1952 (unpublished).

[46] S. W. Akin, Trans. Am. Soc. Mech. Engrs. **72**, 751 (1950).

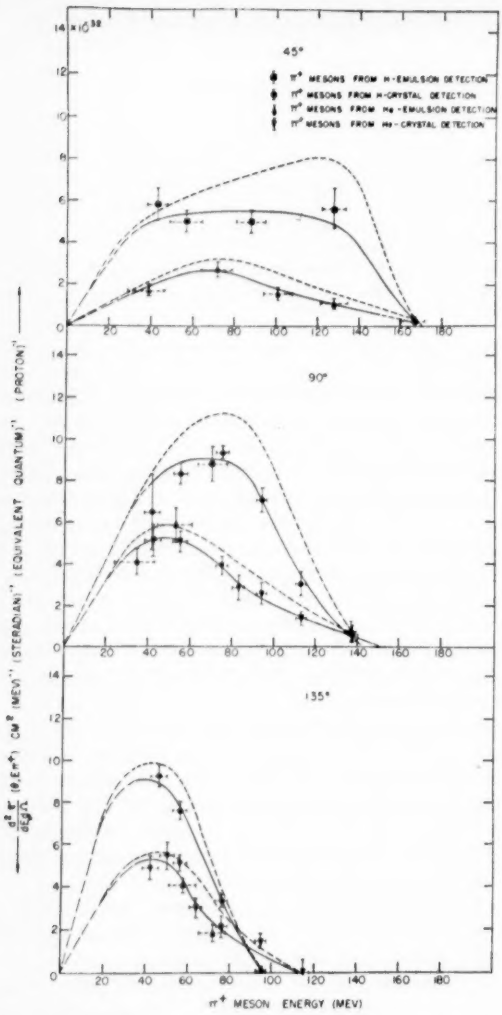

FIG. 1. Energy spectra in the laboratory system for π^+ mesons from helium and hydrogen. The extrapolation to zero meson energy is for the purpose of integration. The dashed curves include the correction for nuclear interaction in the absorbers. Standard deviations are indicated.

of the π-μ endings. The total volume of emulsion scanned for helium was 0.5 cm^3. Cross checks indicated that the efficiency of the scanners was better than 90 percent. (See I.)

Corrections were applied to the data for (1) multiple scattering of the mesons in the absorbers, (2) decays in flight, (3) penetration of the collimating edges, and (4) absorption and scattering of the mesons in the target and absorbers. A plot of these correction factors is given in I. Figures 1, 2, 3, and 4 show the data before and after the correction is included for nuclear interaction.

III. RESULTS OF THE EXPERIMENT

A. π^-/π^+ Ratios

The ratio of π^- to π^+ mesons produced in the target can be expressed in terms of the σ stars and π-μ decays observed in the emulsions. From the data of Adelman and Jones,[35] the number of σ stars observed is 73 percent of the number of π^- mesons stopping in the emulsion. The number of π-μ decays observed is equal to the number of π^+-mesons stopping in the emulsion.[47] By assuming that equal numbers of π^- and π^+ mesons are lost in transit from the target to the emulsions by decay[48] and interaction,[37,49] the π^-/π^+ ratio is simply $[\pi^-/\pi^+]=[1.37\sigma]/[\pi\text{-}\mu]$.

An upper limit for the π^-/π^+ ratio for hydrogen of two percent can be obtained from the fact that 5σ and 301π-μ events were observed in emulsions exposed to hydrogen. It is most probable that these σ events are due to π^- production in the target walls or the collimation system.

250σ, 351π-μ, and 485ρ events were observed in the total volume of emulsion scanned for helium. Table I lists the ratios for the individual angles and energies. The uncertainties listed here and in subsequent data are standard deviations. Within statistics, the ratio is independent of the meson angle and energy. A ratio of approximately one is in agreement with experimental ratios for deuterium, carbon, and other low Z nuclei with equal numbers of neutrons and protons.[3,44,45]

Theoretical calculations have been made for the ratio of the free nucleon reactions (1) and (2) by Brueckner[36] and Watson.[50] In order to make a comparison with helium, the free nucleon calculations would have to be modified for coulombic effects and nuclear binding. These effects can be assumed small, since the π^-/π^+ ratios for deuterium and helium agree within experimental error. Theories which neglect the recoil nucleon current lead to a minus-plus ratio of about one.[50] The fact that the π^-/π^+ ratios for deuterium and carbon are approximately one indicates this is to some extent justified and the interaction of the photon is primarily through the meson currents. As a consequence of this, one would expect $d\sigma(\gamma+p\rightarrow\pi^0+p')=d\sigma(\gamma+n\rightarrow\pi^0+n')$. Recent experimental evidence indicates this is the case.[51]

B. Cross Sections for Helium

1. *Energy Distribution*

The energy distribution for π^+ mesons per equivalent quantum Q are plotted in Fig. 1 for the three production

[47] F. M. Smith, Phys. Rev. **81**, 897 (1951). H. L. Friedman and J. Rainwater, Phys. Rev. **84**, 684 (1951).
[48] Durbin, Loar, and Havens, Phys. Rev. **88**, 179 (1952).
[49] Martin, Anderson, and Yodh, Phys. Rev. **85**, 486 (1952). K. J. Button, Phys. Rev. **88**, 956 (1952). D. Stork, Bull. Am. Phys. Soc. **27**, No. 6, 16 (1952).
[50] K. M. Watson, Phys. Rev. **85**, 852 (1952).
[51] G. Cocconi and A. Silverman, Phys. Rev. **88**, 1230 (1952).

angles of 45°, 90°, and 135°. Data are shown for both helium and hydrogen. The hydrogen cross sections, although published in I, are included to provide a standard for comparison. Figure 2 presents the π^- distribution from helium at 45°. Smooth curves have been drawn through the data and extrapolated to zero meson energy for the purpose of integration. As indicated in I, the angular resolution is about $\pm 16°$. The tails at higher meson energies which indicate mesons of energies higher than those permitted by conservation of energy and momentum for hydrogen at an angle $\bar{\theta}$ are due to mesons allowed through the collimating systems from angles smaller than $\bar{\theta}$.

2. *Differential and Total Cross Sections*

The differential cross sections for helium and hydrogen are presented in Fig. 3. The cross sections were obtained by numerical integration of the data of Fig. 1 and are dependent upon the extrapolation to zero meson energy. The data indicates the peak of the angular distribution lies between 45° and 135°.

The total cross section per proton of helium per Q was obtained from the curves in Fig. 3 by integrating over angles. This requires an extrapolation over angles not measured. Since the solid angle becomes zero at 0° and 180°, the error resulting from this extrapolation should be small. The total cross section for helium for

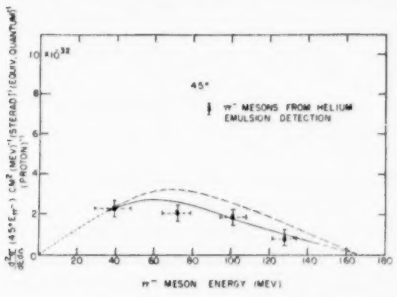

FIG. 2. π^- energy spectra from helium. Standard deviations are indicated.

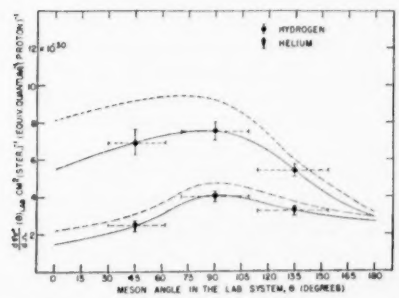

FIG. 3. Differential sections per Q per proton in the laboratory system for π^+ mesons from helium and hydrogen. The smooth curve was drawn for the purpose of integration. The dashed curves include the correction for nuclear interaction in the absorbers. Standard deviations are indicated.

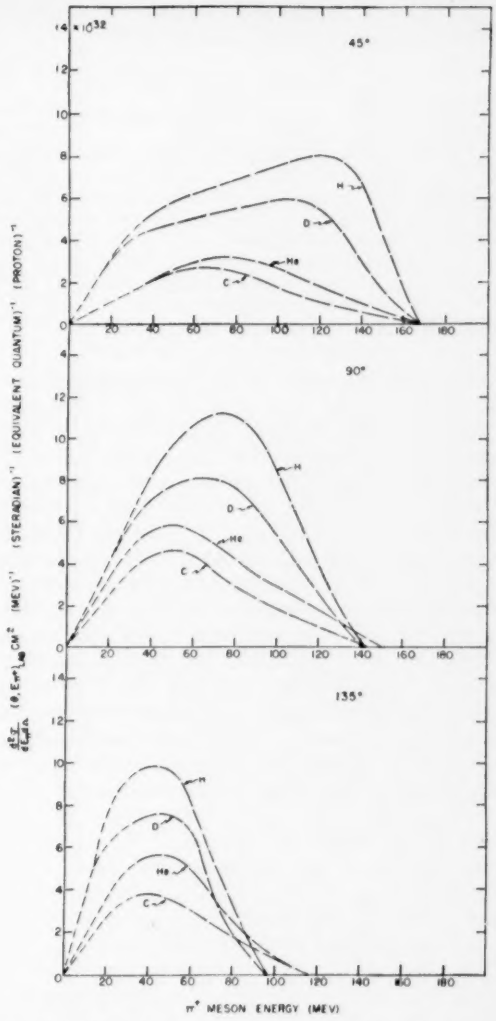

FIG. 4. A plot of the π^+ energy spectra for hydrogen, deuterium, helium, and carbon. The carbon data is from Peterson, Gilbert, and White (see reference 3). The correction for nuclear interaction in the absorbers has been included. The extrapolation to zero meson energy is for the purpose of integration.

π^+ production is

$$\sigma = 4.8 \pm 1.0 \times 10^{-29} \text{ cm}^2 \text{ proton}^{-1} Q^{-1}.$$

This includes a correction of 20 percent for nuclear interaction in the absorbers. The uncertainty listed is that of the absolute beam integration.

C. Comparison of π^+ Production from Hydrogen, Deuterium, Helium, and Carbon

The π^+ energy spectra for hydrogen, deuterium, helium, and carbon are presented in Fig. 4. The cross sections plotted are per proton. The carbon data is from Peterson, Gilbert, and White.[3] The spectra for

TABLE II. π^+ meson cross sections for hydrogen, deuterium, helium, and carbon.[a,b]

Element	$(d\sigma/d\Omega)$ cm²(steradian)$^{-1}Q^{-1}$(proton)$^{-1}$			σ_T cm²Q^{-1}(proton)$^{-1}$
	$45°{}^{+17°}_{-15°}$	$90°\pm16°$	$135°{}^{+15°}_{-17°}$	
Hydrogen[c]	$9.2\pm0.9\times10^{-30}$	$9.3\pm0.6\times10^{-30}$	$6.0\pm0.4\times10^{-30}$	$10.3\pm0.3\times10^{-29}$
Deuterium[c]	6.7 ± 0.7	7.1 ± 0.5	4.6 ± 0.3	7.7 ± 0.3
Helium[c]	3.1 ± 0.3	4.7 ± 0.4	3.8 ± 0.3	4.8 ± 0.2
Carbon[c]	2.6 ± 0.4[a]	3.5 ± 0.3[a]	2.5 ± 0.3[a]	3.8 ± 0.3[a]
Ratio D/H	0.73 ± 0.08	0.76 ± 0.05	0.76 ± 0.06	0.75 ± 0.03
Ratio He/H	0.34 ± 0.05	0.51 ± 0.05	0.63 ± 0.06	0.47 ± 0.04
Ratio C/H	0.28 ± 0.11	0.38 ± 0.15	0.42 ± 0.16	0.36 ± 0.14

[a] Carbon data from Peterson, Gilbert, and White, Phys. Rev. **81**, 1003 (1951).
[b] All data are corrected for nuclear interaction in the absorbers.
[c] In addition to the above standard deviations (except for the ratios), there is an uncertainty of 20 percent in the absolute values of H, D, and He and an uncertainty of 40 percent for C due to beam monitoring.

H, D, and He were obtained with identical geometry. The carbon spectra were obtained with a geometry constructed about a small spherical source with an angular resolution of the detectors of about $\pm7°$.

The ratios of the cross sections for π^+ production, D/H, He/H, and C/H, as obtained from the energy spectra, are tabulated in Table II. The ratios D/H and He/H are dependent only on the relative beam monitoring which has been checked to be accurate to ±2 percent over short periods of time. The ratio C/H is uncertain because of relative beam monitoring over a long period of time. As a check that the beam monitoring had remained fairly constant, the C/H ratios obtained by Mozley[7] were compared with appropriate ratios from the spectra of Fig. 4 and found to be in agreement. A comparison with the C/H data of Steinberger and Bishop[4] gave similar agreement.

It is apparent from the spectra of Fig. 4 that the peaks of the energy distributions of He and C are shifted slightly to lower meson energies relative to the peak of hydrogen. The He/H and C/H ratios listed in Table II indicate the cross sections are reduced more at the angle 45° than at the angle 135°.

The principle reduction in cross sections from the free nucleon reactions (1) and (2) for bound nucleons is due to (a) nuclear binding, (b) exclusion effects, and (c) meson reabsorption. D/H ratios have been considered by a number of authors.[13–19,52] As indicated in I, the D/H ratio is in qualitative agreement with the phenomenological theory.

In He and C the effect of (a) and (b) is to reduce the phase space available for the nucleons in the final state. This reduction is more pronounced when a large portion of the photon momentum is carried away by the meson, leaving the nucleons with little momentum. This then would reduce the cross sections more at small meson angles than at large angles, as is observed. At a given angle, the effect of nuclear binding would be to shift the peak of the meson energy distribution from He and C to a lower energy relative to the meson spectra from free nucleons. At a low Z such as helium, the meson reabsorption (c) should be small compared to the effect of (a) and (b).

[52] H. Feshbach and M. Lax, Phys. Rev. **88**, 509 (1952).

IV. CONCLUSIONS

The most important conclusions of this experiment are:

(1) The minus-plus ratio for helium is close to unity and, within statistics, independent of the angle and energy of the π mesons. This, combined with the fact that the ratio for deuterium is very similar, provides evidence that the recoil nucleon current does not contribute appreciably to photomeson production.

(2) The upper limit for the π^- production cross section from hydrogen is 2 percent of the π^+ cross section.

(3) A proton in helium is essentially one half as effective as a free proton for the photoproduction of π^+ mesons.

(4) The reduction in cross sections for the bound nucleons of helium and carbon is less at backward angles. The peaks of the π^+ energy spectra produced from He and C by 318-Mev bremsstrahlung are shifted to lower energies with respect to the free proton case.

(5) The total cross sections for π^+ production from H, D, He, and C all follow an approximate $A^{\frac{2}{3}}$ dependence. Agreement of the D/H ratios with the phenomenological theory indicate that this dependence is not due to reabsorption of mesons but is due principally to the binding energy and exclusion effects which provide a reduction in cross section such as to approximate an $A^{\frac{2}{3}}$ curve per nucleus for low Z.

Our sincere thanks go to Professor Owen Chamberlain and Professor E. M. McMillan for guidance during the course of this work. We also wish to thank Dr. Barkas and co-workers for suggestions as well as use of the facilities of the Radiation Laboratory Film Program, and the entire synchrotron crew for help in carrying out the bombardments.

Photoneutron Production Excitation Functions to 320 Mev

LAWRENCE W. JONES* AND KENT M. TERWILLIGER*
Radiation Laboratory, Department of Physics, University of California, Berkeley, California
(Received April 15, 1953)

Photoneutron yields from eleven elements were obtained from bremsstrahlung of maximum energy 13.5 to 320 Mev with the reaction, $Cu^{63}(\gamma, n)Cu^{62}$, as a monitor. The yield data were analyzed by a photon difference method to give the excitation functions for photoneutron production. Most of these excitation functions showed the typical resonance shape in the 20-Mev region, a low but finite "tail" to about 80 Mev and a large rise from there to 320 Mev. With the use of a calculated neutron multiplicity $\int_0^\infty \sigma dE$ for tantalum was found to be 5.1 Mev-barns, somewhat higher than $\int_0^\infty \sigma dE$ predicted by Levinger and Bethe for the electric dipole interaction. The rise above 80 Mev is probably due to mesonic interactions. At the meson threshold, with data for the neutron multiplicity from π^- absorption, the photon absorption cross section was found to obey the relation,

$$\sigma = 0.32A^{1.3} \times 10^{-28} \text{ cm}^2.$$

INTRODUCTION

KNOWLEDGE of the magnitude and energy dependence of photonuclear absorption cross sections is basic to the understanding of the interaction of high-energy quanta with nuclei. Previous experimenters,[1–7] measuring induced activities, have shown that the excitation functions for (γ,n) and (γ,p) reactions have large peaks in the neighborhood of 20 Mev. The magnitude of the photonuclear interaction above this 20-Mev region is difficult to measure quantitatively by induced activities because of the limited number and small yield of those reactions which can be measured by this technique. The method of detecting emitted neutrons, however, sums over all the individual reactions to give a fairly quantitative picture of the high-energy photon absorption process.

An indication that large photonuclear interactions involving neutron production exist above the low-energy peaks was found by Eyges[8] from an analysis of an experiment of the authors on neutron production from 320-Mev bremsstrahlung.[9] Kerst[10] also has noted larger neutron yields from 320- than from 22-Mev bremsstrahlung. These results prompted the present determination of photoneutron production cross sections from the region of the low-energy peaks to 320-Mev.

Neutron yields from eleven elements were obtained from 13.5 to 70 Mev with the 70-Mev General Electric synchrotron of the University of California Hospital in San Francisco, and from 80 to 320 Mev with the 320-Mev synchrotron of the University of California Radiation Laboratory at Berkeley. The neutron yields were taken relative to the yield of the $Cu^{63}(\gamma,n)Cu^{62}$ reaction at each bremsstrahlung energy, and cross sections for neutron production were deduced by a photon difference method.

EXPERIMENTAL PROCEDURE

The neutrons were detected at 90 degrees to the beam with a boron trifluoride proportional counter in a long counter geometry of paraffin.[11] The active volume of the counter was 10 inches long, and the paraffin cylinder in which it was embedded was 15 inches long by 8 inches in diameter. This type of counter is reported to be uniformly sensitive to neutrons of from 100 kev to 5 Mev entering parallel to its axis, its sensitivity dropping to 67 percent of maximum for 14- and 18-

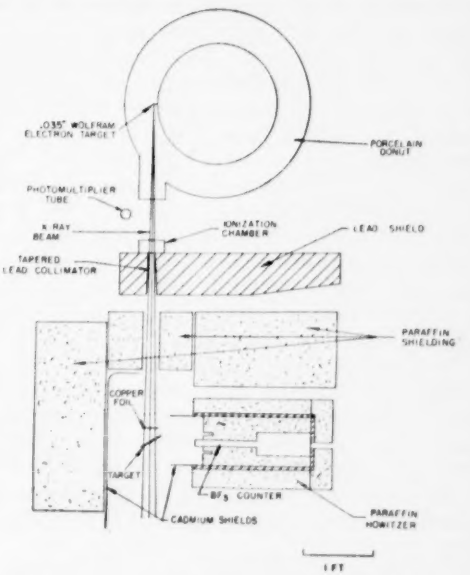

FIG. 1. Schematic overhead layout of the 70-Mev synchrotron and the experimental arrangement.

* Now at the Department of Physics, University of Michigan, Ann Arbor, Michigan.

[1] G. C. Baldwin and G. S. Klaiber, Phys. Rev. **73**, 1156 (1948).
[2] G. M. Almy and B. C. Diven, Phys. Rev. **80**, 407 (1950).
[3] Johns, Katz, Douglas, and Haslam, Phys. Rev. **80**, 1062 (1950).
[4] J. Halpern and A. K. Mann, Phys. Rev. **84**, 840 (1951).
[5] R. Sagane, Phys. Rev. **85**, 926 (1952).
[6] Haslam, Johns, and Horsley, Phys. Rev. **82**, 270 (1951).
[7] L. Katz and A. Cameron, Phys. Rev. **84**, 1115 (1951).
[8] L. Eyges, Phys. Rev. **86**, 325 (1952).
[9] Terwilliger, Jones, and Jarmie, Phys. Rev. **82**, 820 (1951).
[10] D. W. Kerst, private communication.
[11] A. O. Hanson and J. L. McKibben, Phys. Rev. **72**, 673 (1947).

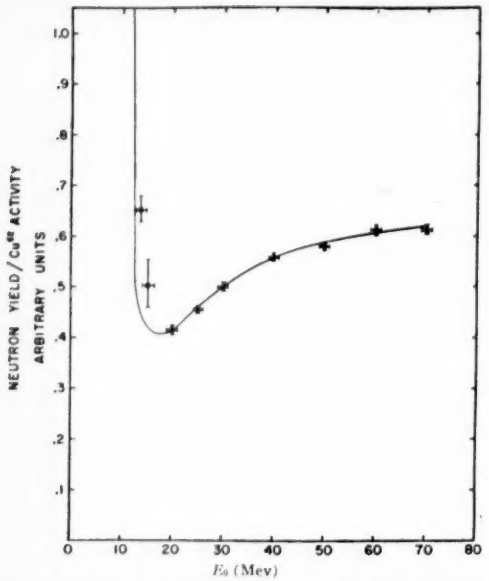

FIG. 2. Neutron yields from copper per unit of induced copper activity as a function of E_0, the maximum bremsstrahlung energy.

Mev neutrons.[12] This response is altered to favor lower energy neutrons by the proximity of the target to the face of the counter.

With both synchrotrons the beam pulse was short, less than 20 microseconds. However, neutron diffusion in the paraffin, with a half-life of about 175 microseconds, made possible high neutron counting rates without large corrections for counter dead time. The counter pulses were clipped to 0.5 microsecond to minimize the pileup of neutrons and of electrons associated with the beam pulse. Electron pulses were biased out by operating the neutron counter at the low-voltage end of its plateau.

A plan view of the experimental arrangement used with the 70-Mev synchrotron is shown in Fig. 1. The synchrotron beam was collimated by a tapered rectangular aperture in an eight-inch lead wall in front of the synchrotron. In addition, 1000 pounds of paraffin faced with cadmium were used to shield the counter from the neutron background.

The beam monitor, a 0.016-inch copper foil, was bombarded along with each target element at each energy. The bombardments were of two-minute duration except at 13.5 Mev where they were four minutes. After a two-minute transfer time, the positron activity of the copper foil was counted for two minutes in a reproducible geometry by a 1B85 Victoreen thyrode Geiger counter.

Similar geometry and procedure were used with the Berkeley synchrotron. In this case at each energy the copper foil method was used to calibrate the beam integrating ionization chamber. Then this chamber was used as a secondary monitor for the neutron counting. This calibration was repeated every time the energy setting was changed. Here the copper foils were bombarded for ten minutes and, after a two-minute changeover, counted for ten minutes.

The beam energy was varied on both machines by maintaining the magnet current pulse at its maximum value and turning off the accelerating voltage before peak magnetic field. The electron energy at the time of radiation was found from the time of rf turnoff with the assumption of a sinusoidally varying magnetic field. The energy at maximum field was determined at Berkeley by Powell *et al.*[13] and by magnetic field measurements at San Francisco. The thresholds for the $C^{12}(\gamma,n)$ and $Cu^{63}(\gamma,n)$ reactions were determined with the San Francisco machine and agreed with known values.

DATA AND ERRORS

Neutron yields per unit of induced copper activity were obtained for each element with the synchrotron of the University of California Hospital for values of maximum bremsstrahlung energy of 13.5, 20, 25, 30, 40, 50, 60, and 70 Mev. Some points were also obtained at 15 and 19 Mev. Elements studied were the natural isotopic mixtures of Be, C, Al, Fe, Cu, Mo, Ag, Ta, W, Pb, and U. The targets were from 0.2 to 0.7 shower unit thick.

With the Berkeley synchrotron, data were taken for values of maximum bremsstrahlung energy of 80, 120, 160, 200, 240, 280, and 320 Mev. Neutron yields were obtained there with similar targets of the above eleven elements.

70-Mev Synchrotron

Each data point above 20 Mev was taken twice and the two yield values were averaged. A typical set of yield data, that for Cu, taken with the San Francisco machine, is shown in Fig. 2. The errors shown are the probable errors and the energy uncertainty which was about one Mev. The yield curve drawn results in a smooth cross section curve (see section on Analysis). The sharp rise of the curve at low energies is due to the lower (γ,n) threshold in Cu^{65}(9.7 Mev) than in the monitoring isotope, Cu^{63}(10.9 Mev).

Twenty-three bombardments of Cu with 40-Mev bremsstrahlung were spaced throughout the experiment to obtain an estimate of the probable error due to random fluctuations of experimental conditions. The results of these runs and the counting errors indicated that all elements except C and Al had probable errors under 1.6 percent for energies 20 Mev and over, and under 8 percent for lower energies. The C and Al errors were under 4 percent at energies above 20 Mev.

Effects such as anisotropy in neutron angular distri-

[12] Barschall, Rosen, Taschek, and Williams, Revs. Modern Phys. **74**, 1 (1951).

[13] Powell, Hartsough, and Hill, Phys. Rev. **81**, 213 (1951).

bution, neutron scattering within the target, and scattering of neutrons from the beam into the counter could cause systematic errors in the yield points above 25 Mev of as much as 15 percent for Be, C, and Al, but under 2 percent for the higher Z elements.

320-Mev Synchrotron

The yield data for Cu from the Berkeley synchrotron are shown in Fig. 3. Since the counting rates were low, no correction was made for neutron counter dead time, which could cause errors of at most 3 percent. Most data points were repeated to insure consistency. These checks and the counting statistics indicated that all data points had probable errors of less than 2 percent. The systematic errors are similar to those for the San Francisco synchrotron.

The maximum energy of the Berkeley synchrotron is 322 ± 6 Mev.[13] It has been taken here as nominally 320 Mev. The relative energy settings were accurate to about 6 Mev.

BREMSSTRAHLUNG

Fundamental to the determination of excitation functions is knowledge of the bremsstrahlung spectra. The spectra used in this experiment for the analysis were obtained by graphically interpolating the representative curves of the basic Bethe-Heitler formula which Rossi and Greisen[14] have plotted for lead, with screening taken into account. Each spectrum is for a thin target and is an average over all angles of the outgoing photons. Schiff[15] has shown that in a finite target multiple scattering causes the spectrum to be independent of angle, so that this integrated Bethe-Heitler spectrum is satisfactory for any fraction of the beam used. Although the Bethe-Heitler formula was derived with the use of the Born approximation, which is not valid for heavy elements, Davies and Bethe[16] have recently shown that the correction term is an additive constant, which would change the magnitude of the bremsstrahlung cross section about 10 percent and the shape considerably less. The bremsstrahlung shape predicted by the Bethe-Heitler formula has been experimentally verified at high energies to within 10 percent.[13,17–19]

Eyges[20] has extended the Bethe-Heitler expression to thick targets by calculating the corrections due to cascade showering. Considering only first-order correction terms, he obtained

$$V\phi'(E_0,E)=V\phi(E_0,E)[1-\tfrac{1}{2}T\{\sigma(E)-\ln(1-V)\}], \quad (1)$$

where ϕ is the Bethe-Heitler spectrum, ϕ' is the corrected spectrum, $V=E/E_0$, E_0 the energy of the incident electrons, E the energy of the radiated quantum, T the target thickness expressed in radiation lengths, and $\sigma(E)$ the cross section of the target material per radiation length for absorption of quanta of energy E.

If the x-ray beam is collimated, Eyges' correction must be modified because of multiple scattering in the target. The average target thickness traversed by an electron with its direction of motion inside the cone subtended by the collimator was used as an effective target thickness $\bar{t}$. From the Williams scattering expression[21] $\bar{t}$ was found to be[22]

$$\bar{t}=\alpha\int_0^T\frac{e^{-\alpha/t}}{t}dt+(1-e^{-\alpha/T})T, \quad (2)$$

where

$$\alpha=\frac{1}{2N}\left(\frac{\theta E_0}{9.2Ze^2}\right)^2,$$

θ is the half-angle subtended by the collimator from the target, and N is the target density in atoms cm^{-2} per radiation length.

The equation for the final corrected spectrum is

$$V\phi'(E_0,E)=V\phi(E_0,E)\times[1-(T-\tfrac{1}{2}\bar{t})\sigma(E)+\tfrac{1}{2}\bar{t}\ln(1-V)]. \quad (3)$$

In both the Berkeley and San Francisco machines the electrons were assumed to traverse the entire target and not just graze the edge. The agreement of the

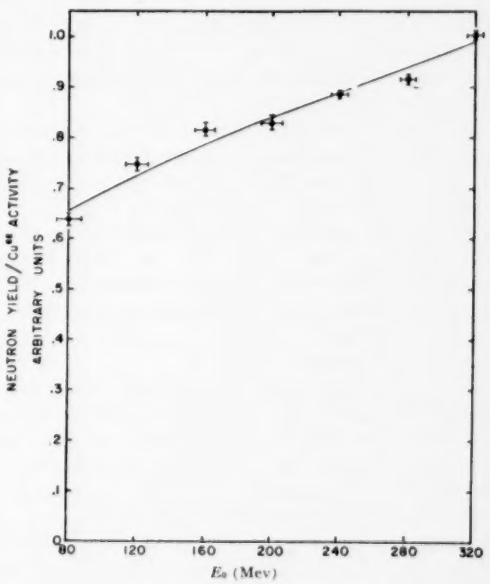

FIG. 3. Neutron yields from copper per unit of induced copper activity as a function of E_0, the maximum bremsstrahlung energy.

[14] B. Rossi and K. Greisen, Revs. Modern Phys. **13**, 253 (1941).
[15] L. I. Schiff, Phys. Rev. **70**, 87 (1946).
[16] H. Davies and H. A. Bethe, Phys. Rev. **87**, 156 (1952).
[17] J. W. Dewire and L. A. Beach, Phys. Rev. **83**, 476 (1951).
[18] R. H. Stokes, Phys. Rev. **84**, 991 (1951).
[19] C. R. Emigh, Phys. Rev. **86**, 1028 (1952).
[20] L. Eyges, Phys. Rev. **81**, 981 (1951).
[21] E. J. Williams, Phys. Rev. **58**, 292 (1940).
[22] L. W. Jones, University of California Radiation Laboratory Report UCRL-1916 (unpublished).

angular spread measurements of Rosengren[23] on the Berkeley synchrotron and Adams[24] on the San Francisco synchrotron with those of Lanzl and Hanson[25] using an externally deflected electron beam indicates that this assumption is justified.

For the energy ranges used, the shape correction to the Bethe-Heitler spectrum was at most 20 percent for the Berkeley 320-Mev synchrotron with a 0.020-inch Pt target and 10 percent for the San Francisco 70-Mev synchrotron with a 0.035-inch W target. Errors in the assumed bremsstrahlung shape affect the derived cross sections linearly.

This calculated bremsstrahlung spectrum is that falling on the front face of the target element being bombarded. The spectrum was further corrected for photon absorption in each neutron target, the correction amounting to as much as 20 percent for some of the targets for high-energy quanta. The targets were not so thick, however, that significant numbers of neutrons were produced from secondary shower quanta.

ANALYSIS

The neutron yields represented the relative values of the ratio

$$\int_0^{E_0} \sigma_n(E)\phi(E_0, E)dE \Big/ \int_0^{E_0} \sigma_c(E)\phi(E_0, E)dE, \quad (4)$$

where $\sigma_n(E)$ is the cross section for neutron production and $\sigma_c(E)$ is the cross section for the $Cu^{63}(\gamma, n)Cu^{62}$ reaction. The excitation functions $\sigma_n(E)$ were calculated from the yield curves by a photon difference method, which has been discussed in the literature.[26] This method will be described briefly here.

The difference in yields for two successive values of E_0 is due to the difference in their bremsstrahlung spectra $\phi(E_0, E)$, the difference occurring over energies below as well as between the two E_0. Therefore, the yield difference must be corrected for the effect of the lower-energy quanta before $\bar{\sigma}_n$, the average cross section for the energy interval, can be obtained. Since each correction term is dependent on the lower-energy cross sections, the $\bar{\sigma}_n$ must be calculated in sequence from low to high energy.

The relative magnitude of each $\phi(E_0, E)$ was calculated from the measured activity of the copper foil monitor with the use of $\sigma_c(E)$. This excitation function has been measured out to 24 Mev by a number of investigators[2,3,27] who monitored their bremsstrahlung with either a calibrated Lucite ion chamber or a pair spectrometer. The shape of their curves agreed to about 10 percent. The curve obtained by Johns *et al.*[3] was used in this analysis. Although their work did not extend above 24 Mev, it indicated that at that energy the cross section was very small. In this analysis the cross section was assumed to be zero above 24 Mev.

The energy increments chosen for the analysis varied from 2.5 to 10 Mev below 70 Mev and were 40 Mev wide above 80 Mev. Above 30 Mev, the yield corrections were usually less than one-half of the yield differences. The $\bar{\sigma}_n$ were assigned to the energy corresponding to the middle of the interval. Since the cross sections are interdependent, errors as small as 2 percent in the chosen yield curves result in oscillations in the successive cross sections. These oscillations were smoothed by successive trail yield curves through the measured yield points. This procedure produces an excitation function which is averaged over neighboring intervals.

The first data point was at 13.5 Mev, and the shapes of the cross-section curves up to that energy were estimated from thresholds and the work of other experimenters on (γ,n) excitation functions. These estimated curves were normalized to the calculated excitation functions from the neutron yield at 13.5 Mev.

The excitation functions obtained on the 70-Mev San Francisco synchrotron were normalized to those obtained on the 320-Mev Berkeley synchrotron through the Berkeley yield at 80 Mev. A change of about 1 percent in the ends of the yield curves was required to match the cross-section curves from the two machines.

The variation with Z of the magnitudes of the cross-section curves was determined independently on the two machines through the relative neutron yields. The results from the two machines agreed to within 5 percent; the mean was used for the final relative magnitudes.

The absolute magnitude of the cross-section curves was determined from the results of a previous experiment[9] by the authors on the neutron yields produced by bombardment with 320-Mev bremsstrahlung. The beam was calibrated by Blocker, Kenney, and Panofsky.[28] The neutron yields were determined by comparison with an Argonne calibrated radium-beryllium source. The absolute magnitude calibration is estimated to be accurate to 15 percent.

RESULTS

The calculated excitation functions are presented in Figs. 4 and 5. The dashed sections represent the estimated curves below 13.5 Mev. Where possible, known cross-section curves by other authors are included on the same graph. The shape and magnitude of the beryllium cross section up to 7 Mev was taken from the theoretical work of Guth and Mullin.[29]

The neutron production cross section $\sigma_n(E)$ used in this experiment may be represented as

$$\sigma_n(E) = \sigma_a(E) \int_0^E \nu(E, \epsilon)P(\epsilon)d\epsilon, \quad (5)$$

[23] J. W. Rosengren, private communication.
[24] G. D. Adams, private communication.
[25] L. H. Lanzl and A. O. Hanson, Phys. Rev. **83**, 959 (1951).
[26] R. Sagane, Phys. Rev. **84**, 586 (1951).
[27] V. E. Krohn, Jr., and E. F. Shrader, Phys. Rev. **87**, 685 (1952).
[28] Blocker, Kenney, and Panofsky, Phys. Rev. **79**, 419 (1950).
[29] E. Guth and C. J. Mullin, Phys. Rev. **76**, 234 (1949).

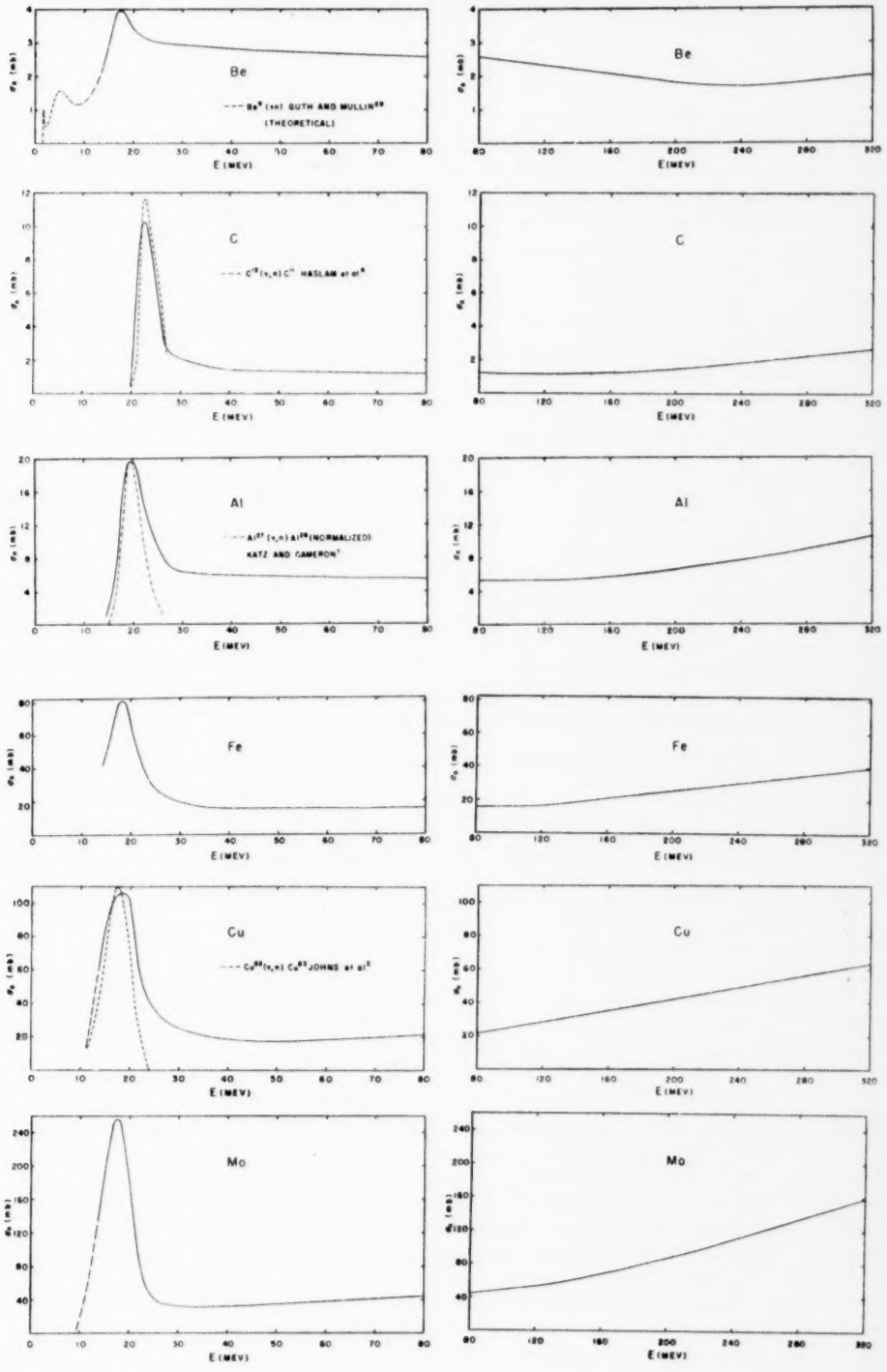

FIG. 4. Curves of cross sections for photoneutron production σ_n as a function of quantum energy E. The curves are extimated up to 13.5 Mev, the first data point.

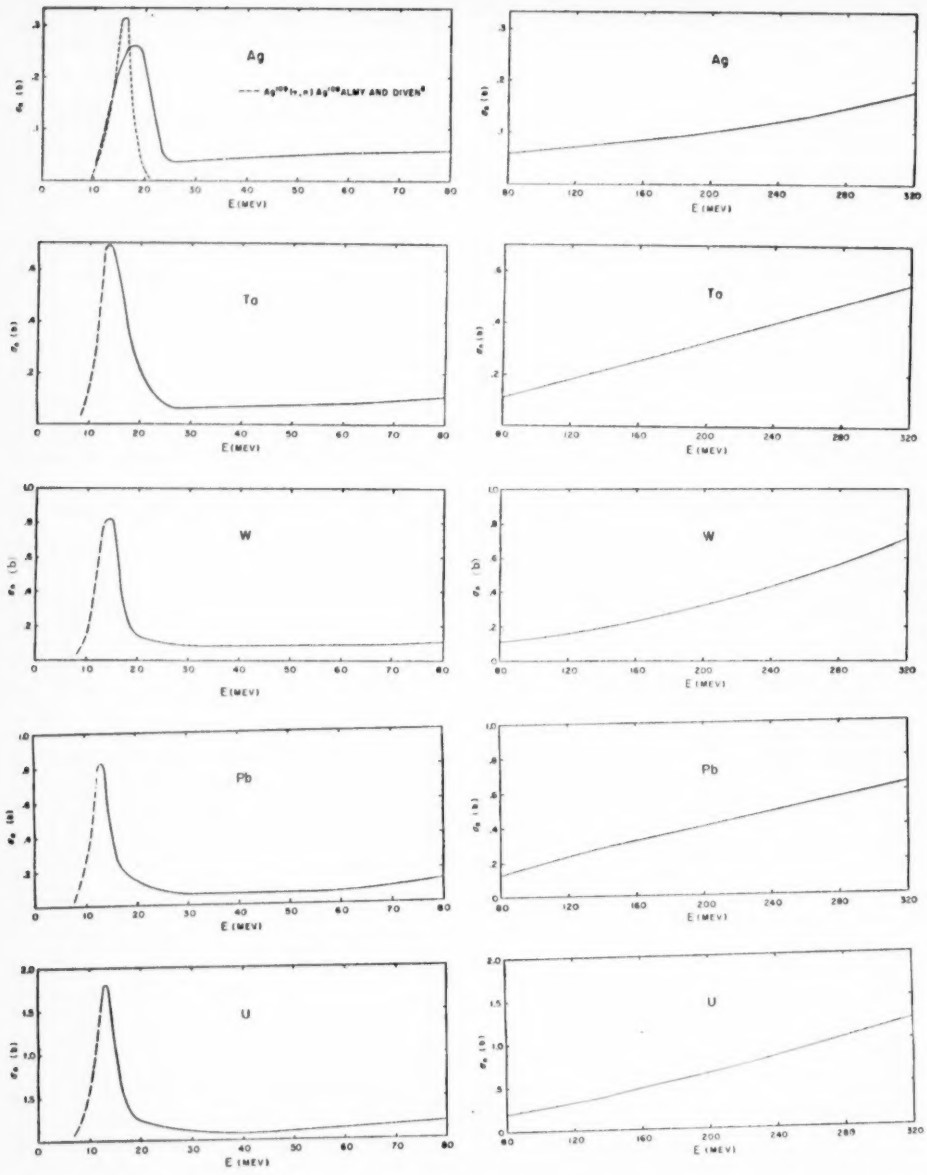

FIG. 5. Curves of cross sections for photoneutron production σ_n as a function of quantum energy E. The curves are estimated up to 13.5 Mev, the first data point.

where $\sigma_a(E)$ is the photon absorption cross section; $\nu(E, \epsilon)$, the probability that a nucleus, having absorbed a photon of energy E, will emit a neutron of energy ϵ; and $P(\epsilon)$, the relative detection efficiency of the neutron counter for neutrons of energy ϵ, being unity for Ra-Be neutrons. If $P(\epsilon)$ were constant, $\sigma_n(E)$ would represent $\sigma_a(E)\nu(E)$, where $\nu(E)$ is the total neutron multiplicity for a nucleus excited to energy E. Since, however, $P(\epsilon)$ for 17-Mev neutrons is less than 0.67 of its value for low-energy neutrons, $\sigma_n(E)$ actually represents only a minimum value of $\sigma_a(E)\nu(E)$.

Some estimate of the failure of the assumption that the counter is uniformly sensitive to all neutrons produced may be made by comparison of the neutron yield data[9] with the photoproton data of Levinthal and Silverman[30] and Keck.[31] It is assumed here that the numbers of neutrons and protons of energies well above the Coulomb barrier are approximately equal, and the validity of this assumption is indicated by rough measurements of Keck and Kerst.[32] From this comparison, a maximum of 20 percent of the photoneutrons

[30] C. Levinthal and A. Silverman, Phys. Rev. **82**, 822 (1951).
[31] J. C. Keck, Phys. Rev. **85**, 410 (1952).
[32] Kerst, Koester, Penfold, and Smith, Phys. Rev. **87**, 197 (1952).

from carbon are undetected when carbon is bombarded by 320-Mev bremsstrahlung. The corresponding figure for copper is 6 percent, and it is less for heavier elements.

The same data, together with those of Kikuchi[33] and the present experiment, can be used to estimate the yield of the $Cu^{63}(\gamma,n)Cu^{62}$ reaction due to quanta of energy greater than 24 Mev. The maximum error in beam monitoring from neglecting a possible high energy "tail" to this reaction is 3 percent. An experimental check on the Berkeley synchrotron in the region from 80 to 320 Mev showed that the ratio of neutron yields from deuterium to copper foil activity was consistent with assuming no tail to the $Cu^{63}(\gamma,n)Cu^{62}$ reaction.

The reaction $Cu^{65}(\gamma,3n)Cu^{62}$ would have the same effect on the monitor activity as such a tail, and it is estimated from the work of Strauch[34] on the reaction $Zn^{66}(\gamma,3n)Zn^{63}$, that the monitoring error can be as much as 3 percent from this source.

Because of these monitoring errors, the small cross sections over the range of 30 to 80 Mev might be low by amounts varying from 15 percent for the lowest Z elements to 100 percent for the highest. In this region the cross sections may have additional errors of from 20 percent for the low Z elements to 50 percent for the highest, because of the experimental errors in the yield points.

The relative areas under the low-energy peaks of the excitation functions are accurate to 10 percent, with the exception of those for Be, C, and Al which are accurate to 20 percent. The same accuracy applies to the areas under the cross-section curves from 80 to 320 Mev. The lower detection efficiency for high-energy neutrons has been neglected in these estimates. The actual curve shape in the low- and high-energy regions is probably good only to 30 percent. The absolute magnitude factor was mentioned in the previous section to be accurate to 15 percent.

DISCUSSION

The shapes and magnitudes of the low-energy peaks agree very well with the (γ,n) cross sections measured by other experimenters using induced activities. The decrease in total neutron cross sections following the peaks is not as fast as that of the (γ,n) curves, indicating the presence of some competing reactions. The drop is sufficient, except in the case of beryllium, to indicate that the photon-absorption cross section has a resonance-like shape in the 20-Mev region.

The areas under the cross-section peaks to 27.5 Mev, plotted in Fig. 6, fit the equation

$$\int_0^{27.5} \sigma_n(E)dE = 5.2\times10^{-4}A^{1.8} \text{ Mev-barns}. \quad (6)$$

Beryllium is a factor of two above the curve, probably as a result of its loosely bound neutron. The integrated cross section predicted by the Levinger and Bethe[35] theory for electric dipole excitation is given by

$$\int_0^{\infty} \sigma_a(E)dE = 0.06\frac{NZ}{A}(1+0.8x) \text{ Mev-barns}, \quad (7)$$

where x is the fraction of neutron-proton exchange force. The experimental increase in the integrated cross section with $A^{1.8}$ rather than A is interpreted as being due to the neutron multiplicity, as Levinger and Bethe have pointed out.[36]

The curves show that the photon-absorption cross section is appreciable in the energy region from 25 to 100 Mev. This is also indicated by the work of others.[34,37]

To obtain a numerical value for the photon-absorption cross section from the neutron production cross section, the number of neutrons emitted must be known. Levinger and Bethe[36] have shown that above the $3n$ threshold the neutron multiplicity can be expressed as the ratio of the excitation energy E to the average energy required to emit a neutron E_b, and they have calculated E_b for five elements from copper to uranium. By drawing a smooth curve through their values and a value obtained for aluminum by assuming equal proton and neutron emission, E_b was estimated for all targets in this experiment from aluminum to uranium. The photon-absorption cross sections at 45 Mev were calculated for these elements by dividing the total neutron cross section by the neutron multiplicity. The elements from Al to Ag fit the linear equation

$$\sigma_a(45) = 0.13A\times10^{-27} \text{ cm}^2, \quad (8)$$

while the four high Z elements lie an average of about 30 percent below this line, well within the estimated error for this region due to error in the assumed monitor reaction cross section.

Levinger and Bethe have calculated the neutron multiplicity curve for Ta^{181}, a single isotope. The photon-absorption cross section curve for Ta^{181} as shown in Fig. 7 was found by dividing the neutron production cross-section curve by their calculated neutron multiplicity. The photon-absorption cross section at low energy from a similar experiment by Whalin and Hanson[38] is shown on the same figure.

The area under the photon-absorption curve for Ta^{181} can be compared with the Levinger and Bethe formula. Levinger and Bethe's theory gives 3.66 Mev-barns for an exchange force fraction one-half, and 4.70 Mev-barns for an exchange force fraction of unity. The experimental integrated cross section is 4.2 Mev-barns to 27.5 Mev and 5.1 Mev-barns to 80 Mev. The absolute accuracy is estimated to be 20 percent. The experimental values are somewhat higher than those predicted by theory.

[33] S. Kikuchi, Phys. Rev. **86**, 41 (1952).
[34] K. Strauch, Phys. Rev. **81**, 973 (1951).
[35] J. S. Levinger and H. A. Bethe, Phys. Rev. **78**, 115 (1950).
[36] J. S. Levinger and H. A. Bethe, Phys. Rev. **85**, 577 (1952).
[37] N. Sugarman and R. Peters, Phys. Rev. **81**, 951 (1951).
[38] E. A. Whalin and A. O. Hanson, Phys. Rev. **89**, 324 (1953).

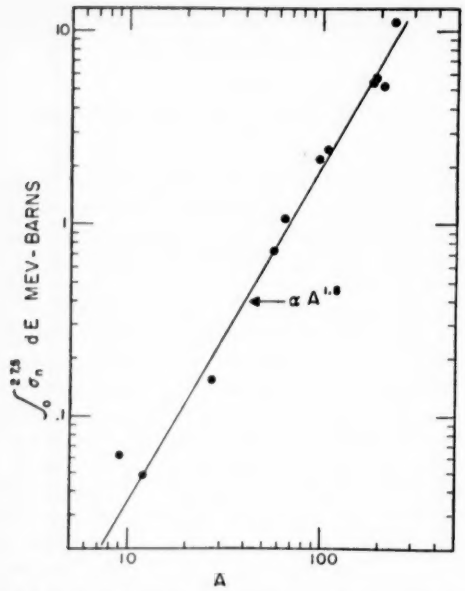

FIG. 6. Values of $\int_0^{27.5}\sigma_n(E)dE$, the integrated cross section for photoneutron production, as a function of atomic weight A.

Above about 80 Mev, most of the neutron production cross sections rise continuously to 320 Mev. The low Z elements fail to do so probably because of the higher energy and limited multiplicity of the emitted neutrons. Levinger and Bethe calculate that it requires an average of 11 Mev to liberate each neutron from Ta^{181} in the region where the statistical model applies, and only neutrons are emitted. At high-excitation energies this is obviously a lower limit. With the use of this figure, however, a lower limit of the photon-absorption cross section curve for Ta^{181} can be obtained. This minimum photon-absorption cross section increases slightly from 80 to 320 Mev, the integrated cross section over that region being about 4 Mev-barns.

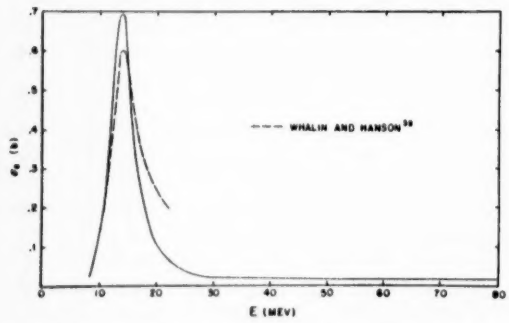

FIG. 7. Cross section for photonuclear absorption in tantalum σ_a as a function of quantum energy E. Calculated from the excitation function for photoneutron production, with the use of the theoretical neutron multiplicity. Also shown are the results of Whalin and Hanson from a similar experiment.

The experimental results at low energy appear to account for the theoretical integrated cross section for electric dipole transitions, while the high-energy results must be due to the same photomesonic interactions responsible for stars, high-energy protons, and real meson production. The cross sections for star production from emulsion nuclei have been found by Miller[39] and Kikuchi[33] to be increasing functions of the photon energy, as is the cross section for photomeson production from hydrogen.[40] These cross sections increase more rapidly with photon energy than the minimum photon-absorption cross section for tantalum obtained in this experiment, but this is at least partially due to the increasing failure of the compound nucleus model at higher energies.

Recent Cornell experiments[41] on neutron production by meson absorption, which used a similar neutron detection system, give an indication of the neutron multiplicity for 140-Mev excitation. The results are given in Table I.

The multiplicity for lead is 30 percent lower than that for bismuth estimated from an extension of Levinger's simplified statistical model. With the use of these multiplicites, photoabsorption cross sections were obtained for those elements for 140-Mev quanta, with Sn being replaced by Ag. These cross sections may be approximately represented by the curve

$$\sigma_a(150)=0.32A^{1.3}\times10^{-28}\text{ cm}^2. \quad (9)$$

The cross sections for photon absorption per nucleon at the meson threshold are comparable in magnitude to those for star production[39] and meson production from hydrogen and deuterium at 200 Mev.[40]

The theory of Huddlestone and Lepore[42] for photodisintegration of deuterium predicts an increase with energy in photon-absorption cross section below the meson threshold, because of photon interaction with the exchange currents. The values of σ_n/E for Ta, W, Pb, and U all show such an increase from 80 to 150 Mev,

TABLE I. Photon-absorption cross sections at 140 Mev. $\sigma_n(150)$ is the cross section for total neutron production by 140-Mev quanta, $\nu(140)$ the neutron multiplicity obtained from π^- absorption,[41] and $\sigma_a(140)$ the cross section for nuclear absorption of 140-Mev quanta.

Element	C	Al	Ag	Pb
$\sigma_n(140)\times10^{-27}$ cm^2	1.2	5.4	80	278
$\nu(140)$	1.6	2.0	6.1[a]	9.3
$\sigma_a(140)=\sigma_n/\nu\times10^{-27}$ cm^2	0.75	2.7	13	30
$\sigma_a/A\times10^{-28}$ cm^2	0.62	1.0	1.2	1.4

[a] Value obtained for Sn.

[39] R. D. Miller, Phys. Rev. **82**, 260 (1951).
[40] K. A. Brueckner and K. M. Watson, Phys. Rev. **86**, 923 (1952).
[41] V. Cocconi Tongiorgi and D. A. Edwards, Phys. Rev. **88**, 145 (1952).
[42] R. H. Huddlestone and J. V. Lepore, Phys. Rev. **87**, 207 (1952).

and presumably the cross sections for photon absorption increase at even a greater rate.

In the energy region from 50 Mev to the meson threshold, the photonuclear interaction may be a combination of photoelectric effect decreasing with energy and a photomesonic effect increasing with energy.

The authors wish to express their gratitude to Professor A. C. Helmholz for his counsel and interest throughout the course of this work and to Mr. George MacFarland and the crew of the Berkeley synchrotron for their cooperation and efficient handling of the machine. Particular thanks are due Dr. G. D. Adams and Dr. R. S. Stone of the University of California Hospital in San Francisco for making their synchrotron available for this work, and to Dr. Adams and his crew for operating the machine during the runs.

PHYSICAL REVIEW VOLUME 91, NUMBER 3 AUGUST 1, 1953

Collision Lengths of Neutral, Penetrating-Shower-Producing Cosmic Radiation in Light and Heavy Water*

DAROL FROMAN, *Los Alamos Scientific Laboratory, Los Alamos, New Mexico*

AND

JAMES KENNEY AND VICTOR H. REGENER, *Department of Physics, University of New Mexico, Albuquerque, New Mexico*

(Received April 6, 1953)

The collision length, L_c, of neutral penetrating-shower-producing cosmic radiation incident through a reinforced concrete roof of thickness 25 g/cm² at Los Alamos, New Mexico, altitude 2280 meters, was measured in light and heavy water. The values obtained were, for H_2O, $L_c = 113 \pm 10$ g/cm² and for D_2O, $L_c = 123 \pm 10$ g/cm². Equal masses of oxygen per unit area in the H_2O and D_2O absorbers were used for a determination of the difference between the collision cross sections of the deuteron and of the proton for the incident particles. The value obtained for this difference was $\sigma_D - \sigma_P = 13 \pm 15$ mb.

I. INTRODUCTION

DURING the past few years much attention has been given hard-shower production by both charged and neutral high-energy cosmic-ray particles. The general purpose of work in this field is to gain an understanding of high-energy nucleon-nucleus and nucleon-nucleon interactions involving, among other phenomena, π-meson production. One of the quantities frequently measured is the collision length, which may be defined as the mean thickness of material, measured in g/cm², through which an incident particle travels before it undergoes a nuclear interaction.

The collision length L_c for a radiation which produces penetrating showers[1] is given by $L_c = (m/\sigma)$ g/cm², where, for a molecular substance, m is the mass of a molecule of the substance and σ is the sum of the effective collision cross sections for the production of penetrating showers in the nuclei composing the molecule.

It has been found that for materials of high atomic mass such as lead, the observed collision length agrees well with the calculated geometric collision length[2] $L_g = m/\sigma_g$. For materials of low atomic mass, the observed collision length is usually greater than the geometric, the difference sometimes being attributed to a "transparency" of nuclei. It is clear, however, that as the atomic number decreases the geometric collision length becomes less meaningful because it is based upon the concept of spherical nuclei of constant, uniform density.

The production of the π mesons of a penetrating shower has been described by two different processes. The plural process, proposed by Heitler and Janossy[3] assumes that the incident particle produces one meson in each collision with a nucleon and that a shower of several mesons is built up through successive collisions with several different nucleons in the same nucleus. The multiple process, proposed by Heisenberg[4] and applied by Fermi[5] in statistical calculations of shower parameters, supposes that several mesons, and possibly some nucleons, are produced in an encounter of the incident particle with a single nucleon. Lewis[6] has summarized the present state of the theory of multiple meson production by collisions of nucleons.

It has now become fairly clear that the multiple process does occur in nature and that multiplications of a shower produced in a first collision with a nucleon can take place within the struck nucleus. Thus, the best description appears to be a kind of plural process

* This document is based on work performed at the Los Alamos Scientific Laboratory of the University of California operated under the auspices of the U. S. Atomic Energy Commission.

[1] For a discussion of this subject and references to the literature, see Bruno Rossi, *High Energy Particles* (Prentice-Hall, Inc., New York, 1952).

[2] In this paper, $\sigma_g = \pi r_0^2 A^{\frac{1}{3}}$, where A is the atomic mass number and $r_0 = 1.37 \times 10^{-13}$ cm.

[3] W. Heitler and L. Janossy, Proc. Phys. Soc. (London) **A62**, 669 (1949).

[4] W. Heisenberg, Z. Physik **126**, 569 (1949).

[5] E. Fermi, Prog. Theoret. Phys. **5**, 570 (1950).

[6] H. W. Lewis, Revs. Modern Phys. **24**, 241 (1952).

not limited to the production of a single meson in each collision with a nucleon, but in which the multiple process is a proper description for each successive collision within the nucleus.

Cosmic-ray particles which produce nuclear interactions are called "N rays." At appreciable depths in the atmosphere, the N rays include primarily protons, neutrons and π mesons. Because of the very short half-lives of the π mesons, most of the N rays observed are protons and neutrons. Certainly the flux of neutral π mesons is very small because of the short mean life, estimated by Carlson, Hooper, and King[7] as about 3×10^{-14} second. This is also true with respect to V_0 particles whose mean life has been estimated as being of the order of 10^{-10} second.[8] Therefore, neutral N rays are believed to consist almost exclusively of high-energy neutrons.

In the measurement of collision lengths of charged N rays by counter arrangements it is difficult to arrive at unambiguous results. However, in 1940 Rossi and Regener[9] devised a coincidence-anticoincidence system which can be used for unambiguous measurements of the collision length of neutral N rays. Adaptations of this system have been used by several experimenters,[10–14] and equipment similar to that used by Pomeroy[12] and Rollosson[13] was used in this experiment.

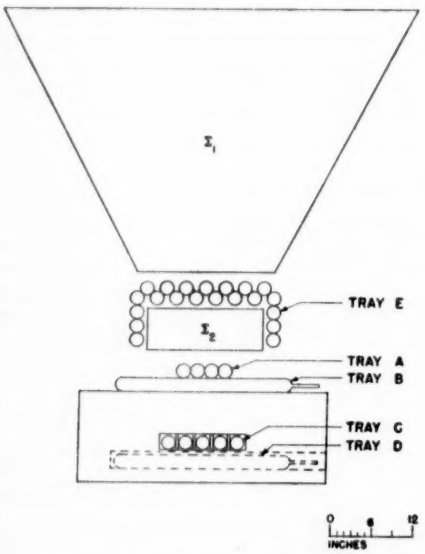

FIG. 1. End view of the apparatus.

[7] Carlson, Hooper, and King, Phil. Mag. **41**, 701 (1950).
[8] Fretter, May, and Nakada, Phys. Rev. **89**, 168 (1953); Leighton, Wanlass, and Anderson, Phys. Rev. **89**, 148 (1953).
[9] Bruno Rossi and Victor H. Regener, Phys. Rev. **58**, 837 (1940).
[10] L. Janossy and G. D. Rochester, Proc. Roy. Soc. (London) **A182**, 180 (1943).
[11] Walker, Walker, and Greisen, Phys. Rev. **80**, 546 (1950).
[12] David Pomeroy, Phys. Rev. **84**, 77 (1951).
[13] G. W. Rollosson, Phys. Rev. **87**, 71 (1952).
[14] H. W. Boehmer and H. S. Bridge, Phys. Rev. **85**, 863 (1952).

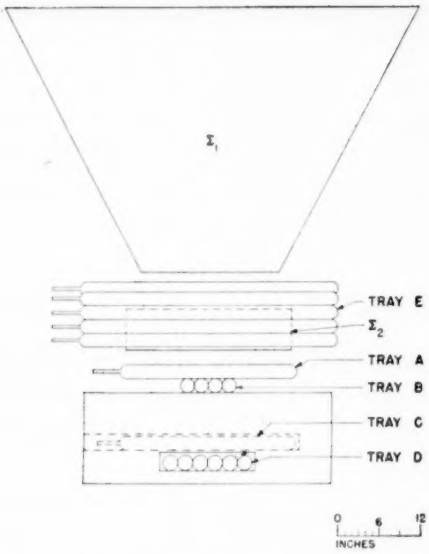

FIG. 2. Side view of the apparatus.

The purpose of this experiment was to measure the collision lengths of neutral N rays (predominantly neutrons) in light and heavy water and to find the difference in the collision cross sections of the deuteron and the proton for these rays.

II. EXPERIMENTAL APPARATUS AND PROCEDURE

Two elevations of the Geiger counter and absorber arrangement are shown in Figs. 1 and 2. All of the equipment below $\sum_1$ was mounted upon a car which could be moved under either of two stainless steel tanks, $\sum_1$, one of which contained H_2O and the other D_2O. The depths of water were adjusted so that the amount of oxygen per cm^2 was the same for both tanks. The two tanks were set up under as nearly identical roof sections as possible, and the positions of the tanks were interchanged twice so that the effect of the slight variation in roof thickness could be eliminated.

The counters were connected to recording equipment in such a manner that counts were recorded when a given counter in tray A and a given counter in tray B were in coincidence with two counters of a certain portion of tray C, and with one counter of a certain portion of tray D, respectively. The choice of those portions of trays C and D which, in combination with given counters in trays A and B contributed to fivefold coincidences, was made in such a way that all straight lines drawn through discharging counters would lie inside $\sum_1$. The requirement for two counters to be discharged in tray C insured that the count represented a shower of at least two ionizing particles, and the thickness of 6 inches of lead between trays B and C insured that recorded showers originating in $\sum_2$ were

made up of penetrating particles. Half-inch lead plates were inserted between adjacent counters in tray C to reduce the registering of local soft showers and knock-on electrons. Except when the background was being counted, $\sum_2$ was filled with lead to a thickness of six inches. Background counts were obtained with this lead removed from $\sum_2$. Fivefold coincidence counts made in this way are designated PS, penetrating showers.

The record of the number of fivefold coincidence counts which appeared under the described conditions, but in anticoincidence with tray E, formed the main portion of the experiment. Events of this type resulted mainly from penetrating showers which orginated in the lead of $\sum_2$ by non-ionizing (neutral) rays. These coincidence-anticoincidence counts are designated NPS.

The equipment was thus designed to record penetrating showers produced in $\sum_2$ by non-ionizing particles which have traversed $\sum_1$ without a nuclear interaction. If the neutral particle had undergone an interaction in $\sum_1$, we assume that it would have been accompanied by charged particles as it reached tray *E*, and the event would not have been recorded as of the NPS type. As the thickness of $\sum_1$ is increased, an exponential decrease in the number of showers produced in $\sum_2$ by non-ionizing primaries is expected. Such an exponential decrease provides a measure of the collision length of the shower-producing radiation in $\sum_1$.

It should be observed that a nuclear collision of the incident neutron in $\sum_1$ might conceivably lead to the transfer of only a small fraction of its energy to ionizing secondaries. These low-energy secondaries might be absorbed in $\sum_1$ before reaching the anticoincidence tray E, and the primary neutron might still be able to produce a penetrating shower in $\sum_2$ and, thus, an NPS count. If this process does happen the magnitude of the effect would certainly be dependent upon the thickness of absorber in $\sum_1$. Thus one could not, in general, expect an exponential decrease of the NPS counts with thickness of absorber in $\sum_1$, and consequently, one could not obtain an unambiguous experimental result for the collision length. However, the data from previous experiments[13–15] performed under similar conditions seem to show an exponential decrease of the NPS rate with thickness in $\sum_1$. This indicates that the primary neutron does not penetrate beyond the distance which is penetrated in $\sum_1$ by its ionizing secondaries. This supports the view that an experiment of the present type does measure the collision length for nuclear interactions of high-energy non-ionizing *N*-rays.

The circuits were arranged in such a way that the discharge of any counter in tray E resulted in the formation of a blocking gate about 100 microseconds long which prevented the recording of any fivefold coincidence on the NPS recorder during the time of this gate. The fivefold coincidence pulse was delayed about 9 microseconds after formation before being fed into the anticoincidence circuit in order to take account of the possibility that a counter in tray E was slow in response. The electronic circuits employed were similar to those used by Pomeroy[12] and by Rollosson,[13] and the counter tubes were of the type described by Regener.[16]

Isotopic analysis of the heavy water showed the hydrogen content to be more than 99 percent deuterium. The correction for the presence of ordinary hydrogen in the heavy water is much less than the relevant statistical errors and it has been neglected. Chemical analyses of the H_2O and D_2O showed the presence of a few parts per million of the more common elements of low and intermediate atomic mass, but the effect of these small amounts of impurity was calculated to be entirely negligible in this experiment. Construction of most of the equipment and preliminary tests were carried out at the Department of Physics of the University of New Mexico. The equipment was then installed at Los Alamos for the duration of the experiment. The elevation was 2280 meters.

Runs, usually of duration about 24 hours each, were made alternately under the tanks containing H_2O and D_2O. The number of penetrating showers PS and NPS and the time were recorded for each run. Similar runs were made with the tanks empty, and some data were taken with fillings of intermediate depth.

Some of the runs were made with lead in position $\sum_2$, some without. A few NPS counts were always observed with no lead in position $\sum_2$. At least some of these arose from showers formed in counter walls and the supports for tray E, and some may have come from wide-angle showers produced in the main lead shield by rays incident at a large zenith angle.

The anticoincidence tray E was not 100 percent efficient. Its inefficiency was measured frequently by moving the equipment away from both tanks, placing tray B above tray E, and connecting two counters in tray C together. Thus single ionizing rays passing through the system could cause counts on the PS recorder but, since these rays would have to pass through tray E, no counts should be recorded on the NPS recorder. However, some NPS counts, arising in part possibly from side showers and accidental coincidences, were always found. The inefficiency ϵ defined as the ratio NPS/PS for this case, was assumed to have the same value during normal operations and this value was used to correct the observed rate of NPS counts. In general, daily checks were made upon the operation of the individual counters and the electronic circuits.

III. CORRECTIONS AND TREATMENT OF DATA

The barometric pressure was recorded and corrections were applied to the data for variations of the pressure from an arbitrary standard value near the mean.

[15] K. Sitte, Phys. Rev. **78**, 714 (1950).

[16] Victor H. Regener, Rev. Sci. Instr. **18**, 267 (1947).

TABLE I. Observed counts and corrections.

No. of runs	Σ_1 in g/cm²	Σ_2	PS counts, obs	NPS counts, obs	Corrections to NPS counts N-S Av	Ineff.	Pressure	NPS corrected
45	85.09, D_2O	6 in. Pb	35 210	2459	−4.05	−444.0	−8.86	2002.1
16	85.09, D_2O	0	15 824	386	−1.06	−199.3	+1.07	186.7
34	76.6, H_2O	6 in. Pb	28 035	1962	−8.19	−354.0	−15.89	1583.9
15	76.6, H_2O	0	17 733	400	− 2.09	−223.5	−0.10	174.3
11	0	6 in. Pb	9868	1068	+14.00	−124.5	−35.24	922.3
8	0	0	8487	292	+5.11	−106.9	−8.85	181.4
4	37.6, H_2O	6 in. Pb	3332	293	−5.12	−42.0	−7.32	238.6
4	37.6, H_2O	0	4863	112	−1.96	−61.3	−3.26	45.5
1	50.8, H_2O	6 in. Pb	688	65	−1.14	−8.7	...[a]	55.2
1	50.8, H_2O	0	610	14	−0.24	−7.7	...[a]	6.1
1	27.0, H_2O	6 in. Pb	484	44	−0.77	−6.1	...[a]	37.1
1	27.0, H_2O	0	1094	27	−0.47	−13.8	...[a]	12.7

[a] The barometric pressure was not read, but the correction is negligible compared with the statistical error for a small number of counts.

The absorption of the roof was not quite the same for the two tank positions, designated N (north) and S (south), and the times spent with the equipment in each position for each arrangement of $\sum_1$ and $\sum_2$ were usually somewhat different. A weighted average of the ratio of the NPS counting rates in the two positions for the same absorber conditions showed that the counting rate in the north position exceeded that in the south position by 3.5 percent. That is, each differed from the average by 1.75 percent. Let t_N and t_S be the times spent in positions N and S, respectively, and let N_N and N_S be the corresponding numbers of NPS counts in the two positions. Then, in order to reduce the total number of counts to the basis of average position, the following corrections were applied:

$$+0.0175N_S(t_S-t_N)/t_S, \text{ if } t_S>t_N,$$

and

$$-0.0175N_N(t_N-t_S)/t_N, \text{ if } t_N>t_S.$$

All data were reduced to average values for the N and S positions by applying the correction terms given above.

A correction for inefficiency ϵ of tray E was made by subtracting the quantity $\epsilon\times$PS from the observed number of NPS counts for each configuration of the absorbers $\sum_1$ and $\sum_2$.

The absorption length of neutral, penetrating-shower-producing rays in air is[12] 115 g/cm² = 3.33 inches Hg. Thus the intensity of incident radiation at pressure p (measured in inches Hg) is given by

$$I_p=I_{p0}\exp[-(p-p_0)/3.33]=I_{p0}\exp(-0.3\Delta p)\approx I_{p0}(1-0.3\Delta p),$$

where I_{p0} is the intensity expected at an arbitrary pressure p_0, chosen near the mean pressure, and $\Delta p=p-p_0$. Thus, in order to bring the results to a common barometric pressure basis, a correction of $0.3\Delta p\times$NPS was added to the NPS count for each run after the correction for inefficiency of tray E had been made.

The background NPS counts, obtained with the lead removed from $\sum_2$, were corrected in the same manner as the other NPS counts. As will be seen later, the background counting rate varies, within experimental error, at the same exponential rate with depth of water in $\sum_1$ as does the NPS counting rate when lead is present at $\sum_2$. Thus, for calculations of collision lengths it does not matter, except for the accumulation of errors, whether or not the background rate is subtracted from the otherwise corrected NPS rates.

Let σ_P, σ_D, and σ_O be the collision cross sections of the hydrogen, deuterium, and oxygen nuclei, respectively, for neutral N rays, and let L_{c1} and L_{c2} be the collision lengths for these rays in light and heavy water, respectively. Let R_0, R_1, and R_2 be the corrected rates of production of penetrating showers in $\sum_2$ by neutral N rays with $\sum_1=0$ (the empty steel tank), with $\sum_1=x_1$ g/cm² H_2O and with $\sum_1=x_2$ g/cm² D_2O, respectively. Let m_1 and m_2 be the molecular masses of light and heavy water, respectively. Then, if the number of penetrating showers produced in $\sum_2$ by neutral N rays is a decreasing exponential function of the depth of water in $\sum_1$,

$$R_1=R_0\exp(-x_1/L_{c1}),$$

and (1)

$$R_2=R_0\exp(-x_2/L_{c2}),$$

where

$$L_{c1}=m_1/(2\sigma_P+\sigma_O),$$

and (2)

$$L_{c2}=m_2/(2\sigma_D+\sigma_O).$$

From the four equations above,

$$R_1/R_2=\exp(x_2/L_{c2}-x_1/L_{c1})=\exp\{2[(x_2\sigma_D/m_2)-(x_1\sigma_P/m_1)]+[(x_2/m_2)-(x_1/m_1)]\sigma_O\}. \quad (3)$$

If the depths of water are chosen such that

$$x_2/m_2=x_1/m_1, \quad (4)$$

as was done for a part of this experiment, (3) reduces to $R_1/R_2=\exp[2x_1(\sigma_D-\sigma_P)/m_1]$, from which

$$\sigma_D-\sigma_P=(m_1/2x_1)\ln(R_1/R_2). \quad (5)$$

From (1) and (2) we get

$$L_{c1}=x_1/\ln(R_0/R_1), \quad (6)$$

$$L_{c2}=x_2/\ln(R_0/R_2). \quad (7)$$

Equations (5), (6), and (7) were used to calculate the results of this experiment.

IV. EXPERIMENTAL DATA

The inefficiency of tray E was determined in 24 runs which resulted in a total of 80 851 PS counts and 1020 NPS counts. This gives $\epsilon = 1020/80851 = 0.0126 \pm 0.0004$. Table I gives the magnitudes of the various corrections and the corrected values of the total NPS counts.

Table II gives the total time of running under each condition, the corrected total NPS counts, and the values of the corrected counting rates. All errors quoted represent standard deviations.

The uncorrected NPS counting rates obtained in individual runs under six different combinations of $\sum_1$ and $\sum_2$, and the individual values of the inefficiency, are plotted against the date of observation in Fig. 3. Some of the deviations of the individual points from the mean values are reduced when corrections are made for the barometric pressure and for the position (north or south) of the apparatus. However, it is clear from observation of Fig. 3 that no large change in the sensitivity of the detection equipment took place during the period of the experiment.

The logarithms of the corrected NPS counting rates observed with $\sum_1$ composed of light water are plotted in Fig. 4 against depth of water for $\sum_2 = 0$ and for $\sum_2 = 6$ inches Pb. Both curves have the same slope within experimental error. One interpretation of this fact is that most of the background counts ($\sum_2 = 0$) arise from rays incident through $\sum_1$ and thus are subject to absorption by the water in it.

Examination of the data in Table II shows that, for $\sum_2 = 6$ inches Pb, the counting rate with $\sum_1 = 85.09$ g/cm² of D_2O is slightly, but insignificantly, less than that with $\sum_1 = 76.6$ g/cm² of H_2O. These depths of

TABLE II. Rates of production of penetrating showers by neutral N rays.

No. of runs	Σ_1 in g/cm²	Σ_2	Total time in hours	Corrected total NPS counts	NPS counting rate in hr^{-1}
45	85.09, D_2O	6 in. Pb	1097.8	2002.1±50	1.825±0.045
16	85.09, D_2O	0	364	186.7±20	0.512±0.055
34	76.6, H_2O	6 in. Pb	855.6	1583.9±44	1.851±0.051
15	76.6, H_2O	0	392.4	174.3±20	0.445±0.051
11	0	6 in. Pb	253.7	922.3±34	3.64 ±0.13
8	0	0	193.4	181.4±17	0.94 ±0.09
4	37.6, H_2O	6 in. Pb	94.7	238.6±17	2.52 ±0.18
4	37.6, H_2O	0	96.4	45.5±10.6	0.47 ±0.11
1	50.8, H_2O	6 in. Pb	22	55.2± 8.1	2.51 ±0.37
1	50.8, H_2O	0	15	6.1± 3.8	0.41 ±0.25
1	27.0, H_2O	6 in. Pb	14	37.1± 6.6	2.65 ±0.47
1	27.0, H_2O	0	24	12.7± 5.2	0.53 ±0.22

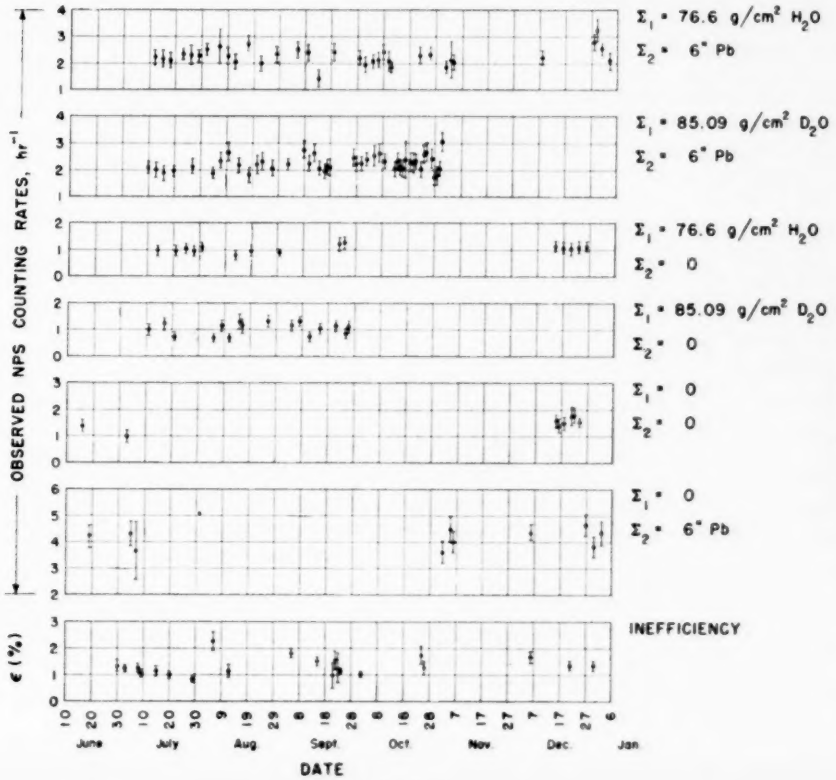

FIG. 3. Uncorrected counting rates and inefficiency as observed throughout the period of experimentation.

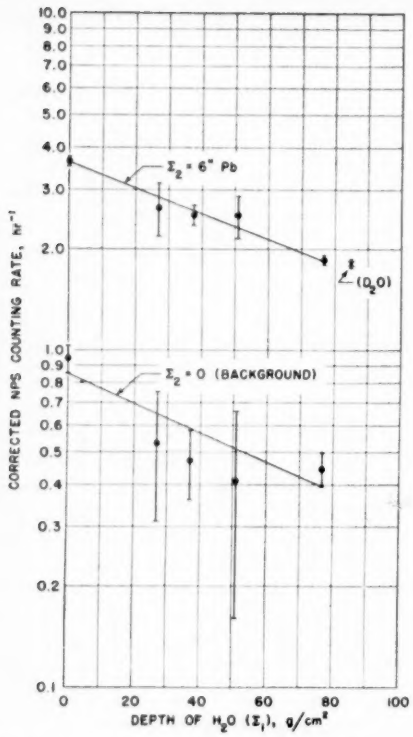

FIG. 4. Absorption of neutral N rays by light water.

heavy and light water contain the same amounts of oxygen per unit area, i.e., they satisfy Eq. (4). Thus the small difference in these counting rates has the right sign to correspond with the cross section of the deuteron being greater than that of the proton, even though this difference is less than its statistical error. The difference between the corresponding background rates ($\sum_2=0$) has the opposite sign, but it is also less than its statistical error. There is no obvious reason for the background to be less when $\sum_1$ is filled with light water than when it is filled with the corresponding depth of heavy water and, possibly, the reverse might be expected. If the true background with light water is equal to or greater than that for heavy water, perhaps the best value of the background for both cases would be the weighted average of the two values given in Table II. This average is 0.477 ± 0.037 count per hour. However, the statistical errors are sufficiently large to include the possibility that the true background values are equal, or even inverted in magnitude, and the value of $\sigma_D-\sigma_P$ has been calculated using the individual background values observed in the experiment.

V. RESULTS

Using the data of Table II, Eq. (5) gives $\sigma_D-\sigma_P=13\pm15$ millibarns. (If the average background rate had been used, as indicated in the preceding paragraph, the result would have been $\sigma_D-\sigma_P=4\pm12$ mb.) Similarly, Eqs. (6) and (7) give the collision length in H_2O, $L_{c1}=113\pm12$ g/cm² and in D_2O, $L_{c2}=123\pm13$ g/cm². If the background values ($\sum_2=0$) are not subtracted from the corrected counting rates, the values of L_{c1} and L_{c2} obtained are the same as above but the calculated standard deviations are ±9 g/cm² in each case. An estimated standard deviation of ±10 g/cm² for each collision length is perhaps a reasonable value. The value of the collision length in H_2O is in reasonable agreement with Rollosson's[13] value of 98 ± 13 g/cm² measured in New Mexico at an altitude of 2770 meters. The geometrical collision lengths are $L_{g1}=61$ g/cm² in H_2O and $L_{g2}=59$ g/cm² in D_2O.

It should be noted that the measured difference of about 13 millibarns between the cross sections of the deuteron and the proton is small compared with $\pi r_0^2=59$ millibarns, the "geometric" cross section of the proton. One might expect the loosely bound deuteron to have a cross section equal to the sum of the proton and neutron cross sections. On this basis $\sigma_D-\sigma_P$ would be a measure of the (n,n) cross section which would be expected to be about the same size as the (n,p) cross section. Thus, it seems reasonable, and consistent with the rather large value obtained for the collision length in water, to assume that the absolute cross sections for penetrating-shower production in hydrogen and deuterium are both small. In fact, a collision length in water as large as 113 g/cm² seems to point to a degree of "transparency" even for the oxygen nucleus.

VI. ACKNOWLEDGMENTS

The authors wish to thank Dr. Charles Metz and his associates at Los Alamos for making the chemical and isotopic analyses of the two types of water used in the experiment. Financial aid to the cosmic-ray program at the Physics Department of the University of New Mexico from the Research Corporation and from the National Science Foundation is gratefully acknowledged.

The Theory of Quantized Fields. II

JULIAN SCHWINGER
Harvard University, Cambridge, Massachusetts
(Received February 19, 1953)

The arguments leading to the formulation of the action principle for a general field are presented. In association with the complete reduction of all numerical matrices into symmetrical and antisymmetrical parts, the general field is decomposed into two sets, which are identified with Bose-Einstein and Fermi-Dirac fields. The spin restriction on the two kinds of fields is inferred from the time reflection invariance requirement. The consistency of the theory is verified in terms of a criterion involving the various generators of infinitesimal transformations. Following a discussion of charged fields, the electromagnetic field is introduced to satisfy the postulate of general gauge invariance. As an aspect of the latter, it is recognized that the electromagnetic field and charged fields are not kinematically independent. After a discussion of the field strength commutation relations, the independent dynamical variables of the electromagnetic field are exhibited in terms of a special gauge.

THE general program of this series[1] is the construction of a theory of quantized fields in terms of a single fundamental dynamical principle. We shall first present a revised account of the developments contained in the initial paper.

THE DYNAMICAL PRINCIPLE

The transformation functions connecting various representations have the two fundamental properties

$$(\alpha'|\gamma')=\int(\alpha'|\beta')d\beta'(\beta'|\gamma'),$$

$$(\alpha'|\beta')^*=(\beta'|\alpha'),$$

where $\int d\beta'$ symbolizes both integration and summation over the eigenvalue spectrum. If $\delta(\alpha'|\beta')$ is any infinitesimal alteration of the transformation function, we may write

$$\delta(\alpha'|\beta')=i(\alpha'|\delta W_{\alpha\beta}|\beta'), \tag{1}$$

which serves as the definition of the infinitesimal operator $\delta W_{\alpha\beta}$. The requirement that any infinitesimal alteration maintain the multiplicative composition law of transformation functions implies an additive composition law for the infinitesimal operators,

$$\delta W_{\alpha\gamma}=\delta W_{\alpha\beta}+\delta W_{\beta\gamma}. \tag{2}$$

If the α and β representations are identical, we infer that

$$\delta W_{\alpha\alpha}=0,$$

which expresses the fixed orthonormality requirements on the eigenvectors of a given representation. On identifying the α and γ representations, we learn that

$$\delta W_{\beta\alpha}=-\delta W_{\alpha\beta}.$$

The second property of transformation functions implies that

$$\begin{aligned}-i(\alpha'|\delta W_{\alpha\beta}|\beta')^*&=-i(\beta'|\delta W_{\alpha\beta}{}^\dagger|\alpha')\\&=i(\beta'|\delta W_{\beta\alpha}|\alpha'),\end{aligned}$$

or

$$\delta W_{\alpha\beta}{}^\dagger=\delta W_{\alpha\beta};$$

the infinitesimal operators $\delta W_{\alpha\beta}$ are Hermitian.

The $\delta W_{\alpha\beta}$ possess another additivity property referring to the composition of two dynamically independent systems. Thus, if I and II designate such systems,

$$(\alpha_{\rm I}'\alpha_{\rm II}'|\beta_{\rm I}'\beta_{\rm II}')=(\alpha_{\rm I}'|\beta_{\rm I}')(\alpha_{\rm II}'|\beta_{\rm II}'),$$

and if $\delta W_{\alpha\beta}{}^{\rm I}$ and $\delta W_{\alpha\beta}{}^{\rm II}$ are the operators characterizing infinitesimal changes of the separate transformation functions, that of the composite system is

$$\delta W_{\alpha\beta}=\delta W_{\alpha\beta}{}^{\rm I}+\delta W_{\alpha\beta}{}^{\rm II}.$$

Infinitesimal alterations of eigenvectors that preserve the orthonormality properties have the form

$$\delta\Psi(\alpha')=-iG_\alpha\Psi(\alpha'),$$
$$\delta\Psi(\alpha')^\dagger=i\Psi(\alpha')^\dagger G_\alpha,$$

where the generator G_α is an infinitesimal Hermitian operator which possesses an additivity property for the composition of dynamically independent systems. If the two eigenvectors of a transformation function are varied independently, the resulting change of the transformation function has the general structure (1), with

$$\delta W_{\alpha\beta}=G_\alpha-G_\beta.$$

The vector

$$\Psi(\alpha')+\delta\Psi(\alpha')=(1-iG_\alpha)\Psi(\alpha'),$$

can be characterized as an eigenvector of the operator set

$$\bar\alpha=(1-iG_\alpha)\alpha(1+iG_\alpha)=\alpha-\delta\alpha,$$

with the eigenvalues α'. Here

$$\delta\alpha=-i[\alpha,G_\alpha].$$

This infinitesimal unitary transformation of the eigenvector $\Psi(\alpha')$ induces a transformation of any operator F such that

$$(\alpha'|F|\alpha'')=(\bar\alpha'|\bar F|\bar\alpha'').$$

[1] J. Schwinger, Phys. Rev. **82**, 914 (1951), Part I.

We write this in the form

$$(\bar{\alpha}'|F|\bar{\alpha}'')-(\alpha'|F|\alpha'')=(\bar{\alpha}'|(F-\bar{F})|\bar{\alpha}''),$$

or, in virtue of the infinitesimal nature of the transformation,

$$\delta(\alpha'|F|\alpha'')=(\alpha'|\delta F|\alpha''),$$

where the left side refers to the change in the eigenvectors for a fixed F, while the right side provides an equivalent variation of the operator F, given by

$$\delta F=F-\bar{F}=-i[F, G_\sigma].$$

If the change consists in the alteration of some parameter τ, upon which the dynamical variables depend, and which may occur explicitly in F, we have

$$\begin{aligned}\bar{F}&=F-(\delta F)_\tau\\&=F+\delta_\tau F-\partial_\tau F,\end{aligned}$$

where $\delta_\tau F$ is the total alteration in F, from which is subtracted $\partial_\tau F$, the change in F associated with the explicit appearance of τ, since the latter cannot be produced by an operator transformation. We thereby obtain the "equation of motion" with respect to the parameter τ,

$$\delta_\tau F=\partial_\tau F+i[F, G_\tau]. \tag{3}$$

For dynamical systems obeying the postulate of local action, complete descriptions are provided by sets of physical quantities, ζ, associated with space-like surfaces, σ. An infinitesimal alteration of the general transformation function $(\zeta_1'\sigma_1|\zeta_2''\sigma_2)$ is characterized by

$$\delta(\zeta_1'\sigma_1|\zeta_2''\sigma_2)=i(\zeta_1'\sigma_1|\delta W_{12}|\zeta_2''\sigma_2). \tag{4}$$

Here the indices 1 and 2 refer both to the choice of complete set of commuting operators ζ, and to the space-like surface σ. We can, in particular, consider transformations between the same set of operators on different surfaces, or between different sets of commuting operators on the same surface, as in

$$\delta(\zeta'\sigma|\bar{\zeta}'\sigma)=i(\zeta'\sigma|\delta W|\bar{\zeta}'\sigma). \tag{5}$$

One type of change of the general transformation function consists in the introduction, independently on σ_1 and on σ_2, of infinitesimal unitary transformations of the operators, including displacements of these surfaces. The transformations will be generated by operators G_1 and G_2, constructed from dynamical variables on σ_1 and σ_2, respectively, and

$$\delta W_{12}=G_1-G_2. \tag{6}$$

When the transformation function connects two different sets of operators on the same surface, which are subjected to infinitesimal transformations generated by G and $\bar{G}$, respectively, we have, referring to (5),

$$\delta W=G-\bar{G}. \tag{7}$$

Since physical phenomena at distinct points on a space-like surface are dynamically independent, a generator G must have the additive form

$$G=\int_\sigma d\sigma G_{(0)}(x)=\int_\sigma d\sigma_\mu G_\mu(x),$$

where $d\sigma$ is the numerical measure of an element of space-like area and $G_{(0)}(x)$ is to be regarded as the time-like component of a vector in a local coordinate system based on σ in order to give the surface integral an invariant form. If one can interpret $G_\mu(x)$ on σ_1, and on σ_2, as the values of a vector defined at all points, the difference of surface integrals in (6) can be transformed into the volume integral

$$\delta W_{12}=\int_{\sigma_2}^{\sigma_1}(dx)\partial_\mu G_\mu(x),$$

$$(\partial_\mu=\partial/\partial x_\mu).$$

A second type of transformation function alteration is obtained on considering that the transformation connecting ζ_1, σ_1, and ζ_2, σ_2 can be constructed through the intermediary of an infinite succession of transformations relating operators on infinitesimally neighboring surfaces. According to the general additivity property (2),

$$\delta W_{12}=\sum_{\sigma_2}^{\sigma_1}\delta W_{\sigma+d\sigma,\sigma},$$

where $\delta W_{\sigma+d\sigma,\sigma}$ characterizes a modification of the transformation function connecting infinitesimally differing complete sets of operators on the infinitesimally separated surfaces σ and $\sigma+d\sigma$. If the choice of intermediate operators depends continuously upon the surface, we shall have

$$\delta W_{\sigma,\sigma}=0,$$

and, referring again to the dynamical independence of phenomena at points separated by a space-like interval, with the consequent additivity property, we see that $\delta W_{\sigma+d\sigma,\sigma}$ will have the general form

$$\delta W_{\sigma+d\sigma,\sigma}=\int_\sigma^{\sigma+d\sigma}(dx)\delta\mathfrak{L}(x).$$

Therefore

$$\delta W_{12}=\int_{\sigma_2}^{\sigma_1}(dx)\delta\mathfrak{L}(x). \tag{8}$$

The combination of these two types of modifications is described by

$$\delta W_{12}=G_1-G_2+\int_{\sigma_2}^{\sigma_1}(dx)\delta\mathfrak{L}(x),$$

which involves dynamical variables on the surfaces σ_1, σ_2, and in the interior of the volume bounded by these surfaces. On the other hand, we can write this as the

volume integral

$$\delta W_{12}=\int_{\sigma_2}^{\sigma_1}(dx)[\partial_\mu G_\mu(x)+\delta\mathfrak{L}(x)],$$

which indicates, conversely, that any part of $\delta\mathfrak{L}(x)$, possessing the form of a divergence, contributes only to the generation of unitary transformations on σ_1 and σ_2.

The fundamental dynamical principle is contained in the postulate that there exists a class of transformation function alterations for which the characterizing operators δW_{12} are obtained by appropriate variation of a single operator W_{12},

$$\delta W_{12}=\delta(W_{12}).$$

Of course, this principle must be implemented by the explicit specification of that class.

The operator W_{12}, the action integral operator, evidently possess the form

$$W_{12}=\int_{\sigma_2}^{\sigma_1}(dx)\mathfrak{L}(x).$$

The Hermitian requirement on δW_{12} is satisfied if W_{12} is Hermitian, which implies the same property for $\mathfrak{L}(x)$, the Lagrange function operator. In order that relations between states on σ_1 and σ_2 be invariantly characterized, the Lagrange function must be a scalar with respect to the transformations of the orthochronous[2] Lorentz group, which preserve the temporal order of σ_1 and σ_2. A dynamical system is specified by exhibiting the Lagrange function in terms of a set of fundamental dynamical variables in the infinitesimal neighborhood of the point x. Contained in this Lagrange function will be certain numerical parameters, which may be functions of x. Any change of these parameters modifies the structure of the Lagrange function and is thus an alteration of the dynamical system. Accordingly, infinitesimal changes of the dynamical system are described by

$$\delta W_{12}=\int_{\sigma_2}^{\sigma_1}(dx)\delta\mathfrak{L}(x),$$

where $\delta\mathfrak{L}=\delta(\mathfrak{L})$, and the numerical parameters are the object of variation. This form is in agreement with (8). For a fixed dynamical system, W_{12} can be altered by displacing the surfaces σ_1, σ_2 and by varying the dynamical variables contained in the Lagrange function. The transformation function $(\zeta_1'\sigma_1|\zeta_2''\sigma_2)$ describes the relation between two states of the given system so that a change in the transformation function can only arise from alterations of the states on σ_1 and σ_2. Hence, for a fixed dynamical system we must have

$$\delta W_{12}=G_1-G_2,$$

where $\delta W_{12}=\delta(W_{12})$ and the objects of variation here are σ_1, σ_2, and the dynamical variables of which $\mathfrak{L}$ is a function.

The latter statement is the operator principle of stationary action. It asserts that W_{12} must be stationary with respect to variations of the dynamical variables in the interior of the region defined by σ_1 and σ_2, since G_1 and G_2 only contain dynamical variables associated with the boundaries of the region. This principle implies equations of motion for the dynamical variables, that is to say, field equations, and provides expressions for the generators G_1 and G_2. The class of variations to which our postulate refers can now be defined through the requirement that this information concerning field equations and infinitesimal unitary transformations be self-consistent.

There exists much freedom within this class, as may be inferred from the remark that two Lagrange functions, differing by the divergence of a vector, describe the same dynamical system. Thus

$$\bar{\mathfrak{L}}(x)=\mathfrak{L}(x)-\partial_\mu f_\mu(x),$$

yields

$$\bar{W}_{12}=W_{12}-(W_1-W_2), \tag{9}$$

where, on each surface,

$$W=\int_\sigma d\sigma_\mu f_\mu=\int_\sigma d\sigma\, f_{(n)}.$$

Accordingly, the stationary action principle for $\bar{W}_{12}$ is satisfied if it is obeyed by W_{12}, since

$$\delta\bar{W}_{12}=\bar{G}_1-\bar{G}_2.$$

Here

$$\delta W_1=G_1-\bar{G}_1,\quad \delta W_2=G_2-\bar{G}_2,$$

define $\bar{G}_1$ and $\bar{G}_2$, which are new generators of infinitesimal unitary transformations on σ_1 and σ_2, respectively. The latter equations possess the form (7), and thus characterize transformation functions connecting two different representations on a common surface. Indeed, with a suitably elaborate notation, we recognize in (9) the additivity property of action operators,

$$W(\bar{\zeta}_1\sigma_1,\bar{\zeta}_2\sigma_2)=W(\bar{\zeta}_1\sigma_1,\zeta_1\sigma_1)+W(\zeta_1\sigma_1,\zeta_2\sigma_2)+W(\zeta_2\sigma_2,\bar{\zeta}_2\sigma_2),$$

where, for example,

$$W_1=-W(\bar{\zeta}_1\sigma_1,\zeta_1\sigma_1)=W(\zeta_1\sigma_1,\bar{\zeta}_1\sigma_1),$$

and

$$W_2=W(\zeta_2\sigma_2,\bar{\zeta}_2\sigma_2).$$

To be consistent with the postulate of local action, the field equations must be differential equations of finite order. One can always convert such equations into systems of first order equations by suitable adjunction of variables. We shall designate the fundamental dynamical variables that obey first-order field equations by $\chi_r(x)$, which form the components of the general field operator $\chi(x)$. With no loss in generality, we take

[2] This name was suggested by H. J. Bhabha, Revs. Modern Phys. **21**, 451 (1949).

$\chi(x)$ to be a Hermitian operator,

$$\chi_r(x)^\dagger = \chi_r(x).$$

If the Lagrange function is to yield field equations of the desired structure, it must be linear in the first derivatives of the field operators with respect to the space-time coordinates. Furthermore, if these field equations are to emerge as explicit equations of motion for field components, that part of the Lagrange function containing first coordinate derivatives must be bilinear in the field components. With these preliminary remarks, we write the following general expression for the Lagrange function,

$$\mathfrak{L} = \tfrac{1}{2}(\chi\mathfrak{A}_\mu\partial_\mu\chi - \partial_\mu\chi\mathfrak{A}_\mu\chi) - \mathfrak{C}(\chi), \tag{10}$$

in which a matrix notation is employed,

$$\chi\mathfrak{A}_\mu\partial_\mu\chi = \chi_r(\mathfrak{A}_\mu)_{rs}\partial_\mu\chi_s.$$

The derivative terms have been symmetrized with respect to the operation of integration by parts, a process which adds a divergence to the Lagrange function, and is thus without effect on the structure of the dynamical system. In order that $\mathfrak{L}$ be a Hermitian operator, the general function $\mathfrak{C}$ must possess this character,

$$\mathfrak{C}(\chi)^\dagger = \mathfrak{C}(\chi),$$

and the numerical matrices $\mathfrak{A}_\mu$; $\mu = 0, 1, 2, 3$ ($x_4 = ix_0$, $\mathfrak{A}_4 = i\mathfrak{A}_0$) must be skew-Hermitian,

$$\mathfrak{A}_\mu{}^\dagger = \mathfrak{A}_\mu{}^{tr*} = -\mathfrak{A}_\mu; \quad \mu = 0, 1, 2, 3.$$

Although we are interested in complete dynamical systems, it is advantageous mathematically to employ devices based upon the properties of external sources. Accordingly, we add to (10) a term designed to describe the generation of the field $\chi(x)$ by an external source $\xi(x)$, which is to be regarded as a field quantity of the same general nature as $\chi(x)$,

$$\mathfrak{L}_{source} = \tfrac{1}{2}(\xi\mathfrak{B}\chi + \chi\mathfrak{B}\xi). \tag{11}$$

This is a Hermitian operator if $\mathfrak{B}$ is a Hermitian matrix,

$$\mathfrak{B}^\dagger = \mathfrak{B}.$$

For the source concept to be meaningful, all components of χ must occur coupled with the source components in (11), which requires that $\mathfrak{B}$ be a nonsingular numerical matrix.

An orthochronous Lorentz transformation

$$'x_\mu = r_{\mu\nu}x_\nu + l_\mu,$$
$$r^{tr}r = 1, \quad r_{44} > 0,$$

induces a linear transformation on the field components,

$$'\chi = L\chi = \chi L^{tr},$$

where L must be a real matrix,

$$L^* = L,$$

to maintain the Hermiticity of $'\chi$. The scalar requirement on $\mathfrak{L}$ is satisfied if $\mathfrak{C}$ is a scalar,

$$\mathfrak{C}(L\chi) = \mathfrak{C}(\chi),$$

and if

$$L^{tr}\mathfrak{A}_\mu L = r_{\mu\nu}\mathfrak{A}_\nu. \tag{12}$$

We shall suppose that the source possesses the same transformation properties as the field. The condition for the source term of the Lagrange function to be a scalar is then given by

$$L^{tr}\mathfrak{B}L = \mathfrak{B}. \tag{13}$$

Note that $\mathfrak{A}_\mu{}^{tr}$ and $\mathfrak{B}^{tr}$ also obey Eqs. (12) and (13), respectively, and that these equations can be combined into

$$L^{-1}(\mathfrak{B}^{-1}\mathfrak{A}_\mu)L = r_{\mu\nu}(\mathfrak{B}^{-1}\mathfrak{A}_\nu),$$

in view of the nonsingular character of $\mathfrak{B}$.

For an infinitesimal Lorentz transformation,

$$'x_\mu = x_\mu - \epsilon_{\mu\nu}x_\nu + \epsilon_\mu, \quad \epsilon_{\mu\nu} = -\epsilon_{\nu\mu},$$

the matrix L can be written

$$L = 1 - i\tfrac{1}{2}\epsilon_{\mu\nu}S_{\mu\nu}, \tag{14}$$

where

$$S_{\mu\nu}{}^* = -S_{\mu\nu}; \quad \mu, \nu = 0, \cdots 3. \tag{15}$$

The infinitesimal version of (13) is

$$-S_{\mu\nu}{}^{tr} = \mathfrak{B}S_{\mu\nu}\mathfrak{B}^{-1} = S_{\mu\nu}{}^\dagger$$

or

$$(\mathfrak{B}S_{\mu\nu})^\dagger = (\mathfrak{B}S_{\mu\nu}),$$

in which the complex conjugate statements refer to the components indicated in (15). Similarly,

$$\mathfrak{A}_\mu S_{\nu\lambda} - S_{\nu\lambda}{}^\dagger\mathfrak{A}_\mu = i(\delta_{\mu\lambda}\mathfrak{A}_\nu - \delta_{\mu\nu}\mathfrak{A}_\lambda) \tag{16}$$

and

$$[\mathfrak{B}^{-1}\mathfrak{A}_\mu, S_{\nu\lambda}] = i(\delta_{\mu\lambda}\mathfrak{B}^{-1}\mathfrak{A}_\nu - \delta_{\mu\nu}\mathfrak{B}^{-1}\mathfrak{A}_\lambda).$$

If one views $'\chi = (1 - i\tfrac{1}{2}\epsilon_{\mu\nu}S_{\mu\nu})\chi$ as a field in the original coordinate system and thus subject to the same dependence upon that coordinate system as χ, it is inferred that

$$L^{-1}S_{\mu\nu}L = r_{\mu\lambda}r_{\nu\kappa}S_{\lambda\kappa}.$$

For infinitesimal transformations, this reads

$$i[S_{\mu\nu}, S_{\lambda\kappa}] = \delta_{\mu\kappa}S_{\nu\lambda} - \delta_{\nu\kappa}S_{\mu\lambda} + \delta_{\nu\lambda}S_{\mu\kappa} - \delta_{\mu\lambda}S_{\nu\kappa}.$$

In performing the variation of the action integral, we shall treat the two types of quantities, coordinates and field variables, on somewhat the same footing, although the former are numbers and the latter operators. We introduce an arbitrary variation of the coordinates, δx_μ, throughout the interior of the region, but subject to the condition that the boundaries remain plane surfaces,

$$\partial_\mu\delta x_\nu + \partial_\nu\delta x_\mu = 0, \tag{17}$$

on σ_1 and σ_2. The field components $\chi_r(x)$ are dependent both upon the coordinate system and the "intrinsic field." Under a rotation of the coordinate system, the field components are altered in the manner described

by (14). Accordingly, we write the general variation of the field as the sum of an intrinsic field variation, and of the variation induced by the local rotation of the coordinate system,

$$\delta(\chi)=\delta\chi-i\tfrac{1}{2}(\partial_\mu\delta x_\nu)S_{\mu\nu}\chi,$$

where the antisymmetry of $S_{\mu\nu}$ ensures that only the rotation part of the coordinate displacement is effective. For the source field, a prescribed function of the coordinates, we have

$$\delta(\xi)=\delta x_\mu\partial_\mu\xi. \tag{18}$$

We also remark that

$$\delta(dx)=(dx)\partial_\mu\delta x_\mu,$$

and

$$\delta(\partial_\mu)=-(\partial_\mu\delta x_\nu)\partial_\nu,$$

whence

$$\delta(\partial_\mu\chi)=\partial_\mu\delta(\chi)-(\partial_\mu\delta x_\nu)\partial_\nu\chi. \tag{19}$$

The Lorentz invariance of $\mathfrak{L}$ produces a significant simplification, in computing the contribution to $\delta(\mathfrak{L})$ from the coordinate induced variation of χ. Thus, if $\partial_\mu\delta x_\nu$ were antisymmetrical and constant, its coefficient in the variation of the Lagrange function would vanish identically, save for the source term since the rotation induced change of ξ is not present in (18). Accordingly, for the general coordinate variation of (10), there remains only those terms in which $\partial_\mu\delta x_\nu$ is differentiated, or occurs in the dilation combination, $\partial_\mu\delta x_\nu+\partial_\nu\delta x_\mu$. Both types are contained entirely in (19), which leads to

$$\begin{aligned}\delta(\mathfrak{L})=\delta\mathfrak{L}&-\tfrac{1}{2}(\partial_\mu\delta x_\nu+\partial_\nu\delta x_\mu)\tfrac{1}{2}(\chi\mathfrak{A}_\mu\partial_\nu\chi-\partial_\nu\chi\mathfrak{A}_\mu\chi)\\&-i\tfrac{1}{2}(\partial_\mu\partial_\nu\delta x_\lambda)\tfrac{1}{2}\chi(\mathfrak{A}_\mu S_{\nu\lambda}+S_{\nu\lambda}{}^\dagger\mathfrak{A}_\mu)\chi\\&-i\tfrac{1}{4}(\partial_\mu\delta x_\nu)(\xi\mathfrak{B}S_{\mu\nu}\chi-\chi S_{\mu\nu}{}^\dagger\mathfrak{B}\xi).\end{aligned}$$

In virtue of the symmetry of the second derivative,

$$\begin{aligned}&(\partial_\mu\partial_\nu\delta x_\lambda)\chi(\mathfrak{A}_\mu S_{\nu\lambda}+S_{\nu\lambda}{}^\dagger\mathfrak{A}_\mu)\chi\\&\quad=(\partial_\mu(\partial_\nu\delta x_\lambda+\partial_\lambda\delta x_\nu))\chi(\mathfrak{A}_\nu S_{\mu\lambda}+S_{\mu\lambda}{}^\dagger\mathfrak{A}_\nu)\chi\\&\qquad\rightarrow-(\partial_\nu\delta x_\lambda+\partial_\lambda\delta x_\nu)\partial_\mu[\chi(\mathfrak{A}_\nu S_{\mu\lambda}+S_{\mu\lambda}{}^\dagger\mathfrak{A}_\nu)\chi],\end{aligned}$$

where the last step expresses the result of an integration by parts, for which the integrated term vanishes, since the dilation tensor is zero on the boundaries (Eq. (17)). Collecting the coefficients of $\partial_\mu\delta x_\nu$ into the tensor $T_{\mu\nu}$, we have

$$\begin{aligned}\delta(W_{12})&=\int_{\sigma_2}^{\sigma_1}(dx)[\delta\mathfrak{L}+(\partial_\mu\delta x_\nu)T_{\mu\nu}]\\&=\int_{\sigma_2}^{\sigma_1}(dx)[\delta\mathfrak{L}-\delta x_\nu\partial_\mu T_{\mu\nu}+\partial_\mu(T_{\mu\nu}\delta x_\nu)],\end{aligned}$$

where

$$\begin{aligned}T_{\mu\nu}=\mathfrak{L}\delta_{\mu\nu}&-\tfrac{1}{2}(\chi\mathfrak{A}_{(\mu}\partial_{\nu)}\chi-\partial_{(\nu}\chi\mathfrak{A}_{\mu)}\chi)\\&-i\tfrac{1}{4}(\xi\mathfrak{B}S_{\mu\nu}\chi-\chi S_{\mu\nu}{}^\dagger\mathfrak{B}\xi)\\&+i\tfrac{1}{2}\partial_\lambda[\chi(\mathfrak{A}_{(\mu}S_{\lambda\nu)}+S_{\lambda(\nu}{}^\dagger\mathfrak{A}_{\mu)})\chi],\end{aligned} \tag{20}$$

and we have employed a notation for the symmetrical part of a tensor,

$$\mathfrak{A}_{(\mu}\partial_{\nu)}=\tfrac{1}{2}(\mathfrak{A}_\mu\partial_\nu+\mathfrak{A}_\nu\partial_\mu).$$

The expression for $\delta\mathfrak{L}$ is

$$\begin{aligned}\delta\mathfrak{L}=\delta\chi\mathfrak{A}_\mu\partial_\mu\chi&-\partial_\mu\chi\mathfrak{A}_\mu\delta\chi-\delta\mathfrak{C}+\tfrac{1}{2}(\delta\chi\mathfrak{B}\xi+\xi\mathfrak{B}\delta\chi)\\&+\delta x_\mu\tfrac{1}{2}(\chi\mathfrak{B}\partial_\mu\xi+\partial_\mu\xi\mathfrak{B}\chi)+\partial_\mu[\tfrac{1}{2}(\chi\mathfrak{A}_\mu\delta\chi-\delta\chi\mathfrak{A}_\mu\chi)].\end{aligned}$$

Hence, on applying the principle of stationary action to coordinate and field variations, separately, we obtain

$$\partial_\mu T_{\mu\nu}=\tfrac{1}{2}(\chi\mathfrak{B}\partial_\mu\xi+\partial_\mu\xi\mathfrak{B}\chi),$$

and

$$\delta\mathfrak{C}=\delta\chi\mathfrak{A}_\mu\partial_\mu\chi-\partial_\mu\chi\mathfrak{A}_\mu\delta\chi+\tfrac{1}{2}(\delta\chi\mathfrak{B}\xi+\xi\mathfrak{B}\delta\chi), \tag{21}$$

while the surface terms yield, on σ_1 and σ_2, the infinitesimal generator

$$G=\int_\sigma d\sigma_\mu[\tfrac{1}{2}(\chi\mathfrak{A}_\mu\delta\chi-\delta\chi\mathfrak{A}_\mu\chi)+T_{\mu\nu}\delta x_\nu].$$

The operator $\mathfrak{C}$ is an arbitrary, invariant function of the field χ. If its variation is to possess the form (21), with $\delta\chi$ appearing on the left and on the right, the latter must possess elementary operator properties, characterizing the class of variations to which the action principle refers. Thus, we should be able to displace $\delta\chi$ entirely to the left, or to the right, in the structure of $\delta\mathfrak{C}$,

$$\delta\mathfrak{C}=\delta\chi(\partial_l\mathfrak{C}/\partial\chi)=(\partial_r\mathfrak{C}/\partial\chi)\delta\chi,$$

which defines the left and right derivatives of $\mathfrak{C}$ with respect to χ. In view of the complete symmetry between left and right in the process of multiplication, we infer that the expressions with $\delta\chi$ on the left and on the right are, in fact, identical. The field equations, therefore, possess the two equivalent forms

$$\begin{aligned}2\mathfrak{A}_\mu\partial_\mu\chi&=(\partial_l\mathfrak{C}/\partial\chi)-\mathfrak{B}\xi,\\-\partial_\mu\chi 2\mathfrak{A}_\mu&=(\partial_r\mathfrak{C}/\partial\chi)-\xi\mathfrak{B},\end{aligned}$$

and G can be equivalently written

$$\begin{aligned}G&=\int_\sigma d\sigma_\mu[\chi\mathfrak{A}_\mu\delta\chi+T_{\mu\nu}\delta x_\nu]\\&=\int_\sigma d\sigma_\mu[-\delta\chi\mathfrak{A}_\mu\chi+T_{\mu\nu}\delta x_\nu].\end{aligned} \tag{22}$$

In keeping with the restriction of the stationary action principle to fixed dynamical systems, the external source has not been altered. If we now introduce an infinitesimal variation of ξ, and extend the argument of the previous paragraph to $\delta\xi$, we obtain the two equivalent expressions for the change induced in W_{12},

$$\delta_\xi W_{12}=\int_{\sigma_2}^{\sigma_1}(dx)\delta\xi\mathfrak{B}\chi=\int_{\sigma_2}^{\sigma_1}(dx)\chi\mathfrak{B}\delta\xi.$$

The corresponding modification in the relation between

states on σ_1 and on σ_2 can be ascribed to the individual states only if one introduces a convention, of the nature of a boundary condition. Thus, we may suppose that the state on σ_2 is unaffected by varying the external source in the region between σ_1 and σ_2. In this "retarded" description, $\delta_\xi W_{12}$ generates the infinitesimal transformation of the state on σ_1. An alternative, "advanced" description corresponds to $-\delta_\xi W_{12}$ generating the change in the state on σ_2, with a fixed state on σ_1. These are just the simplest of possible boundary conditions.

The suitability of the designations, retarded and advanced, can be seen by considering the matrix of an operator constructed from dynamical variables on some surface σ, intermediate between σ_1 and σ_2,

$$(\zeta_1'\sigma_1|F(\sigma)|\zeta_2''\sigma_2)$$
$$=\int(\zeta_1'\sigma_1|\zeta'\sigma)d\zeta'(\zeta'\sigma|F(\sigma)|\zeta''\sigma)d\zeta''(\zeta''\sigma|\zeta_2''\sigma_2).$$

An infinitesimal change of the source ξ produces the following change in the matrix element,

$$\begin{aligned}\delta_\xi(\zeta_1'\sigma_1|F(\sigma)|\zeta_2''\sigma_2)&=(\zeta_1'\sigma_1|(\partial_\xi F(\sigma)+i\delta_\xi W_{1\sigma}F(\sigma)+iF(\sigma)\delta_\xi W_{\sigma 2})|\zeta_2''\sigma_2)\\&=(\zeta_1'\sigma_1|(\partial_\xi F(\sigma)+i(F(\sigma)\delta_\xi W_{12})_+)|\zeta_2''\sigma_2),\end{aligned}$$

in which we have allowed for the possibility that $F(\sigma)$ may be explicitly dependent upon the source, and introduced a notation for temporally ordered products. The matrix element depends upon the external source through the operator $F(\sigma)$, and the eigenvectors on σ_1 and σ_2. One thereby gets various expressions for $\delta_\xi F(\sigma)$, depending upon the boundary conditions that are adopted. Thus, if the state on σ_2 is prescribed, we find

$$\begin{aligned}\delta_\xi F(\sigma)]_{\rm ret}&=\partial_\xi F(\sigma)+i(F(\sigma)\delta_\xi W_{12})_+-i\delta W_{12}F(\sigma)\\&=\partial_\xi F(\sigma)+i[F(\sigma),\delta_\xi W_{\sigma 2}],\end{aligned}\qquad(23)$$

which only involves changes in the source prior to, or on σ. The opposite convention yields the analogous result

$$\begin{aligned}\delta_\xi F(\sigma)]_{\rm adv}&=\partial_\xi F(\sigma)+i(F(\sigma)\delta_\xi W_{12})_+-iF(\sigma)\delta W_{12}\\&=\partial_\xi F(\sigma)-i[F(\sigma),\delta_\xi W_{1\sigma}].\end{aligned}$$

Note that

$$\delta_\xi F(\sigma)]_{\rm ret}-\delta_\xi F(\sigma)]_{\rm adv}=i[F(\sigma),\delta_\xi W_{12}].$$

The operator G of Eq. (22) consists of two parts,

$$G=G_\chi+G_x,$$

where

$$G_\chi=\int_\sigma d\sigma_\mu\chi\mathfrak{N}_\mu\delta\chi=-\int_\sigma d\sigma_\mu\delta\chi\mathfrak{N}_\mu\chi,$$

and

$$G_x=\int d\sigma_\mu T_{\mu\nu}\delta x_\nu=\epsilon_\nu P_\nu+\tfrac{1}{2}\epsilon_{\mu\nu}J_{\mu\nu}.$$

The latter form of G_x is a consequence of the restriction to plane space-like surfaces, limiting displacements to infinitesimal translations and rotations,

$$\delta x_\nu=\epsilon_\nu+\epsilon_{\mu\nu}x_\mu,$$

with the associated operators, the energy-momentum vector

$$P_\nu=\int d\sigma_\mu T_{\mu\nu},$$

and angular momentum tensor

$$J_{\mu\nu}=\int d\sigma_\lambda M_{\lambda\mu\nu},$$

$$M_{\lambda\mu\nu}=x_\mu T_{\lambda\nu}-x_\nu T_{\lambda\mu}.$$

The operator G_x evidently generates the infinitesimal transformation of an eigenvector, produced by the displacement of the surface to which it refers. With the notation

$$\delta_x\Psi(\zeta'\sigma)=(\epsilon_\nu\delta_\nu+\tfrac{1}{2}\epsilon_{\mu\nu}\delta_{\mu\nu})\Psi(\zeta'\sigma),$$

we have

$$i\delta_\nu\Psi(\zeta'\sigma)=P_\nu\Psi(\zeta'\sigma),\quad -i\delta_\nu\Psi(\zeta'\sigma)^\dagger=\Psi(\zeta'\sigma)^\dagger P_\nu,$$

and

$$i\delta_{\mu\nu}\Psi(\zeta'\sigma)=J_{\mu\nu}\Psi(\zeta'\sigma),\quad -i\delta_{\mu\nu}\Psi(\zeta'\sigma)^\dagger=\Psi(\zeta'\sigma)^\dagger J_{\mu\nu}.$$

If $F(\sigma)$ is an arbitrary function of dynamical variables on σ, and possibly of nondynamical parameters dependent on σ, we use the notation

$$\delta_x F(\sigma)=(\epsilon_\nu\delta_\nu+\tfrac{1}{2}\epsilon_{\mu\nu}\delta_{\mu\nu})F(\sigma),$$
$$\partial_x F(\sigma)=(\epsilon_\nu\partial_\nu+\tfrac{1}{2}\epsilon_{\mu\nu}\partial_{\mu\nu})F(\sigma),$$

to distinguish between the total change on displacement, and that occasioned by the explicit appearance of nondynamical parameters. On referring to Eq. (3), we see that

$$\delta_\nu F(\sigma)=\partial_\nu F(\sigma)+i[F(\sigma),P_\nu],$$
$$\delta_{\mu\nu}F(\sigma)=\partial_{\mu\nu}F(\sigma)+i[F(\sigma),J_{\mu\nu}].$$

The proper interpretation of the generating operator G_χ can be obtained by noting its equivalence with an appropriately chosen infinitesimal variation of the external source. Consider the following infinitesimal surface distribution on the negative side of σ,

$$\mathfrak{B}\delta\xi=\mathfrak{N}_{(0)}\delta\chi\delta(x_{(0)}),\qquad(24)$$

which is not incompatible with the operator properties of these variations. We have assumed, for simplicity, that the equation of the surface σ is $x_{(0)}=0$. With this choice,

$$\delta_\xi W_{12}=\int_\sigma d\sigma\chi\mathfrak{N}_{(0)}\delta\chi=G_\chi.$$

The change that is produced in χ can be deduced from

the variation of the field equatons,

$$2\mathfrak{A}_\mu\partial_\mu\delta_\xi\chi-\delta_\xi(\partial_i\mathfrak{K}/\partial\chi)=-\mathfrak{B}\delta\xi$$
$$=-\mathfrak{A}_{(0)}\delta\chi\delta(x_{(0)}).$$

Evidently there is a discontinuity in $\delta_\xi\chi$, on crossing the surface distribution $\delta\xi$, which is given by

$$2\mathfrak{A}_{(0)}\delta_\xi\chi]=-\mathfrak{A}_{(0)}\delta\chi.$$

In the retarded description, say, $\delta_\xi\chi$ is zero prior to the source bearing surface, so that the discontinuity in $\delta_\xi\chi$ is the change induced in χ on (the positive side of) σ. Thus, the surface variation of the external source simulates the transformation generated by G_χ, in which $\mathfrak{A}_{(0)}\chi$ on σ is replaced by

$$\mathfrak{A}_{(0)}\bar{\chi}=\mathfrak{A}_{(0)}\chi+\mathfrak{A}_{(0)}\delta_\xi\chi$$
$$=\mathfrak{A}_{(0)}\chi-\tfrac{1}{2}\mathfrak{A}_{(0)}\delta\chi. \tag{25}$$

The matrix $\mathfrak{A}_{(0)}$ has been retained in this statement since it is a singular matrix, in general. The number of components of χ that appear independently in (25) equals the rank of the matrix $\mathfrak{A}_{(0)}$, and this is the number of independent component field equations that are equations of motion, in that they contain time-like derivatives. The expression of (25) in terms of the generator G_χ is

$$[\mathfrak{A}_{(0)}\chi, G_\chi]=i\tfrac{1}{2}\mathfrak{A}_{(0)}\delta\chi. \tag{26}$$

The factor of $\frac{1}{2}$ that appears in this result stems from the treatment of all components of $\mathfrak{A}_{(0)}\chi$ on the same footing; we have not divided them into two sets of which one is fixed and the other varied.* If F is an arbitrary function of $\mathfrak{A}_{(0)}\chi$ on σ, we write

$$[F, G_\chi]=i(\delta F)_\chi=i\tfrac{1}{2}\delta F,$$

in which the components of $\mathfrak{A}_{(0)}\chi$ are the objects of variation. When the field equations that are equations of constraint prove sufficient to express all components of χ in terms of $\mathfrak{A}_{(0)}\chi$, we can extend (26) into

$$[\chi, G_\chi]=i\tfrac{1}{2}\delta\chi.$$

Of course, one must distinguish between these variations, in which only the $\mathfrak{A}_{(0)}\chi$ are independent, and the independent variations of all components of χ which produce the equations of constraint from the action principle.

In order to facilitate the explicit construction of the field commutation relations, we shall introduce a reducibility hypothesis, which is associated with the Lorentz invariant process of separating the matrices $\mathfrak{A}_\mu$, $\mathfrak{B}$ into symmetrical and antisymmetrical parts. We require that the field and the source decompose into two sets, of the first kind $\chi^{(1)}=\phi$, $\xi^{(1)}=\zeta$, and of the second kind, $\chi^{(2)}=\psi$, $\xi^{(2)}=\eta$, as a concomitant of the decomposition

$$\mathfrak{A}_\mu=\mathfrak{A}_\mu{}^{(1)}+\mathfrak{A}_\mu{}^{(2)}, \qquad \mathfrak{B}=\mathfrak{B}^{(1)}+\mathfrak{B}^{(2)},$$
$$\mathfrak{A}_\mu{}^{(1)\mathrm{tr}}=-\mathfrak{A}_\mu{}^{(1)}, \qquad \mathfrak{B}^{(1)\mathrm{tr}}=\mathfrak{B}^{(1)},$$
$$\mathfrak{A}_\mu{}^{(2)\mathrm{tr}}=\mathfrak{A}_\mu{}^{(2)}, \qquad \mathfrak{B}^{(2)\mathrm{tr}}=-\mathfrak{B}^{(2)}.$$

The matrices of the first kind are real ($\mu=0, \cdots 3$), and those of the second kind are imaginary. We shall not write the distinguishing index when no confusion is possible.

According to this reducibility hypothesis, the field equations in the two equivalent forms

$$2\mathfrak{A}_\mu\partial_\mu\chi=(\partial_i\mathfrak{K}/\partial\chi)-\mathfrak{B}\xi,$$
$$-2\mathfrak{A}_\mu{}^{\mathrm{tr}}\partial_\mu\chi=(\partial_r\mathfrak{K}/\partial\chi)-\mathfrak{B}^{\mathrm{tr}}\xi,$$

separate into the two sets

$$2\mathfrak{A}_\mu\partial_\mu\phi=(\partial\mathfrak{K}/\partial\phi)-\mathfrak{B}\zeta, \quad (\partial_i\mathfrak{K}/\partial\phi)=(\partial_r\mathfrak{K}/\partial\phi),$$

and

$$2\mathfrak{A}_\mu\partial_\mu\psi=(\partial_i\mathfrak{K}/\partial\psi)-\mathfrak{B}\eta, \quad (\partial_i\mathfrak{K}/\partial\psi)=-(\partial_r\mathfrak{K}/\partial\psi).$$

Furthermore, the generator

$$G_\chi=\int d\sigma\chi\mathfrak{A}_{(0)}\delta\chi=\int d\sigma(-\mathfrak{A}_{(0)}{}^{\mathrm{tr}}\delta\chi)\chi,$$

decomposes into $G_\phi+G_\psi$, where

$$G_\phi=\int d\sigma\phi\mathfrak{A}_{(0)}\delta\phi=\int d\sigma(\mathfrak{A}_{(0)}\delta\phi)\phi,$$

and

$$G_\psi=\int d\sigma\psi\mathfrak{A}_{(0)}\delta\psi=\int d\sigma(-\mathfrak{A}_{(0)}\delta\psi)\psi. \tag{27}$$

These results reflect the form assumed by the Lagrange function,

$$\mathfrak{L}=\tfrac{1}{2}\{\phi\mathfrak{A}_\mu, \partial_\mu\phi\}+\tfrac{1}{2}[\psi\mathfrak{A}_\mu, \partial_\mu\psi]-\mathfrak{K}(\phi,\psi)$$
$$+\tfrac{1}{2}\{\zeta\mathfrak{B}, \phi\}+\tfrac{1}{2}[\eta\mathfrak{B}, \psi].$$

The equivalence between left and right derivatives of the arbitrary function $\mathfrak{K}$, with respect to field components of the first kind, and of the two expressions for G_ϕ, shows that $\delta\phi$ commutes with all fields at the same point. It is compatible with the field equations to extend this statement to fields at arbitrary points,

$$[\phi(x), \delta\phi(x')]=[\psi(x), \delta\phi(x')]=0,$$

provided the source components are included,

$$[\zeta(x), \delta\phi(x')]=[\eta(x), \delta\phi(x')]=0.$$

It follows from (27) that the relation between ψ and $\delta\psi$ is one of anticommutivity. The opposite signs of the left and right derivatives of $\mathfrak{K}$ with respect to ψ is then accounted for by

$$[\phi(x), \delta\psi(x')]=\{\psi(x), \delta\psi(x')\}=0,$$

provided only that $\mathfrak{K}$ is an even function of the vari-

* *Note added in proof:*—Further discussion of this point will be found in a paper submitted to the *Philosophical Magazine*.

ables of the second kind. The inclusion of the source components

$$[\zeta(x), \delta\psi(x')]=\{\eta(x), \delta\psi(x')\}=0,$$

insures compatibility with the field equations. We have now obtained the explicit characterization of the class of variations to which our fundamental postulate refers.

Let us also notice that

$$\delta_\xi W_{12}=\int_{\sigma_2}^{\sigma_1}(dx)\chi\mathfrak{B}\delta\xi=\int_{\sigma_2}^{\sigma_1}(dx)(\mathfrak{B}^{\mathrm{tr}}\delta\xi)\chi,$$

decomposes into $\delta_\xi W_{12}+\delta_\eta W_{12}$, where

$$\delta_\xi W_{12}=\int_{\sigma_2}^{\sigma_1}(dx)\phi\mathfrak{B}\delta\zeta=\int_{\sigma_2}^{\sigma_1}(dx)(\mathfrak{B}\delta\zeta)\phi,$$

and

$$\delta_\eta W_{12}=\int_{\sigma_2}^{\sigma_1}(dx)\psi\mathfrak{B}\delta\eta=\int_{\sigma_2}^{\sigma_1}(dx)(-\mathfrak{B}\delta\eta)\psi.$$

We can conclude that source variations have the same operator properties as field variations, as already exploited in Eq. (24).

The operator properties of $\mathfrak{A}_{(0)}\chi$ on a given σ can now be deduced from (26), with the results

$$\begin{aligned}&[\mathfrak{A}_{(0)}\phi(x), \phi(x')\mathfrak{A}_{(0)}]=i\tfrac{1}{2}\mathfrak{A}_{(0)}\delta_\sigma(x-x'),\\ &[\mathfrak{A}_{(0)}\phi(x), \psi(x')\mathfrak{A}_{(0)}]=0,\\ &\{\mathfrak{A}_{(0)}\psi(x), \psi(x')\mathfrak{A}_{(0)}\}=i\tfrac{1}{2}\mathfrak{A}_{(0)}\delta_\sigma(x-x'),\end{aligned}\tag{28}$$

in which $\delta_\sigma(x-x')$ is the three-dimensional delta function appropriate to the surface σ. The numerical forms of these commutators and anticommutators insures their consistency with the operator properties of $\delta\mathfrak{A}_{(0)}\phi$ and $\delta\mathfrak{A}_{(0)}\psi$. The dynamical variables of the first and second kind thus describe Bose-Einstein and Fermi-Dirac fields, respectively, which are unified in the general field χ.

Since the rank of the antisymmetrical matrix $\mathfrak{A}_{(0)}{}^{(1)}$ is necessarily even, there are an even number of independent field components of the first kind, say $2n^{(1)}$. One can always arrange the matrix $\mathfrak{A}_{(0)}{}^{(1)}$ so that all elements are zero beyond the first $2n^{(1)}$ rows and columns. We shall denote this nonsingular submatrix of dimensionality $2n^{(1)}$ by $\mathfrak{A}_{(0)}{}^{(1)}$, and the associated independent components of ϕ by $\boldsymbol{\phi}$. The first commutation relation of (28) can then be written

$$[\boldsymbol{\phi}(x), \boldsymbol{\phi}(x')]=i\tfrac{1}{2}\mathfrak{A}_{(0)}{}^{-1}\delta_\sigma(x-x').$$

The matrix $\mathfrak{B}^{(2)}$, associated with Fermi-Dirac fields, is antisymmetrical and nonsingular. Hence the total number of field components of the second kind is even. If we allow for the possibility that $\mathfrak{A}_{(0)}{}^{(2)}$ may be singular, and arrange the rows and columns so that the nonsingular submatrix $\mathfrak{A}_{(0)}{}^{(2)}$ is associated with the independent components $\boldsymbol{\psi}$, we obtain

$$\{\boldsymbol{\psi}(x), \boldsymbol{\psi}(x')\}=i\tfrac{1}{2}\mathfrak{A}_{(0)}{}^{-1}\delta_\sigma(x-x'),$$

which requires that the real, symmetrical matrix $i\mathfrak{A}_{(0)}{}^{(2)-1}$ be positive definite.

We shall argue that the number of independent field components of the second kind, the dimensionality of $\mathfrak{A}_{(0)}{}^{(2)}$, must be even, $2n^{(2)}$. Let us imagine that, by a suitable real transformation, $\mathfrak{A}_{(0)}{}^{(2)}$ is brought into diagonal form. If the number of components in $\boldsymbol{\psi}$ is odd, the product of all these components at a given point commutes with $\boldsymbol{\psi}$ at that point. Thus, as far as the algebra of operators at a given point is concerned, this product is a multiple of the unit operator (the necessary commutivity with $\boldsymbol{\psi}$ at other points on σ can always be achieved), which contradicts the assumption that all components of $\boldsymbol{\psi}$ are independent.

The relation between invariance under time reflection, and the connection between spin and statistics, may be noted here. The time reflection transformation

$${}'x_4=-x_4, \quad {}'x_k=x_k,$$

induces a transformation of the field

$${}'\chi=L_4\chi,$$

such that

$$L_4{}^{\mathrm{tr}}\mathfrak{A}_4L_4=-\mathfrak{A}_4, \quad L_4{}^{\mathrm{tr}}\mathfrak{A}_kL_4=\mathfrak{A}_k,\tag{29}$$

and

$$L_4{}^{\mathrm{tr}}\mathfrak{B}L_4=\mathfrak{B}, \quad \mathfrak{C}(L_4\chi)=\mathfrak{C}(\chi).$$

However, this preservation of the form of the Lagrange function is only apparent, for fields of the second kind. Since $-i\mathfrak{A}_{(0)}{}^{(2)}$ is a non-negative matrix, one can only satisfy the first equation of (29) with an imaginary $L_4{}^{(2)}$ which produces skew-Hermitian field components ${}'\boldsymbol{\chi}^{(2)}$. But the invariance of the Lagrange function is not the correct criterion for invariance under time reflection. The reversal of the time sense inverts the order of σ_1 and σ_2, and thus introduces a minus sign in the action integral, which can only be compensated by changing the sign of i in (4). We shall describe this as a transformation from the algebra of the operators χ to the complex conjugate algebra of operators χ^*. Since the linear transformation designed to maintain the form of $\mathfrak{L}(\phi, \partial_\mu\phi; \psi, \partial_\mu\psi)$ has effectively replaced $\mathfrak{L}$ with $\mathfrak{L}(\phi, \partial_\mu\phi; i\psi, i\partial_\mu\psi)$, the criterion for invariance reads

$$\mathfrak{L}(\phi, \partial_\mu\phi; i\psi, i\partial_\mu\psi)^*=\mathfrak{L}(\phi^*, \partial_\mu\phi^*; \psi^*, \partial_\mu\psi^*).$$

The derivative term in $\mathfrak{L}$ is indeed invariant since the matrices $\mathfrak{A}_\mu{}^{(1)}$ and $\mathfrak{A}_\mu{}^{(2)}$ are real and imaginary, respectively. We describe this by saying that the theory is kinematically invariant under time reflection. In order that it be dynamically invariant, $\mathfrak{C}$ must be such that

$$\mathfrak{C}(\phi, i\psi)^*=\mathfrak{C}(\phi^*, \psi^*).$$

Since $\mathfrak{C}$ is an even function of the components of ψ, the latter are to be paired with the aid of imaginary matrices, characteristic of the variables of the second kind. The source term is invariant if source and field transform in the same way.

The correlation between spin and statistics enters on

observing that an imaginary L_4 is characteristic of half-integral spin fields. We can prove this by remarking that all the transformation properties of L_4 are satisfied by

$$L_4=\exp(-\tfrac{1}{2}\pi iS_{14})L_1\exp(\tfrac{1}{2}\pi iS_{14})=\exp(-\pi iS_{14})L_1,$$

where L_1 is the matrix describing the reflection of the first space axis. The latter form is a consequence of

$$L_1^{-1}S_{14}L_1=-S_{14}.$$

The essential point with regard to the reality of L_4 is that $S_{14}=iS_{10}$ is a real matrix, whence

$$L_4^*=\exp(\pi iS_{14})L_1=\exp(2\pi iS_{14})L_4.$$

Now S_{14} must possess the same eigenvalues as S_{12}, say, which implies that L_4 is real for an integral spin field, and imaginary for a half-integral spin field. The requirement of time reflection invariance thus restricts fields of the first (B.E.) and second (F.D.) kind to integral and half-integral spins, respectively. This correlation is also satisfactory in that it identifies the double-valued, half-integral spin fields with fields of the second kind, of which $\mathfrak{L}$ is an even function.

We have introduced several kinds of generators of infinitesimal transformations. A criterion for consistency is obtained from the alternative evaluations of the commutator of two such generators,

$$[G_a, G_b]=i(\delta G_a)_b=-i(\delta G_b)_a,$$

namely

$$(\delta G_a)_b+(\delta G_b)_a=0.$$

As a first example, we consider the two generators

$$G_x=\epsilon_\nu P_\nu(\sigma_1)+\tfrac{1}{2}\epsilon_{\mu\nu}J_{\mu\nu}(\sigma_1),$$

and

$$G_\xi=\int_{\sigma_2}^{\sigma_1}(dx)\chi\mathfrak{B}\delta\xi,$$

in the retarded description. In preparation for the test, we remark that

$$P_\nu(\sigma_1)-P_\nu(\sigma_2)=\int_{\sigma_2}^{\sigma_1}(dx)\partial_\mu T_{\mu\nu}$$

$$=\int_{\sigma_2}^{\sigma_1}(dx)\tfrac{1}{2}(\chi\mathfrak{B}\partial_\nu\xi+\partial_\nu\xi\mathfrak{B}\chi),$$

and that

$$J_{\mu\nu}(\sigma_1)-J_{\mu\nu}(\sigma_2)=\int_{\sigma_2}^{\sigma_1}(dx)\partial_\lambda M_{\lambda\mu\nu}$$

$$=\int_{\sigma_2}^{\sigma_1}(dx)[x_\mu\partial_\lambda T_{\lambda\nu}-x_\nu\partial_\lambda T_{\lambda\mu}+T_{\mu\nu}-T_{\nu\mu}].$$

Since

$$T_{\mu\nu}-T_{\nu\mu}=-i\tfrac{1}{2}(\xi\mathfrak{B}S_{\mu\nu}\chi-\chi S_{\mu\nu}{}^\dagger\mathfrak{B}\xi),$$

we have

$$J_{\mu\nu}(\sigma_1)-J_{\mu\nu}(\sigma_2)=\int_{\sigma_2}^{\sigma_1}(dx)\tfrac{1}{2}[\chi\mathfrak{B}(x_\mu\partial_\nu-x_\nu\partial_\mu+iS_{\mu\nu})\xi+(x_\mu\partial_\nu-x_\nu\partial_\mu+iS_{\mu\nu})\xi\mathfrak{B}\chi].$$

In the absence of an external source, $T_{\mu\nu}$ is symmetrical and divergenceless, and P_ν, $J_{\mu\nu}$ are conserved. For simplicity, we shall confine our verification to the situation of no source, in which the infinitesimal $\delta\xi$ is distributed in the region between σ_1 and σ_2. Hence

$$\delta_\xi P_\nu(\sigma_1)=-\int_{\sigma_2}^{\sigma_1}(dx)\partial_\nu\chi\mathfrak{B}\delta\xi,$$

and

$$\delta_\xi J_{\mu\nu}(\sigma_1)=-\int_{\sigma_2}^{\sigma_1}(dx)(x_\mu\partial_\nu-x_\nu\partial_\mu+iS_{\mu\nu})\chi\mathfrak{B}\delta\xi.$$

The consistency requirement

$$(\delta G_\xi)_x=\int_{\sigma_2}^{\sigma_1}(dx)(\delta\chi)_x\mathfrak{B}\delta\xi=\delta_\xi G_x,$$

then demands that

$$-(\delta\chi)_x=\epsilon_\nu\partial_\nu\chi+\tfrac{1}{2}\epsilon_{\mu\nu}(x_\mu\partial_\nu-x_\nu\partial_\mu+iS_{\mu\nu})\chi, \qquad (30)$$

which is indeed true in virtue of the equivalence between $(\delta\chi(x))_x$, induced by the displacement δx_μ, and $'\chi(x)-\chi(x)$, induced by the coordinate transformation $'x_\mu=x_\mu+\delta x_\mu$.

Alternative forms of P_ν and $J_{\mu\nu}$ are convenient for testing the consistency of G_x and G_χ. The following relations derived from (16),

$$\chi\mathfrak{A}_\nu\partial_\mu\chi-\chi\mathfrak{A}_\mu\partial_\nu\chi=i\chi(\mathfrak{A}_\lambda S_{\mu\nu}-S_{\mu\nu}{}^\dagger\mathfrak{A}_\lambda)\partial_\lambda\chi,$$

$$\partial_\mu\chi\mathfrak{A}_\nu\chi-\partial_\nu\chi\mathfrak{A}_\mu\chi=i\partial_\lambda\chi(\mathfrak{A}_\lambda S_{\mu\nu}-S_{\mu\nu}{}^\dagger\mathfrak{A}_\lambda)\chi,$$

enable us to write $T_{\mu\nu}$ as

$$T_{\mu\nu}=\mathfrak{L}\delta_{\mu\nu}-\tfrac{1}{2}(\chi\mathfrak{A}_\mu\partial_\nu\chi-\partial_\nu\chi\mathfrak{A}_\mu\chi)+\partial_\lambda s_{\lambda\mu\nu}+\rho_{\mu\nu},$$

where

$$s_{\lambda\mu\nu}=-s_{\mu\lambda\nu}=i\tfrac{1}{4}\chi(2\mathfrak{A}_{(\mu}S_{\lambda\nu)}+2S_{\lambda(\nu}{}^\dagger\mathfrak{A}_{\mu)}-\mathfrak{A}_\lambda S_{\mu\nu}-S_{\mu\nu}{}^\dagger\mathfrak{A}_\lambda)\chi,$$

and

$$\rho_{\mu\nu}=-i\tfrac{1}{4}[S_{\mu\nu}\chi(\partial_\lambda\mathfrak{K}/\partial\chi)+(\partial_\lambda\mathfrak{K}/\partial\chi)S_{\mu\nu}\chi].$$

In virtue of the antisymmetry of $s_{\lambda\mu\nu}$ in the first two indices, $\partial_\lambda s_{\lambda\mu\nu}$ is automatically divergenceless and does not contribute to the energy-momentum vector P_ν,

$$P_\nu=\int d\sigma_\mu[\mathfrak{L}\delta_{\mu\nu}-\tfrac{1}{2}(\chi\mathfrak{A}_\mu\partial_\nu\chi-\partial_\nu\chi\mathfrak{A}_\mu\chi)+\rho_{\mu\nu}],$$

but does enter in

$$J_{\mu\nu}=\int d\sigma_\lambda[-\tfrac{1}{2}\chi\mathfrak{A}_\lambda(x_\mu\partial_\nu-x_\nu\partial_\mu+iS_{\mu\nu})\chi+\tfrac{1}{2}(x_\mu\partial_\nu-x_\nu\partial_\mu+iS_{\mu\nu})\chi\mathfrak{A}_\lambda\chi+x_\mu\rho_{\lambda\nu}-x_\nu\rho_{\lambda\mu}]+\int(d\sigma_\nu x_\mu-d\sigma_\mu x_\nu)\mathfrak{L}.$$

The components of P_ν in a local coordinate system are

$$P_{(0)}=\int d\sigma[\mathcal{H}-\chi\mathfrak{N}_{(k)}\partial_{(k)}\chi-\tfrac{1}{2}(\xi\mathfrak{B}\chi+\chi\mathfrak{B}\xi)],$$
$$P_{(k)}=\int d\sigma[-\chi\mathfrak{N}_{(0)}\partial_{(k)}\chi+\rho_{(0)(k)}], \tag{31}$$

while those of $J_{\mu\nu}$ are

$$J_{(0)(k)}=x_{(0)}P_{(k)}-\int d\sigma x_{(k)}[\mathcal{H}-\tfrac{1}{2}(\chi\mathfrak{N}_{(l)}\partial_{(l)}\chi-\partial_{(l)}\chi\mathfrak{N}_{(l)}\chi)-\tfrac{1}{2}(\xi\mathfrak{B}\chi+\chi\mathfrak{B}\xi)]$$
$$-\tfrac{1}{2}i\int d\sigma\chi(\mathfrak{N}_{(0)}S_{(0)(k)}+S_{(0)(k)}{}^{\dagger}\mathfrak{N}_{(0)})\chi, \tag{32}$$

$$J_{(k)(l)}=\int d\sigma[-\chi\mathfrak{N}_{(0)}(x_{(k)}\partial_{(l)}-x_{(l)}\partial_{(k)}+iS_{(k)(l)})\chi+x_{(k)}\rho_{(0)(l)}-x_{(l)}\rho_{(0)(k)}].$$

The quantity $\rho_{\mu\nu}$ is closely related to the infinitesimal expression of the scalar character of $\mathcal{H}$,

$$\mathcal{H}(\chi-i\tfrac{1}{2}\epsilon_{\mu\nu}S_{\mu\nu}\chi)-\mathcal{H}(\chi)=0.$$

We can, indeed, conclude that

$$\rho_{\mu\nu}=0,$$

if $\mathcal{H}$ is no more than quadratic in the components of various independent fields. We shall also prove this without the latter restriction, but, for simplicity, with the limitation that there are no equations of constraint. The commutation relations equivalent to (30),

$$[\chi, P_\nu]=-i\partial_\nu\chi,$$
$$[\chi, J_{\mu\nu}]=-i(x_\mu\partial_\nu-x_\nu\partial_\mu+iS_{\mu\nu})\chi,$$

imply that

$$[\chi, N_{\mu\nu}]=S_{\mu\nu}\chi,$$

where

$$N_{\mu\nu}=J_{\mu\nu}-x_\mu P_\nu+x_\nu P_\mu.$$

This enables one to express the scalar requirement on $\mathcal{H}$ in the form

$$[\mathcal{H}, N_{\mu\nu}]=0.$$

The components

$$N_{(0)(k)}=\int d\sigma'(x_{(k)}-x_{(k)}{}')[\mathcal{H}(x')-\tfrac{1}{2}(\chi\mathfrak{N}_{(l)}\partial_{(l)}{}'\chi-\partial_{(l)}{}'\chi\mathfrak{N}_{(l)}\chi)-\tfrac{1}{2}(\xi\mathfrak{B}\chi+\chi\mathfrak{B}\xi)$$
$$-\tfrac{1}{2}i\int d\sigma\chi(\mathfrak{N}_{(0)}S_{(0)(k)}+S_{(0)(k)}{}^{\dagger}\mathfrak{N}_{(0)})\chi,$$

do not involve the unknown $\rho_{(0)(k)}$. According to our simplifying assumption of no constraint equations, the commutators (anticommutators) of all field components at x and x' contain the three-dimensional delta function $\delta_\sigma(x-x')$ and therefore vanish when multiplied by $x_{(k)}-x_{(k)}{}'$. Furthermore,

$$[\mathcal{H}(x), \chi(x')]\mathfrak{N}_{(0)}=\tfrac{1}{2}i(\partial_\sigma\mathcal{H}/\partial\chi)\delta_\sigma(x-x'),$$

and

$$\mathfrak{N}_{(0)}[\chi(x'), \mathcal{H}(x)]=\tfrac{1}{2}i(\partial_\sigma\mathcal{H}/\partial\chi)\delta_\sigma(x-x'),$$

from which we obtain

$$[\mathcal{H}, N_{(0)(k)}]=2i\rho_{(0)(k)}=0.$$

With this information, the proof is easily extended to all components of $\rho_{\mu\nu}$.

The consistency of the generators G_ϵ and G_χ requires that

$$\tfrac{1}{2}\delta_\chi(\epsilon_\nu P_\nu+\tfrac{1}{2}\epsilon_{\mu\nu}J_{\mu\nu})=-\int d\sigma(\delta\chi)_x\mathfrak{N}_{(0)}\delta\chi,$$

or

$$\delta_\chi P_\nu=\int d\sigma\partial_\nu\chi 2\mathfrak{N}_{(0)}\delta\chi,$$

$$\delta_\chi J_{\mu\nu}=\int d\sigma(x_\mu\partial_\nu-x_\nu\partial_\mu+iS_{\mu\nu})\chi 2\mathfrak{N}_{(0)}\delta\chi,$$

which can now be verified from the expressions (31) and (32), with $\rho_{(0)(k)}=0$.

CHARGED FIELDS

Our considerations thus far specifically exclude the electromagnetic field (and the gravitational field). We introduce the concept of charge by requiring that the Lagrange function be invariant under constant phase (special gauge) transformations, the infinitesimal version of which is

$$'\chi=(1-i\delta\lambda\mathcal{E})\chi.$$

Here $\delta\lambda$ is a constant, and $\mathcal{E}$ is an imaginary matrix which can be viewed as a rotation matrix referring to a space other than the four-dimensional world. The invariance requirement implies that

$$\mathcal{E}^{\dagger}=\mathfrak{B}\mathcal{E}\mathfrak{B}^{-1},$$

or

$$(\mathfrak{B}\mathcal{E})^{\dagger}=\mathfrak{B}\mathcal{E},$$

and

$$[\mathcal{E}, \mathfrak{B}^{-1}\mathfrak{N}_\mu]=[\mathcal{E}, S_{\mu\nu}]=0,$$

and that

$$\mathcal{H}(\chi-i\delta\lambda\mathcal{E}\chi)-\mathcal{H}(\chi)=0.$$

We now write the general variation as

$$\delta(\chi)=\delta\chi-i\tfrac{1}{2}(\partial_\mu\delta x_\nu)S_{\mu\nu}\chi-i\delta\lambda\mathcal{E}\chi,$$

where $\delta\lambda$, characterizing a local phase transformation, is an arbitrary function of x, consistent with constant values on σ_1 and on σ_2. The additional contribution to $\delta(\mathcal{L})$ thereby produced is

$$j_\mu\partial_\mu\delta\lambda-i\tfrac{1}{2}(\xi\mathfrak{B}\mathcal{E}\chi-\chi\mathfrak{B}\mathcal{E}\xi)\delta\lambda,$$

where

$$j_\mu=-i\chi\mathfrak{N}_\mu\mathcal{E}\chi$$

is the charge-current vector. The stationary action principle requires that

$$\partial_\mu j_\mu = -i\tfrac{1}{2}(\xi\mathfrak{B}\mathcal{E}\chi - \chi\mathfrak{B}\mathcal{E}\xi), \tag{33}$$

and yields as the phase transformation generator

$$G_\lambda = \int_\sigma d\sigma_\mu j_\mu \delta\lambda = Q\delta\lambda,$$

where Q is the charge operator.

The integral statement derived from (33),

$$Q(\sigma_1) - Q(\sigma_2) = \int_{\sigma_2}^{\sigma_1} (dx) i\tfrac{1}{2}(\chi\mathfrak{B}\mathcal{E}\xi - \xi\mathfrak{B}\mathcal{E}\chi),$$

becomes the conservation of charge in the absence of an external source. If an infinitesimal source is introduced in the region bounded by σ_1 and σ_2, we then have, in the retarded description,

$$\delta_\xi Q(\sigma_1) = -i\int_{\sigma_2}^{\sigma_1} (dx)\delta\xi\mathfrak{B}\mathcal{E}\chi$$

$$= i[Q(\sigma_1), G_\xi],$$

whence

$$[\chi, Q] = \mathcal{E}\chi.$$

This commutation relation also follows directly from the significance of G_λ, indicating the consistency of the latter with G_ξ.

We shall suppose that the matrix $\mathfrak{B}$ is an element of the algebra generated by $\mathfrak{B}^{-1}\mathfrak{A}_\mu$ and $S_{\mu\nu}$. It follows that $\mathfrak{B}$ commutes with $\mathcal{E}$, and therefore that the latter is explicitly Hermitian,

$$\mathcal{E}^\dagger = \mathcal{E}.$$

Such an antisymmetrical, imaginary matrix possesses real eigenvalues which are symmetrically distributed about zero; nonvanishing eigenvalues occur in oppositely signed pairs. Since $\mathcal{E}$ commutes with all members of the above-mentioned algebra, the charge-bearing character of a given field depends upon the reducibility of this algebra. Thus, if the algebra for a certain kind of field is irreducible, the only matrix commuting with all members of the algebra is the symmetrical unit matrix. Hence $\mathcal{E}=0$, and the field is electrically neutral. If, however, the matrix algebra is reducible to two similar algebras, as in

$$\mathfrak{A}_\mu = \begin{pmatrix} \mathfrak{A}_\mu & 0 \\ 0 & \mathfrak{A}_\mu \end{pmatrix}, \tag{34}$$

the matrix $\mathcal{E}$ exists and has the form (with the same partitioning)

$$\mathcal{E} = e\begin{pmatrix} 0 & -i \\ i & 0 \end{pmatrix}. \tag{35}$$

This describes a charged field, composed of particles with charges $\pm e$, the eigenvalues of $\mathcal{E}$. If three similar algebras are involved, the field contains particles with charges $0, \pm e$.

To present $\mathcal{E}$ as a diagonal matrix, we must forego the choice of Hermitian field components. Thus, for the example of a charged F.D. field, where the field components decompose into $\psi_{(1)}, \psi_{(2)}$, corresponding to the structures (34) and (35), the mutually Hermitian conjugate operators

$$\psi_{(+)} = \psi_{(1)} - i\psi_{(2)}, \quad \psi_{(-)} = \psi_{(1)} + i\psi_{(2)},$$

are associated with eigenvalues $+e$ and $-e$, respectively. On introducing these field components, the derivative term in the Lagrange function, the electric current vector, and the commutation relations, respectively, read

$$\tfrac{1}{4}[\psi_{(-)}\mathfrak{A}_\mu, \partial_\mu\psi_{(+)}] + \tfrac{1}{4}[\psi_{(+)}\mathfrak{A}_\mu, \partial_\mu\psi_{(-)}], \tag{36}$$

$$-ie\tfrac{1}{2}(\psi_{(-)}\mathfrak{A}_\mu\psi_{(+)} - \psi_{(+)}\mathfrak{A}_\mu\psi_{(-)}), \tag{37}$$

and

$$\begin{aligned}&\{\mathfrak{A}_{(0)}\psi_{(+)}(x), \psi_{(+)}(x')\mathfrak{A}_{(0)}\} \\ &\quad = \{\mathfrak{A}_{(0)}\psi_{(-)}(x), \psi_{(-)}(x')\mathfrak{A}_{(0)}\} = 0, \\ &\{\mathfrak{A}_{(0)}\psi_{(+)}(x), \psi_{(-)}(x')\mathfrak{A}_{(0)}\} \\ &\quad = \{\mathfrak{A}_{(0)}\psi_{(-)}(x), \psi_{(+)}(x')\mathfrak{A}_{(0)}\} = i\mathfrak{A}_{(0)}\delta_\sigma(x-x').\end{aligned} \tag{38}$$

There is evident symmetry with respect to the substitution $\psi_{(+)} \leftrightarrow \psi_{(-)}$, $e \leftrightarrow -e$.

Since $\psi_{(+)}$ and $\psi_{(-)}$ are Hermitian conjugate operators, we can arbitrarily select one as the primary non-Hermitian field. We shall write

$$\mathfrak{B}^{-1}\mathfrak{A}_\mu = i\gamma_\mu,$$

and

$$\psi_{(+)} = \psi, \quad \psi_{(-)}\mathfrak{B} = \psi^\dagger\mathfrak{B} = \bar{\psi}.$$

This yields the following forms for (36), (37), and (38):

$$\begin{aligned}&\tfrac{1}{4}[\bar{\psi}\gamma_\mu, i\partial_\mu\psi] - \tfrac{1}{4}[i\partial_\mu\bar{\psi}\gamma_\mu, \psi], \\ &\quad e\tfrac{1}{2}[\bar{\psi}\gamma_\mu, \psi],\end{aligned} \tag{39}$$

and

$$\begin{aligned}&\{\gamma_{(0)}\psi(x), \gamma_{(0)}\psi(x')\} = \{\bar{\psi}(x)\gamma_{(0)}, \bar{\psi}(x')\gamma_{(0)}\} = 0, \\ &\{\gamma_{(0)}\psi(x), \bar{\psi}(x')\gamma_{(0)}\} = \gamma_{(0)}\delta_\sigma(x-x').\end{aligned} \tag{40}$$

To express the now slightly obscured symmetry between positive and negative charge, we call $\psi_{(-)}$ the charge conjugate field

$$\psi^c = (-\mathfrak{B}^{-1})\bar{\psi}, \tag{41}$$

and state this symmetry as invariance under the substitution $\psi \leftrightarrow \psi^c$, $e \leftrightarrow -e$.

The matrices γ_μ; $\mu = 0, \cdots 3$, obey

$$\gamma_\mu{}^\dagger = \mathfrak{B}\gamma_\mu\mathfrak{B}^{-1},$$

and

$$\gamma_\mu{}^{tr} = -\mathfrak{B}\gamma_\mu\mathfrak{B}^{-1}, \tag{42}$$

since they are purely imaginary matrices. One should also recall that $\mathfrak{B}$ is an antisymmetrical, imaginary matrix. If we were to depart from these special struc-

tures by subjecting all matrices to an arbitrary unitary transformation, we should find that the only formal changes occur in (41) and (42), where the matrix $\mathfrak{B}$ appears modified by an orthogonal, rather than a unitary transformation. Hence, in a general representation these equations read

$$\psi^c = C\bar{\psi},$$
$$\gamma_\mu{}^{\mathrm{tr}} = -C^{-1}\gamma_\mu C,$$

where C still exhibits the symmetry of $\mathfrak{B}$, appropriate to the example of a half-integral spin field,

$$C^{\mathrm{tr}} = -C.$$

The commutation relations (40) are in the canonical form which corresponds to the division of the independent field components into two sets, such that one has vanishing anticommutators (commutators, for an integral spin field) among members of the same set. The generator of changes in ψ and $\bar{\psi}$, Eq. (27) in the notation of the charged half-integral spin field example, is

$$G(\psi, \bar{\psi}) = \tfrac{1}{2}i\int d\sigma(\bar{\psi}\gamma_{(0)}\delta\psi - \delta\bar{\psi}\gamma_{(0)}\psi),$$

which can be deduced directly from the Lagrange function derivative term (39). Associated with the freedom of altering the Lagrange function by the addition of a divergence, are various expressions for generating operators of changes in the field components. Thus, we have the following two simple possibilities for the derivative term and the associated generating operator,

$$\tfrac{1}{2}[\bar{\psi}\gamma_\mu, i\partial_\mu\psi],$$
$$G(\psi) = i\int d\sigma\bar{\psi}\gamma_{(0)}\delta\psi,$$

and

$$-\tfrac{1}{2}[i\partial_\mu\bar{\psi}\gamma_\mu, \psi],$$
$$G(\bar{\psi}) = -i\int d\sigma\delta\bar{\psi}\gamma_{(0)}\psi.$$

Evidently $G(\psi)$, for example, in the generator of alterations in the components $\gamma_{(0)}\psi$, with no change in $\bar{\psi}\gamma_{(0)}$. The associated commutation relations,

$$[\gamma_{(0)}\psi, G(\psi)] = i\gamma_{(0)}\delta\psi,$$
$$[\bar{\psi}\gamma_{(0)}, G(\psi)] = 0,$$

are satisfied in virtue of (40), and, conversely, in conjunction with the analogous statements for $G(\bar{\psi})$, imply these operator properties of the field components. The connection with the generator in the symmetrical treatment of all field components is given by

$$G(\psi, \bar{\psi}) = \tfrac{1}{2}G(\psi) + \tfrac{1}{2}G(\bar{\psi}),$$

which indicates the origin of the factor (1/2) in the general Eq. (26).

THE ELECTROMAGNETIC FIELD

The postulate of general gauge invariance motivates the introduction of the electromagnetic field. If all fields and sources are subjected to the general gauge transformation,

$$'\chi = \exp\{-i\lambda(x)\mathcal{E}\}\chi = \chi\exp(i\lambda(x)\mathcal{E}),$$

the Lagrange function we have been considering alters in the following manner,

$$'\mathfrak{L} = \mathfrak{L} + j_\mu\partial_\mu\lambda.$$

The addition of the electromagnetic field Lagrange function,

$$\mathfrak{L}_{\mathrm{emf}} = \tfrac{1}{2}\{j_\mu, A_\mu\} - \tfrac{1}{4}\{F_{\mu\nu}, \partial_\mu A_\nu - \partial_\nu A_\mu\} + \tfrac{1}{4}F_{\mu\nu}{}^2 + J_\mu A_\mu, \quad (43)$$

provides a compensating quantity through the associated gauge transformation

$$'A_\mu = A_\mu - \partial_\mu\lambda.$$

The term involving the external current J_μ is effectively gauge invariant if

$$\partial_\mu J_\mu = 0,$$

since the modification is in the form of a divergence. In the same sense, there is no objection to employing a form of the Lagrange function in which the second term of (43) is replaced by

$$\tfrac{1}{2}\{\partial_\mu F_{\mu\nu}, A_\nu\}. \quad (44)$$

We write the general variation of A_μ in the form

$$\delta(A_\mu) = \delta A_\mu - (\partial_\mu\delta x_\nu)A_\nu$$
$$= \delta A_\mu - \tfrac{1}{2}(\partial_\mu\delta x_\nu - \partial_\nu\delta x_\mu)A_\nu - \tfrac{1}{2}(\partial_\mu\delta x_\nu + \partial_\nu\delta x_\mu)A_\nu,$$

which ascribes to A_μ the same transformation properties as the gradient of a scalar, thus preserving the possibility of gauge transformations under arbitrary coordinate deformations. In a similar way,

$$\delta(F_{\mu\nu}) = \delta F_{\mu\nu} - (\partial_\mu\delta x_\lambda)F_{\lambda\nu} - (\partial_\nu\delta x_\lambda)F_{\mu\lambda}.$$

With regard to the derivation of the electromagnetic field equations from the action principle, it should be noted that general gauge invariance requires that the sources of charged fields depend implicitly upon the vector potential A_μ. We express this dependence by

$$\delta_A\xi(x') = \int (dx)(\delta\xi(x')/\delta A_\mu(x))\delta A_\mu(x).$$

Since the infinitesimal gauge transformation, $\delta A_\mu = -\partial_\mu\delta\lambda$, must induce the change $\delta\xi = -i\delta\lambda\mathcal{E}\xi$, we learn that

$$\partial_\mu(\delta\xi(x')/\delta A_\mu(x)) = -i\mathcal{E}\xi(x)\delta(x-x'). \quad (45)$$

One obtains the following field equations on varying

$F_{\mu\nu}$ and A_ν in the complete Lagrange function,

$$F_{\mu\nu}=\partial_\mu A_\nu-\partial_\nu A_\mu, \tag{46}$$

$$\partial_\nu F_{\mu\nu}=j_\mu+k_\mu+J_\mu, \tag{47}$$

where

$$k_\mu(x)=\tfrac{1}{2}\int (dx')[(\delta\xi(x')/\delta A_\mu(x))\mathfrak{B}\chi(x') +\chi(x')\mathfrak{B}(\delta\xi(x')/\delta A_\mu(x))],$$

is the contribution to the total current vector associated with charged field sources. We derive from (45) that

$$\partial_\mu k_\mu=i\tfrac{1}{2}(\xi\mathfrak{B}\mathcal{E}\chi-\chi\mathfrak{B}\mathcal{E}\xi).$$

But the total current vector is divergenceless in consequence of the electromagnetic field equations. Therefore

$$\partial_\mu j_\mu=-i\tfrac{1}{2}(\xi\mathfrak{B}\mathcal{E}\chi-\chi\mathfrak{B}\mathcal{E}\xi),$$

which is in agreement with (33).

After removing the terms in $\delta(\mathfrak{L}_{\text{emf}})$ that contribute to the field equations, we are left with

$$\delta(\mathfrak{L}_{\text{emf}})=\tfrac{1}{2}\{\delta j_\mu, A_\mu\}-\partial_\mu(F_{\mu\nu}\delta A_\nu)+A_\mu\partial_\nu J_\mu\delta x_\nu -\tfrac{1}{2}(\partial_\mu\delta x_\nu+\partial_\nu\delta x_\mu)(\tfrac{1}{2}\{j_\mu, A_\nu\}-\tfrac{1}{2}\{F_{\mu\lambda}, F_{\nu\lambda}\}) -(\partial_\mu\delta x_\nu)J_\mu A_\nu, \tag{48}$$

in which

$$\tfrac{1}{2}\{\delta j_\mu, A_\mu\}=-i\delta\chi\mathfrak{A}_\mu\mathcal{E}\{\chi, A_\mu\}=-i\{A_\mu, \chi\}\mathfrak{A}_\mu\mathcal{E}\delta\chi.$$

This term alters the field equations of charged fields,

$$2\mathfrak{A}_\mu(\partial_\mu\chi-i\mathcal{E}\tfrac{1}{2}\{A_\mu, \chi\})=(\partial_\mu\mathfrak{C}/\partial\chi)-\mathfrak{B}\xi,$$

$$-(\partial_\mu\chi+i\tfrac{1}{2}\{\chi, A_\mu\}\mathcal{E})2\mathfrak{A}_\mu=(\partial_\nu\mathfrak{C}/\partial\chi)-\xi\mathfrak{B}.$$

We have anticipated that not all components of A_μ commute with χ. The tensor $T_{\mu\nu}$ is now obtained as

$$T_{\mu\nu}=\cdots+\tfrac{1}{2}\{F_{\mu\lambda}, F_{\nu\lambda}\}-\tfrac{1}{2}\{j_\mu, A_\nu\}-J_\mu A_\nu, \tag{49}$$

where $\cdots$ stands for (20), but with $\mathfrak{L}$ the complete Lagrange function. The action principle supplies the differential equation

$$\partial_\mu T_{\mu\nu}=\tfrac{1}{2}(\chi\mathfrak{B}\partial_\nu\xi+\partial_\nu\xi\mathfrak{B}\chi)+A_\mu\partial_\nu J_\mu. \tag{50}$$

The divergence term in (48) yields the infinitesimal generator

$$G_A=-\int d\sigma_\mu F_{\mu\nu}\delta A_\nu=-\int d\sigma F_{(0)(k)}\delta A_{(k)}, \tag{51}$$

while the Lagrange function with the derivative term (44) would give

$$G_F=\int d\sigma_\mu\delta F_{\mu\nu}A_\nu=\int d\sigma\delta F_{(0)(k)}A_{(k)}. \tag{52}$$

The change in the action integral produced by a variation of the external current J_μ is given by

$$\delta_J W_{12}=\int_{\sigma_2}^{\sigma_1}(dx)\delta J_\mu A_\mu.$$

If δJ_μ has the explicitly divergenceless form

$$\delta J_\mu=\partial_\nu\delta M_{\mu\nu}, \quad M_{\mu\nu}=-M_{\nu\mu}, \tag{53}$$

where $\delta M_{\mu\nu}$ vanishes on σ_1 and σ_2, we find that

$$\delta_J W_{12}=\int_{\sigma_2}^{\sigma_1}(dx)\tfrac{1}{2}\delta M_{\mu\nu}F_{\mu\nu},$$

which makes it unnecessary to introduce an external source that is directly coupled to the field strength tensor $F_{\mu\nu}$.

The special nature of the electromagnetic field[3] is apparent in the form of the operator (52) generating changes in the local electric field components. Since one of the field equations is the equation of constraint

$$\partial_{(k)}F_{(0)(k)}=j_{(0)}+k_{(0)}+J_{(0)}, \tag{54}$$

the three variations $\delta F_{(0)(k)}$ cannot be arbitrarily assigned; the electromagnetic field and charged fields are not kinematically independent. This is evidently an aspect of the gauge invariance that links the two types of fields. Alternatively, we see from (51) that $A_{(0)}$ is not a dynamical variable subject to independent variations. But there is no field equation that expresses $A_{(0)}$ in terms of independent dynamical variables, in virtue of the arbitrariness associated with the existence of gauge transformations. Furthermore, a variation of $A_{(k)}$ in the form of a gradient, that is, a gauge transformation, yields a generating operator which, in consequence of (54), no longer contains electromagnetic field dynamical variables. Thus, in either form, (51) or (52), there are only two kinematically independent variations of the electromagnetic field quantities.

We now apply these generators to deduce commutation properties for the gauge invariant field strength components. According to the effect of a variation $\delta A_{(k)}$, upon the local components of $F_{\mu\nu}$ we have

$$[F_{(0)(k)}, G_A]=0,$$

$$[F_{(k)(l)}, G_A]=i(\partial_{(k)}\delta A_{(l)}-\partial_{(l)}\delta A_{(k)}),$$

whence

$$[F_{(0)(k)}(x), F_{(0)(l)}(x')]=0, \tag{55}$$

and

$$[F_{(k)(l)}(x), F_{(0)(m)}(x')] =i(\delta_{(k)(m)}\partial_{(l)}-\delta_{(l)(m)}\partial_{(k)})\delta_\sigma(x-x'). \tag{56}$$

In using G_F, we must restrict the electric field variation according to

$$\partial_{(k)}\delta F_{(0)(k)}=0,$$

which is identically satisfied on writing

$$\delta F_{(0)(k)}=\partial_{(l)}\delta Z_{(k)(l)}, \quad Z_{(k)(l)}=-Z_{(l)(k)}.$$

[3] Papers dealing with the situation peculiar to the electromagnetic field are legion. Of the older literature, the closest in spirit to our procedure is that of W. Pauli, *Handbuch der Physik* (Edwards Brothers, Ann Arbor, 1943), Vol. 24.

This yields the form

$$G_F=\int d\sigma\tfrac{1}{2}F_{(k)(l)}\delta Z_{(k)(l)}.$$

The expression of changes induced by $\delta F_{(0)(k)}$,

$$[F_{(k)(l)}, G_F]=0,$$
$$[F_{(0)(k)}, G_F]=i\delta F_{(0)(k)},$$

then provides the commutation properties

$$[F_{(k)(l)}(x), F_{(m)(n)}(x')]=0,$$
$$[F_{(0)(k)}(x), F_{(l)(m)}(x')] \tag{57}$$
$$=i(\delta_{(k)(l)}\partial_{(m)}-\delta_{(k)(m)}\partial_{(l)})\delta_\sigma(x-x').$$

where the latter is equivalent to (56).

An alternative derivation employs an infinitesimal change in the external source, distributed on (the negative side of) σ, $x_{(0)}=0$,

$$\delta M_{\mu\nu}=\delta m_{\mu\nu}\delta(x_{(0)}),$$

for which the associated generator is

$$G_m=\int d\sigma[\tfrac{1}{2}\delta m_{(k)(l)}F_{(k)(l)}-\delta m_{(0)(k)}F_{(0)(k)}].$$

The alteration produced in the field components follows from the field Eq. (47), and the form of (46) given by

$$\partial_\mu F_{\nu\lambda}+\partial_\nu F_{\lambda\mu}+\partial_\lambda F_{\mu\nu}=0. \tag{58}$$

Thus,

$$\partial_{(0)}(\delta F_{(0)(l)}-\delta M_{(0)(l)})=-\partial_{(k)}\delta F_{(k)(l)}+\partial_{(k)}\delta M_{(k)(l)},$$
$$\partial_{(0)}\delta F_{(k)(l)}=\partial_{(l)}\delta F_{(0)(k)}-\partial_{(k)}\delta F_{(0)(l)},$$

which yields the following discontinuities in $\delta F_{\mu\nu}$ on crossing the surface,

$$\delta F_{(0)(l)}]=\partial_{(k)}\delta m_{(k)(l)},$$
$$\delta F_{(k)(l)}]=\partial_{(l)}\delta m_{(0)(k)}-\partial_{(k)}\delta m_{(0)(l)}.$$

In the retarded description, these discontinuities are the actual changes in the field components on σ. On referring to the general formula (23), we obtain

$$\partial_{(k)}\delta m_{(k)(l)}=i[F_{(0)(l)}, G_m],$$
$$\partial_{(l)}\delta m_{(0)(k)}-\partial_{(k)}\delta m_{(0)(l)}=i[F_{(k)(l)}, G_m].$$

In view of the arbitrary values of $\delta m_{\mu\nu}$ on σ, these equations imply field strength commutation relations, which are identical with (55) and (57).

We give a related procedure which also illustrates the possibility of evaluating commutators of field quantities at points in time-like relation. The two field Eqs. (47) and (58) can be combined into (we incorporate k_ν with j_ν)

$$-\partial_\lambda{}^2F_{\mu\nu}=\partial_\mu(j_\nu+J_\nu)-\partial_\nu(j_\mu+J_\mu).$$

A change in the external current, of the form (53), yields

$$-\partial_\lambda{}^2\delta_M F_{\mu\nu}-\partial_\mu\delta_M j_\nu+\partial_\nu\delta_M j_\mu$$
$$=\partial_\mu\partial_\lambda\delta M_{\nu\lambda}-\partial_\nu\partial_\lambda\delta M_{\mu\lambda}, \tag{59}$$

where, in the retarded description

$$\delta_M F_{\mu\nu}(x)=i\left[F_{\mu\nu}(x), \int_{\sigma_2}^{\sigma}(dx')\tfrac{1}{2}\delta M_{\lambda\kappa}(x')F_{\lambda\kappa}(x')\right]$$
$$=\int_{\sigma_2}^{\sigma_1}(dx')\tfrac{1}{2}\delta M_{\lambda\kappa}(x')\eta_+(x-x')i$$
$$\times[F_{\mu\nu}(x), F_{\lambda\kappa}(x')],$$

and η_+ is the discontinuous function

$$\eta_+(x-x')=1, \quad x_0>x_0'$$
$$=0, \quad x_0<x_0'.$$

We have a similar expression for $\delta_M j_\nu(x)$. On comparing the coefficients of $\delta M_{\lambda\kappa}(x')$ in (59) (our two treatments employing external sources are thus distinguished by surface and volume distributions of $\delta M_{\mu\nu}$, respectively), we find

$$-\partial_\lambda{}^2\eta_+(x-x')i[F_{\mu\nu}(x), F_{\lambda\kappa}(x')]$$
$$-\partial_\mu\eta_+(x-x')i[j_\nu(x), F_{\lambda\kappa}(x')]$$
$$+\partial_\nu\eta_+(x-x')i[j_\mu(x), F_{\lambda\kappa}(x')]$$
$$=(\delta_{\nu\lambda}\partial_\mu\partial_\kappa-\delta_{\nu\kappa}\partial_\mu\partial_\lambda-\delta_{\mu\lambda}\partial_\nu\partial_\kappa$$
$$+\delta_{\mu\kappa}\partial_\nu\partial_\lambda)\delta(x-x'). \tag{60}$$

The value of $i[F_{\mu\nu}(x), F_{\lambda\kappa}(x')]$, for equal times, is then obtained from the coefficient of the differentiated delta function of the time coordinate, with the anticipated result.

In the approximation that neglects the dynamical relation between currents and fields at points in time-like relation, the differential Eq. (60) has the solution

$$\eta_+(x-x')i[F_{\mu\nu}(x), F_{\lambda\kappa}(x')]$$
$$=(\delta_{\nu\lambda}\partial_\mu\partial_\kappa-\delta_{\nu\kappa}\partial_\mu\partial_\lambda-\delta_{\mu\lambda}\partial_\nu\partial_\kappa+\delta_{\mu\kappa}\partial_\nu\partial_\lambda)D_{\rm ret}(x-x'),$$

where $D_{\rm ret}(x-x')$ is the familiar retarded solution of

$$-\partial_\lambda{}^2D_{\rm ret}=\delta(x-x'). \tag{61}$$

Had we employed the advanced description, η_+ would be replaced by $-\eta_-$, where

$$\eta_-(x-x')=0, \quad x_0>x_0'$$
$$=1, \quad x_0<x_0',$$

and the advanced solution of (61) would appear. Subtracting these two results, we find

$$i[F_{\mu\nu}(x), F_{\lambda\kappa}(x')]$$
$$=(\delta_{\nu\lambda}\partial_\mu\partial_\kappa-\delta_{\nu\kappa}\partial_\mu\partial_\lambda-\delta_{\mu\lambda}\partial_\nu\partial_\kappa+\delta_{\mu\kappa}\partial_\nu\partial_\lambda)D(x-x'),$$

in which $D(x-x')$ is the homogeneous solution of (61) provided by

$$D=D_{\rm ret}-D_{\rm adv}.$$

The kinematical relation between the electromagnetic field and charged fields, on a given σ, is most clearly indicated in a special choice of gauge, the so-called radiation gauge,

$$\partial_{(k)}A_{(k)}=0. \tag{62}$$

With this choice, the constraint equation for the electric field reads

$$\partial_{(k)}F_{(0)(k)}=-\partial_{(k)}{}^2A_{(0)}=j_{(0)}+J_{(0)},$$

so that the scalar potential is completely determined by the charge density,

$$A_{(0)}(x)=\int_\sigma d\sigma' \mathfrak{D}_\sigma(x-x')(j_{(0)}(x')+J_{(0)}(x')),$$

where

$$\mathfrak{D}_\sigma(x-x')=(1/4\pi)[(x_{(k)}-x_{(k)}{}')^2]^{-\frac{1}{2}}.$$

Evidently, $A_{(0)}$ does not commute with the components of charged fields. In this gauge, then, the dependence of the electric field upon the charged fields is made explicit through the decomposition of the electric field into transverse and longitudinal parts,

$$\begin{aligned}F_{(0)(k)}&=-\partial_{(0)}A_{(k)}-\partial_{(k)}A_{(0)}\\&=F_{(0)(k)}{}^{(T)}+F_{(0)(k)}{}^{(L)}.\end{aligned}$$

The inference that the transverse fields are the independent dynamical variables of the electromagnetic field in this gauge is confirmed on examining the generators G_A and G_F. Indeed,

$$G_A=-\int d\sigma F_{(0)(k)}\delta A_{(k)}=-\int d\sigma F_{(0)(k)}{}^{(T)}\delta A_{(k)},$$

and

$$G_F=\int d\sigma \delta F_{(0)(k)}A_{(k)}=\int d\sigma \delta F_{(0)(k)}{}^{(T)}A_{(k)},$$

in view of the transverse nature of $A_{(k)}$, Eq. (62). We can now derive the commutation properties of these dynamical variables from

$$\begin{aligned}&[A_{(k)},G_A]=i\delta A_{(k)}, &&[F_{(0)(k)}{}^{(T)},G_A]=0,\\&[F_{(0)(k)}{}^{(T)},G_F]=i\delta F_{(0)(k)}{}^{(T)}, &&[A_{(k)},G_F]=0,\end{aligned}$$

on taking into account the restrictions

$$\partial_{(k)}\delta A_{(k)}=\partial_{(k)}\delta F_{(0)(k)}{}^{(T)}=0,$$

produced by the transverse nature of these quantities. The Lagrange multiplier device permits us to deduce that

$$i[A_{(k)}(x),F_{(0)(l)}{}^{(T)}(x')]=\delta_{(k)(l)}\delta_\sigma(x-x')+\partial_{(l)}\lambda_{(k)}.$$

The divergenceless character of the transverse electric field supplied the information

$$\partial_{(l)}{}'^2\lambda_{(k)}=\partial_{(k)}\delta_\sigma(x-x'),$$

whence

$$\lambda_{(k)}=-\partial_{(k)}\mathfrak{D}_\sigma(x-x').$$

The resulting commutator

$$\begin{aligned}&i[A_{(k)}(x),F_{(0)(l)}{}^{(T)}(x')]\\&\quad=\delta_{(k)(l)}\delta_\sigma(x-x')-\partial_{(k)}\partial_{(l)}{}'\mathfrak{D}_\sigma(x-x')\\&\quad=(\delta_{(k)(l)}\delta_\sigma(x-x'))^{(T)},\end{aligned}$$

is also consistent with the transverse nature of $A_{(k)}$. The remaining commutation relations are

$$[A_{(k)}(x),A_{(l)}(x')]=[F_{(0)(k)}{}^{(T)}(x),F_{(0)(l)}{}^{(T)}(x')]=0.$$

We shall use the device of the external current to derive the commutation relations between the electromagnetic field tensor and the displacement generators P_ν, $J_{\mu\nu}$. According to (49) and (50),

$$P_\nu(\sigma_1)-P_\nu(\sigma_2)=\int_{\sigma_2}^{\sigma_1}(dx)[\cdots+A_\lambda\partial_\nu J_\lambda],$$

$$\begin{aligned}J_{\mu\nu}(\sigma_1)-J_{\mu\nu}(\sigma_2)=\int_{\sigma_2}^{\sigma_1}(dx)[&\cdots+A_\lambda(x_\mu\partial_\nu-x_\nu\partial_\mu)J_\lambda\\&+A_\mu J_\nu-A_\nu J_\mu],\end{aligned}$$

in which we have indicated only the terms containing the external current. We consider an infinitesimal change in the latter possessing the form (53). In the retarded description, the resulting changes of P_ν and $J_{\mu\nu}$ on σ_1 are

$$\delta_M P_\nu(\sigma_1)=-\int_{\sigma_2}^{\sigma_1}(dx)\tfrac{1}{2}\delta M_{\lambda\kappa}\partial_\nu F_{\lambda\kappa},$$

$$\begin{aligned}\delta_M J_{\mu\nu}(\sigma_1)=-\int_{\sigma_2}^{\sigma_1}(dx)[&\tfrac{1}{2}\delta M_{\lambda\kappa}(x_\mu\partial_\nu-x_\nu\partial_\mu)F_{\lambda\kappa}\\&+\delta M_{\lambda\nu}F_{\mu\nu}-\delta M_{\lambda\mu}F_{\nu\lambda}].\end{aligned}$$

When expressed in terms of the generator

$$G_M=\int_{\sigma_2}^{\sigma_1}(dx)\tfrac{1}{2}\delta M_{\lambda\kappa}F_{\lambda\kappa},$$

the following commutators are encountered,

$$\begin{aligned}&i[F_{\lambda\kappa},P_\nu]=\partial_\nu F_{\lambda\kappa},\\&i[F_{\lambda\kappa},J_{\mu\nu}]=(x_\mu\partial_\nu-x_\nu\partial_\mu)F_{\lambda\kappa}+\delta_{\nu\kappa}F_{\mu\lambda}\\&\qquad\qquad-\delta_{\mu\kappa}F_{\nu\lambda}+\delta_{\mu\lambda}F_{\nu\kappa}-\delta_{\nu\lambda}F_{\mu\kappa}.\end{aligned}$$

Finally, we remark that the extension of (31) to include the electromagnetic field, in the radiation gauge, is

$$\begin{aligned}P_{(0)}=\int d\sigma[&\tfrac{1}{2}(F_{(0)(k)}{}^{(T)})^2+\tfrac{1}{4}(F_{(k)(l)})^2\\&+\mathfrak{C}-\chi\mathfrak{N}_{(k)}(\partial_{(k)}-i\mathcal{E}A_{(k)})\chi\\&-J_{(k)}A_{(k)}+\tfrac{1}{2}(j_{(0)}+J_{(0)})A_{(0)}-\tfrac{1}{2}(\xi\mathfrak{B}\chi+\chi\mathfrak{B}\xi)],\end{aligned}$$

and

$$P_{(k)}=\int d\sigma[\tfrac{1}{2}\{F_{(0)(l)}{}^{(T)}, F_{(k)(l)}\}-\chi\mathfrak{A}_{(0)}\partial_{(k)}\chi].$$

In arriving at the expression for $P_{(0)}$, the noncommutivity of $A_{(0)}$ with χ must be taken into consideration, but produces no actual contribution. A variation of each of the independent fields yields

$$\delta P_\mu=\int d\sigma[\delta F_{(0)(k)}{}^{(T)}\partial_\mu A_{(k)}-\delta A_{(k)}\partial_\mu F_{(0)(k)}{}^{(T)}-\delta\chi 2\mathfrak{A}_{(0)}\partial_\mu\chi],$$

which confirms the consistency of the translation generator with the various field variation generators.

PHYSICAL REVIEW VOLUME 91, NUMBER 3 AUGUST 1, 1953

The Theory of Quantized Fields. III

JULIAN SCHWINGER
Harvard University, Cambridge, Massachusetts
(Received March 31, 1953)

In this paper we discuss the electromagnetic field, as perturbed by a prescribed current. All quantities of physical interest in various situations, eigenvalues, eigenfunctions, and transition probabilities, are derived from a general transformation function which is expressed in a non-Hermitian representation. The problems treated are: the determination of the energy-momentum eigenvalues and eigenfunctions for the isolated electromagnetic field, and the energy eigenvalues and eigenfunctions for the field perturbed by a time-independent current; the evaluation of transition probabilities and photon number expectation values for a time-dependent current that departs from zero only within a finite time interval, and for a time-dependent current that assumes non-vanishing time-independent values initially and finally. The results are applied in a discussion of the infrared catastrophe and of the adiabatic theorem. It is shown how the latter can be exploited to give a uniform formulation for all problems requiring the evaluation of transition probabilities or eigenvalue displacements.

INTRODUCTION

WE shall approach the general problem of coupled fields through the simpler situation presented by a single field which is externally perturbed. In this paper we illustrate the treatment of a Bose-Einstein system by discussing the Maxwell field with a prescribed electric current. A succeeding paper will be devoted to the Dirac field.

The solution to all dynamical questions is obtained by constructing the transformation function linking two descriptions of the system that are associated with different space-like surfaces. Thus, for a closed system, the general transformation function can be expressed as

$$(\zeta_1'\sigma_1|\zeta_2''\sigma_2)=\sum_{\gamma',\gamma''}(\zeta_1'|\gamma')(\gamma'\sigma_1|\gamma''\sigma_2)(\gamma''|\zeta_2''),$$

where the γ are a complete set of compatible constants of the motion, in terms of which the energy-momentum vector P_μ can be exhibited. In the γ representation, the effect of an infinitesimal translation of σ_1 is given by

$$\delta_\epsilon(\gamma'\sigma_1|\gamma''\sigma_2)=i(\gamma'\sigma_1|P_\mu\delta\epsilon_\mu|\gamma''\sigma_2)=iP_\mu'\delta\epsilon_\mu(\gamma'\sigma_1|\gamma''\sigma_2),$$

where $P_\mu'=P_\mu(\gamma')$. Accordingly, if σ_1 is parallel to σ_2, and is generated from the latter by the translation X_μ, we have

$$(\gamma'\sigma_1|\gamma''\sigma_2)=\delta(\gamma',\gamma'')\exp(iP_\mu'X_\mu),$$

and

$$(\zeta_1'\sigma_1|\zeta_2''\sigma_2)=\sum_{\gamma'}(\zeta_1'|\gamma')\exp(iP_\mu'X_\mu)(\gamma'|\zeta_2''). \quad (1)$$

This shows how a knowledge of the transformation function that relates two conveniently chosen representations on parallel surfaces yields all the eigenvalues and eigenfunctions of P_μ.

Another illustration of the utility of transformation functions relates to the situation in which the same system is externally perturbed, in the interior of the space-time region bounded by σ_1 and σ_2. The transformation function $(\gamma'\sigma_1|\gamma''\sigma_2)$, inferred from the knowledge of $(\zeta_1'\sigma_1|\zeta_2''\sigma_2)$, then yields the probability of a transition from the initial state γ'' to the final state γ',

$$p(\gamma',\gamma'')=|(\gamma'\sigma_1|\gamma''\sigma_2)|^2. \quad (2)$$

Representations of particular convenience are suggested by the characterization of the vacuum state for a complete system. The vacuum is the state of minimum energy. If this natural origin of energy is adjusted to zero, the vacuum can be described as that state presenting identical properties to all observers, $P_\mu\Psi_0=J_{\mu\nu}\Psi_0=0$, and is therefore independent of the surface σ. Now, if the general field component χ is analyzed into contributions of various frequencies, χ_{p0}, we have $[\chi_{p0}, P_0]=p_0\chi_{p0}$, or $P_0\chi_{p0}=\chi_{p0}(P_0-p_0)$. When this relation, involving a positive frequency, $p_0>0$, is

applied to the vacuum state vector, we obtain

$$P_0(\chi_{p0}\Psi_0) = -p_0(\chi_{p0}\Psi_0).$$

Hence

$$\chi_{p0}\Psi_0 = 0, \quad p_0 > 0, \tag{3}$$

since this state, of energy less than that of the vacuum, must be nonexistent. A similar discussion yields

$$\Psi_0^\dagger \chi_{p0} = 0, \quad p_0 < 0,$$

which is the statement adjoint to (3). The vector Ψ_0 is thus characterized as the right eigenvector of the positive frequency parts of the field components, $\chi^{(+)}$, with zero eigenvalues, and $\Psi_0^\dagger$ appears as the left eigenvector, with zero eigenvalues, of the $\chi^{(-)}$, the negative frequency parts of the field components. It should be noted that the decomposition into positive and negative frequency parts is invariant under orthochronous Lorentz transformations. The complete sets of eigenvectors of these types will evidently be of particular value for the construction of energy eigenstates.

THE MAXWELL FIELD

Elementary descriptions of the electromagnetic field on a given σ are provided by the alternative complete sets of commuting operators, the transverse potential $A_k(x)$, and the transverse electric field[1] $F_{0k}(x)$. Following the suggestion of the preceding section, we employ instead the non-Hermitian operators, $F_{0k}^{(+)}(x)$ and $F_{0k}^{(-)}(x)$, which in the absence of an external current, are the positive and negative frequency parts of $F_{0k}(x)$. The transverse field equations, for zero current, are

$$-\partial_0 A_k = F_{0k}, \quad \partial_0 F_{0k} = -\partial_l^2 A_k = \omega^2 A_k,$$

where ω, as a coordinate operator, is defined by the matrix

$$(\mathbf{x}|\omega|\mathbf{x}') = \int \frac{(d\mathbf{k})}{(2\pi)^3} |\mathbf{k}| \exp(i\mathbf{k}\cdot(\mathbf{x}-\mathbf{x}')),$$

which is symmetrical and positive-definite. On writing

$$F_{0k} = F_{0k}^{(+)} + F_{0k}^{(-)}, \quad A_k = A_k^{(+)} + A_k^{(-)},$$

where

$$F_{0k}^{(\pm)} = \pm i\omega A_k^{(\pm)} = \tfrac{1}{2}(F_{0k} \pm i\omega A_k),$$

the equations of motion assume the form

$$\partial_0 F_{0k}^{(\pm)} = \mp i\omega F_{0k}^{(\pm)},$$

which, in virtue of the positive-definite nature of ω, confirms the interpretation of $F_{0k}^{(\pm)}$.

The canonical form of the infinitesimal generators

$$G_A = \int d\sigma(-F_{0k})\delta A_k, \quad G_F = \int d\sigma A_k \delta F_{0k},$$

can be extended to the generators of infinitesimal changes in the non-Hermitian operators $F_{0k}^{(\pm)}$, in the sense of the transformation equation $G - \bar{G} = \delta(W)$. Thus

$$G_F = \int d\sigma (A_k^{(+)} + A_k^{(-)})(\delta F_{0k}^{(+)} + \delta F_{0k}^{(-)})$$

$$= \int d\sigma 2A_k^{(-)}\delta F_{0k}^{(+)} + \delta\Big[\int d\sigma (\tfrac{1}{2}A_k^{(+)}F_{0k}^{(+)} + \tfrac{1}{2}A_k^{(-)}F_{0k}^{(-)} + A_k^{(+)}F_{0k}^{(-)})\Big],$$

and

$$G_F = \int d\sigma 2A_k^{(+)}\delta F_{0k}^{(-)} + \delta\Big[\int d\sigma (\tfrac{1}{2}A_k^{(+)}F_{0k}^{(+)} + \tfrac{1}{2}A_k^{(-)}F_{0k}^{(-)} + A_k^{(-)}F_{0k}^{(+)})\Big],$$

which yields

$$G_F^{(+)} = \int d\sigma 2A_k^{(-)}\delta F_{0k}^{(+)} = 2i\int d\sigma F_{0k}^{(-)}\omega^{-1}\delta F_{0k}^{(+)},$$

and

$$G_F^{(-)} = \int d\sigma 2A_k^{(+)}\delta F_{0k}^{(-)} = -2i\int d\sigma F_{0k}^{(+)}\omega^{-1}\delta F_{0k}^{(-)}.$$

The commutation relations on σ, implied by these generators, are

$$[F_{0k}^{(+)}(x), F_{0l}^{(+)}(x')] = [F_{0k}^{(-)}(x), F_{0l}^{(-)}(x')] = 0,$$

and

$$[F_{0k}^{(+)}(x), 2A_{0l}^{(-)}(x')] = [F_{0k}^{(-)}(x), 2A_{0l}^{(+)}(x')] = i(\delta_{kl}\delta_\sigma(x-x'))^{(T)}.$$

The latter can also be written

$$[F_{0k}^{(+)}(x), F_{0l}^{(-)}(x')] = \tfrac{1}{2}(\delta_{kl}(\mathbf{x}|\omega|\mathbf{x}'))^{(T)}. \tag{4}$$

These operator properties can be verified directly from those of F_{0k} and A_k.

It should be noted that there exists some freedom in choosing the generator for a given set of independent variables. Thus,

$${}'G_F^{(+)} = \int d\sigma 2A_k \delta F_{0k}^{(+)}$$

is also a generator of infinitesimal changes in $F_{0k}^{(+)}$, since

$$G_F^{(+)} - {}'G_F^{(+)} = -\int d\sigma 2A_k^{(+)}\delta F_{0k}^{(+)}$$

$$= 2i\int d\sigma F_{0k}^{(+)}\omega^{-1}\delta F_{0k}^{(+)}$$

$$= \delta\Big[i\int d\sigma F_{0k}^{(+)}\omega^{-1}F_{0k}^{(+)}\Big].$$

[1] When no confusion is likely, we shall not employ the more complete notation $F_{(0)(k)}{}^{(T)}(x)$, which indicates that these are the transverse field components, relative to a local coordinate system based on σ.

Similarly,

$$'G_{F^{(-)}}=\int d\sigma 2A_k\delta F_{0k}{}^{(-)}$$

is an alternative generator of changes in $F_{0k}{}^{(-)}$,

$$G_{F^{(-)}}-'G_{F^{(-)}}=\delta\left[-i\int d\sigma F_{0k}{}^{(-)}\omega^{-1}F_{0k}{}^{(-)}\right].$$

The eigenvector concept can be extended to non-Hermitian operators, with some limitations. We introduce the right eigenvector of the complete set of commuting operators, $F_{0k}{}^{(+)}(x)$ on σ,

$$F_{0k}{}^{(+)}(x)\Psi(F^{(+)'}\sigma)=F_{0k}{}^{(+)'}(x)\Psi(F^{(+)'}\sigma),$$

and the left eigenvector of the complete set, $F_{0k}{}^{(-)}(x)$ on σ,

$$\Phi(F^{(-)'}\sigma)F_{0k}{}^{(-)}(x)=\Phi(F^{(-)'}\sigma)F_{0k}{}^{(-)'}(x).$$

In virtue of the relation $F_{0k}{}^{(-)}(x)=F_{0k}{}^{(+)}(x)^\dagger$, these eigenvectors and eigenvalues are connected by

$$\Phi(F^{(-)'}\sigma)=\Psi(F^{(+)'}\sigma)^\dagger,\quad F_{0k}{}^{(-)'}(x)=F_{0k}{}^{(+)'}(x)^*. \tag{5}$$

However, the right eigenvector of the $F_{0k}{}^{(-)}$ and the left eigenvector of the $F_{0k}{}^{(+)}$ do not exist. This can be inferred from the commutator (4), in the form

$$[{}'F_{0k}{}^{(-)}(x)^\dagger,\ {}'F_{0l}{}^{(-)}(x')]=\tfrac{1}{2}(\delta_{kl}(\mathbf{x}|\omega|\mathbf{x}'))^{(T)},$$

where

$${}'F_{0k}{}^{(-)}(x)=F_{0k}{}^{(-)}(x)-F_{0k}{}^{(-)'}(x).$$

When applied to the hypothetical eigenvector $\Psi(F^{(-)'}\sigma)$, this relation yields

$$-{}'F_{0l}{}^{(-)}(x')\ {}'F_{0k}{}^{(-)}(x)^\dagger\Psi(F^{(-)'}\sigma)=\tfrac{1}{2}(\delta_{kl}(\mathbf{x}|\omega|\mathbf{x}'))^{(T)}\Psi(F^{(-)'}\sigma).$$

The contradiction between the negative-definite nature of the operator on the left, and the positive-definite character of the numerical quantity on the right establishes the nonexistence[2] of $\Psi(F^{(-)'}\sigma)$, and similarly, of $\Phi(F^{(+)'}\sigma)$.

Let us consider the significance of the change induced in the eigenvectors $\Psi(F^{(+)'}\sigma)$ and $\Phi(F^{(-)'}\sigma)$ by the respective generators $G_{F^{(+)}}$ and $G_{F^{(-)}}$, according to the mutually Hermitian conjugate equations,

$$\delta\Psi(F^{(+)'}\sigma)=-iG_{F^{(+)}}\Psi(F^{(+)'}\sigma),$$
$$\delta\Phi(F^{(-)'}\sigma)=i\Phi(F^{(-)'}\sigma)G_{F^{(-)}}.$$

Now $\Psi(F^{(+)'}\sigma)+\delta\Psi(F^{(+)'}\sigma)$ is the eigenvector of the operator set $F_{0k}{}^{(+)}-\delta F_{0k}{}^{(+)}$, with the eigenvalues $F_{0k}{}^{(+)'}$. Since the $\delta F_{0k}{}^{(+)}$ are arbitrary infinitesimal numbers, this vector is also the eigenvector of the $F_{0k}{}^{(+)}$ with the eigenvalues $F_{0k}{}^{(+)'}+\delta F_{0k}{}^{(+)}$. Hence the alteration of the eigenvector $\Psi(F^{(+)'}\sigma)$ is that associated with the change of the eigenvalues by $\delta F_{0k}{}^{(+)}$. A similar statement applies to $\delta\Phi(F^{(-)'}\sigma)$.

The relation between the eigenvectors $\Psi(F^{(+)'}\sigma)$ and ${}'\Psi(F^{(+)'}\sigma)$, which are affected analogously by the respective generators $G_{F^{(+)}}$ and ${}'G_{F^{(+)}}$, can be deduced from

$$\begin{aligned}\delta'\Psi(F^{(+)'}\sigma)&=-i\,'G_{F^{(+)}}{}'\Psi(F^{(+)'}\sigma)\\&=-iG_{F^{(+)}}{}'\Psi(F^{(+)'}\sigma)\\&\quad-\delta\left(\int d\sigma F_{0k}{}^{(+)'}\omega^{-1}F_{0k}{}^{(+)'}\right){}'\Psi(F^{(+)'}\sigma),\end{aligned}$$

namely,

$$\begin{aligned}{}'\Psi(F^{(+)'}\sigma)&=\exp\left(-\int d\sigma F_{0k}{}^{(+)'}\omega^{-1}F_{0k}{}^{(+)'}\right)\Psi(F^{(+)'}\sigma)\\&=\exp\left(-i\int d\sigma A_k{}^{(+)'}F_{0k}{}^{(+)'}\right)\Psi(F^{(+)'}\sigma).\end{aligned}\tag{6}$$

The adjoint equation reads

$$\begin{aligned}{}'\Phi(F^{(-)'}\sigma)&=\exp\left(-\int d\sigma F_{0k}{}^{(-)'}\omega^{-1}F_{0k}{}^{(-)'}\right)\Phi(F^{(-)'}\sigma)\\&=\exp\left(i\int d\sigma A_k{}^{(-)'}F_{0k}{}^{(-)'}\right)\Phi(F^{(-)'}\sigma).\end{aligned}\tag{7}$$

We shall now discuss the Maxwell field under the influence of a prescribed current distribution $J_\mu(x)$. It is convenient, initially, to describe the relations between states on the two arbitrary plane surfaces, σ_1 and σ_2, by means of the transformation function

$${}'(F^{(-)'}\sigma_1|F^{(+)'}\sigma_2)=({}'\Phi(F^{(-)'}\sigma_1)\,{}'\Psi(F^{(+)'}\sigma_2)). \tag{8}$$

The dependence of this transformation function on the eigenvalues $F_{(0)(k)}{}^{(-)'}$ and $F_{(0)(k)}{}^{(+)'}$ is indicated by

$$\begin{aligned}&\delta_F\,'(F^{(-)'}\sigma_1|F^{(+)'}\sigma_2)\\&=i\,'(F^{(-)'}\sigma_1|[{}'G_{F^{(-)}}(\sigma_1)-{}'G_{F^{(+)}}(\sigma_2)]|F^{(+)'}\sigma_2)\\&=2i\,'\left(F^{(-)'}\sigma_1\left|\left[\int_{\sigma_1}d\sigma_\mu\delta F_{\mu\nu}{}^{(-)'}A_\nu\right.\right.\right.\\&\qquad\left.\left.\left.-\int_{\sigma_2}d\sigma_\mu\delta F_{\mu\nu}{}^{(+)'}A_\nu\right]\right|F^{(+)'}\sigma_2\right),\end{aligned}\tag{9}$$

while an infinitesimal change of the external current produces the alteration

$$\begin{aligned}&\delta_J\,'(F^{(-)'}\sigma_1|F^{(+)'}\sigma_2)\\&=i\,'\left(F^{(-)'}\sigma_1\left|\int_{\sigma_2}^{\sigma_1}(dx)\delta J_\mu A_\mu\right|F^{(+)'}\sigma_2\right).\end{aligned}\tag{10}$$

The current variations are subject to the restriction

[2] It is evident from the discussion of the first section, that this is related to the nonexistence of a state with *maximum* energy.

$\partial_\mu \delta J_\mu = 0$. Accordingly, if we rewrite (10) in the notation

$$(\delta/\delta J_\mu(x))\,{}'(F^{(-)\prime}\sigma_1|F^{(+)\prime}\sigma_2) = i\,{}'(F^{(-)\prime}\sigma_1|A_\mu(x)|F^{(+)\prime}\sigma_2), \quad (11)$$

we are at liberty to add an arbitrary gradient to $A_\mu(x)$. Since this coincides with the freedom of gauge transformations, we do not indicate it explicitly.

The advantage provided by the transformation function (8) rests in the possibility of combining (9) and (11) into

$$\delta_F\,{}'(F^{(-)\prime}\sigma_1|F^{(+)\prime}\sigma_2) = \left[2\int_{\sigma_1} d\sigma_\mu \delta F_{\mu\nu}{}^{(-)\prime}(\delta/\delta J_\nu) - 2\int_{\sigma_2} d\sigma_\mu \delta F_{\mu\nu}{}^{(+)\prime}(\delta/\delta J_\nu)\right] \times {}'(F^{(-)\prime}\sigma_1|F^{(+)\prime}\sigma_2),$$

which possesses the formal solution

$$'(F^{(-)\prime}\sigma_1|F^{(+)\prime}\sigma_2) = \exp\left[2\int_{\sigma_1} d\sigma_\mu F_{\mu\nu}{}^{(-)\prime}(\delta/\delta J_\nu) - 2\int_{\sigma_2} d\sigma_\mu F_{\mu\nu}{}^{(+)\prime}(\delta/\delta J_\nu)\right] {}'(0\sigma_1|0\sigma_2). \quad (12)$$

The problem is thus reduced to the construction of the transformation function referring to null eigenvalues.

We shall write[3]

$$(0\sigma_1|0\sigma_2) = \exp(i\mathfrak{W}_0),$$

and

$$(0\sigma_1|A_\mu(x)|0\sigma_2)/(0\sigma_1|0\sigma_2) = \langle A_\mu(x)\rangle.$$

In this notation, the dependence of the null eigenvalue transformation function upon the external current is described by

$$(\delta/\delta J_\mu(x))\mathfrak{W}_0 = \langle A_\mu(x)\rangle,$$

or

$$\delta\mathfrak{W}_0 = \int_{-\infty}^{\infty} (dx)\delta J_\mu(x)\langle A_\mu(x)\rangle, \quad (13)$$

in which we have extended the integration over the entirety of space-time by supposing that the current vanishes externally to the region of interest, the volume bounded by σ_1 and σ_2. According to the operator field equation

$$\partial_\nu F_{\mu\nu} = -\partial_\nu{}^2 A_\mu + \partial_\mu \partial_\nu A_\nu = J_\mu,$$

the numerical quantity $\langle A_\mu(x)\rangle$ obeys the differential equation

$$-\partial_\nu{}^2\langle A_\mu\rangle + \partial_\mu\partial_\nu\langle A_\nu\rangle = J_\mu. \quad (14)$$

Now the gauge ambiguity of $\langle A_\mu\rangle$ is completely without effect in (13), since J_μ vanishes on the boundary of the extended region. Therefore, for the purpose of constructing $\mathfrak{W}_0$, we can replace the differential equation (14) with

$$-\partial_\nu{}^2\langle A_\mu\rangle = J_\mu. \quad (15)$$

We are concerned with the solution of this equation that is compatible with the boundary conditions

$$\langle F_{(0)(k)}{}^{(-)}\rangle = 0, \text{ on } \sigma_1, \quad \langle F_{(0)(k)}{}^{(+)}\rangle = 0, \text{ on } \sigma_2,$$

which follow from the nature of the null eigenvalue states on σ_1 and σ_2. Since the current vector is zero in the external region, we can rephrase these boundary conditions as the requirement that the field shall contain only positive frequencies in the domain constituting the future of σ_1, and only negative frequencies in the region prior to σ_2. This excludes a possible homogeneous solution of (15), whence

$$\langle A_\mu(x)\rangle = \int_{-\infty}^{\infty} (dx')D_+(x-x')J_\mu(x'), \quad (16)$$

in which $D_+(x-x')$ is the Green's function defined by

$$-\partial_\nu{}^2 D_+(x-x') = \delta(x-x'),$$

together with the statement that it contains only positive frequencies for $x_0 > x_0'$, and only negative frequencies for $x_0 < x_0'$. It therefore satisfies the temporal analog of the outgoing wave or radiation condition familiar in the spatial description of a harmonic source.[4]

The expression of (16) provided by

$$(\delta/\delta J_\nu(x'))\langle A_\mu(x)\rangle = (\delta/\delta J_\mu(x))(\delta/\delta J_\nu(x'))\mathfrak{W}_0 = \delta_{\mu\nu}D_+(x-x'),$$

indicates that $D_+(x-x')$ is a symmetrical function of x and x'. Accordingly, the integral of (13) is

$$\mathfrak{W}_0 = \frac{1}{2}\int_{-\infty}^{\infty} (dx)(dx')J_\mu(x)D_+(x-x')J_\mu(x'), \quad (17)$$

apart from the additive constant which is the value of $\mathfrak{W}_0$ for the isolated electromagnetic field ($J_\mu = 0$). It is an advantage of the representation we have been employing that this integration constant has the value zero. Indeed, the null eigenvalue states of the complete system provided by the electromagnetic field with no external current are just the σ-independent vacuum state, whence

$$J_\mu = 0: \quad (0\sigma_1|0\sigma_2) = 1, \quad \mathfrak{W}_0 = 0.$$

The differential operator appearing in (12) has the effect of inducing the substitution

$$J_\mu(x) \to J_\mu(x) + 2[\delta_\mu(x,\sigma_1)F_{\mu\nu}{}^{(-)\prime}(x) - \delta_\mu(x,\sigma_2)F_{\mu\nu}{}^{(+)\prime}(x)]$$

in $\mathfrak{W}_0$. Here $\delta_\mu(x,\sigma)$ represents a one-dimensional delta

[3] The dash is omitted, since there is no distinction between the eigenvectors $\Psi(F^{(+)\prime}\sigma)$ and $'\Psi(F^{(+)\prime}\sigma)$, for zero eigenvalues.

[4] Green's functions of this type have been discussed by E. C. G. Stueckelberg, Helv. Phys. Acta **19**, 242 (1946); and R. P. Feynman, Phys. Rev. **76**, 749 (1949).

function, which is defined by

$$\int (dx)\delta_\mu(x,\sigma)f_\mu(x)=\int_\sigma d\sigma_\mu f_\mu(x).$$

Hence

$$'(F^{(-)'}\sigma_1|F^{(+)'}\sigma_2)=\exp(i'\mathfrak{W}),$$

where

$$\begin{aligned}'\mathfrak{W}=\mathfrak{W}_0&+2\int_{\sigma_1} d\sigma_\mu F_{\mu\nu}{}^{(-)'}(x)\langle A_\nu(x)\rangle\\ &-2\int_{\sigma_2} d\sigma_\mu F_{\mu\nu}{}^{(+)'}(x)\langle A_\nu(x)\rangle\\ &+2\int_{\sigma_1} d\sigma_\mu\int_{\sigma_1} d\sigma_\nu' F_{\mu\lambda}{}^{(-)'}(x)D_+(x-x')F_{\nu\lambda}{}^{(-)'}(x')\\ &+2\int_{\sigma_2} d\sigma_\mu\int_{\sigma_2} d\sigma_\nu' F_{\mu\lambda}{}^{(+)'}(x)D_+(x-x')F_{\nu\lambda}{}^{(+)'}(x')\\ &-4\int_{\sigma_1} d\sigma_\mu\int_{\sigma_2} d\sigma_\nu' F_{\mu\lambda}{}^{(-)'}(x)D_+(x-x')F_{\nu\lambda}{}^{(+)'}(x').\end{aligned}\tag{18}$$

The following symbolic form of the Green's function $D_+(x-x')$,

$$D_+(x-x')=\tfrac{1}{2}i\omega^{-1}\exp(-i\omega|x_0-x_0'|)\delta(\mathbf{x}-\mathbf{x}'),\tag{19}$$

shows that

$$x_0=x_0':\quad D_+(x-x')=\tfrac{1}{2}i(\mathbf{x}|\omega^{-1}|\mathbf{x}'),$$

which identifies the double surface integrals, referring to a single surface, in (18), with the factors appearing in (6) and (7), Our result is therefore expressed more simply as

$$(F^{(-)'}\sigma_1|F^{(+)'}\sigma_2)=\exp(i\mathfrak{W}),\tag{20}$$

with

$$\begin{aligned}\mathfrak{W}=\mathfrak{W}_0&+2\int_{\sigma_1} d\sigma_\mu F_{\mu\nu}{}^{(-)'}(x)\langle A_\nu(x)\rangle\\ &-2\int_{\sigma_2} d\sigma_\mu F_{\mu\nu}{}^{(+)'}(x)\langle A_\nu(x)\rangle\\ &-4\int_{\sigma_1} d\sigma_\mu\int_{\sigma_2} d\sigma_\nu' F_{\mu\lambda}{}^{(-)'}(x)D_+(x-x')F_{\nu\lambda}{}^{(+)'}(x').\end{aligned}$$

In particular,

$$\begin{aligned}J_\mu=0:\quad &(F^{(-)'}\sigma_1|F^{(+)'}\sigma_2)\\ &=\exp\Big[-4i\int_{\sigma_1} d\sigma_\mu\int_{\sigma^2} d\sigma_\nu' F_{\mu\lambda}{}^{(-)'}(x)\\ &\qquad\times D_+(x-x')F_{\nu\lambda}{}^{(+)'}(x')\Big].\end{aligned}\tag{21}$$

APPLICATIONS

Explicit forms of the Green's function $D_+(x-x')$ are required for further work. The Fourier integral version of the three-dimensional delta function in (19) yields

$$D_+(x-x')=\frac{1}{2}\frac{1}{i}\int\frac{(d\mathbf{k})}{(2\pi)^3}\frac{1}{k_0}\begin{cases}e^{ik(x-x')}, & x_0>x_0'\\ e^{-ik(x-x')}, & x_0<x_0',\end{cases}\tag{22}$$

where $k_0=|\mathbf{k}|$ is a *positive* frequency. The invariance of this structure is more evident in the four-dimensional transcription

$$D_+(x-x')=i\int\frac{(dk)}{(2\pi)^3}\delta(k^2)e^{ik(x-x')},$$

in which the integration is restricted to positive frequencies for $x_0>x_0'$, and to negative frequencies for $x_0<x_0'$. No conditions on the domain of integration are involved in the alternative four-dimensional form

$$D_+(x-x')=\int\frac{(dk)}{(2\pi)^4}\frac{1}{k^2-i\epsilon}e^{ik(x-x')},\quad \epsilon\to+0.$$

We shall express the tensor Green's function, $\delta_{\mu\nu}D_+(x-x')$, with the aid of four orthonormal vectors associated with each plane wave,

$$\delta_{\mu\nu}=\sum_{\lambda=1}^{4}e_\mu(\lambda k)e_\nu(\lambda k).$$

We choose the first two vectors to obey the conditions

$$\lambda=1,2:\quad n_\mu e_\mu(\lambda k)=k_\mu e_\mu(\lambda k)=0,$$

in which n_μ is an arbitrary time-like unit vector,

$$n_\mu{}^2=-1.$$

The remaining two are given explicitly by

$$e_\mu(3k)=n_\mu+k_\mu/(n_\nu k_\nu),\quad n_\mu e_\mu(3k)=0,$$

and

$$e_\mu(4k)=in_\mu.$$

Thus, employing the three-dimensional form (22), we have

$$\begin{aligned}\delta_{\mu\nu}D_+(x-x')=\frac{1}{2}\frac{1}{i}\sum_{\lambda=1}^{4}\int\frac{(d\mathbf{k})}{(2\pi)^3}\frac{1}{k_0}&e_\mu(\lambda k)\\ &\times e^{\pm ikx}e_\nu(\lambda k)e^{\mp ikx'}.\end{aligned}\tag{23}$$

For applications referring to parallel surfaces, there is a useful alternative form of $\mathfrak{W}_0$, which corresponds to the construction of $\langle A_\mu\rangle$ in the radiation gauge common to both surfaces,

$$\langle A_0(x)\rangle_{\text{r.g.}}=\int(dx')\mathfrak{D}(x-x')J_0(x'),$$

$$\langle A_k(x)\rangle_{\text{r.g.}}=\int(dx')D_+(x-x')J_k{}^{(T)}(x'),$$

where

$$\mathfrak{D}(x-x')=\delta(x_0-x_0')\mathfrak{D}(\mathbf{x}-\mathbf{x}'),$$

and

$$\mathfrak{D}(\mathbf{x}-\mathbf{x}')=(1/4\pi)|\mathbf{x}-\mathbf{x}'|^{-1}.$$

Thus,

$$\mathfrak{W}_0=\tfrac{1}{2}\int(dx)(dx')[J_k^{(T)}(x)D_+(x-x')J_k^{(T)}(x') - J_0(x)\mathfrak{D}(x-x')J_0(x')]. \quad (24)$$

The direct proof of equivalence with (17) employs the expression for the longitudinal current,

$$J_k^{(L)}(x)=\partial_k\int(dx')\mathfrak{D}(x-x')\partial_0'J_0(x'),$$

and the identity

$$D_+(x-x')=\mathfrak{D}(x-x') + \partial_0\partial_0'\int(dx'')D_+(x-x'')\mathfrak{D}(x''-x'). \quad (25)$$

The latter, incidentally, can be expressed in the symbolic form

$$\tfrac{1}{2}i\omega^{-1}e^{-i\omega|x_0-x_0'|}\delta(\mathbf{x}-\mathbf{x}')=\omega^{-2}\delta(x_0-x_0')\delta(\mathbf{x}-\mathbf{x}') + \partial_0\partial_0'[\tfrac{1}{2}i\omega^{-3}e^{-i\omega|x_0-x_0'|}\delta(\mathbf{x}-\mathbf{x}')]. \quad (26)$$

Zero Current

We shall use the appropriate form of the transformation function, (21), to illustrate the construction of the eigenvalues and eigenfunctions of P_μ for a complete system. It is supposed that the surface σ_1 is obtained from σ_2 by a translation X, which brings the point x_2 of σ_2 into the point x_1. Since the surfaces are parallel, and the eigenvalues refer to transverse fields, one can write (21) as

$$(F^{(-)\prime}\sigma_1|F^{(+)\prime}\sigma_2) =\exp\Big[-4i\int_{\sigma_1}d\sigma\int_{\sigma_2}d\sigma' F_{0m}^{(-)\prime}(x) \times(\delta_{mn}D_+(x-x'))^{(T)}F_{0n}^{(+)\prime}(x')\Big].$$

With the time-like vector n_μ identified with the common normal to both surfaces, we see that the $e_\mu(\lambda k)$, $\lambda=1,2,3$ are pure space vectors, while the fourth vector possesses only a time component. Furthermore, the first two vectors are orthogonal to $\mathbf{k}$, which the third vector parallels. Hence,

$$x_0>x_0':\quad(\delta_{mn}D_+(x-x'))^{(T)}=\frac{1}{2}\frac{1}{-i}\sum_{\lambda=1,2}\sum_{k}\left(\frac{(d\mathbf{k})}{(2\pi)^3}\frac{1}{k_0}\right)^{\frac{1}{2}} \times e_m(\lambda k)e^{ikx}\left(\frac{(d\mathbf{k})}{(2\pi)^3}\frac{1}{k_0}\right)^{\frac{1}{2}}e_n(\lambda k)e^{-ikx'},$$

where we have also replaced the integration with respect to $\mathbf{k}$ by a summation over cells of volume $(d\mathbf{k})$.

On defining

$$a_{\lambda k}^{(-)}(\sigma_1)=-i\left(\frac{(d\mathbf{k})}{(2\pi)^3}\frac{2}{k_0}\right)^{\frac{1}{2}}\int_{\sigma_1}d\sigma \times F_{0m}^{(-)}(x)e_m(\lambda k)e^{ik(x-x_1)}, \quad (27)$$

and

$$a_{\lambda k}^{(+)}(\sigma_2)=i\left(\frac{(d\mathbf{k})}{(2\pi)^3}\frac{2}{k_0}\right)^{\frac{1}{2}}\int_{\sigma_2}d\sigma \times e^{-ik(x-x_2)}e_m(\lambda k)F_{0m}^{(+)}(x), \quad (28)$$

which are correspondingly constructed linear combinations of the $F_{0m}^{(-)}$ on σ_1, and of the $F_{0m}^{(+)}$ on σ_2, we obtain

$$(F^{(-)\prime}\sigma_1|F^{(+)\prime}\sigma_2)=\exp[\sum_{\lambda k}e^{ikX}a_{\lambda k}^{(-)\prime}a_{\lambda k}^{(+)\prime}] =\prod_{\lambda k}\exp[e^{ikX}a_{\lambda k}^{(-)\prime}a_{\lambda k}^{(+)\prime}] =\prod_{\lambda k}\sum_{n_{\lambda k}=0}^{\infty}e^{inkX}\frac{(a^{(-)\prime})^n}{(n!)^{\frac{1}{2}}}\frac{(a^{(+)\prime})^n}{(n!)^{\frac{1}{2}}},$$

or

$$(F^{(-)\prime}\sigma_1|F^{(+)\prime}\sigma_2)=\sum_n\left(\prod_{\lambda k}\frac{(a^{(-)\prime})^n}{(n!)^{\frac{1}{2}}}\right) \times\exp[i(\sum_{\lambda k}nk_\mu)X_\mu]\left(\prod_{\lambda k}\frac{(a^{(+)\prime})^n}{(n!)^{\frac{1}{2}}}\right).$$

A comparison with (1) shows that

$$P_\mu'=P_\mu(n)=\sum_{\lambda k}n_{\lambda k}k_\mu,\quad n_{\lambda k}=0,1,2,\cdots, \quad (29)$$

where, in particular,

$$P_0'=\sum_{\lambda k}n_{\lambda k}k_0\geq 0,$$

and that

$$(F^{(-)\prime}|n)=\prod_{\lambda k}\frac{(a^{(-)\prime})^n}{(n!)^{\frac{1}{2}}},\quad (n|F^{(+)\prime})=\prod_{\lambda k}\frac{(a^{(+)\prime})^n}{(n!)^{\frac{1}{2}}}.$$

The occupation numbers $n_{\lambda k}$ provide the complete set of constants of the motion.

Note that if the eigenvalues at corresponding points are in the relation $F_{0m}^{(-)\prime}=F_{0m}^{(+)\prime *}$, we have $a_{\lambda k}^{(-)\prime}=a_{\lambda k}^{(+)\prime *}$, and therefore $(F^{(-)\prime}|n)=(n|F^{(+)\prime})^*$, as required by (5). With the knowledge of these simple eigenfunctions, one can construct eigenfunctions for any other representation of interest. We can also present our results without reference to a representation. On remarking that the vacuum state eigenfunction is

$(F^{(+)\prime}\sigma|0)=1$, we can write

$$(F^{(+)\prime}\sigma|n\sigma)=\left(\prod_{\lambda k}\frac{(a_{\lambda k}{}^{(+)\prime})^n}{(n!)^{\frac{1}{2}}}\right)(F^{(+)\prime}\sigma|0)$$

$$=\left(F^{(+)\prime}\sigma\left|\prod_{\lambda k}\frac{(a_{\lambda k}{}^{(+)}(\sigma))^n}{(n!)^{\frac{1}{2}}}\right|0\right).$$

Therefore,

$$\Psi(n\sigma)=\left(\prod_{\lambda k}\frac{(a^{(+)}(\sigma))^n}{(n!)^{\frac{1}{2}}}\right)\Psi_0,$$

and

$$\Psi(n\sigma)^\dagger=\Psi_0{}^\dagger\prod_{\lambda k}\frac{(a^{(-)}(\sigma))^n}{(n!)^{\frac{1}{2}}},$$

are the eigenvectors of the state with photon occupation numbers, $n_{\lambda k}$.

Time Independent Current

In this situation, $J_\mu(x)=J_\mu(\mathbf{x})$, the energy operator P_0 is still a constant of the motion, and its eigenvalues and eigenfunctions are obtained from the transformation function that characterizes the time translation

$$T=t_1-t_2,$$

where t_1 and t_2 are the time coordinates that label σ_1 and σ_2.

On employing the form (24) for $\mathcal{W}_0$ we get

$$\mathcal{W}_0=-E(0)T+\tfrac{1}{2}\int(d\mathbf{x})(d\mathbf{x}')J_k(\mathbf{x})J_k(\mathbf{x}')$$

$$\times\int_{t_2}^{t_1}dx_0dx_0'[D_+(x-x')-\mathfrak{D}(x-x')],$$

where

$$E(0)=-\tfrac{1}{2}\int(d\mathbf{x})(d\mathbf{x}')J_\mu(\mathbf{x})\mathfrak{D}(\mathbf{x}-\mathbf{x}')J_\mu(\mathbf{x}').$$

According to the symbolic form (26),

$$\int_{t_2}^{t_1}dx_0dx_0'[D_+(x-x')-\mathfrak{D}(x-x')]$$

$$=\int_{t_2}^{t_1}dx_0dx_0'\partial_0\partial_0'[\tfrac{1}{2}i\omega^{-3}e^{-i\omega|x_0-x_0'|}\delta(\mathbf{x}-\mathbf{x}')]$$

$$=i\omega^{-3}(1-e^{-i\omega T})\delta(\mathbf{x}-\mathbf{x}'),$$

so that

$$\mathcal{W}_0=-E(0)T+\tfrac{1}{2}i\int(d\mathbf{x})J_k\omega^{-3}(1-e^{-i\omega T})J_k.$$

Furthermore,

$$x_0=t_1\colon\quad\langle A_k(x)\rangle=\int_{t_2}^{t_1}dx_0'\tfrac{1}{2}i\omega^{-1}e^{-i\omega(t_1-x_0')}J_k(\mathbf{x})$$

$$=\tfrac{1}{2}\omega^{-2}(1-e^{-i\omega T})J_k(\mathbf{x}),$$

and

$$x_0=t_2\colon\quad\langle A_k(x)\rangle=\int_{t_2}^{t_1}dx_0'\tfrac{1}{2}i\omega^{-1}e^{-i\omega(x_0'-t_2)}J_k(\mathbf{x})$$

$$=\tfrac{1}{2}\omega^{-2}(1-e^{-i\omega T})J_k(\mathbf{x}).$$

The transformation function (20) is thus obtained as

$$\frac{(F^{(-)\prime}\sigma_1|F^{(+)\prime}\sigma_2)}{(F^{(-)\prime}|F^{(+)\prime})}$$

$$=\exp\left[-iE(0)T-2\int(d\mathbf{x})(F_{0k}{}^{(-)\prime}+\tfrac{1}{2}i\omega^{-1}J_k)\right.$$

$$\left.\times\frac{1-e^{-i\omega T}}{\omega}(F_{0k}{}^{(+)\prime}-\tfrac{1}{2}i\omega^{-1}J_k)\right],\quad(30)$$

in which we have divided by the transformation function referring to a common surface,

$$(F^{(-)\prime}|F^{(+)\prime})$$

$$=\exp\left[-4i\int_\sigma d\sigma d\sigma' F_{0k}{}^{(-)\prime}(x)D_+(x-x')F_{0k}{}^{(+)\prime}(x')\right]$$

$$=\exp\left[2\int(d\mathbf{x})F_{0k}{}^{(-)\prime}\omega^{-1}F_{0k}{}^{(+)\prime}\right].$$

It is evidently desirable to employ a new description, characterized by the eigenvalues $\bar{F}_{0k}{}^{(\pm)\prime}$, where

$$\bar{F}_{0k}{}^{(\pm)}=F_{0k}{}^{(\pm)}\mp\tfrac{1}{2}i\omega^{-1}J_k,$$

and

$$\bar{A}_k{}^{(\pm)}=A_k{}^{(\pm)}-\tfrac{1}{2}\omega^{-2}J_k.\quad(31)$$

The relation between the eigenvectors $\Psi(\bar{F}^{(+)\prime}\sigma)$ and $\Psi(F^{(+)\prime}\sigma)$ can be inferred from the generator

$$G(\bar{F}^{(+)})=\int d\sigma 2\bar{A}_k{}^{(-)}\delta\bar{F}_{0k}{}^{(+)}$$

$$=\int d\sigma(2A_k{}^{(-)}-\omega^{-2}J_k)\delta F_{0k}{}^{(+)}$$

$$=G(F^{(+)})-\delta\left[\int d\sigma J_k\omega^{-2}\tfrac{1}{2}(F_{0k}{}^{(+)}+\bar{F}_{0k}{}^{(+)})\right],$$

where we have maintained the symmetry between $F_{0k}{}^{(+)}$ and $\bar{F}_{0k}{}^{(+)}$ that accompanies the substitution $J_k\rightarrow-J_k$. Thus,

$$\Psi(\bar{F}^{(+)\prime}\sigma)$$

$$=\exp\left[i\int d\sigma J_k\omega^{-2}\tfrac{1}{2}(F_{0k}{}^{(+)\prime}+\bar{F}_{0k}{}^{(+)\prime})\right]\Psi(F^{(+)\prime}\sigma)$$

$$=\exp\left[i\int d\sigma J_k\omega^{-2}F_{0k}{}^{(+)\prime}+\tfrac{1}{4}\int d\sigma J_k\omega^{-3}J_k\right]\Psi(F^{(+)\prime}\sigma),$$

and

$$\Phi(\bar{F}^{(-)\prime}\sigma)=\exp\Big[-i\int d\sigma J_k\omega^{-2}F_{0k}{}^{(-)\prime}+\tfrac{1}{4}\int d\sigma J_k\omega^{-3}J_k\Big]\Phi(F^{(-)\prime}\sigma).$$

In further confirmation, observe that

$$(\bar{F}^{(-)\prime}|\bar{F}^{(+)\prime})=\exp\Big[2\int d\sigma\bar{F}_{0k}{}^{(-)\prime}\omega^{-1}\bar{F}_{0k}{}^{(+)\prime}\Big]$$

$$=\exp\Big[-i\int d\sigma J_k\omega^{-2}F_{0k}{}^{(-)\prime}+\tfrac{1}{4}\int d\sigma J_k\omega^{-3}J_k\Big]\times(F^{(-)\prime}|F^{(+)\prime})\exp\Big[i\int d\sigma J_k\omega^{-2}F_{0k}{}^{(+)\prime}+\tfrac{1}{4}\int d\sigma J_k\omega^{-3}J_k\Big],$$

which results in the same eigenvector transformation properties. Since these conversion factors do not refer explicitly to the surface, the transformation function ratio in (30) preserves its structure on introducing the new representations. Therefore,

$$(\bar{F}^{(-)\prime}\sigma_1|\bar{F}^{(+)\prime}\sigma_2)=\exp(i\bar{\bar{\mathfrak{W}}}),\tag{32}$$

where

$$\bar{\bar{\mathfrak{W}}}=-E(0)T-2i\int(d\mathbf{x})\bar{F}_{0k}{}^{(-)\prime}\omega^{-1}e^{-i\omega T}\bar{F}_{0k}{}^{(+)\prime}$$

$$=-E(0)T-4\int_{\sigma_1}d\sigma\int_{\sigma_2}d\sigma'\bar{F}_{0k}{}^{(-)\prime}(x)D_+(x-x')\times\bar{F}_{0k}{}^{(+)\prime}(x').$$

Apart from the factor $\exp(-iE(0)T)$, this transformation function is identical in form with (21). The expanded version of (32) is, therefore,

$$(\bar{F}^{(-)\prime}\sigma_1|\bar{F}^{(+)\prime}\sigma_2)=\sum_n(\bar{F}^{(-)\prime}|n)e^{-iP_0'T}(n|\bar{F}^{(+)\prime}),$$

where

$$P_0'=E(0)+\sum_{\lambda k}n_{\lambda k}k_0,\quad n_{\lambda k}=0,1,2,\cdots,$$

and

$$(n|\bar{F}^{(+)\prime})=\prod_{\lambda k}\frac{(\bar{a}^{(+)\prime})^n}{(n!)^{\frac{1}{2}}},\quad(\bar{F}^{(-)\prime}|n)=\prod_{\lambda k}\frac{(\bar{a}^{(-)\prime})^n}{(n!)^{\frac{1}{2}}}.$$

We see that $E(0)$ is to be interpreted as the energy of the photon vacuum, the state of minimum energy, $n_{\lambda k}=0$. With respect to this displaced origin, the energy eigenvalues are the same as in the absence of a current. One may say that the field $\bar{F}_{0k}$ describes pure radiation, which is without coupling to the external current. Indeed, (31), written as

$$\bar{A}_k{}^{(\pm)}(x)=A_k{}^{(\pm)}(x)-\tfrac{1}{2}\int(dx')\mathfrak{D}(x-x')J_k(x'),$$

represents the removal from $A_k(x)$ of the time-independent potential produced by the static current, which is allocated equally to $A_k{}^{(+)}$ and to $A_k{}^{(-)}$. In view of this uncoupling of the static field and the radiation field, one can assign momentum as well as energy eigenvalues to the radiation quanta, as given by (29).

Time Dependent Currents

We shall now discuss the class of problems in which the physical information contained in the general transformation function (20) refers to transition probabilities rather than eigenvalues. Let us first suppose that the current is zero on σ_2, varies in an arbitrary manner in the region between the parallel surfaces σ_1 and σ_2, but again reduces to zero on σ_1. Thus, the physical states on σ_1 and σ_2 are those of the isolated electromagnetic field, and we wish to compute the probabilities of the transitions induced by this perturbing current.

Now,

$$2\int_{\sigma_1}d\sigma F_{0m}{}^{(-)\prime}(x)\langle A_m(x)\rangle=2\int_{\sigma_1}d\sigma F_{0m}{}^{(-)\prime}(x)\int_{\sigma_2}^{\sigma_1}(dx')(\delta_{mn}D_+(x-x'))^{(T)}J_n(x')=-\textstyle\sum_{\lambda k}a_{\lambda k}{}^{(-)\prime}e^{ikx_1}J_{\lambda k},$$

and

$$2\int_{\sigma_2}d\sigma F_{0m}{}^{(+)\prime}(x)\langle A_m(x)\rangle=2\int_{\sigma_2}d\sigma F_{0m}{}^{(+)\prime}(x)\int_{\sigma_2}^{\sigma_1}(dx')(\delta_{mn}D_+(x-x'))^{(T)}J_n(x')=\textstyle\sum_{\lambda k}a_{\lambda k}{}^{(+)\prime}e^{-ikx_2}J_{\lambda k}{}^*,$$

where

$$J_{\lambda k}=\left(\frac{(d\mathbf{k})}{(2\pi)^3}\frac{1}{2k_0}\right)^{\frac{1}{2}}\int_{-\infty}^{\infty}(dx)e_m(\lambda k)e^{-ikx}J_m(x).\tag{33}$$

The quantity $\mathfrak{W}$, determining the transformation function $(F^{(-)\prime}\sigma_1|F^{(+)\prime}\sigma_2)$, is thus obtained in the form

$$\mathfrak{W}=\mathfrak{W}_0-\textstyle\sum_{\lambda k}[a_{\lambda k}{}^{(-)\prime}e^{ikx_1}J_{\lambda k}+a_{\lambda k}{}^{(+)\prime}e^{-ikx_2}J_{\lambda k}{}^*+ia_{\lambda k}{}^{(-)\prime}e^{ikx_1}a_{\lambda k}{}^{(+)\prime}e^{ikx_2}].$$

The transformation function then serves, according to

$$(F^{(-)}\sigma_1|F^{(+)\prime}\sigma_2)=\sum_{n,n'}(F^{(-)\prime}|n)(n\sigma_1|n'\sigma_2)(n'|F^{(+)\prime}),$$

as a generating function for $(n\sigma_1|n'\sigma_2)$, from which the transition probabilities are found in the manner of (2).

It is somewhat more convenient to deal with the elements of the matrix

$$(n|S|n')=e^{-iP(n)x_1}(n\sigma_1|n'\sigma_2)e^{iP(n')x_2},$$

$$p(n,n')=|(n|S|n')|^2,$$

since they are independent of σ_1 and σ_2, provided the current vanishes on these surfaces. The following substitution, representing a transformation to a common reference surface,

$$a_{\lambda k}{}^{(-)\prime}e^{ikx_1}\longrightarrow a_{\lambda k}{}^{(-)\prime}, \quad a_{\lambda k}{}^{(+)\prime}e^{-ikx_2}\longrightarrow a_{\lambda k}{}^{(+)\prime},$$

yields the generating function

$$\exp(i\mathcal{W}_0)\prod_{\lambda k}\exp[a^{(-)\prime}a^{(+)\prime}-ia^{(-)\prime}J-ia^{(+)\prime}J^*] \qquad (34)$$
$$=\sum_{n,n'}(F^{(-)\prime}|n)(n|S|n')(n'|F^{(+)\prime}).$$

On picking out the coefficient of a particular $(F^{(-)\prime}|n)$, we obtain the partial generating function

$$\exp(i\mathcal{W}_0)\prod_{\lambda k}\left[\frac{(a^{(+)\prime}-iJ)^n}{(n!)^{\frac{1}{2}}}\exp(-ia^{(+)\prime}J^*)\right]$$
$$=\sum_{n'}(n|S|n')(n'|F^{(+)\prime}), \quad (35$$

and, similarly,

$$\exp(i\mathcal{W}_0)\prod_{\lambda k}\left[\frac{(a^{(-)\prime}-iJ^*)^{n'}}{(n'!)^{\frac{1}{2}}}\exp(-ia^{(-)\prime}J)\right]$$
$$=\sum_{n}(F^{(-)\prime}|n)(n|S|n'). \quad (36)$$

Preliminary to a direct verification of the unitary property of the operator S, we evaluate the imaginary part of $\mathcal{W}_0$. According to (24),

$$2\ \mathrm{Im}\,\mathcal{W}_0=\int(dx)(dx')J_m(x)$$
$$\times\mathrm{Im}(\delta_{mn}D_+(x-x'))^{(T)}J_n(x'),$$

where, referring to (23),

$$\mathrm{Im}(\delta_{mn}D_+(x-x'))^{(T)}$$
$$=\mathrm{Re}\sum_{\lambda=1,2}\int\frac{(d\mathbf{k})}{(2\pi)^3}\frac{1}{2k_0}e_m(\lambda k)e^{ikx}e_n(\lambda k)e^{-ikx'}.$$

This form is valid without restriction on x_0-x_0'. Hence,

$$2\ \mathrm{Im}\,\mathcal{W}_0=\sum_{\lambda k}|J_{\lambda k}|^2.$$

Alternatively, the invariant expression (17) yields

$$2\ \mathrm{Im}\,\mathcal{W}_0=\int(dx)(dx')J_\mu(x)\ \mathrm{Im}\,D_+(x-x')J_\mu(x'),$$

with

$$\mathrm{Im}\,D_+(x-x')=\mathrm{Re}\int\frac{(d\mathbf{k})}{(2\pi)^3}\frac{1}{2k_0}e^{ikx}e^{-ikx'},$$

which can be written

$$2\ \mathrm{Im}\,\mathcal{W}_0=\sum_k I_k.$$

Here

$$I_k=\frac{(d\mathbf{k})}{(2\pi)^3}\frac{1}{2k_0}\left|\int(dx)e^{-ikx}J_\mu(x)\right|^2=\sum_{\lambda=1,2}|J_{\lambda k}|^2,$$

in which it must be understood that the complex conjugation does not extend to $J_4=iJ_0$. The necessary equivalence of the two evaluations indicates the complete cancellation of the integrals associated with $\lambda=3$ and 4.

Let us multiply (35) with the complex conjugate equation,

$$\exp(-i\mathcal{W}_0{}^*)\prod_{\lambda k}\left[\frac{(a^{(-)\prime}+iJ^*)^n}{(n!)^{\frac{1}{2}}}\exp(ia^{(-)\prime}J)\right]$$
$$=\sum_{n'}(F^{(-)\prime}|n')(n'|S^\dagger|n), \quad (37)$$

and perform the summation with respect to n,

$$(F^{(-)\prime}|S^\dagger S|F^{(+)\prime})$$
$$=\prod_{\lambda k}\exp[-|J|^2+(a^{(-)}+iJ^*)(a^{(+)}-iJ)$$
$$+ia^{(-)}J-ia^{(+)}J^*]$$
$$=\prod_{\lambda k}\exp(a^{(-)\prime}a^{(+)\prime})=(F^{(-)\prime}|F^{(+)\prime}),$$

whence $S^\dagger S=1$. A symmetry property of S may be noted here. The invariance of the generating function (34), under the substitution

$$a_{\lambda k}{}^{(+)\prime}\longrightarrow a_{\lambda k}{}^{(-)\prime}(J_{\lambda k}/J_{\lambda k}{}^*),$$
$$a_{\lambda k}{}^{(-)\prime}\longrightarrow a_{\lambda k}{}^{(+)\prime}(J_{\lambda k}{}^*/J_{\lambda k}),$$

shows that

$$(n|S|n')=(n'|S|n)\prod_{\lambda k}(J/J^*)^{n-n'},$$

which has the consequence $p(n,n')=p(n',n)$.

As an elementary application of the generating function, we place $n_{\lambda k}'=0$ in (36), which yields

$$(n|S|0)=\exp(i\mathcal{W}_0)\prod_{\lambda k}\frac{(-iJ)^n}{(n!)^{\frac{1}{2}}},$$

and

$$p(n,0)=\prod_{\lambda k}\left[\frac{(|J|^2)^n}{n!}\exp(-|J|^2)\right], \qquad (38)$$

for the situation in which no quanta are present initially. If we are not concerned with the polarization of the emitted quanta, we can employ the binomial theorem to replace (38) with

$$p(n,0)=\prod_k\left[\frac{(I_k)^n}{n!}\exp(-I_k)\right].$$

The general matrix element of S is obtained as

$$(n|S|n')=\exp(i\mathcal{W}_0)\prod_{\lambda k}\left[\frac{i^{n+n'}}{(n!n'!)^{\frac{1}{2}}}J^nJ^{*n'}f_{n,n'}(|J|^2)\right],$$

where the function $f_{n,n'}(x)$, which is symmetrical in n

and n', is given by

$$f_{n,n'}(x)=x^{-n'}e^{x}(d/dx)^{n}(-x)^{n'}e^{-x}$$
$$=x^{-n}e^{x}(d/dx)^{n'}(-x)^{n}e^{-x}$$
$$=(-1)^{n_>-n_<}n_<!\,x^{-n+n_<}L_{n_<}^{(n_>-n_<)}(x).$$

In the indicated relation to the Laguerre polynomials,[5] $n_>$ and $n_<$ represent the greater and lesser of the integers n and n'. The general transition probability is thus obtained as

$$p(n,n')=\prod_{\lambda k}\left[\frac{n_<!}{n_>!}(|J|^2)^{n_>-n_<}(L_{n_<}^{(n_>-n_<)}(|J|^2))^2\right.$$
$$\left.\times\exp(-|J|^2)\right]. \quad (39)$$

In particular, the probability that there be no change in the numbers of quanta is

$$p(n,n)=\prod_{\lambda k}[(L_n^{(0)}(|J|^2))^2\exp(-|J|^2)].$$

Should the quantum numbers n and n' be large in comparison with unity and $\Delta n=n-n'\ll n,\ n'$, for a particular mode of the radiation field, we can replace the factor in the transition probability referring to that mode with the Bessel function asymptotic form $[J_{\Delta n}(2n^{\frac{1}{2}}|J|)]^2$.

One can devise another generating function for the transition probabilities which has the further advantage of yielding the expectation values of powers of the final occupation numbers. We first perform the substitution $a_{\lambda k}^{(+)\prime}\to a_{\lambda k}^{(+)\prime}e^{-i\gamma_{\lambda k}}$ in (35), where the $\gamma_{\lambda k}$ are arbitrary constants. The result,

$$\exp(i\mathfrak{W}_0)\prod_{\lambda k}\left[\frac{(a^{(+)\prime}-ie^{i\gamma}J)^n}{(n!)^{\frac{1}{2}}}\exp(-ia^{(+)}e^{-i\gamma}J^*)\right]$$
$$=\sum_{n'}\Big[\prod_{\lambda k}\exp(i\gamma(n-n'))\Big](n|S|n')(n'|F^{(+)}),$$

is then multiplied by (37) and the summation with respect to n performed. This gives

$$\sum(F^{(-)\prime}|n')(n'|S^\dagger|n)\Big[\prod_{\lambda k}\exp(i\gamma(n-n''))\Big]$$
$$\times(n|S|n'')(n''|F^{(+)\prime})$$
$$=\prod_{\lambda k}\exp[a^{(-)\prime}a^{(+)\prime}-ia^{(-)\prime}(e^{i\gamma}-1)J$$
$$-ia^{(+)\prime}(e^{-i\gamma}-1)J^*+(e^{i\gamma}-1)|J|^2],$$

which exhibits the same structure as (34). On confining our attention to the diagonal matrix elements, $n_{\lambda k}'=n_{\lambda k}''$, we find

$$\sum_n\Big[\prod_{\lambda k}\exp(i\gamma(n-n'))\Big]p(n,n')=\Big\langle\prod_{\lambda k}\exp(i\gamma(n-n'))\Big\rangle_{n'}$$
$$=\prod_{\lambda k}[L_{n'}^{(0)}((e^{i\gamma}-1)(e^{-i\gamma}-1)|J|^2)$$
$$\times\exp((e^{i\gamma}-1)|J|^2)]. \quad (40)$$

The right side thus serves as a generating function for the transition probabilities if developed in positive and negative powers of the $e^{i\gamma_{\lambda k}}$. The expansion in powers of the $\gamma_{\lambda k}$ exhibits it as the generator of expectation values of all powers of the quantities $n_{\lambda k}-n_{\lambda k}'$.

The alternative presentation of this result,

$$\Big\langle\prod_{\lambda k}(1+x_{\lambda k})^{n-n'}\Big\rangle_{n'}$$
$$=\prod_{\lambda k}\left[L_{n'}^{(0)}\left(-\frac{x^2}{1+x}|J|^2\right)\exp(x|J|^2)\right],$$

supplies the expectation values of products successively decreasing by unity. Thus, in the special example referring to the vacuum as the initial state, where

$$\Big\langle\prod_{\lambda k}(1+x)^n\Big\rangle_0=\prod_{\lambda k}\exp(x|J|^2),$$

we find, for a particular mode,

$$\langle n!/(n-k)!\rangle_0=(|J|^2)^k,$$

which is characteristic of the Poisson distribution. The first two expectation values, derived from the general generating function, are

$$\langle(n_{\lambda k}-n_{\lambda k}')\rangle_{n'}=|J_{\lambda k}|^2 \quad (41)$$

and

$$\langle(n_{\lambda k}-n_{\lambda k}')^2\rangle_{n'}=\langle(n_{\lambda k}-n_{\lambda k}')\rangle_{n'}{}^2+(2n_{\lambda k}'+1)|J_{\lambda k}|^2.$$

We need hardly remark on the statistical independence of different modes.

If we are not interested in the polarizations of the emitted quanta, it suffices to identify the parameters distinguishing the different polarizations, $\gamma_{\lambda k}=\gamma_k$. To obtain statements referring also to unpolarized incident quanta, we must average, with equal weight, over the various polarized photon numbers that are consistent with a given number of photons in a certain propagation mode, $n_{1k}'+n_{2k}'=n_k'$. This can be accomplished with the aid of the addition theorem for the Laguerre polynomials. The resulting generating function, without reference to polarization, is

$$\sum_n[\textstyle\prod_k\exp(i\gamma(n-n'))]p(n,n')$$
$$=\langle\textstyle\prod_k\exp(i\gamma(n-n'))\rangle_{n'}$$
$$=\textstyle\prod_k[(n'+1)^{-1}L_{n'}^{(1)}((e^{i\gamma}-1)(e^{-i\gamma}-1)I)$$
$$\times\exp((e^{i\gamma}-1)I)].$$

[5] We employ the definition of W. Magnus and F. Oberhettinger, *Special Functions of Mathematical Physics* (Chelsea Publishing Company, New York, 1949), p. 84.

Some expectation values are $\langle(n_k-n_k')\rangle_{n'}=I_k$ and

$$\langle(n_k-n_k')^2\rangle_{n'}=\langle(n_k-n_k')\rangle_{n'}{}^2+(n_k'+1)I_k.$$

For the second example that is concerned with the evaluation of transition probabilities, we suppose that the current is time-independent in the vicinity of σ_2, varies in an arbitrary manner in the region between the parallel surfaces σ_1 and σ_2, but again becomes time-independent in the neighborhood of σ_1. These limiting forms, $J_\mu(\mathbf{x}, 1)$ and $J_\mu(\mathbf{x}, 2)$, need not be the same.

On each surface, we use the description appropriate to the current on that surface,

$$\begin{aligned}(\bar{F}^{(-)\prime}\sigma_1|\,\bar{F}^{(+)\prime}\sigma_2)&\\ =\exp\Big[&-i\int d\sigma J_k(1)\omega^{-2}F_{0k}{}^{(-)\prime}\\ &+\tfrac{1}{4}\int d\sigma J_k(1)\omega^{-3}J_k(1)\Big](F^{(-)\prime}\sigma_1|\,F^{(+)\prime}\sigma_2)\\ &\times\exp\Big[i\int d\sigma J_k(2)\omega^{-2}F_{0k}{}^{(+)\prime}\\ &+\tfrac{1}{4}\int d\sigma J_k(2)\omega^{-3}J_k(2)\Big],\end{aligned}\tag{42}$$

where

$$\bar{F}_{0k}{}^{(-)}=F_{0k}{}^{(-)}+\tfrac{1}{2}i\omega^{-1}J_k(1),\ \bar{F}_{0k}{}^{(+)}=F_{0k}{}^{(+)}-\tfrac{1}{2}i\omega^{-1}J_k(2).$$

Were the current constant, this transformation function would possess the form (32). Accordingly, it must be possible to express all additional contributions in terms of the time derivative of the current. The manner in which this occurs can be illustrated with the evaluation of

$$\begin{aligned}&\int_{\sigma_1} d\sigma F_{0k}{}^{(-)\prime}(x)\langle A_k(x)\rangle\\ &=-\int_{\sigma_1} d\sigma F_{0k}{}^{(-)\prime}(x)\int_{t_2}^{t_1} dx_0'\int(d\mathbf{x}')\partial_0'\\ &\qquad\times D_+(x-x')i\omega^{-1}J_k(x')\\ &=\int_{\sigma_1} d\sigma F_{0k}{}^{(-)\prime}\tfrac{1}{2}\omega^{-2}J_k(1)+\int_{\sigma_1} d\sigma\int_{\sigma_2} d\sigma' F_{0k}{}^{(-)\prime}(x)\\ &\qquad\times D_+(x-x')i\omega^{-1}J_k(\mathbf{x}', 2)\\ &\quad+\int_{\sigma_1} d\sigma F_{0k}{}^{(-)\prime}(x)\int_{\sigma_2}^{\sigma_1}(dx')D_+(x-x')i\omega^{-1}\partial_0'J_k(x').\end{aligned}$$

The terms containing $J_k(1)$ and $J_k(2)$ are canceled on expressing (42) as a function of the variables $\bar{F}_{0k}{}^{(-)\prime}$ and $\bar{F}_{0k}{}^{(+)\prime}$. Carrying out a similar reduction of $\mathfrak{W}_0$ with the aid of (25), we obtain

$$\begin{aligned}&(\bar{F}^{(-)\prime}\sigma_1|\,\bar{F}^{(+)\prime}\sigma_2)\\ &=\exp\Big[i\bar{\mathfrak{W}}_0-4i\int_{\sigma_1} d\sigma\int_{\sigma_2} d\sigma'\bar{F}_{0k}{}^{(-)\prime}(x)D_+(x-x')\\ &\qquad\times\bar{F}_{0k}{}^{(+)\prime}(x')+2i\int_{\sigma_1} d\sigma\bar{F}_{0k}{}^{(-)\prime}(x)\int_{\sigma_2}^{\sigma_1}(dx')\\ &\qquad\times D_+(x-x')i\omega^{-1}\partial_0'J_k(x')\\ &\qquad+2i\int_{\sigma_2} d\sigma\bar{F}_{0k}{}^{(+)\prime}(x)\int_{\sigma_2}^{\sigma_1}\\ &\qquad\qquad\times D_+(x-x')i\omega^{-1}\partial_0'J_k(x')\Big],\end{aligned}$$

where

$$\begin{aligned}\bar{\mathfrak{W}}_0=&\tfrac{1}{2}\int_{\sigma_2}^{\sigma_1}(dx)(dx')[J_k{}^{(T)}(x)J_k{}^{(T)}(x')-J_0(x)J_0(x')]\\ &\times\mathfrak{D}(x-x')+\tfrac{1}{2}\int_{\sigma_2}^{\sigma_1}(dx)(dx')\partial_0J_k{}^{(T)}(x)\omega^{-1}\\ &\qquad\times D_1(x-x')\omega^{-1}\partial_0'J_k{}^{(T)}(x').\end{aligned}$$

The introduction of the variables $\bar{a}_{\lambda k}{}^{(-)}$ and $\bar{a}_{\lambda k}{}^{(+)}$, in the manner of (27) and (28), brings this transformation function into the form

$$\begin{aligned}&(\bar{F}^{(-)\prime}\sigma_1|\,\bar{F}^{(+)\prime}\sigma_2)\\ &=\exp(i\bar{\mathfrak{W}}_0)\prod_{\lambda k}\exp[\bar{a}^{(-)\prime}e^{ikx_1}\bar{a}^{(+)\prime}e^{-ikx_2}\\ &\qquad-i\bar{a}^{(-)\prime}e^{ikx_1}\bar{J}-i\bar{a}^{(+)\prime}e^{-ikx_2}\bar{J}^*],\end{aligned}\tag{43}$$

where

$$\bar{J}_{\lambda k}=\left(\frac{(d\mathbf{k})}{(2\pi)^3}\frac{1}{2k_0}\right)^{\frac{1}{2}}\int_{-\infty}^{\infty}(dx)e_m(\lambda k)e^{-ikx}(i/k_0)\partial_0J_m(x)\tag{44}$$

is expressed as an integral over all space-time by supposing that the current in the extended domain exhibits the time-independent value appropriate to the nearest surface bounding the region of interest. In order to present this result as a generating function for the surface independent unitary matrix

$$(n|\,S|\,n')=e^{-iP(n,1)x_1}(n\sigma_1|\,n'\sigma_2)e^{iP(n',2)x_2},$$
$$P_0(n)=E(0)+\textstyle\sum_{\lambda k}n_{\lambda k}k_0,$$

a further rearrangement of $\bar{\mathfrak{W}}_0$ is required. Indeed, the first term of this quantity is

$$\begin{aligned}-\int_{t_2}^{t_1} dx_0E(0, x_0)=&-[t_1E(0, 1)-t_2E(0, 2)]\\ &+\int_{-\infty}^{\infty} dx_0x_0\partial_0E(0, x_0).\end{aligned}$$

The substitution

$$\bar{a}^{(-)\prime}e^{ikx_1}\to\bar{a}^{(-)\prime},\quad \bar{a}^{(+)\prime}e^{ikx_2}\to\bar{a}^{(+)\prime},$$

now yields the required generating function

$$\exp(iw_0)\prod_{\lambda k}[\bar{a}^{(-)\prime}\bar{a}^{(+)\prime}-i\bar{a}^{(-)\prime}\bar{J}-i\bar{a}^{(+)\prime}\bar{J}^*]$$
$$=\sum_{n,n'}(\bar{F}^{(-)\prime}|n)(n|S|n')(n'|\bar{F}^{(+)\prime}), \quad (45)$$

where

$$w_0=\int_{-\infty}^{\infty}dx_0x_0\partial_0E(0,x_0)+\tfrac{1}{2}\int_{-\infty}^{\infty}(dx)(dx')$$
$$+\partial_0J_k{}^{(T)}(x)\omega^{-1}D_+(x-x')\omega^{-1}\partial_0{}'J_k{}^{(T)}(x') \quad (46)$$

is such that

$$2\ \mathrm{Im}\ w_0=\textstyle\sum_{\lambda k}|\bar{J}_{\lambda k}|^2.$$

The generating function (45) is identical in structure with (34). Hence the transition probabilities and expectation values are given by (39) and (40), with $\bar{J}_{\lambda k}$ replacing $J_{\lambda k}$. If the current is zero on the boundaries of the region, an integration by parts reduces $\bar{J}_{\lambda k}$ to $J_{\lambda k}$. Notice also that if the current is time-independent, (45) asserts that $(n|S|n')=\delta(n,n')$, attesting to the stationary character of the states labeled by the photon numbers.

The infrared catastrophe.—According to (41), the average number of photons emitted into a particular mode is given by

$$|\bar{J}_{\lambda k}|^2=\frac{(d\mathbf{k})}{(2\pi)^3}\frac{1}{2k_0{}^3}\left|\int_{-\infty}^{\infty}(dx)e_m(\lambda k)e^{-ikx}\partial_0J_m(x)\right|^2.$$

We shall now consider frequencies that are sufficiently low for the wavelength to be large in comparison with the linear dimensions of the spatio-temporal region in which the current changes. The average number of photons, of either polarization, that emerge in a range of such low frequencies is then

$$\int\frac{(d\mathbf{k})}{(2\pi)^3}\frac{1}{2k_0{}^3}\left|\int_{-\infty}^{\infty}(dx)\partial_0J_\mu(x)\right|^2$$
$$=\frac{1}{4\pi^2}\int\frac{dk_0}{k_0}\left|\int(d\mathbf{x})(J_\mu(\mathbf{x},1)-J_\mu(\mathbf{x},2))\right|^2,$$

which becomes infinite as the lower frequency limit approaches zero. Any time variation of the current thus produces a logarithmically infinite number of zero frequency photons—a fact well-known as the "infrared catastrophe." Accordingly, we find a zero probability for the emission of a finite number of photons. To avoid this type of statement we recognize that in any experimental arrangement there is a minimum detectable frequency, $k_{0,\min}$, such that we have no knowledge of the number of photons emitted into modes with frequencies less than $k_{0,\min}$. If we sum the general transition probability (39) over all final occupation numbers referring to these unobservable modes, we are left with the same expression constructed only from the observable modes. The latter will yield nonvanishing probabilities for the emission of a finite number of photons, each transition probability being dependent upon $k_{0,\min}$ through the factor

$$\exp(-\sum_{\lambda k}|\bar{J}_{\lambda k}|^2)=\exp\left[-\int_{k_{0,\min}}^{\infty}\frac{(d\mathbf{k})}{(2\pi)^3}\frac{1}{2k_0{}^3}\right.$$
$$\left.\times\left|\int_{-\infty}^{\infty}(dx)e^{-ikx}\partial_0J_\mu(x)\right|^2\right].$$

This quantity represents the probability that no (observable) photon will be emitted, if none are present initially.

The adiabatic theorem.—This important statement refers to the situation in which the current changes from its initial to its final value at a rate determined by the total elapsed time $T=t_1-t_2$. We are particularly interested in the limit in which T becomes very large compared to the periods of all observable modes, $k_{0,\min}T\to\infty$. The above description of the current time variation is expressed quantitatively by

$$\int(d\mathbf{x})e_m(\lambda k)e^{-i\mathbf{k}\cdot\mathbf{x}}J_m(x)=j_{\lambda k}(\zeta), \quad \zeta=(x_0-t_2)/T.$$

Hence the integral occurring in (44) is essentially determined by

$$\int_0^1d\zeta e^{ik_0T\zeta}j'(\zeta).$$

Now, according to the Riemann-Lebesgue lemma,[6]

$$\operatorname*{Lim}_{k_0T\to\infty}\left|\int_0^1d\zeta e^{ik_0T\zeta}j'(\zeta)\right|=0, \quad (47)$$

provided only that

$$\int_0^1d\zeta|\,j'(\zeta)|<\infty.$$

This suffices to establish that

$$\operatorname*{Lim}_{T\to\infty}|\bar{J}_{\lambda k}|^2=0.$$

If $j_{\lambda k}{}'(\zeta)$ is of limited total fluctuation, the integral in (47) approaches zero as $(k_0T)^{-1}$, which enables us to satisfy

$$\operatorname*{Lim}_{T\to\infty}\sum_{\lambda k}|\bar{J}_{\lambda k}|^2=0,$$

without essential restriction on the spatial distribution of the current (it must not be as singular as the gradient of a delta function). Under these conditions we obtain the probability zero for any change in the photon numbers, despite the alteration in the current.

[6] E. T. Whittaker and G. N. Watson, *Modern Analysis* (Macmillan Company, New York, 1927), p. 172.

This theorem can be exploited to give a uniform expression for the results of all problems involving transition probabilities. Thus, in the integration over the extended region in (44), it is supposed that the current is constant in the exterior region. If we were to replace these constant currents by currents decreasing adiabatically to zero at infinity, the null contribution from the external region would not be affected. But we would have succeeded in substituting for the original problem one in which the current vanishes on the boundaries of the extended region. Accordingly, we can integrate by parts in (44) and regain the form (33) appropriate to null currents on the boundaries. The most general problem requiring the evaluation of transition probabilities between stationary states, involves initial and final currents that are time-independent with respect to different reference systems. When modified with the aid of the adiabatic device, this situation also falls into the class of problems covered by (34).

The adiabatic device is also applicable to eigenvalue problems. Thus, we can use the transformation function (34), appropriate to zero current on the boundary surfaces, to construct the energy eigenvalues for the situation of a time-independent current. We suppose that the current, which is zero on the surface $\sigma_{-\infty}$, grows adiabatically and maintains a constant value between surfaces σ_2 and σ_1, and reduces adiabatically to zero on σ_∞. The designations $\sigma_{\pm\infty}$ refer to the fact that the adiabatic theorem involves the limit of infinite temporal separation between σ_∞ and σ_1, and between σ_2 and $\sigma_{-\infty}$. Then

$$(n\sigma_\infty|n'\sigma_{-\infty})=\delta(n,n')\exp[i\mathcal{W}_0+iP(n)(x_\infty-x_{-\infty})],$$

where [reversing the integration by parts in the first term of (46)],

$$\mathcal{W}_0=-\int_{-\infty}^{\infty}dx_0E(0,x_0),$$

and

$$\exp(i\mathcal{W}_0)=\exp\left(-i\int_{t_1}^{\infty}dx_0E(0,x_0)\right)$$

$$\times\exp(-iE(0)(t_1-t_2))\exp\left(-i\int_{-\infty}^{t_2}dx_0E(0,x_0)\right).$$

On recalling the composition property of transformation functions, we recognize immediately that

$$(n\sigma_1|n'\sigma_2)=\delta(n,n')\times\exp[-iE(0)(t_1-t_2)+iP(n)(x_1-x_2)],$$

which shows that, in the presence of a time-independent current, the energy eigenvalues of the radiation field are displaced by $E(0)$.

The methods discussed in this paper and illustrated for the electromagnetic field are equally applicable to other Bose-Einstein systems, such as the symmetrical pseudoscalar meson field.

PHYSICAL REVIEW VOLUME 91, NUMBER 3 AUGUST 1, 1953

Convergence of the Adiabatic Nuclear Potential

ABRAHAM KLEIN*
Harvard University, Cambridge, Massachusetts
(Received March 30, 1953)

The leading term of the potential of order $4n$, n an arbitrary integer, of the pseudoscalar theory with pseudoscalar coupling is computed by a method which takes advantage of the special pair character of this term. It is shown that the coefficients increase with n as $n!(n-1)!$; thus, despite the decreasing ranges, the unrenormalized potentials grow enormously with n, even in the nonrelativistic domain. The breakdown of the expansion in μ/M for a given order is also indicated. A weakness of the discussion is that it does not include radiative corrections.

I. INTRODUCTION

IN a previous paper,[1] it was shown how the relativistic two-body equation could be made the exclusive basis for the discussion of nuclear forces in the nonrelativistic domain. The methods developed were extensively illustrated by the computation of various terms of the two-, three-, and four-body potentials in the symmetric pseudoscalar theory with pseudoscalar (direct) coupling. No serious attempt was made, however, to present theoretical evidence that would render plausible the implied model[2] of, for example, the neutron-proton system.

To justify the model, there are at least three points that require serious investigation: the hard core, higher order potentials, and radiative corrections. One should like to justify the assumption of a hard core, a *sine qua non*, because of the singular character of the potentials in the asymptotic region. On this matter, we shall be silent. Even assuming a reasonable cut-off radius,

* Jr. Fellow, Society of Fellows.
[1] A. Klein, Phys. Rev. **90**, 1101 (1953). Hereafter referred to as A.
[2] M. M. Lévy, Phys. Rev. **88**, 725 (1952).

$\mu r \lesssim 0.5$, one must show that the potentials of higher order than those taken into account become progressively smaller in the nonrelativistic domain. In view of recent discussions of the S matrix,[3] one would tend to be skeptical of this possibility.

In an effort to obtain a definite result, we have focused attention on the potentials of order $4n$ in the symmetric $ps-ps$ theory. In Sec. II we compare the fourth- and eighth-order potentials, each computed to relative order μ/M compared to the leading term of the given order. All but the μ/M term of eighth order were calculated in **A**, and the latter is obtained here by the same three-dimensional methods. Because of its coefficient and functional dependence, this term proves to be larger in magnitude than the "leading" term for significant separations of the two particles, heralding a breakdown of the expansion in powers of μ/M for a given power of $g^2/4\pi$. This tendency is evident even in fourth order, where the combination of two-pair and one-pair potentials effectively cancels, so that there is no possibility of fitting the singlet $n-p$ scattering data[4] with their sum.

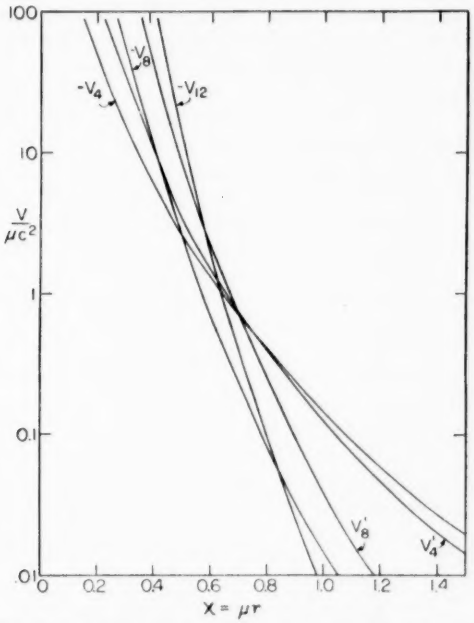

FIG. 1. Plot of the leading terms of the fourth-, eighth-, and twelfth-order potentials for $g^2/4\pi = 10$. The unprimed potentials are generated by matrix elements with the maximum number of pairs, the primed potentials by matrix elements with one pair fewer.

In Sec. III a method is presented which, although not a rigorous one, renders plausible nevertheless a definite result for the $2n$-pair potential of order $4n$, n arbitrary. Aside from the satisfaction of achieving an analytic form for this term, the main result, based upon the combinatorial aspects of the problem, is that the coefficients increase with n as $n!(n-1)!$. This dependence soon overwhelms the reduction brought about by the higher powers of the effective coupling constant,[5] $(g^2/4\pi) \times (\mu/2M)$ and by the decreasing range of the functions

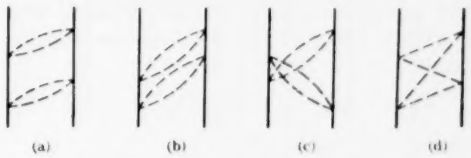

FIG. 2. Diagrams representative of the four types of four-pair matrix elements in eighth order.

involved, even for $\mu r \gtrsim 1$, and is aided in this at distances $\mu r < 1$ by the increasingly stronger singularities at the origin. The mere enumeration of possibilities also makes it apparent that the breakdown of the μ/M expansion becomes progressively worse for higher order terms, though the methods employed do not suffice to determine the exact coefficients.

A weakness in the above discussion is that it refers only to "bare" potentials, i.e., the possible damping due to radiative corrections has not been taken into account. It has been pointed out by Wentzel[6] and more recently by Brueckner,[7] however, that nucleon self-energy effects may severely depress virtual nucleon pair formation. Although it is hardly possible to alter the conclusions of the previous paragraph on the basis of their work alone, one can, in an optimistic moment, envisage that at the very least the strong damping of the pair terms may serve to reduce the effective coupling constant to the point where the theory approaches the probable asymptotic status of electrodynamics.[8] For the no-pair terms have a reasonably small effective expansion parameter,[2] $(g^2/4\pi)(\mu/2M)^2 < 0.1$. It is hardly more likely, however, that higher order potentials of the no-pair variety form a convergent sequence than do the terms discussed in this paper. It would appear, therefore, that the justification by meson-theoretical methods of an adiabatic potential based upon low order terms only has yet to be provided.

The appendix contains a derivation, by the methods of Sec. III, of the n-pair term of the n-body force.

II. EIGHTH-ORDER POTENTIALS

We begin this section with a statement of results and shall discuss some of the relevant aspects of the

[3] C. A. Hurst, Phys. Rev. **85**, 920 (1952); S. Hori, Progr. Theoret. Phys. **8**, 569 (1952); W. Thirring, Helv. Phys. Acta **26**, 33 (1953).

[4] Contrary to what was implied in the concluding discussion of *A*. The remarks there are applicable if one includes the terms of relative order $(\mu/M)^2$ compared to the two-pair terms. As indicated by our later discussion, these may be the decisive terms anyway because of radiative corrections to the pair terms.

[5] Assuming $g^2/4\pi \sim 10$. If $g^2/4\pi \geq 15$, $(g^2/4\pi)(\mu/2M) \geq 1$ and the situation is so much the worse.

[6] G. Wentzel, Phys. Rev. **86**, 802 (1952).

[7] K. Brueckner, Phys. Rev. **90**, 476 (1953).

[8] F. J. Dyson, Phys. Rev. **85**, 631 (1952).

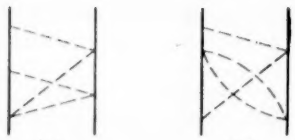

FIG. 3. Diagrams representative of the three-pair matrix elements in eighth order. Diagram (a) is one of six possible configurations, determined by the position of the pair vertex relative to the single vertices and by which particle has the single vertices.

derivation thereafter. It was shown in **A** that to relative order μ/M the fourth-order potential consists of two terms, the two-pair term ($x=\mu r$),

$$V_4(x)=-3\mu(g^2/4\pi)^2(\mu/2M)^2(2/\pi)K_1(2x)/x^2, \quad (1)$$

and the one-pair term[9]

$$V_4'(x)=6\mu(g^2/4\pi)^2(\mu/2M)^3(1+1/x)^2e^{-2x}/x^2. \quad (2)$$

In eighth order the corresponding potentials are the leading four-pair term, also derived in **A**,

$$V_8(x)=-6\mu(g^2/4\pi)^4(\mu/2M)^4(2/\pi)K_1(4x)/x^4, \quad (3)$$

and the leading three-pair term

$$V_8'(x)=24\mu(g^2/4\pi)^4(\mu/2M)^5(1+1/x)^2e^{-4x}/x^4. \quad (4)$$

Equation (4) can be derived by the method employed in **A**, and it will be indicated below that it is the only term of its order which need be considered in the nonrelativistic domain.

Equations (1)–(4) are plotted in Fig. 1, together with $V_{12}(x)$, the leading six-pair term of twelfth-order, which is derived in the next section. The graph is confined to the region $x<1.5$. Several facts emerge clearly. It is seen first that the sum of $V_4(x)$ and $V_4'(x)$ is much smaller in magnitude than $V_4(x)$ and becomes repulsive for $x<0.75$. There is then no hope of fitting the singlet $n-p$ scattering data with such a potential. Further, it is seen that $V_8'(x)$ is almost uniformly larger than $|V_8(x)|$ and that their sum is of greater magnitude than the corresponding fourth-order result. We are confronted with a breakdown of the significance of a factor of μ/M in front of a potential, which is due, as will be seen below, to the greater number of ways of realizing a matrix element with the fewer number of pairs; there is also no evidence of the convergence of the power series in $g^2/4\pi$. In fact, the opposite tendency is evident upon comparison of V_8 and V_{12}, with the latter predominating for $x<0.9$. The nonconvergence indicated here will be established in the next section.

We turn now to a consideration of the features associated with the derivations of Eqs. (3) and (4) which will form the basis of certain generalizations of relevance in our later work. To derive Eq. (3), for example, we recorded all possible four-pair matrix elements involving at most one pair at a time. These could be enumerated without ambiguity by reference to the 4! distinct Feynman diagrams of eighth order for the exchange of four mesons. One then finds only four distinct sets of matrix elements in the nonrelativistic limit, prototypes of which are given in Fig. 2. In order to clarify the essential features, we have preferred to use the pictorial representation associated with the equivalent pair theory.

According to the theory of **A**, matrix elements of the type of Fig. 2(a) were not considered since they were reducible in the three-dimensional sense defined there. It was next found that the sum of all matrix elements of types (b) and (c) were canceled (in the nonrelativistic limit) by iteration of velocity-dependent corrections[10] to the leading two-pair fourth-order potential. Equation (3) then resulted from the summation of all matrix elements of type (d), those for which, in the terminology of pair theory,[11] the meson lines form a closed perimeter.

The cancellation of the matrix elements represented by Figs. 2(b) and (c) is a phenomenon which has been found to occur in every analogous situation encountered in our calculations.[10] Although it hardly appears possible within the present context to prove[12] that it will always occur, that it should happen is eminently reasonable upon physical grounds; for both (b) and (c) can be regarded as retardation corrections to (a), so that one might expect them to disappear in the adiabatic limit. In any case, in our work in the next section we shall consider only potentials of order $4n$ in which all $2n$ lines are connected and thus form a perimeter.

In the derivation of Eq. (4) one encounters a similar situation. Thus, it is matrix elements of the kind represented by Fig. 3(a) that add up to Eq. (4), whereas those like Fig. 3(b) can be canceled if one defines a suitable unperturbed problem and then considers velocity-dependent corrections thereto. It is clear that as one pushes the computation of potentials to higher order in $g^2/4\pi$ and μ/M, one must suitably extend the set of potentials to be included in the unperturbed non-

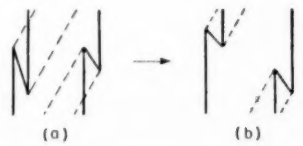

FIG. 4. Diagrams illustrating part of four-pair matrix element with two pairs allowed at a given time [diagram (a)] which is not canceled by leading four-pair terms because of its relation to a [diagram (b)] reducible four-pair term.

[9] The existence of this term has been questioned by some authors. Eq. (2) has been independently verified by Dr. S. Drell using a method based upon the canonical transformation of Dyson, F. J. Dyson, Phys. Rev. **73**, 929 (1948). The universal agreement of the existence of the term in the neutral theory would seem to guarantee that there is a corresponding term in the symmetrical theory.

[10] See Sec. IV C of reference 1.

[11] G. Wentzel, Helv. Phys. Acta **15**, 111 (1942).

[12] It is easy enough to verify, however, that the signs are always appropriate for the concellation. This problem is under further investigation. See Y. Nambu, Prog. Theoret. Phys. **5**, 614 (1950).

relativistic problem. Thus, one considers here, for the first time, velocity-dependent corrections to the one-pair fourth-order potential.

A few final remarks are in order. The assertion that Eq. (4) is the only μ/M "correction" to Eq. (3) must be substantiated by a proof that there are no four-pair static potentials of relative order μ/M. One method of procedure would be to fall back upon the pair analogy. With the pair method of computation one merely never sees such terms, at least in fourth order. By our techniques, the proof consists in demonstrating that the first-order expansion of the pair denominators of the leading pair terms cancels the nonrelativistic limit of matrix elements which can have two pairs at a time, as was shown to be the case in fourth order in **A**. This occurs in eighth order everywhere except where the leading pair matrix element is a reducible one, but the μ/M term with which it should combine is not. Thus, one can think of a matrix element with overlapping pairs, such that when one removes the overlap, there remains an intermediate state with only two nucleons and no mesons as illustrated in Fig. 4. The matrix elements related to Fig. 4 (a) give rise to a large μ/M potential given by

$$V_8^{(b)}(x) = -36\mu(g^2/4\pi)^4(\mu/2M)^5(2/\pi)^2 \times[K_1(2x)]^2/x^4. \quad (5)$$

But even this potential can be omitted in the adiabatic limit if one considers velocity-dependent corrections to the leading two-pair potential of fourth order which arise from the expansion of pair denominators[13] and uses the iteration method of **A**. If one were to extend these methods to four-pair terms of still higher order in μ/M, one should be led to the conclusion that the largest pair contribution to the potential of order $4n$ accounts for the complete *nonrelaitvistic* potential of that order arising from matrix elements with the maximum number of pairs. The correctness of this result will be assumed in the developments that follow.[14]

III. POTENTIAL OF ORDER $4n$

A. Preliminaries

We attack in this section the problem of obtaining the potential of order $4n$ which is the sum of matrix elements with $2n$ pairs. This problem has two aspects, that of obtaining an analytic form and that of obtaining the general coefficient. Since we are interested only in the adiabatic limit, it is a more concise and useful procedure to define the potential directly from the appropriate form of the relativistic two-body equation rather than through the intermediary of the three-dimensional formalism. We shall then rely on our previous experience, as discussed in the last section, to help us select the terms of interest.

Our starting point is the equation[15]

$$[\tfrac{1}{2}W+p_0-E_p][\tfrac{1}{2}W-p_0-E_p]\psi_{++}(x) = \int d^4x'd^4X' \exp[iW(X_0-X_0')] \times I(x,x';X-X')\psi_{++}(x'), \quad (6)$$

from which we have eliminated negative-energy components of the wave function by the method explained in **A**, and therefore the interaction kernel $I(x,x';X-X')$ contains reducible elements in both the four-dimensional and the three-dimensional sense. Multiplying through by the sum of the inverses of the operators that stand on the left-hand side of Eq. (6), we obtain the equation

$$(W-2E_p)\psi_{++}(x) = (2\pi)^{-4}\int d^4p'd^4x''d^4x'd^4X'e^{ip'(x-x'')}\{[\tfrac{1}{2}W+p_0'-E_{p'}]^{-1}+[\tfrac{1}{2}W-p_0'-E_{p'}]^{-1}\} \times\exp[iW(X_0-X_0')]I(x'',x';X-X')\psi_{++}(x') = -i(2\pi)^{-3}\int d\mathbf{p}'d^4x''d^4x'd^4X' \times\exp[i\mathbf{p}'\cdot(\mathbf{r}-\mathbf{r}'')-i(E_{p'}-\tfrac{1}{2}W)|x_0-x_0''|]\exp[iW(X_0-X_0')]I(x'',x';X-X')\psi_{++}(x'). \quad (7)$$

According to Appendix A of **A**, the wave function on the right-hand side of Eq. (7) can be represented as

$$\psi_{++}(x) = (2\pi)^{-2}\int d\mathbf{p} \times\exp[i\mathbf{p}\cdot\mathbf{r}-i(E_p-\tfrac{1}{2}W)|x_0|]\phi_{++}(\mathbf{p}). \quad (8)$$

Taking the nonrelativistic limit consists in the observation that if the wave function $\phi_{++}(p)$ is negligible for $p \gtrsim M$, we may set $E_p \cong M$ and further, ignoring the binding energy, place $E_p-\frac{1}{2}W \cong 0$. The wave function $\psi_{++}(x')$ in Eq. (7) is then independent of x_0, i.e., we have neglected retardation effects. If analogous ap-

[13] In all previous cases it was only the energy denominator associated with intermediate states without pairs that had to be considered. Here also is the first instance of the relevancy of the difference between the pair denominators of **A** and those of Lévy, reference 2. The ambiguity, based upon the fact that our representation is, in a limited sense, a mixed (free and bound) representation, will be even more pronounced in higher order. The remarks of the text are based upon the use of the Lévy denominators.

[14] This assumption may be unjustified, since if one examines the Dyson-transformed Hamiltonian or the similar Foldy Hamiltonian, Berger, Foldy, and Osborn, Phys. Rev. **87**, 1061 (1952), one finds that the theory contains multiple-pair-vertices with smaller effective coupling constants than the single-pair vertices which generate the leading pair terms. The relation of the former to the method of the next section is not completely clear. It is not unlikely, however, that they account for terms like Eq. (5).

[15] The notation follows reference 1. In Eq. (6), $\mathbf{p}$, p_0 are to be understood as differential operators.

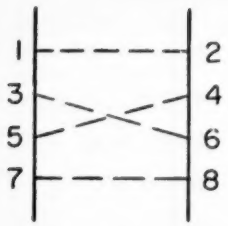

FIG. 5. Eighth-order Feynman diagram which contributes to potential illustrated by Fig. 2(d).

proximations are made uniformly in the right-hand side of Eq. (7), it is easily reduced to the form

$$(W-2E_p)\psi_{++}(\mathbf{r})=-i\int dtd^4x'd^4X'$$
$$\times\exp[i2M(X_0-X_0')]I(x,x';X-X')\psi_{++}(\mathbf{r}'), \quad (9)$$

in which we have recognized explicitly that the left-hand side is independent of x_0 and therefore renamed x_0'' to t. We are now in a position to recognize the potential since the right-hand side of Eq. (9) has the form

$$\int V(\mathbf{r},\mathbf{r}')\psi(\mathbf{r}')d\mathbf{r}',$$

where

$$V(\mathbf{r},\mathbf{r}')=-i\int dtdt'd^4X'$$
$$\times\exp[i2M(X_0-X_0')]I(x,x';X-X'). \quad (10)$$

When we introduce explicit forms for $I(x,x';X-X')$ and make the requisite nonrelativistic approximations in it, $V(\mathbf{r},\mathbf{r}')$ will reduce to the required $V(\mathbf{r})\delta(\mathbf{r}-\mathbf{r}')$.

B. Fourth- and Eighth-Order Potentials

We illustrate the special use we shall make of Eq. (10) by rederiving old results. Consider first the two-pair fourth-order potential. It will prove sufficient to compute for a single Feynman diagram, Fig. 1(b) of **A**, for example, and then to multiply by the sum of the isotopic operators of all contributing diagrams which we shall designate in the general case by T_l, where l is the order of the potential. Thus, for the two-pair part of the fourth-order potential V_{--} we have

$$V_{--}(\mathbf{r},\mathbf{r}')=-i(-ig^2)^2T_4\int dtdt'd^4X'\exp[i2M(X_0-X_0')]\Delta(X-X'-\tfrac{1}{2}(x+x'))\Delta(X-X'+\tfrac{1}{2}(x+x'))$$
$$\times\langle\gamma_0\gamma_5G_-(X-X'+\tfrac{1}{2}(x-x'))\gamma_5\rangle^{(1)}\langle\gamma_0\gamma_5G_-(X-X'-\tfrac{1}{2}(x-x'))\gamma_5\rangle^{(2)}, \quad (11)$$

where $\langle\ \rangle$ denotes spin matrix element and G_- the value of the Green's function for negative values of its time argument; the time integrations are also limited by this ordering. We recall that

$$G(x)=\frac{i}{(2\pi)^3}\int d\mathbf{p}\exp[i\mathbf{p}\cdot\mathbf{r}-iE_p|t|]\frac{[H(\mathbf{p})+E_p\,\mathrm{sgn}t]}{2E_p}\gamma_0. \quad (12)$$

In the adiabatic limit, we set $E_p\cong M$. For $t<0$, therefore, we obtain

$$\langle\gamma_0\gamma_5G_-(x)\gamma_5\rangle\cong-i\delta(\mathbf{r})e^{iMt}, \quad (13)$$

in virtue of the properties[16] of γ_5. Inserting Eq. (13) in Eq. (11) and imposing the spatial connections implied by the δ functions, we obtain

$$V_{--}(\mathbf{r},\mathbf{r}')\to V_4(\mathbf{r})\delta(\mathbf{r}-\mathbf{r}'), \quad (14)$$

$$V_4(\mathbf{r})=-ig^4T_4\int_{-\infty}^{\infty}dt\int dt_3(t_3>t_1)\int dt_4(t_4>t_2)\exp[i2M(t_1+t_2-t_3-t_4)]\Delta(\mathbf{r},t_1-t_4)\Delta(\mathbf{r},t_2-t_3). \quad (15)$$

In Eq. (15) we have preferred to return to individual time coordinates ($t=t_1-t_2$) as we shall do in all subsequent cases. Now the limitations on the allowed values of t_3 and t_4 merely restrict us to the entire two-pair potential, i.e., they specify the number of pairs associated with a single nucleon line. If we are to derive the leading two-pair potential we should establish additional relationships between the time coordinates of the two particles in order to ensure no overlap in time between the pairs. We would then be applying the method of Appendix A of **A** which subdivides Eq. (15) into the sum of all its distinct three-dimensional matrix elements. This is precisely what we must avoid if we are eventually to obtain by reasonable labor a result for arbitrary order. To carry out our program, we must invoke the special property of the pair interactions described in Sec. II, that the sum of *all* pair terms yields in the adiabatic limit only the *leading* pair potential. In short, no error should result from Eq. (15).

Introducing the four-dimensional momentum representations of the meson propagation functions and reversing the orders of integration, we require the time

[16] See Eq. (28) of reference 1.

integrals

$$\int_{-\infty}^{\infty} dt \int_{t_1}^{\infty} dt_3 \int_{t_2}^{\infty} dt_4 \exp[it_1(2M-k_{01})+it_2(2M-k_{02})-it_3(2M-k_{02})-it_4(2M-k_{01})]$$
$$=2\pi(-i)^2(2M-k_{01})^{-1}(2M-k_{02})^{-1}\delta(k_{01}-k_{02}). \tag{16}$$

We may replace $2M-k_0$ by $2M$ since the poles thus neglected do not adequately account for the behavior at small distances anyway because of previous nonrelativistic approximations. This replacement will be made in the future without further comment. As a consequence of Eq. (16) we are left with

$$V_4(r)=i\frac{g^4}{(2M)^2}\frac{1}{(2\pi)^7}T_4\int d\mathbf{k}_1 d\mathbf{k}_2 e^{i(\mathbf{k}_1+\mathbf{k}_2)\cdot\mathbf{r}}\int\frac{dk_0}{(k_0^2-\omega_1^2)(k_0^2-\omega_2^2)}$$
$$=-3\mu(g^2/4\pi)^2(\mu/2M)^2(2/\pi)K_1(2x)/x^2. \tag{17}$$

The integral involved is one of a class evaluated in the appendix. We have also substituted the value $T_4=6$ (two Feynman diagrams).

We demonstrate next that the same technique easily reproduces the potential $V_8(x)$ of Eq. (3). We may begin appositely by computing the quantity T_8. This is best done by reference to Fig. 2(d). The number of Feynman diagrams that contribute (equally) to the potential represented by this figure is 2^4, for each pair-vertex corresponds to two γ_5 vertices and the sequence of these may be interchanged independently of all other vertices. For the potential of order $4n$, the result is 2^{2n}. The reader will then easily convince himself that the quantity T_{4n} has the value 3×2^{2n}, i.e., just three times the value for the neutral theory. Thus $T_8=48$.

We shall carry out the calculation for the interaction of Fig. 5. We consider, therefore,

$$V_8(\mathbf{r},\mathbf{r}')=-i(-ig^2)^4T_8\int dtd^4x_3\cdots d^4x_6dt_7dt_8d\mathbf{R}'$$
$$\times\exp[iM(t_1+t_2-t_7-t_8)]\Delta(x_1-x_2)\Delta(x_3-x_6)\Delta(x_6-x_4)\Delta(x_7-x_8)\langle\ \rangle^{(1)}\langle\ \rangle^{(2)}, \tag{18}$$

with

$$\langle\ \rangle^{(1)}=\langle\gamma_0\gamma_5 G_-(x_1-x_3)\gamma_5 G_+(x_3-x_5)\gamma_5 G_-(x_5-x_7)\gamma_5\rangle^{(1)}$$
$$\cong(-i)^2 i\delta(\mathbf{r}_1-\mathbf{r}_3)\delta(\mathbf{r}_3-\mathbf{r}_5)\delta(\mathbf{r}_5-\mathbf{r}_7)\exp[iM(t_1-2t_3+2t_5-t_7)], \tag{19}$$

with a similar expression holding for $\langle\ \rangle^{(2)}$. Carrying out the spatial integrations, we find for the equation analogous to (15),

$$V_8(\mathbf{r})=ig^8T_8\int dtdt_3\cdots dt_8(t_3>t_1,\ t_1<t_7,\ t_7>t_5\cdots)$$
$$\times\exp[i2M(t_1+t_2-t_3-t_4+t_5+t_6-t_7-t_8)]\Delta(\mathbf{r},t_1-t_2)\Delta(\mathbf{r},t_3-t_6)\Delta(\mathbf{r},t_5-t_4)\Delta(\mathbf{r},t_7-t_8). \tag{20}$$

The time integrations analogous to Eq. (16) will be done in two steps as follows:

$$\int dtdt_3\cdots dt_8\exp[it_1(2M-k_{01})+\cdots]=(-i/2M)^4\int_{-\infty}^{\infty}dt\exp[-i(t_1-t_2)(k_{01}+k_{02}+k_{03}+k_{04})]$$
$$\times\int_{-\infty}^{0}dt_5\exp[-it_5(k_{03}+k_{04})]\int_{-\infty}^{0}dt_6\exp[it_6(k_{02}+k_{04})]\rightarrow$$
$$(-i/2M)^4 2(\pi)^3\delta(k_{01}+k_{02}+k_{03}+k_{04})\delta(k_{03}+k_{04})\delta(k_{02}+k_{04}). \tag{21}$$

The arrow is used in the last stage to indicate that it is a permissible step only in virtue of the symmetry properties of the entire integral, Eq. (20). Physically, it corresponds to the fact that having established the pair-vertices by prior time integrations, reversal of the time sequence of the two-pair-vertices of each particle leaves the inter-

action [or Fig. 2(d)] invariant.[17] As a consequence of Eq. (21), we are left with

$$V_8(\mathbf{r})=i\frac{g^8}{(2M)^4}\frac{1}{(2\pi)^{12}}\frac{T_8}{(2)^3\pi}\int d\mathbf{k}_1\cdots d\mathbf{k}_4\exp[i(\mathbf{k}_1+\mathbf{k}_2+\mathbf{k}_3+\mathbf{k}_4)\cdot\mathbf{r}]$$
$$\times\int dk_0[(k_0^2-\omega_1^2)(k_0^2-\omega_2^2)(k_0^2-\omega_3^2)(k_0^2-\omega_4^2)]^{-1}. \quad (22)$$

In the appendix it is shown that the integral

$$I_{2l}\equiv\frac{i}{\pi}\frac{1}{(2\pi^2)^{2l}}\int d\mathbf{k}_1\cdots d\mathbf{k}_{2l}\exp[i(\mathbf{k}_1+\cdots+\mathbf{k}_{2l})\cdot\mathbf{r}]\int dk_0[(k_0^2-\omega_1^2)\cdots(k_0^2-\omega_{2l}^2)]^{-1}=-(2/\pi)\mu K_1(2l\mu r)/r^{2l}. \quad (23)$$

Equation (22) yields, therefore,

$$V_8(x)=-6\mu(g^2/4\pi)^4(\mu/2M)^4(2/\pi)K_1(4x)/x^4. \quad (24)$$

C. General Result

On the basis of the previous results, we conjecture that the $2n$-pair potential of order $4n$ has the form

$$V_{4n}(x)=-\mu(g^2/4\pi)^{2n}(\mu/2M)^{2n}$$
$$N_{4n}T_{4n}2^{-2n-1}(2/\pi)K_1(2nx)/x^{2n}. \quad (25)$$

Here N_{4n} is the number of distinct perimeters, for starting with twelfth order, this number is greater than unity and as we shall see below increases rapidly with n. Figure 6 shows two of the six perimeters in twelfth order. In writing Eq. (25), we have assumed that each perimeter contributes equally to the potential, at least *on the average*. The inclusion of the factor 2^{-2n-1} [see the factor 2^{-3} in Eq. (22)] assumes that the contributions from the time intervals between the established pair vertices yield half a delta function each, again at least on the average.

To find N_{4n}, we ask for the number of ways of constructing distinct meson-line perimeters, starting from n pair vertices for each particle. The result is

$$N_{4n}=\binom{n}{2}[(n-1)(n-2)][(n-2)(n-3)]\cdots$$
$$=\tfrac{1}{2}n!(n-1)!. \quad (26)$$

We then have

$$N_{4n}T_{4n}2^{-2n-1}=3\times n!(n-1)!, \quad (27)$$

FIG. 6. Two of six twelfth-order perimeters.

and Eq. (25) becomes

$$V_{4n}(x)=-\mu(g^2/4\pi)^{2n}(\mu/2M)^{2n}3$$
$$\times n!(n-1)!(2/\pi)K_1(2nx)/x^{2n}. \quad (28)$$

It can now be stated that in virtue of Eq. (23), there remains but a single point that must be established in order to completely verify Eq. (28); namely, that whenever we encounter an integral of the form

$$\int_{-\infty}^{0}dt e^{-i\lambda t}=\pi\delta(\lambda)+iP(1/\lambda), \quad (29)$$

which arises from time intervals between pair-vertices, we can replace it by merely $\pi\delta(\lambda)$ as a consequence of the structure of the entire expression of which it is a part, as in Eq. (21). Unfortunately, we have been unable thus far to find a general proof of this statement. It is, in fact, not true in the simple form analogous to Eq. (21). What appears to be true is that integrals containing an even number[18] of linear denominators from equations like (29) cancel out when one adds the analogous contributions from different perimeters. This has actually been checked in twelfth order, which is the first nontrivial case. It appears to be a consequence of the topological invariance of the group of perimeters as a whole under the inversion in time order of selected pair vertices, but we have been unable to relate this in a general way to the structure of the integrals encountered.

We believe that this lack of rigor hardly invalidates the general inference to be drawn from Eq. (28). Based alone on the combinatorial aspects of the work, there should be little doubt that the coefficients of higher order potentials increase so rapidly as to render unthinkable the convergence of the unrenormalized potentials.

We have also tentatively applied the same technique of calculation to the set of potentials exemplified by Eqs. (2) and (4), where we claim no validity for it. It is found that the method reproduces the correct analytic

[17] In detail, we carry out the sequence of transformations $k_{01}\leftrightarrow k_{02}$ (and $\mathbf{k}_1\leftrightarrow\mathbf{k}_2$), $k_{03}\leftrightarrow k_{04}$ (and $\mathbf{k}_3\leftrightarrow\mathbf{k}_4$) and then note that $k_{01}+k_{02}=-k_{03}-k_{04}$ in virtue of the integral with respect to t. Half the sum of the original plus the equivalent transformed expression yields the factor $\pi\delta(k_{03}+k_{04})$. Similar steps provide the other δ function.

[18] Those involving an odd number vanish identically.

form of the potential, but starting in eighth order, overestimates the coefficients.[19] Again, however, there can be little doubt that the tendency toward breakdown of the expansion in μ/M for a given power of $g^2/4\pi$ becomes increasingly apparent in higher orders.

Note added in proof:—The central result of this paper, Eq. (28), is incorrect. The correct result is obtained by replacing the factor $n!(n-1)!$ by $2^{2(n-1)}/n$. A derivation of the correct general expression for the pair potentials as well as for certain other series of potentials involving a restricted number of gradient couplings, together with the sum of each series, will be submitted for publication shortly. The series of potentials for pair theory can also be deduced directly from the work of reference 11. The "derivation" given in the present paper goes wrong only at the last stage, Eq. (29) and associated discussion. The special results obtained in Secs. II, IIIb, and the Appendix are, however, subject to no objection. Our conclusions must correspondingly be modified from a bald assertion of nonconvergence to the statement that perturbation theory yields a series of potentials with a finite radius of convergence in inverse distance space. However, for values of the coupling constant presently contemplated, $(g^2/4\pi)\geq 10$, there is an important region outside the cut-off radius where the series either doesn't converge or else the convergence is painfully slow. This will be shown in greater detail in the forthcoming publication.

APPENDIX

In Sec. VI of **A**, the general character of the n-pair term of the n-body force was established, and in addition specific expressions were given for the three and four-body forces. We are now in a position to obtain the result for arbitrary n by means of the technique employed in Sec. III, which applies here without question.

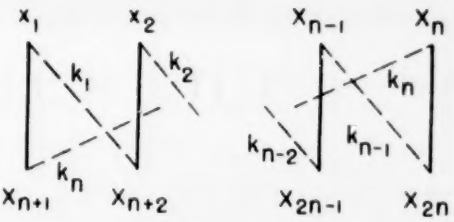

FIG. 7. Representative diagram for the calculation of the n-pair term of the n-body potential.

We recall that this force consists of $(n-1)!/2$ terms, each of similar structure, one for every possible perimeter. Furthermore, it is sufficient to calculate for a single Feynman diagram that contributes to some standard perimeter and multiply the result by $T_n=3\times 2^n$, the isotopic factor for the perimeter. From this single term it is a trivial matter of changing functional arguments to obtain all $(n-1)!/2$ terms.

Consider therefore the interaction of Fig. 7. In complete analogy to Eqs. (18) or (11), it can be shown to contribute the potential

$$V_n(\xi_1\xi_2\cdots\xi_{n-1};\,\xi_1'\cdots\xi_{n-1}')=(-1)^n(-i)^{n-1}(-ig^2)^nT_n\int dt_2dt_3\cdots dt_nd\mathbf{R}'\exp[iM(t_1+t_2+\cdots-t_{n+1}-\cdots t_{2n}]$$
$$\times\Delta(x_1-x_{n+2})\Delta(x_2-x_{n+3})\cdots\Delta(x_n-x_{n+1})\langle\gamma_0\gamma_5G_-(x_1-x_{n+1})\gamma_5\rangle^{(1)}\cdots\langle\gamma_0\gamma_5G_-(x_n-x_{2n})\gamma_5\rangle^{(n)},\quad(A.1)$$

where $\xi_1\cdots\xi_{n-1}$ is the sequence of independent coordinate differences,[20] which defines the particular perimeter considered, $\xi_1=\mathbf{r}_1-\mathbf{r}_2$, $\xi_2=\mathbf{r}_2-\mathbf{r}_3$, $\cdots\xi_n=\mathbf{r}_n-\mathbf{r}_1$, and the time integrations are restricted by the condition that only the n-pair part is to be included ($t_1<t_{n+1}$, etc.). By means of the relationship,

$$\langle\gamma_0\gamma_5G_-(x_1-x_{n+1})\gamma_5\rangle^{(1)}\cdots\langle\gamma_0\gamma_5G_-(x_n-x_{2n})\gamma_5\rangle^{(n)}$$
$$\cong(-i)^n\delta(\mathbf{r}_1-\mathbf{r}_{n+1})\cdots\delta(\mathbf{r}_n-\mathbf{r}_{2n})\cdot e^{iM(t_1-t_{n+1})}\cdots e^{iM(t_n-t_{2n})},\quad(A.2)$$

Eq. (A.1) is reduced to a point potential,

$$V_n(\xi_1\cdots\xi_{n-1},\,\xi_1'\cdots\xi_{n-1}']\rightarrow V_n(\xi_1\cdots\xi_{n-1})\delta(\xi_1-\xi_1')\cdots\delta(\xi_{n-1}-\xi_{n-1}'),\quad(A.3)$$

$$V_n(\xi_1\cdots\xi_{n-1})=(-i)^{n-1}g^{2n}T_n\int dt_2\cdots dt_{2n}\exp[i2M(t_1+t_2+\cdots$$
$$-t_{n+1}-\cdots t_{2n})]\Delta(\xi_1,\,t_1-t_{n+2})\cdots\Delta(\xi_n,\,t_n-t_{n+1}).\quad(A.4)$$

Introducing four-dimensional momentum representations of the Δ functions, we encounter the time integrations

$$\int_{-\infty}^{\infty}dt_2\cdots dt_n\int_{t_1}^{\infty}dt_{n+1}\cdots\int_{t_n}^{\infty}dt_{2n}\exp[it_1(2M-k_{01})+\cdots+it_n(2M-k_{0n})$$
$$-it_{n+1}(2M-k_{0n})-it_{n+2}(2M-k_{01})-\cdots-it_{2n}(2M-k_{0\,n-1})]$$
$$=(-i/2M)^n(2\pi)^{n-1}\delta(k_{01}-k_{02})\delta(k_{02}-k_{03})\cdots\delta(k_{0\,n-1}-k_{0n}).\quad(A.5)$$

[19] One cannot, in full justice, rule out this possibility for Eq. (28).
[20] Note that ξ_n is not independent of the other ξ_i, but satisfies $\Sigma_i\xi_i=0$.

As a consequence of Eq. (A.5), Eq. (A.4) has been reduced to the form

$$V_n(\xi_1\cdots\xi_{n-1})=i(-1)^n\left(\frac{g^2}{4\pi}\right)^n\left(\frac{1}{2M}\right)^n T_n\left(\frac{1}{2\pi^2}\right)^n\frac{1}{2\pi}\int d\mathbf{k}_1\cdots d\mathbf{k}_n$$
$$\times\exp[i(\mathbf{k}_1\cdot\xi_1+\cdots+\mathbf{k}_n\cdot\xi_n)]\int dk_0[(\omega_1^2-k_0^2)\cdots(\omega_n^2-k_0^2)]^{-1}. \quad \text{(A.6)}$$

It remains only to demonstrate that, for $n\geq 2$,

$$I_n\equiv\frac{i}{\pi}\frac{1}{(2\pi^2)^n}\int d\mathbf{k}_1\cdots d\mathbf{k}_n\exp[i(\mathbf{k}_1\cdot\xi_1+\cdots+\mathbf{k}_n\cdot\xi_n)]\int dk_0[(\omega_1^2-k_0^2)\cdots(\omega_n^2-k_0^2)]^{-1}$$
$$=-\mu(2/\pi)K_1[\mu(\xi_1+\xi_2+\cdots+\xi_n)]/\xi_1\xi_2\cdots\xi_n, \quad \text{(A.7)}$$

in order to establish the result[21]

$$V_n(\xi_1\cdots\xi_{n-1})=(-1)^{n-1}3\times 2^{n-1}(g^2/4\pi)^n(\mu/2M)^n(2/\pi)K_1[\mu(\xi_1+\cdots+\xi_n)]/\mu^{n-1}\xi_1\cdots\xi_n, \quad \text{(A.8)}$$

in agreement with a previous derivation.[11]

We may remark that the same method suffices to derive the μ/M corrections to Eq. (A.8) which are analagous to the one-pair potential of fourth order, but we shall not go into detail. We turn rather to the proof of (A.7).

We employ spherical polar coordinates for the three-momentum integrations and immediately carry out the angular integrations. We are left with

$$I_n=\frac{i}{\pi}\left(\frac{2}{\pi}\right)^n\frac{1}{\xi_1\xi_2\cdots\xi_n}\int_{-\infty}^{\infty}dk_0\int_0^{\infty}dk_1k_1\sin k_1\xi_1\cdots dk_nk_n\sin k_n\xi_n[(\omega_1^2-k_0^2)\cdots(\omega_n^2-k_0^2)]^{-1}. \quad \text{(A.9)}$$

Next, consider the factors

$$[\omega_1^2-k_0^2]^{-1}[\omega_2^2-k_0^2]^{-1}=[k_1^2-k_2^2]^{-1}\{[\omega_2^2-k_0^2]^{-1}-[\omega_1^2-k_0^2]^{-1}\}. \quad \text{(A.10)}$$

By means of the formula

$$\int_0^{\infty}\frac{\sin(lk\xi)kdk}{k^2-k_1^2}=\tfrac{1}{2}\pi\cos lk_1\xi, \quad \xi>0, \quad \text{(A.11)}$$

we can carry out the k_1 integral in the first term and the k_2 integral in the second term. We label as k the remaining one of the momenta k_1, k_2 and combine the two terms again, with the result

$$I_n=\frac{i}{\pi}\left(\frac{2}{\pi}\right)^{n-1}\frac{1}{\xi_1\xi_2\cdots\xi_n}\int_{-\infty}^{\infty}dk_0\int_0^{\infty}kdk\sin k(\xi_1+\xi_2)k_3dk_3\sin k_3\xi_3\cdots[(\omega^2-k_0^2)(\omega_3^2-k_0^2)\cdots(\omega_n^2-k_0^2)]^{-1}. \quad \text{(A.12)}$$

We now perform the same sequence of operations with the factors $[(\omega^2-k_0^2)(\omega_3^2-k_0^2)]^{-1}$ and so on, a total of $(n-2)$ such sequences for Eq. (A.11), until we have reduced its structure to

$$I_n=\frac{i}{\pi}\frac{2}{\pi}\frac{1}{\xi_1\xi_2\cdots\xi_n}\int_0^{\infty}dkk\sin k(\xi_1+\cdots+\xi_n)\int_{-\infty}^{\infty}dk_0(\omega^2-k_0^2)^{-1}=-\mu(2/\pi)K_1[\mu(\xi_1+\cdots+\xi_n)]/\xi_1\cdots\xi_n. \quad \text{(A.13)}$$

The last form which is the result desired follows from the equations

$$\int_{-\infty}^{\infty}dk_0[\omega^2-i\eta-k_0^2]=\pi i/\omega, \quad \text{(A.14)}$$

and

$$\int_{-\infty}^{\infty}\frac{dkk\sin k(\xi_1+\cdots+\xi_n)}{\omega}=\mu K_1[\mu(\xi_1+\cdots+\xi_n)].$$

If we take n even and set $\xi_i=r$ for all i, we obtain Eq. (23) of the text.

[21] The demonstration holds also for $n=2$, if we agree that there is only half a perimeter in this case and consequently halve the result. For instead of $2^n=4$ Feynman diagrams, we have only two, the "ladder" and "crossed-quantum" diagrams.

Note on the Low-Energy Properties of the Nucleon-Nucleon Interaction

ROBERT JASTROW*
Institute for Advanced Study, Princeton, New Jersey
(Received April 2, 1953)

A previously proposed model for the nucleon-nucleon interaction consists of the potential yielded by the symmetrical pseudoscalar theory with pseudoscalar coupling, calculated to the fourth order in the coupling constant and cut off by a hard sphere repulsion. Further calculations relating to the low energy properties of this potential have been carried out in which the effect of a variation in the magnitude of the fourth-order term is considered. The computed low-energy constants are found to be insensitive to this variation.

I. INTRODUCTION

IT has been remarked by several authors, with reference to the nuclear forces yielded by the symmetrical pseudoscalar theory with pseudoscalar coupling, that the contribution of fourth order in the coupling constant may equal or outweigh that of second order at low energies.[1-6] It has been suggested, furthermore, that terms of higher order than the fourth may be neglected at distances larger than 0.5×10^{-13} cm.[7] These considerations have led to a model of the nucleon-nucleon interaction consisting of the sum of the second- and fourth-order potentials from the pseudoscalar theory, cut off in an arbitrary manner at a distance of the order of 0.5×10^{-13} cm.

The properties of this potential have been examined on the assumption of a hard sphere cutoff and are in good agreement with experiment.[8,9] The bearing of the comparison with experiment on the status of the pseudoscalar theory is not clear, however, for the model is arbitrary in several respects. In addition to the freedom in choice of a cutoff, the weight of the fourth- relative to the second-order potential is modified to an unknown degree by Lamb shift terms occurring in all higher orders.[10] It is the purpose of the present note to consider the effect of this modification on the low-energy constants.

As in earlier calculations, the potential will be cut off by a hard sphere repulsion representing the effects of nucleon structure at low energies.[11]

The discussion will be based on a nonrelativistic calculation of the interaction. At nonrelativistic energies the pseudoscalar coupling takes the form

$$g\gamma_5\varphi \rightarrow \frac{g}{2m}\boldsymbol{\sigma}\cdot\nabla\varphi+\frac{g^2}{2m}\varphi^2+O(\varphi^4). \tag{1}$$

The gradient term in Eq. (1) leads to the familar second-order result,

$$V^{(2)}=\mu\left(\frac{\mu}{2m}\right)^2\left(\frac{g^2}{4\pi}\right)\frac{\boldsymbol{\tau}_1\cdot\boldsymbol{\tau}_2}{3}\times\left\{\boldsymbol{\sigma}_1\cdot\boldsymbol{\sigma}_2+S_{12}\left(1+\frac{3}{\mu r}+\frac{3}{(\mu r)^2}\right)\right\}\frac{e^{-\mu r}}{\mu r},$$

and the pair term, $g^2\varphi^2/2m$, to the fourth-order potential,

$$V^{(4)}=-\mu\left(\frac{\mu}{2m}\right)^2\left(\frac{g^2}{4\pi}\right)^2\frac{6}{\pi}\frac{K_1(2\mu r)}{(\mu r)^2}.$$

A parameter α will be introduced to describe variations in the ratio $V^{(2)}:V^{(4)}$. The potential to be examined is then

$$V=\infty, \quad r<r_0;$$
$$V=V^{(2)}+\alpha V^{(4)}, \quad r>r_0.$$

The fourth-order term behaves as a $1/r^3$ potential in the region of interest, for the contemplated cut-off distance of 0.5×10^{-13} cm is less than $\frac{1}{2}\mu$ and $K_1(2\mu r)$ $1/2\mu r$ if $2\mu r<1$. For distances less than $1/\mu$, $V^{(2)}$ is dominated by its $1/r^3$ tensor component. Thus the combination, $V^{(2)}+\alpha V^{(4)}$, may be simply described with respect to its low-energy properties as a $1/r^3$ potential with a tensor component whose relative weight is specified by α. This description depends for its validity on the fact that the principal contributions come from

* On leave from the Radiation Laboratory, University of California, Livermore, California.

[1] H. A. Bethe, Phys. Rev. **76**, 191 (1949).

[2] J. V. Lepore and K. M. Watson, Phys. Rev. **76**, 1157 (1949).

[3] Y. Nambu, Prog. Theoret. Phys. (Japan) **5**, 614 (1950).

[4] M. M. Lévy, Phys. Rev. **88**, 725 (1952).

[5] R. P. Feynman, California Institute of Technology notes (unpublished).

[6] Taketani, Machida, and Onuma, Progr. Theoret. Phys. (Japan) **7**, 45 (1952). The gradient coupling theory is discussed from a viewpoint similar to that of the present paper.

[7] See reference 4. However, recent work by A. Klein, Phys. Rev. **89**, 1158 (1953) indicates that the convergence of the series in powers of the coupling constant is in doubt.

[8] M. M. Lévy, Phys. Rev. **86**, 806 (1952).

[9] R. Jastrow, Phys. Rev. **86**, 209 (1952). This report quoted an incorrect value of the quadrupole moment.

[10] The effect of these terms has been estimated by G. Wentzel [Phys. Rev. **86**, 802 (1952)] in a strong coupling calculation of the static interaction produced by the φ^2 coupling alone in Eq. (1). The result differs by a multiplicative factor from the fourth-order potential obtained in weak coupling,

$$V_{\text{pair}}=V^{(4)}\Big/\left(1+\frac{A}{m}\frac{g^2}{4\pi}\right)^2.$$

Here A is a momentum cutoff of the order of m, the nucleon mass. Choosing $A=m$ and $g^2/4\pi\gg1$ as required by the low energy data, one has $V_{\text{pair}}\ll V^{(4)}$. The gradient coupling in Eq. (1) is neglected by Wentzel in comparison with the pair term, although the potentials arising from the two terms are comparable in magnitude if the weight of $V^{(4)}$ is reduced as suggested by his calculation.

[11] Reference 9; also R. Jastrow, Phys. Rev. **81**, 165 (1951).

TABLE I. The low-energy constants calculated from the potential (2) for two values of α. The last column lists the observed values. Distances are in units of 10^{-13} cm.

Coupling constant $(g^2/4\pi)$	10	16	Obs
α	1	$\frac{1}{4}$	—
Deuteron binding energy (E_B)	+2.23	2.23	2.227±0.003
Singlet scattering length (a_s)	−23.7	−23.7	−23.68 ±0.06
Effective range			
Triplet (r_{0t})	1.64	1.89	1.70 ±0.03
Singlet (r_{0s}) n-p	2.53	2.48	2.47 ±0.02
p-p			2.60 ±0.07
Quadrupole moment (Q)	2.12	2.73	2.738±0.016
Percent D state (P_D)	5.1	7.3	4?
Core radius: triplet r_{ct}	0.53	0.61	—
singlet r_{cs}	0.48	0.40	—

distances close to the cut-off radius because of the highly singular nature of the potential. For the same reason, the effective range of the interaction is determined by r_0, rather than by $1/\mu$ or $1/2\mu$. The volume of potential contained in the tail of $V^{(2)}$ is relatively small and can be effective only at higher energies through the excitation of P and D waves.

II. CALCULATION OF THE LOW-ENERGY CONSTANTS

The properties of the potential (2) have been studied for two cases: $\alpha=1$, corresponding to the perturbation treatment of the pair force; and $\alpha=\frac{1}{4}$, representing an arbitrarily chosen diminution in $V^{(4)}$. In each case, the coupling constant was varied to secure the best over-all agreement of the effective ranges with observation.

The wave functions were obtained by integrating inward from large r, starting at 5.6×10^{-13} cm, with initial values taken from asymptotic expressions corresponding to the observed deuteron binding energy or singlet scattering length.[12] The radius of repulsion was determined as the first zero of the wave function during the inward integration.

The results of the calculation, listed in Table I, indicate that the change from $\alpha=1$ to $\alpha=\frac{1}{4}$ has little effect on the low energy constants.[13] The principal variation occurs in the quadrupole moment, whose magnitude is determined by the relative weight of the $1/r^3$ tensor term in $V^{(2)}$ and may be expected to depend directly on α. The improvement in the quadrupole moment resulting from a reduction in α is partially compensated by an increased discrepancy with respect to the triplet range, the over-all agreement being similar for the two values of α.

The calculated D-state probability corresponding to a suitable value of the quadrupole moment is considerably larger than the accepted figure of 4 percent, derived from the magnitude of the deuteron magnetic moment. However, the relation of the magnetic moment to the D-state probability is not well defined, and presumably little importance should be attached to the discrepancy.[14]

III. DISCUSSION

The significance of the agreement with observation is reduced by the insensitivity of the results to changes in α and g, as well as by the availability of four parameters —r_{0s}, r_{0t}, g, and α—for the adjustment of the five calculated constants.[15] The number of parameters may be reduced to three by the requirement of identical radii of repulsion, but it is difficult to justify this assumption on the spin dependence of the inner region.[16] It is possible, however, to obtain more information by increasing the area of comparison with experiment through a consideration of two-body scattering at intermediate energies, sufficiently high to excite P and D waves but low enough to insure the applicability of a static potential. These requirements are satisfied by experiments in the region of 10 to 40 Mev.[17]

Although the reduction in α produces little change, it is of interest that $V^{(2)}$ alone with $\alpha=0$ cannot reproduce the low energy data. The triplet properties may be brought into fair agreement in this case by setting $g^2/4\pi=32$, but the singlet constants provided by $V^{(2)}$ for the same choice of g—a scattering length of -7.5×10^{-13} cm and effective range of 4.0×10^{-13} cm—are in serious disagreement with the observed values. It appears that $V^{(2)}$ cannot account for the singlet and triplet states with one value of the coupling constant and that $V^{(4)}$ must be introduced for this purpose.

I should like to thank Mr. John Killeen and Mr. John Griffith of the Radiation Laboratory of the University of California for valuable advice and assistance in performing the necessary integrations by machine computation.

This work was performed in part under the auspices of the U. S. Atomic Energy Commission.

[12] The $1/r^3$ singularities in the potential made it convenient to use the transformation, $y=\log r$, with subsequent integration in the scale of y.

[13] The quoted experimental values are taken from Taketani *et al.* (reference 6) apart from the n-p and p-p singlet ranges. The deduction of the latter constants from the measured cross sections requires an assumption for the shape-dependent coefficient P in the expansion of $k\cot\delta$ at low energies. According to Hafner, Hornyak, Falk, Snow, and Coor, Phys. Rev. **89**, 204 (1953), Fig. 15, one has $P=-0.04$ for a hard core potential of radius 0.6×10^{-13} cm. Since $P=-0.04$ for a square well also, the appropriate values of the singlet range may be taken from the results for the square well in Fig. 14 of the same paper. These are the values quoted in Table I.

[14] An estimate by H. Miyazawa, Progr. Theoret. Phys. (Japan) **7**, 207 (1952) of the modification of the magnetic moment of one nucleon by the presence of the other leads him to assign the limits of 2 to 8 percent to the D state probability.

[15] It should be noted that the form of the cutoff is also arbitrary. As a consequence, it is difficult to distinguish the contributions of more singular forces than the $1/r^3$ potential, for it is entirely within the spirit of the calculation to replace the hard sphere by a $1/r^4$ or $1/r^5$ repulsion, for example, into whose uncertain magnitude any attractive potential of the same or a higher degree of singularity will be absorbed.

[16] The calculation by Lévy (reference 4) imposes this condition.

[17] Calculations of the p-p cross section at 18 and 32 Mev with the model of Lévy have been carried out by A. Martin and L. Verlet, Phys. Rev. **89**, 519 (1953).

The Similarity Theory of Relativity and the Dirac-Schrödinger Theory of Electrons. II

BANESH HOFFMANN
Queens College, Flushing, New York
(Received February 24, 1953)

The variational principle given in a previous paper under this title is here modified slightly in three stages. First the integral is made similarity-invariant. Then a sign is changed so that a consistent signature for the various terms shall be possible. Finally, a numerical discrepancy that was found on making a detailed comparison with the Jordan theory of the variable gravitational constant is removed, so that the equations of the latter theory for empty space are obtained as a special case of the present theory when all quantities except g_{ab} and ω are set equal to zero.

IN a recent paper[1] I showed that a general type of similarity geometry could form the basis for a unified field theory containing, among other things, the Dirac-Schrödinger equations for scalar electrons in an electromagnetic field, and a scalar field ω related to the scalar used by Jordan in his theory of the variable gravitational constant.

In this paper, I wish to modify the variational principle used in I so as to remove difficulties connected with the signs of certain terms and with the detailed comparison of the field equations with those of Jordan's theory.

The variational principle given in Eq. (25) of I was

$$\delta\int\{\omega(\bar{Z}-20N^2)+(\alpha-1)R\}(-g)^{\frac{1}{2}}dx^1dx^2dx^3dx^4=0. \quad (1)$$

Under a similarity transformation, the quantity in brackets acquires a factor k^{-2} while $(-g)^{\frac{1}{2}}$ acquires a factor k^4. So the integral acquires a factor k^2 and is thus not invariant. Since k is only a numerical parameter, and not an arbitrary function of position, this lack of invariance does not affect the resulting equations nor spoil their invariance. However, it does suggest that a more natural variational principle would be obtained by multiplying the integrand by ω, since ω acquires a factor k^{-2} under a similarity transformation and this would make the integral similarity-invariant. Such a change would not affect those conclusions in I concerned with the cases in which ω was kept constant. It does affect the equations relating to ω, bringing them closer in form to those used by Jordan. It also makes the term involving $10N$ in Eq. (26) of I a pure divergence so that it will not contribute to the field equations. Thus one is tempted to replace (1) by

$$\delta\int\{\omega^2(\bar{Z}-20N^2)+\omega(\alpha-1)R\}(-g)^{\frac{1}{2}}\times dx^1dx^2dx^3dx^4=0. \quad (2)$$

However, closer examination of the field equations belonging to (1) reveals two defects, and these persist in (2). In removing these defects, we shall work with (2) rather than (1) so as to have the integral in the variational principle invariant under similarity transformations.

[1] B. Hoffmann, Phys. Rev. **89**, 52 (1953); hereinafter referred to as I.

Since the ordinary derivatives $\partial\varphi/\partial x^a$, $\partial\omega/\partial x^a$ are also covariant derivatives with respect to g_{ab}, we may denote them by $\varphi_{,a}$ and $\omega_{,a}$, respectively. We have, by the usual formula for the covariant derivative of a vector density,

$$\frac{\omega^2}{(-g)^{\frac{1}{2}}}\frac{\partial}{\partial x^a}\left(\frac{1}{\omega}g^{ab}(-g)^{\frac{1}{2}}\frac{\partial\log\omega}{\partial x^b}\right)=\omega^2\left(\frac{1}{\omega^2}g^{ab}\omega_{,b}\right)_{,a}=g^{ab}\omega_{,ab}-\frac{2}{\omega}g^{ab}\omega_{,a}\omega_{,b}. \quad (3)$$

Also

$$\omega^2\frac{\partial\log\omega}{\partial x^a}\frac{\partial\log\omega}{\partial x^b}=\omega_{,a}\omega_{,b}. \quad (4)$$

So, by Eq. (26) of I, we may write (2) in the form

$$\delta\int\Big[\omega\alpha R+2g^{ab}\omega_{,ab}+\frac{14}{\omega}g^{ab}\omega_{,a}\omega_{,b}-\omega^2\psi^a{}_b\psi^b{}_a-\theta^a{}_b\theta^b{}_a-g^{bd}\psi_a\theta^a{}_b\varphi_{,d}+\frac{1}{2\omega}g^{ab}\varphi_{,a}\varphi_{,b}+20N^2\{\omega g^{ab}(\theta_a-\psi_a\varphi)(\theta_b-\psi_b\varphi)+\varphi^2\}\Big]\times(-g)^{\frac{1}{2}}dx^1dx^2dx^3dx^4=0, \quad (5)$$

where we have omitted the divergence term,

$$10N\frac{\partial}{\partial x^a}\{\omega g^{ab}(-g)^{\frac{1}{2}}(\psi_b\varphi-\theta_b)\},$$

which does not contribute to the field equations.

Consider the following two groups of terms in (5):

$$-\theta^a{}_b\theta^b{}_a+20N^2\omega\theta^a\theta_a, \quad (6)$$

and

$$\omega^{-1}(\tfrac{1}{2}g^{ab}\varphi_{,a}\varphi_{,b}+20N^2\omega\varphi^2). \quad (7)$$

They will refer to particles having real masses if either (a) g_{ab} has signature $+++-$, and $N^2\omega>0$, or (b) g_{ab} has signature $---+$, and $N^2\omega<0$.

But the term involving R in (5) must have a sign opposite to that involving $g^{ab}\varphi_{,a}\varphi_{,b}$, and this can not occur whether ω is positive or negative. Nor can the relative sign of these two terms be changed by altering the signature of g_{ab}. Thus we must change the sign of the constant α, taking it to be negative.

If the gravitational term $\omega\alpha R$ is negative, comparison with the electromagnetic term $-\omega^2\psi^a{}_b\psi^b{}_a$ shows that we must use the signature $---+$; if we take ω to be negative the relative sign of these two terms changes and so we must use the signature $+++-$. In either case we see from (a) and (b) that N must be pure imaginary. So we shall take ω to be positive, g_{ab} to have the signature $---+$, and N to be pure imaginary.

Instead of taking α to be negative we may replace it by $-\alpha$ in (2), and then, to keep the R term positive without spoiling the relative signs of the various terms, we may multiply the whole integrand by -1. The resulting variational principle is

$$\delta\int\{\omega(\alpha+1)R-\omega^2(\bar{Z}-20N^2)\}(-g)^{\frac{1}{2}}dx^1dx^2dx^3dx^4=0, \quad (8)$$

where α is now once more a positive number.

The signs are now in order, and this includes the signs of the Jordan-like ω terms. But there is still a numerical discrepancy to be corrected if we are to relate the scalar ω to Jordan's theory. Jordan's variational principle can be written[2]

$$\delta\int\left\{\omega R-\frac{\zeta}{\omega}g^{ab}\omega_{,a}\omega_{,b}\right\}(-g)^{\frac{1}{2}}dx^1dx^2dx^3dx^4=0, \quad (9)$$

where ζ is a positive number which Jordan later shows[3] should be large but not greater than about 30.

If we consider those terms in (8) that contain only g_{ab} and ω, we have

$$\delta\int\left\{\omega\alpha R-2g^{ab}\omega_{,ab}-\frac{14}{\omega}g^{ab}\omega_{,a}\omega_{,b}\right\}(-g)^{\frac{1}{2}}\times dx^1dx^2dx^3dx^4=0. \quad (10)$$

The term $-2g^{ab}\omega_{,ab}$ may be ignored since it is the divergence of $-2g^{ab}\omega_{,a}$ and thus does not contribute to the field equations. The coefficient 14 in the third term is a fair approximation to the ζ in (9), but this agreement is spoiled by the α multiplying R, since the presence of α means that we have to compare ζ not with 14 but with $14/\alpha$, and α is of the order of magnitude 10^{41}.

One way to remove this discrepancy is to replace (8) by the variational principle,

$$\delta\int\{-5\alpha\bar{R}+6\alpha\omega R-\omega^2(\bar{Z}-20N^2)\}(-g)^{\frac{1}{2}}\times dx^1dx^2dx^3dx^4=0, \quad (11)$$

where[4] $\bar{R}$ is the similarity-invariant curvature scalar formed from the similarity-invariant tensor $\bar{g}_{ab}$.

From Eq. (83) of I and Eq. (3) of the present paper, we have

$$\bar{R}=\omega R-6g^{ab}\omega_{,ab}+\frac{6}{\omega}g^{ab}\omega_{,a}\omega_{,b}. \quad (12)$$

Thus, writing M^2 for $-N^2$, omitting the terms involving $g^{ab}\omega_{,ab}$ and $10N$ because they are divergences, and the numbers 1 and 14 in the quantities $(\alpha-1)$, $(30\alpha+14)$ because α is very large, we may write (11) in the explicit form

$$\delta\int\Big[\alpha\omega R-\frac{30\alpha}{\omega}g^{ab}\omega_{,a}\omega_{,b}+\omega^2\psi^a{}_b\psi^b{}_a+\theta^a{}_b\theta^b{}_a+g^{ab}\psi_a\theta^a{}_b\varphi_{,a}-\frac{1}{2\omega}g^{ab}\varphi_{,a}\varphi_{,b}+20M^2\{\omega g^{ab}(\theta_a-\psi_a\varphi)(\theta_b-\psi_b\varphi)+\varphi^2\}\Big]\times(-g)^{\frac{1}{2}}dx^1dx^2dx^3dx^4=0. \quad (13)$$

This integral contains no imaginary quantities. Thus the field equations will be real, and all the significant field quantities, g_{ab}, ψ_a, θ_a, φ, and ω, will be real.

The integral in (11) involves the numbers 5 and 6 along with the number α. The last has some justification as a well-known fundamental pure number, but the numbers 5 and 6 are arbitrary. In Jordan's theory the whole term $(\zeta/\omega)g^{ab}\omega_{,a}\omega_{,b}$ in (9) was subtracted arbitrarily from the term $R\omega$, and the value of the constant ζ adjusted to avoid disagreement with astronomical data. The numbers 5 and 6 in (11) correspond precisely to this arbitrariness in the Jordan theory, for the modification introduced by means of (11) amounts essentially to the subtraction of $(30\alpha/\omega)g^{ab}\omega_{,a}\omega_{,b}$ from the expression in brackets in (8), coupled with the neglect of small numbers in comparison with α. For the expression in brackets in (11) can be written

$$\{\alpha\omega R-\omega^2(\bar{Z}-20N^2)\}+5\alpha(\bar{R}-\omega R), \quad (14)$$

and the first group of terms is essentially the same as the expression in brackets in (8) while the last term is just $-(30\alpha/\omega)g^{ab}\omega_{,a}\omega_{,b}$ plus a divergence, the number 5 in (14) being chosen so as to give the number 30 here.

If ω is to play the part of a variable gravitational constant, it is desirable to write the parts of (13) that refer to the Maxwell-Dirac-Schrödinger field and the vector field θ_a in such a way that ω^2 appears explicitly as a factor. The Maxwellian part, $\omega^2\psi^a{}_b\psi^b{}_a$, already has this factor. If we introduce new variables $\bar{\theta}_a$, $\bar{\varphi}$, where

$$\bar{\theta}_a=\theta_a/\omega, \quad (15)$$

$$\bar{\varphi}=\varphi/\omega^{\frac{1}{2}}, \quad (16)$$

we may also extract an explicit factor ω^2 from the other terms, and, so far as the pure fields taken individually are concerned, they do not contain ω further except in the mass terms, as in (6) and the parentheses of (7). The interaction terms are intimately linked with ω. Thus, if the present interpretation of ω as Jordan's scalar is correct, it indicates mass changes, and interaction effects between fundamental particles, that involve the variable gravitational constant and thus depend on the epoch of the universe.

[2] See P. Jordan, *Schwerkraft und Weltall* (Vieweg, Braunschweig, 1952), Eq. (4), p. 140. We modify the notation to conform to that used here.

[3] Reference 2, p. 156.

[4] See I, below Eq. (77); also Eqs. (81), (83).

Letters to the Editor

PUBLICATION of brief reports of important discoveries in physics may be secured by addressing them to this department. The closing date for this department is five weeks prior to the date of issue. No proof will be sent to the authors. The Board of Editors does not hold itself responsible for the opinions expressed by the correspondents. Communications should not exceed 600 words in length and should be submitted in duplicate.

Electronic Hall Effect in NaCl*

ALFRED G. REDFIELD†
Physics Department, University of Illinois, Urbana, Illinois
(Received June 3, 1953)

BY applying the pulsed light method of Pohl and his coworkers[1] to the measurement of electronic Hall effect in insulating photoconductors it has been possible to avoid the space-charge difficulties present in previous work.[2,3] The electrode arrangement is shown in Fig. 1. The battery V_L sets up a potential

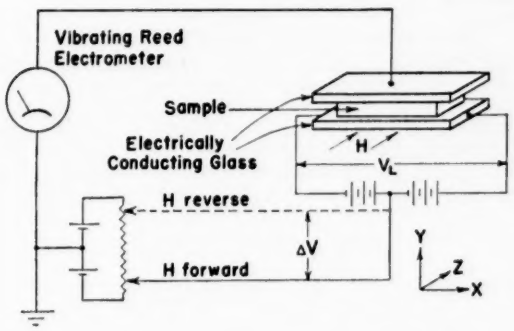

FIG. 1. Electrode arrangement for observing electronic Hall effect in insulating photoconductors.

gradient on the lower surface of the crystal, and thus an inhomogeneous field in the crystal which is, on the average, in the x direction. The upper plate is held at ground potential by the electrometer circuit; the potential of the entire lower plate can be changed with the potentiometer, and moving the potentiometer tap rotates the electric field in the crystal. The electrometer responds only to the component of charge flow which is in the y direction.

In making a measurement, a magnetic field is applied in the z direction, the crystal is illuminated with pulses of light a few seconds in duration, and the potentiometer is adjusted until the electrometer gives zero deflection during illumination. This means that the average charge flow in the crystal is in the x direction parallel to the electrodes, but the average electric field is at an angle, the Hall angle, to the electrodes. To eliminate space charge, the batteries are turned off between each observation of the electrometer, and the crystal is illuminated with a strong light.

The magnetic field is then reversed and the potentiometer is again adjusted as before, so that the average charge flow is again in the x direction but the average electric field has been rotated through twice the Hall angle. Using a theorem of Shockley,[4] it can then be shown rigorously that (for small θ)

$$\frac{2\mu H}{c}=2\theta=\frac{\Delta V}{D}\frac{\int n\tau dv}{\int E_x n\tau dv},$$

where μ is the mobility, H the magnetic field, c the velocity of light, θ the Hall angle, D the thickness of the crystal, n the number of electrons per unit volume released by the light, τ the mean electronic lifetime, and E_x the x component of electric field in the crystal. The integrations are over the volume of the crystal.

This method differs from the conventional one in several ways. First, it is a transient method. Second, the electric field inside the crystal is rotated by external electrodes, rather than by the electrons under study. Finally, no attempt is made to inject or eject electrons through the surface of the crystal. The method cannot be applied directly to crystals having finite dark conductivity. It has already been applied to diamond.[5]

Both additively colored and x-rayed Harshaw NaCl crystals have been studied and the charge released from F centers in these crystals gives a Hall voltage polarity characteristic of electrons. At 82±2°K the mobility is 250±50 cm²/volt sec, and at 200°K the mobility is of the order of forty. The experimental error is due to noise in the conducting plates, F center bleaching, temperature variations, or possibly crystal imperfections. By violently quenching the crystal, its mobility can be reduced to as low as 150 cm²/volt sec at 82°K. These observations are in reasonable agreement with both the theory of Fröhlich and Mott[6] and the more recent calculation of Low and Pines.[7] Work is under way to improve and extend these measurements.

The help of many people in this work is gratefully acknowledged; the author wishes particularly to thank Dr. R. J. Maurer for his frequent suggestions and Dr. C. P. Slichter and his associates for the use of their magnet.

* Partially supported by U. S. Office of Naval Research.
† U. S. Atomic Energy Commission predoctoral Fellow.
[1] R. W. Pohl, Proc. Phys. Soc. (London) **49** (Extra part), 3 (1937).
[2] J. Evans, Phys. Rev. **57**, 47 (1940).
[3] C. C. Klick and R. J. Maurer, Phys. Rev. **81**, 124 (1951).
[4] W. Shockley, J. Appl. Phys. **9**, 635 (1938).
[5] A. Redfield, paper presented at the 1953 North Carolina meeting, Bull. Am. Phys. Soc. **28**, No. 2, 46 (1953).
[6] Fröhlich, Pelzer, and Zienau, Phil. Mag. **41**, 221 (1950).
[7] F. E. Low and D. Pines, Phys. Rev. (to be published).

Some Electrical Properties of Strontium Titanate

ARTHUR LINZ, JR.
Research Laboratory, Titanium Division, National Lead Company, South Amboy, New Jersey
(Received June 8, 1953)

SOME properties of very pure synthetic strontium titanate single crystals grown at this laboratory by the flame fusion technique[1] have been investigated by electrical methods. It was felt that these preliminary measurements would be of interest due to the high dielectric constant of this material and its close relationship to the ferroelectric barium titanate. Strontium titanate, $SrTiO_3$, like barium titanate above its Curie point, is a cubic crystal of the perovskite type.

The dc conductivity as a function of temperature is shown in Fig. 1. These measurements were made at a field strength of 2500 volts per cm with fired-on silver paste electrodes. If the conductivity is represented by the Boltzmann equation $\sigma=\sigma_0 \exp(-\epsilon/kT)$, then for $kT\ll\epsilon$ the activation energy is $E=2\epsilon=0.68$ ev. This is very close to the value found by Cronemeyer[2] for slightly reduced rutile crystals, suggesting a conductivity mechanism similar to that in rutile involving electrons trapped at oxygen vacancies. Preliminary optical density measurements on a clear single crystal plate of strontium titanate have indicated a corresponding absorption peak in the neighborhood of 2μ (0.63 ev). The energy necessary to raise an electron from the valence band to the conduction band can be deduced from the position of the ultraviolet absorption edge at 395 mμ, corresponding to an intrinsic activation energy of 3.15 ev. This assumption will be checked by high-temperature conductivity and photoconductivity measurements.

The dielectric constant ϵ' and the loss tangent tanδ are shown in Fig. 2 as functions of temperature at various frequencies. On the scale shown, there is no substantial difference in the dielectric constant at the three frequencies. From 125°C to −50°C the

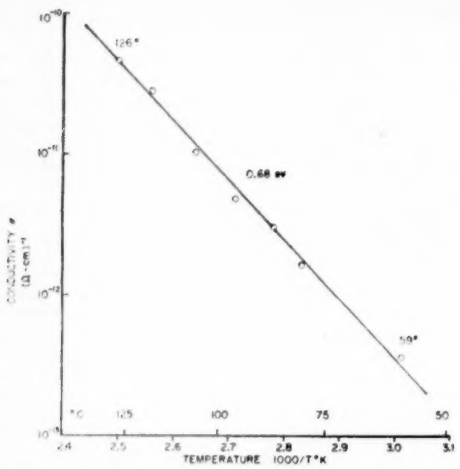

FIG. 1. The dc conductivity as a function of temperature.

dielectric constant can be fitted by a Curie-Weiss law curve, $\epsilon' = C/(T-\theta)$, with $C = 8.5 \times 10^4$, $\theta = 17°$K. However, at $-160°$C, this curve gives a value of $\epsilon' = 880$, compared to a measured value of 815, thus indicating, in agreement with Hulm's results on

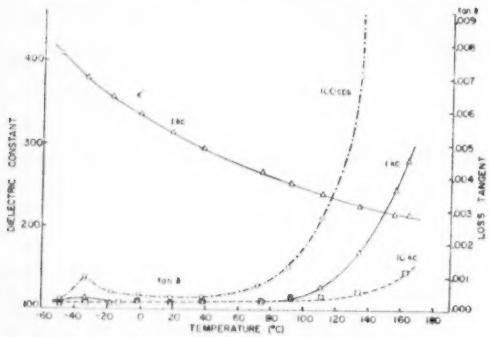

FIG. 2. The dielectric constant ϵ' and the loss tangent tanδ as functions of temperature at various frequencies.

sintered strontium titanate,[2] that a Curie-Weiss law curve based on high-temperature data should not be used to predict a ferroelectric Curie point for this material. It should be noted that the value of the dielectric constant for a single crystal was found

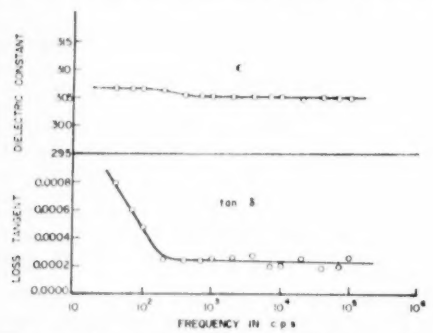

FIG. 3. The dielectric constant and loss tangent as functions of frequency at 25°C.

to be twenty percent higher than values found by Hulm and others[4] for sintered specimens, although the latter values were corrected for porosity. The increase in loss tangent with temperature is presumably the result of the increase in conductivity of the crystal, but the cause of the peak at $-30°$C is not known.

The dielectric constant and loss tangent as functions of frequency at 25°C are shown in Fig. 3. The loss tangent appears to consist of a polarization loss, tan $\delta = 0.00025$, substantially independent of frequency over the range studied, and a conductivity loss approximately inversely proportional to the frequency. The situation is complicated by space-charge effects in the crystal and at the boundaries where diffused silver ions from the electrodes form low-lying electron traps. A more detailed investigation is in progress.

[1] L. Merker and L. E. Lynd, U. S. Patent 2,628,156 (February 10, 1953).
[2] D. C. Cronemeyer, Phys. Rev. **87**, 876 (1952).
[3] J. K. Hulm, Proc. Phys. Soc. (London) **A63**, 1184 (1950).
[4] A. von Hippel *et al.*, Lab. Ins. Res., National Defense Research Committee Report No. 300, 1944 (unpublished).

Evaporation of Copper from Germanium

GEORGE FINN
Sylvania Electric Products, Byaside, New York
(Received June 5, 1953)

BECAUSE of the interest in "thermal" acceptors introduced into germanium by heat treatment[1,2] and because of the fact that these acceptors may be due, at least in part, to copper as an impurity,[3,4] the following results are believed to be significant. It has been found that if germanium is heat treated in a vacuum, the number of acceptors introduced at a given temperature and a given quench time is less than that corresponding to heat treatment in an atmosphere of helium (see Fig. 1).

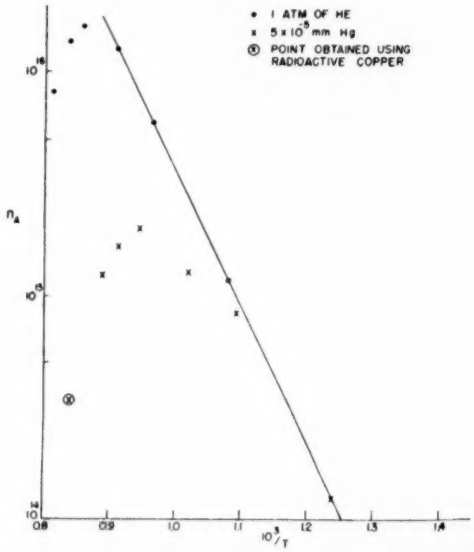

FIG. 1. Number of acceptors introduced as a function of the reciprocal of the heat-treatment temperature for two residual gas pressures.

In addition, radioactive copper was deposited on the surface of several samples of germanium by dipping the germanium in a solution of radioactive copper nitrate. This copper was then diffused into the germanium to within one percent of equilibrium by heating in one atmosphere of helium at 918°C. One of these samples was then etched to remove any excess copper from the

surface and heated for three hours at 918°C at a residual gas pressure of 5×10^{-6} mm mercury. It was found that during the vacuum heating radioactive copper was collected on a cold finger in the vacuum system indicating that copper had evaporated from the germanium. From the change in sample surface count before and after the vacuum heating and from the amount of copper collected on the cold finger, it is estimated that at least 96 percent of the copper was evaporated from the germanium during the vacuum heating. Hall measurements made on the sample show that after the initial heat treatment in helium, the density of added acceptors was $n_A=1.43\times10^{16}/cm^3$, and after the vacuum heat treatment the remaining density of acceptors was $n_A=3.4\times10^{14}/cm^3$.

The evaporation of copper during the vacuum heating corresponds within experimental error to the loss of acceptors as given by Hall measurements.

The author wishes to thank Dr. George Morrison for the work with radioactive tracers and Dr. S. Mayburg and Dr. E. N. Clarke for much helpful discussion.

[1] H. C. Theuerer and J. H. Scaff, J. Metals **191**, 59 (1951).
[2] Fuller, Theuerer, and Van Roosbroeck, Phys. Rev. **85**, 678 (1952).
[3] C. S. Fuller and J. D. Struthers, Phys. Rev. **87**, 526 (1952).
[4] W. P. Slichter and E. D. Kolb, Phys. Rev. **87**, 527 (1952).

Diode Characteristic of a Hollow Cathode*

M. L. Babcock, D. F. Holshouser, and H. Von Foerster
University of Illinois, Urbana, Illinois
(Received June 8, 1953)

IF a current is drawn from an aperture of a hollow cathode, the inside surface of which is coated with Ba–Sr oxide emitting material, a diode characteristic is obtained which does not resemble the typical Child-Langmuir characteristic.

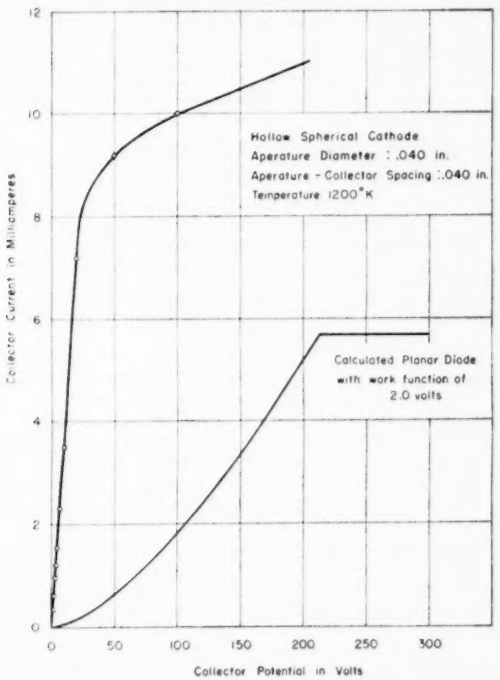

FIG. 1. Comparison of the measured current-voltage characteristic obtained through the aperture of a hollow cathode with the computed characteristic of a planar diode with a cathode area equal to the aperture area.

In Fig. 1 the diode characteristic is plotted for a hollow cathode arrangement in which the current from an aperture of one millimeter diameter is collected by an anode spaced one millimeter distant. This is compared with the curve one would expect from an equivalent planar diode, i.e., one with the same emitting material, with a cathode area equal to the aperture area, and with the same cathode-anode spacing.

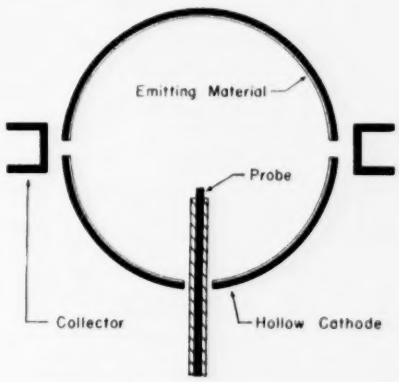

FIG. 2. Schematic diagram of the experimental arrangement used for the study of the characteristic of a spherical hollow cathode.

Three typical features of this characteristic are of particular interest:

(1) The rapid increase of current even if small positive potentials are applied to the collector electrode.

(2) Over the entire potential range higher currents were obtained than are to be expected from the equivalent planar diode.

(3) At potentials above which the planar diode exhibits saturation, the current in this structure continues to increase at a considerable rate.

Figure 2 shows schematically the experimental arrangement being used in these studies. The spherical hollow cathode is heated uniformly and indirectly by a larger concentric heater sphere (not shown in Fig. 2). For purposes of comparison two apertures with their corresponding collector electrodes are provided. Since particular care was taken to avoid spurious effects of any kind, the collector electrodes are water-cooled to eliminate the possibility of thermionic currents in the inverse direction. The inverse impedance under operating conditions is found to be very large indeed; it is of the order of 3×10^8 ohms.

A probe which can be inserted or withdrawn during operation allows the study of the conditions inside of the sphere.

These experiments are a phase of a general study of electron gases in equilibrium[1,2] and will be reported in greater detail in a later article.

* This study is sponsored by the U. S. Office of Naval Research.
[1] H. Von Foerster and H. S. Wu, "Thermodynamics and Statistics of the Electron Gas," Technical Report No. 3-1 and 3-2, ONR contract (unpublished).
[2] D. F. Holshouser, "Stable Spherical Electron Cloud," Progress Report No. 13, ONR contract (unpublished).

A Tentative Theory of Metallic Whisker Growth*

J. D. Eshelby
University of Illinois, Urbana, Illinois
(Received June 4, 1953)

PEACH'S[1] very pretty explanation of the formation of metallic whiskers[2] seems to be ruled out by the observation[3] that they grow at the root. The growth seems to be influenced[4] by the atmosphere over the surface. The energy required to form a

fresh surface may be more than repaid if it is attacked avidly enough by the atmosphere; there is then an effective negative surface tension $-\gamma$. We might have perhaps $\gamma b^2 \sim 1$ ev (b = lattice constant). The ratio γ/μ (μ = shear modulus) would then be about 1A. The surface tension forces on a small hump on the surface [Fig. 1(a)] obviously have the right character (a central pull

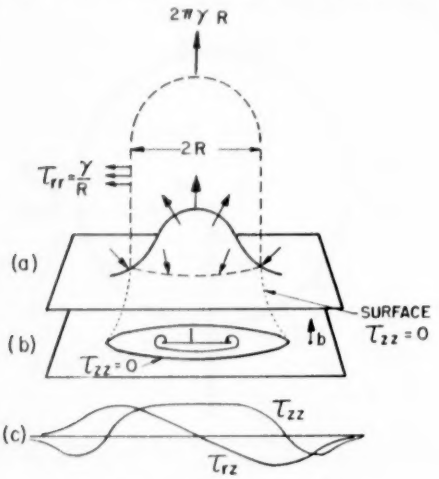

FIG. 1. Model for whisker growth.

surrounded by a restraining pressure) to "wire-draw" it into a whisker according to intuitive ideas of plastic flow. For the observed whisker size ($R \sim 10^{-4}$ cm) the stress of order γ/R in and just below the hump might exceed the actual yield stress, though not the theoretical yield stress ($\sim\mu/20$). However, on this small scale one must consider in detail how flow is catalyzed by dislocation.

The model of Fig. 1 lends itself to rough calculations. A Frank-Read source of length l and vertical Burgers vector b lies in a horizontal plane (b) at a depth of order l below the hump. The stress τ_{zz} [Fig. 1 (c)] makes the source emit a dislocation loop by "climb." The loop expands in the plane (b) until it reaches a radius where $\tau_{zz}=0$. Here the stress τ_{rz} assisted by image forces makes the loop glide vertically, so adding one atomic layer to the base of the hump. When by repetition of this a reasonable whisker has grown, τ_{zz} will be $2\gamma/R$ in the whisker and about γ/R at the source. To operate the source, τ_{zz} must be at least $\mu b/l$. With $\gamma/\mu \sim 1\text{A} \sim b$, this will be so if $R \sim l$. The stress at the source ultimately falls off both for $R \gg l$ and $R \ll l$ if the source depth stays constant. The whisker radius is thus tied to the length of a Frank-Read source, which is usually supposed to be about one micron. The surface $\tau_{zz}=0$ forms a "stress funnel" which guides each loop more or less unerringly to break surface at the base of the whisker, and so keeps its diameter constant. If the motion of the source is not to be stopped by the back-pressure of the vacancies it emits, there must be suitable sinks for them. It can be shown that surface tension changes the volume of a body of any shape with compressibility χ by $\frac{2}{3}\gamma\chi$ times its surface area. For a macroscopic specimen the corresponding mean pressure, $\frac{2}{3}\gamma\chi$ (surface/volume) would fall far short of the value required to make Frank-Read sources in the interior act as the necessary sinks. However, it should not be hard to find them at the surface. Frank[8] has shown that even with positive surface tension it may be energetically an advantage for a dislocation reaching the surface to develop a hollow core. Or again, if we had a depression instead of a hump in Fig. 1 the source would work in reverse, absorbing vacancies and deepening the depression.

We may use a calculation of Mott's[6] to find the rate of growth. He showed that, if a cube has normal stresses P on one pair of opposite faces and $-P$ on another pair, a volume $V \sim NbD(Pb^3/kT)$ of material is transferred from one pair of faces to the other in unit time if there are N points on dislocations which can absorb or emit vacancies and the coefficient of self-diffusion is D. Our case is analogous. P is γ/R times a factor κ depending on the detailed stress-distribution, including a possible stress concentration if successive loops help one another. N is about l/b, the number of lattice sites per loop, times the fraction β (perhaps $\ll 1$) of them which can emit or absorb vacancies times n, the number of loops in transit between source and surface at one time. The rate of change of the whisker length h will thus be

$$\dot{h} = V/\pi R^2 \sim \kappa\beta n D(b/l^2)(\gamma b^3/kT).$$

With the value of D for tin at room temperature,[7] we can get a growth rate of a millimeter or a centimeter per year with $\kappa\beta n \sim 100$ or 1000. The small number of accidental coincidences of sources and suitable surface irregularities may be enough to account for the number of whiskers per unit area. If not, we might suppose that the sources build their own humps by operating initially without stress as the result of a subsaturation of vacancies due to a change of temperature.

Many variations of this model are possible. The transfer of loops to the surface might occur by the formation and joining up of secondary loops in a vertical plane as in "prismatic punching,"[8] where the stress distribution is similar. The whiskers might then be prismatic. Professor Seitz (to whom the writer is indebted for helpful discussions) has suggested a mechanism involving a spiral prismatic dislocation,[9] which is the internal counterpart of spiral growth on the surface and which leaves a screw dislocation along the axis of the whisker.

* Work done under U. S. Office of Naval Research contract.
[1] Milton O. Peach, J. Appl. Phys. **23**, 1401 (1952).
[2] C. Herring and J. K. Galt, Phys. Rev. **85**, 1060 (1952).
[3] S. Eloise Koonce and S. M. Arnold, J. Appl. Phys. **24**, 365 (1953).
[4] Compton, Mendizza, and Arnold, Corrosion **7**, 327 (1951).
[5] F. C. Frank, Acta Cryst. **4**, 497 (1951).
[6] N. F. Mott, *IXe Conseil de Physique (Solvay), Rapports* (Stoops, Brussels, 1952), p. 515; Proc. Phys. Soc. (London) **B64**, 379 (1951), §7.
[7] P. J. Fensham, Australian J. Sci. Research **A3**, 91 (1950).
[8] Frederick Seitz, Phys. Rev. **79**, 723 (1950). Here *ABFE* corresponds to our plane (b) and *DCHG* is the root of the whiskers.
[9] Frederick Seitz, Phys. Rev. **79**, 1003 (1950).

Oxygen-Induced Surface Conductivity on Germanium

EDWARD N. CLARKE
Sylvania Electric Products, Bayside, New York
(Received June 18, 1953)

MOTT has suggested[1] that oxygen may introduce acceptor energy levels on a germanium surface. The present note reports mainly on gas adsorption and resulting surface electrical conductance at a temperature of 197°K.

A very thin high-resistivity (40 ohm-cm at room temperature) n-type single crystal rectangular bridge of germanium was assembled for electrical measurements in a high vacuum system. The voltage probes are germanium and an integral part of the single crystal and are separated by 0.5 cm. The crystal width is 0.2 cm and the thickness about 0.004 cm, made purposely thin to amplify any surface changes. The surface was prepared by etching with an etchant of HF, HNO_3, and H_2O, and then rinsing with H_2O.

The residual gas pressure was reduced to about 5×10^{-8} mm Hg after pumping for 20 hours, and after heating the experimental tube containing the Ge to about 450°C for one half-hour. This treatment decreased the germanium conductance by a factor of two, representing a decrease in conductance of 4×10^{-6} mho. If one assumes a surface carrier mobility of 1000 cm²/volt sec this represents a decrease of 4×10^{10} carriers per cm² of surface. A different carrier concentration will correspond to a different mobility. The germanium was heated to near its melting point for a short period of time (seconds) and then quenched rapidly by radiation

to the surroundings at room temperature. This heating and quenching in a high vacuum may have produced a surface cleaner than the original etched surface, but also has changed the bulk characteristics. As described below, the germanium appears now to be more sensitive to surrounding gases than was the original crystal with etched surface.

After the above heating and quenching, gases at several different pressures were admitted slowly through the vacuum system. Figure 1 shows a typical plot of germanium conductance at 197°K varying as the residual gas pressure varies from 10^{-7} mm Hg to 10^{-3} mm Hg (by shutting off the diffusion pump). Dry argon admitted to the germanium at 0.3 mm Hg for one minute has little effect upon the conductance but dry oxygen at 0.3 mm Hg for one minute increases the conductance by a factor of ten. The largest surface conductance at 197°K obtained during similar observations is 8×10^{-4} mho, representing about 10^{13} carriers per

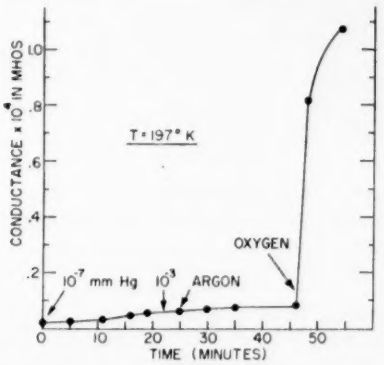

FIG. 1. Dependence of Ge conductance upon surrounding atmosphere. The diffusion pump was shut off at time $t=0$; argon was admitted at $t=25$ min and removed after one min; oxygen was admitted at $t=47$ min and removed after one min.

cm² of surface (if a mobility of 1000 cm²/volt sec is assumed). Oxygen is also adsorbed at room temperature. Initially, it appeared possible to remove most of the absorbed gas (as measured by electrical conductance) by simply heating the experimental tube containing the Ge in a high vacuum at about 450°C for one half-hour. However, Fig. 2 shows that as the number of cycles increased (each cycle corresponding to a maximum conductance with gas adsorption and then a minimum conductance after heating in a high vacuum), the minimum conductance became larger. By the twelfth cycle, heating the tube at 450°C had a much smaller effect in reducing the surface conductance. This might be

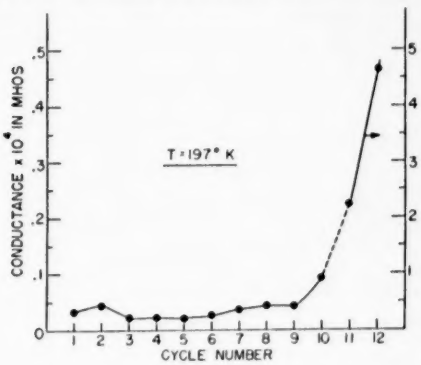

FIG. 2. Conductance of Ge after heating in high vacuum. Each cycle corresponds to a maximum and minimum conductance. Cycles 11 and 12 correspond to right-hand ordinate.

described in terms of a thin layer (oxide) being built up on the surface. It is not unreasonable to assume that oxygen may introduce surface acceptor energy levels resulting in hole conductivity.

Further work will include measurements to determine surface carrier type and surface mobility of carriers.

[1] N. F. Mott, Proc. Inst. Elect. Engrs. (London) **96**, 253 (1949).

Thermally Induced Acceptors in Single Crystal Germanium

R. A. LOGAN
Bell Telephone Laboratories, Murray Hill, New Jersey
(Received June 4, 1953)

WHEN germanium is heated above 600°C and then cooled, it has been shown[1] that the acceptor density increases markedly. This effect is reversible in that prolonged reheating at 475°C "anneals" out these acceptors. More recently, simlar acceptors have been produced in experiments[2] where the cooling time has varied from a very rapid quench to a time of the order of several minutes.

It has been shown[3] that copper as an impurity in germanium has the same activation energy, diffusivity, solid solubility, and "annealing" property as these acceptors. Since no precautions were taken to avoid copper contamination, and since very small concentrations of copper will produce these acceptors, this evidence led to the conclusion[2] that in all of the above experiments copper produced the observed acceptor centers. A method has been developed by which it is possible to heat germanium to high temperature for extended periods of time and avoid copper-like contamination. This makes it possible to examine more closely the phenomena associated with quenching germanium from high temperature.

In these experiments, small samples were cut from single crystal n-type germanium which contained about 6×10^{13} donors per cc. The specimens were cleaned[4] by acid etching followed by a rinse in twice-distilled water. They were then soaked in a strong aqueous KCN solution. The cyanide forms soluble complexes with copper, as well as other metallic ions, which are then removed by rinsing the specimens in twice-distilled water.

To study the effect of rapid quenching from high temperatures, a sample was placed on a carbon boat furnace in a quartz tube and heated in a hydrogen atmosphere by rf induction. A castor oil bath was located about one inch below the boat. The sample could be dropped from the boat into the oil bath in about 0.1 second. If one of the samples was heated at an elevated temperature for one minute and allowed to cool slowly to room temperature by simply turning off the rf heater, no detectable change in resistivity occurred. Resistivity was measured at −78°C, where the measurement was sensitive to impurity concentrations as low as a few times 10^{12} per cc or about one per 10 billion germanium atoms. In this experiment, the sample cooled to 500°C in about 15 seconds and reached room temperature in a few minutes (hereafter this will be referred to as the regular cooling cycle). However, if the sample was quenched in the oil bath, a change in resistivity resulted and acceptor centers were found uniformly throughout the sample. The effects of heating at different temperatures before quenching are shown in Fig. 1.

If the quenched samples were recleaned, as described above, and reheated to a high temperature followed by the regular cooling cycle, they returned to nearly their original resistivity.

It has been proposed[5] that lattice defects such as vacancies and interstitial germanium atoms may act as acceptors in germanium. If the acceptor centers produced by quenching are thermally produced lattice defects,[6] then to a close approximation the density of acceptor centers n_Q present when the sample is in thermal equilibrium at temperature T_Q is given by

$$n_Q = n_L e^{-E/kT_Q},$$

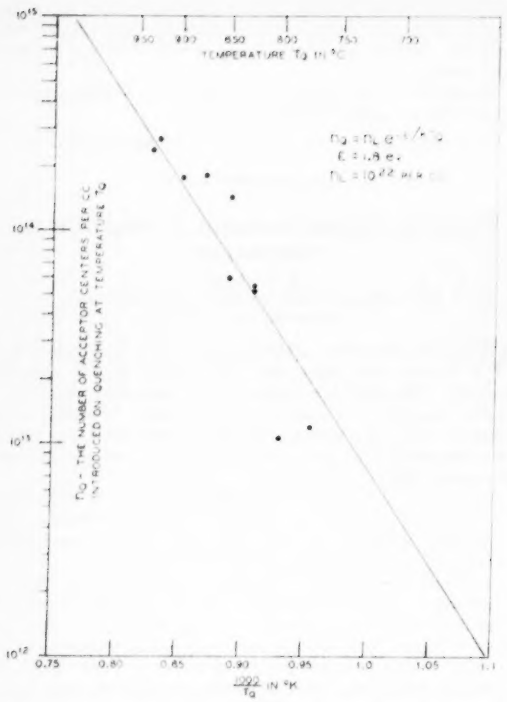

FIG. 1. Temperature dependence of acceptor concentration in quenched germanium samples.

where E is the activation energy for the production of an acceptor center and n_L is the maximum density of lattice sites that could be occupied by acceptors of this type. From theory,[7] n_L is approximately 10^{22} per cc for germanium. If the equilibrium state of the sample at temperature T_Q is essentially "frozen" by the rapid quench, the measured increase in acceptor center density should be very nearly equal to n_Q. In the limit of $T \to \infty$, the curve is made to pass through $n_Q = n_L$ as required theoretically. The activation energy is found to be 1.8 ev per center, which may be compared to the activation energy of 1.2 ev per center for the introduction of copper into the germanium lattice.[3]

If the thermally produced acceptor centers are due to some unknown chemical impurity, then Fig. 1 can be regarded as a plot of the temperature dependence of the solid solubility of this impurity in germanium. There are two ways in which impurities could enter a quenched sample. They could diffuse into the germanium during the quench, although no impurity whose diffusion in germanium has thus far been studied could diffuse uniformly from the surface in this short time. A more likely possibility is that an impurity has diffused into the germanium during the heating time, and that the rapid quench has essentially "frozen" this dispersed impurity which would otherwise "anneal" in the regular cooling cycle. This "annealing" might be similar to (though much faster than) that for copper in germanium. There is, as yet, insufficient evidence to distinguish lattice defects from chemical impurities.

Although the surface treatments described above permit the heating of a test sample to high temperature without resistivity change, there was always a decrease in body lifetime. For example, when a test sample with an original lifetime of 100μsec was heated for one minute at about 825°C, followed by the regular cooling cycle, the average body lifetime was reduced to 19μsec. It is known that recombination centers are formed by some chemical impurities[8] and by lattice imperfections.[9] In the heat treatments performed in these experiments, the cause of the recombination centers has not been ascertained. The preliminary experiments indicate that recombination centers diffuse in rapidly from the surface in a manner similar to copper. This suggests that, in this case, recombination centers may be a chemical impurity which has a marked effect on lifetime while making only a small contribution to the resistivity.

I would like to express appreciation to W. Shockley, M. Sparks, and G. C. Dacey for encouragement in these experiments.

[1] H. C. Theuerer and J. H. Scaff, Trans. Am. Inst. Mining Met. Engrs. **191**, 59 (1951); Fuller, Theuerer, and van Roosbroeck, Phys. Rev. **85**, 678 (1952).
[2] W. E. Taylor, Phys. Rev. **86**, 642 (1952); C. Goldberg, Phys. Rev. **88**, 920 (1952); L. Esaki, Phys. Rev. **89**, 1026 (1953).
[3] C. S. Fuller and J. D. Struthers, Phys. Rev. **87**, 526 (1952); W. P. Slichter and E. D. Kolb, Phys. Rev. **87**, 527 (1952).
[4] This cleaning process was developed in collaboration with M. Sparks.
[5] Lark-Horovitz, Bleuler, Davis, and Tendam, Phys. Rev. **73**, 1256 (1948).
[6] Such defects have been observed in gold by J. W. Kauffman and J. S. Koehler, Phys. Rev. **88**, 194 (1952).
[7] N. F. Mott and R. W. Gurney, *Electron Processes in Ionic Crystals* (Oxford University Press, London, 1940), Chap. II.
[8] I am indebted to J. A. Burton for communication of these results prior to publication. They will be presented at the joint Am. Chem. Soc.-Am. Phys. Soc. Symposium on Impurity Phenomena on June 16, 1953 (to be published in J. Phys. Chem.).
[9] G. L. Pearson (private communication); also, W. Shockley, *Electrons and Holes in Semiconductors* (D. Van Nostrand Company, Inc., New York, 1950), p. 347.

Examples of Multiple Pion Production in n–p Collisions Observed at the Cosmotron*

W. B. FOWLER, R. P. SHUTT, A. M. THORNDIKE, AND W. L. WHITTEMORE
Brookhaven National Laboratory, Upton, New York
(Received June 11, 1953)

ABOUT 100 events attributed to π-meson production by neutrons in hydrogen have been photographed under conditions described in a previous communication.[1] Neutrons produced in a carbon target by the 2.2-Bev proton beam in the Cosmotron passed through appropriate collimators into a hydrogen-filled diffusion cloud chamber located in a field of 11 000 gauss. Two examples of creation of pairs of pions in the gas are shown in Figs. 1 and 2. Data on these events are given in Table I.

Track c in event A can be attributed to a proton from its momentum and estimated ionization density which are given in Table I. Tracks a and b, by the same method, must have been produced by particles much lighter than protons, most probably pions. (Masses of a and b are <400 and <240 electron masses, respectively.) The 6 angles fixing the directions of the 3 tracks with respect to the direction of travel of the incident neutrons were also determined by reprojecting the stereoscopic photographs in space. The resultant p_r of the transverse components of the three momenta is given in Table I. The fact that p_r is not zero also indicates that at least one neutral particle must be involved in addition to the charged ones, which is assumed to be a neutron. The two pions are then produced in the reaction $n+p=n+p+\pi^+ +\pi^-$.

TABLE I. Data on pion-pair events.

		Event A	Event B
Track a (negative charge)	Momentum (Mev/c)	474 ± 50	980 ± 70
	Estimated Ionization density	1 ×minimum	1 ×minimum
Track b (positive charge)	Momentum (Mev/c)	286 ± 20	550 ± 40
	Estimated Ionization density	1 ×minimum	1 ×minimum
Track c (positive charge)	Momentum (Mev/c)	835 ± 50	1260 ± 200
	Estimated Ionization density	1.5 to 2 ×minimum	2 to 3 ×minimum
Resultant transverse momentum, p_r (Mev/c)		268 ± 20	50 ± 60
Sum of forward momenta, p_z (Mev/c)		1260	2770
Sum of energies of charged particles (a,b,c), E_m (Mev)		1140	1950
Energy of incident neutron, E (Mev)		$2060\ {}^{+140}_{-250}$	1980 ± 250

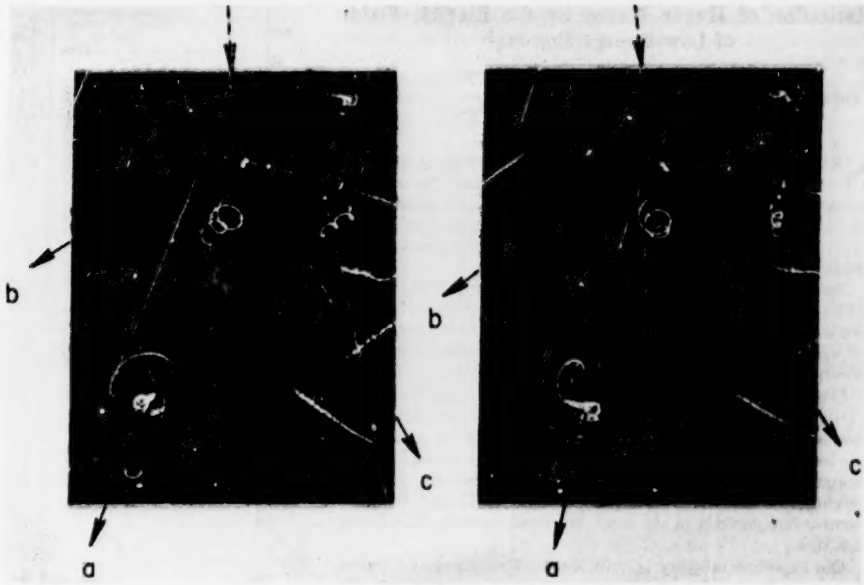

FIG. 1. Stereoscopic photograph of event *A*. Neutron enters in direction of broken arrow. Track *a* is identified as a π^-, track *b* as a π^+, track *c* as a proton. Horizontal black line is sweeping field electrode. Tracks pass underneath electrode.

From the sum p_s of the forward components of the momenta, the sum of the energies E_m of the charged particles (including all kinetic energies and the pion rest energies), and p_r one can calculate the energy E of the incident neutron, the indicated errors having been determined from the uncertainties of the momentum and angle measurements.

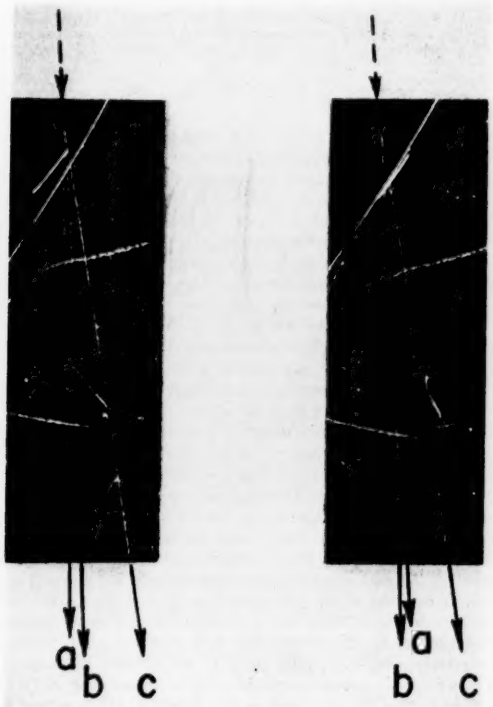

FIG. 2. Stereoscopic photograph of event *B*. Neutron enters in direction of broken arrow. Track *a* is a π^-, track *b* a π^+, track *c* a deuteron.

The energy available for meson creation in the center-of-mass system of incoming neutron and proton is 830 Mev. One can compute that the total energies of π^+ and π^- in the center-of-mass system are 320 and 300 Mev, respectively. Thus only 210 Mev remain for the nucleons in the c.m. system. This indicates the existence of very highly excited states of the nucleons after the collision. There is no obvious angular correlation between the outgoing nucleons and mesons in the c.m. system.

Track *c* in event *B* (Fig. 2) is of interest because of its large momentum and high estimated ionization density which are consistent only with a deuteron track. Track *b* must again be a particle much lighter than a proton, presumably a π^+ (mass <450 electron masses). We interpret this event as following the reaction $n+p=d+\pi^++\pi^-$. As required for this reaction, p_r is zero within the given errors which are mostly caused by uncertainties in the rather small angles involved here. p_s must here be equal to the momentum of the incident neutron. The energy E of the incident neutron calculated from p_s must be equal to E_m. p_s and E_m are indeed quite consistent with each other. Of the available c.m. energy of 810 Mev, the mesons have received about 90 percent. The deuteron passes almost straight backward in the c.m. system while both mesons pass forward.

Of 24 such 3-prong events so far analyzed we have identified the following π-meson production events: 10 definitely $(\pi^++\pi^-)$, 5 either $(\pi^++\pi^-)$ or $(\pi^0+\pi^-)$, 1 definitely $(\pi^0+\pi^-)$ (from momentum balance), 2 definitely single π^-, 4 possibly single π^-, and 2 which could not be determined. Thus at least $\frac{2}{3}$ of these events appear to be due to multiple meson production. The c.m. energy in all of these events was large enough to produce at least 4 mesons. To date we have not observed a single 5-prong event attributable to production of 3 charged mesons by a process such as $n+p=p+p+\pi^++\pi^-+\pi^-$. The possibility of a low meson production multiplicity in nucleon-nucleon collisions, mostly at considerably higher energies, has been indicated by a number of cosmic-ray observers.[2]

* Work performed under the auspices of the U. S. Atomic Energy Commission.

[1] Fowler, Shutt, Thorndike, and Whittemore, Phys. Rev. **90**, 1126 (1953).

[2] See, for example, M. L. Vidale and M. Schein, Phys. Rev. **84**, 593 (1951); G. W. Rollosson, Phys. Rev. **87**, 71 (1952); W. Bosley and H. Muirhead, Phil. Mag. **43**, 783 (1952); A. B. Weaver, Phys. Rev. **90**, 86 (1953); McCusker, Porter, and Wilson, Phys. Rev. **91**, 384 (1953).

Excitation of Heavy Nuclei by the Electric Field of Low-Energy Protons*

CLYDE L. MCCLELLAND AND CLARK GOODMAN
Department of Physics and Laboratory for Nuclear Science, Massachusetts Institute of Technology, Cambridge, Massachusetts
(Received June 16, 1953)

SEVERAL theoretical predictions[1] have been made that heavy charged particles may excite nuclei even though the collision energy is much too small to allow appreciable wave penetration of the Coulomb barrier. Nuclear forces do not take part in this type of inelastic scattering—the excitation of the nucleus results solely from the interaction of the Coulomb fields.

Barnes and Aradine[2] observed the reaction $In^{115}(p,p')In^{115*}$ (4.1 hr) with protons of energy 5.8 Mev and estimated a cross section of about 10^{-29} cm^2. However, there is some question as to whether this reaction involved barrier penetration rather than purely Coulomb excitation.

During the summer of 1952 we observed what appeared to be excitation of a low-lying level in tantalum[3] using protons of such low energy (1.4 to 1.8 Mev) that formation of the compound nucleus is entirely negligible. We observed the prompt monoenergetic gamma rays rather than induced radioactivity. More recently we have examined[4] Ta, Pt, Au, Hg, Tl, and Bi using bombarding energies in the range of proton energies, $E_p=1.4$ to 2.6 Mev.

Our experimental setup is quite simple. Monoenergetic protons from the Rockefeller electrostatic generator strike a metallic target (thick to protons) adjacent to which is the crystal of a NaI(Tl) spectrometer using an RCA 5819 and single channel discriminator. Pulse-height distribution curves are obtained in the usual manner. Co^{57}, Na^{22}, Cs^{137}, Hg^{203}, and Pb (K x-rays) were used for energy calibration.

Figure 1 summarizes the results for three different tantalum targets and a single gold target at proton energies of 1.42 and 1.48 Mev. Each Ta target shows a strong photopeak at 138±5 kev, well resolved from the K x-rays to the left (not plotted). To determine whether this gamma ray was due to impurities in the target or to reactions with scattered protons in the target assembly rather than to the 136-kev first excited state[5] in $_{73}Ta^{181}$, the following steps were taken:

(1) four targets of Ta from two sources were tested;

(2) the targets were cleaned successively with steel wool, emery, acid, water, and alcohol;

(3) iron, vanadium, and carbon targets were tested, since these are the most common bulk impurities in commercial Ta;

(4) an Au target was tested in a similar manner.

The pulse-height distributions from the Fe, V, C, and Au (see Fig. 1) targets were such that these substances could not account for the 138-kev peak in Ta. Our spectrometer would not reveal the 77-kev gammas from $_{79}Au^{197}$ (assuming they were produced) in the presence of the K x-rays. The possibility that the 138-kev line is the result of the pile-up of pulses in the NaI(Tl) crystal is also eliminated by the absence of a similar line in Au at about twice the K x-ray energy.

Another possibility suggested by Professor H. Bethe[4] is that the 138-kev peak is the result of a superposition of K x-rays from the double ionization of the K shell in Ta. We have measured the absorption of the 138-kev line relative to the K x-rays in Pb (~20 mils) and find that the x-rays are attenuated much more markedly than the 138-kev peak. Hence, the 138-kev line does not appear to be composed of lower energy quanta. What is more significant, however, is that the shape of the 138-kev peak was retained after attenuation in the Pb—the effect to be expected for a line spectrum.

The tentative conclusion is that these are $M1$ gammas from the transition $g_{7/2}$, first excited state, to $g_{7/2}$ ground state of $_{73}Ta^{181}$ induced by Coulombian excitation of the nucleus. The basis for discarding barrier penetration at the proton energies used is that the cross section for formation of the compound nucleus alone is

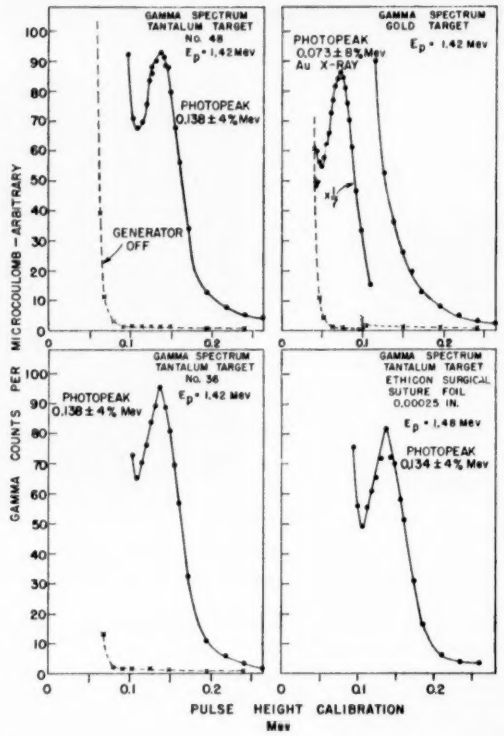

FIG. 1. Pulse-height spectra for Ta and Au. The pulse height has been calibrated with 511-kev annihilation radiation from Na^{22}, and the energy of the gamma ray may be read directly from the position of its photopeak.

only about 10^{-30} cm^2 at $E_p=1.5$ Mev. It would be even smaller for $\sigma(p,p')$.

Because the yield of gammas has been measured only for thick Ta targets, only rough estimates can be made of the observed cross section. We calculate this to be about 0.4 millibarn and essentially constant for $E_p=1.4$ to 1.6 Mev. However, assuming 80 percent internal conversion of the 138-kev gamma, the cross section would be about 8 millibarns.

Naturally we were reluctant to accept the above conclusions without additional experimental evidence. Dr. de-Shalit suggested[6] that we bombard platinum since there are two low-lying levels:[5] a $p_{1/2}$ at 97 kev and an $f_{5/2}$ at 126 kev above the $p_{1/2}$ ground state in $_{78}Pt^{195}$. We have done this, with the results shown in Fig. 2. Clearly there is a peak at about 127 kev for $E_p=1.64$, 1.78, and 2.0 Mev. There is also evidence at these energies, and at 1.51 Mev as well, for some radiation between 90 and 100 kev, since otherwise the curve should dip much more in this region (see corresponding section of Au data in Fig. 1). We, therefore, tentatively conclude that nuclear gammas from $_{78}Pt^{195}$ have been activated by the purely Coulombian process. We are unable at this time to quote a cross section for Pt, but it certainly appears to be substantially less than for Ta for the same proton energy.

The results with Au, Hg, Tl, and Bi are more preliminary than those for Ta and Pt. The first measurements with Au (Fig. 1) show no evidence of the 191-kev radiation[5] from the second to the first excited state. More recent measurements with an improved resolution crystal (Harshaw) show two small peaks which we very tentatively would attribute to 250- and 450-kev gammas. The improved resolution also revealed another higher peak in Ta (not evident in Fig. 1) which increased in height as the proton energy was increased. We would tentatively assign this an energy of about 500 kev. Conceivably this radiation may be from the next

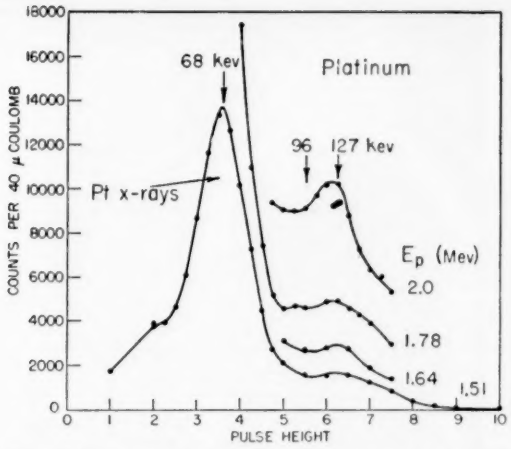

FIG. 2. Pulse-height spectrum of Pt at four proton energies E_p. A small adjustment has been made in the horizontal position of the data taken at $E_p = 2.0$ Mev in order to correct for electronic drift in the spectrometer.

higher level in $_{73}Ta^{181}$ decaying to the ground state. This would imply the presence of 345-kev radiation as well, and some evidence for this has been observed.

After studying the Au radiation, we made an amalgam and examined the increment due to Hg. There is clearly a reproducible break in the curve at an energy of about 200 kev which increases with proton energy. At least two isotopes of Hg are reported to have levels which could account for radiation of this energy.

We examined Tl (cp) and observed a well-resolved peak at 380 ± 10 kev. This radiation does not correspond to transitions between known levels to the best of our knowledge. The 280-kev radiation, from Tl^{203}, if present, would have been obscured by the Compton peak from the 380 kev and the high-energy tail of the x-rays. Preliminary tests on Bi as yet have yielded no significant results.

In the future we plan to use only thin targets since these are not only essential for accurate cross-section measurements, but also result in a greatly reduced x-ray background. We can also further reduce the x-ray background by critical absorption foils, a technique which we have already used successively to a limited extent.

We wish to express our sincere thanks to Professors Deutsch, Feshbach, and Weisskopf, and Dr. de-Shalit and Dr. Ajzenberg for their advice and encouragement.

* This work was supported by the Bureau of Ships and the U. S. Office of Naval Research.

[1] V. F. Weisskopf, Phys. Rev. **53**, 1018 (1938); C. J. Mullin and E. Guth, Phys. Rev. **82**, 141–155 (1951); R. Huby and H. C. Newns, Proc. Phys. Soc. (London) **A64**, 619–632 (1951); K. A. Ter-Martirosian, Zhur. Eksptl. i Teort. Fiz. **22**, 284 (1952); A. Bohr and B. R. Mottelson [see U. S. Office of Naval Research Scientific Notes, May 1, 1953, p. 93 (unpublished)].

[2] S. W. Barnes and P. W. Aradine, Phys. Rev. **55**, 50–52 (1939).

[3] C. L. McClelland, S.M. Thesis, Massachusetts Institute of Technology, August 15, 1952 (unpublished).

[4] These results were reported at the Medium Energy Conference held at the University of Pittsburgh, June 4–6, 1953 (unpublished).

[5] M. Goldhaber and R. D. Hill, Revs. Modern Phys. **24**, 225 (1952).

[6] A. de-Shalit (private communication).

Radiative Corrections to Nuclear Forces in Pseudoscalar Theory*

K. A. BRUECKNER
Indiana University, Bloomington, Indiana
(Received June 5, 1953)

IT has been recently pointed out by the author, Gell-Mann, and Goldberger[1] (in a paper to be referred to as I) that a simple subset of radiative corrections to the nucleon propagation function has the effect of strongly depressing nucleon pair formation in pseudoscalar theory with pseudoscalar coupling. The effects on meson scattering and nuclear forces are then very pronounced. It is the purpose of this note to show that these effects also appear in a simple way in a consistent formulation of the relativistic two-body problem. For this we consider the Bethe-Salpeter equation for the bound state[2] (the consideration of the scattering problem is not essentially different) which has the form

$$\varphi(p_1, p_2) = S_F(p_1) S_F(p_2) \int d^4p_1' d^4p_2' \times G(p_1, p_2; p_1', p_2') \varphi(p_1', p_2'), \quad (1)$$

where $G(p_1, p_2; p_1', p_2')$ is the kernel of the integral equation. A method proposed for attacking this problem is to expand the kernel in a power series in the coupling constant but to attempt to solve the resulting simplified equation exactly. The first approximation to the integral equation [Eq. (1)] can then consistently be assumed to arise from taking all contributions of order g^2 which lead from the state $\varphi(p_1, p_2)$ to the state $\varphi(p_1', p_2')$. These are shown in the form of Feynman diagrams in Fig. 1.

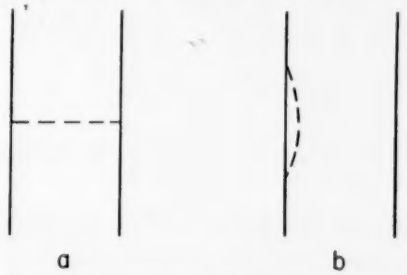

FIG. 1. Feynman diagrams for the g^2 contributions to the kernel.

Diagram (a) of this figure gives rise to the usual "ladder" approximation;[2,3] the second diagram (b) corresponds to a vacuum fluctuation for the nucleon and would give no contribution in a Born approximation calculation. The finite contribution from this graph is, however, not in general zero (vanishing only on the energy shell) and cannot be consistently dropped in this approximation. It can be treated in the following way; in the zeroth approximation (of order g^2) to the kernel, one obtains the following contributions:

$$G^0(p_1, p_2; p_1', p_2') = G^0_{\text{ladder}} \delta(p_1 + p_2 - p_1' - p_2') + G^0_{\text{radiative}} \delta(p_1 - p_1') \delta(p_2 - p_2'), \quad (2)$$

where

$$G^0_{\text{ladder}} = g^2 \boldsymbol{\tau}_1 \cdot \boldsymbol{\tau}_2 (\gamma_5)_1 (\gamma_5)_2 D_F(p_1 - p_1') \quad (3)$$

and

$$G^0_{\text{radiative}} = g^2 \sum_{\lambda=1}^{2} \boldsymbol{\tau}_\lambda \cdot \boldsymbol{\tau}_\lambda \int [\gamma_5 S_F(p_\lambda - k) \gamma_5]_\lambda D_F(k) d^4k. \quad (4)$$

The finite parts of $G^0_{\text{radiative}}$ have been previously evaluated; in the notation of I,

$$G^0_{\text{radiative}} = -(3g^2/16\pi^2)[f(p_1) + f(p_2)]. \quad (5)$$

The only property of $f(p)$ which we shall consider here is that $f(p)$ vanishes on the energy shell but is approximately equal to one if the momentum-energy relation between $\gamma \cdot p$ and M is that of an antiparticle.

The integral equation [Eq. (1)] now becomes

$$\varphi(p_1, p_2) = S_F(p_1) S_F(p_2) \{1 + (3g^2/16\pi^2)[f(p_1) + f(p_2)]\}^{-1} \times \int d^4p_1' d^4p_2' G^0_{\text{ladder}} \delta(p_1 + p_2 - p_1' - p_2') \varphi(p_1', p_2'), \quad (6)$$

which differs from the ladder approximation in that the propagation functions $S_F(p)$ have been replaced by $S_F'(p)$, where

$$S_F'(p_1) S_F'(p_2) = S_F(p_1) S_F(p_2) \{1 + (3g^2/16\pi^2)[f(p_1) + f(p_2)]\}^{-1}.$$

The corresponding modification of the Feynman diagrams which

represent the ladder approximation is to include an infinite set of radiative corrections to each nucleon line corresponding to the successive emission and reabsorption one at a time of any number of mesons. The properties of these modified propagation functions have already been discussed in I; they differ little from the original functions if particles (1) and (2) are moving as nearly free particles. If however pair formation has occurred as is characteristic of the pseudoscalar theory even when the nucleons are interacting rather weakly, then the modification of the propagation functions is very large. Accordingly the effect will be small only if an adiabatic approximation[2,3] is made to the integral equation which does not involve pair formation. The next contributions to the adiabatic approximation to the equation involve the formation of zero, one, or two nucleon pairs, as is shown in Fig. 2, which will be decreased

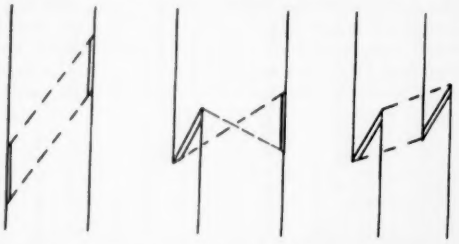

FIG. 2. g^4 contributions to the potential in the adiabatic approximation. The doubled nucleon lines represent propagation functions modified by radiative corrections.

in the nonrelativistic region by factors of approximately one, $(1+3g^2/16\pi^2)$ and $(1+3g^2/8\pi^2)$, respectively. More generally, the radiative effects tend to prevent inversion of the nucleon line in time, i.e., pair formation, which is similar to the result already discussed in I.

Similar comments also apply to the formulation of the relativistic integral equation[4] describing meson-nucleon scattering. In that problem the g^2 kernel includes not only the two usual Compton contributions but also radiative terms for both the meson and nucleon which lead to replacement of S_F and D_F by S_F' and D_F' which differ by damping radiative terms similar to those discussed above.

Finally it may be remarked that while the treatment of the radiative terms in the g^2 kernel as suggested here is fairly nonambiguous, the method of inclusion of radiative effects in higher-order terms in the kernel of Eq. (1) still remains somewhat arbitrary.

The author is indebted to Professor H. Bethe for interesting discussions of this and related problems.

* Supported by a grant from the National Science Foundation.
[1] Brueckner, Gell-Mann, and Goldberger, Phys. Rev. **90**, 476 (1953).
[2] E. E. Salpeter and H. A. Bethe, Phys. Rev. **84**, 1232 (1951).
[3] M. Lévy, Phys. Rev. **88**, 72 (1952).
[4] Compare, for example, Karplus, Kivelson, and Martin, Phys. Rev. **90**, 1072 (1953).

Bubble Chamber Tracks of Penetrating Cosmic-Ray Particles*

DONALD A. GLASER
Harrison M. Randall Laboratory of Physics, University of Michigan, Ann Arbor, Michigan
(Received May 20, 1953)

TRACKS of penetrating cosmic-ray particles passing through an ether-filled bubble chamber under 10 cm of lead have been recorded by flash photography triggered by a twofold vertical coincidence telescope. The bubble chamber consisted of a heavy-walled cylindrical Pyrex bulb 3 cm long and 1 cm inside diameter, which communicates with a pressure-regulating device by means of a Pyrex capillary tube 45 cm long. A thermostated temperature bath of mineral oil surrounded the bulb, maintaining

FIG. 1. Flash duration 20 microseconds, no deliberate delay, temperature 140°C.

the temperature constant within 0.5°C in the range 138°C to 143°C. The pressure-regulating device consisted of a brass cylinder of length 2 cm and inside diameter 3 cm. One end of the cylinder was sealed with a flexible diaphragm of $\frac{1}{8}$-in. Neoprene faced with Teflon to confine the ether and permit variation of its pressure by controlling the pressure of compressed gas on the outside of the diaphragm.

To prepare for taking a picture of a track, the ether was compressed by admitting compressed nitrogen to the pressure regulator at a pressure of 300 pounds per square inch so that no vapor bubbles remained in the system. Then the gas was allowed to escape, so that the ether suddenly became highly superheated at atmospheric pressure. On the average the liquid remained quietly in this unstable condition for several seconds until a violent eruptive boiling occurred. If a coincidence of the vertical counter telescope occurred during this waiting time, a picture was taken by means of a xenon discharge flashlamp. About 5 seconds were required to recompress the ether in preparation for the next event.

Figure 1 shows a track obtained at a temperature of 140°C with a flash duration estimated to be 20 microseconds. In Fig. 2 the duration was reduced to about 5 microseconds, the temperature 141°C. Here one sees a scattering of about 2°.

From these sample pictures several characteristics of bubble chambers and their possible applications to high-energy nuclear physics can be inferred. Because of the relatively high density of the sensitive medium (about 0.5 g/cc under these conditions), there is a good chance of seeing an interesting event occurring in the liquid where most of the secondaries would be visible. Since the particles recorded here are almost certainly fast mu mesons, one concludes that the bubble chamber is sensitive to minimum ionizing particles. Since the bubbles grow so extremely rapidly, there are virtually no distortions of the tracks due to convection

currents in the liquid. Another interesting possibility arising from the rapid bubble growth is that one could take multiple exposure photographs of events so that a measurement of bubble size could tell the relative ages of tracks in the range 0 to 100 microseconds. It should be possible to construct larger bubble chambers, to use liquids of various composition and density, and to calibrate the bubble density along a track in relation to the ionization density.

In order to estimate the conditions under which a bubble chamber will be useful as a detector of ionizing radiation, and to guide the choice of a working liquid, an approximate theory of the stability of charged bubbles in superheated liquids has been developed. To understand the result let us first suppose that as a result of thermal fluctuations a tiny spherical bubble at least several molecular diameters across is formed in the liquid and that a single ion is made inside the bubble by an ionizing event. It is easy to show that the ion will run to the surface of the bubble, and that the energy contribution of its electric field is such as to encourage the collapse of the bubble. If, on the other hand, the bubble contains a number of ions, they will distribute themselves roughly uniformly over the surface and aid its growth. When only two or three ions are present, the result is not clear cut, and depends on the detailed shape of the bubble and the mechanism by which the ions are prevented from escaping into the bulk of the liquid.

The main result of the theory, in the continuously distributed charge approximation, is that for a bubble carrying n charged ions to grow to visible size, the liquid must be superheated so that the normal saturated vapor pressure p_∞ exceeds the actual applied pressure on the system by the amount

$$p_\infty(T)=3/2\left(\frac{4\pi}{n^2e^2}\right)^{1/3}[\sigma(T)]^{4/3}[\epsilon(T)]^{1/3}. \quad (1)$$

This result neglects the dependence of the surface tension σ and dielectric constant ϵ on the curvature of the surface and on the pressure.

To find the temperature at which a bubble chamber will operate, one plots $p_n(T)$ and $p_\infty(T)$ *versus* T on the same graph. The intersections for the various n give the required temperatures and pressures. For diethyl ether the predicted and measured temperatures are closer than 10°C if n is something between 2 and 10.

If ionizing radiation is the limiting factor in an experimental attempt to obtain high superheats in pure liquids, one would expect the present theory to predict maximum attainable superheats. For the few liquids for which good data are available the agreement is within 20°C or better.

In its broad outlines this analysis parallels that of droplet growth in a supersaturated atmosphere. The present multiple-charge modification extends the effect so that ionizing events can make a growth-aiding contribution to the surface free energy of a particle of new phase in any nucleation situation in which the two phases have a difference of dielectric constant. This fact may have interesting consequences for the influence of ionizing radiation on nucleation in supercooled liquids, supersaturated solutions, etc.

* This work was supported by the Michigan Memorial-Phoenix Project and a grant from the Horace H. Rackham School of Graduate Studies.

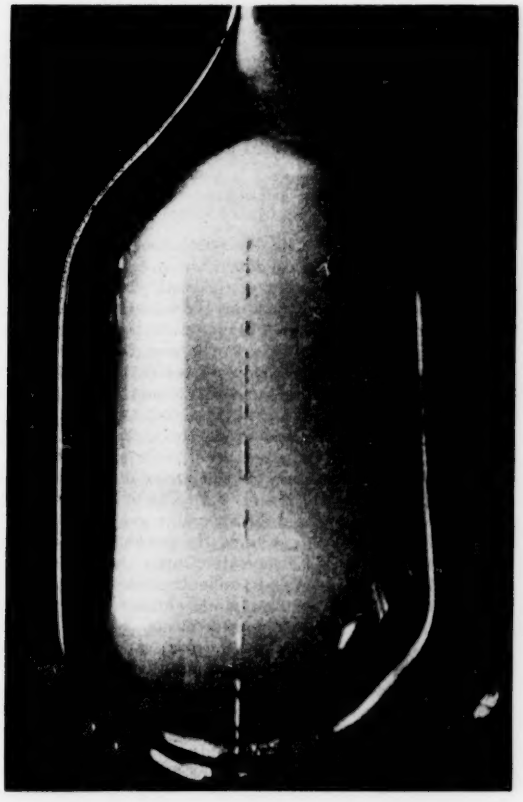

FIG. 2. duration 5 microseconds, no deliberate delay, temperature 141°C.

Patterns in Alpha Spectra of Even-Even Nuclei

FRANK ASARO AND I. PERLMAN
Radiation Laboratory and Department of Chemistry, University of California, Berkeley, California
(Received June 8, 1953)

THE present communication aims to bring out some definite regularities in the spectra of even-even alpha emitters without elaborating particularly on the possible significance of these findings regarding alpha-decay theory and spectroscopic states of heavy nuclei. Most of the data to be discussed were obtained over the range of elements from curium 96 to radium 88 since it is inherently difficult to make the necessary measurements for elements below radium.

We shall first suggest some means to identify the energy states which seem to recur generally and to designate the alpha transitions leading to these states. The first rule for even-even alpha emitters is that the most prominent alpha group leads to the ground state of the product nucleus as would be expected from previous alpha-decay theory. (This is not the case for nuclear types having odd nucleons.) In addition, an alpha group is invariably found which leads to a level with spin 2 and even parity, and the abundance of this group likewise conforms in first approximation with the expectations from unadorned alpha-decay theory. The energy level of this excited state will be termed the *first even-spin state* and lies about 40 kev above the ground state at plutonium, increasing with decreasing mass number as already described.[1,2] In low abundance are found alpha groups leading to other levels which we shall term *second and third even-spin states*. In the few cases for which gamma-ray data are available it seems probable that these levels have even parity as well as even spin and may very well be 4+ and 6+ states. There is some fragmentary evidence in our work that an odd-spin odd-parity state is appearing in a limited region, but this will not be discussed further at present.

Bohr and Mottelson[3] have suggested that nuclides well beyond a closed shell have states in which the nucleus acts as a rigid rotator. The energy of such rotational levels should be proportional to $J(J+1)$, where J is the total angular momentum quantum number. If we consider the 2+ and 4+ states to be rotational states, the ratio of the energies should be 3.3. Figure 1 shows

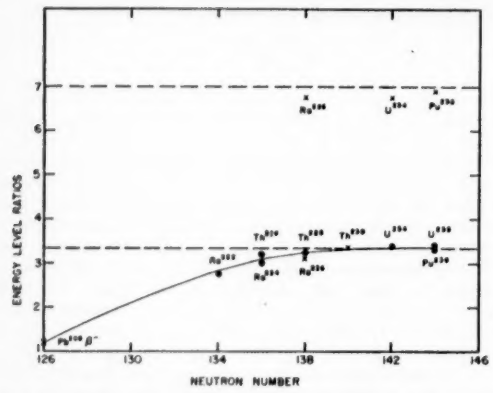

FIG. 1. Energy ratios for the levels of even-even nuclides. ● From alpha-particle spectrograph data. × From gamma-ray data.

experimental ratios for 10 nuclei in the heavy element region plotted against neutron number. It is fairly certain that corresponding states are compared here although in only one case, Cm^{243}, have the necessary measurements been made to establish this state as $4+$.[4] The heaviest nuclei show remarkably close agreement with the expectations for the postulated rotational states and there appears to be a progressive departure from the ratio 3.3 toward lighter nuclei. (There is no convincing justification for plotting these data strictly with respect to neutron number as is done here; in fact, it is not to be expected that the nuclear deformation which defines these levels is simply a function of the neutron number.)

Gamma-ray data have been used to infer the existence of the third *even-spin* state for three species. The ratios of the third to the first levels are indicated in Fig. 1 in relation to the theoretical value 7 for the third rotational state, $J=6$.

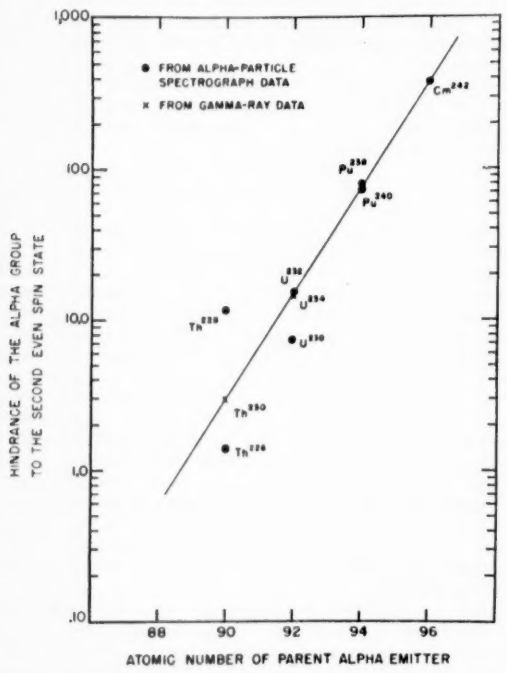

FIG. 2. Relation between the observed partial half-life and that calculated from alpha-decay theory for the alpha group populating the second even-spin state.

In the study of the alpha spectra of most of the nuclides shown in Fig. 1, it became clear that the alpha transitions leading to the second even-spin states were highly hindered. That is, the measured partial half-lives were much longer than expected simply from the energy and nuclear charge. (It will be remembered that the ground-state transitions and those leading to the first even-spin states are in first approximation unhindered.) The Cm^{242} alpha group leading to the second even-spin state, as an example, has a half-life almost *400-fold longer* than expected from theory. On examining this relationship for alpha emitters of lower elements, it was found that as the energy of the second even-spin state increased, the hindrance factor decreased. For the species examined so far, the logarithm of the hindrance factor varies linearly with the atomic number (Fig. 2). There is no quantitative explanation yet known for the close agreement of this function. (It will be noted that a few points lie off the curve.)

If we assume that the same spin change is involved in each of these transitions, an explanation cannot lie in simple fashion in this direction both because of the large hindrance factors in some cases and because of the wide variation. A possible explanation lies in the assumption of a progressive change in charge asymmetry on leaving the closed shells in the vicinity of lead. The potential barrier will then be spherically nonsymmetrical and if the alpha particles of a type have a preferred direction of emission, any progressive change in charge distribution will be reflected in a progressive change in the ease with which the alpha particle can leave.

[1] F. Asaro and I. Perlman, Phys. Rev. **87**, 393 (1952).
[2] S. Rosenblum and M. Valadares, Compt. rend. **235**, 711 (1952).
[3] A. Bohr and B. Mottelson, Phys. Rev. **89**, 316 (1953).
[4] Asaro, Thompson, and Perlman, Phys. Rev. (to be published).

High Altitude Measurements of the Intensity of Cosmic Radiation at Magnetic Latitudes 3°N and 19°N

A. S. RAO, V. K. BALASUBRAHMANYAN, G. S. GOKHALE, and A. W. PEREIRA
Tata Institute of Fundamental Research, Bombay, India
(Received June 8, 1953)

THE total intensity and penetrating component of cosmic radiation in the vertical direction have been measured as a function of altitude at Bangalore, magnetic latitude 3°N, and Delhi, magnetic latitude 19°N, during the years 1951–1953. Quadruple coincidence G.M. counter telescopes without any absorber and with 10 cm of lead absorber in between the counter trays were sent up in free balloon ascents to measure the total intensity and that of the penetrating component, respectively. The geometry of the telescopes was so designed that the most inclined particle recorded by the telescopes would only traverse a thickness of the atmosphere and the absorber 10 percent greater than a particle arriving vertically. The half-angles of the telescopes about the vertical were 13.5° and 24.5°. The temperature inside the gondola which contained the apparatus was maintained between +15°C and +25°C by using the greenhouse effect. The atmospheric pressure and temperature inside the gondola were measured by an aneroid and bi-metallic strip meteorograph of the Olland type. A mercury manometer was also used as an independent check on the pressure measurements. The atmospheric pressure, temperature inside the gondola, and the cosmic-ray data, were transmitted to the ground receiving station where they were recorded automatically on a moving paper tape.

The results obtained at the two stations Bangalore and Delhi are given in Fig. 1 as intensity *vs* pressure curves. Curves A[1] and B give the penetrating component at 3°N and 19°N, respectively, and C and D the total intensities at the above two latitudes. Every curve in the figure is a composite curve of the data obtained in a number of flights. The root-mean-square deviations of the points are marked for each curve.

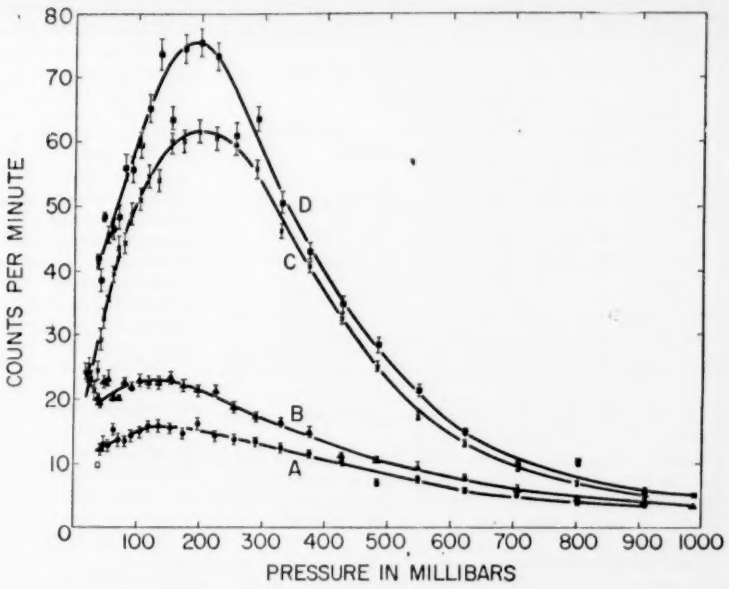

FIG. 1. Vertical intensity of cosmic radiation penetrating 10 cm of lead. A: at Bangalore 3°N(mag). B: at Delhi 19°N(mag). Total vertical intensity of cosmic radiation, C: at Bangalore 3°N(mag), D: at Delhi 19°N(mag).

The intensity of the component penetrating 10 cm of lead absorber at 3°N and 19°N increases continuously with decreasing pressure, reaches a maximum at a pressure of 120 millibars, and then falls with further decrease in pressure. However, the slopes of curves A and B on either side of the maxima differ from each other. The rise of curve B with decreasing pressure before the maximum is much faster than that of curve A, whereas the fall after the maximum is much less steep.

The total intensity at 3°N and 19°N (curves C and D) increases rapidly with decreasing pressure passes through a maximum at 200 millibars and then decreases very rapidly up to the lowest pressure obtained.

There is no detectable shift in position of the maxima between 3°N and 19°N, both in the case of the total intensity and the penetrating component. This may be due to the smallness in difference in the cut-off values of the primary radiation at the two latitudes.

Neher and Pickering[2] reported that there was no detectable increase in the total intensity of cosmic radiation at high altitudes in going from 3°N to 19°N, but our results are in disagreement with this and show that the ratio of the intensities is given by $I_t(19°)/I_t(3°)=1.22$ at the maximum. For the penetrating component at the maximum, the corresponding ratio $I_p(19°)/I_p(3°)$ is 1.46. The latitude effects $I_{19°}/I_{3°}$ for the total radiation and the penetrating component decrease with increasing pressure. The latitude effect at the maximum is much greater for the penetrating component than for the total cosmic radiation as the above figures show, whereas Vidale and Schein[3] found that at 28°, 41°, and 55° the latitude effect for the total intensity was higher than that of the penetrating component.

The primary flux values obtained by extrapolation of the penetrating component curves, uncorrected for showers and accidentals, to the top of the atmosphere at 3°N and 19°N along 77°E geographic longitude are 227 and 364 particles meter^{-2} sterad^{-1} sec^{-1}, respectively. If the correction due to showers and accidentals, which is essential, is considered, the flux values may be smaller by 25 to 30 percent. The shower and accidental measurements have been made, but they are not used to correct the flux values as they do not extend below 75 millibars.

The theoretical analysis of these results, which is in progress, will be published soon.

We wish to express our gratitude to the Atomic Energy Commission, Government of India, for the grants which have made these experiments possible. We wish to express our thanks to Professor H. J. Bhabha for his great interest in the progress of the work and for helpful suggestions and criticism.

[1] Curve A, which has already been published [Phys. Rev. **83**, 173 (1951)], is given here for comparison with the results at 19°N (mag).
[2] H. V. Neher and W. H. Pickering, Phys. Rev. **61**, 407 (1942).
[3] M. Vidale and M. Schein, Phys. Rev. **81**, 1065 (1951).

Measurements of Meson Masses and Related Quantities

F. M. SMITH, W. BIRNBAUM,* AND WALTER H. BARKAS
Radiation Laboratory, Department of Physics, University of California, Berkeley, California
(Received June 12, 1953)

A MESON-MASS measurement program has been completed. The method has been partially described[1,2] and preliminary results[2-4] have been reported at earlier stages of the work. As noted previously,[2] it was discovered that stray mesons coming from points other than the target were interfering with the measurements. Attempts to reduce this effect have been successful, and little evidence of stray mesons remains.

To determine the pion masses, meson and proton ranges and momenta were measured in the same velocity interval. To measure the pion-to-muon mass ratio, similar comparisons were made between pions and muons. In one of the methods employed to find the momentum p_0 of the muon which is emitted when the pion decays at rest, the muon range is compared with the ranges of pions of known momentum and of nearly the same velocity. The decay muons were also compared directly with muons coming from the target in a second type of experiment.

For each particle, the quantity studied statistically is that function of the mass in which the range appears linearly. The dominant term in the variance of this quantity is the range straggling; consequently, it as well as other sources of variance has been examined closely, and the shapes of the measured distribution functions are now understood theoretically.

The stray mesons mentioned above introduced a systematic error of about one percent in the mass values quoted previously. The known systematic effects are now believed to be eliminated,

TABLE I. Values for meson masses and related quantities. The errors quoted are statistical probable errors. The uncertainties in the various quantities are not independent. The mass assumed for the proton is 1836.1 electron masses.

Fundamental mass ratios		
π^+/proton	π^-/proton	π^+/μ^+
0.14888 ± 0.00011	0.14840 ± 0.00017	1.321 ± 0.002

Absolute decay momentum of positive muon
$p_0 = 29.80 \pm 0.04$ Mev/c

Derived masses in units of the electron mass		
π^+	π^-	μ^+
273.4 ± 0.2	272.5 ± 0.3	207.0 ± 0.4

Absolute mass measurements in units of the electron mass[a]		
π^+	μ^+	$\pi^+ - \mu^+$
(273.5 ± 1.2)	(207.1 ± 1.1)	(66.41 ± 0.07)

[a] The bracketed numbers are absolute mass determinations in the derivation of which no use is made of information obtained from the direct comparison of masses with that of the proton, but it is assumed that a neutrino of zero rest mass is emitted in a two-body decay of the pion.

and the statistical errors also have been considerably reduced. Our final results are contained in Table I.

The measured π^+ and π^- masses differ by an amount which is almost significant. If this difference is assumed to be real, an alternative to a true difference between the pion masses is a difference in the stopping cross sections for the positive and negative pions.

Taking the muon/electron mass ratio to be 207, the value of p_0 found implies that the kinetic energy of the muon is 4.12 Mev.

Complete reports of the theoretical and experimental details are being prepared for publication.

The generous assistance of many individuals in the Radiation Laboratory is acknowledged with appreciation.

* Present address: California Research and Development Corporation, Livermore, California.

[1] W. H. Barkas, Proceedings of the Echo Lake Cosmic Ray Symposium, p. 47, June 23–28, 1949 (unpublished).
[2] W. H. Barkas, Am. J. Phys. **20**, 5 (1952).
[3] Barkas, Smith, and Gardner, Phys. Rev. **82**, 102 (1951).
[4] Birnbaum, Smith, and Barkas, Phys. Rev. **83**, 895 (1951).

Origin of Cosmic Rays

J. W. DUNGEY
School of Physics, University of Sydney, New South Wales, Australia
(Received May 18, 1953)

THE most popular class of theories of the origin of cosmic rays supposes that charged particles are accelerated by the electric fields associated with temporally varying magnetic fields. In a broad sense the whole of this class might be called "betatron processes," but there is one subclass[1,2] which resembles the betatron much more closely than the others. The intention here is to point out certain difficulties for this subclass, which have not received sufficient attention, and to survey the other possibilities.

Although magnetic fields which vary with time are observed on the sun and certain stars, it does not follow that "betatron processes" in the narrow sense must occur, but only in the broad sense. Remembering that the magnetic fields are nonuniform in space, the temporal variation of the magnetic field could in principle be the result of a uniform motion of the magnetic field. A Lorentz transformation shows that this case will not account for any cosmic rays.

Riddiford and Butler[2] consider a uniform magnetic field increasing in time, and then the lines of force of the electric field are concentric circles. Consider the case in which the change of the field is very slow compared with the Larmor frequency. The perturbation method[3] may then be used, and it is found that the motion of any charged particle averaged over a Larmor period is given as follows. The average distance of the particle from the the axis where **E** vanishes is proportional to $H^{-\frac{1}{2}}$; the average relativistic momentum perpendicular to **H** is proportional to $H^{\frac{1}{2}}$. This result is just the same as though the particles were contained in a box, and the box were compressed in directions perpendicular to **H** but not parallel to **H**. The question of what causes this compression has not been answered, and it is not plausible that this process should occur on stars with a compression factor sufficient to generate cosmic rays.

The perturbation method is valid in practice except for very weak fields. This case is restricted, however, by a condition $E < vH/c$, where v is of the order of the velocity of mass motion of the gas. This condition is true unless there is a large current density and unless high frequency oscillations occur. If then the perturbation method is in error by a substantial factor, the field cannot extend over a distance much greater than mcv/eH, which is the radius of the orbit of a particle with velocity v. Consequently the highest energy obtained is not many times mc^2.

Investigation of the case when there is a large current density leads to the conclusion that cosmic-ray energies can be attained near a neutral point of the magnetic field.[4,5]

The theory of high frequency oscillations in ionized gases is not far enough advanced to allow the possibility of acceleration by high frequency fields to be discussed.

The general theory of the orbits of particles in magnetic fields In nonuniform motion involves combinations of the special cases discussed here. Fermi[6] has discussed the case of turbulent motion and shown that the particles have a slow average gain of energy.

[1] W. F. G. Swann, Phys. Rev. **43**, 217 (1933).
[2] L. Riddiford and S. T. Butler, Phil. Mag. **43**, 447 (1952).
[3] H. Alfven, *Cosmical Electrodynamics* (Oxford University Press, London, 1950).
[4] R. G. Giovanelli, Monthly Notices Roy. Astron. Soc. **107**, 338 (1948); **108**, 113 (1948).
[5] J. W. Dungey, Phil. Mag. (to be published).
[6] E. Fermi, Phys. Rev. **75**, 1169 (1949).

Fluorescent Light Yields with Alpha, Beta, and Gamma Radiations*

MILTON FURST AND HARTMUT KALLMANN
New York University, Washington Square, New York
(Received June 15, 1953)

THE absolute light yields of various fluorescent materials under high-energy excitation have been investigated previously.[1–3] Recently Bril and Klasens[4] have reported many new results for 20-kev electron excitation. It must be borne in mind that there is a marked decrease in the efficiency of light output with excitation by highly energizing particles for most of the materials except ZnS and CdS. If this is taken into account, the results of Bril and Klasens confirm most of the earlier results in those cases where the same materials were investigated. (The measurements of Bril and Klasens were made with rather highly energizing 20-kev electrons.) Since it has frequently been contended that even traces of impurities, especially with organic substances, influence the fluorescent yield considerably, new measurements of relative efficiencies with pure materials have been made and are presented in Table I. Hard gamma rays from radium, beta particles from Sr 90, and alpha particles from Po were used on all the solid materials. For electrons the values have been adjusted for equal stopping power, and for gamma rays the values were reduced to equal masses; no corrections were made for alpha particles since they were completely absorbed in the materials used. The difference in spectral sensitivity of the 1P28 multiplier for the various materials has not been taken into account. This is serious only for the Radelin powder emitting in the green; if spectral corrections were applied for this material, the values would be close to those of the ZnS (type D, Dupont).

Thin layers of powders, crystals, or liquids were used (of the order of 10 mg/cm^2). No appreciable loss was found in ZnS on account of true absorption in the powder caused by lengthening of the light path by multiple scattering, since the light output was found to be proportional to the thickness of the powder over a considerable range when electrons and gamma rays were used. Anthracene, which also showed no self-absorption in these thicknesses, was tested both as a powder and as a clear transparent

TABLE I. Comparison of fluorescence for various excitations.

Substance	Intensity α particles[a]	β particles[b]	γ rays[c]
Anthracene crystal	4.3	44	71
Anthracene powder	2.5	41	61
Calcium tungstate	3.3	47	46
Diphenyl	1.1	14	22
Radelin (PFG)[d]	30	47	42
Terphenyl (3 g/l) in phenylcyclohexane		20	
ZnS (Type D)	100	100	100

[a] Polonium source.
[b] Strontium 90; values corrected for equal stopping power.
[c] Radium; values corrected for equal mass.
[d] Radelin is also a ZnS-type phosphor.

single crystal (specially purified). Special precautions were taken with the ZnS powders to attain saturation before measurements, and thus maximum light efficiency was obtained.

The crystal values provide the most favorable comparison for the true anthracene fluorescence with that of ZnS. Anthracene of different degrees of purity were found to have practically the same yield, though anthracene powder with just a noticeable yellow color due to oxidation had a light intensity of only 60 percent of that of the pure material. The difference between gamma-ray and beta-particle values for substances like anthracene and $CaWO_4$ may be due to the portion of electrons with smaller energy than the maximum and, therefore, higher energizing power for which the light efficiency is smaller.

The liquid also showed no self-absorption and demonstrated a high efficiency for beta particles. (Its high efficiency for gamma rays was previously determined.[5]) If corrected for zero self-quenching, this efficiency is only 30 percent smaller than that of solid anthracene.

If the absolute yield for ZnS is assumed to be 20 to 25 percent,[1,4] these results show that the absolute yield for anthracene lies between 8 and 10 percent as previously reported. The occurrence of only a small difference between the crystal and powder values for electrons and gamma radiations again shows the very slight absorption even in the powder.

* This work was sponsored by the Signal Corps Engineering Laboratory, Evans Signal Laboratory, Belmar, New Jersey.
[1] Broser, Kallmann, and Martius, Z. Naturforsch. **4a**, 204 (1949).
[2] H. W. Leverenz, *An Introduction to the Luminescence of Solids* (John Wiley and Sons, Inc., New York, 1950), p. 317.
[3] Furst, Kallmann, and Kramer, Phys. Rev. **89**, 416 (1953).
[4] A. Bril and H. A. Klasens, Philips Research Repts. **7**, 401 (1952).
[5] M. Furst and H. Kallmann, Phys. Rev. **85**, 816 (1952).

A Metastable State of V^{52}

T. WIEDLING
*Joint Establishment for Nuclear Energy Research, Kjeller, Lillestrøm, Norway**
(Received June 12, 1953)

VANADIUM is found to have two stable isotopes,[1] V^{50} and V^{51}. After neutron bombardment of vanadium, Amaldi *et al.*[2] found an activity with a 3.75-min half-life. Later Renard[3] reported a 2.6-min state which he ascribed to V^{52}. Cork *et al.*[4] found a half-life of 16 hours.

Spectroscopically pure V_2O_5 was irradiated in the JENER-pile for approximately 30 hours. The half-life was measured and the 16-hour activity was verified.

In order to identify the 16-hour activity, the gamma spectrum was measured with a scintillation spectrometer. Two gamma rays with energies of 59 kev and 96 kev were obtained. Further, eight other lines were detected:

0.539±0.008 Mev,	1.40±0.04 Mev,
0.739±0.010 Mev,	1.76±0.07 Mev,
0.850±0.010 Mev,	2.33±0.07 Mev,
1.00 ±0.06 Mev,	3.2 ±0.1 Mev.

The three lines 0.739 Mev, 1.00 Mev, and 1.40 Mev have been reported[5] for Cr^{52}. The other five also fit the disintegration scheme

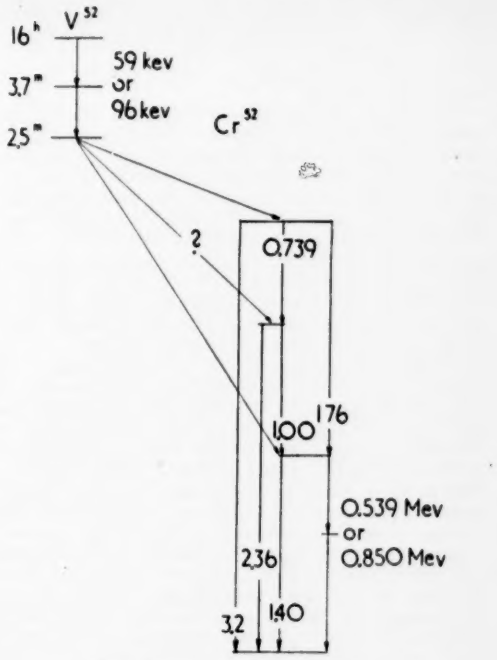

FIG. 1. Tentative decay scheme of V^{52}.

of Cr^{52}. Since the vanadium isotope investigated is a negatron-emitter and thus goes over into Cr, and because the lines detected seem to agree with those of Cr^{52} obtained from the positron-emitter Mn^{52}, it seems probable that the 16-hour activity belongs to an excited state of V^{52}. Thus the low-energy lines probably belong to excited states of V^{52}, the highest level of which has a lifetime of 16 hours and the lower one 3.7 minutes.[3]

The new high-energy lines detected in Cr^{52} make it possible to give the order of the γ rays with energies 0.74 Mev and 1.0 Mev (Fig. 1).

The investigation of vanadium will continue.

* On leave from the Laboratory of Physics, University of Stockholm, Stockholm, Sweden.
[1] W. T. Leland, Phys. Rev. **76**, 1722 (1949).
[2] Amaldi, D'Agostino, Fermi, Pontecorvo, Rasetti, and Segrè, Proc. Roy. Soc. (London) **A149**, 522 (1935).
[3] G. A. Renard, Ann. phys. **5**, 385 (1950).
[4] Cork, Keller, and Stoddard, Phys. Rev. **76**, 575 (1949).
[5] W. C. Peacock and M. Deutsch, Phys. Rev. **69**, 306 (1946).

Total Cross Sections of 408-Mev Protons for Hydrogen and Light Elements*

J. MARSHALL, L. MARSHALL, AND A. V. NEDZEL
Institute for Nuclear Studies, University of Chicago, Chicago, Illinois
(Received June 10, 1953)

THE total cross sections of several light elements for 408-Mev protons have been measured by a transmission method. The cross sections given here were measured in such a way that they include all processes except the Coulomb scattering. A proton beam scattered from the Chicago 170-inch synchrocyclotron was highly collimated and deflected with an auxiliary magnet. Range measurements in copper indicated a mean proton energy of 408±10 Mev at the scatterer.

Two one-inch square×¼-inch thick crystal scintillation counters were connected in fast coincidence to define and monitor the beam. A 9½-inch diameter liquid scintillator counter was placed coaxial with the beam defined by the first two counters and at variable

distance L. It was connected in anticoincidence with the coincidence output of the first two counters so as to count directly the number of particles removed from the beam. Thin scatterers (of 90–95 percent beam transmission) were placed directly after the second crystal counter.

The variable distances L between the thin scatterer and the anticoincidence counter determined the minimum angle θ, by which a proton (and any secondary charged particles) would have to be deflected from the forward direction in order to allow an anticoincidence event to register. The angle θ was varied in each case over a range of small angles, but no angles were used which were so small as to introduce any large effect from Coulomb scattering. Corrections were applied to the results from measurements at the smallest values of θ for the Coulomb scattering. The corrected experimental values were plotted against θ, and in each case lay on a straight line. These straight lines were extended to $\theta=0$ to obtain the total cross sections.

For the determination of the total cross section of liquid hydrogen, the transmission was measured for laboratory angles of 1.5° to 6°. The straight line drawn through the experimental points showed a steep slope in the case of hydrogen, due to the deuterons formed in pion production. These deuterons have about 4-Mev energy in the baricentral system, and of the order of 200 Mev in the laboratory system. Consequently they all come forward within an angle of 8° to the beam giving rise to the observed increase of counting rate with decreasing angle of the large counter. An angular dependence of $0.2+\cos^2\theta$ was assumed for the deuteron production in the baricentral system. The corresponding effect on counting rate calculated as a function of angle (assuming 2 mb for the deuteron production cross section) accounted for most of the slope of this line. The data were corrected for deuteron production and plotted against θ; the line through the corrected points was extrapolated to zero angle, and the assumed deuteron cross section was added to the intercept to give a total hydrogen cross section of 24 mb. This number is insensitive to the quantity assumed for the deuteron production cross section, the final result of 24 mb being obtained for choices of 2, 3, or 4 mb.

For Li, Be, and C, θ was varied from 3.5° to 14° and for D_2O and H_2O, from 2.5 to 8°. In no case was the Coulomb correction more than a few percent. The straight lines determined by the corrected transmissions plotted *versus* θ were extended to $\theta=0$, to give the total cross section for 408-Mev protons not including Coulomb scattering. The values so obtained are as follows:

$$\sigma(\mathrm{H})=24.0\pm1 \text{ mb (liquid hydrogen)}$$
$$\sigma(\mathrm{Li})=194\pm8 \text{ mb (lithium metal)}$$
$$\sigma(\mathrm{Be})=242\pm6 \text{ mb (beryllium metal)}$$
$$\sigma(\mathrm{C})=285\pm14 \text{ mb (graphite)}$$
$$\sigma(\mathrm{D-H})=\tfrac{1}{2}[\sigma(\mathrm{D_2O})-\sigma(\mathrm{H_2O})]=31.6\pm2 \text{ mb}$$
$$\sigma(\mathrm{O})=\sigma(\mathrm{H_2O})-2\sigma(\mathrm{H})=406\pm3 \text{ mb}$$
$$\sigma(\mathrm{D})=\sigma(\mathrm{D-H})\pm\sigma(\mathrm{H})=55.6\pm2.2 \text{ mb}.$$

These total cross sections for 408-Mev protons are closely equal to the corresponding total cross sections for 400-Mev neutrons,[1] in agreement with the hypothesis of charge symmetry. The (p,p) cross section, however, is significantly lower than the (n,p) cross section at the same energy. In order to compare this transmission cross section with (p,p) scattering cross sections it must be corrected for a sizeable meson production, which may be as much as 2 millibarns. The scattering cross section implied here is therefore in agreement with the Berkeley value[2] of 3.5±0.4 mb/sterad at 340 Mev, and with one-half the Carnegie Institute of Technology value[3] of 45±10 mb at 435 Mev. (The factor ½ is needed to allow for the definition of scattering cross section in the case of identical particles.)

* Research sponsored by the U. S. Office of Naval Research and the U. S. Atomic Energy Commission.

[1] V. A. Nedzel, Phys. Rev. **90**, 169 (1953).
[2] O. Chamberlain (private communication).
[3] Clark, Grandey, Kao, and Mann, Bull. Am. Phys. Soc. **28**, No. 3, 43 (1953).

Gamma Radiation from Inelastic Scattering of 2.7-Mev Neutrons

V. E. Scherrer, W. L. Smith, B. A. Allison, and W. R. Faust
Naval Research Laboratory, Washington, D. C.
(Received June 15, 1953)

We have performed some preliminary observations of gamma radiation arising from bombardment of various materials with 2.7-Mev neutrons produced by the $D(d,n)He^3$ reaction. A scatterer, made of the material of interest, was placed 25 cm from the accelerator target and in line with the deuteron beam. Gamma radiation was detected by a Compton spectrometer placed about 10 cm from the scatterer. Some shielding of the spectrometer crystals was provided by a lead bar placed between the accelerator target and spectrometer. The spectrometer crystals were arranged such that the angle of scattering of the incident quanta was 135 degrees. With this arrangement the resolution was about 12 percent full width at half-maximum. Calibration was performed with standard sources of Na^{22}, Cs^{137}, and Co^{60}. Experiments indicated that the energy calibration was essentially independent of the position of the sources from points within the volume normally occupied by the scatterer.

Pulse-height distributions were taken first with the scatterer in position and then removed. The accelerator rate was held constant during the runs so that the neutron yield was the same during both source and background runs. The net counting data in counts per channel per neutron monitor count is plotted in the accompanying figures. Sample probable errors are indicated at a few points. Generally the error was large for small pulse heights due to a large accidental rate produced by neutrons penetrating the spectrometer shield.

Figure 1 shows pulse-height distributions produced by bombardment of a copper scatterer as well as a typical Co^{60} calibration curve. Ordinates, for the latter, are in counts per second per chan-

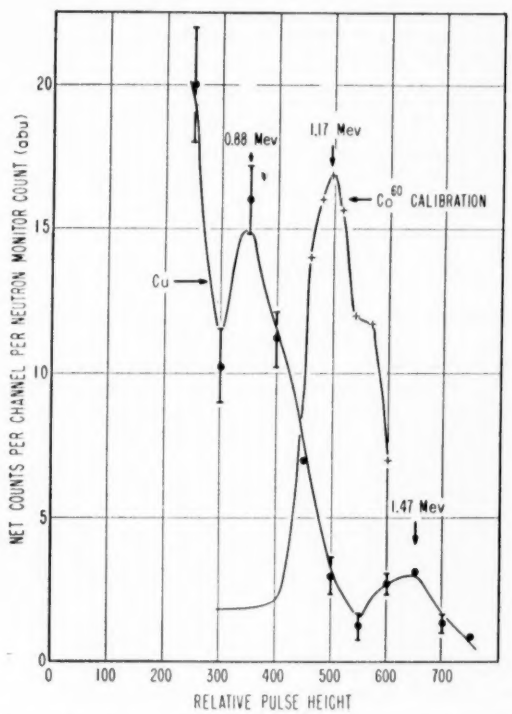

Fig. 1. Compton spectrometer pulse-height distribution produced by gamma rays arising from neutron bombardment of copper.

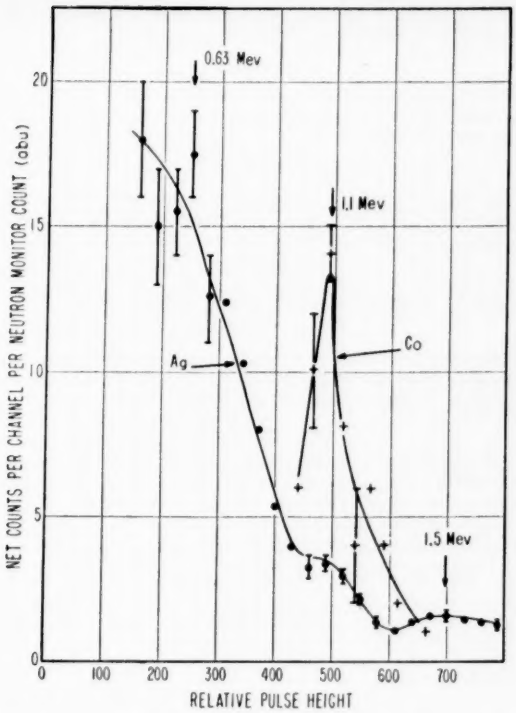

FIG. 2. Compton spectrometer pulse-height distribution produced by gamma rays arising from neutron bombardment of silver and cobalt.

nel. The copper spectrum shows gamma rays at 0.88 Mev as well as a broad smear near 1.47 Mev. The silver pulse-height distribution, shown in Fig. 2, indicates gamma rays at 1.1 and 1.5 Mev. Further data indicate a repeatable maximum near 0.63 Mev, although statistics are too poor on data shown here to definitely establish a gamma ray at that energy. A cobalt scatterer produced the pulse-height distribution also shown in Fig. 2, in which a strong 1.1-Mev gamma ray is quite apparent.

The authors wish to thank Dr. E. H. Krause for his active interest and support and express their appreciation to Mr. A. P. Flanick for aid in performing the experiments.

Interpretation of $0+x\phi$ Type Stars in Photographic Emulsions

C. B. A. McCUSKER AND F. C. ROESLER
Dublin Institute for Advanced Studies, Dublin, Ireland
(Received May 29, 1953)

A NUMBER of observers[1–7] have reported stars in photographic emulsions which are produced by a fast singly charged particle and are remarkable for having a number of shower tracks without any accompanying heavy particles. The primary particle has generally been interpreted as a proton, and there has been a tendency to believe that the stars are the result of a single nucleon-nucleon interaction and that they demonstrate the possibility of the multiple production of mesons.

However, there are a number of features of these stars which argue against this interpretation. In the first place, the stars are produced by primaries of a very wide range of energy (~10 Bev to several thousand Bev) and there is no significant correlation of multiplicity with primary energy. Secondly, almost equal numbers are found with odd and even numbers (n_s) of shower particles. While it is possible to interpret those of even n_s as proton-proton interactions, the law of conservation of charge forbids such an explanation of those of odd n_s. Moreover there are serious difficulties in the way of believing that these latter are the result of the interactions of a primary proton with a peripheral neutron of a nucleus in the photographic emulsion. For, if a single neutron is removed from any of the main stable isotopes of C, N, O, Ag, and Br, the remaining nucleus is radioactive to β decay with a half-life of a few minutes and a β energy of ~1 Mev.[8] Such an electron should easily be observed in the emulsion but none of the events published have recorded its presence.

Thus we may conclude that events of odd n_s are not p-n encounters and we may then either suppose that events of odd and even n_s are due to completely different causes or that neither type of event represents in general, a nucleon-nucleon encounter. The latter hypothesis is obviously the more satisfactory particularly as it seems reasonable to suppose that a struck nucleus may return to equilibrium without the emission of any charged particles. Indeed for excitation energies of less than ~100 Mev this is the normal process.[9] Such an hypothesis at once explains the roughly equal numbers of stars of odd and even n_s and suggests the possibility that the shower particles are due to normal cascading through the nucleus.

[1] C. F. Powell, Repts. Progr. Phys. **13**, 401 (1950).
[2] Hoang Chang Fong, J. phys. et radium (to be published).
[3] E. Pickup and L. Voyvodic, Phys. Rev. **82**, 265 (1951).
[4] E. Pickup and L. Voyvodic, Phys. Rev. **84**, 1190 (1951).
[5] Daniel, Davies, Mulvey, and Perkins, Phil. Mag. **43**, 753 (1952).
[6] Kaplon, Ritson, and Walker, Phys. Rev. **90**, 716 (1953).
[7] K. Gottstein and M. Teucher, Z. Naturforsch. **8a**, 120 (1953).
[8] J. Mattauch and S. Fluegge, *Nuclear Physics Tables* (Interscience Publishers, Inc., New York, 1946).
[9] K. J. Le Couteur, Proc. Phys. Soc. (London) **A63**, 498 (1951).

New Evidence Concerning Extreme Energy Interactions in Heavy Nuclei

C. B. A. McCUSKER AND F. C. ROESLER
Dublin Institute for Advanced Studies, Dublin, Ireland
(Received June 5, 1953)

EXTENDING work with copper targets,[1] Kaplon, Ritson, and Walker (KRW) have now investigated[2] stars produced in lead and in emulsion by $10^{12} \cdots 10^{13}$ ev primaries. We wish to discuss their results in relation to our theory (RM) of the extreme energy cascade.[3] The new evidence may be used to decide which of the two multiplicity functions [RM Eqs. (49) and (54)] and [RM Eq. (55)] or other such functions is the right one.

For primary energies $E' \gtrsim 16A$ (in Bev, A denoting the atomic weight of the target[3]) the jet will develop within an almost cylindrical tunnel. For a given target, the length of the tunnel s depends upon the impact parameter. Measured in nucleon diameters, the median $\bar{s} \approx A^{\frac{1}{3}}$. If the semi-empirical multiplicity function (RM-49 and 54) is approximately correct, one should find experimentally $\bar{n} \propto s^{4/5} \propto A^{4/15}$. If, on the other hand, (RM-55) is the more correct multiplicity function, one should find $\bar{n}_s \approx A^{\frac{1}{3}} + \exp[2A^{\frac{1}{3}}/3]$.

Table I shows the mean multiplicities inferred from observation and the predicted multiplicities including extrapolations for carbon and hydrogen. We have estimated the median tunnel length to be expected in Ilford G-5 emulsion and find it to correspond to that of a nucleus with $A \approx 49$.

The trend of (RM-49 and 54) fits the experimental results very well. By contrast, (RM-55) seems to be ruled out by the observations for lead.

The observed trend of multiplicities and (RM-49 and 54) both demand a (slow) *decrease* of dn_s/ds with s. It seems that no theory based on "plural" production alone can give this, that is make d^2n_s/ds^2 negative for all (even for small) s. (A purely plural theory could make d^2n_s/ds^2 negative for large s, if reabsorption of mesons is taken into account.) An argument which might be

TABLE I. Observed and calculated average numbers of shower particles from different elements at 5000 Bev.

Target		H	C	G-5 emulsion	Cu	Pb
	A	1	12		63	208
Mean multiplicity $E'=5\times10^{13}$ ev.	KRW for	...		14	18	24
Predicted median multiplicities	On (RM-49 and 54)*	5.9	11.5	16.7	18	23.8
	On (RM-55)	3	7	15	18	58

* Normalized to $n_s=18$ for Cu. This normalization does not, within the previous limits of error, represent a change of the empirical constants in (RM-49 and 54).

put forward in defense of a purely "plural" theory of the jets is that, with the method of searching for events in the stacked plates, showers of small multiplicity may be missed. Such a bias might be large in the case of hydrogen but one can hardly expect it to produce large effect in the cases of Cu and Pb. Actually the trend of maximum multiplicities at a given (high) energy with A suffices to decide between the different multiplicity functions.

The trend of (RM-49 and 54) points to $\bar{n}_s=6$ for collisions with hydrogen, i.e., to true multiple production. This multiplicity is in rough agreement with Fermi's statistical theory.[4] The empirical $E'^{\frac{1}{4}}$ law in (RM-49 and 54) is also in agreement with this theory. It has become more and more clear recently[5-8] that (contrary to what was widely believed for about one decade) at low and moderate cosmic-ray energies (i.e., in the $10^9\cdots10^{11}$ ev regions) true multiple production of mesons does not or does but rarely occur. However, the trend of multiplicities observed by Kaplon and Ritson and by Kaplon, Ritson, and Walker does seem to show true multiple production occurring at extreme primary energies (above 10^{12} ev). Arguing on a purely empirical basis, one may say that in this energy domain the total multiplicity increases only slowly with growing A; therefore, very probably, it will decrease only slightly with decreasing A. The results of Kaplon and Ritson and of Kaplon, Ritson, and Walker may well come to be regarded as the first convincing evidence for genuine multiple processes. It is very much to be hoped that these experiments will be continued and extended to other targets.

We are indebted to Dr. Kaplon, Dr. Ritson, and Dr. Walker for sending us their results in advance of publication.

[1] M. F. Kaplon and D. M. Ritson, Phys. Rev. **88**, 386 (1952).
[2] Kaplon, Ritson, and Walker, Phys. Rev. **90**, 716 (1953).
[3] F. C. Roesler and C. B. A. McCusker, Nuovo cimento **10**, 127 (1953).
[4] E. Fermi, Prog. Theoret. Phys. **5**, 570 (1950).
[5] Salant, Hornbostel, Fisk, and Smith, Phys. Rev. **79**, 184 (1950).
[6] Walker, Duller, and Sorrels, Phys. Rev. **86**, 865 (1952).
[7] A. B. Weaver, Phys. Rev. **90**, 86 (1953).
[8] McCusker, Porter, and Wilson, Phys. Rev. **91**, 384 (1953).

Construction of Conservation Equations for for Nonlocal Field Theories*

CHRISTOPHER GREGORY
University of Hawaii, Honolulu, Hawaii
(Received April 22, 1953)

IN certain cases it is not too difficult to construct nonlocal stress-energy-momentum tensors by inspection or by comparison with well-known local field expressions for the stress-energy-momentum tensor. For these cases, the operator field equations involve commutators of the fields with the displacement operators p_μ. The question arises as to the construction of the stress-energy-momentum tensor when the operator field equations involve the operator fields and the displacement operator in an arbitrary way. Some time ago[1] an operator identity was found which had as a result shown the existence of a nonlocal vector function N^μ which satisfied a conservation equation $[P_\mu,N^\mu]_-=0$. It is the purpose of this note to point out that this identity could be of use in constructing stress-energy-momentum tensors.

Let us consider an operator function L of a set of operators f_A. Then the first variation of L is of the form

$$\delta L=F_B{}^A\delta f_A G^B, \tag{1}$$

where A and B denote collection of indices, and the F's and G's are operators. Now if we consider the trace of ΓL, where Γ is any operator, we have

$$\delta\mathrm{Tr}\Gamma L=\mathrm{Tr}(L\delta\Gamma+G^B\Gamma F_B{}^A\delta f_A), \tag{2}$$

upon using (1) and the properties of tracing operation. If the variations in (2) arise from an infinitesimal similarity transformation, then as in reference 1, we must conclude

$$[\Gamma,L]_-+[f_A,G^B\Gamma F_B{}^A]_-\equiv0. \tag{3}$$

If Γ is a c number, we obtain the result of reference 1,

$$[f_A,G^BF_B{}^A]_-\equiv0. \tag{4}$$

If we identify f_μ, $\mu=0$, 1, 2, 3 to be the displacement operators and the rest of the A's to be collection of indices specifying the fields, say A', then (4) may be expressed as

$$[p_\mu,G^BF_B{}^\mu]_-\equiv-[f_{A'},G^BF_B{}^{A'}]_-. \tag{5}$$

Consequently, we discover that there exists a vector operator $N^\mu=G^BF_B{}^\mu$ which satisfies a conservation equation if $f_{A'}$ commutes with $G^BF_B{}^{A'}$. One way this may be assured is by taking $G^BF_B{}^{A'}=0$ (field equations).

Similarly, if we set $\Gamma=p^\nu$ in (3), we obtain

$$[p_\mu,\eta^{\mu\nu}L+G^Bp^\nu F_B{}^\nu]_-=-[f_{A'},G^Bp^\nu F_B{}^{A'}]_-, \tag{6}$$

where $\eta^{\mu\nu}$ is the flat space metric tensor. Consequently, we conclude that if the right-hand side of (6) is zero, then

$$[p_\mu,T^{\mu\nu}]_-=0, \tag{7}$$

where

$$T^{\mu\nu}\equiv\eta^{\mu\nu}L+G^Bp^\mu F_B{}^\nu. \tag{8}$$

Application of this method to the simple case $4L_\pm=[p^\mu,U]_\pm\times[p_\mu,U]_\pm$, involving a scalar field U, with $[A,B]_\pm\equiv AB\pm BA$, shows that the right-hand side of (5) and (6) vanish if the field equations are satisfied. Aside from a constant, $T_\pm{}^{\mu\nu}$ turns out to be

$$4T_\pm{}^{\mu\nu}=\eta^{\mu\nu}[p^\alpha,U]_\pm[p_\alpha,U]_\pm-[p^\mu,U]_\pm[p^\nu,U]_\pm-[p^\nu,U]_\pm[p^\mu,U]_\pm,$$

where U satisfies the field equations $[p^\mu,[p_\mu,U]_\pm]_\pm=0$.

* Supported by the U. S. Office of Naval Research.
[1] C. Gregory, Phys. Rev. **78**, 479 (1950).

Auger Electron Intensities*

R. D. HILL
Physics Department, University of Illinois, Urbana, Illinois
(Received June 15, 1953)

THE difficulty of making accurate calculations of the Auger effect lies in obtaining accurate electron wave functions. This problem is similar to the closely allied problem of electron internal conversion where improved calculations with accurate relativistic wave functions have been performed[1] only recently.

Since the evaluation of a conversion coefficient of a nuclear γ transition does not depend on the particular model of the nucleus but only on the nature of the atomic electrons which interact with the radiation field arising from the nuclear transition, it might not seem unreasonable that the same conversion coefficients would also approximately apply for atomic x transitions. It might further be expected that this approximation would be better for K series x-ray conversions in the L shell and also for high atomic-number atoms, for which the K orbits are closer to nuclear dimensions.

An estimate of the relative Auger electron intensities has been carried out with the heuristic viewpoint that Auger transition intensities are proportional to the products of the separate L to K x-transition probabilities and the L subshell conversion coeffi-

TABLE I. Auger line intensities arising from internal conversion of $E1$ radiation.

Auger line	K–L_1L_1	K–L_1L_{II}	K–L_1L_{III}	K–$L_{II}L_{II}$	K–$L_{II}L_{III}$	K–$L_{III}L_{III}$
Calculated intensity	zero	0.87	1.65	0.235	1.46	0.805
Experimental intensity	1.0	1.71	1.20	0.32	1.44	0.805

cients. The $K\alpha_1$ and $K\alpha_2$ x-rays arise from $E1$ transitions between the L_{III} and K levels and the L_{II} and K levels, respectively. Conversion coefficients for these radiations in the L subshells can be obtained from the theoretical computations of Gellman, Griffith, and Stanley.[1] Although these calculations are admittedly approximate, they have been observed[2,3] to describe L-conversion experiments reasonably well.

In Table I, the relative intensities of the L Auger lines for mercury ($Z=80$) have been computed. In these computations it was assumed that the $K\alpha_1$ intensity was twice the $K\alpha_2$ intensity and that the conversion coefficient in a particular subshell was reduced proportionately to the fraction of electrons in the subshell at the instant of conversion. The relative experimental intensities in gold ($Z=79$) due to Mihelich[4] are also given in Table I.

The calculated intensities, except for those lines including an L_I subshell contribution, are in excellent agreement with experiment. The L_I discrepancy can now be somewhat removed by

TABLE II. Auger line intensities arising from internal conversion of $M1$ and $E1$ radiation.

Auger line	K–L_1L_1	K–L_1L_{II}	K–L_1L_{III}	K–$L_{II}L_{II}$	K–$L_{II}L_{III}$	K–$L_{III}L_{III}$
Calculated intensity	1.0	1.02	1.65	0.235	1.46	0.805
Intensity (theory[a])	1.0	5.5	5.3			
Intensity (theory[b])	1.0	1.14	2.28			
Intensity (expt.[c])	1.0	1.71	1.20	0.32	1.44	0.805

[a] See reference 5.
[b] See reference 6.
[c] See reference 4.

allowing the existence of a small amount of magnetic dipole radiation in the K series x-rays. An $M1$ transition may occur in the "forbidden" electron jump between the L_I and K levels, and on account of the high preferential conversion of $M1$ radiation in the L_I subshell, the K–L_1L_1 Auger line can be brought up to the observed strength by assuming only about 1 percent of $M1$ radiation.

In Table II, the relative Auger line intensities for mercury are given for an $M1$ intensity of 1.47 percent of the total $E1$ x-ray intensity. Other intensities listed in the table are the relativistic theory calculations of Massey and Burhop,[5] the nonrelativistic theory calculations of Burhop,[6] and the experimental values of of Mihelich,[4] all for $Z=79$. With the exception of the K–L_1L_{II} and K–L_1L_{III} lines, for which the calculated intensities are reversed, the agreement with experiment of the calculated values is surprisingly good and superior to that of existing theoretical intensities.

It is uncertain whether the remaining lack of agreement is due to the approximate nature of the conversion coefficients, or to the inaccuracy of the assumptions (for example, the size of the radiation source), or to the experimental uncertainties.

Finally it should be pointed out that Hulubei[7] in 1947 observed satellite x-ray lines on the long wavelength side of the $K\alpha_2$ lines. Although he considered at that time the possibility of L_I to K electron jumps, he believed these lines arose from some process in which the $K\alpha_{1,2}$ x-rays lost energy to electrons in external shells. These and other satellite lines have more recently been observed by Groven and Morlet,[8] who now interpret them as arising from L_I to K jumps modified slightly by different electron screening effects. According to Hulubei, exposures of approximately 100 times those required for the $K\alpha_{1,2}$ lines were needed to bring out the satellite lines. There seems little doubt that the satellite lines are to be identified with the magnetic dipole transitions which give rise to the strong K–L_1L_I Auger line.

* Assisted by the joint program of the U. S. Office of Naval Research and the U. S. Atomic Energy Commission.
[1] Gellman, Griffith, and Stanley, Phys. Rev. **85**, 944 (1952).
[2] J. W. Mihelich, Phys. Rev. **87**, 646 (1952).
[3] J. B. Swan and R. D. Hill, Phys. Rev. **91**, 424 (1953); Australian J. Phys. (to be published).
[4] J. W. Mihelich, Phys. Rev. **88**, 415 (1952). Other experimental results are summarized by E. H. S. Burhop, *The Auger Effect* (Cambridge University Press, Cambridge, 1952).
[5] H. S. W. Massey and E. H. S. Burhop, Proc. Roy. Soc. (London) **A153**, 661 (1936).
[6] E. H. S. Burhop, Proc. Roy. Soc. (London) **A148**, 272 (1935).
[7] H. Hulubei, Compt. rend. **224**, 770 (1947).
[8] L. Groven and J. Morlet, Acad. roy. Belge, Classe sci., Mem. **37**, 630 (1951).

Connection between Fusion Theory of Bosons and Nonlocal Field Theory

SATOSI WATANABE
United States Naval Postgraduate School, Monterey, California
(Received June 11, 1953)

FOLLOWING the original idea of de Broglie,[1] the quanta of a pseudoscalar field and a vector field are considered as composite particles resulting from the "fusion" of a spinor particle and its antiparticle. As Heisenberg emphasized,[2] we have to assume an attractive force of yet unknown nature between the constituent particles in order that such a fusion theory may become physically meaningful. If the pair of component fermions are thus performing relative motion, it is to be expected that the resulting boson field can be described as a kind of nonlocal field in the sense of Yukawa's theory.[3] The aim of the present work is to demonstrate by an example the mathematical feasibility of such correlation of the fusion theory with the nonlocal field theory.

The two-particle wave function $\Psi_{rs}(x', x'')$ (r, s: Dirac indices) is assumed to transform like $\psi_r(x')\bar{\Psi}_s(x'')$ for the Lorentz transformation and to obey a relativistic two-body wave equation,[4]

$$(D(x')+mE_5)\Psi(x', x'')(D(x'')-mE_5) = g^2W(x', x'')O'^{\alpha}\Psi(x', x'')O''^{\alpha}, \quad (1)$$

with

$$D(x')=-i(\partial/\partial x'_\mu)E_\mu, \quad O''=J\bar{O}'J^{-1}, \quad (2)$$

where the ordinary rule of matrix multiplication is assumed for the 4-4-Dirac indices. $W(x', x'')$ is an invariant "potential," which may be a function or an operator.[5] The O's are some matrices with Dirac indices ($\hbar=c=1$).

In addition to (1), $\Psi(x', x'')$ is assumed to satisfy

$$(D(x')+D(x'')+\kappa E_5)\Psi(x', x'')=0, \quad (3)$$

which amounts physically to a condition for formation of a pseudoscalar or vector particle.[6] The compatibility of (1) and (3) is indirectly verified by the existence of a common solution. The mass κ of the composite particle must be $2m$ plus a certain term due to the interaction.

We now expand Ψ with the help of the 16 units of the E system,

$$\Psi=(iU+U^\mu E_\mu E_5)+(VE_5+V^\mu E_\mu+\tfrac{1}{2}iV^{\mu\nu}E_\mu E_\nu E_5). \quad (4)$$

By virtue of the transformation property of Ψ, the quantities in the first pair of parentheses transform like pseudoscalar field quantities and those in the second pair like vector field quantities. Equations (1) and (3) can now be rewritten as a set of nonlocal equations for the U's and V's with respect to the variables

$$X^\mu=(x^{\mu'}+x^{\mu''})/2, \quad r^\mu=x^{\mu'}-x^{\mu''}. \quad (5)$$

As an illustration, a particular type of "oscillator potential" is considered,

$$O'=-O''E_5,$$
$$g^2=4/\lambda^4, \tag{6}$$
$$W=-[(r_\mu r_\nu\partial^2/\partial X_\mu\partial X_\nu)/(\partial^2/\partial X_\lambda\partial X^\lambda)].$$

The resulting equations for the pseudoscalar field are[7]

$$\{(\partial^2/\partial X_\mu\partial X^\mu)-\kappa^2\}U=0, \tag{7}$$
$$\{(\partial^2/\partial r_\mu\partial r^\mu)-(\kappa-2m)^2/4-4(r_\mu r_\nu\partial^2/\partial X_\mu\partial X_\nu)/(\kappa^2\lambda^4)\}U=0, \tag{8}$$
$$\{(\partial^2/\partial X_\mu\partial r_\nu)-(\partial^2/\partial X_\nu\partial r_\mu)\}U=0, \tag{9}$$
$$U^\mu=(1/\kappa)(\partial U/\partial X_\mu). \tag{10}$$

Equations (7), (8), and (9) can certainly be satisfied by a U which is a plane wave with respect to X^μ and an oscillator function with argument $K_\mu r^\mu$, where K^μ is the momentum four-vector of the composite particle. The possible values of the mass κ of the composite particle are determined by Eq. (8). For instance, the simplest solution

$$U(X,r)=\int(\alpha K)^4U(K)\exp(iK_\mu X^\mu)\delta(K_\mu K^\mu+\kappa^2)\times\exp[-(K_\mu r^\mu)^2/(\kappa^2\lambda^2)]. \tag{11}$$

gives

$$\kappa=2m\pm2\sqrt{2}/\lambda. \tag{12}$$

The vector field is completely separated from the pseudoscalar field and can be dealt with in a similar fashion.

More importance should be attached to the method presented here than to the particular type of nonlocal field derived by it.

[1] L. de Broglie, Compt. rend. **198**, 135 (1934) and subsequent papers and monographs.
[2] W. Heisenberg, Z. Naturforsch. **5a**, 251 (1950); **5a**, 367 (1950); **6a**, 281 (1951); his article in the monograph: *Louis de Broglie* (Paris, 1952), p. 284. See also L. de Broglie, J. phys. et radium **12**, 509 (1951); M. A. Tonnelat, J. phys. et radium **12**, 516 (1951).
[3] H. Yukawa, Phys. Rev. **77**, 219 (1950); **80**, 1047 (1950).
[4] $\bar{\psi}=-\psi^\dagger\gamma_4$, $E_a=i\gamma_5\gamma_a$ $(a=1, 2, 3)$, $E_0=-J=\gamma_4\gamma_5$, $E_5=\gamma_5$. $\bar{O}$ means the Hermitian conjugate of O. For the notations see S. Watanabe, Phys. Rev. **84**, 1008 (1951).
[5] If the "force" is produced through the intermediary of another field, W will become in the lowest approximation Δp and Eq. (1) will reduce to Nambu's equation, the charge conjugate representation being used for one of the particles. Y. Nambu, Prog. Theoret. Phys. **5**, 614 (1950), Eq. (82). However, we should rather expect, with Heisenberg (Ref. 2) that W is not of such a type.
[6] Regarded as an equation with respect to X^μ, condition (3) becomes identical with the wave equation used by the author in his 4×4-matrix formalism of meson theory. S. Watanabe, Sci. Papers Inst. Phys.Chem. Research (Tokyo) **39**, 157 (1941), Eq. (5.2) through Eq. (5.5).
[7] Reasoning from a different point of view, H. Yukawa also has come to consider a type of equation similar to (8) [private communication from Professor Yukawa, and also Phys. Rev. **91**, 415, 416 (1953)].

Scintillations Produced by Alpha Particles in CsI

BEAT HAHN
Department of Physics, University of Neuchâtel, Neuchâtel, Switzerland
(Received June 8, 1953)

CRYSTALS of CsI (without activator) at 77°K show an abnormally high absolute efficiency of luminescence under α-particle bombardment, of about 35 percent, and the individual light pulses have a short decay time of 0.5 μsec.[1] Such crystals are colorless, emit light in the blue region of the spectrum, and are nonhygroscopic. Moreover they have a high density (4.5 g/cm^3) and constituents of high atomic number ($Z=55$ and 53), resulting in a relatively large absorption coefficient (per cm) for γ and x-rays. CsI crystals used in combination with an RCA photomultiplier 5819 and a pulse-height selector are therefore suitable for energy measurements of charged particles and γ rays. It should be mentioned that CsI is a quasi-monoatomic substance. Some results with α particles will be presented here.

The surface of a CsI crystal (5×5×2 mm) is irradiated with collimated α particles. The α source, mounted on a Pt foil, is located at a distance of 1 mm from the crystal surface. There is a space between the crystal and multiplier cathode and no "light contact" is provided. An Al mirror serves as a light reflector. The complete assembly is mounted on the upper end of a copper rod, which is immersed in liquid nitrogen.

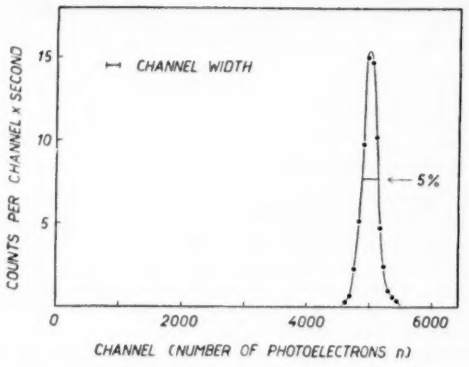

FIG. 1. Pulse spectrum for Po alpha line.

The pulse spectrum, which corresponds to the Po α line, is shown in Fig. 1. The pulse height is expressed in terms of the number n of photoelectrons liberated at the multiplier cathode during one scintillation (about 1000 photoelectrons per Mev). The channel width of the single-channel pulse-height selector used

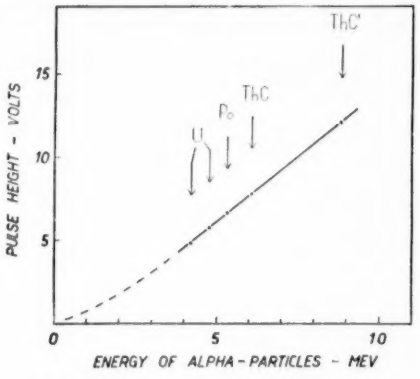

FIG. 2. Energy response of CsI for alpha particles.

in this experiment is indicated in the figure. The resulting full width at half-maximum of the distribution is 5 percent, being only about 20 percent larger than the minimum width expected from the formula:

$$x_h=2.34\left\{\frac{1}{n}(1+\delta_g^2)\right\}^{\frac{1}{2}},$$

where δ_g means the relative standard deviation of the tube multiplication.

With the aim of investigating the energy response of CsI crystals to α particles, a thin source composed of U, Po, and ThB mounted on the same Pt foil, was used. Consequently the α lines

TABLE I. Ratio of the pulse heights for the α particles from ThC and ThC'.

Crystal	$h_{ThC}/h_{ThC'}$	References
Anthracene	0.53	a, b
Stilbene	0.52	a
Naphtalene	0.53	a
NaI(Tl)	0.57	b
KI(Tl)	0.60	a
CsI	0.64	
Energy ratio	0.69	

[a] Harding, Flowers, and Eppstein, Nature **163**, 990 (1949).
[b] Taylor, Remley, Jentschke, and Kruger, Phys. Rev. **83**, 169 (1951).

of U^{238}, U^{234}, Po^{210}, ThC, and ThC′ with 4.18, 4.76, 5.30, 6.05, and 8.78 Mev would be expected. The resulting pulse-height distribution shows the five maxima well separated. The energy response is shown in Fig. 2. The measured values lie on a straight line, which intersects the x axis at about 1 Mev. The errors correspond to the radii of the circles. The ratio of the pulse heights for the α particles from ThC and ThC′ is given in Table I for several crystals. Of the crystals listed, the response of CsI is most nearly proportional to energy.

The author wishes to express his most sincere gratitude to Professor J. Rossel and to Dr. J. Bonanomi for their valuable advice.

[1] B. Hahn and J. Rossel, Helv. Phys. Acta **26**, 271 (1953); J. Bonanomi and J. Rossel, Helv. Phys. Acta **25**, 725 (1952).

CONTENTS—Continued

Letters to the Editor:

Electronic Hall Effect in NaCl . . . . . Alfred G. Redfield 753

Some Electrical Properties of Strontium Titanate . . . . . Arthur Linz, Jr. 753

Evaporation of Copper from Germanium . . . . . George Finn 754

Diode Characteristic of a Hollow Cathode . . . . . M. L. Babcock, D. F. Holshouser, and H. Von Foerster 755

Tentative Theory of Metallic Whisker Growth . . . . . J. D. Eshelby 755

Oxygen-Induced Surface Conductivity on Germanium . . . . . Edward N. Clarke 756

Thermally Induced Acceptors in Single Crystal Germanium . . . . . R. A. Logan 757

Examples of Multiple Pion Production in π-p Collisions Observed at the Cosmotron . . . . . W. B. Fowler, R. P. Shutt, A. M. Thorndike, and W. L. Whittemore 758

Excitation of Heavy Nuclei by the Electric Field of Low-Energy Protons . . . . . Clyde L. McClelland and Clark Goodman 760

Radiative Corrections to Nuclear Forces in Pseudoscalar Theory . . . . . K. A. Brueckner 761

Bubble Chamber Tracks of Penetrating Cosmic-Ray Particles . . . . . Donald A. Glaser 762

Protons in Alpha Spectra of Even-Even Nuclei . . . . . Frank Asaro and I. Perlman 763

High Altitude Measurements of the Intensity of Cosmic Radiation at Magnetic Latitudes 3°N and 19°N . . A. S. Rao, V. K. Balasubrahmanyam, G. S. Gokhale, and A. W. Pereira 764

Measurements of Meson Masses and Related Quantities . . . . . F. M. Smith, W. Birnbaum, and Walter H. Barkas 765

Origin of Cosmic Rays . . . . . J. W. Dungey 766

Fluorescent Light Yields with Alpha, Beta, and Gamma Radiations . . . . . Milton Furst and Hartmut Kallmann 766

Metastable State of V^{50} . . . . . T. Wiedling 767

Total Cross Sections of 400-Mev Protons for Hydrogen and Light Elements . . . . . J. Marshall, L. Marshall, and A. V. Nedzel 767

Gamma Radiation from Inelastic Scattering of 2.7-Mev Neutrons . . . . . V. E. Scherrer, W. L. Smith, B. A. Allison, and W. R. Faust 768

Interpretation of $O^+ \times \beta$ Type Stars in Photographic Emulsions . . . . . C. B. A. McCusker and F. C. Roesler 769

New Evidence Concerning Extensive Energy Interactions in Heavy Nuclei . . . . . C. B. A. McCusker and F. C. Roesler 769

Construction of Conservation Equations for Nonlocal Field Theories . . . Christopher Gregory 770

Auger Electron Intensities . . . . . R. D. Hill 770

Connection between Fusion Theory of Baryons and Nonlocal Field Theory . . Satosi Watanabe 771

Scintillations Produced by Alpha Particles in CsI . . . . . Beat Hahn 772

CONTENTS

THE PHYSICAL REVIEW SECOND SERIES, VOLUME 91, NO. 3 AUGUST 1, 1953

Straggling Distributions for Electrons in Passing through Thin Foils . . . F. Kulf and R. D. Birkhoff 505
Current Density Tables for Field Emission Theory . . . W. W. Dolan 510
Surface Tension of Liquid Silicon and Germanium . . . Paul H. Kaik and Wendell Van Horn 512
Double Hysteresis Loop of $BaTiO_3$ at the Curie Point . . . Walter J. Merz 513
n-Type Surface Conductivity on p-Type Germanium . . . W. L. Brown 518
Generalized Self-Consistent Field Method . . . J. C. Slater 528
Band Structures of One-Dimensional Crystals with Square-Well Potentials . . . G. Allen 531
Photoemission from Silver into AgCl, KBr, NaCl, and New Bands of Photosensitivity in AgCl . M. A. Gilleo 534
Electron Ejection from Ta by He^+, He^{++}, and He_2 . . . Homer D. Hagstrum 543
Reversible Bleaching of a Band in the Absorption Spectrum of Diamond . . . Peter Pringsheim 551
Diffusion Currents in the Semiconductor Hall Effect . . . Rolf Landauer and John Swanson 555
Photoemission of Tungsten in the Region of Predicted Schottky Deviations . . . E. E. Ender, J. J. Ruddick, and A. H. Weber 561
Storage of Energy in Silver Activated Potassium Chloride . . . C. E. Mandeville and H. O. Albrecht 566
Photocurrent, Space-Charge Building, and Field Emission in Alkali Halide Crystals . . . A. von Hippel, E. P. Gross, J. G. Jelatis, and M. Geller 568
Current Carrier Mobility Ratio in Semiconductors . . . L. P. Hunter 579
Secondary Electron Emission of Crystalline MgO . . . J. B. Johnson and K. G. McKay 582
Theory of Alpha-Decay. I . . . Joseph J. Devaney 587
Long-Lived Delayed Neutrons from Fission . . . J. W. Kunstadter, J. J. Floyd, and L. B. Borst 594
New Neutron Scattering Cross Sections for Rare Earth Nuclides . . . W. C. Koehler and E. O. Wollan 597
Gamma Radiation from B^{11} Bombarded by Protons . . . Torben Huus and Robert B. Day 599
Excitation Curves for α Particles from B^{11} Bombarded with Protons . . . Olof Backman, Torben Huus, and Czeneky Zupancic 606
Analysis of Angular Correlation and Angular Distribution Data . . . M. E. Rose 610
Gamma-Gamma Angular Correlation in Hf^{177} . . . E. D. Klema and F. K. McGowan 616
Hyperfine Structure and Nuclear Moments of Pr^{141} . . . Hin Lew 619
Nuclear Magnetic Resonance in Solid Hydrogen . . . F. Reif and E. M. Purcell 631
New Nuclides Produced in Chlorine Spallation . . . Manfred Lindner 642
Theory of (d,p) and (d,n) Reactions . . . E. Gerjuoy 643
Correction for Finite Angular Resolution in Directional Correlation Measurements . . . J. S. Lawson, Jr., and H. Frauenfelder 649
Radioactivity of Cu^{67} . . . Harry T. Easterday 653
Fission Cross Section of Uranium-234 . . . R. W. Lamphere 655
Photoneutron Cross Sections . . . R. Montalbetti, L. Katz, and J. Goldemberg 659
Neutrons from the Proton Bombardment of Be^9 . . . Fay Ajzenberg and W. W. Buechner 674
Energy Levels in Be^9 from the Reaction $Li^6(He^3,p)Be^9$ . . . W. E. Kunz, C. D. Moak, and W. M. Good 676
Production of Positive Pions by 341-Mev Protons on Protons . . . W. F. Cartwright, C. Richman, M. N. Whitehead, and H. A. Wilcox 687
Effects of Geohava and Lower Latitudes of Changes in Energy and Composition of Solar Cosmic Rays . . . V. Sarabhai and R. P. Kane 688
Anisotropic Distribution of Secondaries in Extensive Energy Cosmic-Ray Stars . . . Frank C. Rossler and C. B. A. McCusker 690
Production of Charged Photomesons from Helium. Hydrogen-Helium Ratios. II . . . M. J. Jakobson, A. G. Schutz, and R. S. White 695
Photoneutron Production Excitation Functions to 320 Mev . Lawrence W. Jones and Kent M. Terwilliger 699
Collision Lengths of Neutral, Penetrating-Shower-Producing Cosmic Radiation in Light and Heavy Water . . . Darol Froman, James Kenney, and Victor H. Regener 707
Theory of Quantized Fields. II . . . Julian Schwinger 715
Theory of Quantized Fields. III . . . Julian Schwinger 728
Convergence of the Adiabatic Nuclear Potential . . . Abraham Klein 740
Note on the Low-Energy Properties of the Nucleon-Nucleon Interaction . . . Robert Jastrow 749
Similarity Theory of Relativity and the Dirac-Schrödinger Theory of Electrons . . . Banesh Hoffmann 751

(continued on cover three)

LANCASTER PRESS, INC., LANCASTER, PA.